Conference Proceedings of the Society for Experimental Mechanics Series

Gaetan Kerschen · Douglas Adams · Alex Carrella *Editors*

Topics in Nonlinear Dynamics, Volume 1

Proceedings of the 31st IMAC, A Conference on Structural Dynamics, 2013

SEM

Springer

Conference Proceedings of the Society for Experimental Mechanics Series

Series Editor

Tom Proulx
Society for Experimental Mechanics, Inc.,
Bethel, CT, USA

For further volumes:
http://www.springer.com/series/8922

Gaetan Kerschen • Douglas Adams • Alex Carrella
Editors

Topics in Nonlinear Dynamics, Volume 1

Proceedings of the 31st IMAC, A Conference on Structural Dynamics, 2013

Springer

Editors
Gaetan Kerschen
University of Liege
Liege, Belgium

Alex Carrella
LMS International
Brussels, Belgium

Douglas Adams
School of Mechanical Engineering
Purdue University
West Lafayette, USA

ISSN 2191-5644 ISSN 2191-5652 (electronic)
ISBN 978-1-4614-6569-0 ISBN 978-1-4614-6570-6 (eBook)
DOI 10.1007/978-1-4614-6570-6
Springer New York Heidelberg Dordrecht London

Library of Congress Control Number: 2013932475

Preface

Topics in Nonlinear Dynamics represents one of seven volumes of technical papers presented at the 31st IMAC, A Conference and Exposition on Structural Dynamics, 2013 organized by the Society for Experimental Mechanics, and held in Garden Grove, California February 11–14, 2013. The full proceedings also include volumes on Experimental Dynamics Substructuring; Dynamics of Bridges; Dynamics of Civil Structures; Model Validation and Uncertainty Quantification; Special Topics in Structural Dynamics; and, Modal Analysis.

Each collection presents early findings from experimental and computational investigations on an important area within Structural Dynamics. Nonlinearity is one of these areas.

The vast majority of real engineering structures behave nonlinearly. Therefore, it is necessary to include nonlinear effects in all the steps of the engineering design: in the experimental analysis tools (so that the nonlinear parameters can be correctly ***identified***) and in the mathematical and numerical models of the structure (in order to run accurate ***simulations***). In so doing, it will be possible to create a model representative of the reality which (once ***validated***) can be used for better predictions.

Several nonlinear sessions will address theoretical and numerical aspects of nonlinear dynamics (covering rigorous theoretical formulations and robust computational algorithms) as well as experimental techniques and analysis methods. There are papers dedicated to nonlinearity in practice where real-life examples of nonlinear structures will be discussed. Finally, a number of papers will discuss an interesting shift in paradigm: nonlinearities are not always detrimental, but instead they can be exploited for better engineering designs.

The organizers would like to thank the authors, presenters, session organizers, and session chairs for their participation in this track.

Liege, Belgium — Gaetan Kerschen
West Lafayette, USA — Douglas Adams
Brussels, Belgium — Alex Carrella

Contents

Chapter 1
International Space Station 2A Array Modal Analysis

Michael Laible, Kristin Fitzpatrick, and Michael Grygier

Abstract On December 9th 2009, the International Space Station (ISS) 2A solar array mast experienced prolonged longeron shadowing during a Soyuz undocking. Analytical reconstruction of induced thermal and dynamic structural loads showed an exceedance of the mast buckling limit. Possible structural damage to the solar array mast could have occurred during this event. A Low fidelity video survey of the 2A mast showed no obvious damage of the mast longerons or battens. The decision was made to conduct an on-orbit dynamic test of the 2A array on December 18th, 2009. The test included thruster pluming on the array while photogrammetry data was recorded. The test was similar to other Dedicated Thruster Firings (DTFs) that were performed to measure structural frequency and damping of a solar array. Results of the DTF indicated lower frequency mast modes than model predictions, thus leading to speculation of mast damage.

A detailed nonlinear analysis was performed on the 2A array model to assess possible solutions to modal differences. The setup of the parametric nonlinear trade study included the use of a detailed array model and the reduced mass and stiffness matrices of the entire ISS being applied to the array interface. The study revealed that the array attachment structure is nonlinear and thus was the source of error in the model prediction of mast modes. In addition, a detailed study was performed to determine mast mode sensitivity to mast longeron damage. This sensitivity study was performed to assess if the ISS program has sufficient instrumentation for mast damage detection.

Keywords Non-linear • Modal analysis • Photogrammetry • Damage detection

1.1 Introduction

The on-orbit construction of the International Space Station (ISS) began in November 1998, and was completed in July of 2011. The ISS consists of eight solar arrays for power generation. Each array is mounted on a rotating gear box for solar tracking and is deployed with a four longer on mast. Each mast is made of 32 bays consisting of longerons, fixed battens, flexible battens, and cable diagonals. Early in the ISS assembly process it was noted that thermal and dynamic conditions exist that could buckle a solar array mast longeron. This condition exists when one longeron is shadowed by another structure, thus causing asymmetric thermal loading in the mast longeron.

The ISS program developed a software tool to predict longeron shadowing events and to minimize periods of extreme loads. During the 19S Soyuz undocking December 1, 2009, the vehicle was in a long period of solar array longeron shadowing. The analysis predicted extreme loads in array 2A longeron and possible buckling. It was determined that an on-orbit test should be performed to analyze the dynamic response of the 2A array to check for damage.

This test produced a significant frequency difference in the first In Plane Array Mode compared to the analytical model and the other arrays. The ISS program requested a complete analysis of this event to determine if the 2A array was damaged

M. Laible (✉) • K. Fitzpatrick
The Boeing Company, 3700 Bay Area Blvd., Houston, TX, USA
e-mail: michael.r.laible@boeing.com; kristin.l.fitzpatrick@boeing.com

M. Grygier
NASA, Johnson Space Center, Houston, TX, USA
e-mail: Michael.S.Grygier@nasa.gov

G. Kerschen et al. (eds.), *Topics in Nonlinear Dynamics, Volume 1: Proceedings of the 31st IMAC, A Conference on Structural Dynamics, 2013*, Conference Proceedings of the Society for Experimental Mechanics Series 35,
DOI 10.1007/978-1-4614-6570-6_1,

or not. This paper documents the analysis performed and investigates possible solutions to the dynamic differences of this array. In addition to the dynamic analysis, analysis was performed to determine if a longeron did fail, can the failure be detected from existing on-orbit instrumentation.

Section 1.2 of this report presents the background of longeron shadowing and the specific 2A longeron shadowing event. Section 1.3 describes both the linear and nonlinear 2A array modal analyses performed and a comparison to the other ISS arrays. Section 1.4 outlines the analysis performed to determine if we can detect mast damage utilizing the instrumentation on-board ISS. Section 1.5 discusses the conclusions.

1.2 Problem Description

1.2.1 ISS Array Longeron Shadowing

The ISS has eight solar arrays, each consisting of a mast, two solar cell blankets, and four blanket boxes. These masts are attached to the Beta Gimbal Assembly (BGA) and can rotate independently about the long axis of the mast. Figure 1.1 illustrates the ISS configuration with the eight arrays rotated independently and the 2A Array; the focus of this paper.

Each mast is made up of four longerons as shown in Fig. 1.2. If one longeron is shadowed and the others heated, two longerons will be in compression and others will be in tension. This can cause buckling of the longerons. Typical buckling and temperature values are shown in Fig. 1.2.The buckling starts at a combined dynamic and thermal load of 1,340 lbs [1].

The ISS program performs a detailed longeron shadowing analysis and values are reported real-time. The ISS mission operation personnel will receive a warning if a longeron is shadowed and loads are at max limit values. When 1the warning is received the BGA is rotated to eliminate longeron shadowing.

1.2.2 2A Anomoly

During an ISS maneuver in December, 2009, the 2A Array experienced Longeron Shadowing for an extended period of time. Post flight analysis proved that the limit load was exceeded and that buckling could have occurred. To ensure structural integrity a detailed photo review was performed with no noticeable damage reported.

The ISS program then determined that a Dedicated Thruster Firing (DTF) test should be performed on the 2A Array to determine the modal structural properties. Instrumentation does not exist on the array mast itself; therefore, photogrammetry data was recorded and analyzed to determine the modal parameters of the array. The Image Science and Analysis Group (ISAG), at NASA JSC received analog video taken during the 2A DTF from two ISS external cameras [2]. Figure 1.3 illustrates the camera views and jet plume direction toward the 2A Array. The thruster firing lasted for 1 s and was designed to excite the modes of the 2A Array.

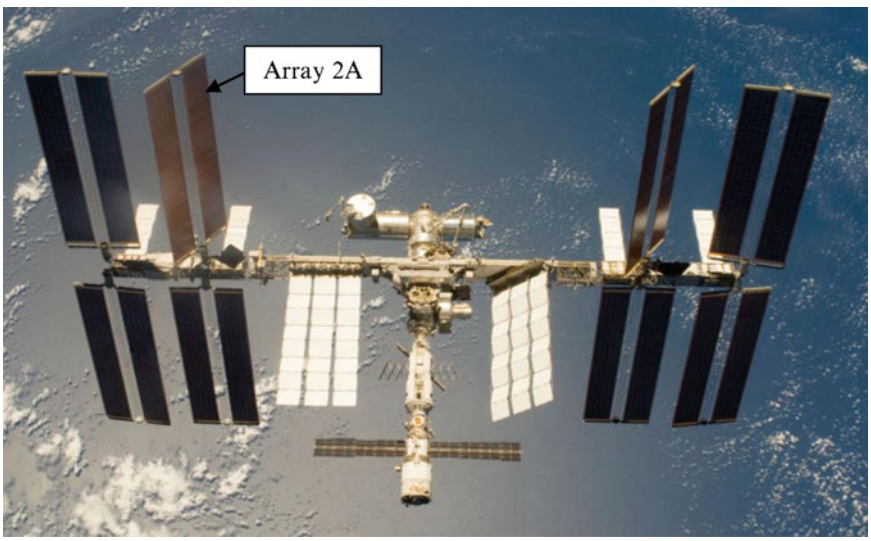

Fig. 1.1 International space station assembly complete

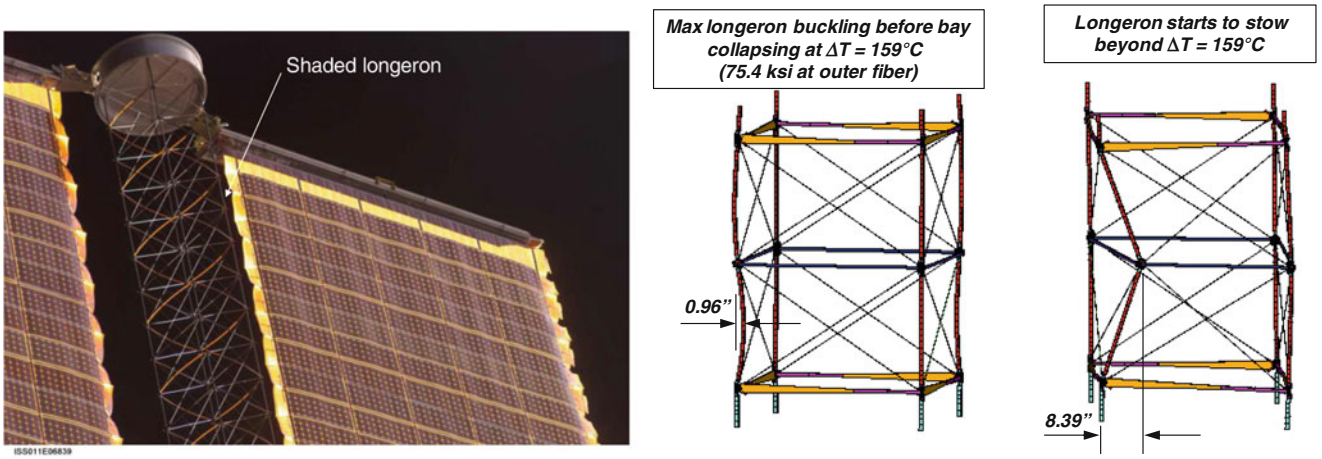

Fig. 1.2 Solar array shadowing and thermal buckling

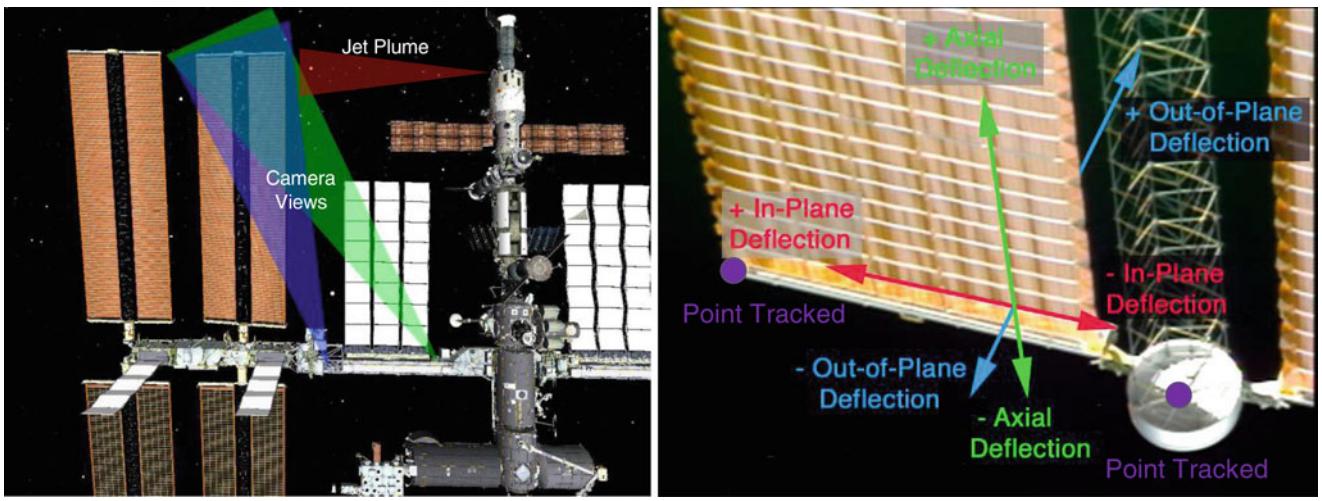

Fig. 1.3 ISS camera views, jet plume and photogrammetry coordinate frame

The ISAG used their image processing software to track two points at the end of the 2A Solar Array Wing (SAW), Fig. 1.3. One point was on the mast cap located at the end of the mast of the solar array. The second tracked point was on the tip of the blanket box at the end of the solar array. The motion of each point was tracked in the video recorded from each of the two cameras and used to compute the relative displacement of the SAW tip in each axis, defined by the plane of the array during the DTF. Due to the high mathematical correlation between the axial and out of plane motion, the calculations were conducted in a way which constrains the axial position to a fixed value of 0. This constraint is acceptable given that the motion of the array in the axial direction is significantly less than the In Plane (IP) or Out Of Plane (OOP) motions. The major modes observed from this DTF and previous DTF's are the first OOP and first IP modes. The frequency of the OOP and IP modes found for other arrays are between 0.06–0.0675 Hz and 0.09–0.099 Hz, respectively.

When the photogrammetric analysis was completed, the time history data was low-pass filtered and the FFT was also computed. The OOP frequency was within the expected range but the IP frequency was 14% lower. The displacement time history and FFT of the array mast cap is illustrated in Fig. 1.4.

The Eigensystem Realization Algorithm (ERA) [3] was utilized to extract the modal parameters from the detrended photogrammetry data sets. The Modal Assurance Criterion (MAC) was calculated between the extracted mode shapes and the analytical model mode shapes. The comparison results between the extracted modal parameters from the data and the analytical modal parameters are summarized in Table 1.1. The frequency of the first OOP test mode matched within 5% of the first 2A OOP analytical mode. The frequency difference between the first IP test mode and IP analytical mode ranged from 14 to 17%.

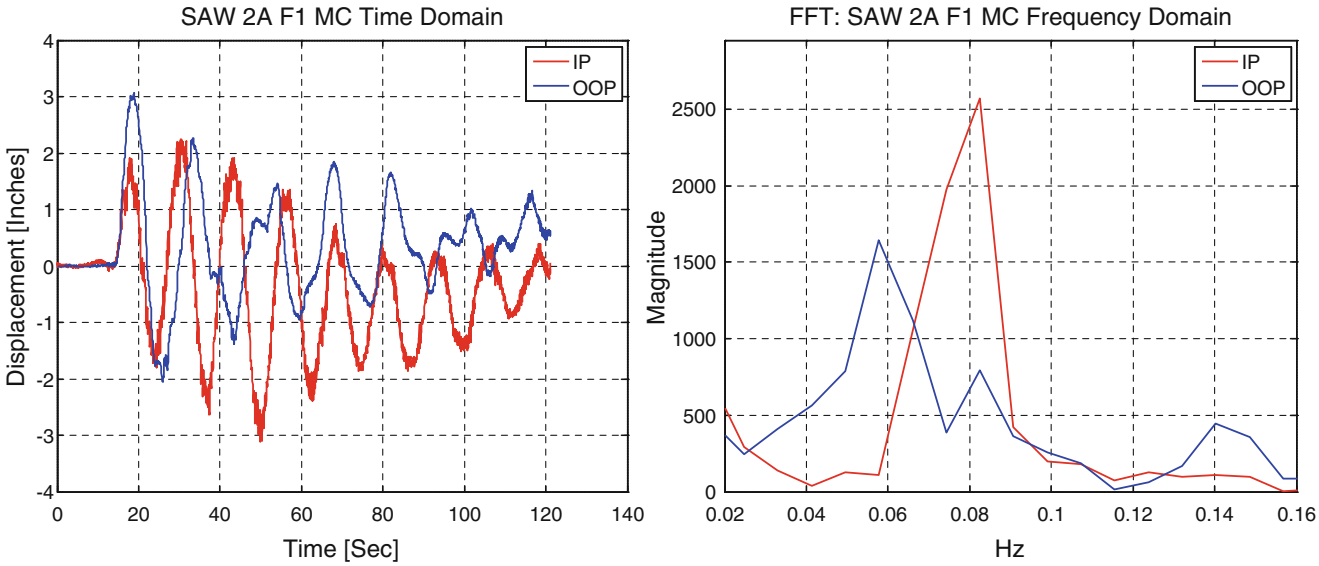

Fig. 1.4 Mast cap displacement time history and FFT

Table 1.1 2A array test modes versus analytical model modes

Test data				Analysis data				
Mode #	Freq (Hz)	Damp (%)	EMAC (%)	Mode #	Freq. (Hz)	Freq. diff (%)	MAC	Mode description
				9	0.0597	2.68	0.951	All SAWs OOP
				10	0.0613	0.0	0.948	All SAWs OOP
1	0.0613	4.6	92.42	12	0.0648	−5.40	0.942	Port SAWs OOP
				14	0.0651	−5.84	0.943	Port SAWs OOP
				16	0.0665	−7.82	0.940	Port SAWs OOP
2	0.0798	3.3	96.12	17	0.0933	−14.47	0.909	Port SAWs IP
				19	0.0964	−17.22	0.904	Port SAWs IP
				22	0.0971	−17.82	0.902	Port SAWs IP

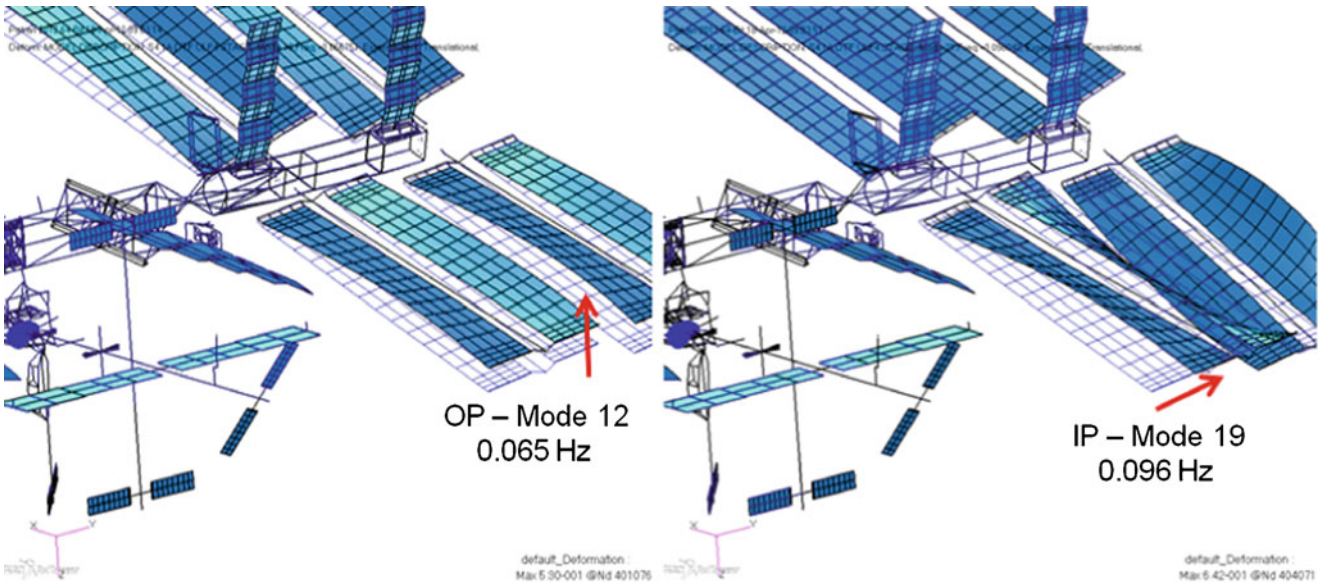

Fig. 1.5 Analytical array out of plane and in plane

Figure 1.5 illustrates the analytical mode shape of the OOP and IP modes. The figure is the MSC PATRAN model of the ISS system model, zoomed in on the 2A array. The mode number and frequency is shown for the OOP and IP 2A array modes.

1.3 2A Array Modal Analysis

The 2A Solar array had experienced a sustained longeron shadow event. The analytical reconstruction of the event showed an excedence in the limit loads when combining the dynamic and thermal loads. An on-orbit dynamics test was performed and the IP mast mode was found to be 14% lower than what was expected when compared with the analytical dynamic model. In addition, the first IP 2A Array test mode was lower than what was previously seen with any other array on-orbit test. The large frequency difference between the IP test and analytical mode was a concern to the program and resulted in the request of a more detailed analysis to determine the cause of the difference.

The following detailed analysis was conducted to determine why the first IP Array mode was lower and if damage of the array could be detected with modal analysis.

1.3.1 Linear Analysis

The ISS loads system model is made up of over 90 super elements and has 35,000 dof. Each model takes about 60 min of computer time for the SOL 103. When performing time domain solutions (SOL 109 or 129) the time increases dramatically. This is an unmanageable model when performing parametric runs and numerous failure analysis time domain runs. To simplify the problem, a stiffness matrix was developed using the NASTRAN DMIG option with the boundary conditions being constrained at the approximate CG of the ISS and the other boundary being the four grids that the Solar array BGA attaches to ISS.

In addition, the solar array model used during nominal loads analysis has a simplified mast (one Center Bar, ten pieces) and did not model the individual longerons. To perform parametric studies of failed longerons the detailed mast model would have to be integrated into the simplified system model. Figure 1.6 illustrates the baseline loads model (left) and the detailed mast model delivered from the developer (right). The highlighted CBARS are the longerons used for the failed analysis. The far right is a close up of the longeron model and cross battens. In failed longeron cases the complete connection is removed at positions depicted in Fig. 1.6 (MID and BASE).

The detailed array model was compared against the simplified baseline array model. A modal solution was performed with both models being constrained at the base coordinate frame as shown in Fig. 1.6. The frequency differences between the modes of each model were all within a $1/2\%$. Once the model comparison was complete the detailed mast model was attached into the station stiffness and sensitivity studies were performed. Figure 1.7 illustrates the station stiffness model with the detailed mast and array models.

The first run was the SOL 106, a non-linear solution, which involved pulling the blankets tight to the baseline spring tension. The blanket elements were pre-stressed in order to account for the effect of the blanket tension load. The blanket tension load was analyzed using geometric non-linear static analysis sequence (NASTRAN SOL 106) [4]. The differential stiffness matrix and coupled mass matrix are used in normal mode analysis solution sequence (NASTRAN SOL 103) and the EXTSEOUT card to build the DMIG of the array, PCH and ASM files. This is performed by restarting the SOL 106 run and using the EXTSEOUT card.

Now the ISS system model can be replicated by a NASTRAN run using the ISS DMIG, Solar array DMIG, and detailed four-bar BGA assembly. The time domain and modal solution runs could be performed with minimum computer time. Again this model is shown in Fig. 1.7 which also notes the chosen failed longerons for the analysis. These longerons were chosen from a separate analysis, which showed that these areas are the most likely to fail.

The Boeing Loads and Dynamics group performs thruster plume analysis on all station arrays. The program that performs the analysis uses plume jet mass flow and impinges on individual plates modeling the array. The output is a force on each individual grid. The program has been validated with other array displacement checks. A special routine was developed to map force values and vectors for each array blanket. These force values were mapped to every array blanket and the mast cap. The array wing displacement was plotted and compared to the on-orbit data. These comparison plots are shown in Fig. 1.8. As can be seen by the displacement time history plots, the frequency of the on-orbit data and analytical data does not compare for the IP mode. This also was seen in the frequency domain.

In addition to the time domain runs, a parametric study was performed using the modal solution. Several models were created to conduct the parametric study; the Baseline array (BL 081), Baseline array with MID longeron partially failed

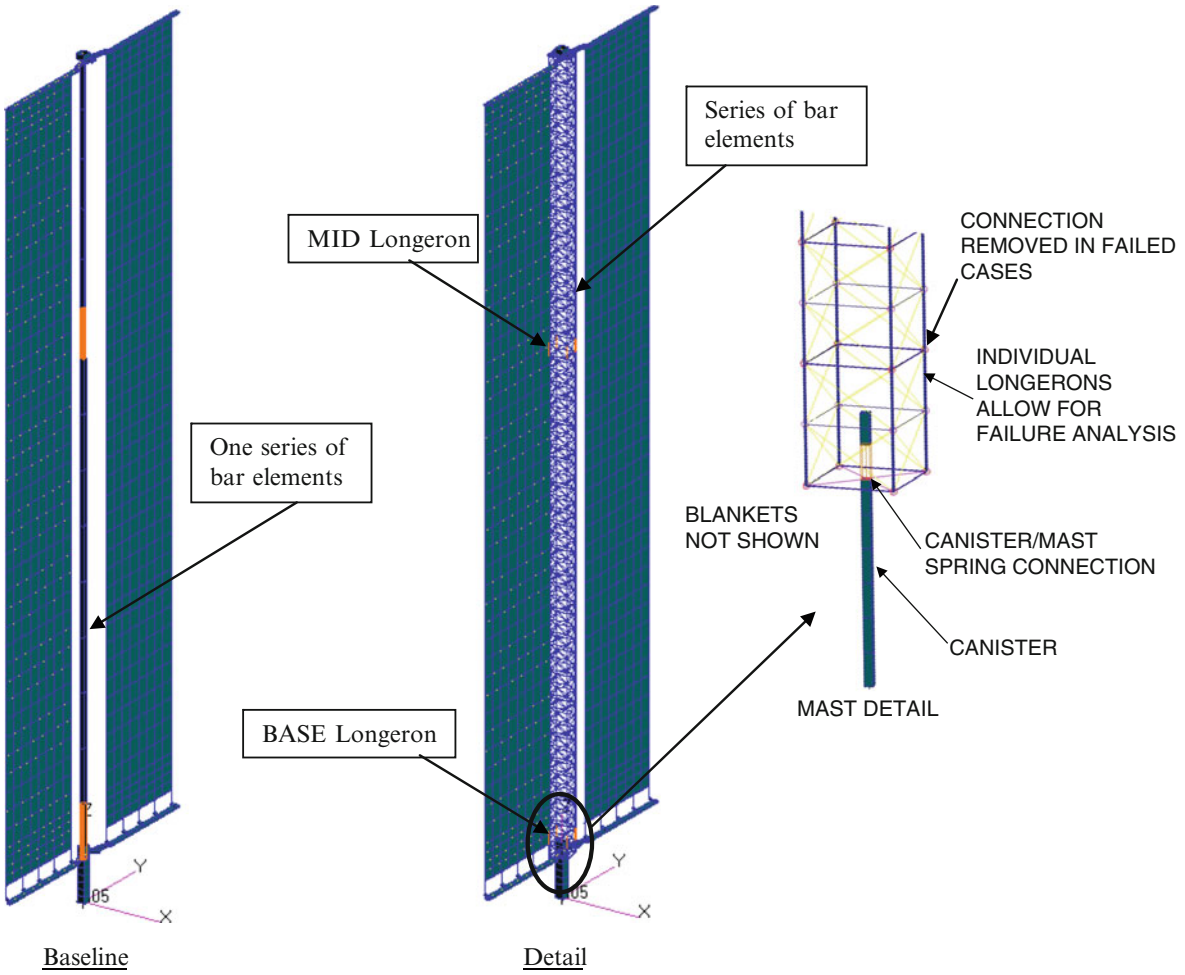

Fig. 1.6 Baseline versus detailed array model

(BL 081 MD1) and total fail (BL 081 MD1 TL), and the base longeron partially failed (BL 081 BS1) and base longeron totally failed (BL 081 BS1 TL). The results of this parametric study are shown in Table 1.2. As can be noted the Base longeron totally failed still shows a 10% frequency difference from the on-orbit test IP frequency.

These results indicate that the on-orbit IP frequency difference between the on orbit test and the analytical model cannot be explained by a longeron failure alone. Other areas had to be investigated.

After a more detailed look of the system, it was determined that the IP mode stress was greatest in the four-bar linkages, which attaches the BGA to the ISS truss. In fact, the first two modes are dominated by the four-bar/BGA assembly. A detailed picture of the four-bar assembly is shown in Fig. 1.9.

1.3.2 Non-linear Analysis

To get a better understanding of the four-bar assembly mechanism and the inherent non-linearities, the ground test documents were reviewed. The ground test data illustrated an initial slippage followed by a high degree of bi-linearity, most notably between the ± My cases. Figure 1.10 shows the strain gauge location and the derived moment output from the My input. The test data showed that some of the deflections were different in the plus and minus loading cases. Within each load case, the deflection verses load curves were relatively linear, but two curves emerged in some of the plus and minus load cases that were not (My shown in Fig. 1.10) [5–7].

This observation in the ground test data means that there was uneven slippage in some of the four-bar to clevis connections. After ten iterations of the ground test the best agreement between the model and linear data required stiffness values be

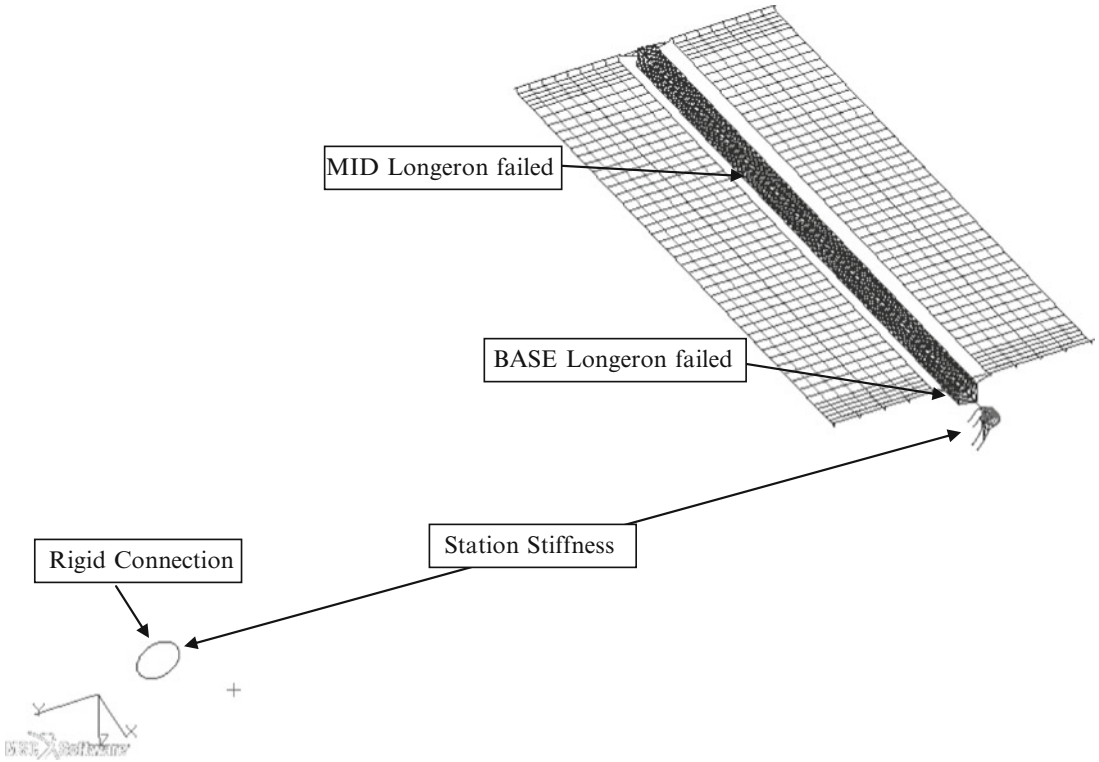

Fig. 1.7 ISS stiffness with detailed BGA and array model

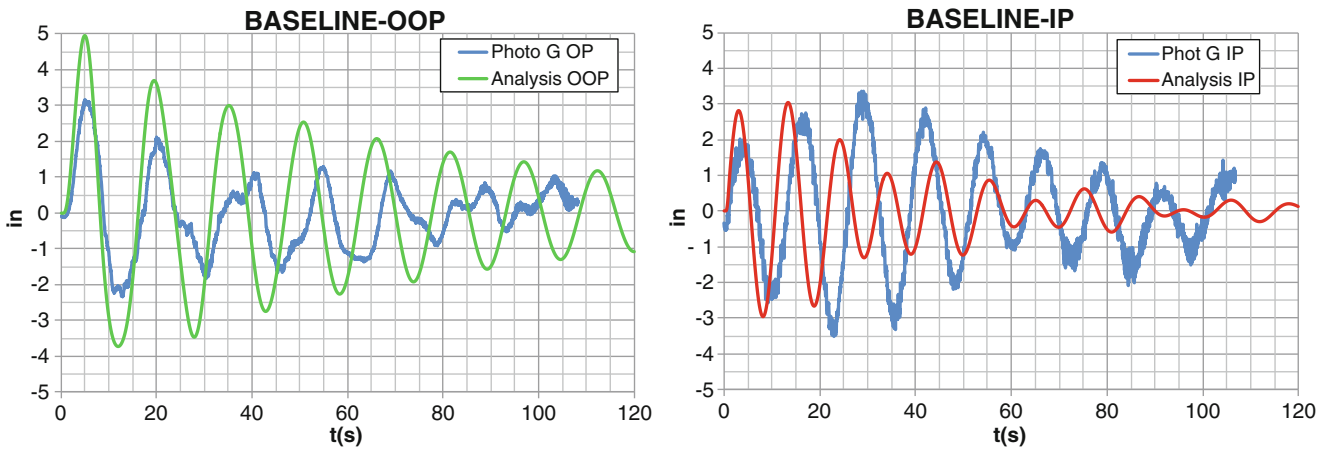

Fig. 1.8 Time domain comparison of out of plane and in plane test and baseline analytical data

Table 1.2 Array frequency comparison

Mode description	2A DTF	BL 081	% diff test	BL 081 MD1	BL 081 MD1 TL	BL 081 BS1	BL 081 BS1 TL	% diff test
OP	0.0602	0.0649	8	0.0646	0.0644	0.0635	0.0634	5
IP	0.0814	0.0969	17	0.0929	0.0926	0.0903	0.0898	10
TOR & IP	0.103	0.0934	−10	0.0957	0.0953	0.0945	0.0945	−9
Mast OP	0.152	0.1519	0	0.1519	0.1519	0.1517	0.1517	0

adjusted in the model four-bar to clevis springs, Mx (in-lb) = 450,000 to 900,000, My (in-lb) 650,000 to 2,280,000, and Mz (in-lb) 600,000 to 6,000,000. These new stiffness values were developed to correlate to the linear slope of the test data, thus the model is expected to be stiffer.

All reports indicate that the non-linearities are mechanism slippage and are in the four-bar to IEA clevis connection.

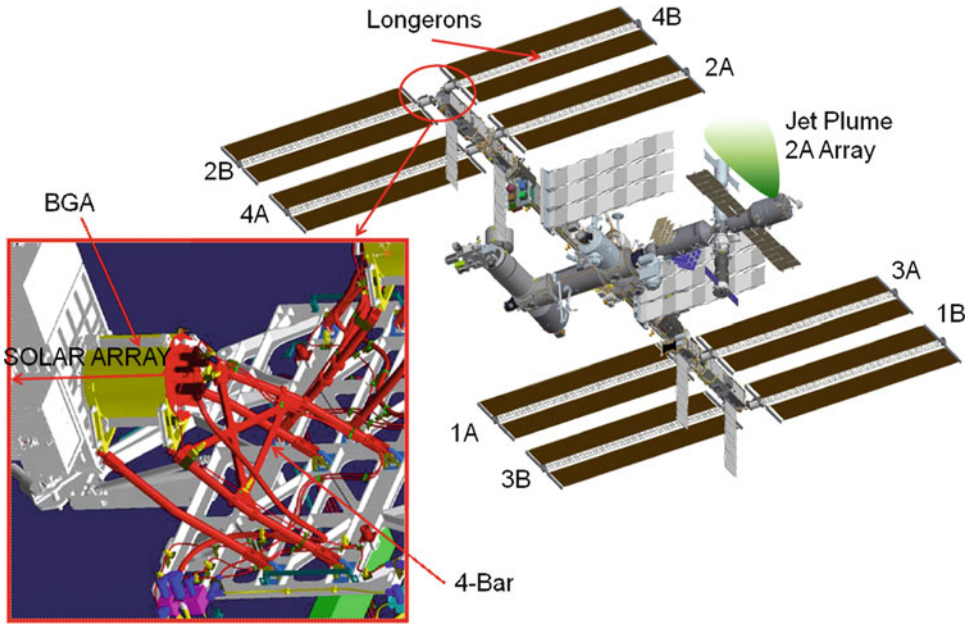

Fig. 1.9 ISS four-bar assembly

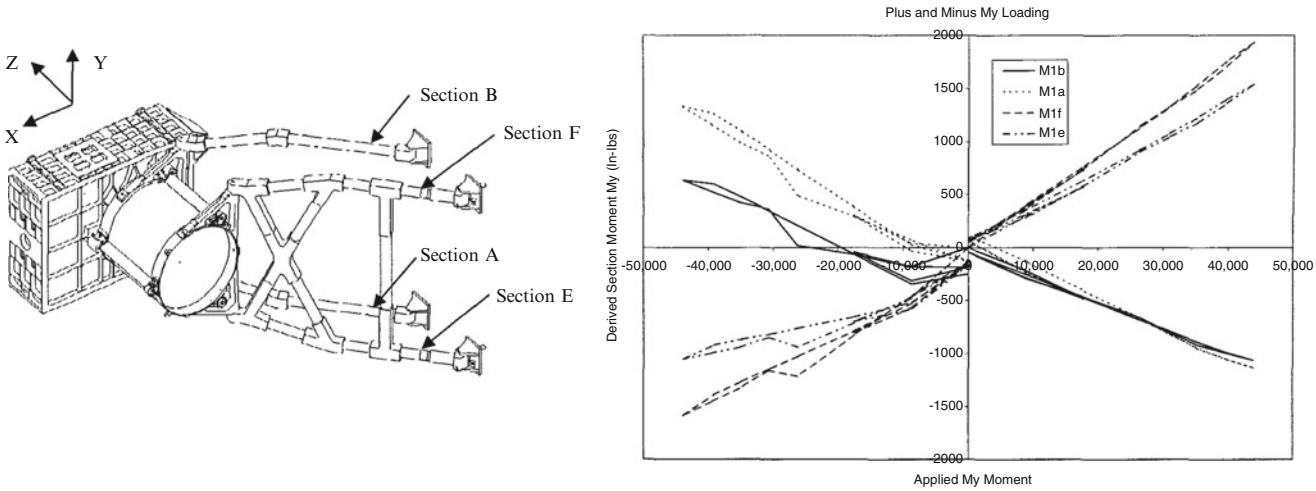

Fig. 1.10 Ground test four-bar assembly and ground test stiffness data

The ground test documents showed that non-linearities exist in the four bar connections. As noted earlier, the four-bar connections dominate the first two modes, OOP and IP. At this point a more detailed analysis was performed on the on-orbit data using the Boeing Test Analysis Correlation Solutions (BTACS) program. The BTACS system identification tool includes a method that extracts modal parameters within a set window over a prescribed period of time within the data set. The photogrammetry displacement data was analyzed using the system identification tool of the BTACS program. The modal parameters were computed every 0.67 s using a window of 60 s of data.

The frequency values, of the extracted modes, were then plotted for each time increment where the color of the data point represented the EMAC value, red being greater than 90% and orange greater than 80%. Figure 1.11 shows the results of the BTACS system identification analysis of the on-orbit data array data showing non-linearities of the first OOP and first IP Modes. The frequency of the OOP mode ranged from 0.06 to 0.068 Hz and IP 0.079 to 0.09 Hz over time, as the amplitude of the array displacement diminished.

To better understand the mechanism of the four-bar clevis to truss connection, on-orbit photos were reviewed. As previously noted the ground test documents indicate that the non-linearities were most likely coming from the four-bar to truss clevis connection. Figure 1.12 depicts the on-orbit photos showing the placement and close-up of the four-bar to clevis connection.

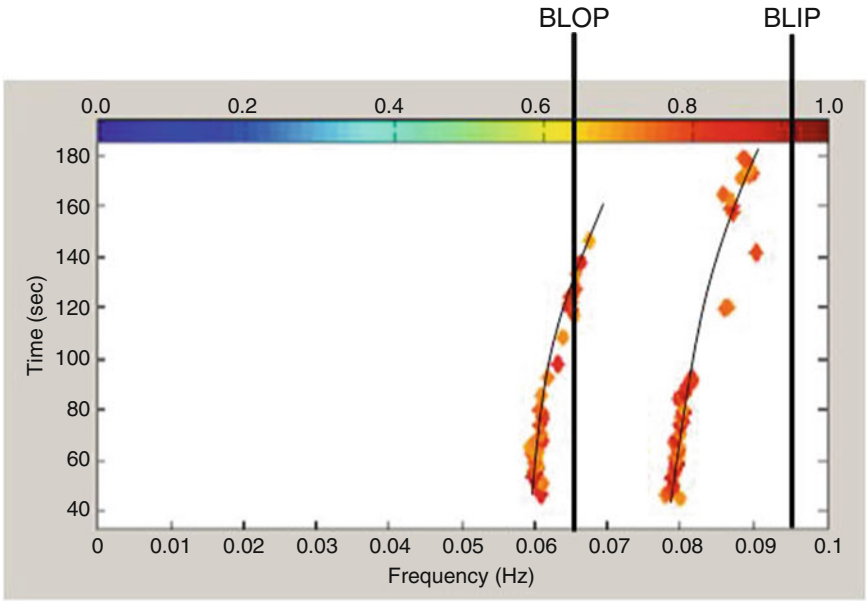

Fig. 1.11 Photogrammetry data mode frequencies vs time

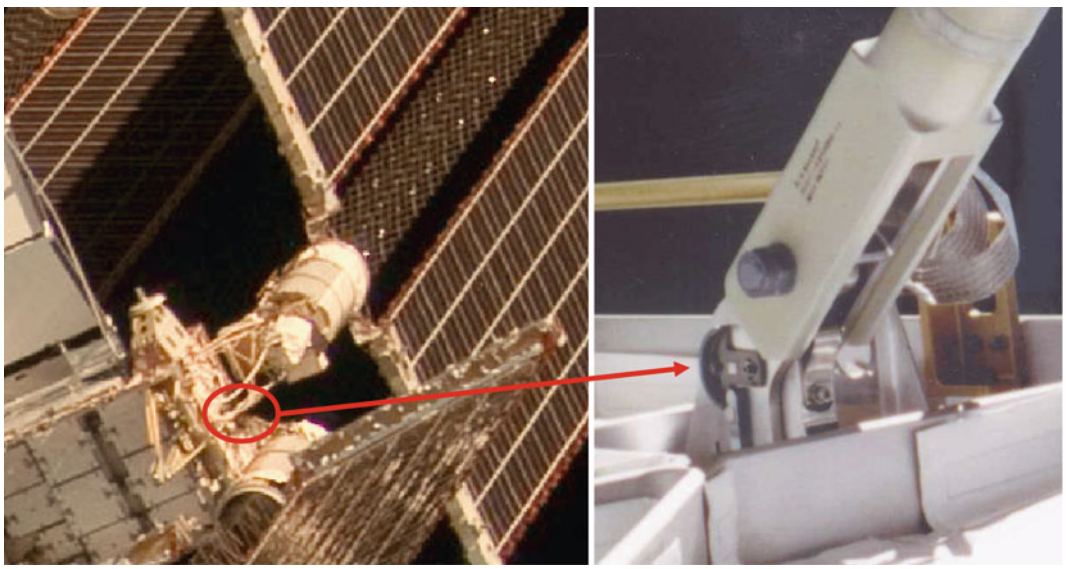

Fig. 1.12 Four-bar to truss mechanism

Table 1.3 BGA to truss spring values

	Baseline (in-lb)	Ground test – BL 081 (in-lb)	Modified – BL 081 DOF 1,3,5 front (in-lb)
CELAS2 DOF1	5,500,000	5,500,000	5,000
CELAS2 DOF2	5,000,000	5,000,000	5,000,000
CELAS2 DOF3	300,000	300,000	5,000
CELAS2 DOF4	450,000	900,000	900,000
CELAS2 DOF5	650,000	2,280,000	2,280
CELAS2 DOF6	600,000	6,000,000	6,000,000

Figure 1.12 illustrates the pin mechanism that locks the four-bar in the extended position (far right). This pin connection is modeled as a set of springs in the BGA detailed NASTRAN [8] model. During the ground test it was decided to correlate the model to the linear stiff portion of the test data, thus increasing the rotational spring values as shown in Table 1.3, Colum 3 (Ground test BL 081). The original values of the model are shown in column 2 (Original).

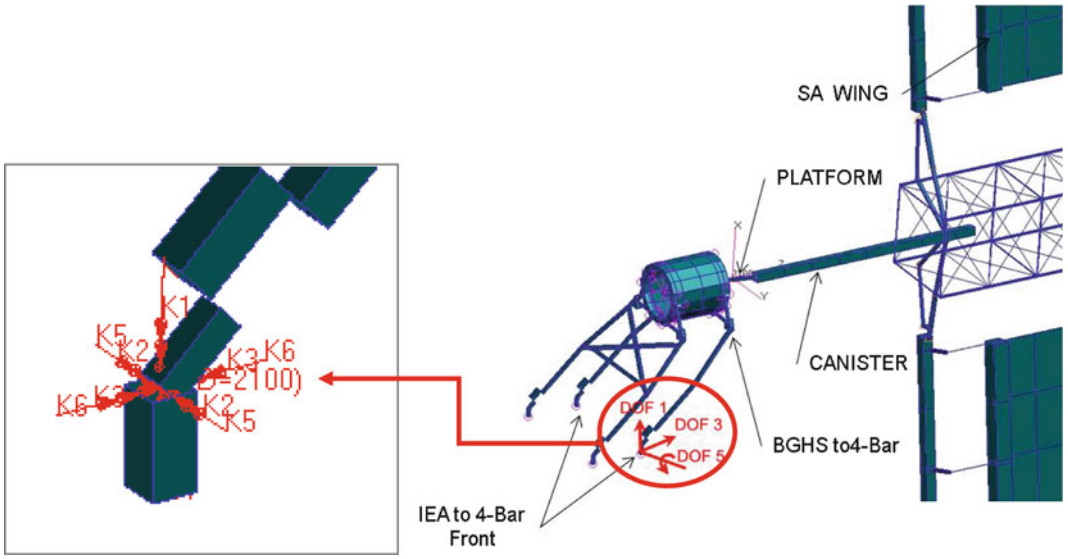

Fig. 1.13 Modified BGA description

Table 1.4 Analytical results of modified BGA

On-orbit test		BL 081 (Hz)	% diff test	BL 081 DOF 1, 3, 5 front (Hz)	% diff test
0.0602	OOP	0.065	8	0.061	1
0.0814	IP	0.097	17	0.079	−3
0.103	TOR	0.096	−7	0.096	−7
0.152		0.152	0	0.151	−1

Table 1.5 GAP stiffness values

	GAP Disp (in)	GAP closed stiffness (in-lb)	GAP open stiffness (in-lb)
DOF1	0.00005	5,500,000	5,000
DOF2	No gap	5,000,000	5,000,000
DOF3	0.0001	300,000	5,000
DOF4	No gap	900,000	900,000
DOF5	No gap	2,280	2,280
DOF6	No gap	6,000,000	6,000,000

A series of NASTRAN runs were performed modifying the four-bar to truss spring values. It was found that modifying the front two connections in DOF 1, 3, and 5 (see Fig. 1.13) would impact the frequency of the IP mode while having negligible effects on the frequency of the other modes. Column 4 of Table 1.3 contains the final spring values used for the analysis.

After all the runs with spring reductions were complete, the final OOP and IP mode frequency values were checked against the baseline mode and the on-orbit test. Table 1.4 illustrates the final frequency values and the percent frequency difference from the on-orbit test. The modified spring values changed the frequency of the IP mode without affecting the frequency other modes. These results allowed for a plausible explanation of the modal discrepancies of the IP frequency difference. It must be noted that this is a linear solution and that we saw non-linear results from the on-orbit test.

To account for the non-linear results seen in the on orbit photogrammetry data, GAP elements were used for the four-bar to truss clevis connection. The solution 129 was used for this analysis. Numerous runs were performed using GAP elements and the NOLIN card. The final analysis was performed using the NASTRAN GAP elements with varying axial stiffness values depending on open or closed gap. To model the on-orbit structure the stiffness was modeled to be less with an open gap. The closed gap stiffness is the same as the baseline A recap of the GAP card values are shown in Table 1.5.

The GAP elements were used on the four-bar to truss clevis on the front locations only. The initial gap open was determined by performing nominal plume runs and plotting the relative displacement between the GRIDS with the baseline spring constant. The exact GAP opened value was determined after several runs and acceptable results were achieved.

Once the proper GAP parameters were achieved, a time domain SOL 129 was performed. When performing non-linear transient analysis, the damping value is specified with the W3 parameter and is the damping at a specified mode. The frequency used for this was a split between OOP and IP mode and was valued at 2%. The comparison time domain of the

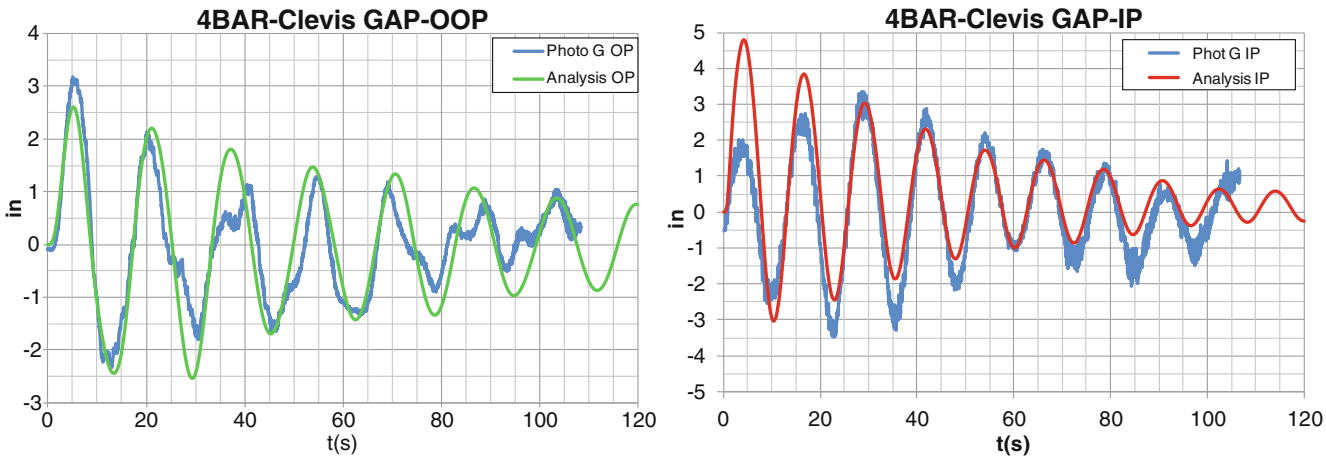

Fig. 1.14 On-orbit versus analytical non-linear time domain data

Fig. 1.15 Relative displacement of front four-bar clevis

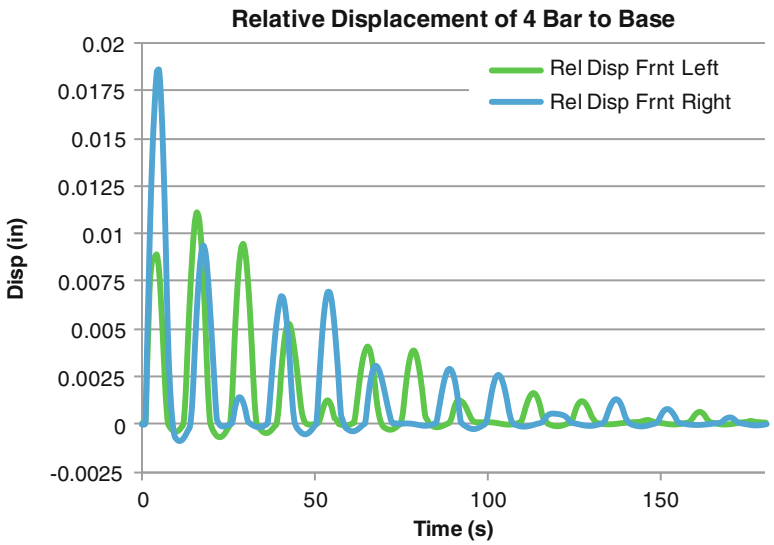

on-orbit test data and the non-linear analytical data is shown in Fig. 1.14. As can be noted the comparison is much better than the baseline (Fig. 1.8) and considered to be a good analytical representation of the on-orbit structure.

In addition to the time domain of the individual OOP and IP displacement of the array, the overall relative displacement of the spring grids were plotted. Figure 1.15 shows the relative displacement of the front four-bars to truss clevis. The maximum displacement is 0.0175". This displacement is a little more than double the complete tolerance stack up of the four-bar mechanism. The tolerance stack up of the four-bar clevis to truss connection is 0.0073".

For a 'quick look' analysis the softened springs were used on the boundary connections of the starboard truss IEA super element and the 2A BGA super element in the full detailed ISS system model. This model has all eight arrays thus it will have eight OOP modes, eight IP modes, and eight torsional array modes.

Table 1.6 compares the system model baseline modes and the 2A array reduced boundary connection model modes. It is noted, in bold, the 2A IP array mode of the modified model is lowered by the amount seen on-orbit. The mode shape comparison of the test modes and the modified model modes matched, and with the lower frequency value, would have deemed the array nominal if this was in the original analytical model when compared to on orbit 2A DTF.

1.4 Mast Damage Sensitivity Study

In addition to the analysis performed to investigate the array mode frequency difference, it was asked if the current ISS instrumentation would allow for mast damage to be detected. A detailed study was performed to investigate if a longeron failure could be detected with current instrumentation.

Table 1.6 ISS modal comparison of baseline and modified

Baseline mode (Hz)	Mode description (baseline)	DOF 135 mode (Hz)	Mode description (modified)	% diff
0.05973	OOP PORT/STBD	0.05884	OOP PORT/2A	−1.5
0.06134	OOP PORT/STBD	0.06071	OOP PORT/STBD	−1.0
0.06472	OOP STBD	0.06472	OOP STBD	0.0
0.06484	OOP PORT/2A	0.06294	OOP PORT/2A	−3.0
0.06499	OOP STBD	0.06499	OOP STBD	0.0
0.06511	OOP PORT	0.06497	OOP PORT	−0.2
0.06566	OOP STBD	0.06566	OOP STBD	0.0
0.06648	OOP PORT	0.06628	OOP PORT	−0.3
0.09333	IP PORT sym	**0.08128**	**IP 2a**	**−14.8**
0.09566	IP STBD sym	0.09568	IP STBD sym	0.0
0.09639	**IP PORT/2a**	0.09473	IP PORT sym	−1.8
0.09664	IP STBD anti-sym	0.09664	IP STBD anti-sym	0.0
0.09676	IP STBD	0.09676	IP STBD anti-sym	0.0
0.09707	IP PORT, STBD anti-sym	0.09700	IP PORT anti-sym, STBD	−0.1
0.09713	IP PORT anti-sym, STBD	0.09713	IP PORT, STBD anti-sym	0.0
0.09812	IP PORT anti-sym	0.09811	IP PORT anti-sym	0.0
0.09961	TOR STBD	0.09961	TOR STBD	0.0
0.09968	TOR STBD	0.09968	TOR STBD	0.0
0.09974	TOR STBD	0.09974	TOR STBD	0.0
0.09976	TOR PORT	0.09978	TOR PORT	0.0
0.09977	TOR STBD	0.09977	TOR STBD	0.0
0.09995	TOR PORT	0.09967	TOR PORT	−0.3
0.10025	TOR PORT	0.10022	TOR PORT	0.0
0.10036	TOR PORT	0.10036	TOR PORT	0.0

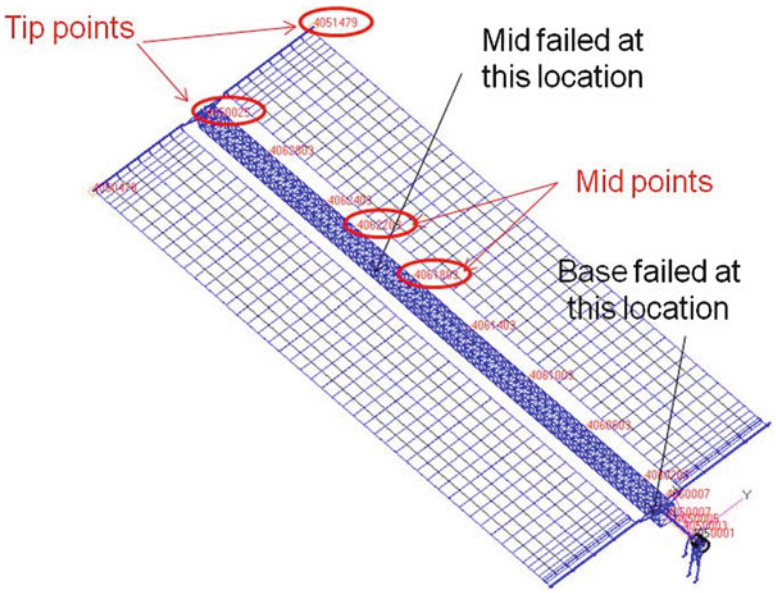

Fig. 1.16 Array camera viewing locations

The only instrumentation on orbit to measure ISS array modes is the photogrammetry system. The photogrammetry analysis needs at least two cameras on each area being investigated. It is possible but very difficult to get four cameras dedicated for an array test. For this study it was decided to use four cameras. Figure 1.16 illustrates the two areas the cameras would be pointed, one set at the tip and one set at the midpoint, spanning the most credible failure area.

A set of SOL 103, modal solution, runs were performed on the baseline array model, failed at mid model, and failed at base model. The modal parameters for each model was output and compared to the baseline model modal parameters. For each run the frequency difference and MAC was calculated. The baseline model has over 700 modes from 0 to 5.5 Hz. To reduce the amount of modes to investigate, only modes containing 2% or greater kinetic energy in the array mast were saved. This reduced the problem down to 60 modes. It also must be mentioned that this is a total failure of the longeron and does not assume partial fractures.

Table 1.7 BGA at 81° damaged at MID

Nom freq	Fail freq	MAC	% diff freq	Mode description	% KE mast
0.093	0.090	0.758	−3.2	Torsion	3
0.6777	0.6247	0.823	−7.8	Mast bending with blanket (anti) bending	5
1.5107	1.259	0.745	−16.7	Out plane bending with lower blink box	20
1.5107	**1.2868**	**0.722**	**−14.8**	**Added mode from mid damage**	**20**
2.3272	2.2607	0.752	−2.9	Good first in plane bending	24
4.344	4.06	0.642	−6.5	45° plane second bending	2
4.3824	4.6232	0.545	5.5	Out plane second bending	52

Table 1.8 BGA at 81° damaged at base

BL freq	Fail freq	MAC	% diff freq	Mode description	% KE mast
0.093	0.090	0.758	−3.4	Torsion	19.2
1.001	0.980	0.924	−2.1	Mast in plane first bending	9
2.327	2.254	0.984	−3.1	Good first in plane bending	24
4.344	4.083	0.602	−6.0	45° plane second bending	2
4.382	4.083	0.915	−6.8	Out plane second bending	52

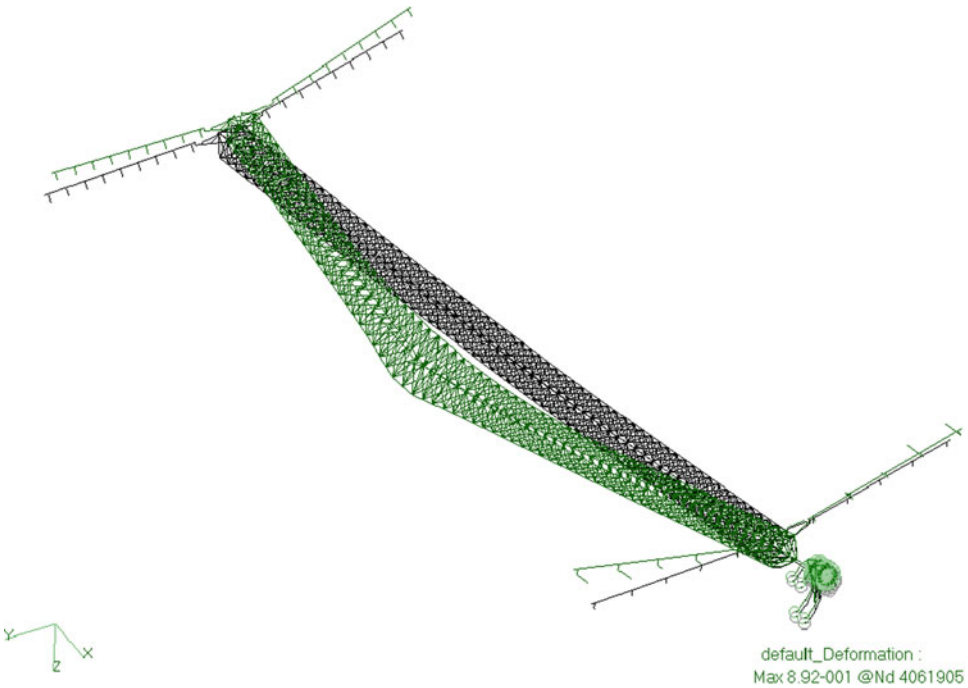

Fig. 1.17 Mast mode shape comparison with MID longeron failure

Once the major modes were selected, the MAC was calculated using the four grids as noted in Fig. 1.16. Table 1.7 summarizes the data results for the mast failed at mid model and Table 1.8 summarizes the data for the mast failed at base model.

Table 1.7 is the summary of the failed longeron at the mid point of the mast. The torsion mode has a low MAC between the baseline and damaged model but it would be difficult to detect this with the cameras available and determining if this is the results of the four-bar contribution or mast damage. The next possible mode for detecting mast damage was the 0.677 Hz mast bending mode. The failed mast does show a lower MAC value and mode frequency. The best possibility of damage detection is the additional mode in the failed case at 1.2868 Hz (highlighted in bold). When performing the MAC the best match is the baseline mode at 1.5107 Hz. This mode would be the best mode to detect a total longeron failure at mid mast and the comparison mode shape is illustrated in Fig. 1.17. Some other modes exist above 4 Hz but it is difficult on orbit to physically excite modes at that high of a frequency and the reliability of photogrammetry to capture the modes at that frequency is unknown, due to the frame rate of the cameras of 15 or 30 Hz.

Table 1.8 illustrates the frequency difference and MAC values between baseline model and the failed longeron at the base of the mast model. Once again the first torsion mode may be difficult to determine if the difference is caused by the mast

or four-bar damage but with the higher KE it should be easier to excite on orbit. The modes above 4 Hz seem to have the best chance of detecting mast damage, but again the modes at this high a frequency are difficult to excite on orbit and it is unknown if modes in this frequency range can be reliably detected using photogrammetry.

The final conclusions are that a mast failure can be detected with modes above 1 Hz for MID failure and above 2 Hz for the base failure. The limitation of the mast failure detection using existing photogrammetry is the ability of only having two areas to track. Mode shape differences are easier to detect when tracking four or more areas. An exhaustive study of the optimal tracking areas was not performed and could be an area of improvement. In addition, the program is developing high definition cameras that would enhance the detection process but would still be limited to tracking only two areas.

1.5 Conclusions

The 2A ISS array was subjected to extreme limit loads from a longeron shadowing event. The longeron shadowing event may cause a thermal buckling of the longeron on the ISS solar array mast. To check for structural integrity of the array, a photo survey was conducted and an on-orbit modal test was performed. No damage was found from the photo survey but the on-orbit modal test showed a frequency difference in the first IP Array mode. Through analysis it was found that this frequency shift could not be explained by mast damage alone, but in fact may be a non-linear characteristic of the BGA four-bar clevis to truss attachment. Modal solutions proved that by softening the front four-bars that the first IP mode frequency was lowered without affecting the other modes' frequencies. This was exactly what was observed in the on-orbit test. A simplified station model was developed with the detailed solar array model to perform time domain NASTRAN runs. The time domain runs were performed with the soft front four-bars with good results but still was not matching the on-orbit data.

It was found that the on-orbit 2A array displacement data increases in frequency as displacement amplitude decreases. This indicates a non-linear mechanism. This non-linear phenomenon was modeled using NASTRAN gaps with the baseline stiffness of the front four-bars when the Gap was closed and when it was opened the soft spring values were applied. The time domain displacement results matched the on-orbit test. It was concluded that the non-linearities could be attributed to gaps, gaps with pre-loads, and thermal effects. It was also determined that if a longeron on the array mast was damaged, completely separated, that it would be difficult to measure with current instrumentation, but with additional and higher quality cameras, it would be possible.

References

1. Solar array mast buckling report, ATK Space Systems 1163D3883, 10 June 2010
2. P4-2A photogrammetry results, NASA-JSC-Image Science and Analysis Group, 5 Jan 2010
3. Juang JN, Pappa RS (1985) An eigensystem realization algorithm for modal parameter identification and model reduction. J Guid 8(5):620–627
4. Space station PG-2 fully deployed solar array nastran dynamic model, EM NO. SSSA57, Lockheed Martin Missiles and Space, C. C. Tang, 10 Feb 1997
5. BGA static test on-orbit deployed loads model correlation, Boeing Memorandum EID-05475, 6 April 2000
6. BGA on-orbit static test/Finite element model correlation, Boeing Memorandum EID-05379, 18 April 2000
7. Qualification mast canister stiffness, strength, and structural alignment test report, Lockheed 518D972, 24 May 1996
8. MSC/NASTRAN quick reference guide, MSC/NASTRAN, 2008

Chapter 2
Experimental Non-linear Modal Testing of an Aircraft Engine Casing Assembly

Dario Di Maio, Paul Bennett, Christoph Schwingshackl, and David J. Ewins

Abstract This paper aims to present experimental work on an aircraft engine casing assembly. Nowadays single components of casings can be modeled with such high accuracy that they can be validated by carrying out the model validation process using measured data from a sector of the entire assembly. This smart validation process can be achieved by carrying out the modal analysis with a Scanning LDV (Laser Doppler Vibrometer) system which allows good spatial resolution of the measured mode shapes. The validation process can be assumed valid under linear response conditions obtainable for low vibration amplitudes. Casings are typically connected together by joints which may or may not respond non-linearly under high levels of vibration. Therefore, prior to conducting any non-linear validation, the mode(s) responding non-linearly must be identified beforehand in order to correctly specify the non-linear modal testing required. The work presented here will use a large civil engine casing assembly comprising a Combustion Chamber Outer Casing (CCOC), High Intermediate Pressure Turbine Casing (HIPTC) and Low Pressure Turbine Casing (LPTC.) The Fine Mesh Finite Element Model (FMFEM) was successfully validated using linear modal analysis test data. One of the objectives of this work is to define the key points for conducting non-linear modal testing of such large casing assemblies and sub-assemblies. One outcome of the experimental work was a set of recommendations for performing measurements, which should be carried out within the frequency bandwidth selected during the model validation process. Experimentally derived non-linear response curves are presented in this paper.

Keywords Joints • Non-linear testing • Aircraft engine casing • Scanning LDV

2.1 Introduction

A civil aircraft engine casing assembly comprising a Combustion Chamber Outer Casing (CCOC), High Intermediate Pressure Turbine Casing (HIPTC) and Low Pressure Turbine Casing (LPTC) Fine Mesh Finite Element Model (FMFEM) was successfully validated using linear modal analysis test data [1] and (Private communication University of Bristol-Rolls-Royce). One of the objectives of this project was to define guide-lines for conducting non-linear modal testing of such large casing assemblies and sub-assemblies. The key aim was to produce a set of recommendations for performing measurements, which should be carried out within the frequency bandwidth selected during the model validation process. The validation process of the full assembly was performed using two measurement methods: (i) accelerometers and a roving instrumented impact hammer and (ii) using a Scanning Laser Doppler Vibrometry (SLDV) system and electromagnetic shaker. The first validation was carried out with the casing assembly supported vertically by bungees, whereas the second was tested with the assembly suspended horizontally.

D. Di Maio (✉) • D.J. Ewins
University of Bristol, Bristol, UK,
e-mail: dario.dimaio@bristol.ac.uk

P. Bennett
Rolls-Royce plc, London, UK

C. Schwingshackl
Imperial College London, London, UK

G. Kerschen et al. (eds.), *Topics in Nonlinear Dynamics, Volume 1: Proceedings of the 31st IMAC, A Conference on Structural Dynamics, 2013*, Conference Proceedings of the Society for Experimental Mechanics Series 35,
DOI 10.1007/978-1-4614-6570-6_2,

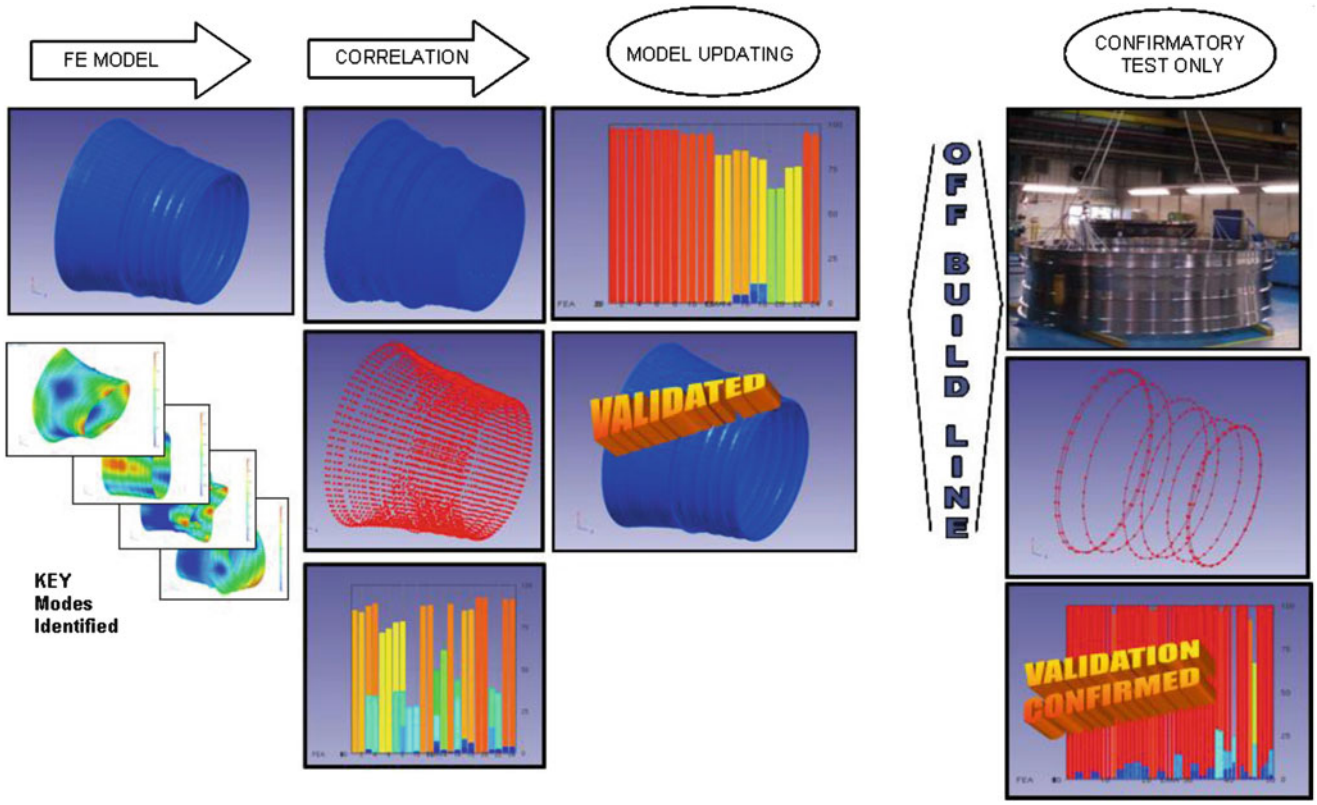

Fig. 2.1 Schematic of a validation of an assembly model

Non-linear testing was initially started with the casing suspended horizontally. It was later decided to rotate the test structure and continue testing with it suspended vertically because some of the natural frequencies obtained from the horizontal tests had shifted slightly.

The assembly has over 50 modes below 1 kHz which makes selection of the most suitable modes for non linear testing difficult.

The testing was divided into five distinct stages

(i) Linear FMFEM model validation
(ii) Mode shape selection
(iii) Qualitative assessment of non linearity using force control method (low excitation levels)
(iv) Quantitative assessment of non linearity of selected resonances using force control method
(v) Higher amplitude modal testing using amplitude control method of those modes identified as non linear.

Using this approach those resonances likely to exhibit the strongest non linear behaviours can be quickly shortlisted. For the assembly the bolted flanges are responsible for most (if not all) of the non linearity of the structure. The testing presented here was focused mainly on excitation of modes with significant casing flange response.

For some engine components, the 'physics' of the undamped FE model are completely represented when analysed in a Free-Free state (i.e. no boundary conditions or external loads applied). In other words, the accuracy of the normal modes prediction of such FE models (i.e. the natural frequencies and mode shapes) are most strongly dependant on the fidelity of the FE model geometry, the material properties used, selection of element type(s) and the degree of FE mesh refinement employed. In fact, for lightly damped, solid, isotropic components at room temperature, the accuracy of the FE model normal modes analysis, for all practical purposes, depends only on these parameters for low levels of excitation.

Early on in the development program, prior to the manufacture of hardware, only nominal geometry models are usually available. Even so, it is clear that if FE models of high geometric fidelity and mesh refinement are generated (i.e. FMFEMs) the resulting predictions of frequencies and mode shapes can be used, well in advance of any Modal Testing, to help validate the less refined and more idealised Whole Engine Models (WEM) required early on in an Engine Development Program. The effort required to produce FMFEMs is now considerably less than might be expected (typically only 2–3 days) depending on the component complexity and the quality of the 3D geometry initially provided. Figure 2.1 shows how a validation of a

linear WEM assembly model can be performed very quickly using FMFEM models where modal testing plays an important part in confirming the quality of the validation process.

At this time it is felt that some limited, confirmatory testing, of the actual component hardware would still be advantageous. This would primarily be to confirm that the test hardware supplied was close to its design intent. It has been shown recently that the use of new technologies such as Scanning LDV systems can be used to rapidly validate FMFEMs. Such short test times can be fitted neatly within modern development engine build programmes with minimal disruption. One of the key advantages of performing modal testing with an SLDV system is its ability to measure mode shapes with high spatial resolution very quickly. Visualization of the mode shapes helped to rapidly identify those resonances which were more likely to exhibit a non-linear response. Reviewing such high fidelity depictions of the assembly mode shapes was very useful for understanding which modes were likely to exercise the casing flanges, the greatest potential source of the assembly non-linearity. This approach was found to be extremely useful for the initial experimental assessment of the casing's likely non linear responses.

2.2 Test Planning for Rapid Validation of FMFEM Axisymmetric Casings and Assemblies

2.2.1 Contrast with WEM Model Validation Testing

For WEM models current validation processes require that all key modes are acquired during the modal test model correlation and to permit any subsequent Computational Model Updating (CMU) required later. When Test Planning for FMFEMs only those key modes need to be acquired which confirm, with high confidence, that the FMFEM closely represents the dynamic behaviour of the test component and so was a valid reference for previous validation of the WEM model.

Modal Test Planning and Validation of WEM models starts with the WEM model itself, however when a FMFEM model has already been used to 'validate' the less detailed WEM model earlier in the engine development programme then a smaller scale modal test can be planned. For example, Test Planning the validation of WEM models will usually make provision to acquire both orthogonal modes from each mode pair. However, when validating large, *strongly* axisymmetric FMFEM models usually only one orthogonal mode from each pair need be acquired on test, since a strong correlation with one of the orthogonal modes would imply a similarly strong correlation for the other. High confidence in the FMFEM also makes it very unlikely that the modal validation test data will need to be used as a reference for any CMU later.

2.2.2 Reducing Modal Test Times

There are three main areas in which to speed up the validation testing required for FMFEMs. This section illustrates some suggestions to reduce the model validation test time required for FMFEM components and/or subassemblies from delivery of the hardware to the test area.

For large casing structures modal test setup times can still be lengthy despite the apparent simplicity of the Free-Free boundary conditions required. However, by using the FMFEM model it becomes possible to predict the test component's fundamental Free-Free mode and mass with high confidence. Using this information the number and stiffness of the suspension points required can be calculated in advance and can be made ready prior to the test hardware's arrival.

Correctly marking up the test hardware prior to modal testing is critical, as it locates the test positions carefully chosen during Test Planning onto the actual test hardware. Mistakes made during marking-up are often difficult to evaluate post test and will artificially reduce the correlation with the FMFEM model.

The large amount of geometric detail in FMFEMs can be utilised to simplify marking-up of the test hardware enormously. A large number of features (e.g. flange holes, casing holes, casing bosses, etc.) within the FMFEM can now also be accurately located on the test hardware itself. Higher initial confidence in the FMFEM also means that fewer test points are required for validation, i.e. additional test points that would otherwise have been specified to extract both orthogonal mode pairs or to aid mode visualisation are no longer required.

It will be shown that for large axisymmetric component casings (and subassemblies) test data will usually only be required from a sector of the test hardware in order to validate its corresponding FMFEM model with high confidence. Since only one side of the component needs to be tested, non-contact 'line of sight' dynamic measurement methods (e.g. SLDV) can

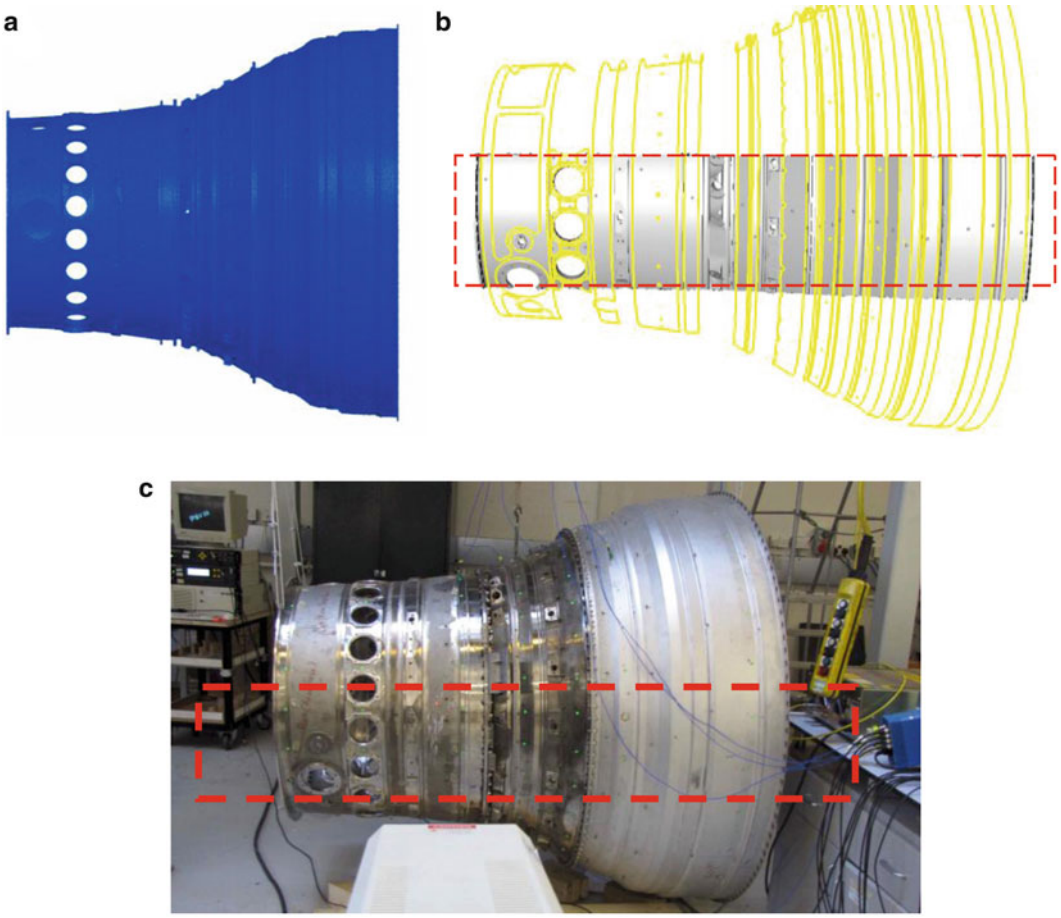

Fig. 2.2 FE model **(a)**, target sector **(b)** and test setup **(c)**. **(a)** Mesh Finite Element Model (FMFEM) of the COC/HPTIPT/LPT casing assembly. **(b)** Target sector used for the Test planning of COC/HPTIPT/LPT casing assembly FMFEM. **(c)** Setup showing the target sector of the FMFEM on the real COC/HPTIPT/LPT casing assembly

be employed efficiently. When SLDV is used the acquisition can also be automated to give high density area scans. It is essential to confirm in advance, using Test Planning, that the chosen sector scan is likely to provide sufficient high quality data in order to validate the target FMFEM modes.

2.2.3 Sector Test Planning for Large Axisymmetric FMFEMs

Figure 2.2a shows a FMFEM model of a large Civil Engine casing sub-assembly. This FMFEM model has over 12 million degrees of freedom and the casing flanges have been modelled (simplistically) as rigidly fixed together. Using the Rolls-Royce in-house FE code it is possible to quickly 'hide' all but a sector of the full assembly model, Fig. 2.2b, and export selected nodal displacements from that sector only. Figure 2.2c shows how closely the geometry of the FMFEM sector matches the actual test hardware; a number of the same features can be clearly identified on both (e.g. casing holes, bosses, etc.). Note, not all sector faces are chosen for inclusion in Test Planning, highly angular faces (e.g. bosses, flange radii, etc.) have not been included and so appear uniformly dark blue (i.e. no displacement data exported) in Fig. 2.2c.

The first 30 FMFEM modes were included in Test Planning. The displacement data and sector FE mesh were combined and converted into a format that could be read directly into FEMtools [2]. Using FEMtools it was possible to quickly produce an autoMAC of the sector displacement patterns from the first 30 FMFEM modes. This was one of the key aims of Test Planning – to eliminate or minimise any spatial aliasing, i.e. to ensure that enough test points are included so that *all modes of interest* could be unambiguously differentiated.

In this way testing a 'sector' of the FMFEM was 'simulated' in order to determine how many test points might be required to clearly differentiate the first 30 modes of the sub-assembly on test. The autoMAC of a good test plan will have

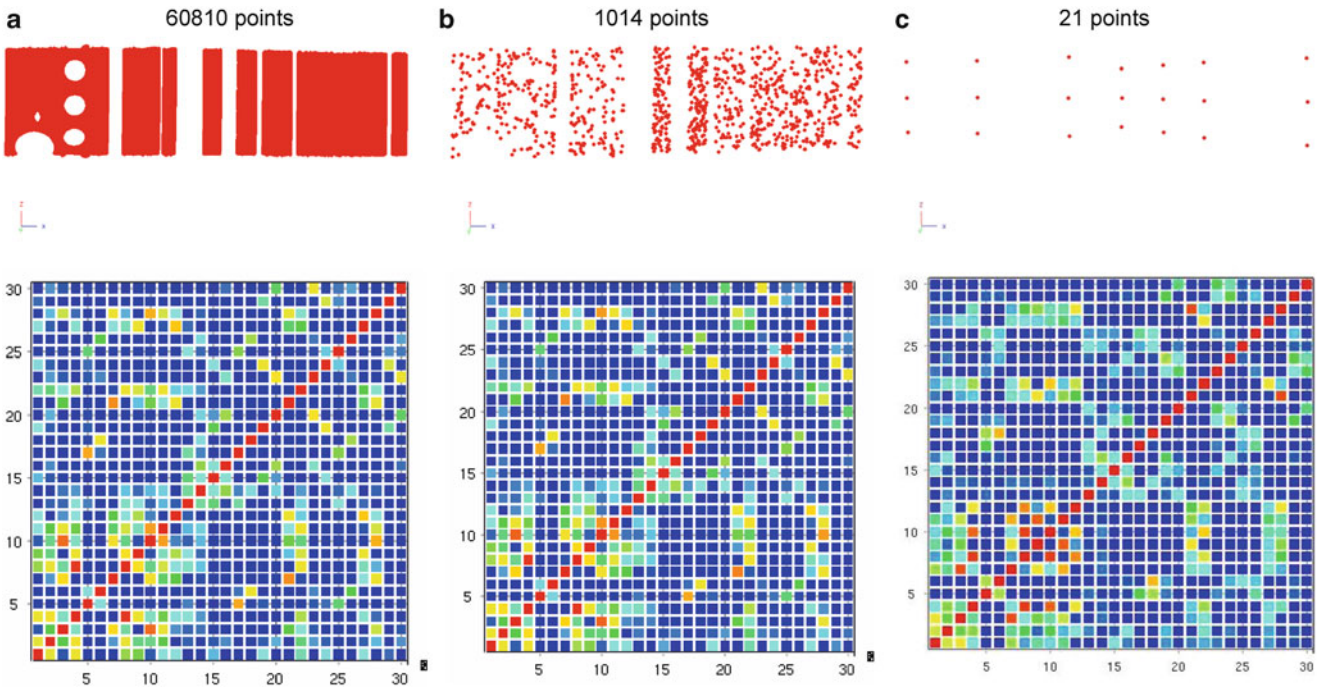

Fig. 2.3 Predicted variation in the autoMAC of first 30 modes of the FMFEM sector due to a reduction in test point density

low off-diagonal terms for all modes of interest. Figure 2.3 shows the effect on the autoMAC for a reducing number of test points assumed from (a) all 60,810 points exported from the FMFEM; to (b) a subset of 1,014 points; to (c) where only 21 points were selected. Assuming 60,810 test points is obviously impractical, however, the resulting autoMAC does provide a useful datum against which to assess how decreasing test point density might adversely affect the resulting test.

It can be seen that a reduction from 60,810 to 1,014 test points, a far more likely scan density for this structure, has had little detrimental effect on the autoMAC. A Test Plan is usually deemed satisfactory if the off diagonal terms of the simulated test autoMAC are less than 40% for all key modes unless they are already well separated (>25%) in frequency. In other words, no two modes on test should look too much alike unless they can also be differentiated (with high confidence) using frequency difference alone. The near identical autoMAC's of Fig. 2.3a, b show that using 1,014 test points would be functionally as good as using 60,810 points.

What may be a little more surprising is that the autoMAC from a very small (but carefully chosen) number of test points, i.e. the 21 points of Fig. 2.3c, is still reasonable. While there are now some obvious differences when compared with the larger tests, its autoMAC suggests that test data from just these 21 points would still lead to a satisfactory modal test.

The number and location of the accelerometers required for the modal test should always be confirmed using Test Simulation. A key advantage for FMFEM validation testing is that it becomes possible, during Test Simulation, to confirm a number of suitable accelerometer positions which also take advantage of the very high geometry fidelity to the actual test hardware. Through careful Test Planning, the number and position of the test accelerometers required can be chosen such that they that are simple to attach accurately, and very quickly, to the test hardware.

2.3 Test Case: SILOET 2.3.2: Full Assembly COC\HPTIPT\LPT FMFEM

In order to demonstrate the applicability of the above approach it was decided to conduct some rapid testing of the large Civil casing sub-assembly shown in of Fig. 2.2a, at the University of Bristol as part of the SILOET Research Program. The Test Planning and Test Simulation outlined in Sect. 2.2.3 were carried out by Rolls-Royce and an impact hammer modal test was conducted at the University of Bristol using just the 21 points of Figs. 2.3c and 2.10 off pre-selected reference accelerometer positions around the assembly. The location of these 21 points on the test hardware has been shown in Fig. 2.4.

The results of the testing are shown in Table 2.1 where it can be seen that there is strong correlation with the FMFEM predictions for at least 1 of each orthogonal mode pair up to mode pair 12. Table 2.1 compares the FMFEM correlation

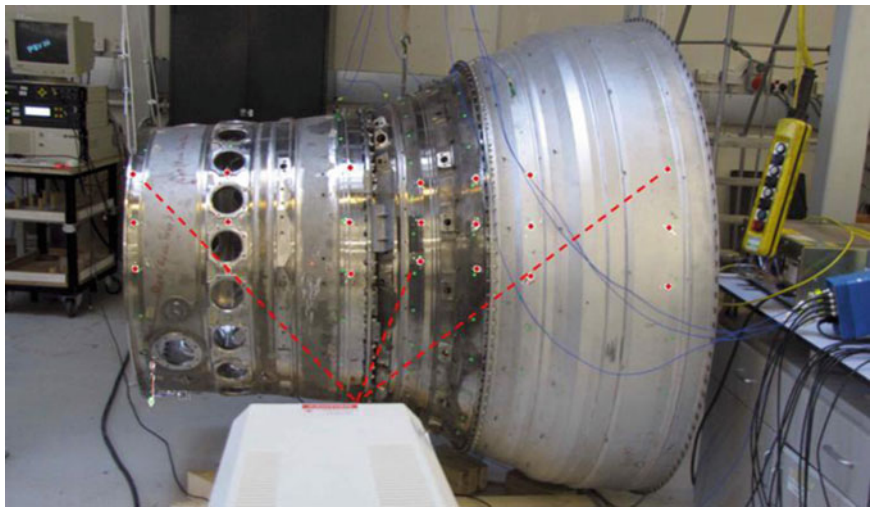

Fig. 2.4 Location of the 21 measurement points

Table 2.1 Correlation of FMFEM model against modal test data. Comparison of rapid sector test FMFEM correlation with that of the full modal test

					Full test		Rapid test	
Mode pair	FMFEM mode	Hz	TEST mode	Hz	Freq. diff. (%)	MAC	Freq. diff. (%)	MAC
1	1	39.3	1	39.1	0.4	97.8	−0.9	91.3
	2	40.1	2	39.7	1.1	94.4	2.5	80.9
2	3	53.7	3	53.1	1.1	99.0	1.1	96.3
	4	53.8	4	53.2	1.2	99.2	1.1	89.1
3	5	58.7	5	58.5	0.3	97.4	−0.4	95.2
	6	58.7	6	58.9	−0.3	97.1	0.4	90
4	7	84.5	7	82.3	2.7	99.5	2.7	97.8
	8	84.6	8	82.4	2.7	99.1	2.7	94.4
5	9	129.3	9	125.7	2.9	98.8	2.8	96.1
	10	129.3	10	125.8	2.8	99.0	2.9	90.6
6	11	185.5	11	180.5	2.8	97.3	2.8	98.5
6	12	185.6	12	180.6	2.8	96.9	2.8	79.3
7	13	201.8	13	187.7	7.5	85.9	7.5	92.2
	14	203.0	14	189.4	7.2	96.3	7.2	95.2
8	15	206.8	15	201.1	2.9	96.9	0.4	97.1
	16	209.9	16	206.0	1.9	97.3	4.4	96.4
9	17	241.2	17	229.8	4.9	92.2	4.9	94.8
	18	242.4	18	230.3	5.3	91.6	5.3	89.5
10	19	244.8	19	232.7	5.2	98.4	5.2	97.3
	20	245.0	20	233.2	5.0	93.1	5.1	90.9
11	21	249.6	21	242.6	2.9	98.9	2.9	96.6
	22	249.7	22	243.0	2.8	99.1	2.8	93.4
12	23	290.1	23	283.5	2.3	99.4	1.9	93.5
	24	290.5	24	284.8	2.0	99.4	2.5	96.2

results of the 21 point sector test and those of the larger 200 point whole annulus test. The 21 point 'sector' test and 200 point 'full' modal test results compare well in almost all cases, and very well for at least one of the orthogonal modes in each pair – which was the original aim of the Test Planning. For both tests mode pair 7, 9 and 10 are outside the current FMFEM acceptance criteria and this is likely due to the simplistic modelling of the flange joints in the FMFEM (fully fixed) causing it to over predict the frequencies for these modes. The advantage of SLDV scanning is that it can be completely automated and gives very high test point density (typically 1,000+ points). However, it generally uses a 'contacting' excitation system (e.g. a small Electromagnetic (EM) shaker) which can have a negative impact on the extraction of the orthogonal mode pairs of the large axisymmetric components/sub-assemblies and also on their measured frequencies (due to mass attachment effects).

2.4 Test Setup for Non-linear Large Assembly Tests

2.4.1 Preliminary Measurements

The initial assessment of the casing assembly's non linearity was started with it suspended horizontally. The ten off reference accelerometer positions used during the linear validation of the assembly were also used for the non linear testing to provide continuity. Figure 2.5 shows the initial non linear test set-up, and the LDS V200 electromagnetic shaker (20 N dynamic range) attached to the HPIPT of the casing.

Although a commercially available system was used for the non-linear testing, a customised acquisition panel was created in LabVIEW (a National Instruments software package) to support the initial investigation. The test data acquired was analysed using the ICATS modal analysis software suite [3].

A broadband sine step excitation (500 Hz bandwidth) was selected to excite a pre-chosen subset of the casing resonances for non linear assessment. Figure 2.6 shows in red boxes the resonances selected at 58, 206, 232 and 460 Hz, respectively. Neither the force nor amplitude was experimentally controlled but instead, as a first pass check, the selected resonances were excited at increasing levels in order to visually detect any changes in the resulting FRFs, that might be suggestive of underlying non linearity.

As a quick first pass check, neither the force nor amplitude was experimentally controlled but instead the selected resonances were excited at increasing levels in order to visually detect any changes in the resulting FRFs, which might be suggestive of underlying non linearity. In order to excite to higher amplitudes a further trial was carried out with a larger shaker LDS V400 which has a 190 N dynamic range.

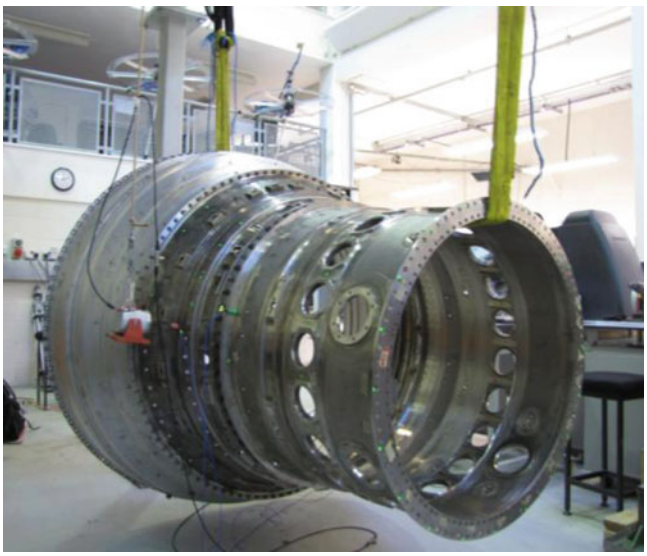

Fig. 2.5 Test rig setup horizontally

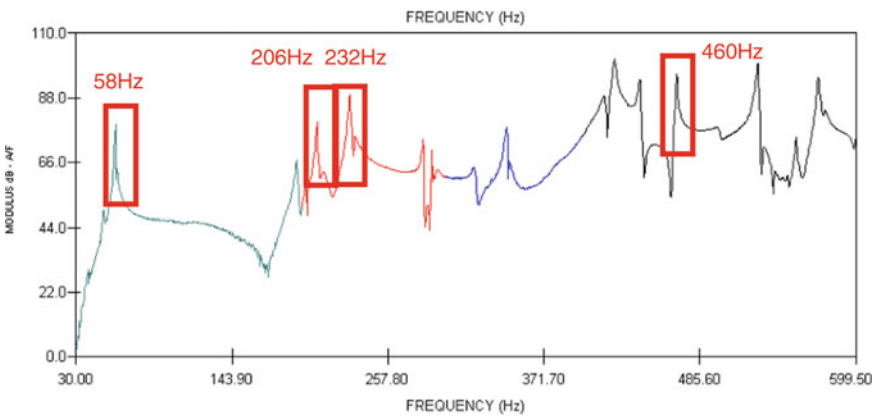

Fig. 2.6 Broad band excitation for resonance's selected

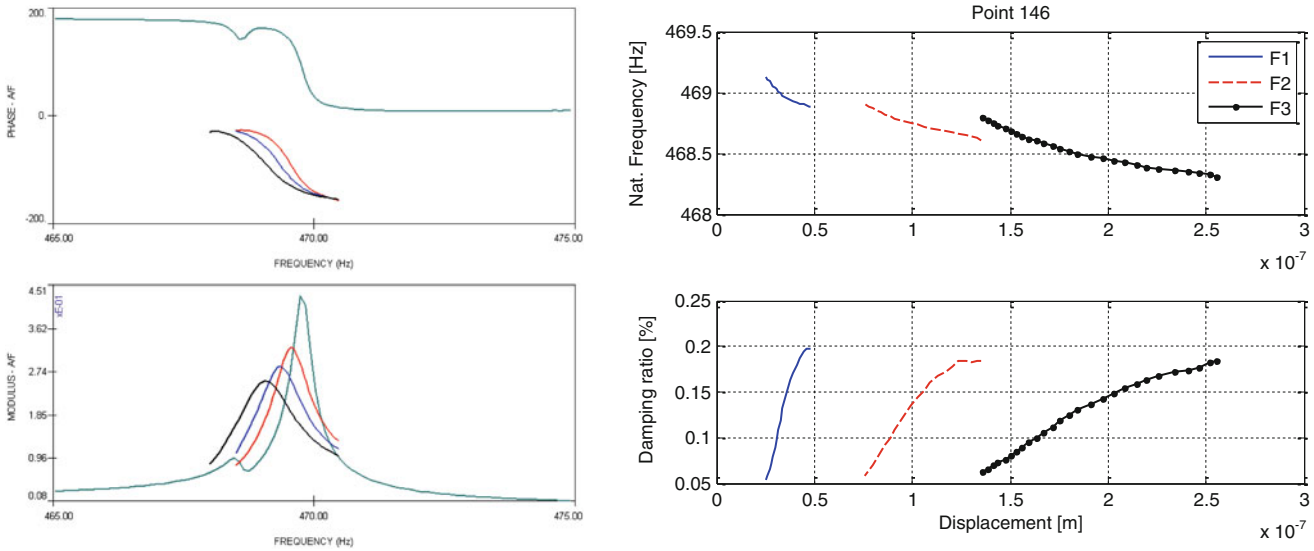

Fig. 2.7 Post-processing of FRFs using CONCERTO software

The non linear behaviour of the structure was confirmed by the frequency shift of the FRFs. Figure 2.7 shows the FRFs measured around 467 Hz when post processed by CONCERTO [4]. The plots show how the natural frequency varies with increased displacement, confirming the non linear behaviour of the assembly.

2.4.2 Importance of Vibration Settling Time

An important check before conducting a modal test is to assess the settling time of response, especially for lightly damped structures. The longer the settling time the longer the pause required before test measurement acquisition. Figure 2.8 shows a time history plot of all ten off accelerometers attached to the assembly for the excitation of the first of the resonances shown in Fig. 2.6. It is clear that a suitable time of 5 s might be required for vibrations to settle down for the casing assembly. Figure 2.9 shows the effect that having an incorrect settling time can have on the FRFs. Different structures can have very different settling times and so a preliminary check would be a sensible.

2.4.3 Final Test Setup and Preliminary Non-linear Testing

Following the initial assessment, it was decided to suspend the structure vertically. Despite the successful validation of the assembly model from test data obtained both vertically and horizontally supported, it was felt that the straps looping longitudinally along the assembly (when hung horizontally) was contributing significantly to the structural damping at the contact locations. Other suspension methods were considered, but none provided as much confidence when testing at larger amplitudes as hanging the assembly vertically suspended from the much stiffer CCOC. In addition, when a comparison of FRFs was made (using a reduced modal test) with the specimen supported both horizontally and vertically, they were found to be different, as shown in Fig. 2.10. The FRFs shown were both measured at position 146 with the excitation at position 25.

With the preliminary testing giving confidence that the assembly was exhibiting non linear behaviour, it was important to consider whether it would be possible to quickly identify which modes might respond more non-linearly than the others. The FMFEM mode shapes below 500 Hz were reviewed and a modal test carried out along a sector of the test assembly. The details of the test planning and FE model correlation are outlined in Sect. 2.2. As the bolted flanges were the most likely sources of non linearity those mode shapes with large deflections across the flange areas were considered first. For example the mode shape at 129 Hz (shown on the left-hand side of Fig. 2.11) responds locally around the unconstrained edge of the LPT whereas the mode shape at 202 Hz (shown on the right-hand side of Fig. 2.11) responds significantly across CCOC-HPIPT and HPIPT-LPT bolted flanges.

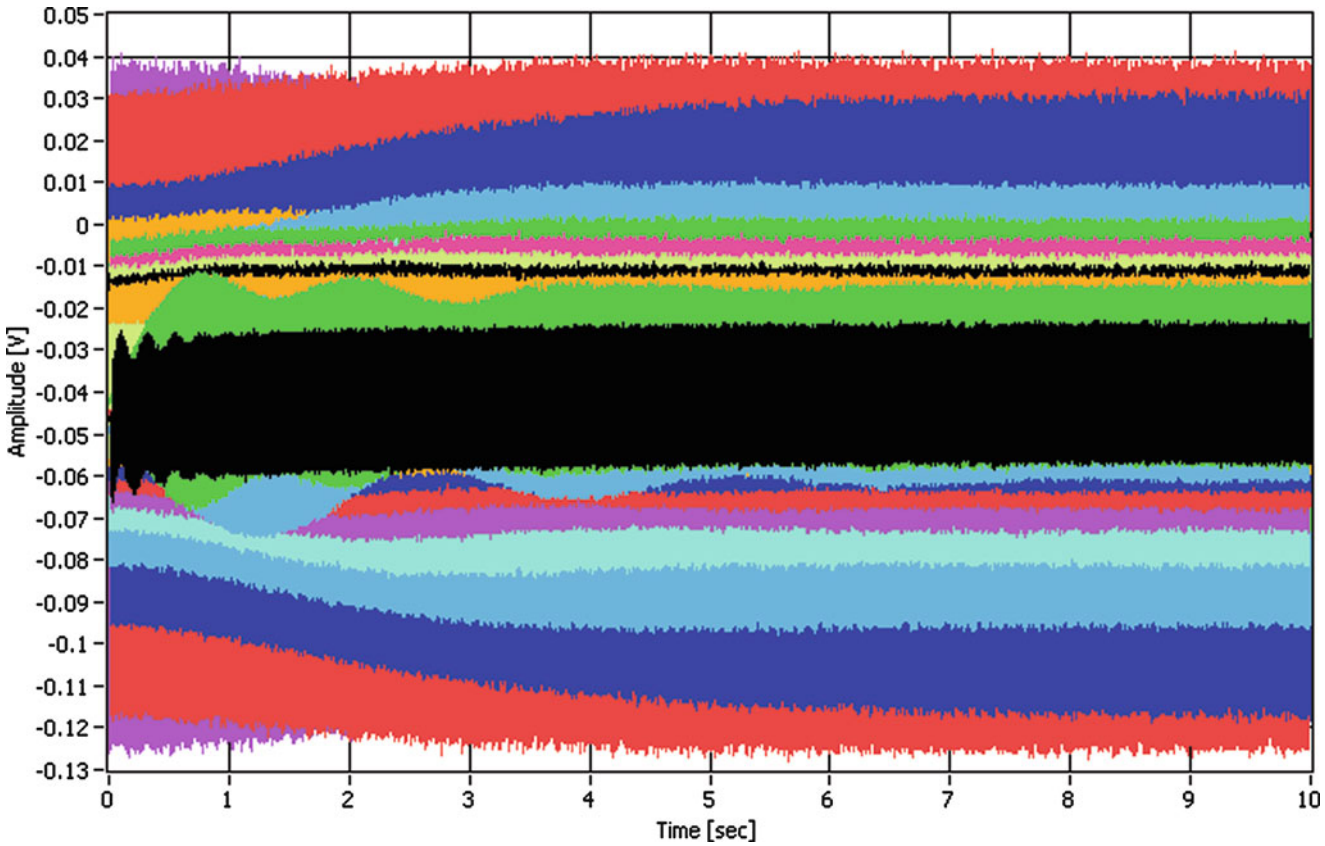

Fig. 2.8 Acquired time signal

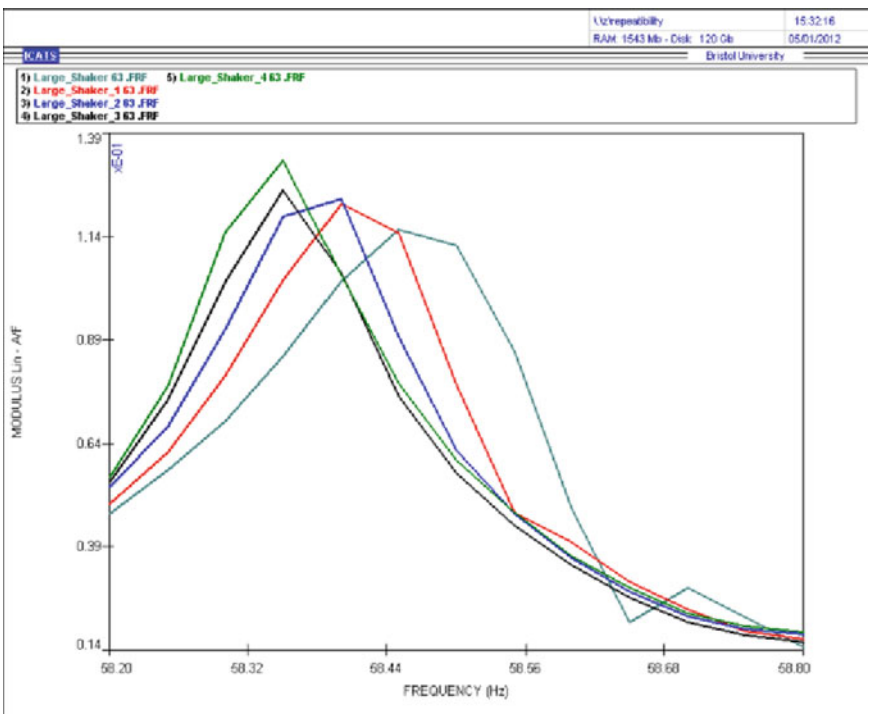

Fig. 2.9 Effect of incorrect settling time during testing

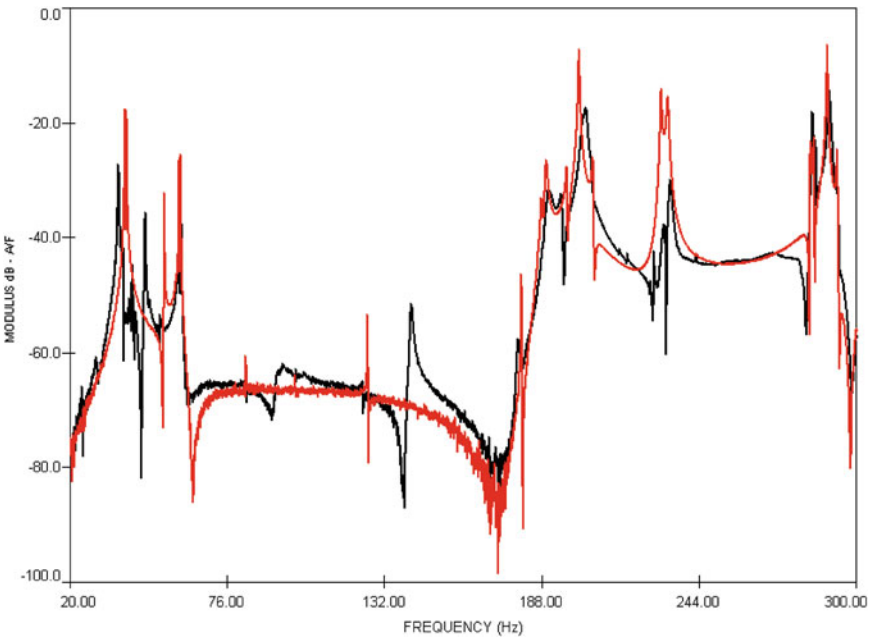

Fig. 2.10 Comparison of FRFs measured horizontally *(black)* and vertically *(red)* (color figure online)

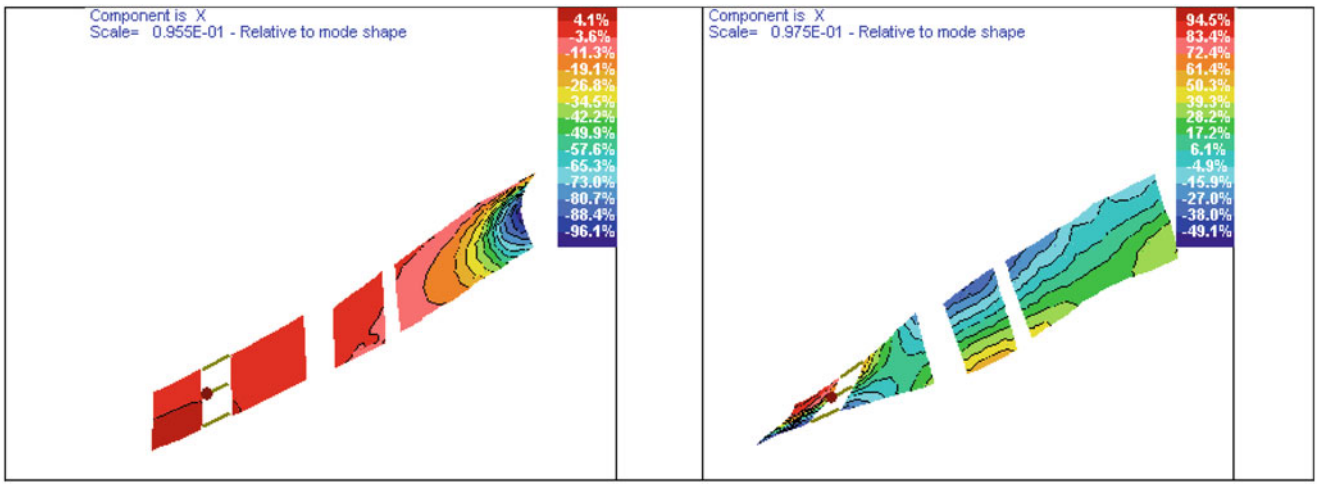

Fig. 2.11 Identification of resonances for non linear testing using mode shapes

This qualitative assessment of the resonances using mode shapes from experimental data (or FMFEM predictions if available) can help to quickly shortlist the resonances to be tested further. The validity of this approach was tested by measuring FRFs at low and high excitation levels and comparing modes which presented small and large frequency shifts. Figure 2.12 shows two FRFs measured using low and high excitation levels; measurements were again carried out without force control. Figures 2.13 and 2.14 show a zoom of the FRFs where Figs. 2.15 and 2.16 show the mode shapes, respectively. These examples have been chosen to demonstrate that mode shapes can be used as good indicators when selecting resonances for non linear testing. The mode shown in Fig. 2.15 looks more likely to exercise the flanges, and has a corresponding high frequency shift its FRFs (as shown in Fig. 2.13), than the far more local (to the LPT) mode shape of which has a correspondingly small change in the FRFs as shown in Fig. 2.14. The mode shapes of such casings can be extremely useful tools for identifying areas of such test structures which are likely to respond linearly. This approach was used to down select the resonances for further, higher amplitude, non linear testing.

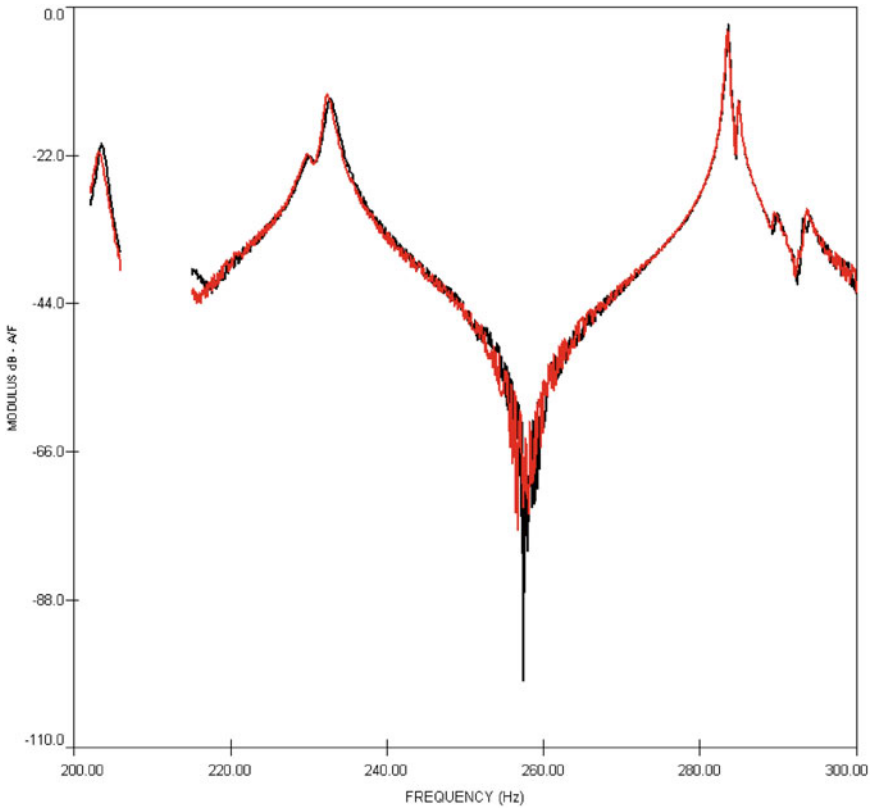

Fig. 2.12 FRFs obtained from *high* and *low* level of excitations; *red* and *black*, respectively (color figure online)

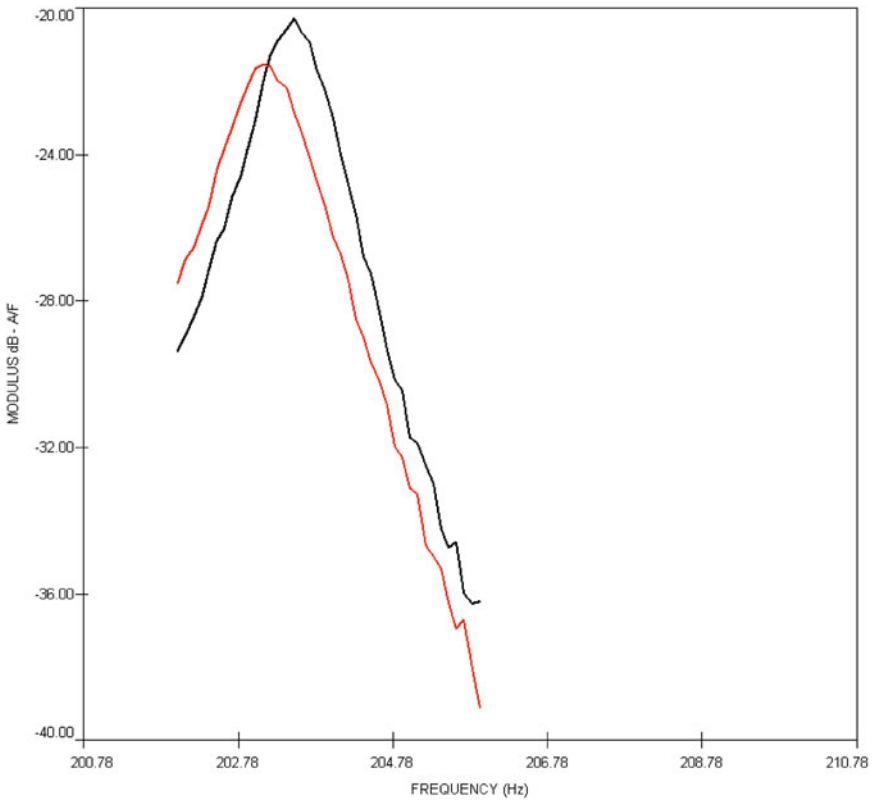

Fig. 2.13 FRFs (zoom) around 202 Hz

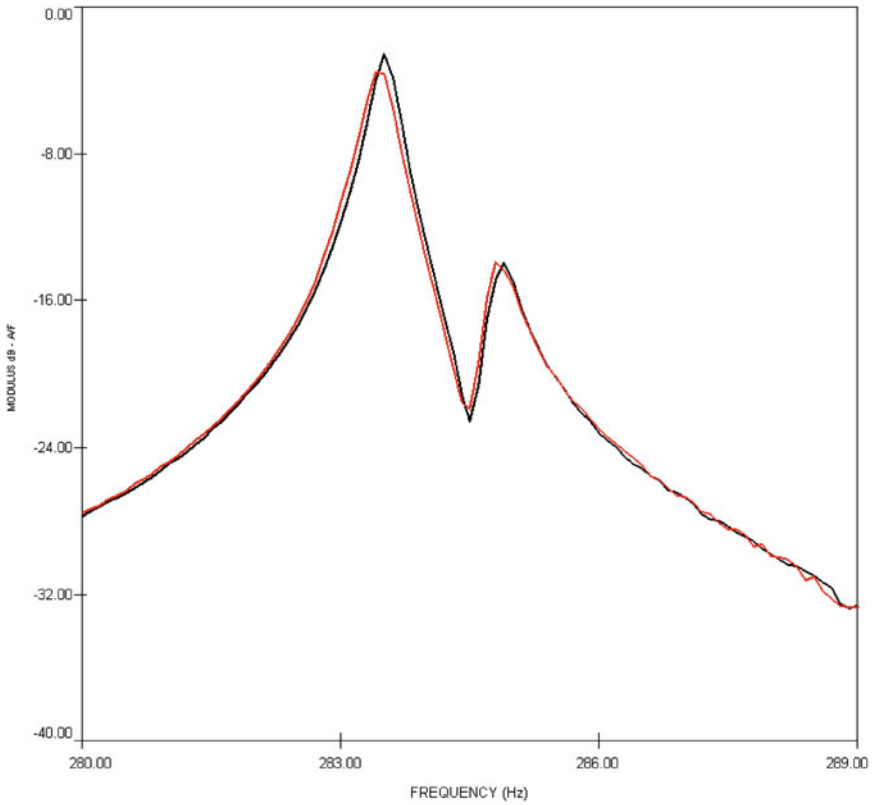

Fig. 2.14 FRFs (zoom) around 284 Hz

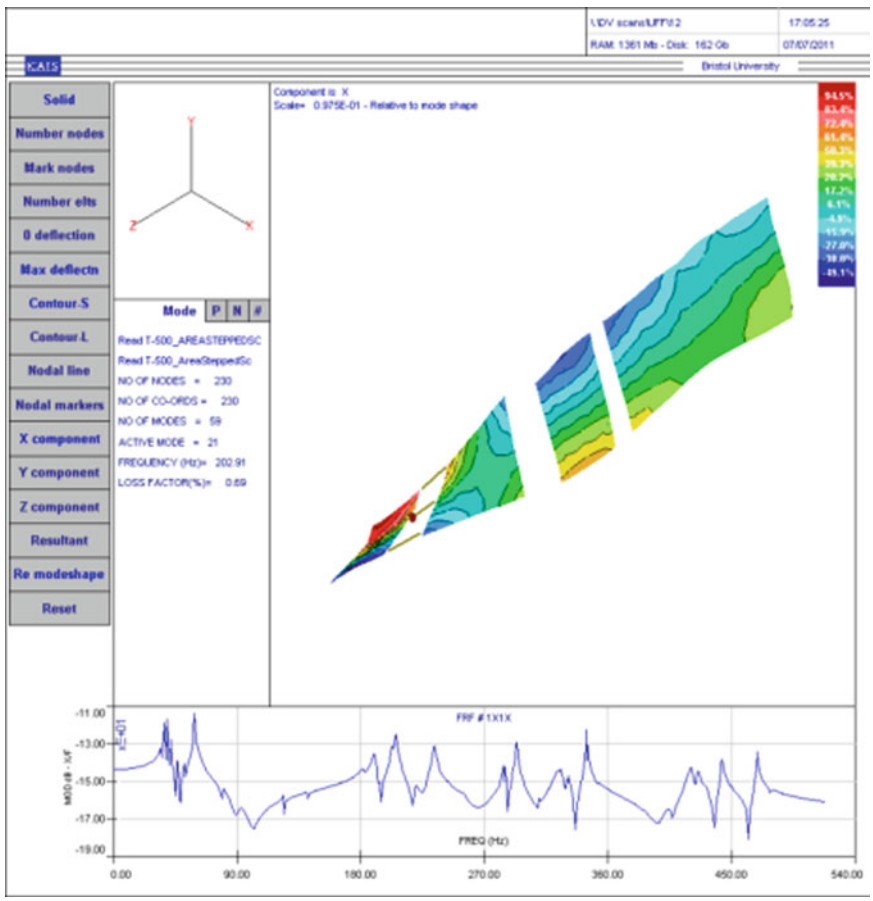

Fig. 2.15 Mode shape at 202.9 Hz

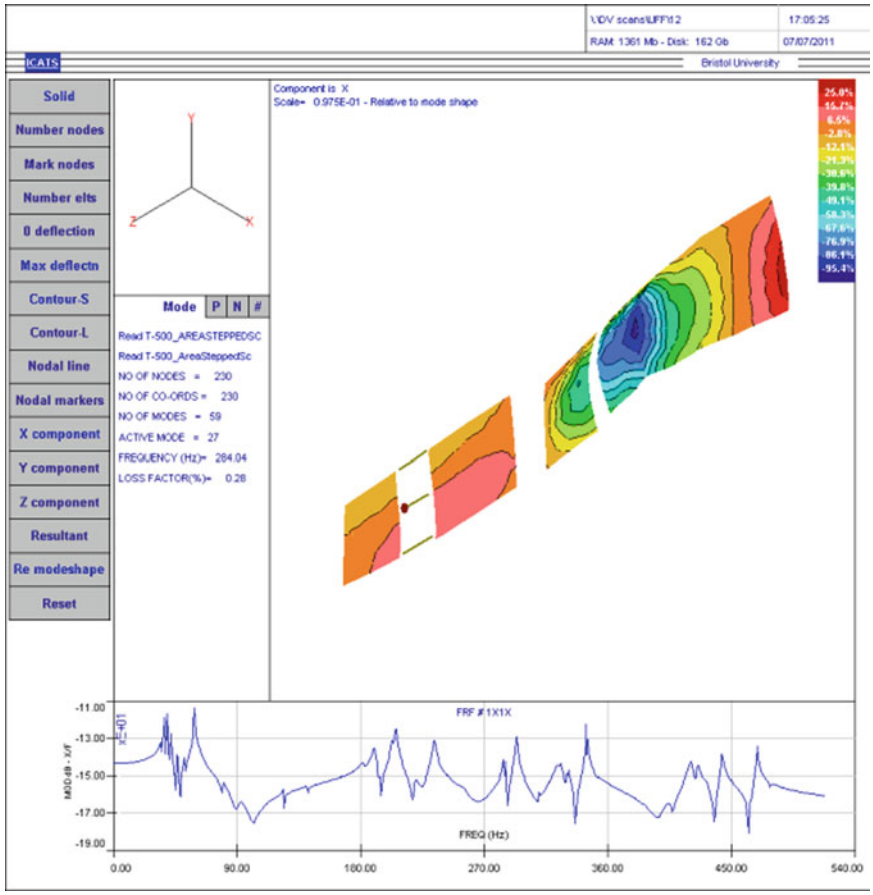

Fig. 2.16 Mode shape at 284 Hz

2.5 Non-linear Testing Method

This section aims to design guidance for conducting sensibly non linear modal testing. A schematic of the process used for the initial study of the non linear behaviour of the casing assembly has been shown in Fig. 2.17.

Having measured some non linearity from the casing assembly, it was decided to produce a test matrix so as to quantify more precisely which resonances would respond non-linearly at higher excitation levels. The test matrix was also designed to highlight more clearly the influence of excitation position. It was decided to use a commercially available system for carrying out the testing. The Dynamics laboratory of Blade (University of Bristol) has an LMS data acquisition system and this was used for the remainder of the work presented. The LMS system has several excitation options and the decision was made to use the stepped sine excitation with either (i) no force or amplitude control; (ii) force control or (iii) amplitude control. The third option is the only one which permits a subsequent linear modal analysis of the resulting FRFs. Using amplitude control, response at every frequency point is measured for a given acceleration level and the output FRFs are effectively linearised and so can be processed using existing linear modal analysis tools.

The test matrix covered:

(i) Two frequency bandwidths
(ii) Excitation of the test structure at six different positions; two points for each component
(iii) Excitation at three excitation levels using the force control method

and

(iv) Excitation at three acceleration levels using the amplitude control method.

When attaching the shaker to the CCOC casing (e.g. as in Figs. 2.18, 2.19, 2.20, 2.21, 2.22, and 2.23), care was taken to ensure that it was correctly aligned with the stinger rod. Misalignment of the shaker and its stinger rod can 'corrupt' the excitation and so compromise post-processing of the test data.

It was noticed that some measurement parameters specified in the test matrix were redundant. For example, initially three levels of excitation force had been chosen but it was later decided, to reduce the testing time, this could be lowered to just

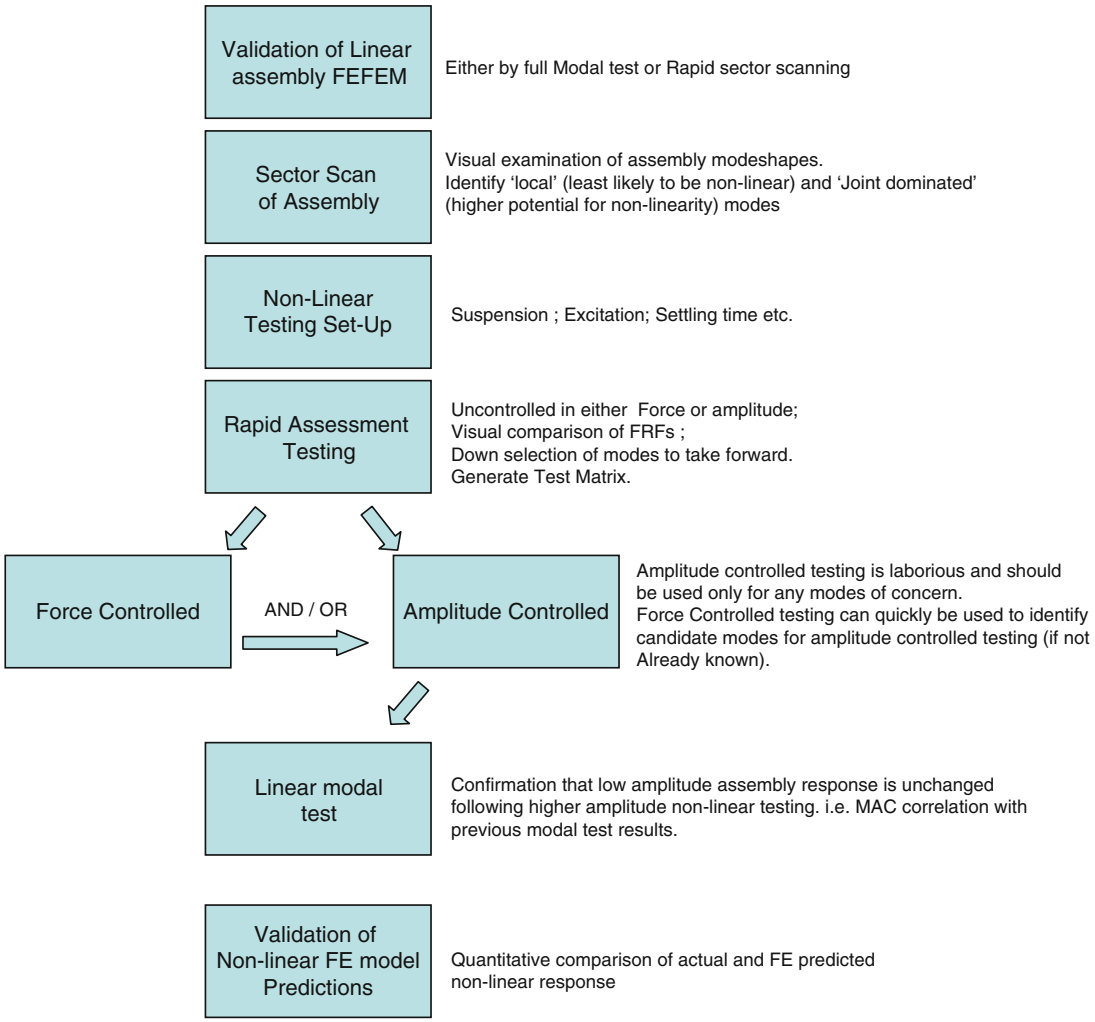

Fig. 2.17 Schematic process for non-linear behavior study

Fig. 2.18 Position 1

Fig. 2.19 Position 2

Fig. 2.20 Position 3

two. To assess any natural frequency shift of the test modes excitation levels of either 1 and 30 N, or 1 and 50 N were used. The lowest force level (i.e. 1 N) could always be achieved whereas the higher force levels could not always be achieved. It can be noted that FRFs measured for the lowest force levels looked, on occasion, quite noisy. This was a consequence of the poor Signal-To-Noise-Ratio (SNR) at low excitation levels and for future testing a minimum allowable SNR should be specified. For some modes the excitation levels of 50 N could also not be achieved either because the force control could not be maintained and/or of the power of the shaker was inadequate at that frequency. However, as this was intended to be an explorative approach, to be confirmed later by more rigorous testing using amplitude control; this was considered acceptable.

Measurements of FRFs for low (black) and high (red) excitation levels are presented in Fig. 2.24 for the response at the point 119. Measurement point 119 was chosen because of its proximity to the flange, as shown in Fig. 2.25, and thereby

Fig. 2.21 Position 4

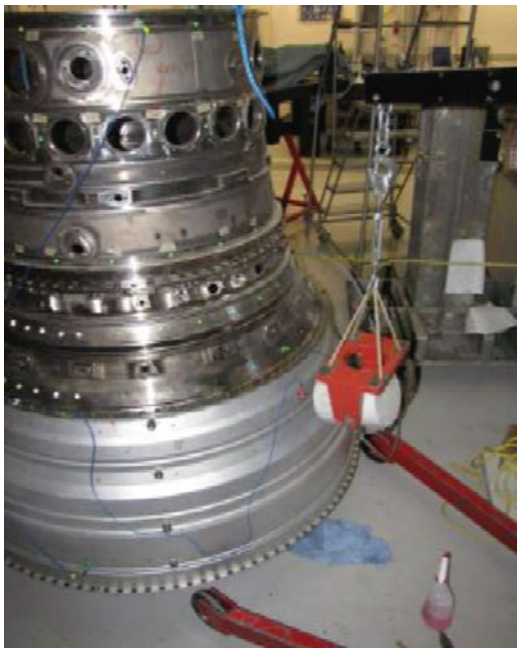

Fig. 2.22 Position 5

thought to be capable of capturing more non-linear effects than the other accelerometers. This point was also used as the reference when carrying out amplitude controlled measurements.

All modes selected exhibited a frequency shift with increased excitation force, due to the non-linear behaviour of the flange joints. The quantitative assessment of the non linearity of the target modes was carried out using amplitude control so as to be able to analyse FRFs using currently available linear modal analysis tools.

As stated above the accelerometer position for the amplitude controlled testing was measurement point 119. Only one position at the time can be used for amplitude control, as the response from the remaining nine off accelerometers will be uncontrolled. If required, amplitude control measurements could have been carried out individually for the other accelerometers positions taking each one in turn. However, due to time limitations this could not be done as it would have increased the required testing time nearly tenfold. Careful selection of which measurement point(s) to use for amplitude controlled testing is essential to avoid wasting the available, and usually highly limited, test time. Using of the preliminary (and much quicker) force controlled testing can act as a effective guide to avoid poor choices.

Fig. 2.23 Position 6

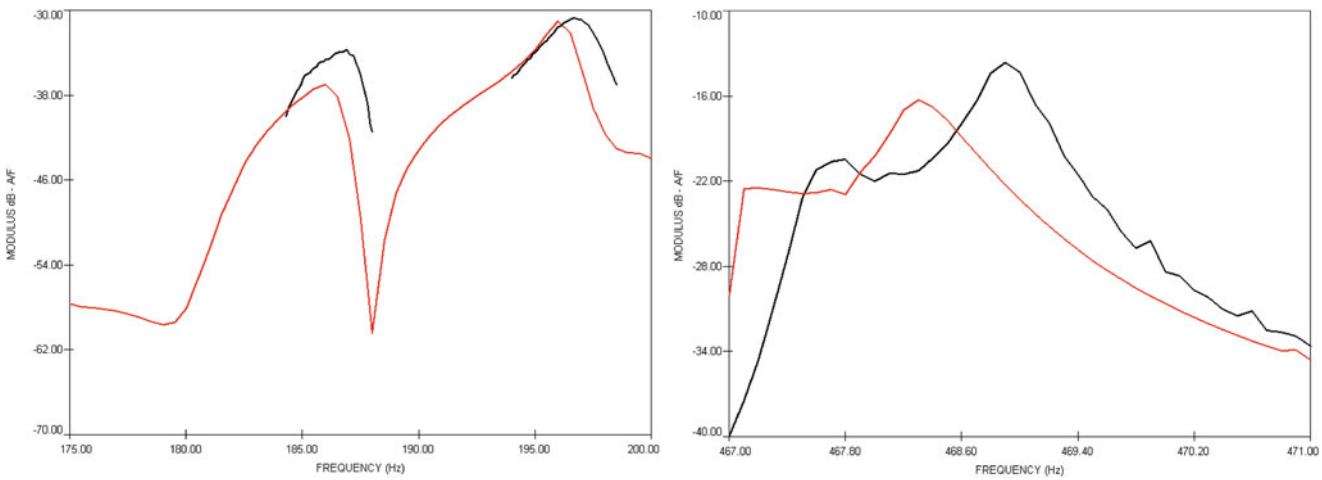

Fig. 2.24 FRFs measured at point 119 with different force levels, high in *red* and low in *black*, respectively. Excitation position 1 (color figure online)

Fig. 2.25 Response measurement point 119, *red box* (color figure online)

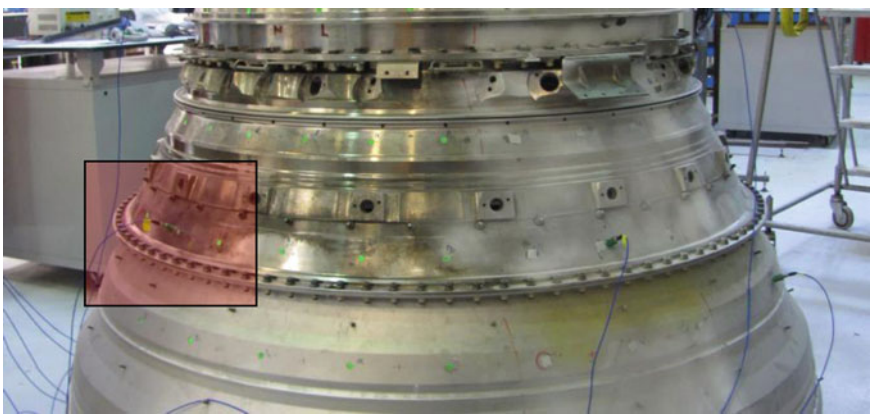

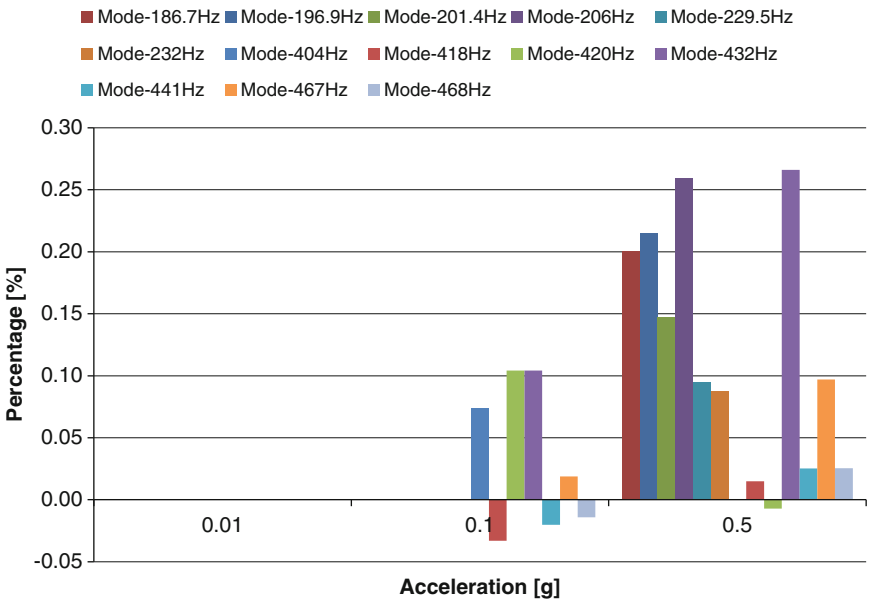

Fig. 2.26 Natural frequency shift with increased acceleration with excitation position 1 and response measurement at point 119

Figure 2.26 shows the observed frequency shifts (when compared with the linear modal analysis results) of the target resonances, for increasing levels of acceleration. FRF measurements were performed for most resonances at 0.01, 0.1 and 0.5 g. However, it can be seen that some resonances were not measured at 0.1 g. The aim of the post-processing was to be able to identify those resonances which were responding more non-linearly than the others. The modes at 186.7, 196.9, 206 and 432 Hz exhibited noticeable non-linear behaviour compared with the other modes. Although, the frequency shifts seen are quite small, such plots indicate which resonances are good candidates for higher amplitude testing.

2.5.1 Test Results for SILOET 2.3.2 Test Case

Completion of the test matrix produced some interesting results. The preliminary scoping performed using the force control method was able to identify the key resonances to be selected for amplitude control testing. The amplitude controlled testing focussed on achieving much higher levels of vibration in order to observe more consistent non linear behaviour of the structure. Based on the testing carried out it was decided to use excitation position 1 because of the higher quality test data that resulted. Positions 2–6 were discarded because

(i) Not all modes could be excited,

and

(ii) When modes were excited they did not present non linear behaviour.

Measurements were repeated for two modes (i) 194.6 Hz and (ii) 205.4 Hz. The first was not predicted by the FMFEM even though it was measured during both the VIVACE [1] and current SILOET testing of the fully assembled structure. Figure 2.27 shows a set of FRFs obtained during the linear modal analysis; the excitation position for the impact hammer was at point 134. The plot shows clearly the presence of a mode at approx. 194.6 Hz which was not predicted. The most likely explanation is that the FMFEM, which had a simplistic 'fully fixed' boundary conditions between the flange mating faces, could not correctly predict modes which have significant separation of the flange faces of the bolted test structure. Figures 2.28 and 2.29 present the mode shape in the plane Z-X and Y-X, respectively. Table 2.1 showed that there are other mode pairs (7, 9 and 10) for which the FMFEM poorly predicted the assembly frequencies, again strongly suggesting that, although quick, there is a need to replace the overly stiff 'fully fixed' representation of the bolting with something more detailed. Figures2.30 and 2.31 show mode shapes measured at 194.6 and 205.4 Hz, respectively, using SLDV measurement method.

Mode at 194.6 Hz was tested up to nine excitation levels, 0.1, 0.5, 1, 1.5, 2, 3, 4, 4.5 and 5 g, respectively. Mode at 205.4 Hz was tested using excitation levels of 0.1, 1, 2, 3, 5, 7, 9 and 11 g, respectively. Modal analysis was performed for calculating natural frequencies and damping loss factors, as shown in Figs. 2.32 and 2.33, respectively. It is of interest that

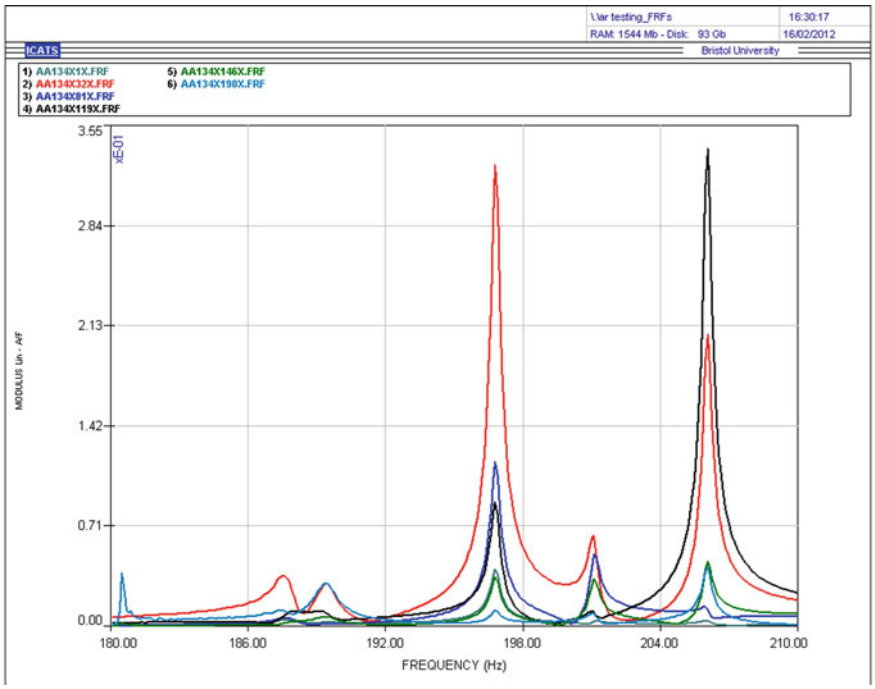

Fig. 2.27 FRFs measured with impact hammer (excitation point-134) response at points 32 *(top red)*, 1, 81, 119, 146 and 190, respectively (color figure online)

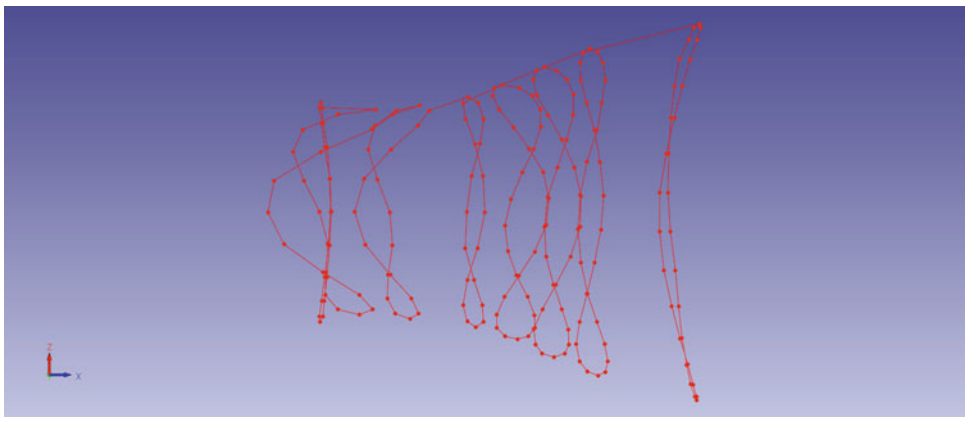

Fig. 2.28 Mode of vibration at 196 Hz (plane Z-X)

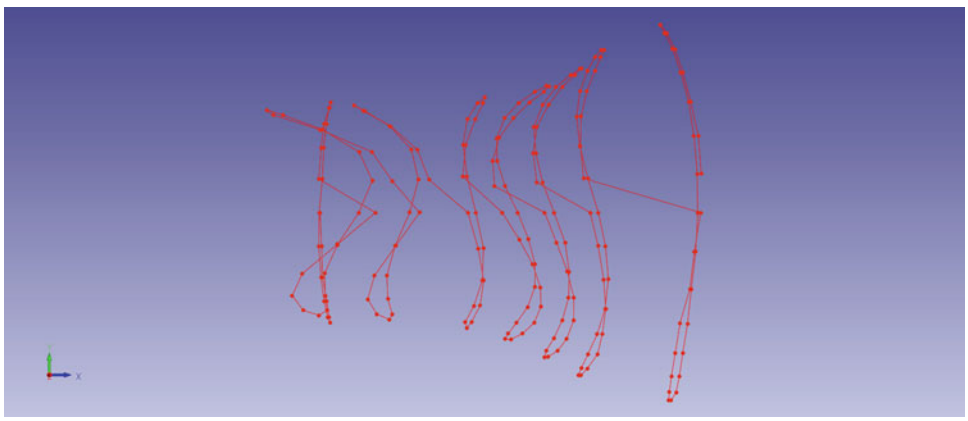

Fig. 2.29 Mode of vibration at 196 Hz (plane Y-X)

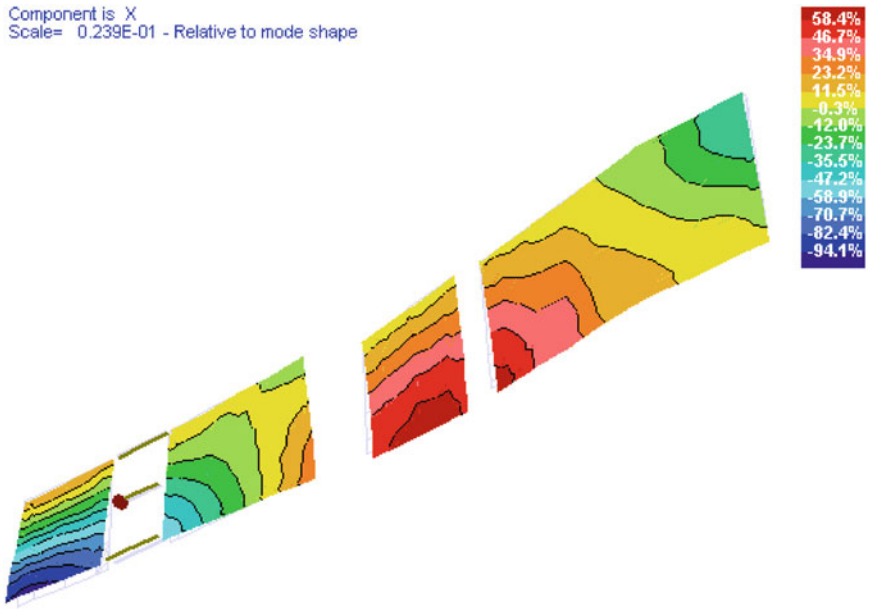

Fig. 2.30 Measured mode at 194.6 Hz using sector scanning SLDV measurement method

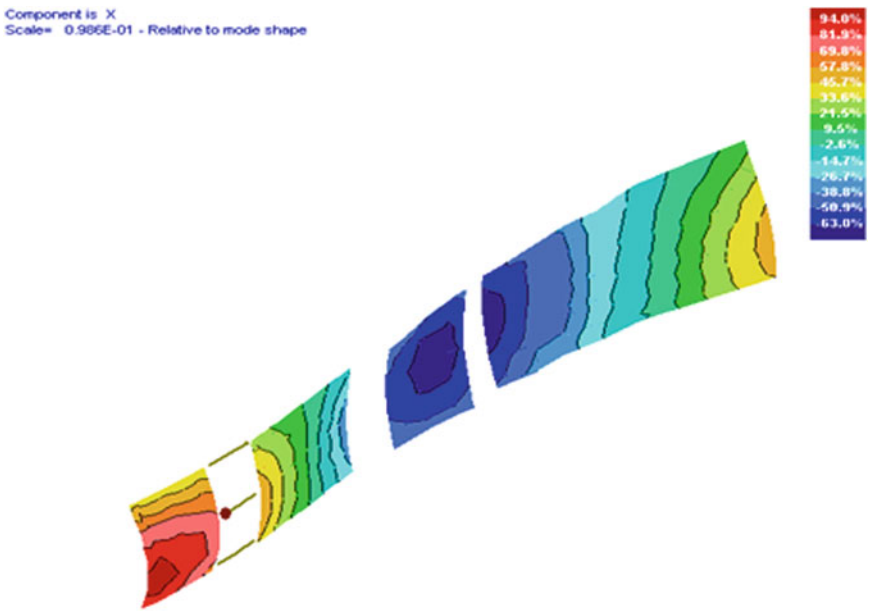

Fig. 2.31 Measured mode at 205.4 Hz using sector scanning SLDV measurement method

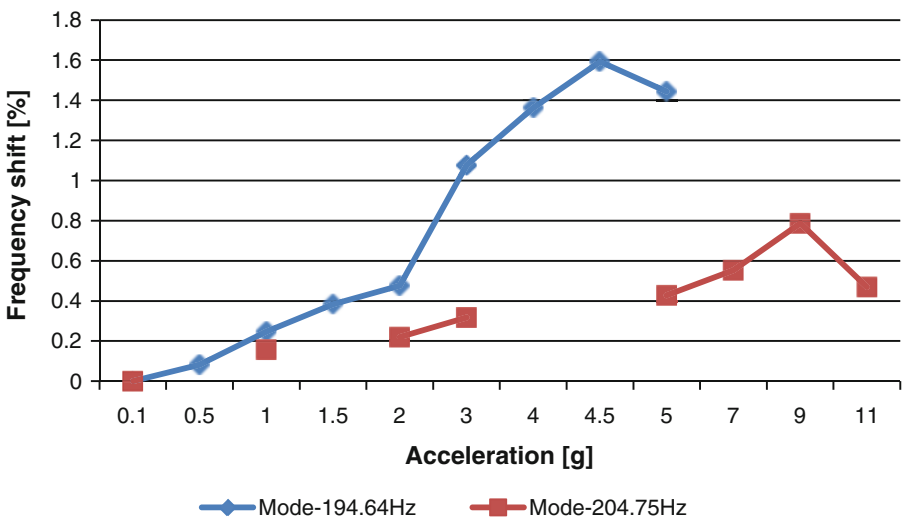

Fig. 2.32 Comparison of frequency shifts at different vibration levels

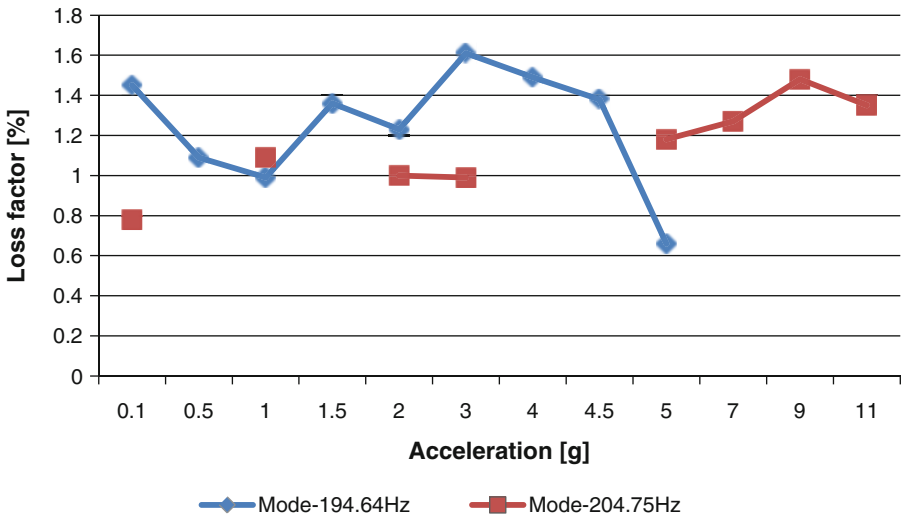

Fig. 2.33 Comparison of loss factors at different vibration levels

both frequency shift plots show a drop for the last measurement that is 5 and 11 g, respectively. These two FRFs present a quite flat shape and it is possible that either the modal analysis was not very accurate because the small number of frequency point for the curve fitting or response behaviour of the flanges not fully captured at these vibration levels with FRFs. Such experiments are at the limit of the commercial software's capability. The results at 5 and 11 g should be treated with caution until they have been confirmed by additional testing.

The results presented here tend to confirm that the approach of Fig. 2.17 for performing non linear modal testing is valid. The initial selection of modes using either FMFEM or experimental mode shapes helped to quickly shortlist the resonances for the modal testing. Screening these modes using the force control method helped to quickly identify the resonances to consider for the amplitude control testing. Finally, the FRFs measured using amplitude control helped confirm the resonances whose non linear behaviour should be studied in greater detail.

While it is clear that FMFEMs are capable of predicting modes of single components and also of sub-assemblies, they can omit or miscalculate those resonances which exhibit strong non linearity.

2.6 Conclusions

A set of criteria have been listed so as to give guidance for non linear testing of large casing assemblies. It is important to perform test planning using the FEM so as to identify the best excitation positions for EM shaker. The experimental work with a civil aircraft engine casing has shown that some of the positions chosen for exciting the structure were not optimal because some modes could not be excited either sufficiently, or at all. There are no additional precautions in suspending the test structure than the ones already applied for linear testing.

The alignment of shaker and stinger rod must be very accurate. This becomes even more important as the levels of excitation are far higher than those of linear testing. Any misalignment between shaker-stinger-load cell will introduce unnecessary errors.

The settling time must be estimated correctly before trials are started. It was shown that an incorrect choice of settling time can lead to misinterpretation of the acquired FRFs. This can be a simple as acquiring the time history data from the test structure for a single impact where the time taken for the vibrations to decay would make a suitable settling time.

The use of mode shapes obtained either from FE models or from modal analysis performed with SLDV measurement method on sector(s) of a specimen is very beneficial for identification of resonances. All mode shapes presenting large levels of vibrations in the areas of, for example, bolted flanges can be confidently selected for the next measurement phase.

Quick measurements made at low and high excitation levels, but without controlling the excitation force, can highlight signs of non linear behaviours in the test structure. Although only a qualitative assessment it is still very helpful in the early stages of testing.

Measurement of FRFs using the force control method can be carried out for the selected modes. Two excitation levels, one low and one high, is usually enough to identify those modes with the highest frequency shifts due to non linearity.

All accelerometers included in the test planning for the linear modal analysis should be used for the force control measurement method. The analysis of all measured FRFs can help to identify those resonances responding more non-linearly than the others and so help to select a smaller number for subsequent amplitude control measurements. This will also help identify the best measurement positions for conducting an amplitude control.

The final phase of non linear modal testing is the measurement of FRFs using amplitude control. This technique is time consuming and so it is advisable to use it only for those modes which are definitely thought to be non linear. The FRFs resulting from amplitude controlled testing can be post-processed using currently available linear modal analysis tools.

Non linear behaviour was observed and measured for a mode which presents a strong out of plane vibration of the flanges.

Acknowledgements We would like to acknowledge Rolls-Royce for having supported this research work.

References

1. Garcia J (2008) Development of valid models for structural dynamic analysis. PhD thesis, Imperial College London
2. FEMtools v3.3. Dynamic design solutions. www.femtools.com
3. ICATS, modal analysis software, ICON Suite, 58 Prince's Gate Exhibition Road, London SW7 2PG
4. A. Carrella, D. J. Ewins, Identifying and quantifying structural nonlinearities in engineering applications from measured frequency response functions. Mech Syst Signal Process. doi:10.1016/j.ymssp.2010.09.011

Chapter 3
Nonlinear Dynamic Analysis of a Track Bridge Structure Designed for a Floating Bridge

H. Sedarat, A. Kozak, I. Talebinejad, V. Jacob, A. Krimotat, T. Cooper, J. Sleavin, and P. Cornish

Abstract The addition of Light Rail Trains (LRT) to the Homer M. Hadley Memorial Bridge, the widest floating bridge in the world located in Seattle, Washington, is currently in its design process. The design team has concluded that a transition Track Bridge (TB) is necessary to accommodate large movements induced by the floating bridge in relation to the fixed approach structures and to provide reliable LRT service along the I-90 corridor. Dynamic train-structure interaction analysis was required to evaluate the TB performance and ride quality. A high fidelity finite element model of the bridge was developed along with two TBs. Each TB has been designed with 34 double-concave Friction Pendulum Bearings (FPBs) supporting bearer bars at both ends. The FPB model includes bottom and top plates and a slider in between, all modeled with solid elements. Simulation of frictional contact interaction between the plates and slider allows limited transverse movement of the rail under moving train loads. In addition to numerical analysis, component and full scale tests have been planned to examine the TB kinematics as well as FPB behavior. This paper presents a unique multi-scale FE analysis of a train-structure interaction system which includes detailed model of TBs incorporated in the global model of the floating bridge.

Keywords Dynamic analysis • Floating bridge • Light rail train • Track bridge system • Friction pendulum bearing

3.1 Introduction

The Homer M. Hadley Memorial Bridge is the widest and fifth-longest floating bridge in the world owned and operated by the Washington State Department of Transportation (WSDOT). It carries westbound and reversible lanes of Interstate 90 between Seattle and Mercer Island, Washington. The entire bridge structure spanning approximately 5,700 ft (1,737 m) includes concrete box girder approach spans supported by deep foundations, a floating span supported by pontoons and transition spans connecting approach and floating spans [1] (Fig. 3.1).

As a part of the programmed light rail extension referred to as the East Link Project, Sound Transit (ST) proposes to install Light Rail Transit (LRT) tracks on the I-90 floating bridge. The placement of light rail across the floating bridge, with no precedent in the civil engineering practice, presents unique challenges including the design of a Track Bridge (TB) system to accommodate multidimensional movements at the existing expansion joints where transition span is connected to approach and floating spans. The purpose of TB is to support the rails under Light Rail Vehicle (LRV) loading while allowing the imposed deflections due to floating bridge movements to be distributed over a sufficiently long length of track to satisfy the rail profile requirements. Figure 3.2 shows two track bridges: the exterior one on the left side connecting approach span to the transition span and the interior one on the right side connecting transition span to the floating span.

Given the importance of the existing floating bridge and complex design of the TB system, detailed nonlinear finite element analysis was required to provide validation of the TB design prior to full-scale testing and prior to its installation

H. Sedarat • A. Kozak • I. Talebinejad (✉) • V. Jacob • A. Krimotat
SC Solutions Inc., Sunnyvale, CA, USA
e-mail: hassan@scsolutions.com; italebinejad@scsolutions.com

T. Cooper
Parsons Brinckerhoff, New York, NY, USA

J. Sleavin • P. Cornish
Sound Transit, St, Seattle, WA, USA

G. Kerschen et al. (eds.), *Topics in Nonlinear Dynamics, Volume 1: Proceedings of the 31st IMAC, A Conference on Structural Dynamics, 2013*, Conference Proceedings of the Society for Experimental Mechanics Series 35,
DOI 10.1007/978-1-4614-6570-6_3,

Fig. 3.1 The twin spans of the Homer M. Hadley Memorial Bridge *(left)* and the Lacey V. Murrow Memorial Bridge *(right)*, looking east toward Mercer Island (Courtesy of Sound Transit)

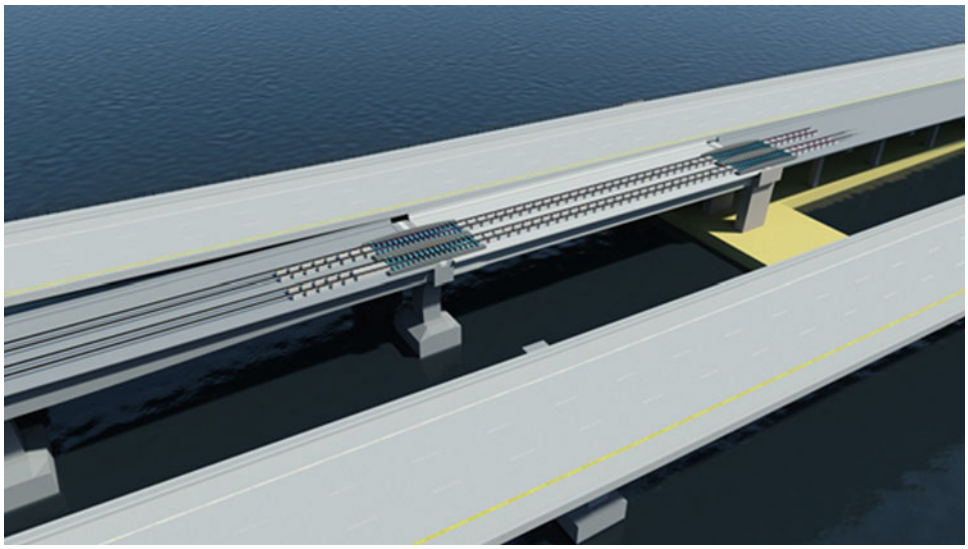

Fig. 3.2 Exterior track bridge *(left)* and interior track bridge *(right)* – (Courtesy of Parsons Brinckerhoff)

on the I-90 structure. This paper describes development, testing, and execution of a high-fidelity finite element model of the bridge along with two TBs. The LRV train was separately modeled as a coupled system with rail, which includes the stiffness of the fasteners as well as dynamic characteristics of the vehicle. The bridge model was analyzed for a set of loading scenarios including different storm conditions and train speeds. Rail stresses, bearer bar movements and TB stress contours were extracted from the model to evaluate the structural performance. A profile time-history of the rail was also an output; through an iterative process with other team members, this information was used to evaluate the internal response of the LRV's as they passed over the TBs. It should be mentioned that the main focus of this paper is on the finite element modeling and performance of the TB under storm condition and train loading. However, a brief explanation on finite element modeling of the floating bridge and LRV train is also presented in the following section.

3.2 Finite Element Model of the Bridge and LRV Train

A detailed three dimensional model of the bridge containing all the structural components of the bridge was developed using ADINA software [2]. This model includes approach, transition and floating spans of the west side of the bridge with total length of 2,100 ft (640 m). The as-built drawings of SR 90 3rd Lake Washington Floating Bridge, Approaches and Transition

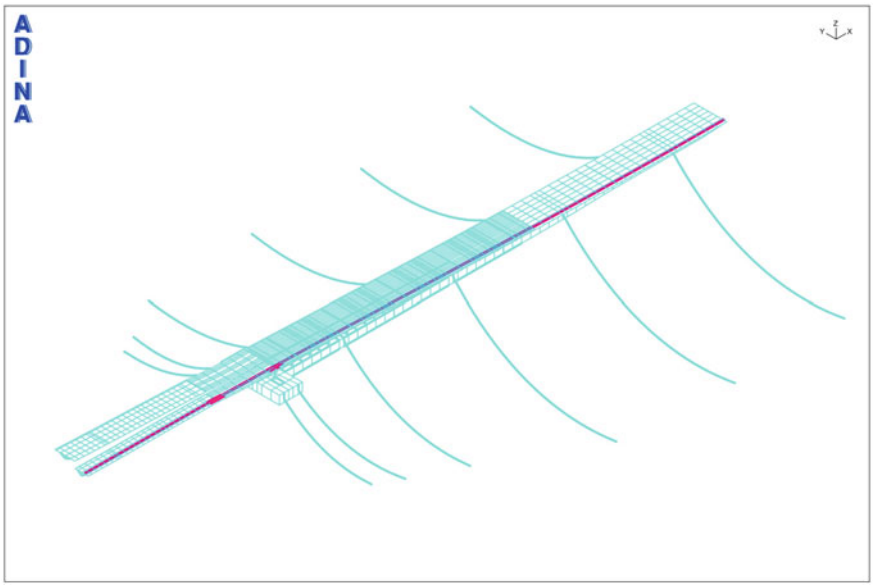

Fig. 3.3 Isometric view of the FE model of the bridge

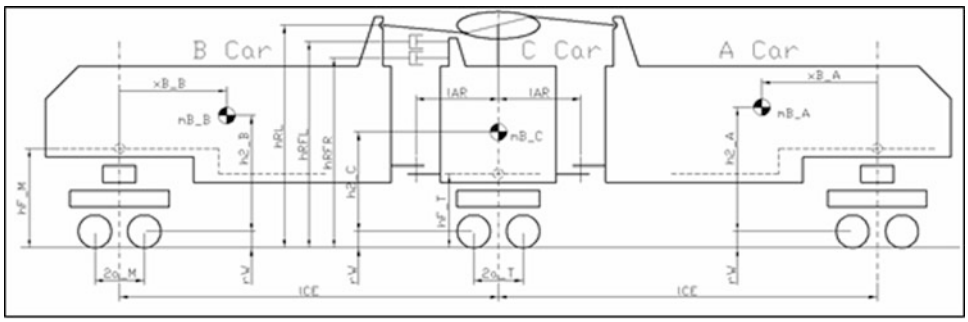

Fig. 3.4 Different components of the LRV train

Spans were used to generate a detailed three-dimensional model of the floating bridge. The transition span is seated on pile foundations while the floating span is supported by pontoons. The transition spans connect the approach and floating spans. An isometric view of the bridge model including two TBs is shown in Fig. 3.3.

Pontoons were modeled explicitly using elastic shell elements. The floatation was provided by a set of nonlinear springs to simulate variable buoyancy forces due to water. The cable anchors, connecting pontoons to the bottom of Lake Washington, were modeled explicitly using beam elements. All piers connecting deck to the pontoons were modeled with linear elastic beam elements. The slabs were modeled using eight-noded shell elements with linear elastic material properties. The FE models of two TBs were inserted in a detailed model of the I-90 Bridge (TBs are shown in red in Fig. 3.3). Detail description on finite element modeling of the TB is presented later.

A dynamic model of the LRV train was developed based on the information obtained from the manufacturer (KINKISHARYO International, LLC) and confirmed/ modified through independent physical testing of the vehicle suspension system. The train schematic shown in Fig. 3.4 is a three-section passenger vehicle with articulation joints between the bodies. The primary suspension system of the train model includes a set of springs representing longitudinal, vertical, and lateral stiffness as well as damping characteristics of the system. The secondary suspension system of the LRV is an air suspension consisting of airbags and air reservoirs which was simulated by nonlinear springs and dashpots to include the effects of damping due to air flow in the orifices between the reservoirs and airbags. The finite element model of the vehicle is shown in Fig. 3.5. All components of the train including train body, bolsters, bogies, axle, axle boxes and wheels were modeled explicitly.

Parametric loading cases were defined as shown in Table 3.1. Each case includes a combination of bridge movements due to storm condition (pitch, yaw and roll) along with a LRV train passing over the bridge. These parametric loading conditions provide an envelope of environmental conditions the bridge is expected to experience. Roll represents the rotation of the floating span about longitudinal x-axis, while yaw and pitch are the rotations about vertical z-axis and transverse y-axis respectively.

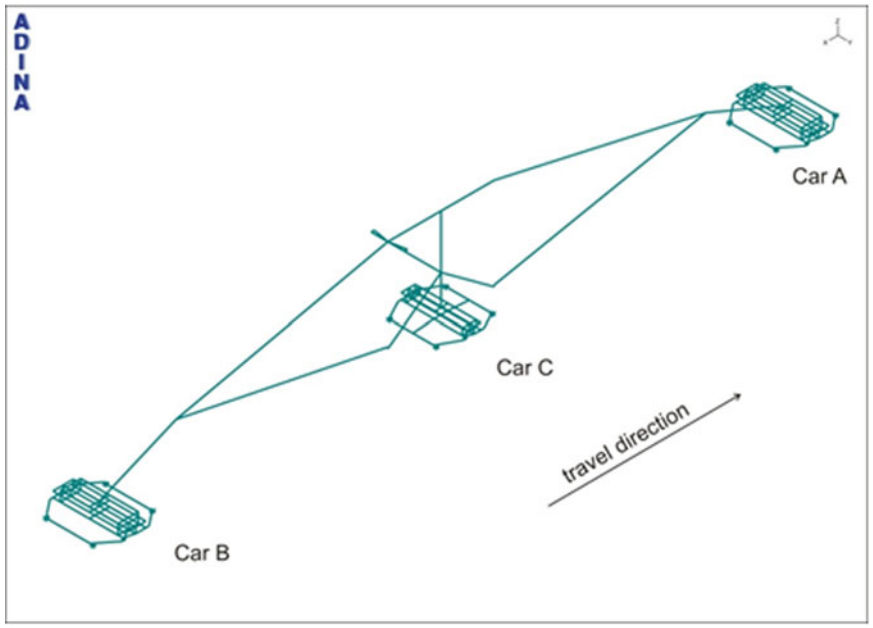

Fig. 3.5 Vehicle dynamic model

Table 3.1 Different loading scenarios

	Speed (MPH)	Pitch (○)	Yaw (○)	Roll (○)
Case 0 (neutral)	55	0.0	0.0	0.0
Case 1 (service)	55	0.5 down	0.0	0.0
Case 2 (service)	55	0.5 down	0.1	0.0
Case 3 (service)	55	0.5 down	0.0	0.7
Case 5 (service)	55	0.5 down	0.1	0.7
Case 9a (restricted)	55	1.0 down	0.5	1.0
Case 9b (restricted)	40	1.0 down	0.5	1.0
Case 9c (restricted)	20	1.0 down	0.5	1.0

3.3 Finite Element Model of the Track Bridge

The LRT system includes TBs, running rails and guard rails. TB has different components as shown in Fig. 3.6. Each TB is connected to the bridge deck through six (6) supports. For both exterior and interior TBs, supports on the transition span are free to move in longitudinal direction and fixed in transverse and vertical directions. Supports on the floating span (for interior TB) and approach span (for exterior TB) are fixed for all translational movements. Center bearings are only fixed in vertical direction and free in transverse and longitudinal directions. All the supports are free to rotate. A detailed three-dimensional FE model of a TB including wings, edge beams, vertical stiffeners, bearer bars and 34 double-concave Friction Pendulum Bearings (FPBs) was developed in ADINA (Fig. 3.7). Material properties for the TB components (rails, fasteners, etc.) are based on the Basis of Design Report (BODR) [3].

Rails modeled with elastic beam elements are supported by vertical, transverse and longitudinal nonlinear springs representing fastener properties. Wings were modeled with eight-noded shell elements with elastic properties. The wing has a trapezoidal shape, with minimum width of 21 in. (53.34 cm) and a maximum width equal to 56 in. (142.24 cm). Edge beams were modeled with eight-noded shell elements with elastic properties. Vertical stiffeners modeled with eight-noded shell elements are located under each bearing. Bearer bars were linear elastic beam elements supporting rail and guard rails and are sitting on a FPB at each end. These bearings are positioned on a curve which has a radius of 140 ft (42.67 m). The purpose of FPB is to provide limited transverse movement of the rails under train loading and to center bearer bars after the train is passed over the TB. Figure 3.8 shows components of a FPB including two concave plates on top and bottom and a slider in between. The slider flanges move within the slots of the plates. While the slider is free to move in transverse direction, its vertical and longitudinal movements are limited.

Figure 3.9 shows the finite element model of a FPB. The FPB model includes the bottom and top plates and slider, all modeled with solid elements. The slots are modeled with shell elements with spherical surfaces that match those of the top and bottom plates. Each shell is connected to the corresponding plate and moves together with the plate as a rigid body.

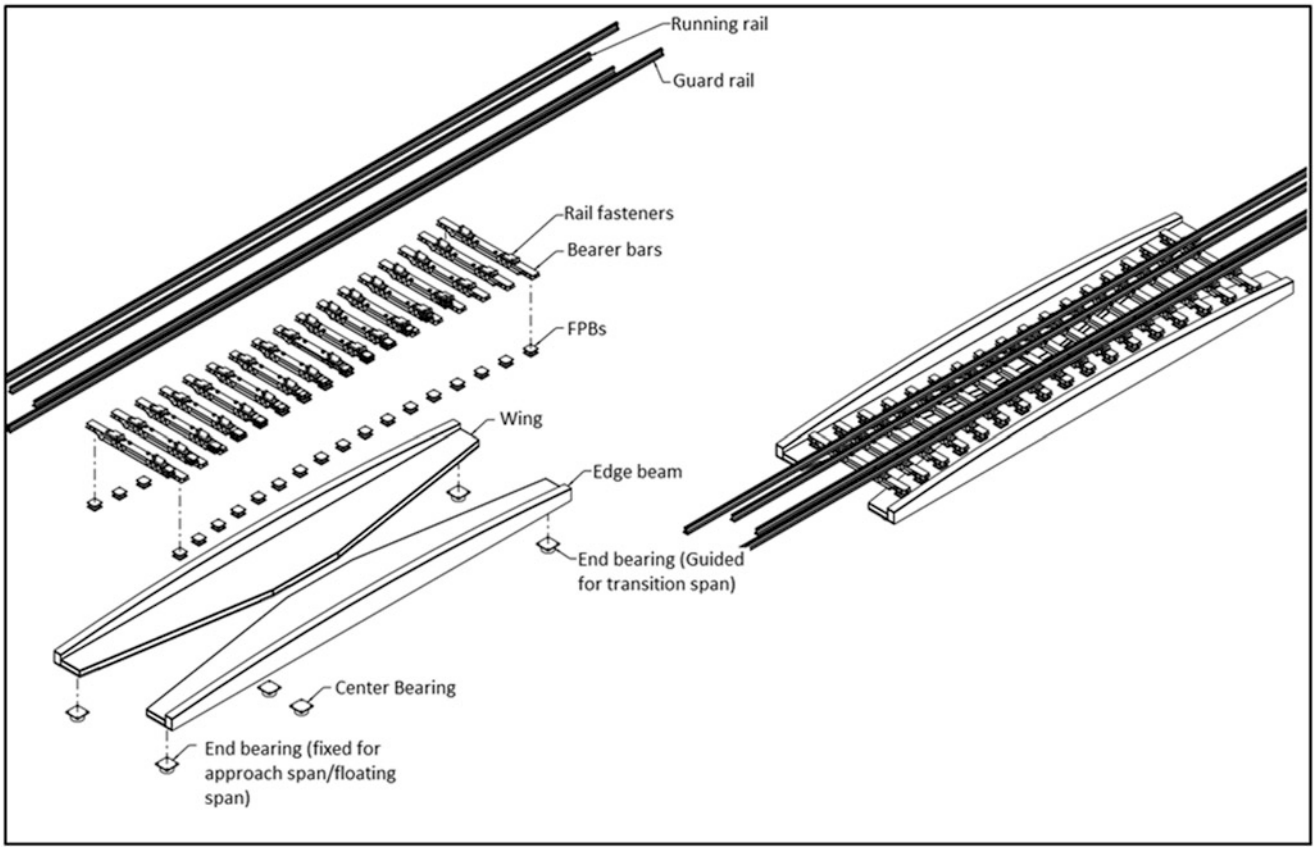

Fig. 3.6 Track bridge components (Courtesy of Parsons Brinckerhoff)

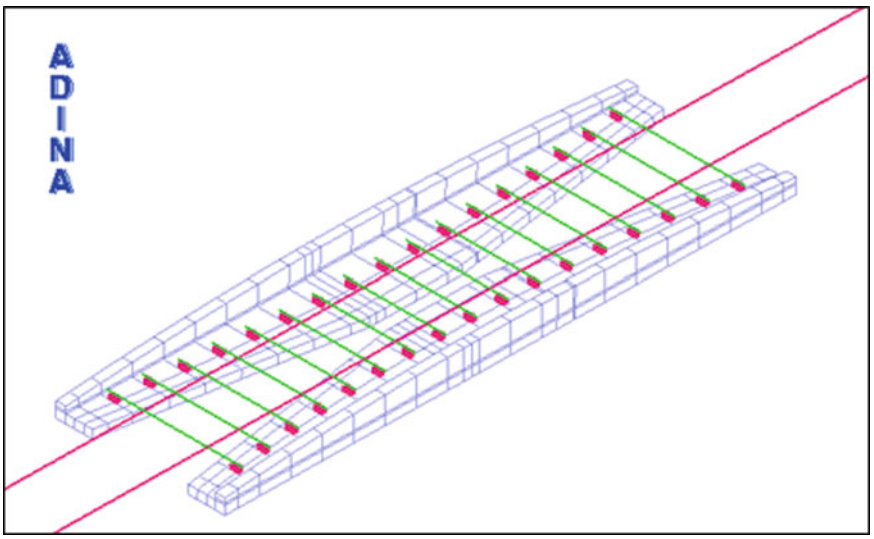

Fig. 3.7 Finite element model of the track bridge

This model provides a mechanism that prevents excessive uplift. Figure 3.9 shows each of the components separately with the four contact surfaces as described below:

- Contact 1 is between the bottom plate and bottom of the slider.
- Contact 2 is between the top plate and top of the slider.
- Contact 3 is between the upward side of the slider bottom flange and the bottom plate slot.
- Contact 4 is between the downward side of the slider top flange and the top plate slot.

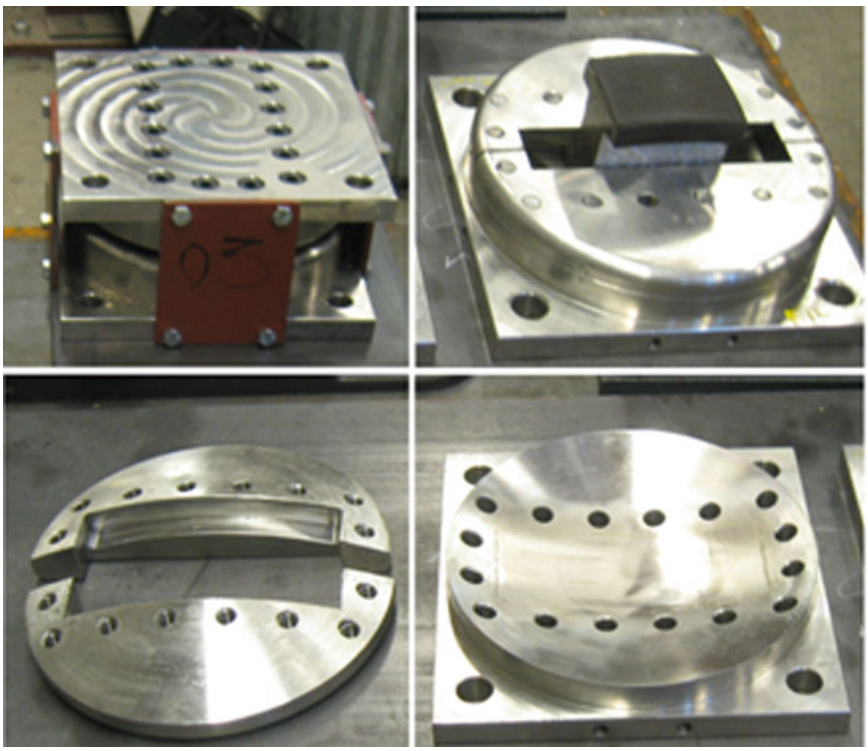

Fig. 3.8 Friction pendulum bearing

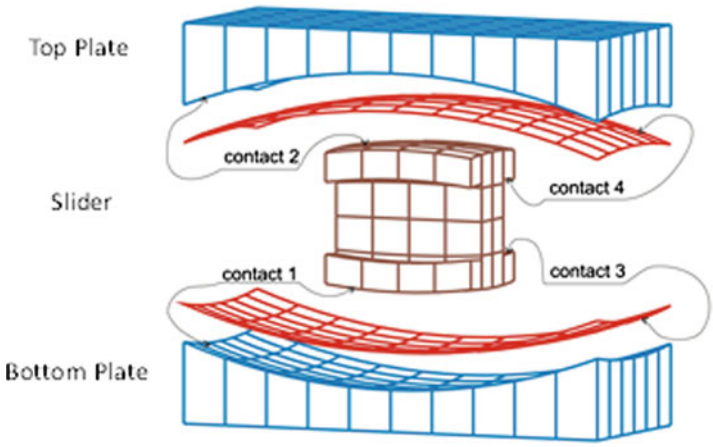

Fig. 3.9 Finite element model of a friction pendulum bearing

There are 0.75 in. (1.91 cm) gaps between the slider flanges and slot shell surfaces. If a downward force is applied to the top plate (regular condition), only contacts 1 and 2 between the slider and bearing plates are engaged. When an upward force is applied to the top plate (uplift), the contacts 1 and 2 become disengaged. After both gaps are exhausted (1.5 in relative vertical displacement of the plates), contacts 3 and 4 become engaged. Simulation of frictional contact interaction between the plates and slider (Fig. 3.10) allows limited transverse movement of the rail under moving train. The relative longitudinal displacement and rotations of the bearing plates are controlled by a set of nonlinear truss/spring elements.

Once the detailed model of the TB was developed and prior to its installation in global model of the bridge, a series of analyses were performed to study the kinematics of bearer bars and FPBs and to investigate whether the system locks due to the bridge movements. Using the global FE model of the bridge, the displacements characterizing the basic movements of the bridge due to storm condition (roll, pitch and yaw) were extracted at the locations where the TB was supposed to be connected to the deck (Fig. 3.11). These displacements were applied to the six support locations in the detailed stand-alone FE model of the track bridge. The forces in the bearer bars and the movements of the double FPBs were monitored. No locking in the system was observed. Then, this stand-alone model was inserted in two locations in the global model of the bridge as shown in Fig. 3.3.

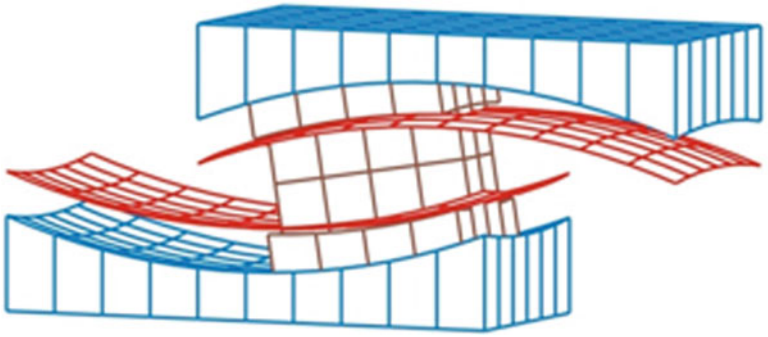

Fig. 3.10 Typical sliding deformation of friction pendulum bearing

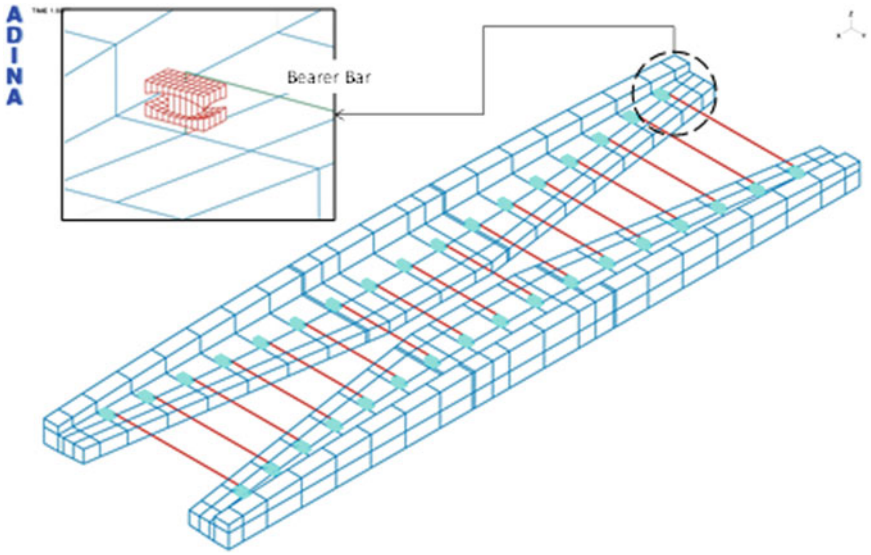

Fig. 3.11 Stand-alone detailed model of TB

3.4 Results

Several analyses were performed to study the performance of the track bridge system under a combination of bridge movements due to storm and LRV train loading. In this section, some of the results pertaining to case 5 (Table 3.1) are presented. Figure 3.12 shows rail normal stresses with a maximum of 16 ksi (110 MPa) at the location of the interior track bridge. Figure 3.13 shows the maximum bearer bar transverse movements for both exterior and interior track bridges. Each track bridge has 17 FPBs seated on each wing (total of 34 for each TB). The maximum relative displacement is about 0.5 in. (1.27 cm). Figures 3.14 and 3.15 show the tensile stress distribution in the interior and exterior TBs under LRV train loading. The maximum tensile stress is 11.59 ksi (80 MPa) and 11.84 ksi (81.6 MPa) for interior and exterior TBs respectively. Rail stresses, bearer bar movements and stress distribution in the TB components extracted for all analysis cases were found to be in the acceptable range.

3.5 Conclusion

This study pertains to the bridge–train interaction analysis of Homer M. Hadley Memorial Bridge located in Seattle, Washington. The finite element model of the bridge includes approach, transition and floating segments of the west part of the bridge along with two track bridges. The track bridge is an essential component of the LRT system which provides smooth and flexible connection of tracks of the fixed and transition spans as well as the transition and floating spans of the bridge.

– This is a unique multi-scale finite element model including 68 10 in.-diameter friction pendulum bearings incorporated in the global model of the west part of Homer M. Hadley Memorial Bridge spanning about 2,100 ft.

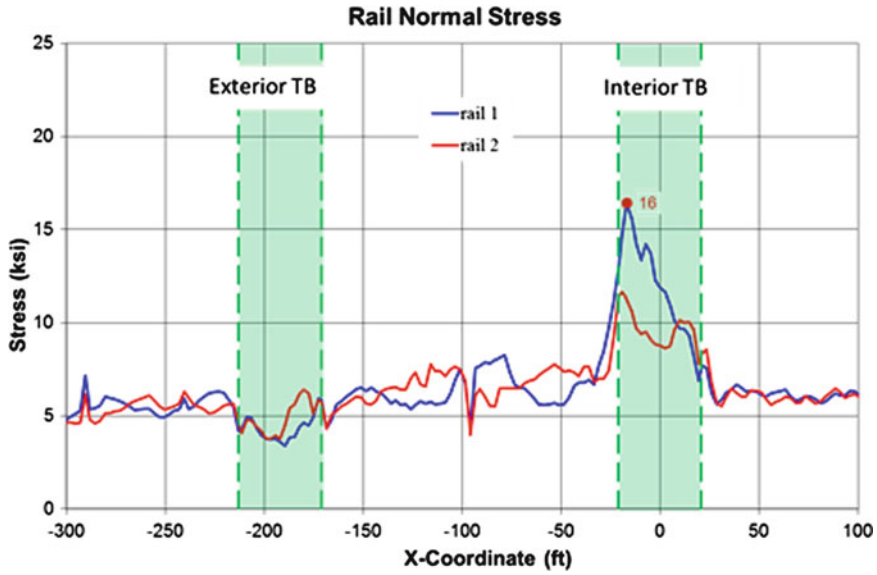

Fig. 3.12 Rail stresses due to LRV train loading

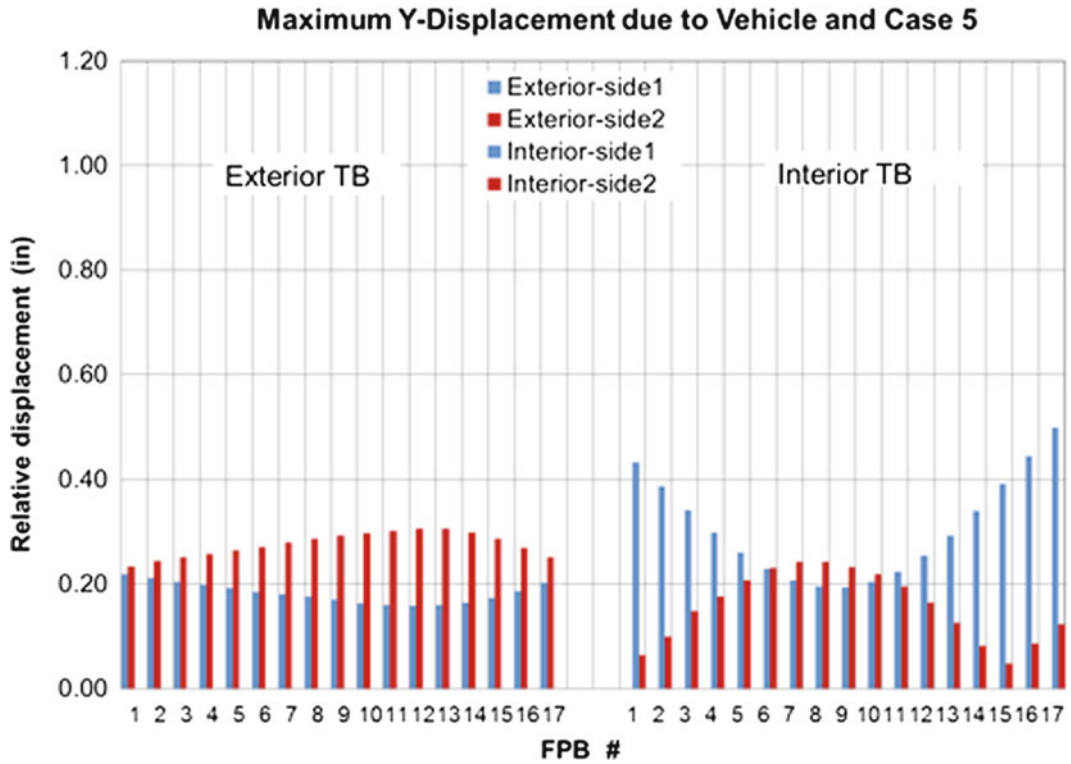

Fig. 3.13 Bearer bar transverse movements

- The track bridge model incorporates all structural components presented in a detailed way necessary for the design purposes. It includes the detailed friction pendulum bearing model which simulates all important mechanical features (friction, returning force, stoppers) and provides stable dynamic behavior under the moving load.
- The LRV train was separately modeled as a coupled system with rail, which includes stiffness of the fasteners as well as dynamic characteristics of the vehicle.
- Due to high efficiency of the developed finite element model of all components of the bridge, detailed analysis of the track bridge components was feasible using computers of regular capacity within reasonable computational time.

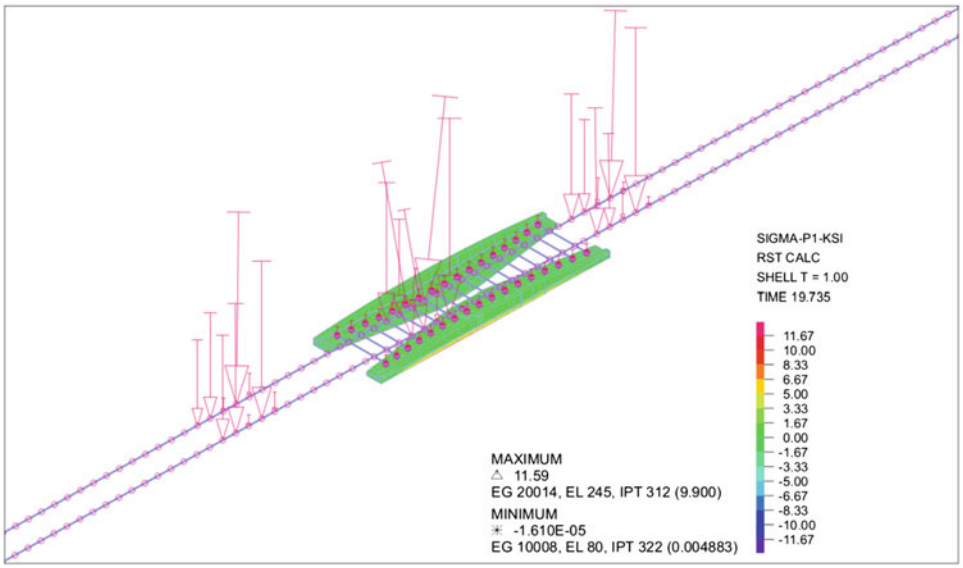

Fig. 3.14 Interior TB-vehicle position which creates the maximum tensile stress in the TB components

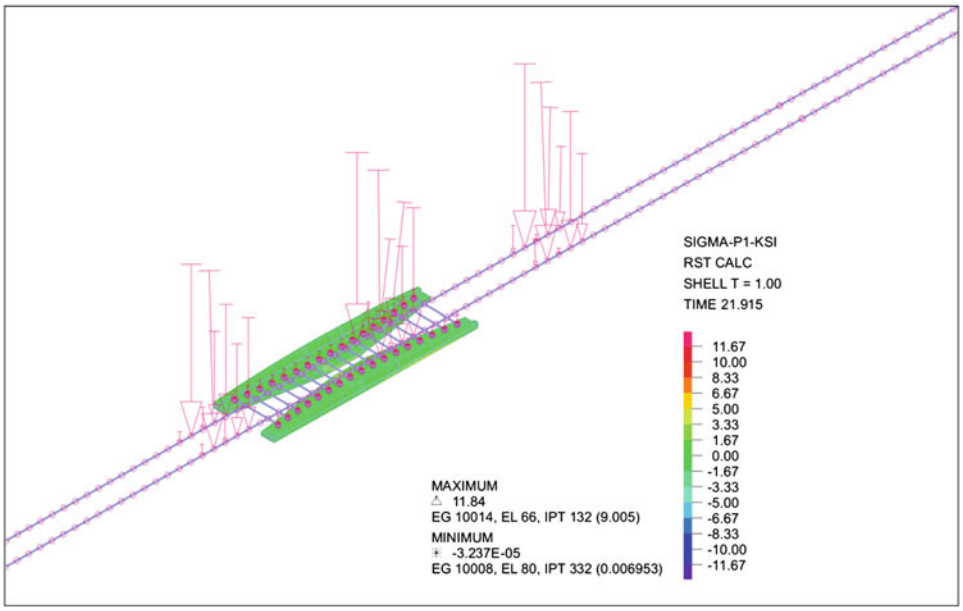

Fig. 3.15 Exterior TB-vehicle position which creates the maximum tensile stress in the TB components

– The bridge model was analyzed for a set of loading scenarios including different storm conditions and train speeds. Stress distribution in the track bridge components, rail stresses and bearer bar movements extracted for each loading scenarios, were found to be in the acceptable range.
– In addition to numerical analysis, component and full scale tests have been planned to examine the TB kinematics as well as FPB behavior.

References

1. As-built drawings – SR s 3rd Lake Washington Floating Bridge, Approaches and transition spans
2. Automatic Dynamic Incremental Nonlinear Analysis, ADINA, ADINA, R&D, www.adina.com
3. Draft Basis of Design Report (BODR), February 2012, prepared by Parsons Brinckerhoff

Chapter 4
Experiment-Based Assessment of *NLBeam* for Modeling Geometrically Nonlinear Dynamic Deformations

Lisa Dangora, Julie Harvie, Katie Wichman, and D.J. Luscher

Abstract As the wind energy industry expands, larger wind turbines are being developed to harvest more energy for a given plant site. It has also been noted that gear boxes within the wind turbines are wearing out faster than expected. One possible explanation is that current modeling approaches employed in wind turbine design do not adequately account for nonlinearities associated with the large deformations in wind turbine blades. A finite element code, *NLBeam*, has been developed to account for nonlinearities using geometrically exact beam theory. To validate the code, experiments were conducted on a surrogate aluminum blade and the results were compared to simulation results from *NLBeam*. Further development of the *NLBeam* code will be based off of this research. In the future, *NLBeam* will be coupled with *WindBlade*, a computational fluid dynamics based software which has been developed at Los Alamos National Laboratory to study fluid-structure interaction between turbines within wind plants.

Keywords Geometrically exact beam theory • Model validation • Wind turbine

4.1 Introduction

In recent years, the wind energy industry has made significant advancements and continues to rapidly expand. To accommodate the increase in demand, wind power plants are making efforts to optimize efficiency by strategic placement of turbines [1]. Additionally, manufacturers are producing larger turbines to achieve higher capacities. Larger deformation of wind turbine blades may be anticipated as the designed blade length continues to increase. Such deformation, especially finite rotations, may no longer be regarded as geometrically linear and will affect the air flow throughout the entire wind plant. Consider for example, the aerodynamic force on an aerofoil section depends upon the relative wind velocity and orientation (angle-of-attack) of that section with respect to the wind. Clearly, the orientation of a section depends upon the torsion of the blade and the relative velocity depends, in part, on the dynamic response of the blade itself.

WindBlade, a computational fluid dynamics (CFD) computer code, was developed at Los Alamos National Laboratory (LANL) to simulate the complex flow pattern induced by turbine – turbine interactions [2]. Currently, *WindBlade* utilizes rigid body dynamics to simulate the response of turbine blades. Thus, modeling form error is introduced into *WindBlade* because it does not represent the dynamic structural deformation of turbine blades subjected to aerodynamic loading. A supplemental finite element (FE) code, *NLBeam*, was developed to account for such structural dynamics in a geometrically nonlinear manner with tractable computational cost. The FE code uses geometrically exact beam theory to model the blades. Ultimately, fluid-structure interactions will be incorporated into plant-scale simulations by coupling *NLBeam* with

L. Dangora • J. Harvie
Department of Mechanical Engineering, University of Massachusetts – Lowell, Lowell, MA 01854, USA
e-mail: lisadangora@gmail.com; harvie.julie@gmail.com;

K. Wichman
Department of Engineering Physics, University of Wisconsin – Madison, Madison, WI 53706, USA
e-mail: katiewichman08@gmail.com

D.J. Luscher (✉)
Theoretical Division, Los Alamos National Laboratory, Los Alamos, NM 87545, USA
e-mail: djl@Lanl.gov

G. Kerschen et al. (eds.), *Topics in Nonlinear Dynamics, Volume 1: Proceedings of the 31st IMAC, A Conference on Structural Dynamics, 2013*, Conference Proceedings of the Society for Experimental Mechanics Series 35,
DOI 10.1007/978-1-4614-6570-6_4,

WindBlade. This paper aims to validate aspects of the structural dynamic code, *NLBeam*, by comparing the results of experiments conducted on surrogate aluminum blades to simulation results from *NLBeam*.

Previous work towards the experimental validation of structural dynamics simulation capabilities of *NLBeam* under generally nonlinear deformations illuminated the importance of carefully controlled experimental boundary conditions [3]. In that work, aluminum beams with simple geometry and well-characterized material properties were used to eliminate potential sources of material nonlinearity and reduce variability that would likely accompany the use of realistic wind turbine blades. Thus, the focus was to isolate and characterize the ability of *NLBeam* to model purely geometric nonlinearity. Three beams of differing geometries were clamped directly to a shaker in various configurations. Accelerometers were utilized to obtain experimental data at specified locations along the beam during excitation. In order to compare the experimental data to the FE model, displacement boundary conditions needed to be applied to the model consistent with those realized in experiment. *NLBeam* accommodates displacement (but not velocity or acceleration) time history data as boundary conditions; consequently, measured acceleration data was numerically integrated to determine boundary displacement information. Due to the amplification of noise during integration, various data processing techniques such as filtering were employed. Also, issues were encountered from the high rotational momentum that was introduced from the mass being attached to the tip of the beam. The rotational momentum caused the base to undergo a rocking motion, which introduced additional nonlinearities into the system. Furthermore, testing performed at resonant frequencies caused discrepancies between model and experimental data because *NLBeam* simulations did not include material damping; thus, the amplitudes of the experimental and model results did not match well for some cases.

During the research presented in this paper, improvements were made to the previous experimental approach to mitigate the aforementioned issues. Several experiments were conducted to determine the accuracy of various aspects of the code. The code was assessed for linear and nonlinear situations in both static and dynamic experiments. The cases were also compared to results from commercially available software in a code-to-code comparison. Continued development of *NLBeam* will be guided by the results of this research.

4.2 Theoretical Background

NLBeam utilizes the geometrically exact beam theory [3] in order to properly account for arbitrarily large rotations of beam cross sections. Thus, the geometric nonlinearities present in the related equations of motion are attributed to finite rotations. Here, we present a brief overview of the theory; for more details cf., for example, [4–7]. The kinematic picture corresponding to this theory is depicted in Fig. 4.1.

A global inertial coordinate system is described by the orthonormal base vectors, $\boldsymbol{E}_1, \boldsymbol{E}_2, \boldsymbol{E}_3$. The upper curve shows the undeformed beam reference axis at $t = t_0$. A position along the reference axis is described by the arc length, s, and the corresponding point is denoted by the position vector, $\mathbf{x}_0^r(s)$. The cross section of the undeformed beam is perpendicular to the line of centroids and can be described using the orthonormal base vectors, $\boldsymbol{B}_1, \boldsymbol{B}_2, \boldsymbol{B}_3$. In the reference configuration, the cross section is always perpendicular to the reference axis, thus $\boldsymbol{B}_1(s) = \boldsymbol{x}_0^{r'}(s)$, where the prime $(')$ indicates the derivative with respect to the variable s. After some time $t > t_0$ the beam has deformed, for example, as shown in the lower curve. It is assumed that each cross section is rigidly deformed, thus deformation of a cross section (for example Poisson expansion) is neglected. The vector $\mathbf{x}^r$ locates any point along the deformed reference axis and the orthogonal triad, $\boldsymbol{b}_1, \boldsymbol{b}_2, \boldsymbol{b}_3$ defines the orientation of cross section at that point. The relation between the $\boldsymbol{B}_i$ and $\boldsymbol{b}_i$is described using the rotation matrixs, $\boldsymbol{\Lambda}$,

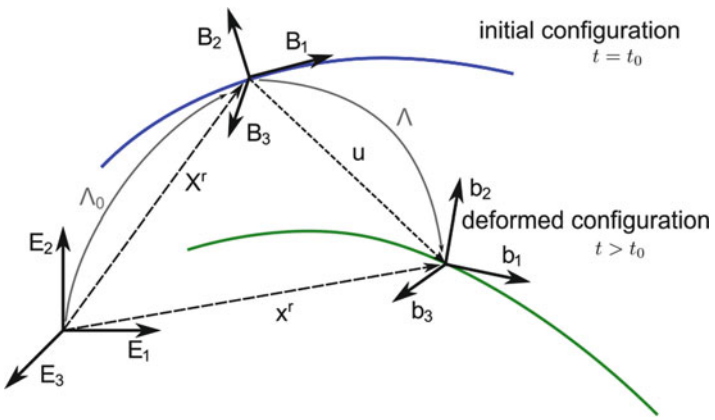

Fig. 4.1 Illustration of configurations and orientations for nonlinear kinematic behavior

i.e., $\boldsymbol{b}_i = \boldsymbol{\Lambda}\boldsymbol{B}_i$. Thus, $\boldsymbol{\Lambda}$ is an element within the special orthogonal group, $SO(3)$ such that $\det(\boldsymbol{\Lambda}) = 1$ and $\boldsymbol{\Lambda}^{-1} = \boldsymbol{\Lambda}^T$. The relative displacement between the two configurations is described by the vector $\mathbf{u}^r$.

Using this information the location of any point (including points off the reference axis) in the beam's undeformed configuration can be expressed as

$$\boldsymbol{x}_0 = \boldsymbol{x}_0^r + \xi_0 \tag{4.1}$$

where ξ_0 is the position of a point within the cross section defined with respect to the origin of basis $\boldsymbol{B}_i$, whose coefficients are $\{0, x_2, x_3\}$ within the $\boldsymbol{B_i}$ coordinate system. The location of the same point in the deformed configuration can be expressed using the same vector coefficients, $\{0, x_2, x_3\}$ but with respect to the b_i coordinate system.

Using this information any point in the beam's deformed configuration can be described by

$$\boldsymbol{x} = \boldsymbol{x}_0^r + \boldsymbol{u}^r + \Lambda\,\xi_0 \tag{4.2}$$

Note that this equation reflects six deformational degrees of freedom, viz. three coefficients of the vector $\boldsymbol{u_r}$ and three unique rotational parameters defining the rotation matrix Λ. Explicit contributions due to cross sectional warping are omitted here. In this paper, an isotropic material obeying Hooke's law is assumed and thus the constitutive relationship describing the relationship between continuum stresses, $\boldsymbol{\sigma}$, and strains, $\boldsymbol{\varepsilon}$, is given by

$$\boldsymbol{\sigma} = \boldsymbol{\lambda}\,\mathrm{Tr}[\boldsymbol{\varepsilon}]\mathbf{I} + 2\mu\boldsymbol{\varepsilon} \tag{4.3}$$

The material properties are described using the elastic shear modulus, μ, and the Lamé constant, λ. $\mathbf{I}$ denotes a second order identity matrix and $\mathrm{Tr}[*]$ is the sum of the diagonal coefficients of matrix $*$. The elastic shear modulus and Lamé constant are calculated using Young's modulus, E, and Poisson ratio, ν, as

$$\mu = \frac{E}{2(1+\nu)} \text{ and } \lambda = \frac{\nu E}{(1+\nu)(1-2\nu)} \tag{4.4}$$

Although this paper assumes an isotropic material, *NLBeam* can be used for any elastically anisotropic material model such as an orthotropic linear elastic model for a composite material. The sectional strains and curvature are computed, respectively, by

$$\begin{aligned} \boldsymbol{\gamma} &= \frac{\partial \boldsymbol{x}^r}{\partial s} - \boldsymbol{b}_1 \\ \hat{\kappa} &= \boldsymbol{\Lambda}'\boldsymbol{\Lambda}^T \end{aligned} \tag{4.5}$$

For convenience in consideration of the definition of sectional constitutive response, these kinematic deformation measures are rotated into the beam's reference coordinate system, i.e.,

$$\begin{aligned} \Gamma &= \boldsymbol{\Lambda}^T\boldsymbol{\gamma} \\ \boldsymbol{K} &= \boldsymbol{\Lambda}^T\kappa \end{aligned} \tag{4.6}$$

Consistently, the sectional strain energy along any point of the beam is defined as

$$U = \frac{1}{2}\left\{\begin{array}{c}\boldsymbol{\Gamma}\\ \boldsymbol{K}\end{array}\right\}^T [\boldsymbol{C}] \left\{\begin{array}{c}\boldsymbol{\Gamma}\\ \boldsymbol{K}\end{array}\right\} \tag{4.7}$$

Where C represents the sectional stiffness matrix. In general, *NLBeam* utilizes a generally anisotropic generalized Timoshenko sectional stiffness that is able to represent composite materials. However, for this research, a homogenous, isotropic material with a symmetric cross section was the focus, thus a simplified stiffness matrix was used, i.e.,

$$[\boldsymbol{C}] = \mathrm{Diag}\,[EA, GA_2, GA_3, GJ, EI_2, EI_3] \tag{4.8}$$

Where $\mathrm{Diag}[*]$ represents a diagonal matrix with $*$ as the terms along the diagonal. A is the area of the cross section, I_2 and I_3 are the area moments of inertia with respect to the cross sectional axes, G is the shear modulus, J is the polar geometric moment of inertia of the cross section, and A_2 and A_3 are the effective shear areas along the corresponding cross sectional axes. Differentiation of the strain energy with respect to cross sectional strains and curvature yields the cross sectional forces and moments

$$\boldsymbol{F}_N = \frac{\partial U}{\partial \boldsymbol{\Gamma}} \text{ and } \boldsymbol{F}_M = \frac{\partial U}{\partial \boldsymbol{K}} \tag{4.9}$$

The strong form of conservation of linear and angular momentum for a three-dimensional continuum are expressed, respectively, by the equations

$$\begin{aligned} \nabla \cdot \boldsymbol{\sigma} + \rho \boldsymbol{\sigma} &= \rho \ddot{\boldsymbol{u}} \\ \boldsymbol{\sigma} &= \boldsymbol{\sigma}^T \end{aligned} \tag{4.10}$$

This semi-discrete weak form of these equations can be expressed using the finite element nodal residual system of equations. The total residual force at each node, I, has contributions due to the cross-sectional stress (mat), cross-sectional inertia (dyn) and external applied forces (ext). To satisfy conservation of momentum, these contributions must sum to zero at each discrete node.

$$\boldsymbol{R}_I = \boldsymbol{R}_I^{mat} + \boldsymbol{R}_I^{dyn} + \boldsymbol{R}_I^{ext} = 0 \tag{4.11}$$

The individual residual contributors can be calculated as follows.

$$\begin{aligned} \boldsymbol{R}_I^{mat} &= \int_0^L \begin{bmatrix} N_I' \boldsymbol{I} & 0 \\ N_I \tilde{r}' & N_I' \boldsymbol{I} \end{bmatrix} \begin{Bmatrix} \boldsymbol{\Lambda} \cdot \boldsymbol{F}_N \\ \boldsymbol{\Lambda} \cdot \boldsymbol{F}_M \end{Bmatrix} dx_1 \\ \boldsymbol{R}_I^{dyn} &= \int_0^L N_I(\boldsymbol{x}_1) \begin{Bmatrix} \rho A \ddot{\boldsymbol{u}} \\ \tilde{\boldsymbol{W}} \boldsymbol{J}_\rho \boldsymbol{W} + \boldsymbol{J}_\rho \boldsymbol{A} \end{Bmatrix} dx_1 \\ \boldsymbol{R}_I^{ext} &= -\int_0^L \begin{Bmatrix} N_I \rho A \mathbf{f_b} \\ 0 \end{Bmatrix} dx + \sum_k N_I(\boldsymbol{x}_1^k) \begin{Bmatrix} \boldsymbol{\Lambda} \cdot \bar{\mathbf{f}}_k \\ \boldsymbol{\Lambda} \cdot \bar{\mathbf{m}}_k \end{Bmatrix} \end{aligned} \tag{4.12}$$

Where $\boldsymbol{W}$ and $\boldsymbol{A}$ are the angular velocities and accelerations for a point on the beam reference axis, $\boldsymbol{J}_\rho$ is the cross-sectional inertia tensor, $\bar{\mathbf{f}}$ and $\bar{\mathbf{m}}$ are concentrated forces and moments and N_I is the shape function. *NLBeam* utilizes a three-noded quadratic (Lagrange interpolating polynomial) shape function. Equation 4.12 reflects a nonlinear system of equations in which the independent variables are the nodal degrees of freedom comprising reference axis displacements, u, and rotations, $\boldsymbol{\Lambda}$. This system is solved using a Newton-Raphson iterative scheme.

4.3 Numerical Modeling

Ultimately, this research culminated in a comparison of simulation results using *NLBeam* with results from linear models, as well as from experiments, for both static and dynamic cases. For the static cases, a linear model was derived from beam bending theory assuming small deformation and expressed analytically. For the dynamic cases, a linear model was constructed using Abaqus. Of course, in both cases, the nonlinear model was defined using *NLBeam* reflecting the geometrically exact beam theory discussed in the previous section.

4.3.1 Linear Model

The experimental configuration for static response was sufficiently simple that the linear response of the beam could easily be computed using analytical expressions. The geometrically-linear analytical model was based on Euler-Bernoulli beam theory. Assumptions associated with this theory include: a slender beam (long relative to thickness); strictly lateral loading; and small deformation (displacements and rotations). Because the surrogate blade was subjected to large deformations in the experiments, assumptions for lateral loading conditions and small deflections were not satisfied in all cases. The static experiments discussed subsequently consisted of applying a tip load to the surrogate blade in a cantilevered test configuration and quantitative comparisons are made regarding the displacements at the cantilever tip. Accordingly, the linear model for the horizontal cantilever condition is expressed simply as

$$\delta = \frac{PL^3}{3EI} \tag{4.13}$$

Table 4.1 Material and sectional properties of surrogate blade

Parameter	Value	Units
Elastic modulus	68.9	GPa
Shear modulus	26.0	GPa
Cross sectional area	83.4	mm^2
Area moment of inertia (x-axis)	4,500	mm^4
Area moment of inertia (z-axis)	74.8	mm^4
Product area moment of inertia	0.00	mm^4
Polar moment of inertia	4,580	mm^4
Mass moment of inertia (x-axis)	12.4	$kg\,mm^2$
Mass moment of inertia (z-axis)	12.4	$kg\,mm^2$
Product mass moment of inertia	0.00	$kg\,mm^2$

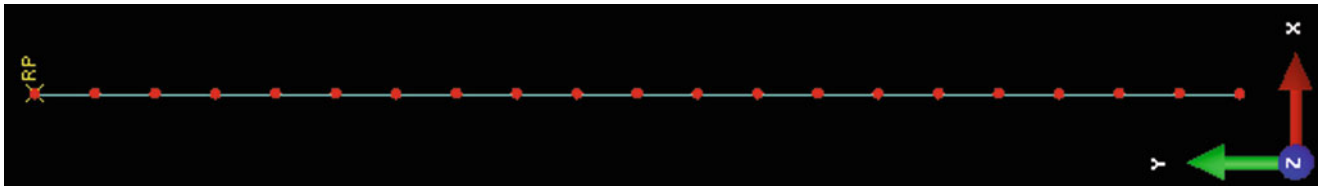

Fig. 4.2 Finite element mesh and coordinate system used for simulations in this work

Where P is the applied load, L is the effective length from the clamped base to the location of the load, E is the elastic modulus, and I is the area moment of inertia. A pseudo-linear model was considered for the vertical cantilever condition since the applied moment is implicitly dependent on displacement. The pseudo-linear model is governed by the equation

$$\Delta = \frac{PL^3}{3EI} + \frac{ML^2}{2EI} \tag{4.14}$$

Where M is the applied moment at the clamped interface due to the tip mass displacement.

A geometrically linear finite element model for simulating various dynamic response cases was developed in Abaqus using parameters in congruence with those employed in the nonlinear *NLBeam* model as specified in Table 4.1. Three-noded quadratic beam elements were used in the analysis and the beam was discretized into ten elements with a total of 21 nodes. A point mass was included at the beam tip to simulate the added weights attached to the free end of the surrogate blade. The boundary conditions at the base were created such that displacements and rotations were not permitted for the y and z axes in accordance with the coordinate system shown in Fig. 4.2. The rotations about the x axis were also constrained. The measured base displacement from the experimental data was imported into the Abaqus model and applied as a dynamic boundary condition on the boundary node in the x direction to generate the base excitation.

4.3.2 NLBeam Model

For both static and dynamic cases, geometrically nonlinear simulations were generated using a finite element model comprising of quadratic beam elements in *NLBeam*. Each beam element has three nodes with six degrees of freedom – three translational and three rotational. The combined element/cross section behavior is defined through several cross-sectional properties; the relevant parameters are listed in Table 4.1. Ten elements and 21 nodes were used in all models and a mesh convergence study was performed to justify the mesh size chosen.

4.3.3 Mesh Refinement Study

A mesh refinement study was performed to identify the optimal number of elements needed to predict an accurate solution in both static and dynamic cases while minimizing computational time. The numerical accuracy of the *NLBeam* model was quantified using the verification of asymptotic convergence. The governing equation for this solution verification is defined as

$$y^{Ref} \approx y(\Delta x) + \beta \cdot \Delta x^p \tag{4.15}$$

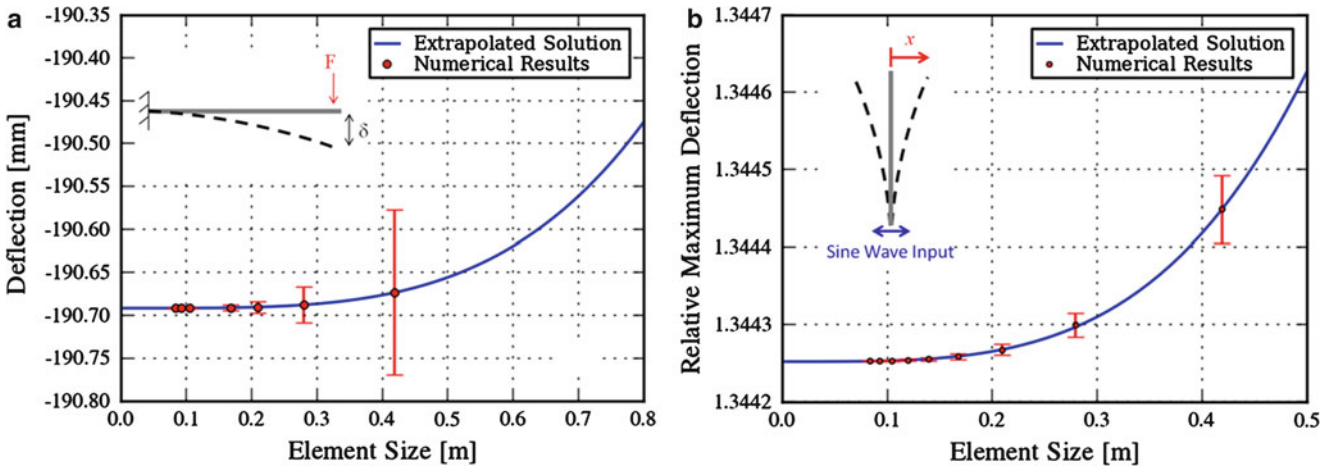

Fig. 4.3 Mesh refinement results for (**a**) static case and (**b**) dynamic case

Where y^{Ref} is the converged value, $y(\Delta x)$ is the output at a given mesh size, Δx, β is a constant coefficient, and p is the order of convergence. The order of convergence can be determined using the results of three different mesh sizes. The calculation is

$$p = \frac{\log\left(\frac{y(\Delta x_{\mathrm{m}}) - y(\Delta x_{\mathrm{c}})}{y(\Delta x_{\mathrm{f}}) - y(\Delta x_{\mathrm{m}})}\right)}{\log(R)}, \text{ where } \mathrm{R} = \frac{\Delta x_{\mathrm{m}}}{\Delta x_{\mathrm{f}}} = \frac{\Delta x_{\mathrm{c}}}{\Delta x_{\mathrm{m}}} \tag{4.16}$$

and the subscripts c, m, and f describe the mesh (coarse, medium, or fine). Once Eq. 4.16 is solved, the extrapolated converged solution value can be estimated by

$$y^{Ref} = y(\Delta x_f) + \frac{y(\Delta x_{\mathrm{f}}) - y(\Delta x_{\mathrm{m}})}{\mathrm{R}^{\mathrm{p}} - 1} \tag{4.17}$$

and, subsequently, the coefficient β can be determined using Eq. 4.15. Solutions from a minimum of three finite element meshes are needed to perform this sequence of calculations.

A mesh refinement study was performed for a cantilevered beam under a static tip load, $F = 5N$, as depicted in the inset of Fig. 4.3a. The computed tip displacement versus element size is plotted in Fig. 4.3a. Equations 4.15 through 4.17 were used to fit the convergence ansatz to observed convergence behavior from simulation results and extrapolated to the converged solution as the element size approaches zero. The solution had converged to within the machine precision at a mesh size of 105 mm corresponding to eight elements along the beam length.

A similar mesh refinement study was repeated for a dynamically excited cantilever beam. A sinusoidal base excitation was input to the *NLBeam* code as a displacement boundary condition consistent with the depiction in the inset of Fig. 4.3b. The maximum relative tip displacement is plotted versus element size in Fig. 4.3b. Similarly to the static case, Eqs. 4.15 through 4.17 were used to fit a convergence behavior to these simulation points. The solution was converged to within machine precision at a mesh size of 93 mm; this corresponded to nine elements along the beam length.

Although both the static and dynamic solutions were "fully converged" at nine elements along the length, a mesh consisting of ten elements was chosen for the final model as a matter of convenience in comparing to experimental data. Ideally, comparison between experimental and numerical results is directly facilitated by locating FE model nodes at the exact locations along the beam where physical measurements were taken. As such, the ten element model allowed for two more tracking points than the nine element model and the added computational cost was negligible.

4.3.4 Sensitivity Analysis

To assess the potential importance of uncertainty or variability of input parameters used in the *NLBeam* model to the computed results, a sensitivity analysis was performed. Based on engineering judgment and consideration of the analytical expression for tip deflection of a cantilever beam, attention was restricted to the parameters comprising thickness, width, and

Table 4.2 Effect of varying parameters in NLBeam on deflection of cantilever beam

Parameter	Nominal value	Minimum value	Maximum value	Maximum deflection difference (mm)
Thickness	3.28 mm	3.24 mm	3.32 mm	6.3
Width	25.44 mm	25.00 mm	26.00 mm	3.7
Length	83.89 cm	83.39 cm	83.89 cm	3.4
Elastic modulus	69 Gpa	66 Gpa	72 Gpa	7.1

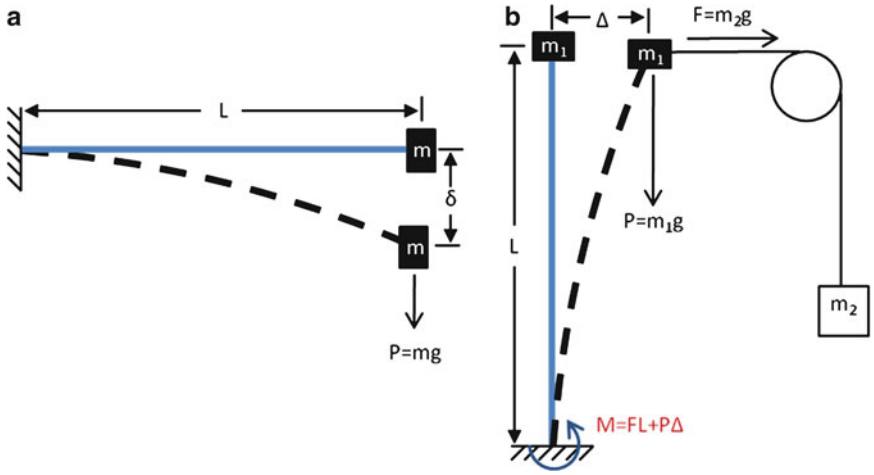

Fig. 4.4 Static test setup for **(a)** horizontal and **(b)** vertical configurations

length of the beam, as well as elastic modulus of the material. The nominal values, as displayed in Table 4.2, were initially established using either measured values or typical values from the literature [8]. The authors set a reasonable range of values for each parameter using either physical tolerances or engineering judgment. A static cantilever simulation, as shown in Fig. 4.4a, was run in *NLBeam* while changing each parameter individually between the range of values. The deflection at the tip of the beam was recorded for all cases, and the maximum difference between the deflections of those cases compared to the nominal case is shown in Table 4.2. As shown, the maximum difference in deflection varies at most 7.1 mm. The most extreme changes in computed results are on the order of the estimated accuracy of the calibrated experimental diagnostics. Thus, it was concluded that nominal values are sufficient for use in this research.

4.4 Experimental Approach

4.4.1 Static Bending Experiments

As mentioned previously, experiments conducted on the aluminum prismatic surrogate blades provide the basis for assessment of simulation results. For static cases, experiments consisted of cantilevering the surrogate blade with a relatively fixed base in vertical and horizontal configurations (separately) as shown in Fig. 4.4. To create the fixed cantilever condition for the horizontal case, the specimen was clamped between two rectangular plates at the base as shown in Fig. 4.5a, thus minimizing rotations at the fixed end. During each experiment, images were collected using a high-speed camera. The positions of specifically marked locations on the beam (shown in Fig. 4.5b) were tracked throughout the sequence of images from each experiment to define the beam displacement field using the image tracking software ProAnalyst. As shown in Fig. 4.5b, there is a deflection of the test specimen due to its own weight in the horizontal configuration. Consequently, all experimental measurements and comparisons with simulations are expressed relative to this initial deflection.

Cylinders of known mass were suspended from the tip of the surrogate blade by lightweight line and the corresponding tip displacements were recorded. In this fashion, the beam was loaded using tip masses from 200 to 700 g in increments of 100 g.

Predictions employing linear beam theory for the corresponding tip deflections were computed by using Eq. 4.13. Likewise, simulations reflecting geometrically nonlinear response were conducted using the *NLBeam* model for this static case. An initially deformed configuration was established by simulating the response of the blade under gravity. The resulting displacement field was used as a baseline by subtracting the displacements from subsequent simulations of blade response under gravity and tip loads to calculate relative static deflections for comparison with experimental values.

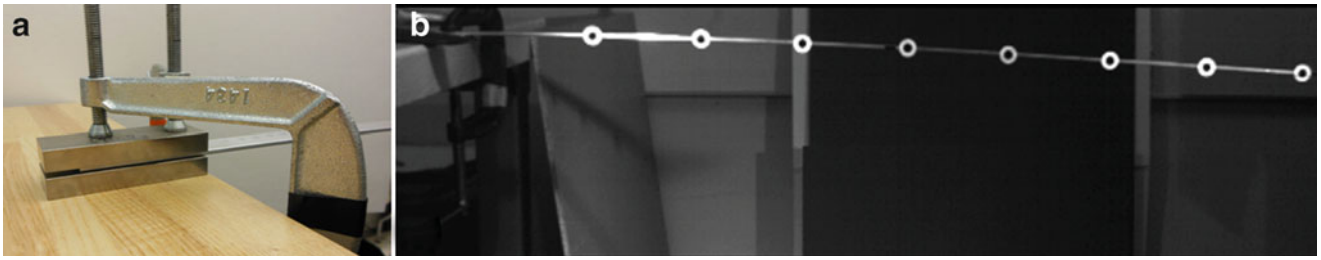

Fig. 4.5 **(a)** Cantilever condition and **(b)** initial deflection due to beam weight

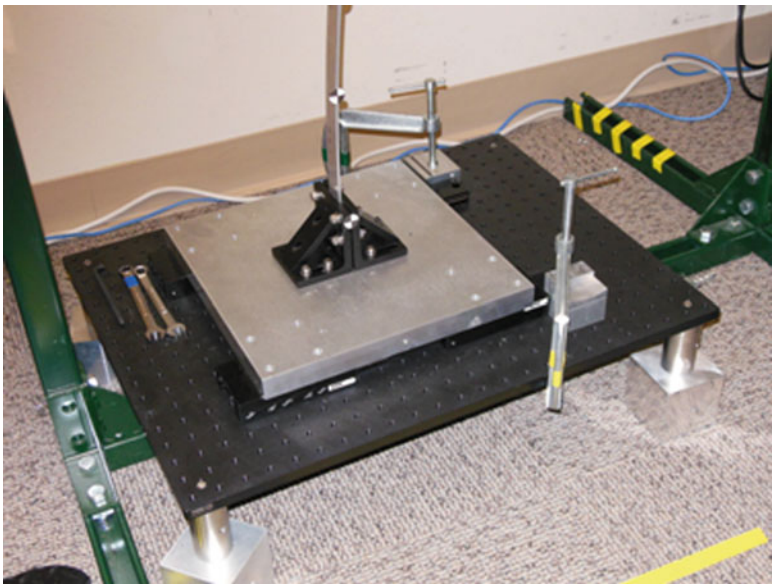

Fig. 4.6 Photograph of fixture used to support test subject in vertical configuration

To emphasize geometric nonlinearity, experiments were also conducted with the beam cantilevered vertically from its base in a sliding table clamping fixture. This fixture was designed to support the beam in a fixed-free vertical configuration enabling both static fixed and dynamically driven base excitation experiments with design features to eliminate base rocking experienced in previous efforts [3]. The fixture, as shown in Fig. 4.6, consisted of a massive steel plate attached to a base plate on lubricated gliders. The beam was sandwiched between two L-brackets, in turn bolted to the plate. The gliders enable the base plate to be easily translated along one direction for dynamic test cases, but can be sufficiently restrained using blocks as shown in Fig. 4.6.

To perform the vertical static validation, various masses were suspended from the pulley and the elongation of the spring was measured to estimate the applied force. Simultaneously, the displacement of the tip of the beam was measured using the aforementioned image tracking software. These tests were performed for three cases: no tip mass, intermediate tip mass (381 g), and large tip mass (780 g).

To achieve a variable load perpendicular to the face of the beam tip, a pulley system was constructed. As shown in Fig. 4.7, a pulley was attached to a plate on the frame surrounding the beam to allow the pulley to be vertically realigned, ultimately achieving a purely horizontal force applied at the tip. Again, a strong lightweight line was used to connect the tip of the beam to a variable hanging mass, m_2, while employing the pulley system. Because the pulley is not frictionless, a spring was connected between the pulley and the tip of the beam to characterize the actual force that was input to the beam. The spring stiffness was determined from calibration in a purely vertical condition to determine the amount of elongation that occurred due to known mass loadings, thus achieving a relatively effective low-force mechanical load cell.

4.4.2 Dynamic Experiments

The modal characteristics of the test article were experimentally obtained in order to identify effective input excitation frequencies for driving large displacements. Modal characterization tests were conducted using a force transducer secured

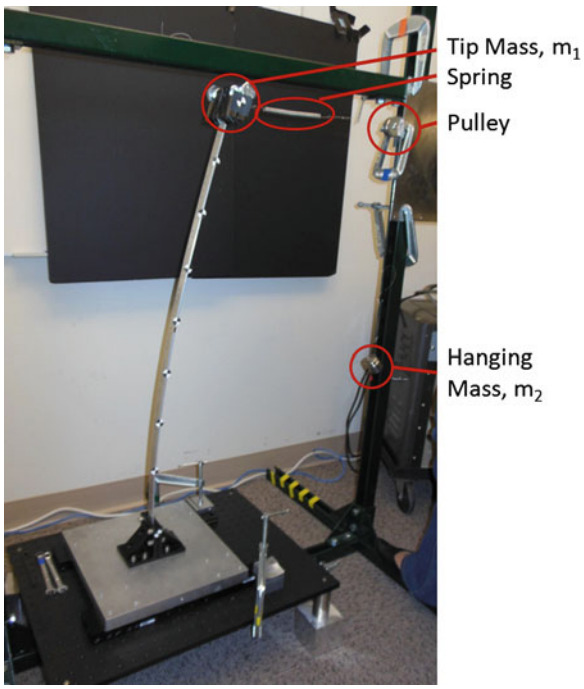

Fig. 4.7 Experimental test setup used for static vertical testing

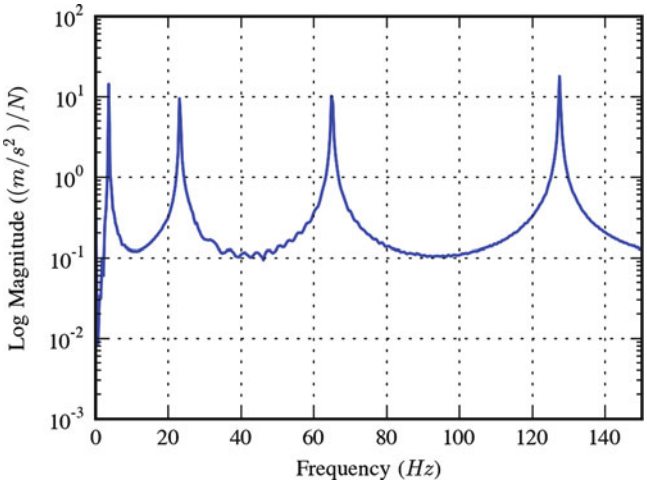

Fig. 4.8 Frequency response function used to determine natural frequencies of beam without tip mass

Table 4.3 First four natural frequency and damping values for beam without tip mass

Mode	Freq (Hz)	Damping (%)
1	3.64	0.316
2	23.18	0.265
3	64.99	0.095
4	127.48	0.104

to the base fixture inline with the shaker attachment and an accelerometer was secured to the tip of the beam. A shaker was used to transmit a chirp signal to base excitation of the beam. The frequency response function (FRF) between the accelerometer and force transducer was measured using an LDS Dactron to collect data and subsequently post-processed in RT Pro Photon. The procedure was repeated to characterize modal response for each of the considered tip masses. When configured with the largest tip mass (780 g), the first natural frequency was below the measurable range of the accelerometer. For that case, a sinusoidal input whose frequency was swept over a range was used to estimate the first natural frequency as the input frequency at which the beam achieved maximum response amplitudes. For example, the computed frequency response function for the beam without any tip mass is shown in Fig. 4.8. Four distinct peaks are observed within the 150 Hz bandwidth that was measured. Using ME'scope, curves were fit to each of the distinct peaks to provide estimates of frequency and damping values for these four modes as reported in Table 4.3.

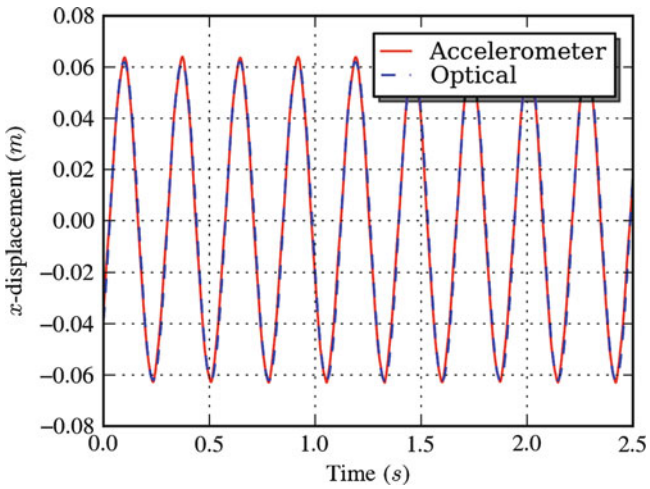

Fig. 4.9 Comparison of displacement data from optical system and accelerometer

When the intermediate tip mass (381 g) was added, the first natural frequency dropped to approximately 1.10 Hz. With the larger tip mass (780 g) the first natural frequency fell to 0.65 Hz. Results of this characterization were used to set experimental parameters, calibrate experimental diagnostics, and to help understand source of discrepancy between experiment and simulation in some cases as discussed below.

For example, application of a sinusoidal base excitation to the specimen at its natural frequency should achieve a nearly pure sinusoid output with negligible response at higher-order modes. This simple case was used to determine the accuracy of the optical measurement system. Under a nearly pure sinusoidal base excitation at the first natural frequency, the tip response was measured using an accelerometer as well as high-speed camera. The optical system measures displacements, while, of course, the accelerometer measures acceleration. Integration of the tip acceleration time history ought to be consistent with the measured displacement time history; however, numerical integration of an acceleration time history would be sensitive to noise. On the other hand, the anticipated analytical expression for tip displacement

$$x(t) = \sin(\omega t) \tag{4.18}$$

where x is displacement, ω is the angular frequency, and t is time, provides a direct means to compute the displacement time history from acceleration data, i.e.,

$$x(t) = -a(t)/\omega^2 \tag{4.19}$$

where a is acceleration. Displacement results of such a comparison are shown in Fig. 4.9 for the case of vertical cantilever with no tip mass under base excitation at the first resonant frequency. Clearly, the displacement obtained from the accelerometer and optical system are in strong agreement, thus giving confidence in the optical measurement system.

A 'pluck test', i.e., free vibration of the test specimen from an initial tip displacement in a vertically cantilevered configuration, was used to confirm estimates of first natural frequencies and to characterize damping and damped natural frequencies. The logarithmic decay of displacement time history at the tip, for example cf. Fig. 4.10, was analyzed to estimate damped natural frequency and damping of the first mode. For each case considered, two temporal points at maximum amplitude were chosen and the logarithmic decrement was calculated using

$$\zeta = \frac{1}{2\pi n} \ln\left(\frac{x_1}{x_n}\right) \tag{4.20}$$

where n is the number of cycles between the selected points and x represents the displacement at each time point. The damped period of response was estimated as

$$T_d = \frac{t_n - t_1}{n} \tag{4.21}$$

where t represents the time at each point.

One phenomenon that was present in experimental and simulation results for several cases was beating, which can occur when a structure is excited close to, but not exactly at, one of its natural frequencies. Because the two signals have similar frequencies, they will alternately interfere both constructively and destructively as time proceeds. This beating phenomenon can be seen in the pedagogical response time history displayed in Fig. 4.11. The overlying beating behavior, outlined with a red dashed line, reflects the frequency of beating.

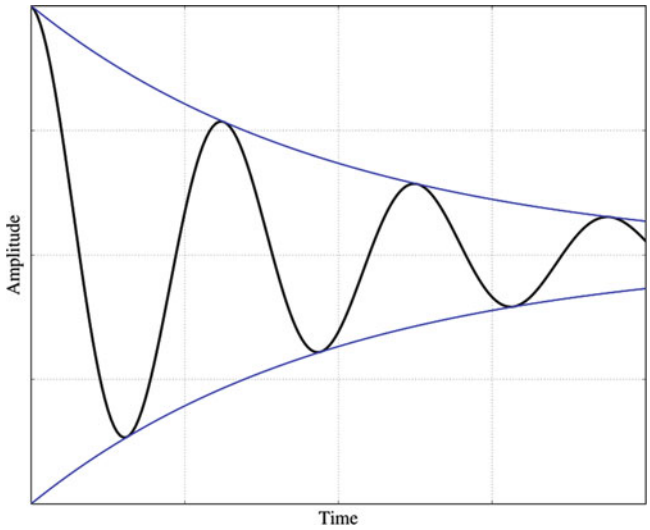

Fig. 4.10 Theoretical logarithmic decay of free response due to initial displacement

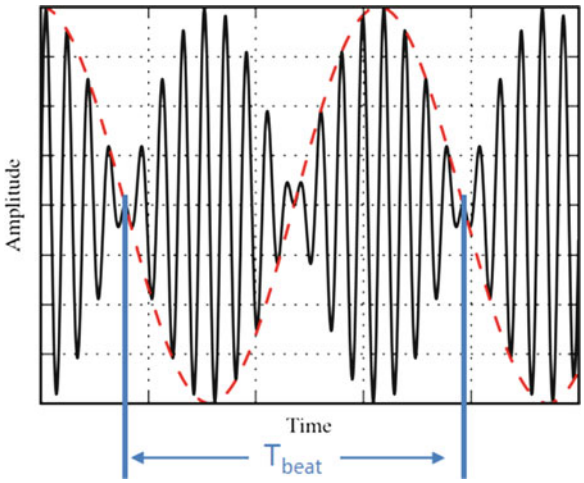

Fig. 4.11 Demonstration of beating phenomenon

The beat frequency of the resulting motion can be computed by

$$\varepsilon = \left| \frac{\omega - \Omega}{2} \right| \tag{4.22}$$

where ω and Ω are a resonant frequency of the system and the input excitation frequency, respectively [9]. The period of the beating signal is simply $T_{beat} = 1/\varepsilon$. The beating periods were estimated following this approach for several relevant cases as discussed subsequently.

4.5 Results and Discussion

4.5.1 Comparison of Model and Experiment Under Static Loading

The results from the horizontal static testing are presented in Fig. 4.12 and Table 4.4. Tip deflections are plotted versus tip mass for experiment, NLBeam simulations, and linear beam solution in Fig. 4.12. For small tip loads, experiment, linear theory, and *NLBeam* simulations agree fairly well. As the tip load increases, the rotational angle increases and there is a geometric stiffening effect introduced as more of the weight of the tip mass is resisted by axial stress in the beam. The geometric stiffening can be seen in results from *NLBeam* and experiment which follow a similar trend. However, because

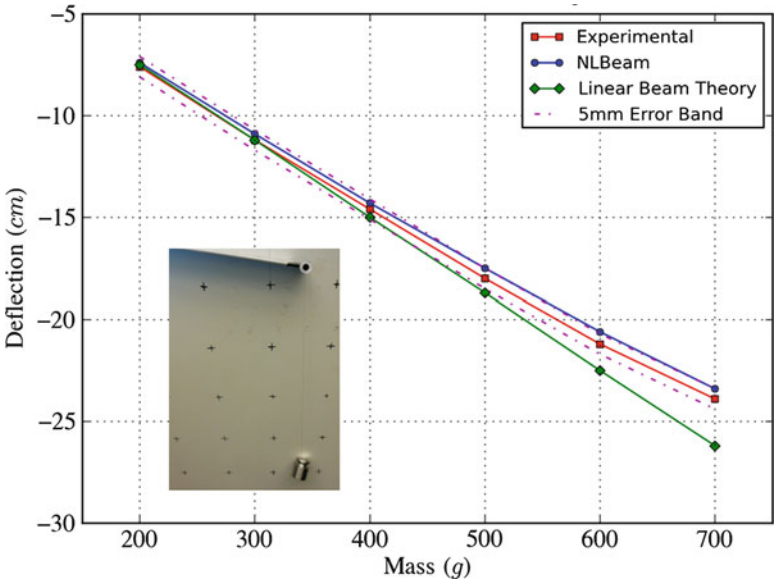

Fig. 4.12 Net static deflection of a horizontal beam

Table 4.4 Static deflection comparison for horizontal configuration

Mass (g)	Percent difference from experiment *NLBeam* (%)	Linear beam theory (%)
200	3	1
300	3	0
400	2	3
500	3	4
600	3	6
700	2	10

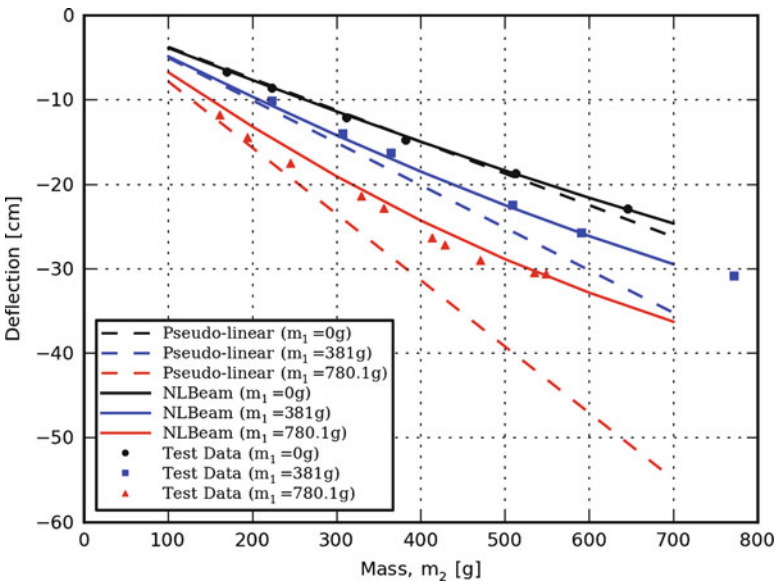

Fig. 4.13 Static deflection of a vertically cantilievered beam with various tip masses (m_1) under increasing values of horizontal load (m_2)

the linear beam theory does not account for the nonlinearity introduced by geometric stiffening, the linear beam theory calculations overpredict the tip deflection at displacements beyond 15 cm. Table 4.4 summarizes the percent difference in computed vertical tip displacement for these cases.

Results from the vertically cantilevered static deflection tests are presented in Fig. 4.13. *NLBeam* simulation results compare more favorably to experiment than linear beam theory for all three values of tip mass (m_1). Considering first the case of no tip mass, i.e., $m_1 = 0$, experiment, *NLBeam*, and linear beam theory are in reasonable agreement up to a tip defection near 20 cm. Beyond that the geometric stiffening observed in the horizontal static test case becomes apparent and calculations using linear beam theory diverge from tip deflection observed in experiment and *NLBeam* simulation results.

Table 4.5 Comparison of first natural frequency and damping values computed using logarithmic-decrement approach

	Experiment		*NLBeam*		ABAQUS	
	Freq (Hz)	ζ (%)	Freq (Hz)	ζ (%)	Freq (Hz)	ζ (%)
No tip mass	3.631	0.335	3.745	0.027	3.803	0 % unless otherwise specified
Intermediate tip mass	1.103	0.070	1.230	0.008	1.248	
Large tip mass	0.650	0.067	0.884	0.006	0.897	

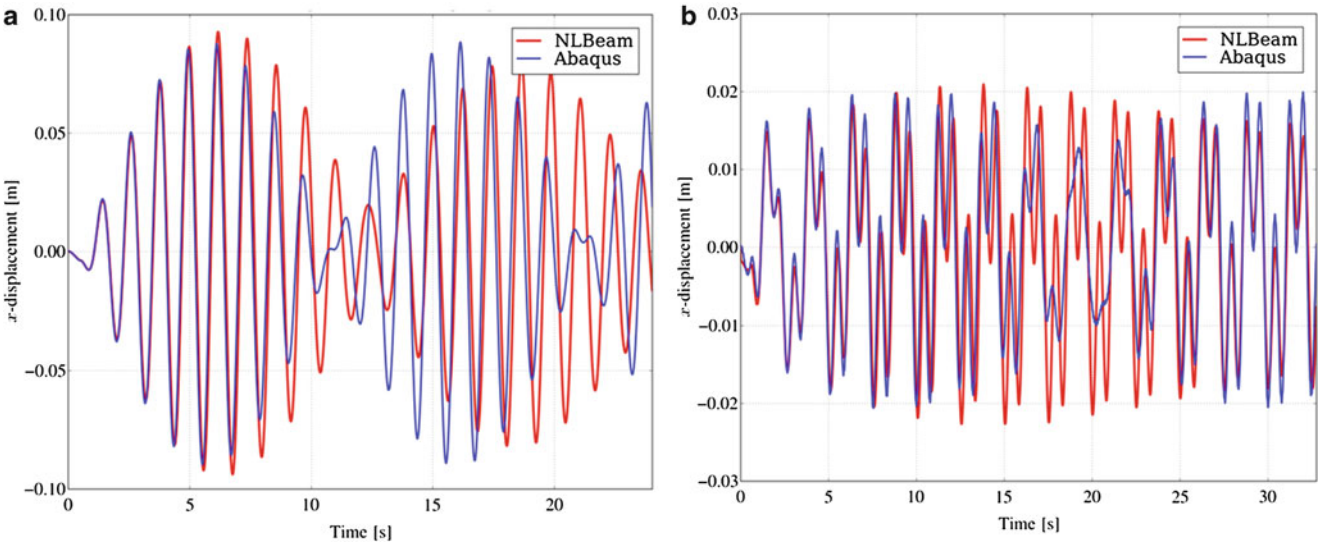

Fig. 4.14 Code-to-code comparison of *NLBeam* with Abaqus for **(a)** simple beating and **(b)** more complex responses

This geometric stiffening effect is observed in experimental and *NLBeam* simulation results for each case shown in Fig. 4.13, although the behavior becomes more pronounced for increasing values of tip mass (m_1). Furthermore, as the tip mass (m_1) is increased, the relationship between horizontal force (attributed to m_2) and tip deflection becomes softer, an additional manifestation of geometric nonlinearity. The behavior exhibited by experiments is captured well by the *NLBeam* simulation over the ranges of m_1 and m_2 considered here. With an intermediate tip mass, the pseudo-linear model is able to accurately predict the response up to a displacement of 10 cm. For the case of a large tip mass, error is prevalent in the pseudo-linear results over the entire range of the experiment. While the pseudo-linear model accounts for the softening effect observed as the tip mass increases, it cannot account for the stiffening effect seen as the deformations enter a nonlinear region.

4.5.2 Comparison of Model and Experiment Under Dynamic Base Excitation

Simulations of the 'pluck test' for the vertically cantilevered configuration with zero, small, and large tip masses were conducted using the geometrically nonlinear model in *NLBeam* and a geometrically linear beam model in Abaqus. The logarithmic decrement approach (discussed previously) was used to characterize results from experiments, *NLBeam*, and Abaqus and are presented in Table 4.5. Note that the frequencies identified from pluck test experimental data are in agreement with those obtained from the experimentally measured FRF. There are small discrepancies in frequency and damping values estimated from experimental and simulation results. The discrepancies between results with no tip mass suggest that there is an inherent difference in the original modeling assumptions, e.g., boundary conditions, cross-sectional dimensions. Additional discrepancy is introduced upon addition of mass blocks because they were modeled as nodal masses absent of any rotary inertia; in reality, these blocks reflect an additional rotary inertia about their point of application. At the time of this research, *NLBeam* did not explicitly include nodal contributions of rotary inertia. While one could add a small chunk of an additional stiff beam element to reflect this rotary inertia, this was not pursued in the scope of the research.

As a preliminary step to code verification, a code-to-code comparison was performed to compare *NLBeam* with commercially available software, Abaqus. Comparisons were made between *NLBeam* and Abaqus simulation results for several experimental cases, two of which are presented in Fig. 4.14. Figure 4.14a compares simulation results for the case

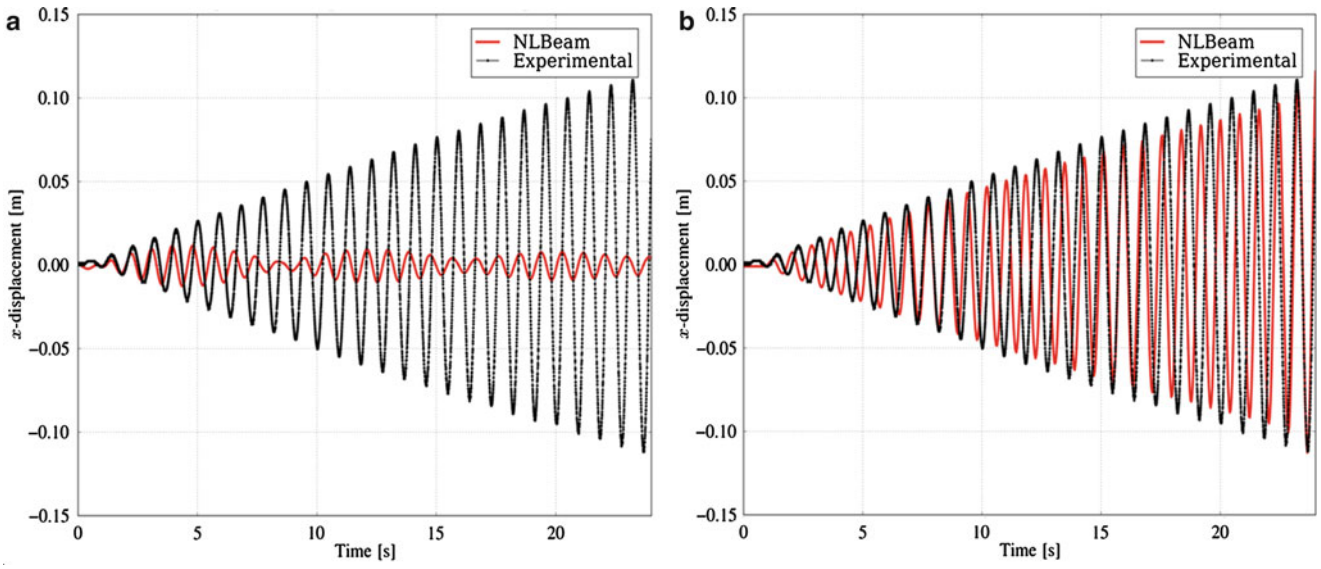

Fig. 4.15 Excitation at **(a)** experimental resonant frequency and at **(b)** each system's resonant frequency

with large tip mass and a quasi-sinusoidal base excitation at 0.8 Hz. Note, the shaker apparatus was unable to cleanly amplify a pure sinusoidal wave at all input magnitudes, so the input excitation was not a pure sinusoid. The actual displacement time history of the base of the experiment was used as input boundary conditions for the model.

Results from both models exhibit beating; however, there is a noticeable difference in the beat frequency between these two codes caused by differences in the distance of the excitation frequency from each system's resonance. For this case, the differences between the driving frequency and resonant frequency were 0.097 and 0.084 Hz for Abaqus and *NLBeam* respectively. Simulation results agreed extremely well through the first six seconds with close match in both frequency and amplitude between models. The discrepancy that grows subsequently is attributed to the difference in beat frequency, in turn attributed to small differences in natural frequency (cf. Table 4.5.) Thus, slight differences in modal characteristics result in potentially substantial differences in dynamic response time histories when excitation is near a resonance for lightly damped systems. Results in Fig. 4.14b are for the experiment case comprising a small tip mass (381 g) under sinusoidal excitation at 0.4 Hz. Again, beating is evident from the response time history but it is not as profound as in the case shown in Fig. 4.14a. It should be noted that geometrically nonlinear model employed in *NLBeam* and the geometrically linear model employed in Abaqus would not be expected to give similar results for large deformation cases. Excitations for these simulations were selected such that tip displacements remained effectively small.

A dynamic experiment was performed on resonance by exciting the base of the physical structure (cantilevered beam with 381 g tip mass) with a sinusoidal input at the first natural frequency of the system.

The displacement time-history results from this initial comparison are plotted in Fig. 4.15a. Clearly, there is poor agreement between experimental and simulation results due to differences in each system's resonant frequencies as seen in Table 4.5. The experiment is exhibiting response of a lightly damped structure to excitation at resonance, while the *NLBeam* simulation is not. In order to excite the *NLBeam* model at resonance, the time axis of the input boundary conditions was scaled to align the excitation frequency with the estimated resonant frequency of the model. Note that the input base displacement magnitudes were not changed, only the time values were uniformly scaled. Results from this simulation compare favorably to the experimental results as shown in Fig. 4.15b. Of course, the periods are not aligned because of the difference in resonant frequencies.

Additional cases with excitation further from resonance were investigated. For example, Fig. 4.16 compares the tip displacement results between experiment and *NLBeam* simulations for no tip mass with a base excitation frequency of 3.04 Hz. Recall from Table 4.5 that (for zero tip mass), the first resonant frequencies were estimated as 3.63 and 3.75 Hz for experiment and model, respectively. From Fig. 4.16a, it is evident that model and experiment exhibit similar displacement amplitudes after 30 s of response. However, the initial response ($t < 15$ s) does not compare as well. The experimental response decays more slowly from an initial transient than the *NLBeam* results, perhaps suggesting that *NLBeam* has a higher damping value. Figure 4.16b shows reasonable agreement in these results for $(15\,\text{s} < t < 20\,\text{s})$. These results are typical of other cases investigated.

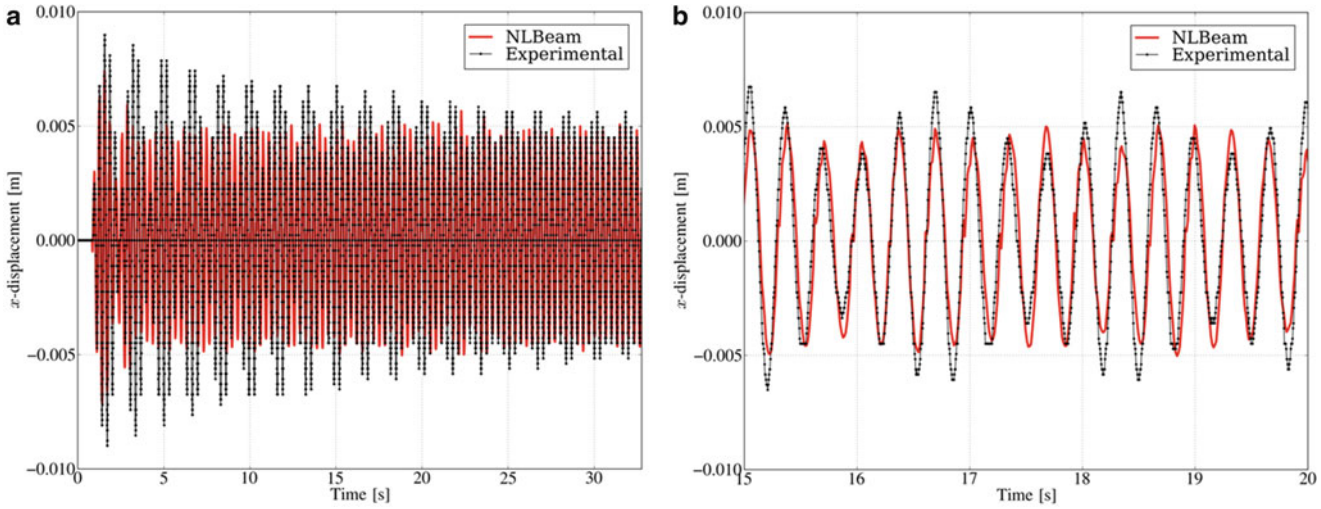

Fig. 4.16 **(a)** Off resonance response of beam without tip mass and **(b)** zoomed in section

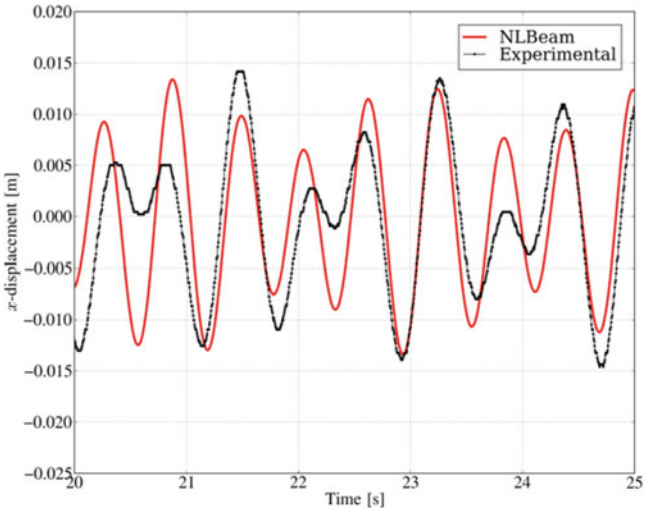

Fig. 4.17 Tip displacement time history response for off-resonance excitation (1.7 Hz) with intermediate tip mass

After validating the response of the beam off resonance without a tip mass, the intermediate mass was attached to the tip of the beam and experiments were run. Figure 4.17 compares *NLBeam* and experimental displacement results for off-resonance excitation of the surrogate blade with a mass of 381 g attached to the free end. The *NLBeam* simulation and the physical response appear to follow the same trend as the local maxima and minima occur at the same time; however, there are noticeable difference in the amplitudes of the two time traces. The peaks in the *NLBeam* data are relatively predictable and generally larger than the experimental amplitudes overall.

To further examine and compare frequency content of the dynamic response, FFTs of the response time-history data were computed for this off-resonance case. The time history data and the corresponding FFT are shown on the left and right of Fig. 4.18 respectively. For both experiment and simulation results, the first FFT peak occurs at the resonant frequency of the beam and the second peak occurs at the frequency of the base excitation. In experimental results, more energy is associated with response at the natural frequency than the base excitation frequency. The opposite is true of the *NLBeam* simulation results, i.e., more energy is associated with response at base excitation frequency than the unforced resonant frequency. Consequently, the discrepancy in time histories shown in Fig. 4.17 are simply due to this difference in energy distribution over two competing response frequencies. Eventually, the actual dynamic response would be dominated by the base excitation frequency. Thus, *NLBeam* model is redistributing energy into the base excitation response frequency earlier than the experiment, i.e., the model is exhibiting more damping than the experiment. This behavior is more important for lightly damped systems where the transient period is longer.

A case of off-resonance base excitation for with the largest tip mass attached to the beam was investigated. Figure 4.19a shows the response of *NLBeam* model and the experiment due to an input signal at 0.80 Hz. For reference, the first resonant

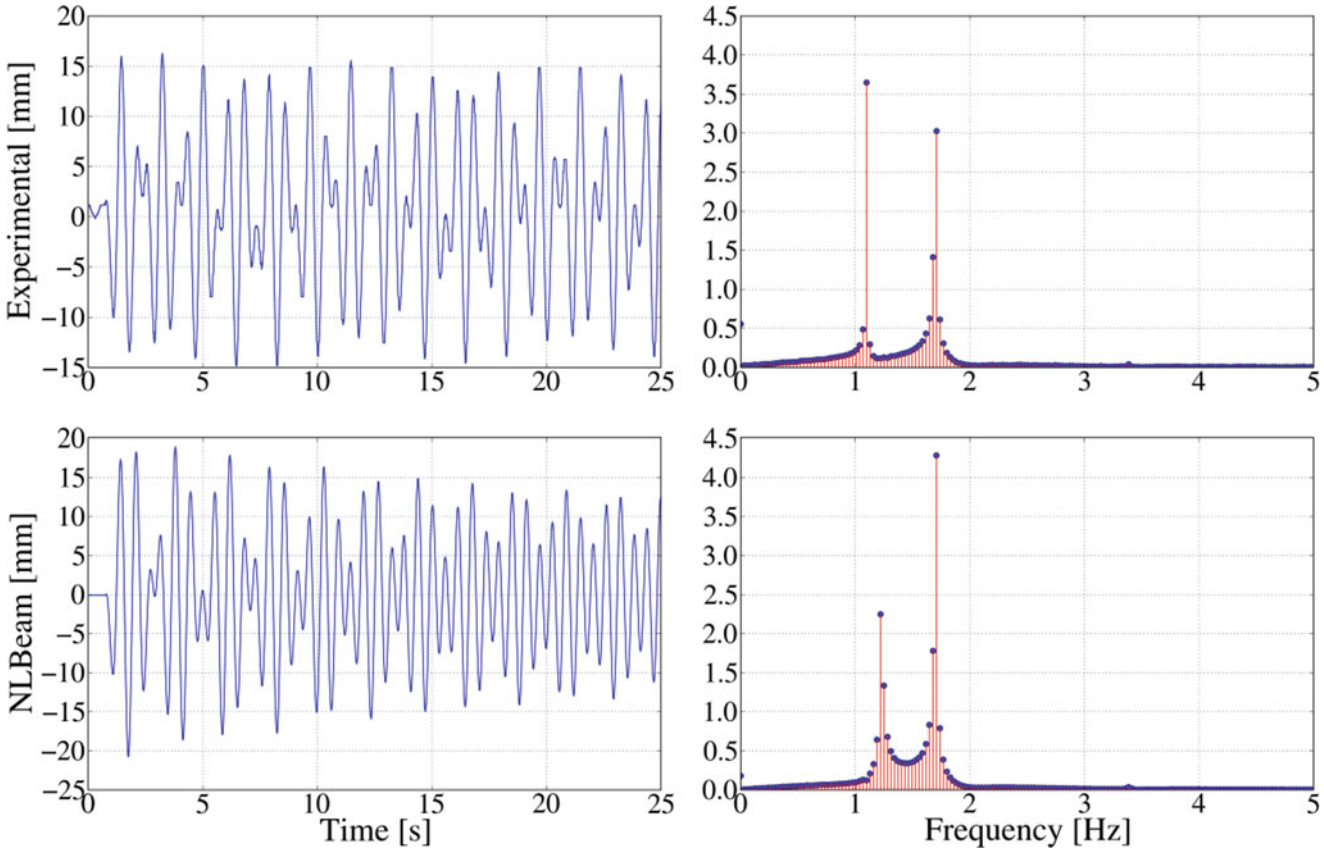

Fig. 4.18 Time traces and resulting Fast Fourier Transforms for experimental and *NLBeam* results of previous case

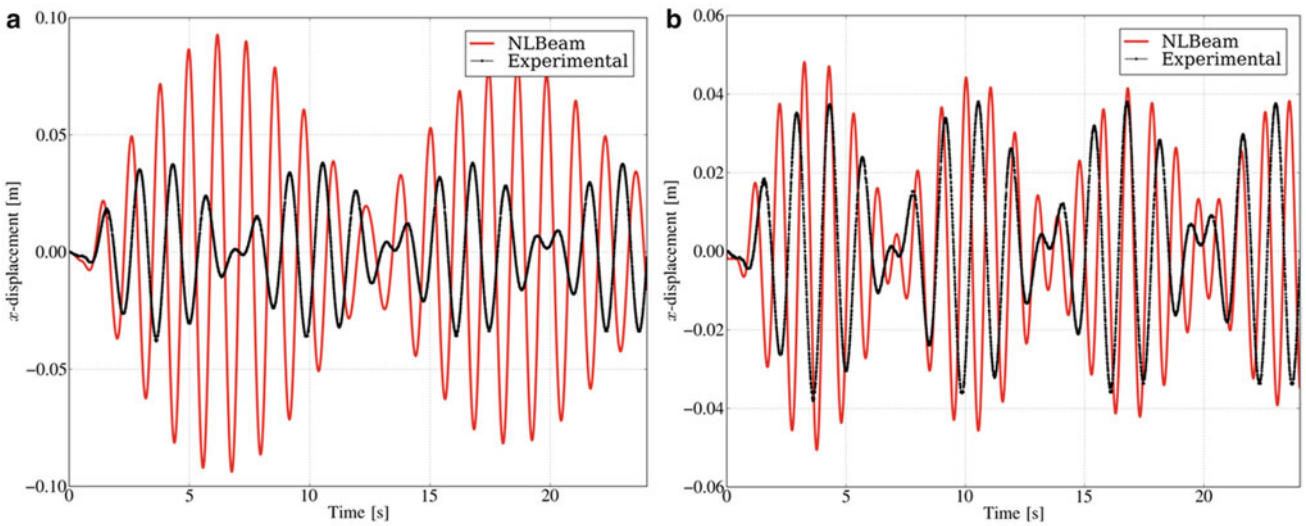

Fig. 4.19 Beating phenomenon seen at **(a)** different beat frequencies and **(b)** same beat frequencies

frequency in this configuration was approximately 0.65 Hz in the experiment and 0.88 in the *NLBeam* simulations. The difference between the experiment resonant frequency and base excitation frequency was roughly 0.15 Hz, whereas the difference between model resonant frequency and base excitation frequency was only 0.08 Hz. Consequently, the beating frequency in simulation results is approximately twice that observed in experimental data.

To isolate the discrepancy in results attributed to the different in beating frequency, the time scale of the base excitation displacement boundary condition applied to *NLBeam* was subsequently scaled such that the difference between resonant

and input frequencies is approximately 0.15 Hz for both simulation and experiment. As shown in Fig. 4.19b, the results compare well when the beating frequencies of the model and experiment are nearly equal. Initially, the *NLBeam* model over predicts displacement amplitudes, however, the amplitudes are in good agreement after approximately 20 s. In this case, the difference in simulation and experiment results during the initial transient suggest that *NLBeam* exhibits less damping than the experiment. This is consistent with expectations, because the only sources of damping in *NLBeam* are numerical damping associated with the Newmark integration scheme and gyroscopic forces associated with the rotational velocity. The damping for these cases is dominated by the time integration scheme which introduces numerical damping associated in larger proportions to higher frequencies.

4.6 Conclusions

A combined experimental and modeling effort was used to assess the ability for *NLBeam*, a finite element implementation of the geometrically exact beam theory, to represent generally geometrically nonlinear static and dynamic responses of slender beams. The investigation focused on test specimens described with simple and accurately measurable geometric parameters, i.e., rectangular cross section, and well-characterized linearly elastic material, i.e., aluminum. Using such simple test specimen as a surrogate for highly complex wind turbine blades isolates the ability to properly model finite deformations. However, for all of the dynamic excitation cases considered, it was difficult to drive response to regimes where geometric nonlinearity was emphatically crucial. Additional experimental techniques to distinguish the importance of nonlinearity need to be developed in order to better understand limitations of small deformation assumptions.

Overall, there was good agreement between experiment and simulation results for static displacement under both small and large deformation regimes. Under dynamic base excitation consistent with small deformation approximations, code-to-code comparisons between a geometrically linear model in Abaqus and the *NLBeam* model reinforce confidence in the newly developed code. Additional code verification was conducted by means of a grid convergence study performed for both static and dynamic cases. From comparison of simulation and experiment results for a variety of base excitation cases, it is clear that properly capturing the beating in structural response is highly sensitive to small errors in resonant frequency of the model. Typically, beating is a transient phenomenon that decays rapidly in time, however, the decay time may be significant in lightly damped systems. This may seem an unimportant part of the response for driving improvements to models, however, it is likely the extreme excursions in structural response (for example root bending moment or strain) are observed during such transients. Clearly, properly capturing the physical damping in a model is important in correctly simulating these transient events. Also, it is notable that the same sensitivity applies to *actual* deviations in input excitation frequency and *actual* changes in system resonant frequency attributable to, e.g., temperature changes or ice buildup. Transient response is perhaps less important for wind-turbines because the blades exhibit significantly more damping than simple surrogates, but this investigation clearly motivates consideration of such effects.

Results from this research motivate additional work in several areas. Firstly, the importance of energy dissipation, i.e., damping, to the structural dynamic response for these cases motivates development of a physics-based damping model to add dissipative forces to equations of motion in *NLBeam*. In particular, simple material damping is relevant to this investigation; perhaps more detailed viscoelastic and frictional mechanisms would become important when considering composite materials. As discussed previously, the motivation of this work led to the selection of simple geometry and materials for test specimens. The next step in increasing relevance to the structural dynamics of wind turbines is to address composite materials and include initial curvature (especially twist) of cross sections along the reference axis. Ideally, these extensions would be first made independently, and then subsequently with realistic wind turbine blades. The research conducted here has focused on validation of kinematic variables, namely, displacement and acceleration. Extending the considered kinematic variables to include strain and curvature is relatively straightforward and should be included in future work. On the other hand, of paramount importance is validating simulations of structural forces and moments transmitted through the base. Measuring this aspect of structural dynamic response is not trivial.

There are a number of enhancements that would benefit future experiments. For example, computing the harmonic distortion of a response time history can quantify system nonlinearity. However, in order to calculate harmonic distortion, a purely sinusoidal input of a single frequency must be used to excite the system. The equipment used in this research was not capable of driving a sufficiently pure sinusoidal mechanical response over the range of input magnitudes employed. Additionally, it would be beneficial to use two high-speed cameras, one focused on capturing base motion and one focused on tip response, to get more accurate measurements at both locations.

Acknowledgements Dangora, Harvie, and Wichman would like to acknowledge the Engineering Institute at Los Alamos National Laboratory (Dr. Charles Farrar, Director) for providing the funding and equipment used in conducting this research. The authors gratefully acknowledge Ian Fleming, Dr. Steve Anton, and Dr. Francois Hemez for their training, support, and expertise, respectively. Luscher is grateful for the support of the Laboratory Directed Research and Development (LDRD) project on Intelligent Wind Turbines (IWT) at Los Alamos National Laboratory (Dr. Curtt Ammerman, PI).

References

1. Samorani M, The wind farm layout optimization problem. http://leeds-phdstudents.colorado.edu/samoranm/papers/Wind.pdf
2. US Department of Energy (2010) HIGRAD/Windblade wind generation modeling and simulation. http://techportal.eere.energy.gov/technology.do/techID=276
3. Dalton S, Monahan L, Stevenson I et al (2012) Towards the experimental assessment of NLBeam for modeling large deformation structural dynamics. In: Proceedings of the 30th international odal analysis conference. Jacksonville
4. Reissner E (1981) On finite deformations of space-curved beams. J Appl Math Phys 32(6):734–744.
5. Simo J (1985) A finite strain beam formulation. The three-dimensional dynamic problem - part 1. Comp Methods Appl Mech Eng 49(1):55–70.
6. Simo J, Vu-Quoc L (1986) A three-dimensional finite-strain rod model. Part 2: computational aspects. Comp Methods Appl Mech Eng 58(1):79–116.
7. Hodges DH, Yu W (2007) A rigorous, engineer-friendly approach for modelling realistic, composite rotor blades. Wind Energy 10(December 2006):179–193.
8. The Engineering ToolBox, Elastic properties and young modulus for some materials. http://www.engineeringtoolbox.com/young-modulus-d_417.html
9. Tedesco J, McDougal W, Ross C (1999) Structural dynamics theory and applications. Addison Wesley Longman, Inc., Menlo Park

Chapter 5
Identification of Restoring Force Surfaces in Nonlinear MDOF Systems from FRF Data Using Nonlinearity Matrix

Murat Aykan and H. Nevzat Özgüven

Abstract The sensitivity of the response characteristics of a nonlinear structure to load level may prevent us to predict the linear behavior of a nonlinear system. The nonlinear identification method recently proposed by the authors is based on the measured linear and nonlinear Frequency Response Functions (FRFs). The method is easy to implement and requires standard testing methods. The data required is limited with measured linear and nonlinear FRFs. In order to obtain the linear FRFs in a nonlinear system, it is the general practice to use low level forcing, unless the nonlinearity is due to dry friction. However, depending on the level of nonlinearity it may not be possible to lower the harmonic forcing amplitude beyond a practical limit, and this may not be sufficient to obtain linear FRFs. The approach presented in this study aims to perform the nonlinear identification directly from a series of measured nonlinear FRFs. It is shown that Restoring Force Surfaces (RFS) can be identified more accurately by employing this approach. The verification of the method is demonstrated with simulated and experimental case studies.

Keywords Nonlinear structural dynamics • Nonlinear identification • Parametric nonlinear identification • Nonlinear structures • Nonlinear vibration testing

5.1 Introduction

Traditionally, for system identification in structural dynamics, we tend to apply linear identification theories, which are well established [1, 2]. However, with the increasing need to understand nonlinear characteristics of complicated structures, there were several studies published on nonlinear system identification. For instance, see [3–15]. Nonlinearities can be localized at joints or boundaries or else the structure itself can be nonlinear. There are various types of nonlinearities, such as hardening stiffness, clearance, coulomb friction etc. [4].

Nonlinear system identification methods can be divided into two groups as time and frequency domain methods [11], and time domain methods can be further divided as discrete and continuous time methods [5]. Most of the methods available require some foreknown data for the system. Some methods require all or part of mass, stiffness and damping values [7–9] whereas some methods [10–14] require linear frequency response function (FRF) of the analyzed structure. In these methods nonlinearity type is usually foreknown or determined by inspecting the describing function footprints (DFF) visually. However, although the user interpretation may be possible for a single type of nonlinearity, it may not be so easy when there is more than one type of nonlinearity present in the system [4].

The Restoring Force Surface (RFS) method, proposed by Masri et al. [9], constitutes one of the first attempts to identify nonlinear structures. A variant of this method was later independently developed by Crawley et al. [16, 17] and was named as force-state mapping method. Masri et al. [18] extended the RFS method to MDOF systems in 1982.

M. Aykan (✉)
Department of Mechanical Engineering, Middle East Technical University, Ankara 06800, Turkey

Defense Systems Technologies Division, ASELSAN Inc., Ankara, 06172, Turkey
e-mail: maykan@aselsan.com.tr

H.N. Özgüven
Defense Systems Technologies Division, ASELSAN Inc., Ankara, 06172, Turkey
e-mail: ozguven@metu.edu.tr

G. Kerschen et al. (eds.), *Topics in Nonlinear Dynamics, Volume 1: Proceedings of the 31st IMAC, A Conference on Structural Dynamics, 2013*, Conference Proceedings of the Society for Experimental Mechanics Series 35,
DOI 10.1007/978-1-4614-6570-6_5,

The RFS method requires the time histories of the displacement and its derivatives, and the applied force to be measured or calculated. Furthermore, the mass and damping matrices can be needed. In theory, the RFS method is applicable to MDOF systems. However, a number of practical considerations diminish this capability, and its scope is practically bound to systems with a few degrees of freedom only [19].

The RFS method has been studied experimentally for several systems with few degrees of freedom. Kerschen et al. [20] demonstrated experimental identification of impacting cantilever beams with symmetrical or asymmetrical piecewise linear stiffness using the RFS method. Another experimental application of the RFS method studied by Kerschen et al. [21] was the VTT benchmark, which consists of wire rope isolators mounted between a load mass and a base mass. The RFS method was also used in vehicle suspension system characterization [22]. Recently, Noel et al. [19] demonstrated the application of the RFS method for an elastomeric connection on a real life spacecraft structure.

There are studies in the literature obtaining the nonlinear RFS [23, 24] using variants of RFS method or other similar approaches like neural networks and optimization [5, 25]. Application of optimization methods in nonlinear system identification is rather a new and promising approach. The major disadvantage of these methods is generally the computational time required.

Nonlinearity identification method presented in this study is an improved version of the method developed earlier by Özer et al. [11]. The improvement includes performing the nonlinear identification directly from a series of measured nonlinear FRFs without the need to measure the linear FRFs. Furthermore, it is shown that Restoring Force Surfaces (RFS) can be identified more accurately by employing this approach.

5.2 Theory

Representation of nonlinear forces in matrix multiplication form using describing functions has been first given by Tanrıkulu et al. [26], and employed in identification of structural nonlinearities by Özer et al. [11]. The method presented here is based on the basic theory of the identification method which is given in detail in reference [11]. Here, only the related equations are given with a brief summary.

The nonlinear internal forces in the system can be expressed in matrix form using describing functions. This approach makes it possible to represent the nonlinear stiffness and damping properties of the system in compact form as a response dependent matrix which can easily be included into the dynamic stiffness matrix of the linear system in the frequency domain. From the mathematical expressions of the FRF matrix of the nonlinear system $[H^{NL}]$ and FRF matrix of the linear part of the system $[H]$ (see reference [11] for details) the response dependent "nonlinearity matrix" $[\Delta(x,\dot{\chi})]$ can be obtained as

$$[\Delta] = \left[H^{NL}\right]^{-1} - [H]^{-1} \tag{5.1}$$

where the elements of the nonlinearity matrix are expressed in terms of describing functions v [26].

In general applications, the linear model of the system can be obtained by using FEM, and experiments are made only on the nonlinear system. Alternatively, the FRFs of the underlying linear system can be obtained from FRF measurements in the system at very low forcing levels, where the nonlinear internal forces will be negligible. However, when there is only friction type of nonlinearity, FRFs measured at low amplitude of vibration will not represent FRFs of the underlying linear system; on the contrary, the FRFs measured at high response levels will represent FRFs of the linear counterpart. Comparison of FRFs measured at different response levels will reveal whether or not there is only friction type of nonlinearity so that the FRF measured at high response level can be taken as the FRF for the underlying linear system. Yet, if the system has multiple nonlinearities including friction type of nonlinearity, it may be difficult to measure the FRF of the underlying linear system experimentally, and using finite element model of the system seems to be the only alternative to obtain linear FRF of the linear counterpart.

In an attempt to obtain the nonlinearity matrix directly from nonlinear FRFs, the following methodology is proposed;

The nonlinearity matrix at forcing level F_1 can be defined as

$$[\Delta_1] = \left[H_1^{NL}\right]^{-1} - [H]^{-1} \tag{5.2}$$

Changing the forcing to another level F_2, Eq. (5.2) becomes

$$[\Delta_2] = \left[H_2^{NL}\right]^{-1} - [H]^{-1} \tag{5.3}$$

Subtracting Eq. (5.2) from Eq. (5.3) yields

$$[\Delta_2] - [\Delta_1] = \left[H_2^{NL}\right]^{-1} - \left[H_1^{NL}\right]^{-1} \tag{5.4}$$

For a SDOF system, Eq. (5.4) reduces to

$$\Delta_2 - \Delta_1 = \frac{1}{H_2^{NL}} - \frac{1}{H_1^{NL}} \tag{5.5}$$

where the nonlinearity matrix reduces to the describing function ν.

The describing function will be a function of the displacement amplitude only, when there is displacement dependent nonlinearity in the system. As the values Δ_1 and Δ_2 are obtained from the same describing function, evaluated at two different displacement amplitude levels; if a polynomial form (as shown below) is assumed for the describing function and nonlinear FRFs at two load levels (H_1^{NL} and H_2^{NL}) are measured experimentally, the coefficients of the function that describes the nonlinearity can be calculated:

$$\Delta(X) = \sum_{i=1}^{\infty} c_i X^i \tag{5.6}$$

where X represents the amplitude of the harmonic response.

For a MDOF system the difference matrix ($[\Delta_2] - [\Delta_1]$) is obtained from Eq. (5.4). Then, a polynomial is fitted to each element of the difference matrix separately and the coefficients of the functions that describe the nonlinearities at different coordinates can be calculated. The only difference between one nonlinear location and multiple nonlinear locations will be the number of curve fitting operations required.

5.2.1 Application of the Method

The first step is to test the nonlinear structure at two excitation levels. Equation (5.4) requires having the inverses of the measured nonlinear FRFs, and therefore is sensitive to noise. In order to minimize this effect, the excitation levels can be chosen high enough or averaging can be performed. However, if the forcing levels are high then friction type nonlinearities will not depict themselves in the measured values. In order to identify friction type nonlinear elements a low forcing test can also be performed. Equation (5.4) will give a complex result, whose real part represents the stiffness nonlinearity and the imaginary part represents the damping nonlinearity.

In order to solve Eq. (5.4) we need as many equations as the order of the polynomial that has been assumed. These equations can be generated from the nonlinear FRF values, which have distinct displacement values for each frequency. In other words, if we assume a polynomial, for instance up to the third order for the nonlinearity, we will need three equations. The following equations show the calculation procedure:

$$(c_1X_2 + c_2X_2^2 + c_3X_2^3) - (c_1X_1 + c_2X_1^2 + c_3X_1^3) = \tfrac{1}{H_2^{NL}} - \tfrac{1}{H_1^{NL}} \tag{5.7}$$

$$\begin{bmatrix} X_2 - X_1 & X_2^2 - X_1^2 & X_2^3 - X_1^3 \end{bmatrix} \begin{bmatrix} c_1 \\ c_2 \\ c_3 \end{bmatrix} = \tfrac{1}{H_2^{NL}} - \tfrac{1}{H_1^{NL}} \tag{5.8}$$

$$\begin{bmatrix} x_2(\omega_1) - x_1(\omega_1) & X_2^2(\omega_1) - X_1^2(\omega_1) & X_2^3(\omega_1) - X_1^3(\omega_1) \\ x_2(\omega_2) - x_1(\omega_2) & X_2^2(\omega_2) - X_1^2(\omega_2) & X_2^3(\omega_2) - X_1^3(\omega_2) \\ x_2(\omega_3) - x_1(\omega_3) & X_2^2(\omega_3) - X_1^2(\omega_3) & X_2^3(\omega_3) - X_1^3(\omega_3) \end{bmatrix} \begin{bmatrix} c_1 \\ c_2 \\ c_3 \end{bmatrix} = \begin{bmatrix} \frac{1}{H_2^{NL}(\omega_1)} - \frac{1}{H_1^{NL}(\omega_1)} \\ \frac{1}{H_2^{NL}(\omega_2)} - \frac{1}{H_1^{NL}(\omega_2)} \\ \frac{1}{H_2^{NL}(\omega_3)} - \frac{1}{H_1^{NL}(\omega_3)} \end{bmatrix} \tag{5.9}$$

where ω represents the response frequency.

The FRF values at each frequency give us one equation. In general we will have more frequency values than the number of equations that is required to solve the equation for unknown coefficients. Thus, if we use "n" frequencies, Eq. (5.9) can be expanded as

$$\begin{bmatrix} x_2(\omega_1)-x_1(\omega_1) & X_2^2(\omega_1)-X_1^2(\omega_1) & X_2^3(\omega_1)-X_1^3(\omega_1) \\ x_2(\omega_2)-x_1(\omega_2) & X_2^2(\omega_2)-X_1^2(\omega_2) & X_2^3(\omega_2)-X_1^3(\omega_2) \\ x_2(\omega_3)-x_1(\omega_3) & X_2^2(\omega_3)-X_1^2(\omega_3) & X_2^3(\omega_3)-X_1^3(\omega_3) \\ \vdots & \vdots & \vdots \\ x_2(\omega_n)-x_1(\omega_n) & X_2^2(\omega_n)-X_1^2(\omega_n) & X_2^3(\omega_n)-X_1^3(\omega_n) \end{bmatrix} \begin{bmatrix} c_1 \\ c_2 \\ c_3 \end{bmatrix} = \begin{bmatrix} \frac{1}{H_2^{NL}(\omega_1)} - \frac{1}{H_1^{NL}(\omega_1)} \\ \frac{1}{H_2^{NL}(\omega_2)} - \frac{1}{H_1^{NL}(\omega_2)} \\ \frac{1}{H_2^{NL}(\omega_3)} - \frac{1}{H_1^{NL}(\omega_3)} \\ \vdots \\ \frac{1}{H_2^{NL}(\omega_n)} - \frac{1}{H_1^{NL}(\omega_n)} \end{bmatrix} \tag{5.10}$$

Equation (5.10) can be solved by pseudo inversion which will give us a least square fit solution for the polynomial coefficients. After successful identification of high forcing effective nonlinearities, the linear FRFs can be evaluated from Eq. (5.2). Thus, using Eq. (5.2) again with nonlinear FRFs obtained from low forcing level, and calculated linear FRFs, we can obtain the describing function values for low forcing nonlinearities such as friction.

The describing function inversion approach introduced recently [27] can now easily be integrated to the method proposed here. The verification and effective application of the method are shown with the case studies and experimental studies given next.

5.3 Case Studies

5.3.1 Case Study 1

The nonlinear identification approach proposed in this study is applied to a SDOF discrete system with a nonlinear elastic element represented by k_1^* (a linear stiffness of 1,000 N/m with a backlash of 0.005 m) and a coulomb friction element $c_1^*(= 0.001 sgn(\dot{x})N)$, as shown in Fig. 5.1.

The numerical values of the linear system elements are given as follows:

$$\begin{aligned} k_1 &= 500\,\mathrm{N/m} \\ c_1 &= 5\,\mathrm{Ns/m} \\ m_1 &= 1\,\mathrm{kg} \end{aligned} \tag{5.11}$$

The time response of the system is first calculated with MATLAB by using the ordinary differential equation solver ODE45. The simulation was run for 32 s at each frequency to ensure that transients die out. The frequency range used during the simulations is between 0.0625 and 16 Hz with frequency increments of 0.0625 Hz. Three forcing levels (0.01, 3, 20 N) are used, in turn, in the simulations. The FRF functions obtained are presented in Fig. 5.1. Before using the calculated FRFs as simulated experimental data, they are polluted by using the "rand" function of MATLAB with zero mean, normal distribution and standard deviation of 5 % of the maximum amplitude of the FRF value. A sample comparison for the nonlinear FRFs (H_{11}) is given in Fig. 5.2 for three different forcing levels.

Using the method proposed, the describing functions representing these nonlinear elements are calculated from simulated experimental results and are plotted in Fig. 5.3.

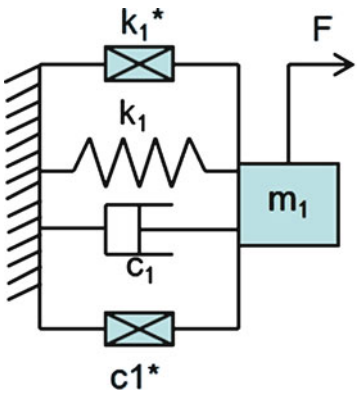

Fig. 5.1 SDOF discrete system with two nonlinear elements

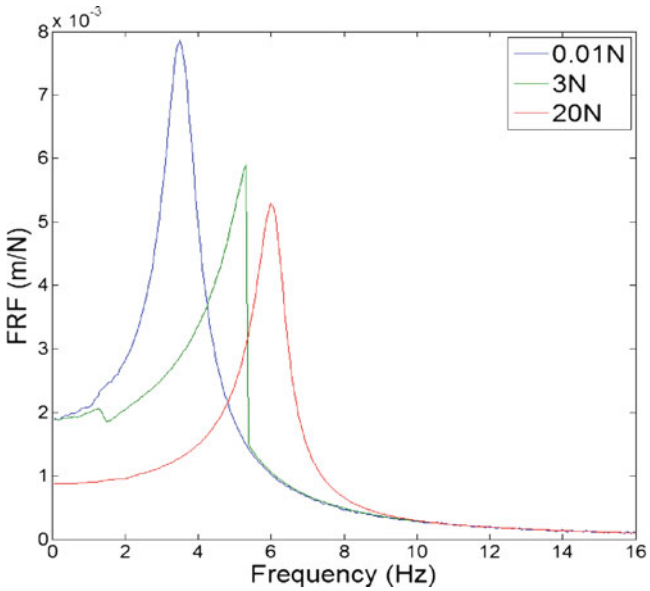

Fig. 5.2 Nonlinear FRF plots for different forcing levels

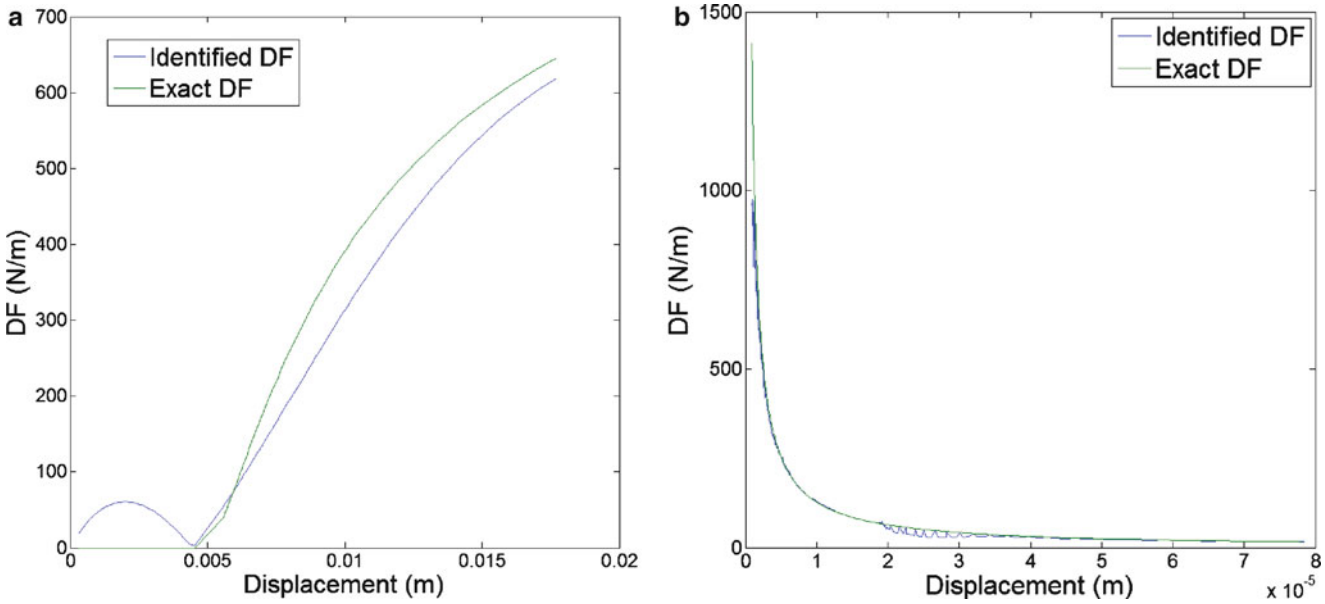

Fig. 5.3 Identified and exact DFs, (**a**) stiffness type (*backlash*) nonlinear element, (**b**) damping type (*friction*) nonlinear element

Alternatively, the types of nonlinear elements can be identified more easily if DF inversion method proposed in the previous study [27] is used. The calculated RF plots are presented in Fig. 5.4. By first fitting curves to the calculated RF plots, parametric identification can easily be made.

Although the DF inversion formulations are based on polynomial type describing functions, it is shown in this case study that they work, with an acceptable accuracy, for even discontinuous nonlinearities such as backlash, as well as for multiple nonlinearities.

5.3.2 Case Study 2

The proposed method is again applied to the same SDOF discrete system with a nonlinear elastic element represented by k_1^* (a nonlinear hardening cubic spring $= 10^6 x^2$ N/m) and a coulomb friction element $c_1^*(= 0.001 = \text{sgn}(\dot{x})\text{N})$, as shown in Fig. 5.1. The nonlinear FRFs (H_{11}) are given in Fig. 5.5 for three different forcing levels.

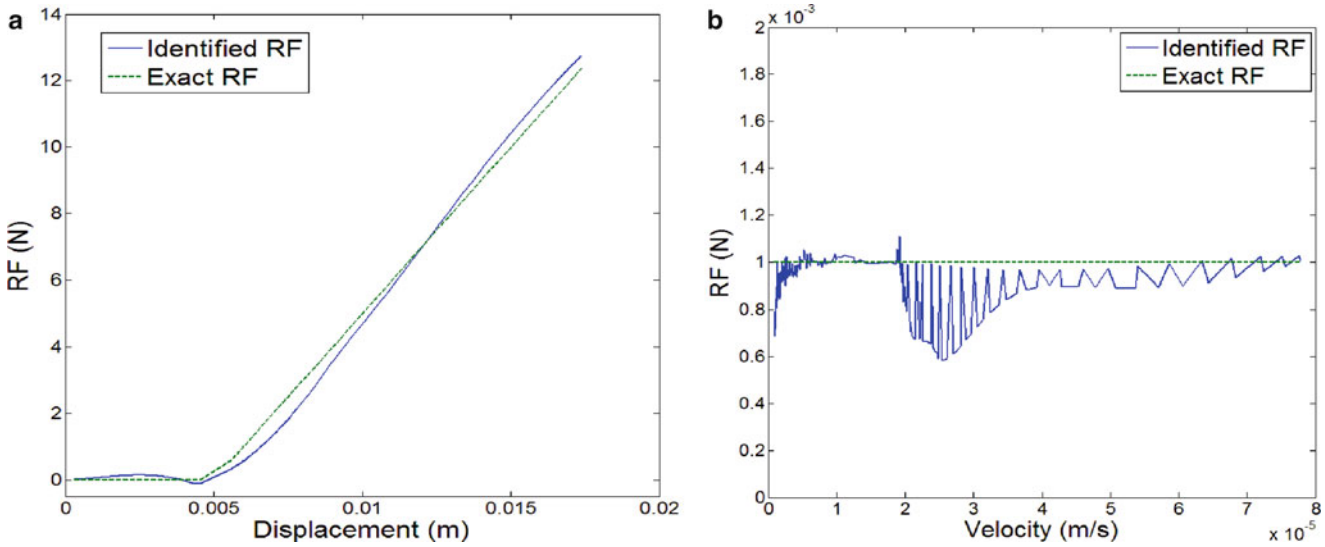

Fig. 5.4 Identified and exact RF plots, (a) stiffness type (*backlash*) nonlinear element, (b) damping type (*friction*) nonlinear element

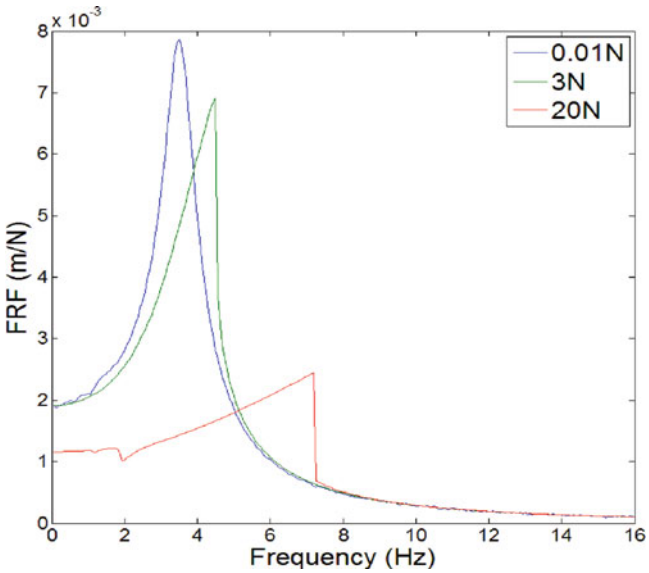

Fig. 5.5 Nonlinear FRF plots for different forcing levels

Following the same procedure we obtain the describing functions representing these nonlinear elements as given in Fig. 5.6.

Similarly, the types of nonlinear elements can be identified more easily if DF inversion method is used. These plots are given in Fig. 5.7.

5.3.3 Case Study-3

The nonlinear identification approach proposed in this study is applied to a 4 DOF discrete system with a nonlinear elastic element represented by k_4^* (a linear stiffness of 100 N/m with a backlash of 0.005 m) and a nonlinear hardening cubic spring $k_4^{**}(= 10^6 x^2\,\mathrm{N/m})$ between coordinates 3 and 4, as shown in Fig. 5.8.

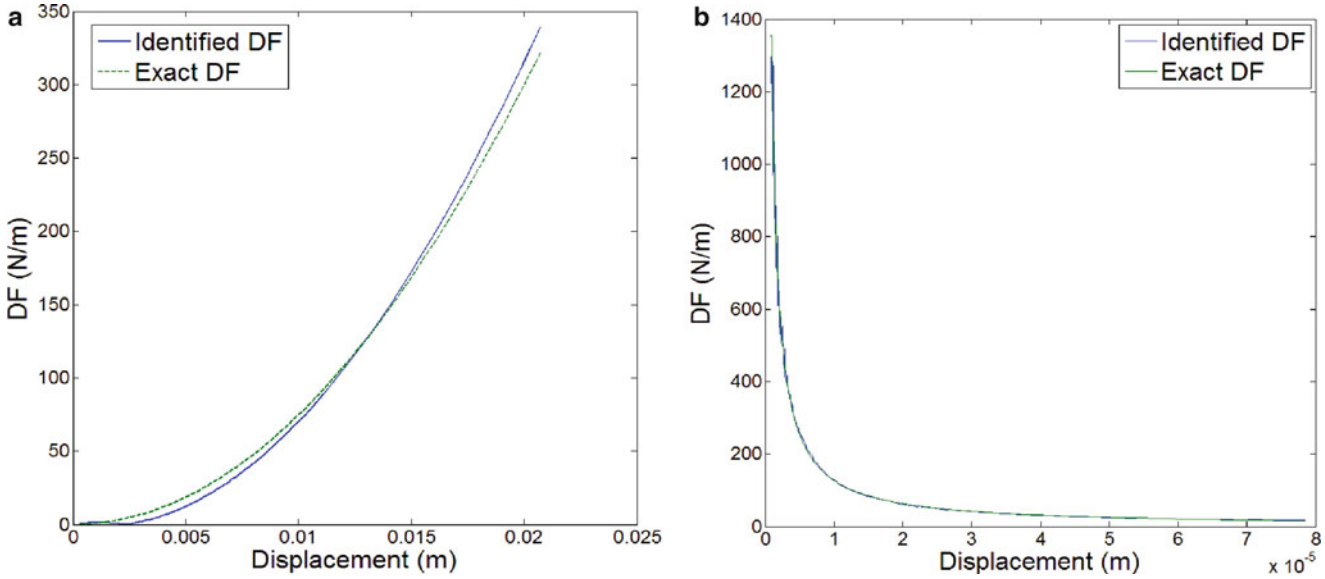

Fig. 5.6 Identified and exact DFs, (a) stiffness type (*cubic stiffness*) nonlinear element, (b) damping type (*friction*) nonlinear element

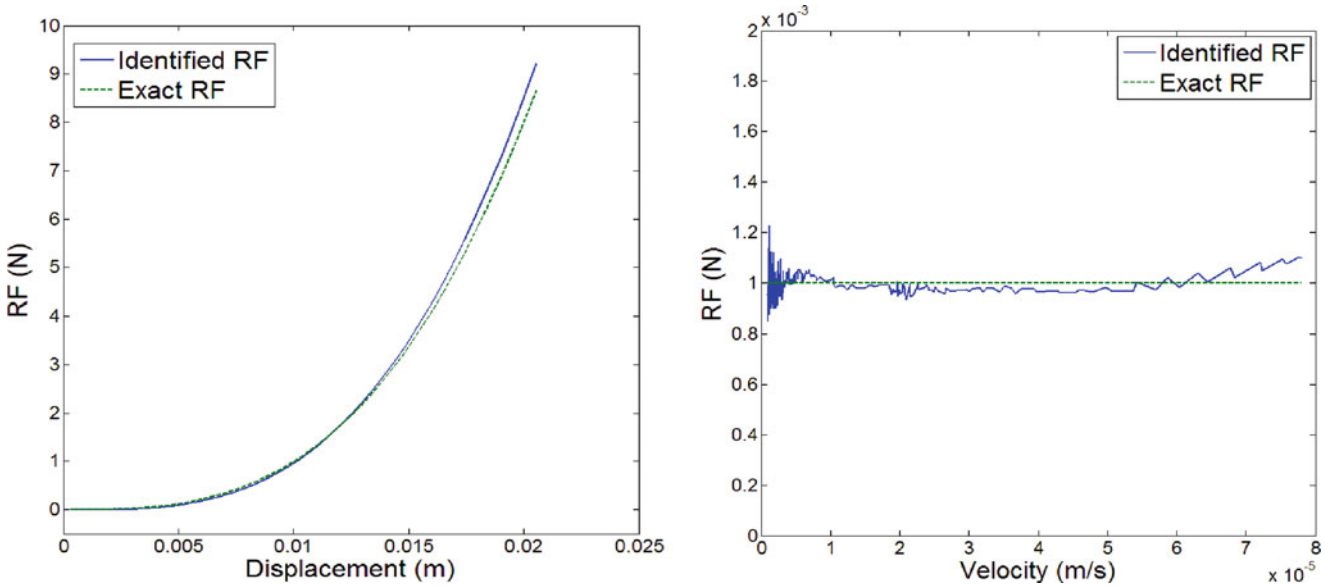

Fig. 5.7 Identified and exact RF plots, (a) stiffness type (*cubic stiffness*) nonlinear element, (b) damping type (*friction*) nonlinear element

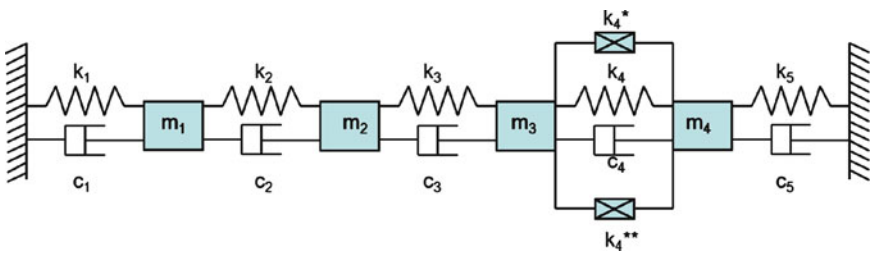

Fig. 5.8 Four DOFs discrete system with two nonlinear elements

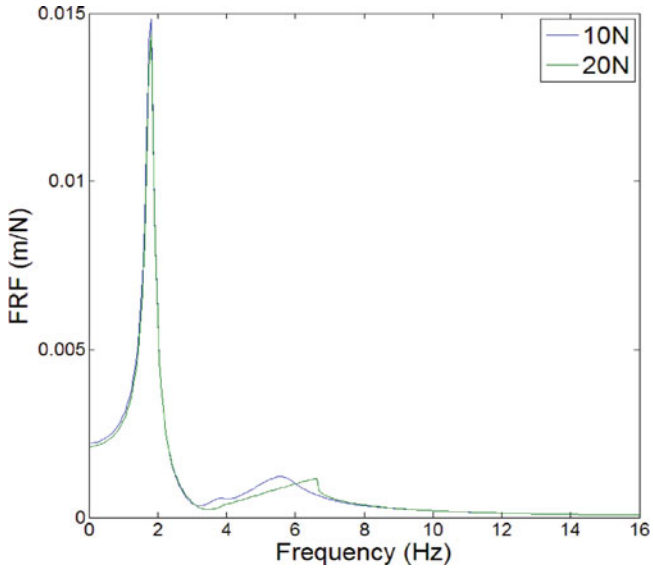

Fig. 5.9 Nonlinear FRF plots for different forcing levels

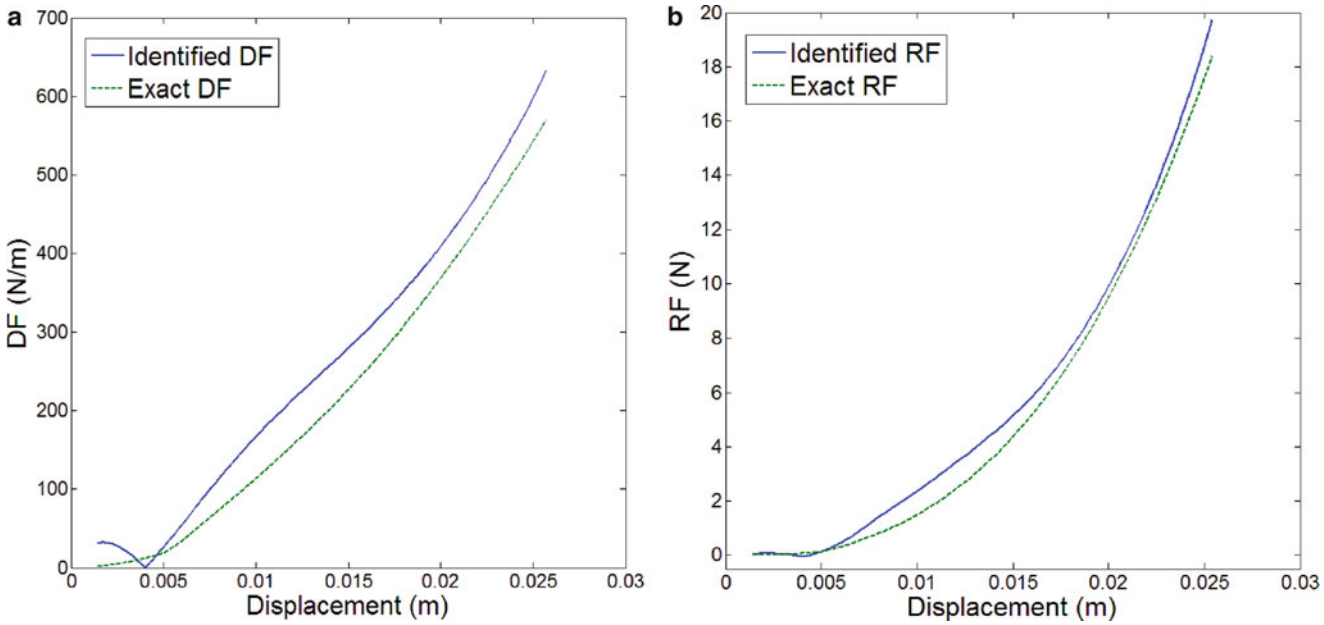

Fig. 5.10 Identified and exact, (a) DFs, (b) RFs

The numerical values of the linear system elements are given as follows:

$$\begin{aligned} k_1 &= k_2 = k_3 = k_4 = k_5 = 500\,\mathrm{N/m} \\ c_1 &= c_2 = c_3 = c_4 = c_5 = 5\,\mathrm{Ns/m} \\ m_1 &= 0.5\,\mathrm{kg}, \quad m_2 = 1\,\mathrm{kg}, \quad m_3 = 1.5\,\mathrm{kg}, \quad m_4 = 3\,\mathrm{kg} \end{aligned} \tag{5.12}$$

A sample comparison for the nonlinear and linear FRFs (H_{11}) is given in Fig. 5.9.

In this case study, the forcing is first applied from third coordinate with two forcing levels, and then from fourth coordinate. Employing the method suggested and by using FRFs of the third and fourth coordinates only, the describing functions representing these nonlinear elements are obtained as given in Fig. 5.10. As it is the case in the previous example, the total restoring force of nonlinear elements can be identified more easily when DF inversion method is used.

5.4 Experimental Study

The proposed approach is also tested on the experimental setup used in a recent study [28]. The tests carried out in previous study [28] were repeated with better frequency resolution (0.1 Hz) and force control. The experimental setup and FRF plots obtained with constant amplitude harmonic forces are given in Figs. 5.11 and 5.12, respectively.

The test rig consists of a linear cantilever beam with its free end held between two thin identical beams which generate cubic spring effect. The cantilever beam and the thin nonlinear beams were manufactured from St37 steel. The beam can be taken as a single DOF system with a nonlinear cubic stiffness located between the ground and the equivalent mass representing the cantilever beam. This test rig is preferred for its simplicity in modeling the dynamic system since the thin beams yield only hardening stiffness nonlinearity and the structure itself can be modeled as a single degree of freedom system.

For a single degree of freedom system, the nonlinearity matrix reduces to the describing function defining the nonlinearity [11]:

$$v = \frac{H - H^{NL}}{H^{NL} H} \tag{5.13}$$

As discussed in Sect. 5.2, the method requires the linear FRFs. Thus, we may assume that the lowest force level that we can achieve gives the linear FRF. However, the method proposed in this study shows that the linear FRF may not always be obtained accurately by low forcing even though there is no friction type of nonlinearity (Fig. 5.13).

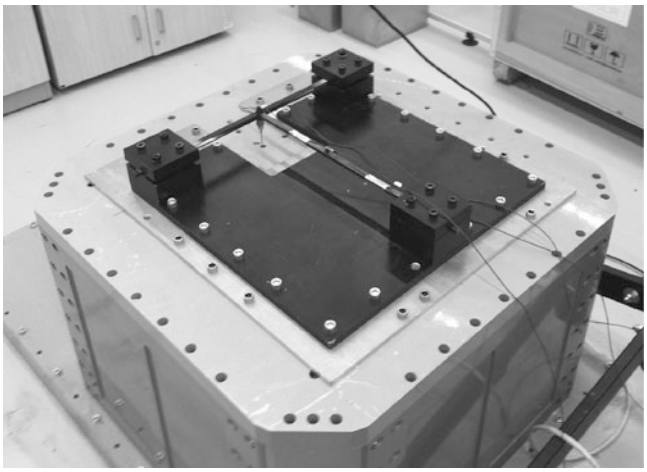

Fig. 5.11 Setup used in the experimental study

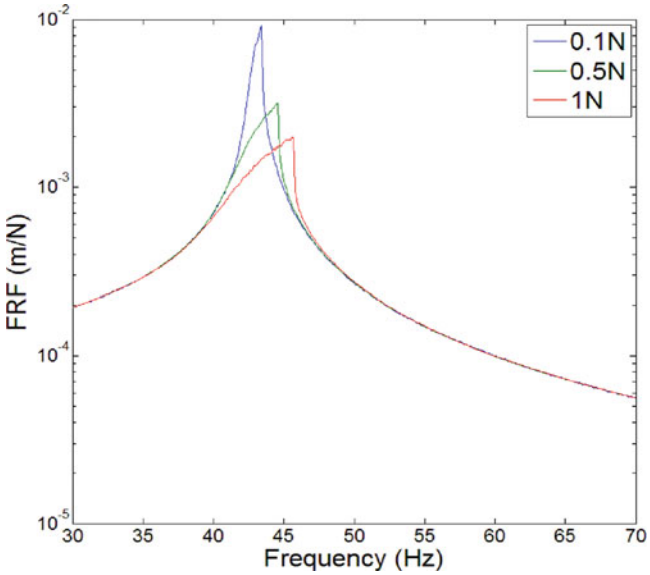

Fig. 5.12 Constant force driving point FRF curves for different forcing levels

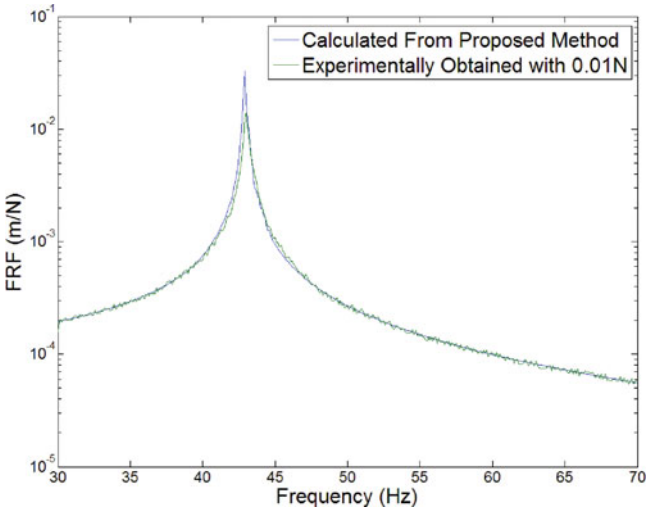

Fig. 5.13 Linear FRF curves

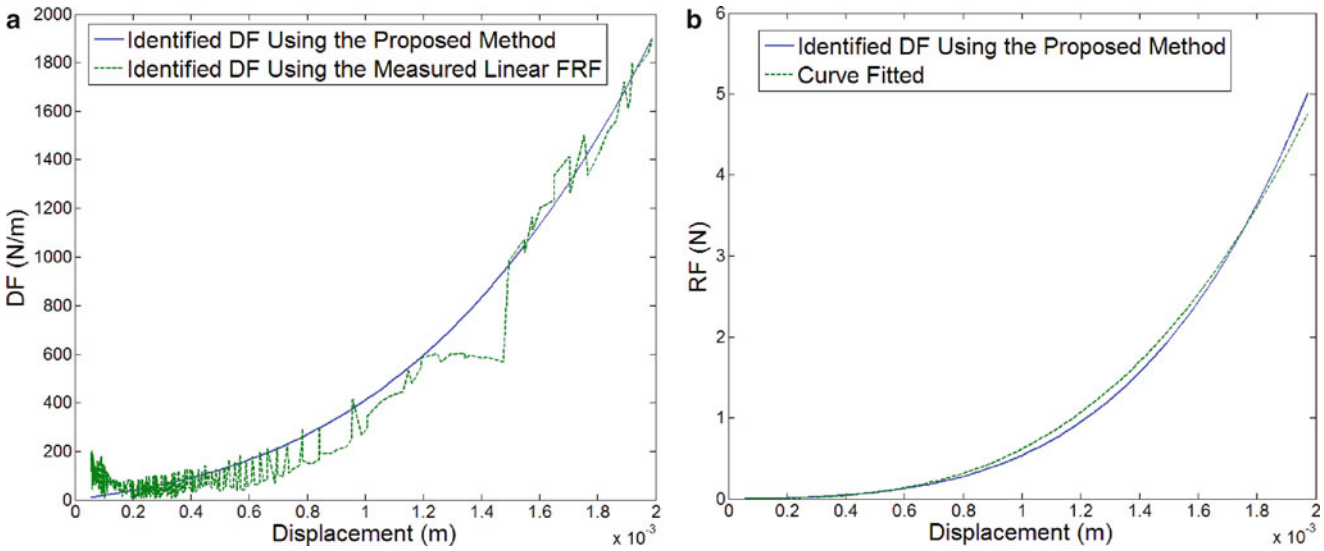

Fig. 5.14 (**a**) DF curve and fitted curve, (**b**) RF curve and fitted curve

If we cannot apply sufficiently low forcing level or if there is friction type of nonlinearity in the system then the approach proposed becomes more valuable. The describing function representation of the nonlinearity (ν) can be graphically shown as a function of response amplitude, which makes it possible to identify the type of nonlinearity and to make parametric identification by using curve fitting (Fig. 5.14a). The restoring force plot is also given in Fig. 5.14b. From Fig. 5.14b the nonlinearity coefficient is found by curve fitting as $6.18\ 10^8\,\mathrm{N/m^2}$.

The nonlinear FRFs are calculated [11] using the identified nonlinearity coefficient at forcing levels of 0.5 and 1 N and are compared with experimentally measured values in Fig. 5.15. As can be seen from the figure, better agreements are obtained between experimental and predicted responses with the new method.

5.5 Conclusions

It was recently shown [27] with an experimental case study that the method developed by Özer et al. [11] for detecting, localizing and parametrically identifying nonlinearity in MDOF systems is a promising method that can be used in industrial applications. In the study presented here some improvements are suggested to eliminate some of the practical limitations of the previously developed method. The verification of the approach proposed is demonstrated with three case studies. The main improvement is obtaining the nonlinearity matrix directly from nonlinear FRFs eliminating the need for obtaining linear FRFs.

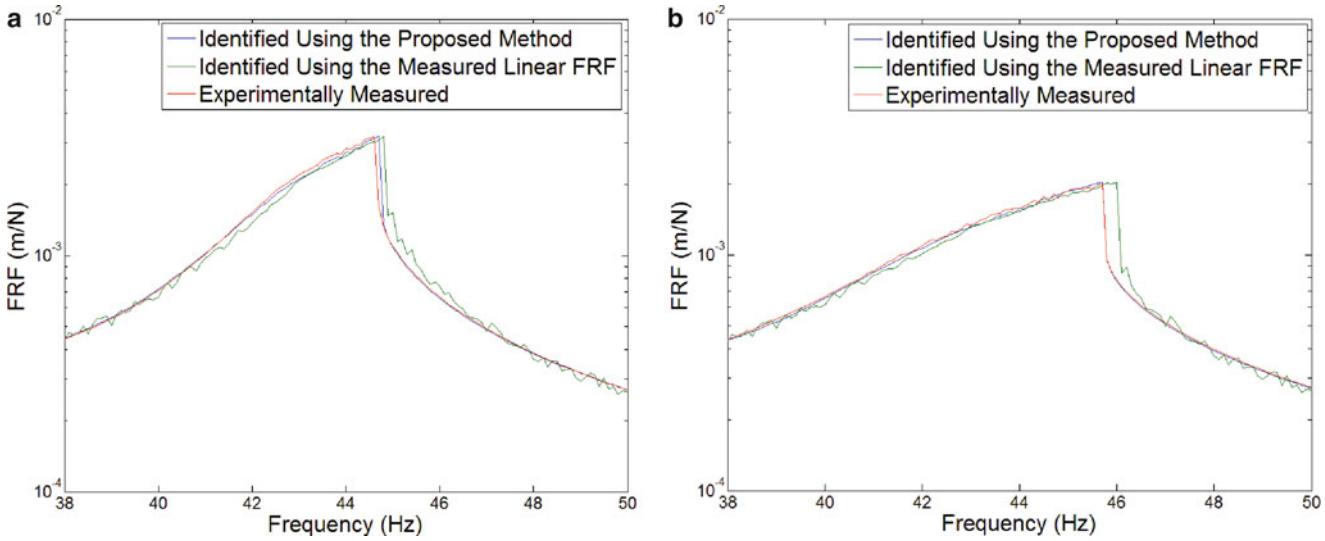

Fig. 5.15 Identified and measured nonlinear FRF curves at forcing level of (**a**) 0.5 N, (**b**) 1 N

The original method requires dynamic stiffness matrix of the linear part of the system which can be obtained by constructing a numerical model for the system and updating it using experimental measurements. Alternatively, low forcing measurements can be used to obtain the linear FRFs. However, low forcing testing may not always give the linear FRFs accurately when nonlinearity is high, and furthermore, if nonlinearity is due to dry friction, low forcing level testing will not give linear FRFs at all, since its effect will be dominant at low level vibrations. For this type of nonlinearity, on the contrary, high forcing testing will yield the linear FRFs. To overcome such problems, in the approach developed in this study it is proposed to test the structure at two forcing levels and calculate the nonlinearity matrix directly from these measurements.

The approach suggested is first applied to lumped parameter systems and it is shown that identification of nonlinear elements can successfully be achieved even when there is more than one nonlinear element with different characters at the same coordinate.

The application of the approach proposed is also demonstrated on a real structural test system, and it is concluded that the accuracy in parametric determination of nonlinearity by the proposed method gives better results than the method of Özer et al. [11] where low forcing tests were used to obtain linear FRFs. It is concluded in this study that the approach proposed is very promising to be used in practical systems, especially when there are multiple nonlinear elements at the same location.

References

1. Maia NMM, Silva JMM (1997) Theoretical and experimental modal analysis. Research Studies Press, Taunton
2. Ewins DJ (1995) Modal testing: theory and practice. Research Studies Press, Letchworth
3. Kerschen G, Worden K, Vakakis AF, Golinval JC (2006) Past, present and future of nonlinear system identification in structural dynamics. Mech Syst Signal Process 20:505–592
4. Göge D, Sinapius M, Füllekrug U, Link M (2005) Detection and description of non-linear phenomena in experimental modal analysis via linearity plots. Int J Nonlinear Mech 40:27–48
5. Worden K, Tomlinson GR (2001) Nonlinearity in structural dynamics, Institute of Physics Publishing, Bristol
6. Siller HRE (2004) Non-linear modal analysis methods for engineering structures. Ph.D. Thesis in Mechanical Engineering, Imperial College London/University of London
7. Narayanan S, Sekar P (1998) A frequency domain based numeric–analytical method for non-linear dynamical systems. Journal Sound Vib 211:409–424
8. Muravyov AA, Rizzi SA (2003) Determination of nonlinear stiffness with application to random vibration of geometrically nonlinear structures. Comput Struct 81:1513–1523
9. Masri SF, Caughey TK (1979) A nonparametric identification technique for nonlinear dynamic problems. Trans ASME J Appl Mech 46:433–445
10. Elizalde H, İmregun M (2006) An explicit frequency response function formulation for multi-degree-of-freedom non-linear systems. Mech Syst Signal Process 20:1867–1882
11. Özer MB, Özgüven HN, Royston TJ (2009) Identification of structural non-linearities using describing functions and the Sherman–Morrison method. Mech Syst Signal Process 23:30–44

12. Thothadri M, Casas RA, Moon FC, D'andrea R, Johnson CR Jr (2003) Nonlinear system identification of multi-degree-of-freedom systems. Nonlinear Dyn 32:307–322
13. Cermelj P, Boltezar M (2006) Modeling localized nonlinearities using the harmonic nonlinear super model. J Sound Vib 298:1099–1112
14. Nuij PWJM, Bosgra OH, Steinbuch M (2006) Higher-order sinusoidal input describing functions for the analysis of non-linear systems with harmonic responses. Mech Sys. Signal Process 20:1883–1904
15. Adams DE, Allemang RJ (1999) A new derivation of the frequency response function matrix for vibrating non-linear systems. J Sound Vib 227:1083–1108
16. Crawley EF, Aubert AC (1986) Identification of nonlinear structural elements by force-state mapping. AIAA J 24:155–162 (Sects. 3.2, 6.1)
17. Crawley EF, O'Donnell KJ (1986) Identification of nonlinear system parameters in joints using the force-state mapping technique. AIAA Pap 86–1013:659–667 (Sects. 3.2, 6.1)
18. Masri SF, Sass H, Caughey TK (1982) A nonparametric identification of nearly arbitrary nonlinear systems. J Appl Mech 49:619–628
19. Noel JP, Kerschen G, Newerla A (2012) Application of the restoring force surface method to a real-life spacecraft structure. In: Proceedings of the SEM IMAC XXX conference, Jacsonville, vol 3
20. Kerschen G, Golinval JC (2001) Theoretical and experimental identification of a nonlinear beam. J Sound Vib 244(4):597–613
21. Kerschen G, Lenaerts V, Golinval JC (2003) VVT benchmark: application of the restoring force surface method. Mech Syst Signal Process 17(1):189–193
22. Worden K, Hickey D, Haroon M, Adams DE (2009) Nonlinear system identification of automotive dampers: a time and frequency-domain analysis. Mech Syst Signal Process 23:104–126
23. Xueqi C, Qiuhai L, Zhichao H, Tieneng G (2009) A two-step method to identify parameters of piecewise linear systems. J Sound Vib 320:808–821
24. Haroon M, Adams DE, Luk YW, Ferri AA (2005) A time and frequency domain approach for identifying nonlinear mechanical system models in the absence of an input measurement. J Sound Vib 283:1137–1155
25. Liang YC, Feng DP, Cooper JE (2001) Identification of restoring forces in non-linear vibration systems using fuzzy adaptive neural networks. J Sound Vib 242(1):47–58
26. Tanrikulu Ö, Kuran B, Özgüven HN, İmregun M (1993) Forced harmonic response analysis of non-linear structures. AIAA J 31:1313–1320
27. Aykan M, Özgüven HN (2012) Parametric identification of nonlinearity from incomplete FRF data using describing function inversion. In: Proceedings of the SEM IMAC XXX conference, Jacsonville, vol 3
28. Arslan Ö, Aykan M, Özgüven HN (2011) Parametric identification of structural nonlinearities from measured frequency response data. Mech Syst Signal Process 25:1112–1125

Chapter 6
Smooth Projective Noise Reduction for Nonlinear Time Series

David Chelidze

Abstract Many nonlinear or chaotic time series exhibit an innate broad spectrum, which makes noise reduction difficult. Locally projective noise reduction using proper orthogonal decomposition (POD) is one of the most effective tools. It works for both map-like and continuously sampled time series. However, it only looks at geometrical or topological properties of data and does not take into account temporal characteristics of time series. Here we present a new noise reduction method using smooth orthogonal decomposition (SOD) of bundles of locally reconstructed trajectory strands, which imposes temporal smoothness on the filtered time series. It is shown that SOD based noise reduction significantly outperforms the POD based method for the continuously sampled noisy time series.

Keywords Smooth orthogonal decomposition • Nonlinear noise reduction • Proper orthogonal decomposition

6.1 Introduction

Many natural and engineered systems generate nonlinear deterministic time series that are contaminated by random measurement or dynamical noise. Chaotic time series have inherently broad spectrum and are not amenable to conventional spectral noise filtering. Two main methods for filtering noisy chaotic time series [11,12,14] are: (1) model based filtering [1], and (2) projective noise reduction [11]. While model based reduction has some merits for systems with known analytical models [1], projective noise reduction provides a more superior alternative [11] for experimental data. There are other methods like adaptive filtering or wavelet shrinkage [18] method that can work in certain cases, but require opportune selection of parameters or some a priori knowledge of system or noise mechanisms [7].

In this paper we describe a new method of nonlinear noise reduction that is based on a smooth subspace identification [5,6] in the reconstructed phase space [15, 17]. In particular, instead of identifying tangent subspace using proper orthogonal decomposition (POD) of a collection of nearest neighbor points (i.e., as in projective noise reduction scheme), we identify the tangent subspace by smooth orthogonal decomposition (SOD) of a bundle of nearest neighbor trajectory strands. This new method accounts for not only geometrical information in the data, but its temporal characteristics too. As we demonstrate later, this dramatically increases the ability to filter low signal-to-noise-ratio (SNR) time series.

6.2 Smooth Projective Nonlinear Noise Reduction

Both POD-based projective noise reduction [11], and SOD-based smooth projective noise reduction work in the reconstructed phase space of the system generating the noisy time series $\{x_i\}_{i=1}^{N}$. These time series are embedded into a d-dimensional phase space using delay coordinate embedding generating vector-valued trajectory $\{\mathbf{y}_i\}_{i=1}^{N-(d-1)\tau}$:

$$\mathbf{y}_i = \left[x_i, x_{i+\tau}, \ldots x_{i+(d-1)\tau}\right]^T, \tag{6.1}$$

D. Chelidze (✉)
Department of Mechanical, Industrial and Systems Engineering, University of Rhode Island, 92 Upper College Road, Kingston, RI 02881, USA
e-mail: chelidze@egr.uri.edu, http://mcise.uri.edu/chelidze

G. Kerschen et al. (eds.), *Topics in Nonlinear Dynamics, Volume 1: Proceedings of the 31st IMAC, A Conference on Structural Dynamics, 2013*, Conference Proceedings of the Society for Experimental Mechanics Series 35,
DOI 10.1007/978-1-4614-6570-6_6,

where τ is the delay time determined using the first minimum of average mutual information curve for the time series, or by some other nonlinear correlation statistic. The embedding dimension d should be large enough so that actual dynamical attractor is embedded in the phase space, and usually a false nearest neighbor algorithm is used for its estimation.

In the projective noise algorithm, for each point $\mathbf{y}_i$ in the reconstructed phase space, r temporarily uncorrelated nearest neighbor points $\{\mathbf{y}_i^j\}_{j=1}^r$ are determined. The POD is applied to this cloud of nearest neighbor points, and optimal k-dimensional projection of the cloud is obtained providing the needed filtered $\bar{\mathbf{y}}_i$, which in addition is also adjusted accounting for the shift in the projection dues to the trajectory curvature at $\mathbf{y}_i$. The filtered time series $\{\bar{x}_i\}_{i=1}^N$ is obtained by averaging the appropriate coordinates in the adjusted phase space $\{\bar{\mathbf{y}}_i\}_{i=1}^{N-(d-1)\tau}$ points.

In contrast, smooth projective noise reduction works with short strands of the reconstructed phase space trajectory, which are collection of odd numbered l consecutive phase space points. In particular, r nearest neighbor strands are determined by finding the r nearest neighbor points of the middle point of the current strand and forming the associated strands. The collection of these r strands is called a bundle. SOD is applied to each strand in the bundle and the corresponding k-dimensional smoothes approximations are obtained. The filtered middle strand point is determined by averaging the middle points of the strands in the bundle. The filtered time series are obtained just as in the projective noise reduction. The procedure can be applied repeatedly for further smoothing or filtering. For completeness, the details of SOD and smooth subspace approximation are given in the following sections.

6.2.1 Smooth Orthogonal Decomposition

The objective of POD is to obtain the best low-dimensional approximate description of high-dimensional data in a least squares sense [3, 13, 16]. In contrast, SOD is aimed at obtaining the smoothest low-dimensional approximations of high-dimensional dynamical processes [2, 4, 5]. While POD only focuses on the spatial characteristics of the data, SOD considers both its temporal and spatial characteristics.

Consider a case where a field, y, is defined for some n state variables $\{x_i\}_{i=1}^n$ (e.g., a system of n ordinary differential equations, n sensor measurements from some system, etc.). Assume that this field is sampled at exactly m instants of time (e.g., m sets of n simultaneous measurements at n locations). We arrange this data into a $m \times n$ matrix $\mathbf{Y}$, such that element Y_{ij} is the sample taken at the ith time instant from the jth state variable. We also assume that each column of $\mathbf{Y}$ has zero mean (or, alternatively, we subtract the mean value of each column). We are looking for a decomposition of this matrix $\mathbf{Y}$ into:

$$\mathbf{Y} = \mathbf{Q}\Phi^T, \tag{6.2}$$

where the columns of $\mathbf{Q} \in \mathbb{R}^{m\times n}$ are *smooth orthogonal coordinates* (SOCs) and *smooth orthogonal models* (SOMs) are given by the columns of $\Phi \in \mathbb{R}^{n\times n}$. In this decomposition, $\mathbf{Q} \in \mathbb{R}^{m\times n}$ should contain time coordinates sorted by their roughness.

The SOD is accomplished by the following generalized eigenvalue problem[1]:

$$\Sigma_{\mathbf{YY}}\psi_k = \lambda_k \Sigma_{\dot{\mathbf{Y}}\dot{\mathbf{Y}}}\psi_k, \tag{6.3}$$

where $\Sigma_{\mathbf{YY}} = \frac{1}{m}\mathbf{Y}^T\mathbf{Y} \in \mathbb{R}^{n\times n}$ and $\Sigma_{\dot{\mathbf{Y}}\dot{\mathbf{Y}}} = \frac{1}{m}\dot{\mathbf{Y}}^T\dot{\mathbf{Y}} \in \mathbb{R}^{n\times n}$ are auto-covariance matrices for n states and their time derivatives, respectively, λ_k are *smooth orthogonal values* (SOVs), and $\psi_k \in \mathbb{R}^n$ are *smooth projective modes* (SPMs). Higher the value of SOV the smoother is the corresponding SOC.

6.2.2 Smooth Subspace Identification and Data Projection

Equation (6.3) can be solved using a generalized singular value decomposition of the matrix pair $\mathbf{Y}$ and $\dot{\mathbf{Y}}$:

$$\mathbf{Y} = \mathbf{UC}\Phi^T, \quad \dot{\mathbf{Y}} = \mathbf{VS}\Phi^T, \quad \mathbf{C}^T\mathbf{C} + \mathbf{S}^T\mathbf{S} = \mathbf{I}, \tag{6.4}$$

where SOCs are given by the columns of $\mathbf{Q} = \mathbf{UC} \in \mathbb{R}^{m\times n}$ and SOVs are given by the term-by-term division of $\mathrm{diag}(\mathbf{C}^T\mathbf{C})$ and $\mathrm{diag}(\mathbf{S}^T\mathbf{S})$. The resulting SPMs are the columns of the inverse of the transpose of SOMs: $\Psi^{-1} = \Phi^T \in \mathbb{R}^{n\times n}$. In this

[1] Concept similar to SOD called *slow feature analysis* has been used for pattern analysis in neural science [19–26].

paper, we will assume that the SOVs are arranged in decreasing order ($\lambda_1 \geq \lambda_2 \geq \cdots \geq \lambda_n$). Please note that if the identity matrix is substituted for $\Sigma_{\dot{\mathbf{Y}}\dot{\mathbf{Y}}}$ in Eq. (6.3), it reduces to the POD eigenvalue problem that can be solved by the singular value decomposition of matrix $\mathbf{Y}$.

Smoothest k-dimensional approximation to $\mathbf{Y}$ ($k < n$) can be obtained by retaining only k columns of interest in matrices $\mathbf{U}$ and Φ and reducing $\mathbf{C}$ to the corresponding $k \times k$ minor. In effect, we are looking for a projection of $\mathbf{Y}$ onto a k-dimensional smoothest subspace. This k-dimensional smoothest $\bar{\mathbf{Y}}$ is composed of the corresponding reduced matrices $\bar{\mathbf{U}} \in \mathbb{R}^{m\times k}$, $\bar{\mathbf{C}} \in \mathbb{R}^{k\times k}$, and $\bar{\Phi} \in \mathbb{R}^{n\times k}$:

$$\bar{\mathbf{Y}} = \bar{\mathbf{U}}\bar{\mathbf{C}}\bar{\Phi}^T. \tag{6.5}$$

6.3 Description of Smooth Projective Noise Reduction Algorithm

1. Embedding time series into a reconstructed phase space:
   (a) Estimate the appropriate delay time (τ) for data using average mutual information or characteristic length method.
   (b) Using false nearest neighbor algorithm identify the appropriate embedding dimension d.
   (c) Determine the local (k) and global (d) embedding dimensions for trajectory strands.[2]
   (d) Embed time series using global embedding parameters.
2. Smooth Subspace Approximation:
   (a) Partition the embedded points into a kd-tree for fast searching.
   (b) Pad the end points using continuation to deal with edge effects of filtering.
   (c) For each embedded point $\mathbf{y}_i$ construct a strand $\mathbf{Y} = [\mathbf{y}_i, \ldots, \mathbf{y}_{i+l-1}]^T \in \mathbb{R}^{l\times n}$, where l is an odd number representing the length of a strand.
   (d) For the middle point on this strand $\mathbf{y}_{i+(l-1)/2}$, look up r nearest neighbor points that are temporarily uncorrelated, which would be the midpoints of the corresponding nearest neighbor strands $\{\mathbf{Y}^i\}_{i=1}^r$.
   (e) Apply SOD to each of the strands in this bundle, and obtain the corresponding k-dimensional smooth approximations $\{\bar{\mathbf{Y}}^i\}_{i=1}^r$.
   (f) Approximate the base strand by taking the average of all these k-dimensional smooth approximations using weighting that diminishes contribution with increase in the distance from the base strand.
3. Filtering/adjustment:
   (a) Replace the middle point in the base strand by its approximation determined above.
   (b) Average each d smooth adjustment to each point in the time series for estimating filtered point.
4. Repeat the first three steps until data is smoothed out.

6.4 Evaluating Performance of the Algorithm

In this section we evaluate the performance of the algorithm by testing it on a time series generated by a double-well Duffing oscillator:

$$\ddot{x} + 0.25\dot{x} - x + x^3 = 0.3\cos t\,. \tag{6.6}$$

The steady state chaotic response of this system was sampled 30 times per forcing period and totals of 12,000 points were recorded to test the noise reduction algorithm. In addition, 12,000 point normally distributed random signal was generated, and was mixed with the chaotic signal in 1/20, 1/10, 1/5, 2/5, and 4/5 amplitude ratios, which corresponds to 5, 10, 20, 40, and 80% noise in the signal or SNR of 26.02, 20, 13.98, 7.96, and 1.94 dB, respectively.

Results showing the increase in the SNR values after filtering are shown in Fig. 6.1. The POD and SOD-based algorithms were applied iteratively using 16 nearest neighbor points and the bundles of 9 strands, respectively. As seen from these plots the SOD-based filtering provides higher SNR for all noise levels at any iteration. The SNR plots do not tell the whole story,

[2] You may want to use sod of individual strands to get several samples of smooth subspace basis, and then apply sod to the matrix collecting all the basis to find the dimensionality of global bases.

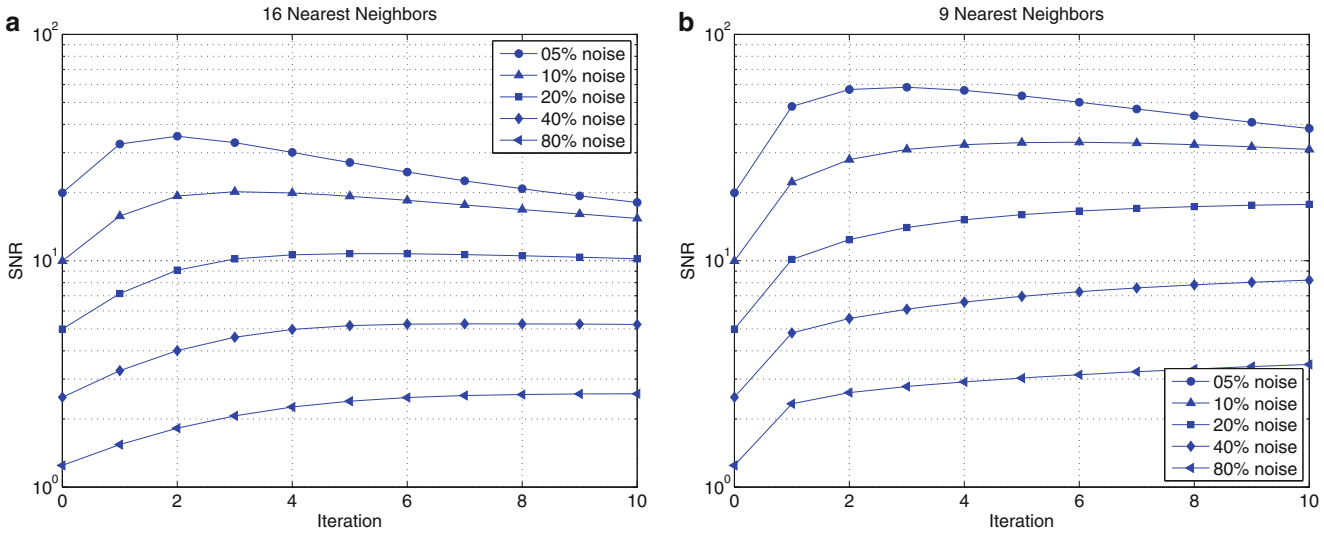

Fig. 6.1 SNR versus the iteration number for POD (*left plot*) and SOD-based (*right plot*) filtering

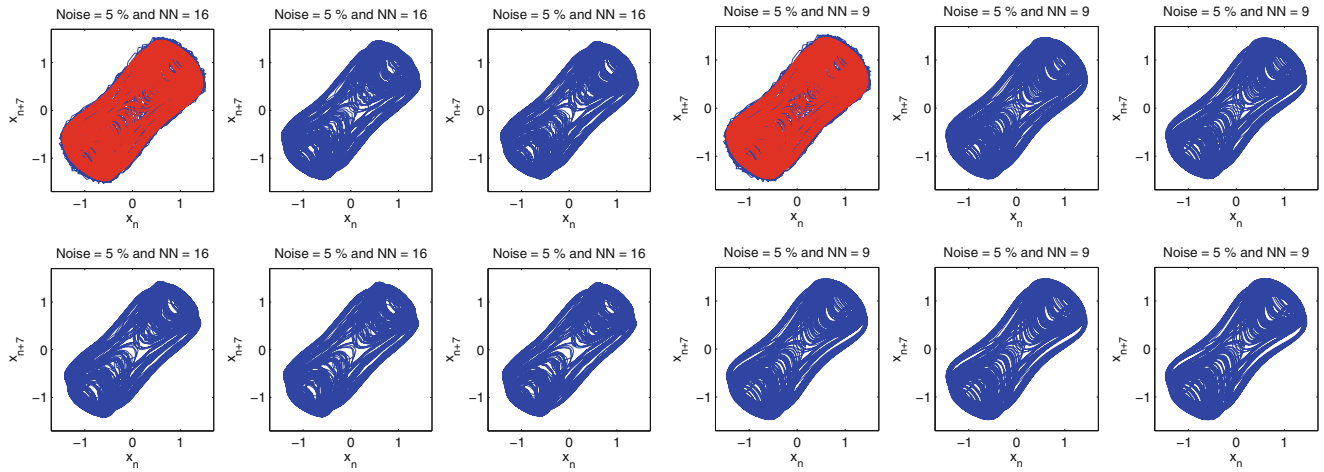

Fig. 6.2 Phase space reconstruction at different iteration stages for POD (*left plots*) and SOD-based (*right plots*) nonlinear noise reduction for a signal with 5% noise. The *red lines* show the clean signal, and *blue lines* show filtering process starting with unfiltered and filtered data after 2, 4, 6, 8, and 10 iterations

we also need to look at trajectories themselves. The corresponding phase portraits are shown in Fig. 6.2 for 5% noise, Fig. 6.3 for 20% noise, and 40% noise is shown in Fig. 6.4. Again, the SOD based noise reduction provides the better approximation of the original phase portrait. Even for a 40% noise level SOD-based reconstruction gives a plausible trajectory after 10 iterations, while POD-based reduction completely fails. However, at this noise level the fine phase space structure is not recovered even after ten successive application of our SOD algorithm, but larger structure of the signal is still present.

To evaluate filtering algorithm effectiveness in recovering the deterministic dynamical properties, we have also calculated largest Lyapunov exponents, and fractal dimensions from the original, noise contaminated, and filtered time series.

The Largest Lyapunov exponent λ_1 characterizes exponential growth of the distance between two points on the attractor that are very close initially. If this small initial distance between points is δ_0 and the distance at a later discrete time n is denote as δ_n, then $\delta_n \sim \delta_0 \exp(\lambda_1 t)$ as $\delta_0 \to 0$. Here we used a modified algorithm by Wolf et al. [27, 28], where for a set of reconstructed points $\mathbf{y}_i$ on their fiducial trajectory, we look up the r temporarily uncorrelated nearest neighbor points and track their average divergence from the fiducial trajectory. The results are shown in Fig. 6.5. Using the scaling regions at near the beginning we can estimate the corresponding largest Lyapunov exponents as given in Table 6.1. The results reflect that for 5% noise level both methods are able to approximate the original divergence curve adequately, with POD-based data having more local variation for small scales. For the 20% noise data, SOD-based filtering provides a much smoother curve that has similar scaling region to the original data. POD-based filtering is close to the original but has large fluctuations at

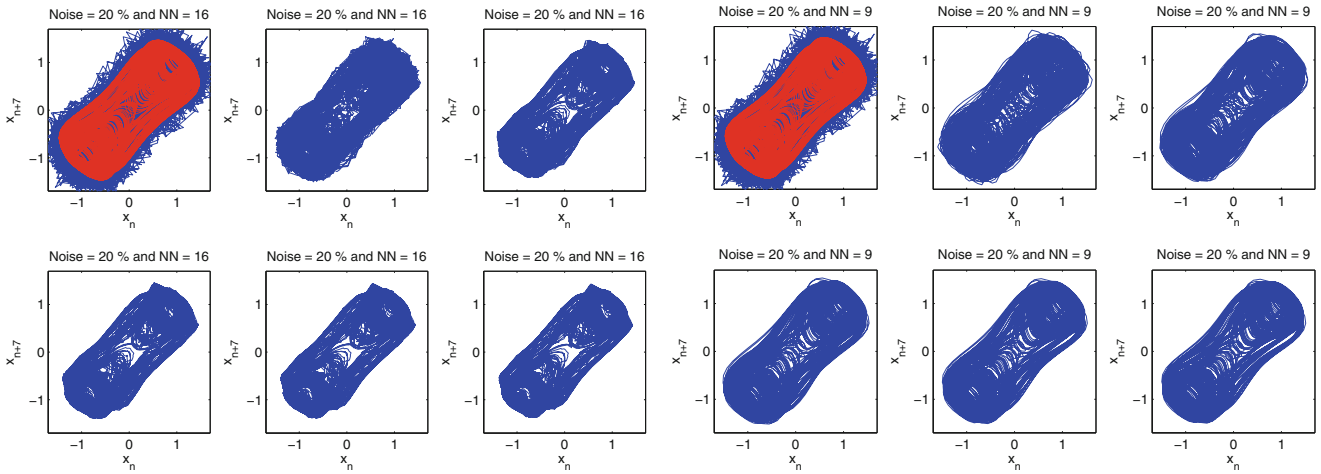

Fig. 6.3 Phase space reconstruction at different iteration stages for POD (*left plots*) and SOD-based (*right plots*) nonlinear noise reduction for a signal with 20% noise. The *red lines* show the clean signal, and *blue lines* show filtering process starting with unfiltered and filtered data after 2, 4, 6, 8, and 10 iterations

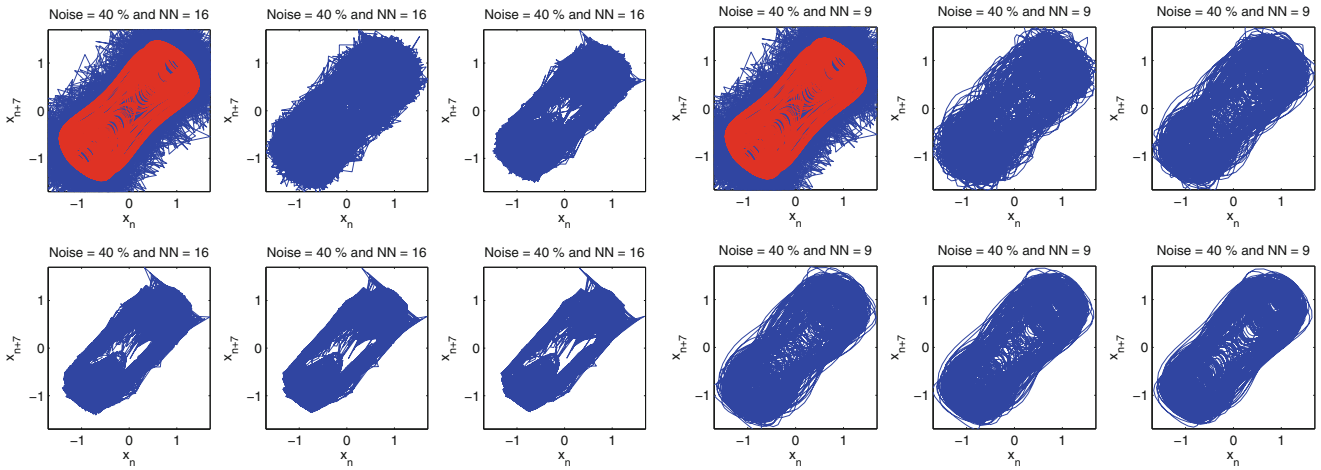

Fig. 6.4 Phase space reconstruction at different iteration stages for POD (*left plots*) and SOD-based (*right plots*) nonlinear noise reduction for a signal with 40% noise. The *red lines* show the clean signal, and *blue lines* show filtering process starting with unfiltered and filtered data after 2, 4, 6, 8, and 10 iterations

small scales. SOD-based algorithm is able to handle noise at both large and small scale structures, while POD is good only for large scale structures.

The correlation dimension characterizes the cumulative distribution of distances on the attractor [8–10], and indicates the minimum number of variables needed to describe the dynamics on the attractor. Here, we used a modified algorithm described in [10], where the correlation sum is estimated for the different length scales ε:

$$C(\varepsilon) = \frac{1}{(N-s)(N-s-1)} \sum_{i=1}^{N} \sum_{j=i+s+1}^{N} \Theta\left(\varepsilon - \left\|\mathbf{y}_i - \mathbf{y}_j\right\|\right) \sim \varepsilon^{D_2}, \tag{6.7}$$

where Θ is a Heaviside step function, N is the total number of points, s is the temporal separation needed to remove correlations, and D_2 is the correlation dimension. The results are shown in Fig. 6.6 for the correlation dimension estimated along the different length scales ε. The clean original signal's D_2 values have a plateau at about 2.2–2.3. The noisy data for both 5 and 20% noise levels looses this plateau, which is fully recovered by SOD filtering for 5% noise, and is still identifiable for 20% noise level. POD filtering, however, failed for 20% noise, and gave inferior result for 5% noise level.

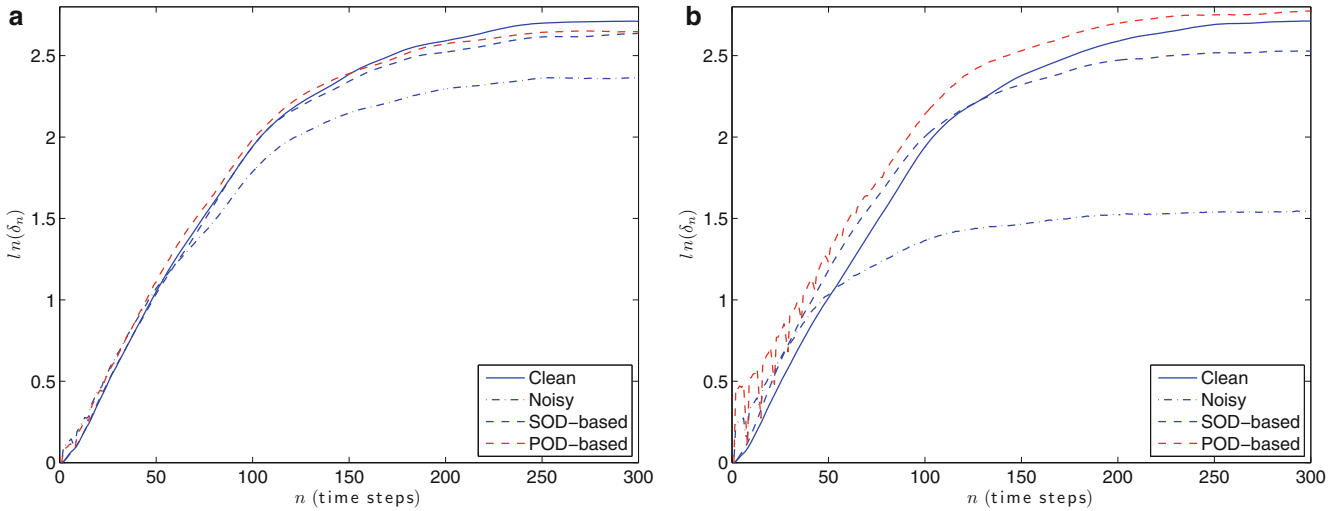

Fig. 6.5 Divergence curves for the largest Lyapunov exponent for a 5% (*left plot*) and 20% (*right plot*) noise levels

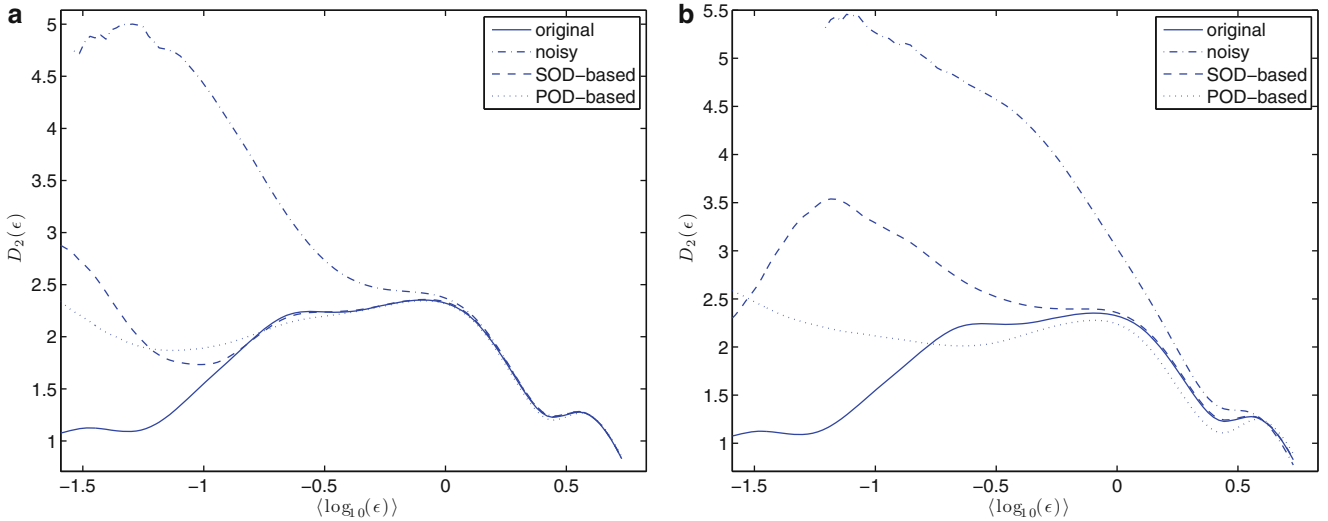

Fig. 6.6 Correlation dimension as a function of length scale for 5% (*left plot*) and 20% (*right plot*) noise levels

Table 6.1 SNR and largest Lyapunov exponent estimated for the original clean and noisy time series, plus for noisy data filtered by POD and SOD-based algorithms

Data type	SNR	Lyapunov exponent
Clean data	–	0.0847 ± 0.0017
5% noise level	26.003	0.0347 ± 0.0001
5% noise POD	31.003	0.0825 ± 0.0026
5% noise SOD	35.326	0.0854 ± 0.0015
20% noise level	13.962	0.0308 ± 0.0019
20% noise POD	20.174	0.0819 ± 0.0031
20% noise SOD	24.984	0.0786 ± 0.0021

6.5 Conclusions

In this paper we have propose a new smooth projective noise reduction (SOD-based) algorithm and compared its performance to the established projective noise reduction (POD-based) algorithm. Using synthetic chaotic time series generated by the two-well Duffing oscillator, we have shown that SOD-based algorithm outperforms POD-based one in terms of effective increase in SNR, better estimates for largest Lyaponov exponent, and the correlation dimension.

Acknowledgements This paper is based upon work supported by the National Science Foundation under Grant No. 1100031.

References

1. Brocker J, Parlitz U, Ogorzalek M (2002) Nonlinear noise reduction. Proc IEEE 90(5):898–918
2. Chatterjee A, Cusumano JP, Chelidze D (2002) Optimal tracking of parameter drift in a chaotic system: experiment and theory. J Sound Vib 250(5):877–901
3. Chatterjee A (2000) An introduction to the proper orthogonal decomposition. Curr Sci 78(7):808–817
4. Chelidze D, Liu M (2008) Reconstructing slow-time dynamics from fast-time measurements. Philos Trans R Soc A 366:729–3087
5. Chelidze D, Zhou W (2006) Smooth orthogonal decomposition-based vibration mode identification. J Sound Vib 292(3):461–473
6. Farooq U, Feeny BF (2008) Smooth orthogonal decomposition for modal analysis of randomly excited systems. J Sound Vib 316(1):137–146
7. Gao J, Sultan H, Hu J, Tung WW (2010) Denoising nonlinear time series by adaptive filtering and wavelet shrinkage: a comparison. IEEE Signal Process Lett 17(3):237–240
8. Grassberger P (1983) Generalized dimensions of strange attractors. Phys Lett A 97(6):227–230
9. Grassberger P, Procaccia I (1983) Characterization of strange attractors. Phys Rev Lett 50(5):346–349
10. Grassberger P, Procaccia V (1983) Measuring the strangeness of strange attractors. Phys D 9(1):189–208
11. Kantz H, Schreiber T (2003) Nonlinear time series analysis, Cambridge University Press, Cambridge
12. Kantz H, Schreiber T, Hoffmann I, Buzug T, Pfister G, Flepp LG, Simonet J, Badii R, Brun E (1993) Nonlinear noise reduction: a case study on experimental data. Phys Rev E 48(2):1529
13. Kerschen G, Golinval J-C, Vakakis AF, Bergman LA (2005) The method of proper orthogonal decomposition for dynamical characterization and order reduction of mechanical systems: an overview. Nonlinear Dyn 41:147–169
14. Kostelich EJ, Schreiber T (1993) Noise reduction in chaotic time-series data: a survey of common methods. Phys Rev E 48(3):1752
15. Liebert W, Pawelzik K, Schuster HG (2007) Optimal embeddings of chaotic attractors from topological considerations. Europhys Lett 14(6):521
16. Rathinam M, Petzold LR (2003) A new look at proper orthogonal decomposition. SIAM J Numer Anal 41(5):1893–1925
17. Sauer T, Yorke JA, Casdagli M (1991) Embedology. J Stat Phys 65(3):579–616
18. Tikkanen PE (1999) Nonlinear wavelet and wavelet packet denoising of electrocardiogram signal. Biol Cybern 80(4):259–267
19. Wiskott L (1998) Learning invariance manifolds. In: Niklasson L, Bodén M, Ziemke T, (eds) Proceedings of the 8th international conference on artificial neural networks, ICANN'98, Skövde, Sept 1998. Perspectives in neural computing. Springer, London, pp 555–560
20. Wiskott L (1998) Learning invariance manifolds. In: Proceedings of the 5th joint symposium on neural computation, San Diego, vol 8. University of California, 16 May 1998, pp 196–203
21. Wiskott L (1999) Learning invariance manifolds. In: Proceeding of the computational neuroscience meeting, CNS'98, Santa Barbara, CA, 1999. Special issue of neurocomputing, 26/27:925–932
22. Wiskott L (1999) Unsupervised learning and generalization of translation invariance in a simple model of the visual system. In: Paaß G (ed) Learning and adaptivity for connectionist models and neural networks, Proceedings Meeting of the GI-Working Group 1.1.2 "Connectionism", Magdeburg, 29 Sept, pp 56–67, Sankt Augustin, 1999. GMD-Forschungszentrum Informationstechnik GmbH. GMD Report 59
23. Wiskott L (2000) Unsupervised learning of invariances in a simple model of the visual system. In: Proceeding of the 9th annual computational neuroscience meeting, CNS 2000, Brugge, 16–20 July 2000, p 157
24. Wiskott L (2001) Unsupervised learning of invariances in a simple model of the visual system. In: Mumford D, Morel J-M, C. von der Malsburg (eds) Proceedings of the mathematical, computational and biological study of vision, Oberwolfach, Mathematisches Forschungsinstitut, 4–10 Nov 2001, pp 21–22
25. Wiskott L (2006) Is slowness a learning principle of visual cortex? In: Proceedings of the japan-germany symposium on computational neuroscience, Saitama, RIKEN Brain Science Institute, 1–4 Feb 2006, p 25
26. Wiskott L, Berkes P (2003) Is slowness a learning principle of the visual cortex? In: Proceeding of the jahrestagung der deutschen zoologischen gesellschaft, Berlin, 9–13 June 2003. Special issue of zoology, 106(4):373–382
27. Wolf A (1986) Quantifying chaos with lyapunov exponents. In: Chaos, pp 273–290
28. Wolf A, Swift JB, Swinney HL, Vastano JA (1985) Determining lyapunov exponents from a time series. Phys D 16(3):285–317

Chapter 7
Nonlinear Finite Element Model Updating of a Large-Scale Infilled Frame Structures Based on Instantaneous Modal Parameters

Eliyar Asgarieh, Babak Moaveni, and Andreas Stavridis

Abstract While linear finite element (FE) model updating has been successfully applied for predicting structural damage as loss of effective stiffness, nonlinear FE model updating can provide improved and more accurate damage identification (i.e., a more comprehensive measure of damage) and can additionally be used as a tool for damage prognosis. The current study is focused on characterizing the nonlinear material behavior in a FE model of a three-story infilled frame using the identified instantaneous natural frequencies and mode shapes. The 2/3-scale, 3-story, 2-bay reinforced concrete frame with masonry infills was subjected to large amplitude earthquake base excitations on a shake table. The deterministic stochastic subspace identification method is used for estimating the instantaneous (during short-time windows) modal parameters of the structure based on the nonlinear response of structure during a seismic base excitation. Parameters of a priori selected hysteretic models (Bouc-Wen) at different finite elements of the structural model are calibrated to minimize the misfit between the identified modal parameters and those from the FE model. The accuracy of the calibrated FE model is assessed through the comparison of the predicted response and natural frequencies obtained from the model with those of the specimen.

Keywords Nonlinear FE model updating • Damage identification • Hysteretic material model • System identification • Instantaneous modal parameters

7.1 Introduction

Identification of a numerical model of a dynamic system is a common interest among researchers in many fields of engineering especially in the field of structural health monitoring. Model-based structural health monitoring methods have been successfully used for damage identification of civil structures [1]. An important class of model based damage identification methods includes finite element (FE) model updating methods. Linear FE model updating, by means of modal parameters identified form the pre and post incident data, has been used successfully for detection, localization, and quantification of structural damage [2–4]. However, linear FE model updating methods cannot be used for predicting the behavior of structures due to future loading events and also are not capable of using the nonlinear data usually recorded during a damaging event. Higher amplitude nonlinear responses will provide a better indication of structural damage than do low amplitude responses. This can be explained by the fact that low amplitude ambient excitations often cannot open the existing cracks in the structural components and therefore damage in these components is not observed from the corresponding dynamic response. Therefore, some researchers have proposed to identify the parameters of nonlinear FE models in which nonlinearity is simulated with hysteretic nonlinear models assigned to their elements [5]. This approach can replace the identification of a time-variant system with the identification of time-invariant parameters of a nonlinear model.

Different methods, mainly based on time-domain data, have been used for identifying hysteretic material models which represent the nonlinearity in components of a structure. Since this usually involves solving an ill-conditioned inverse problem,

E. Asgarieh • B. Moaveni (✉)
Civil Engineering and Environmental Department, Tufts University, Medford, MA, USA
e-mail: eliyar.asgarieh@tufts.edu; babak.moaveni@tufts.edu

A. Stavridis
Department of Civil Engineering, University of Texas at Arlington, Arlington, TX, USA
e-mail: stavridis@uta.edu

G. Kerschen et al. (eds.), *Topics in Nonlinear Dynamics, Volume 1: Proceedings of the 31st IMAC, A Conference on Structural Dynamics, 2013*, Conference Proceedings of the Society for Experimental Mechanics Series 35,
DOI 10.1007/978-1-4614-6570-6_7,

the majority of the proposed approaches use adaptive time-domain methods such as different types of Kalman filters (KF) [5, 6]. Moreover, this estimation is based on nonlinear data; hence, revised versions of KF such as extended KF are applied to solve this issue by linearizing the model to the first order of accuracy [7, 8]. Other refined filters such as Unscented KF and particle filters are proposed to provide higher order of accuracy and robustness [9–11]. However, most applications of these nonlinear identification studies have been on single-degree-of-freedom or simple multi-degree-of-freedom numerical examples. Therefore, there is a need for application of these methods for identification of real-world complex systems.

In this paper, a method based on instantaneous modal identification is proposed for nonlinear model calibration of a large-scale complex structure. The deterministic stochastic subspace identification (DSI) method [12] is used for the estimation of the instantaneous modal parameters of the structure. The accuracy of this method was investigated by the authors in a previous study [13]. Selected parameters of a nonlinear FE model of the test structure are updated to minimize the misfit between the instantaneous modal parameters of the model with the identified ones at selected time instances. The optimum values of the model parameters are found by minimizing the objective function based on the modal residuals. This is achieved using the simulated annealing (SA) global optimization method [14], which is a probabilistic optimization method based on the Monte-Carlo sampling. In the following sections, the FE model of the test structure and the applied system identification method are briefly presented. Then the nonlinear model updating process applied here and the obtained results are discussed.

7.2 Test Structure and Nonlinear FE Model

The test structure is a 2/3-scale, 3-story, 2-bay reinforced-concrete moment-frame with unreinforced masonry infill walls. It was tested on the shake-table of University of California at San Diego (UCSD). Figure 7.1 shows the test structure on the UCSD-NEES shake-table. The structure was damaged progressively as it was subjected to seismic base excitations of increasing intensity [15]. The base excitations were scaled records of the 1989 Loma Prieta earthquake measured at Gilroy three station. The structure was densely instrumented with 289 sensors including accelerometers, strain gages, and displacement transducers. However, only the acceleration measurements at floor levels (two vertical and one longitudinal) are used in this study. Detailed information about the test structure, its instrumentation and dynamic tests are available at [16].

A two-dimensional nonlinear FE model of the structure illustrated in Fig. 7.2, has been created in the structural analysis software OpenSees [17]. In this model, the beams are modeled as linear-elastic Euler-Bernoulli frame elements. The columns of the first story and the infill walls at all three stories are assumed to have nonlinear behavior, while the columns of the second and third stories are modeled as linear-elastic frame elements. The infilled walls are modeled with diagonal struts. All the nonlinear elements are fiber elements with the hysteretic behavior assigned at the fiber sections. A Bouc-Wen model [18, 19] is used to represent the hysteretic material behavior of all nonlinear finite elements. In the process of model updating, parameters α, β, γ and δ_η are considered as updating parameters in the Bouc-Wen model with α as the post-yield to initial stiffness ratio, β and γ defining the shape of the hysteretic curve, and δ_η determining the stiffness degradation parameter. To reduce the number of parameters to be updated, the values of parameters β and γ are assumed to be equal [20].

Fig. 7.1 Three-story test structure on the UCSD-NEES shake table

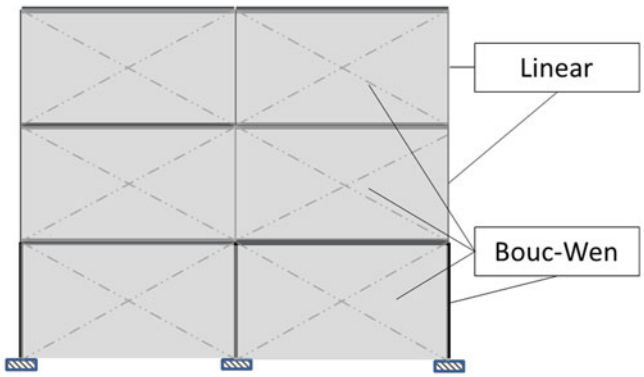

Fig. 7.2 Nonlinear FE model of the specimen used for model updating

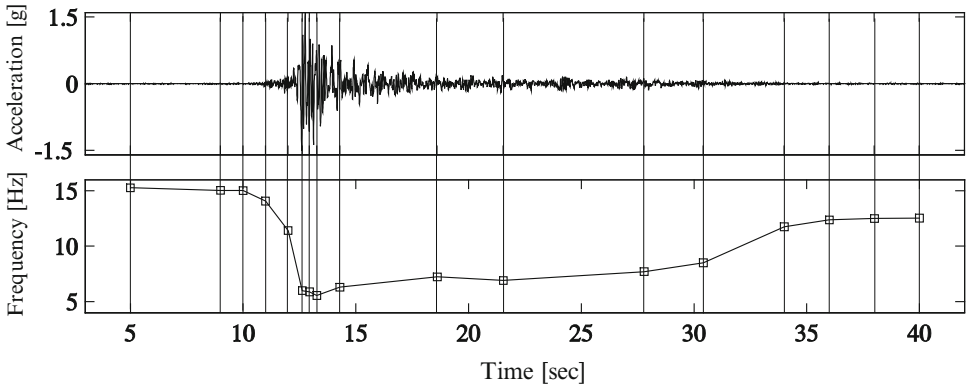

Fig. 7.3 Time history of the 1989 Loma Prieta Gilroy base excitation record (*top*), and identified first mode frequencies at 17 selected time instances (*bottom*)

7.3 System Identification

The short-time DSI method is used to extract the instantaneous modal parameters of the test structure. The DSI is a parametric, input-output system identification method used to realize a state-space model representation of a linear dynamic system. The method is robust against noise as it accounts for both output measurement noise as well as input disturbances. To identify the instantaneous modal parameters of the structure at each time instance a short length of data around each moment is used for identification. In this study time windows of 0.5 s have been used. The performance of this method for short-time modal identification was investigated by the authors in a recent study [13]. Figure 7.3 shows the instantaneous first mode natural frequency of the test structure identified at 17 instances during the 100% of 1989 Loma Prieta Gilroy earthquake record. These instances are arbitrarily selected along the response time history with especial emphasis on the highly nonlinear part of the response. It should be noted that the instantaneous natural frequencies depend on the considered window length and selected time instances but the corresponding natural frequencies of the model are also computed based on these parameters. From Fig. 7.3, it can be observed that the identified natural frequency of the specimen drops significantly during the strong motion part of the base excitation (12–15 s) but it slowly increases as the vibration weakens. The increase in natural frequencies corresponds to the larger tangent stiffness of structure at lower amplitude of response. However, there is a permanent reduction in the natural frequency of structure from before to after the earthquake due to damage.

7.4 Nonlinear Model Updating

The first step in the proposed model updating process is to calibrate the initial stiffness parameters through a linear FE model updating. Three stiffness parameters are updated: (1) stiffness of walls, (2) stiffness of columns in the first story, and (3) stiffness of columns in the second and third stories. The objective function, f, is calculated based on the modal parameter residuals which represent the discrepancies between the identified modal parameters (at the beginning of the earthquake) and the ones from the model.

$$f(\theta) = \mathbf{r}(\theta)^T \mathbf{W} \mathbf{r}(\theta) = \sum_{i=1}^{N_r} w_i r_i(\theta)^2 \tag{7.1}$$

Table 7.1 Updated parameters of column and wall hysteretic models

	Column parameters			Wall parameters			Error metrics	
	α_{column}	β_{column}	$\delta_\eta^{\text{column}}$	α_{wall}	β_{wall}	$\delta_\eta^{\text{wall}}$	f	E_{acc}
Case 1	0.6	950	6.2	0.001	8,890	9.7	2.2	2.1
Case 2	1.0	6,090	1.564	0.02	7,260	7.0	2.6	1.1

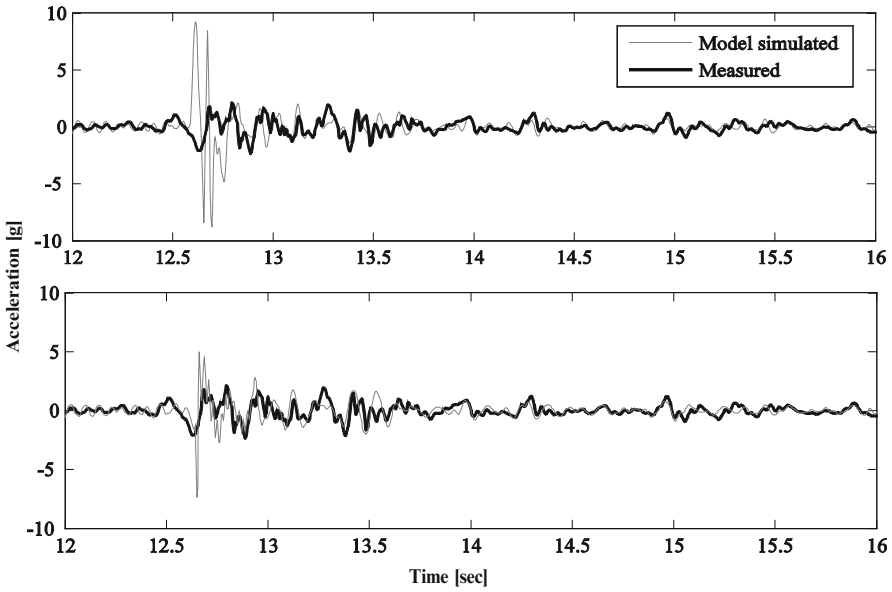

Fig. 7.4 Comparison of roof acceleration responses for Case1 (*top*) and Case2 (*bottom*)

In Eq. (7.1), θ represents the updating parameters, **W** is a diagonal weighting matrix, and **r** denotes the modal residual vector. Natural frequencies and mode shapes of the first two identified longitudinal modes are used in the FE model updating. The stiffness parameters at this step are updated using the identified modal parameters from the low amplitude initial part of response, in which structure behaves relatively linear. The stiffness parameters (moduli of elasticity) for the walls, columns of the first story, and columns of the second and third story are obtained as 3,840, 2,490, and 1,640 Kips/in^2, respectively.

In the second step of the proposed updating process, selected parameters of Bouc-Wen models for two substructures, the walls and the columns, are updated while the initial stiffness values are kept fixed. Two different cases of nonlinear parameter calibrations are performed. In both cases, α, β, and δ_η are updated for each substructure, assuming equal values for β and γ and therefore, decreasing the total updating parameters to six. The six parameters are updated simultaneously in the first case. To update these parameters, an objective function based on instantaneous modal parameters at the 17 instants (shown in Fig. 7.3) is minimized. The simulated annealing method [14] is used for minimizing the objective function.

In the second case, first δ_η is kept fixed for both the walls and columns substructures and the other 4 parameters are updated based on modal parameters at 11 instants during the middle part of the earthquake (11–34 s). Subsequently, the two δ_η parameters are updated while the other four are fixed to their updated values from the previous step, by using 3 initial and 3 final points from the 17 referred points. This process is repeated for a few iterations until no considerable reduction is gained in the objective function. Table 7.1 summarizes the calibrated nonlinear material parameters for the walls and columns for both cases. It should be noted that the considered optimization problem is not uniquely identifiable and therefore different combination of Bouc-Wen parameters provide similar acceleration response as well as modal residuals.

To evaluate the accuracy of the calibrated models, in addition to the objective function, another error metric is defined based on the difference between the horizontal acceleration response measured at the roof and the corresponding accelerations simulated by the update model. This error is computed for the acceleration time-histories over 0–40 s of the earthquake excitation with sampling frequency of 240 Hz. The values of both error metrics are also listed in Table 7.1.

$$E_{acc} = \frac{\|\ddot{\mathbf{x}} - \ddot{\mathbf{x}}^e\|_2}{\|\ddot{\mathbf{x}}^e\|_2} \tag{7.2}$$

The roof acceleration of the updated FE model subjected to the Gilroy earthquake is compared with the response time history measured during the test in Fig. 7.4. It is observed that the updated model, especially in Case 1, cannot estimate accurately the acceleration peaks during the highly nonlinear part of motion but it performs relatively well for moderate and low amplitude part of the response. The high level of nonlinearity during a short segment of data makes it difficult for the

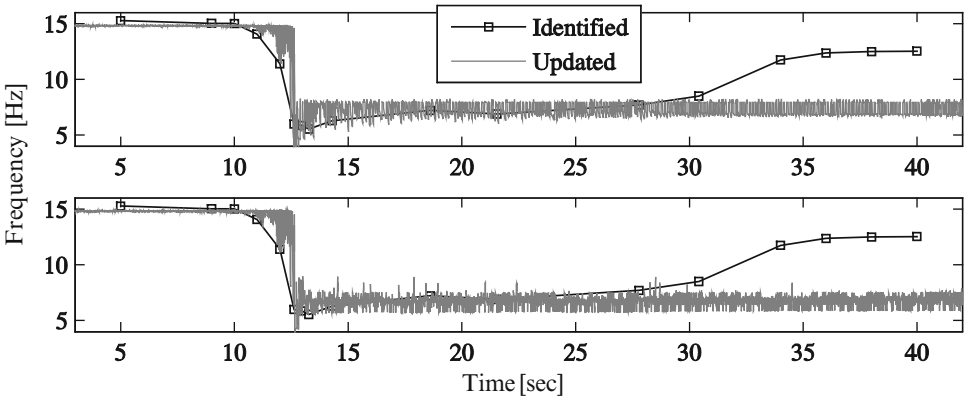

Fig. 7.5 Comparison of instantaneous natural modal frequency of the first mode for Case1 (*top*) and Case2 (*bottom*)

models to simulate the response during this period because most of the data used in the objective function represent lower levels of nonlinearity. The simplicity of the FE model and limited number of updating parameters are other factors for this error. Figure 7.5 compares the instantaneous natural frequencies of the models with those identified from the measured data. It can be seen that the frequencies are in good agreement up to the last part of records before the natural frequencies start to increase. The model cannot capture this regaining of stiffness.

7.5 Conclusions

The instantaneous modal parameters of a large-scale test structure are used for calibration of a nonlinear FE model. Selected parameters of Bouc-Wen models for two substructures (columns and walls) are updated in two different cases. It is observed that the updated models, especially for Case 1, significantly overestimate the acceleration peaks during the highly nonlinear part of motion but it performs relatively well for moderate and low amplitude part of the response. The high level of nonlinearity in this part of the response makes it difficult for the models to simulate the data since most of the data used in the objective function represent lower levels of nonlinearity. The simplicity of the FE model and limited number of updating parameters are other factors for this error. The calibrated models also cannot capture the increase in the tangent stiffness of the specimen as the excitation amplitude subsides.

Although the proposed method had been successfully applied to numerical data, this application to a real-world complex structure suggests that further investigation is required for practical application of the proposed methodology. Accounting for different sources of uncertainty including modeling errors and estimation errors is an important factor to improve the nonlinear structural identification results. This is the topic of ongoing research by the authors.

References

1. Doebling SW, Farrar CR, Prime MB, Shevitz DW (1996) Damage identification in structures and mechanical systems based on changes in their vibration characteristics: a detailed literature survey. Los Alamos National Laboratory Report, LA-13070-MS, Los Alamos
2. Teughels A, De Roeck G (2005) Damage detection and parameter identification by finite element model updating. Arch Comput Methods Eng 12(2):123–164
3. Moaveni B, He X, Conte JP, De Callafon RA (2008) Damage identification of a composite beam using finite element model updating. J Comput Aided Civil Infrastruct Eng 23(5):339–359
4. Moaveni B, He X, Conte JP, Restrepo JI (2010) Damage identification study of a seven-story full-scale building slice tested on the UCSD-NEES shake table. Struct Saf 32(5):347–356
5. Distefano N, Rath A (1974) Sequential identification of hysteretic and viscous models in structural seismic dynamics. Comput Methods Appl Mech Eng 6:219–232
6. Distefano N, Rath A (1975) System identification in nonlinear structural seismic dynamics.Comput Methods Appl Mech Eng 5(3):353–372
7. Hoshiya M, Saito E (1984) Structural identification by extended Kalman filter. J Eng Mech 110(12):1757–1770
8. Lin JS, Zhang Y(1994) Nonlinear structural identification using extended Kalman filter. Comput Struct 52(4) 757–764
9. Wu M, Smyth AW (2007) Application of unscented Kalman filter for real-time nonlinear structural system identification. J Struct Control Health Monit. doi:10.1002/stc.186, Published online in Wiley Inter Science
10. Mariani S, Ghisi A (2007) Unscented Kalman filtering for nonlinear structural dynamics. Nonlinear Dyn 49:131–150

11. Chatzi E, Smyth A (2009) The unscented Kalman filter and particle filter methods for nonlinear structural system identification with non-collocated heterogeneous sensing. Struct Control Health Monit 16:99–123
12. Van Overschee P, De Moore B (1996) Subspace identification for linear systems. Kluwer Academic, Norwell
13. Moaveni B, Asgarieh E (2012) Deterministic-stochastic subspace identification method for identification of nonlinear structures as time-varying linear systems. Mech Syst Signal Process 31:40–45
14. Kirkpatrick S, Gelatt CD, Vecchi MP (1983) Optimization by simulated annealing. Science 220(4598):671–680
15. Stavridis A, Koutromanos I, Shing PB (2012) Shake-table tests of a three-story reinforced concrete frame with masonry infill walls. Earthq Eng Struct Dyn 41:1089–1108. doi:10.1002/eqe.1174
16. Stavridis A. (2009) Analytical and experimental study of seismic performance of reinforced concrete frames infilled with masonry walls. Ph.D. thesis, University of California, San Diego
17. Mazzoni S, Scott MH, McKenna F, Fenves GL et al (2006) Open system for earthquake engineering simulation – user manual (version 1.7.3). Pacific Earthquake Engineering Research Center, University of California, Berkeley
18. Ismail M, Ikhouane F, Rodellar J (2009) The hysteresis Bouc-Wen model, a survey. Arch Comput Methods Eng 16:161–188
19. Ikhouane F, Hurtado JE, Rodellar J (2007) Variation of the hysteresis loop with the Bouc-Wen model parameters. Nonlinear Dyn 48(4):361–380
20. Ma F, Zhang H, Bockstedte A, Foliente GC, Paevere P (2004) Parameter analysis of the differential model of hysteresis. J Appl Mech 71(3):342–349

Chapter 8
Frequency-Domain Subspace Identification of Nonlinear Mechanical Systems: Application to a Solar Array Structure

J.P. Noël, G. Kerschen, E. Foltête, and S. Cogan

Abstract The present paper addresses the experimental identification of a simplified realisation of a solar array structure in folded configuration. To this end, a nonlinear subspace identification technique formulated in the frequency domain, referred to as the FNSI method, is exploited. The frequency response functions of the underlying linear structure and the nonlinear coefficients are estimated by this approach. Nonlinearity is caused by impacts between adjacent panels and friction and gaps appearing in their clamping interfaces. This application is challenging for several reasons, which include high modal density and the complicated nature of the involved nonlinear mechanisms.

Keywords Nonlinear system identification • Subspace method • Frequency domain • Space structure • Experimentall-data

8.1 Introduction

Identification of linear and time-invariant systems is a discipline that has evolved considerably during the last 40 years. The techniques available today are really quite sophisticated and advanced. In particular, subspace algorithms [1, 2] are powerful identification methods that are routinely used for experimental and operational modal analysis [3], but also for advanced processing such as damage detection and structural health monitoring [4]. However, nonlinearity is a frequent occurrence in engineering structures and, for this reason, subspace-based methods have recently been generalised to handle nonlinear systems. In particular, the frequency-domain nonlinear subspace identification (FNSI) method has proved successful [5, 6].

Space structure dynamics is a typical field of application for nonlinear system identification techniques [7]. Indeed, although they are generally modelled as linear systems, space structures are known to be prone to nonlinear phenomena. A specific difficulty encountered is the behaviour of solar generators in their stowed position. In fact, solar panels are folded during the spacecraft launch to save volume and impact one another at specific points, leading to nonlinear boundary conditions. As the excitation level increases, friction and gaps may also appear in the clamping interfaces between adjacent panels. In this context, the objective of the present paper is to address the experimental identification of a simplified realisation of a solar array structure in folded configuration using the FNSI method. The frequency response functions (FRFs) of the underlying linear structure and the nonlinear coefficients will be estimated by this approach. This application is challenging for several reasons, which include high modal density and the complicated nature of the involved nonlinear mechanisms. The paper is organised as follows. Section 8.2 describes the experimental test rig and its instrumentation. The FNSI method is then introduced in Sect. 8.3 and applied to the solar array structure using random and sine-sweep data in Sect. 8.4. The conclusions of this application are finally summarised in Sect. 8.5.

J.P. Noël (✉) • G. Kerschen
Space Structures and Systems Laboratory (S3L), Department of Aerospace and Mechanical Engineering, University of Liège, Liège, Belgium
e-mail: jp.noel@ulg.ac.be; g.kerschen@ulg.ac.be

E. Foltête • S. Cogan
FEMTO-ST Institute, LMARC, Besançon, France
e-mail: emmanuel.foltete@univ-fcomte.fr; scott.cogan@univ-fcomte.fr

G. Kerschen et al. (eds.), *Topics in Nonlinear Dynamics, Volume 1: Proceedings of the 31st IMAC, A Conference on Structural Dynamics, 2013*, Conference Proceedings of the Society for Experimental Mechanics Series 35,
DOI 10.1007/978-1-4614-6570-6_8,

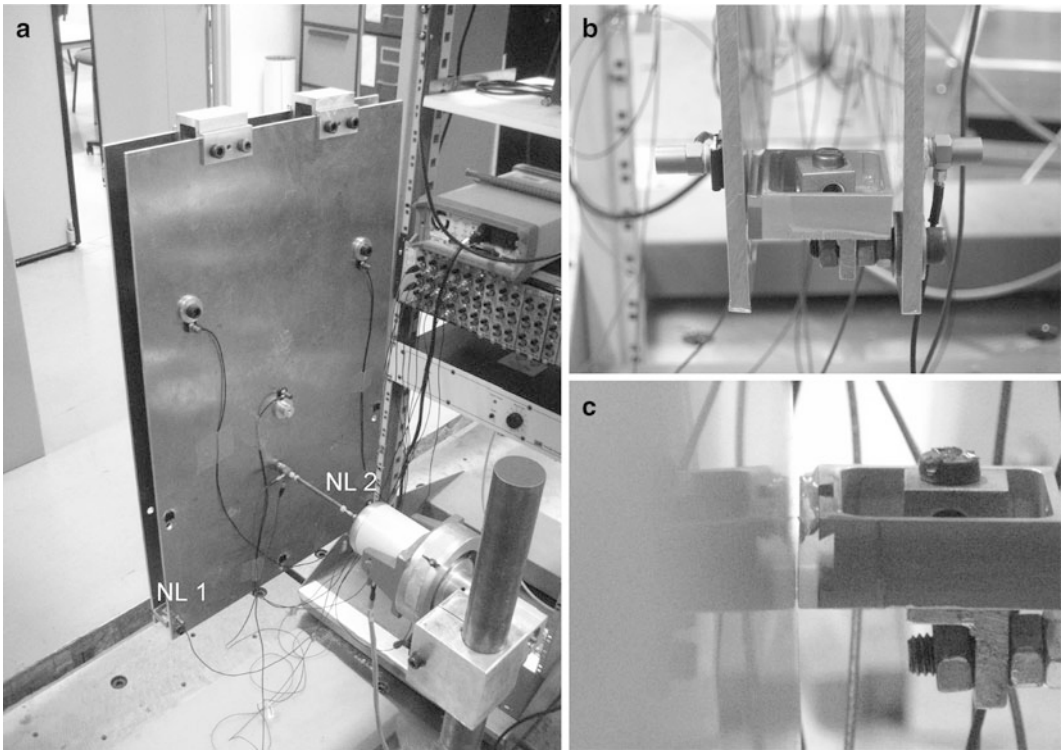

Fig. 8.1 Simplified solar array system. (**a**) Global view of the two aluminium plates clamped together at the *top edge*; (**b**) close-up on the NL 1 snubber connection instrumented with one accelerometer at both ends; (**c**) very thin freeplay between the snubber and the rear panel in NL 2

8.2 Description of a Simplified Solar Array System

In response to the issue raised in the introductory section, a simplified experimental test rig that mimics the complex dynamics of folded solar generators has been built. It consists of two $77 \times 44 \times 0.5\,\text{cm}^3$ parallel aluminium plates clamped together on one edge and connected through three stacking points, as pictured in Fig. 8.1a. The system is mounted in free-free configuration. Imperfect tightening of bolts within the stacking points are suspected to generate friction and clearance. In addition, two solithane snubbers mounted on steel supports are introduced on both corners of the free edge (Fig. 8.1b). They are designed so as to maintain contact and absorb vibrations. At high excitation level however, solithane material nonlinearity may emerge and the loss of contact between adjacent panels may also result in impacts [8]. In this study, a freeplay of less than a millimetre is introduced such that there is no contact at rest (see Fig. 8.1c). This allows the proper definition of a linear regime of motion at low amplitude.

The structure is instrumented with ten accelerometers positioned at both ends of each suspected nonlinearity, i.e. the three stacking points and the two snubbers (Fig. 8.1b). Besides, a 10-Newton shaker, visible in Fig, 8.1a, is used to apply random and sine-sweep excitations, considering a sampling frequency of 6,400 Hz. Acceleration and force signals are recorded at the excitation point, located below the stacking points, through an impedance head. For the sake of conciseness, the present paper will exclusively focus on the identification of the two snubber connections, labelled NL 1 and NL 2, which will be shown to exhibit a combined softening-hardening behaviour.

8.3 Subspace Identification of Nonlinear Mechanical Systems in the Frequency Domain

One way of tackling nonlinear system identification in structural dynamics is to break the problem down into three successive tasks, namely detection, characterisation and parameter estimation [9]. Following nonlinearity detection whose goal is obvious, characterisation is concerned with nonlinearity location and model selection. The model parameters then introduced are generally estimated through least-squares fitting, or nonlinear optimisation. The FNSI method addresses this latter step and so aims at estimating nonlinear stiffness and/or damping coefficients and the FRF matrix of the underlying linear system.

The vibrations of nonlinear systems which possess an underlying linear regime of motion are governed by the time-continuous model

$$M\,\ddot{q}(t) + C\,\dot{q}(t) + K\,q(t) + f(q(t),\dot{q}(t)) = p(t) \tag{8.1}$$

where $M, C, K \in \mathbb{R}^{r\times r}$ are the linear mass, damping and stiffness matrices, respectively; $q(t)$ and $p(t) \in \mathbb{R}^r$ are the generalised displacement and external force vectors, respectively; $f(t) \in \mathbb{R}^r$ is the nonlinear restoring force vector, and r is the number of degrees of freedom (DOFs) of the structure obtained after spatial discretisation. The amplitude, the direction, the location and the frequency content of the excitation $p(t)$ determine in which regime the structure behaves. As in reference [10], the effects of the s lumped nonlinearities are modelled using the summation

$$f(q(t),\dot{q}(t)) = \sum_{j=1}^{s} \mu_j\, b_j\, g_j(q(t),\dot{q}(t)). \tag{8.2}$$

Each term contains an unknown nonlinear coefficient μ_j and the corresponding functional form $g_j(t)$, which is assumed to be known. Nonlinearity location is specified through a vector of boolean values, $b_j \in \mathbb{R}^r$. In the literature about subspace methods, first-order state-space models are universally preferred to the second-order description of the dynamics in Eq. (8.1), because the intrinsic capability of a state-space model to encompass multi-input multi-output systems is attractive. Assuming that displacements are measured and defining the state vector $x = \begin{pmatrix} q^T & \dot{q}^T \end{pmatrix}^T \in \mathbb{R}^n$, the equations of motion are recast into

$$\begin{cases} \dot{x}(t) = A_c\, x(t) + B_c^{nl}\, g(t) + B_c\, p(t) \\ q(t) = C_c\, x(t) + D_c\, p(t) \end{cases} \tag{8.3}$$

where subscript c stands for *continuous-time*; $A_c \in \mathbb{R}^{n\times n}$, $B_c^{nl} \in \mathbb{R}^{n\times s}$, $B_c \in \mathbb{R}^{n\times r}$, $C_c \in \mathbb{R}^{r\times n}$ and $D_c \in \mathbb{R}^{r\times r}$ are the state, nonlinear coefficient, input, output and direct feedthrough matrices, respectively; $g(t) \in \mathbb{R}^s$ gathers the basis functions $g_j(t)$, and $n = 2\,r$. State-space and physical-space matrices correspond through the relations

$$A_c = \begin{pmatrix} 0^{r\times r} & \mathrm{I}^{r\times r} \\ -M^{-1}K & -M^{-1}C \end{pmatrix} \quad B_c^{nl} = \begin{pmatrix} 0^{r\times 1} & 0^{r\times 1} & \dots & 0^{r\times 1} \\ -\mu_1 M^{-1} b_1 & -\mu_2 M^{-1} b_2 & \dots & -\mu_s M^{-1} b_s \end{pmatrix}$$

$$B_c = \begin{pmatrix} 0^{r\times r} \\ M^{-1} \end{pmatrix} \quad C_c = \begin{pmatrix} \mathrm{I}^{r\times r} & 0^{r\times r} \end{pmatrix} \quad D_c = 0^{r\times r} \tag{8.4}$$

where 0 and I are zero and identity matrices, respectively. Given $p(t)$ and $q(t)$, the FNSI method determines the five matrices A_c, B_c^{nl}, B_c, C_c and D_c. The estimation of the nonlinear coefficients μ_j and of the FRFs is subsequently carried out thanks to the conversion from state space to physical space outlined in Sect. 8.3.4.

8.3.1 Equivalent Linear Identification through Feedback

The FNSI method utilises the feedback formulation proposed in [10], and illustrated in Fig. 8.2, for interpreting the dynamics governed by Eq. (8.1). It consists in moving the nonlinear term to the right-hand side of this equation and viewing nonlinear forces as external forces applied to the underlying linear structure. Thus, the internal forces that are nonlinear functions of the outputs act as a feedback to the linear open-loop system. Considering Eq. (8.3), this interpretation boils down to the concatenation of $g(t)$ and $p(t)$ into a single *extended input* vector $e(t) \in \mathbb{R}^{s+r}$:

$$\begin{cases} \dot{x}(t) = A_c\, x(t) + B_c^{e}\, e(q(t),\dot{q}(t)) \\ q(t) = C_c\, x(t) + D_c^{e}\, e(t) \end{cases} \tag{8.5}$$

where $B_c^e = \begin{pmatrix} B_c^{nl} & B_c \end{pmatrix} \in \mathbb{R}^{n\times(s+r)}$ and $D_c^e = \begin{pmatrix} 0^{r\times s} & D_c \end{pmatrix} \in \mathbb{R}^{r\times(s+r)}$. The feedback formulation is particularly appealing, because the inverse problem to be solved is now equivalent to the widely-studied linear state-space identification problem. However, because the FNSI algorithm handles nonlinearities in input-output data, its interpretation and use must be tailored, as detailed in reference [5].

As extensively discussed by Pintelon and Schoukens in [11], tackling system identification problems in the frequency domain is an attractive and versatile alternative. For improved numerical conditioning [12], a discrete-time translation of Eq. (8.5) is first considered, before applying the discrete Fourier transform (DFT). Provided that the time signal $v(t)$ is periodic and observed over an integer number of periods in steady-state conditions, its DFT $V(k)$ is given by

$$V(k) = \frac{1}{\sqrt{M}} \sum_{t=0}^{M-1} v(t)\, e^{-j\,2\pi\,k\,t/M} \tag{8.6}$$

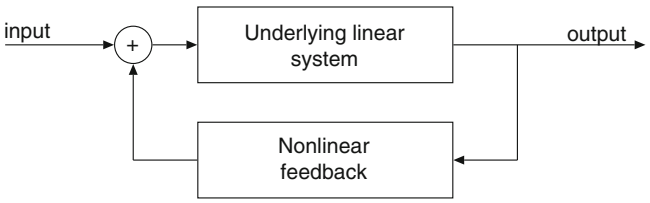

Fig. 8.2 Feedback interpretation of nonlinear mechanical systems [10]

where M is the number of recorded time samples, k is the frequency line and j the imaginary unit. Equations (8.5) eventually write

$$\begin{cases} z_k X(k) = A_d X(k) + B_d^e E(k) \\ Q(k) = C_d X(k) + D_d^e E(k) \end{cases} \tag{8.7}$$

where subscript d stands for *discrete-time*; $z_k = e^{j2\pi k/M}$ is the Z-transform variable, and $X(k)$, $E(k)$ and $Y(k)$ are the DFTs of $x(t)$, $e(t)$ and $y(t)$, respectively.

8.3.2 Output-State-Input Matrix Equation Formulation

In practice, only a limited set of DOFs in $p(t)$ and $q(t)$ are excited and observed, respectively. The identification problem is therefore preferably stated in terms of the *measured* applied forces $u(t) \in \mathbb{R}^{m \leq r}$ and displacements $y(t) \in \mathbb{R}^{l \leq r}$. Accordingly, the extended input vector is $e(t) \in \mathbb{R}^{\sigma = s+m}$. Equations (8.7) become

$$\begin{cases} z_k X(k) = A_d X(k) + B_d^e E(k) \\ Y(k) = C_d X(k) + D_d^e E(k) \end{cases} \tag{8.8}$$

where $Y(k)$ is the DFT of $y(t)$ and the matrices A_d, B_d^e, C_d and D_d^e are now a projection of the original matrices onto the observed and controlled DOFs. In what follows, subscript d indicating discrete-time matrices will be skipped, because no ambiguity is possible.

The measured output frequency spectra matrix is defined as

$$Y_i = \begin{pmatrix} Y(1) & Y(2) & \dots & Y(N) \\ z_1 Y(1) & z_2 Y(2) & \dots & z_N Y(N) \\ z_1^2 Y(1) & z_2^2 Y(2) & \dots & z_N^2 Y(N) \\ \vdots & & & \\ z_1^{i-1} Y(1) & z_2^{i-1} Y(2) & \dots & z_N^{i-1} Y(N) \end{pmatrix} \in \mathbb{R}^{li \times N} \tag{8.9}$$

where i is a user-defined index and N the number of (non-necessarily equidistant) frequency lines exploited in the identification. Defining $\zeta = \mathrm{diag}\,(z_1\, z_2\, \dots\, z_N) \in \mathbb{R}^{N \times N}$, Y_i is recast into

$$Y_i = \left(Y^T \; Y\,\zeta^T \; Y\,\zeta^{2T} \; \dots \; Y\,\zeta^{i-1T} \right)^T. \tag{8.10}$$

The extended input frequency spectra matrix is similarly formed as

$$E_i = \left(E^T \; E\,\zeta^T \; E\,\zeta^{2T} \; \dots \; E\,\zeta^{i-1T} \right)^T \in \mathbb{R}^{\sigma i \times N}. \tag{8.11}$$

Introducing the extended observability matrix

$$\Gamma_i = \left(C^T \; CA^T \; CA^{2T} \; \dots \; CA^{i-2T} \; CA^{i-1T} \right)^T \in \mathbb{R}^{li \times n} \tag{8.12}$$

and the lower-block triangular Toeplitz matrix

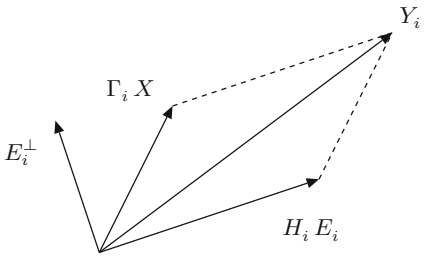

Fig. 8.3 Geometrical interpretation of Eq. (8.14) in a two-dimensional space

$$H_i = \begin{pmatrix} D^e & 0 & 0 & \dots & 0 \\ CB^e & D^e & 0 & \dots & 0 \\ CAB^e & CB^e & D^e & \dots & 0 \\ \vdots & \vdots & \vdots & & \vdots \\ CA^{i-2}B^e & CA^{i-3}B^e & CA^{i-4}B^e & \dots & D^e \end{pmatrix} \in \mathbb{R}^{li \times \sigma i}, \tag{8.13}$$

recursive substitution of Eq. (8.8) results in the output-state-input matrix equation

$$Y_i = \Gamma_i X + H_i E_i \tag{8.14}$$

where $X \in \mathbb{R}^{n \times N}$ is the state spectrum.

Remark that i and N must be chosen to encompass sufficient valuable information to identify the system. The choice of N is discussed in Sect. 8.4 where the possibility to focus on frequency regions of interest will prove to be a major asset of the FNSI method. A physics-based or information-based decision about i is more delicate. Basically, the larger i, the more accurate the identification, since i conveys how system dynamics is included in the data matrices. However, redundant information can affect the conditioning of those matrices, hence imposing bounds to i. There also exists an obvious trade-off between the values of i and N and the time needed to inverse the model.

8.3.3 Estimation of the State Matrices

The FNSI algorithm is a three-step procedure built upon Eq. (8.14). First, an estimate of the extended observability matrix Γ_i is computed. To this end, the term depending on the input and the nonlinearities in Eq. (8.14), namely $H_i E_i$, is eliminated using a geometrical projection. The vector interpretation of Eq. (8.14) depicted in Fig. 8.3 shows that an orthogonal projection onto the orthogonal complement of E_i, denoted $E_i^{\perp}$, cancels the input term.

Matrix Γ_i can then be obtained through a truncated singular value decomposition (SVD) of the result of the projection. The truncation limits the singular value spectrum to genuine elements, hence removing spurious values and reducing the influence of noise and rounding errors on the identification. In addition, the number of retained singular values yields the system order n. From the knowledge of n and Γ_i, the second step consists in computing the matrices A and C thanks to the shift property $\underline{\Gamma i} A = \overline{\Gamma_i}$, where $\underline{\Gamma_i}$ and $\overline{\Gamma_i}$ are the matrix Γ_i without the last and first l rows (or block row), respectively. State matrix A is thus found as the least-squares solution of the overdetermined system of equations $A = \underline{\Gamma i}^{\dagger} \overline{\Gamma_i}$, where $\dagger$ is the pseudo-inverse; output matrix C is extracted from Γ_i as its l first rows. The final step is the estimation of the system matrices B^e and D^e. A robust numerical scheme is described in reference [5]. It exploits the formulation of a set of linear equations in B^e and D^e, explicitly solved in least-squares sense. For the sake of conciseness, it is not detailed herein.

8.3.4 Conversion from State Space to Physical Space

Starting from the identified spate-space model (A, B^e, C, D^e), the estimation of the nonlinear coefficients μ_j and of the FRF matrix of the underlying linear system $H(\omega)$ can be carried out. To that purpose, a transformation back to physical space is achieved through the derivation of a linear relationship between output and extended input spectra in lumped nonlinear structures, extending the concept of FRF [10]:

$$Y(\omega) = H(\omega)\left[\mathrm{I}^{r\times r} - \sum_{j=1}^{s} \mu_j b_j\right] E(\omega) = H^e(\omega) E(\omega) \tag{8.15}$$

where the linear operator $H^e(\omega)$ is the extended FRF matrix. Moreover, in [13], the authors proved that $H^e(\omega)$ is an invariant system property. It can be retrieved, as in linear theory, from the combination of the continuous-time state-space matrices

$$H^e(\omega) = C_c(j\,\omega\,\mathrm{I}^{n\times n} - A_c)^{-1} B_c^e + D_c^e. \tag{8.16}$$

As a result, the nonlinear coefficients identified from the extended FRF matrix are spectral quantities, i.e. they are complex-valued and frequency-dependent. A reliable identification scheme together with an appropriate selection of the nonlinear functional forms should make the imaginary parts much smaller than the corresponding real parts. The frequency dependence of the coefficients should also remain small. These indications will serve as quality criteria in Sect. 8.4.

8.4 Identification of the Snubber Softening-Hardening Nonlinearities

Since the choice was made to introduce a static gap between the two snubbers and the rear panel, a linear analysis of the structure can safely be achieved at low level. To this end, a band-limited (5–350 Hz) white-noise signal was applied to the structure during 90 s considering a root-mean-square (RMS) amplitude of 0.16 N. Figure 8.4 shows the linear properties extracted by the FNSI method for model orders up to 200. The number of block rows i was chosen equal to 100 and measured frequency samples were processed in the excitation band only. This stabilisation diagram leads to the identification of 21 modes, whose natural frequencies and damping ratios are listed in Table 8.1. As expected for an aluminium structure, damping ratios are all very low and are bounded above by 1%. The FRF superimposed in Fig. 8.4 was measured on the front panel in NL 1, and shows an excellent agreement with the estimated linear frequencies. Finally, the deformed shape of mode 10 at 190.60 Hz is depicted in Fig. 8.5 and corresponds to an out-of-phase motion of the two panels. This mode will be found to be of prime importance for nonlinear identification purposes since it is likely to involve impacts for increasing excitation levels.

A second random data set measured at high level (3.82 NRMS) is now analysed to detect and locate in the frequency domain the modes triggering nonlinear mechanisms. Figure 8.6a presents the comparison between the low- and high-level FRFs measured on the front panel in NL 1. One first observes that some peaks are visibly not affected by nonlinearity, e.g.

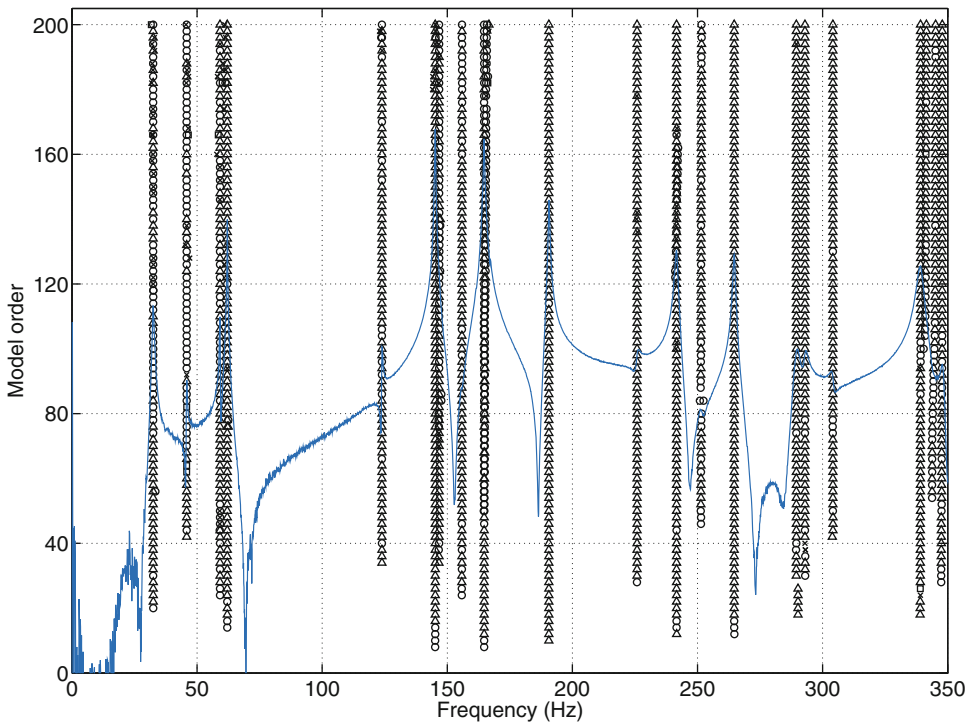

Fig. 8.4 Stabilisation diagram computed by the FNSI method at low level and corresponding FRF measured in NL 1 on the front panel. A cross denotes a pole stabilised in frequency only. Extra-stabilisation in damping and mode shape are given by squares and circles, respectively. Full stabilisation is expressed through a triangle. Stabilisation thresholds in natural frequency, damping ratio and modal assurance criterion (MAC) value were set to 0.1, 1 and 0.99%, respectively

Table 8.1 Identified frequencies and damping ratios in 5–350 Hz using a FNSI stabilisation diagram

Mode	Frequency (Hz)	Damping ratio (%)
1	32.47	0.81
2	45.85	0.44
3	59.17	0.18
4	62.08	0.17
5	123.88	0.14
6	145.18	0.10
7	146.74	0.25
8	155.85	0.37
9	164.73	0.17
10	190.60	0.14
11	225.84	0.35
12	241.62	0.24
13	251.40	0.34
14	264.66	0.17
15	289.48	0.48
16	292.95	0.31
17	304.10	0.27
18	339.16	0.38
19	341.24	0.55
20	344.97	0.19
21	347.80	0.24

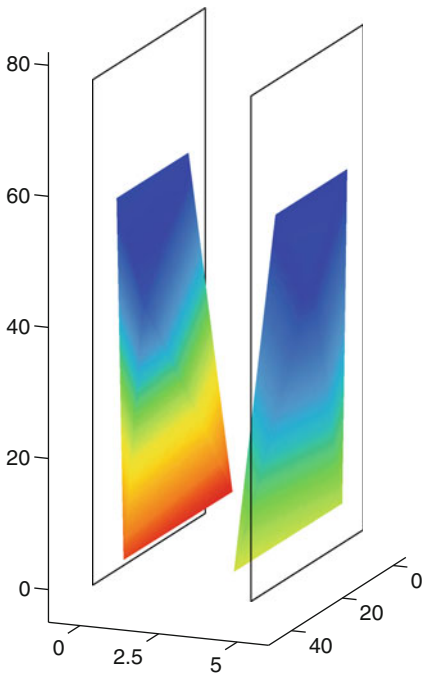

Fig. 8.5 Deformed shape of mode 10 at 190.60 Hz. Geometrical dimensions are given in centimetres

around 59, 62 or 145 Hz. Others clearly suffer from a shift towards lower frequencies, as a symptom of a softening behaviour, e.g. around 241, 264 or 339 Hz. This can arguably be attributed to loosening of bolts within the stacking points but will not be analysed further in the present work for brevity purposes. Eventually, three modes around 32, 46 and 191 Hz exhibit an increase of their resonance frequency and a "noisy" behaviour typical of hardening nonlinearities. They most probably translate the presence of impacts in the measurements. The variety of nonlinear distortions involved in the system response is well illustrated in the frequency close-up provided in Fig. 8.6b where three successive modes are found to manifest linear, softening and hardening behaviour, respectively. In the sequel, we will focus on the identification of the nonlinearities induced by the presence of snubbers, and will further restrict our interest to the mode at 190.60 Hz (see Fig. 8.5) which involves the largest relative displacements between the two panels and hence the most severe impacts.

Following nonlinearity detection, the adequate selection of the describing functions $g_j(t)$ is a key step to the success of the estimation of nonlinear coefficients. In this context, the restoring force surface (RFS) method is worth being utilised since

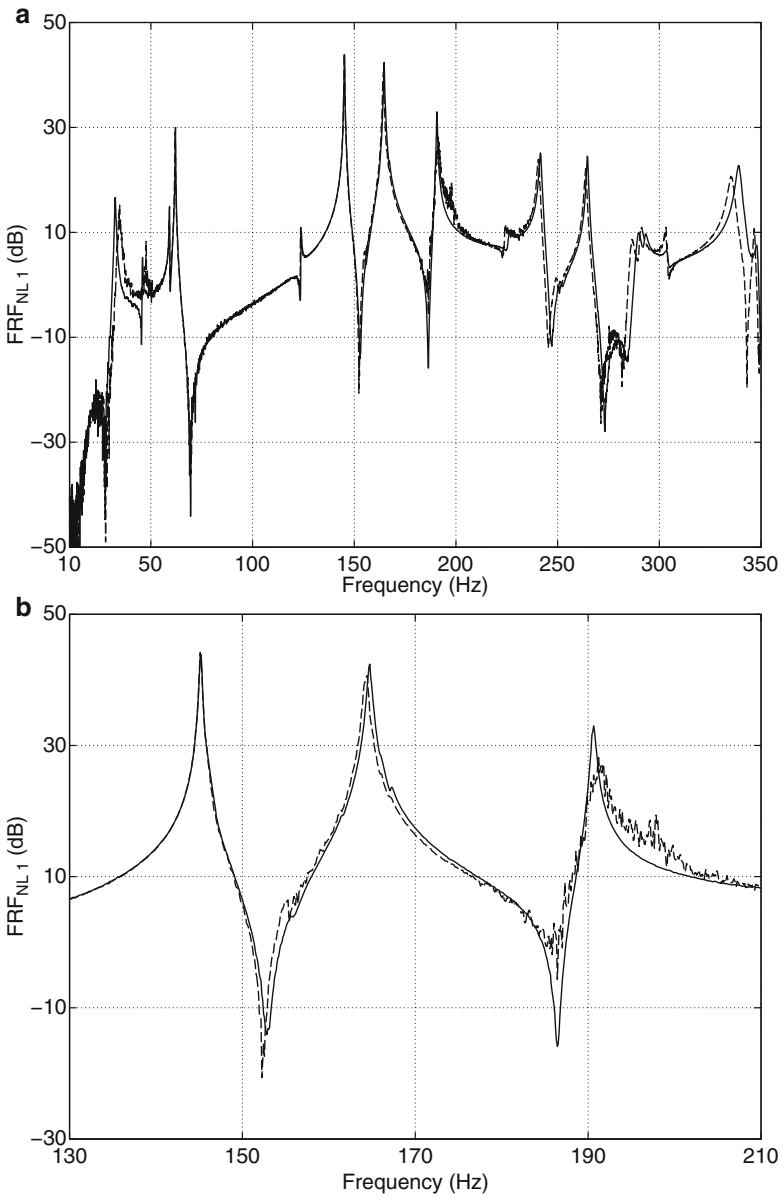

Fig. 8.6 Detection of nonlinearity in the frequency domain using FRF plots measured in NL 1 on the front panel. *Solid line*: 0.16 NRMS; *dashed line*: 3.82 NRMS. (**a**) Full excitation band; (**b**) close-up on three modes exhibiting different nonlinear behaviours

it yields a convenient visualisation of nonlinear effects. The RFS method relies on Newton's second law of motion, written for a single-degree-of-freedom system as

$$m\ddot{x} + f(x,\dot{x}) = p \tag{8.17}$$

where m is the mass, $\ddot{x}$ the acceleration and p the external force and where f encompasses all the restoring forces in the system, being of elastic or dissipative nature. This equation recast into

$$f(x,\dot{x}) = p - m\ddot{x} \tag{8.18}$$

gives a direct access to a nonparametric estimate of the restoring force surface defined by the triplets $(x, \dot{x}, f(x,\dot{x}))$. Applied to more complex systems, the method only provides qualitative information but can still be exploited for nonlinearity characterisation. Figures 8.7a, b depict the stiffness curves computed across the NL 1 and NL 2 connections, respectively. As the use of the RFS method is known to be facilitated when the modes can be isolated in the structural response, a 4-N sine-sweep excitation is here considered. Both curves present a large increase of stiffness in negative relative displacements which is the clear indication of impacts between the snubbers of the rear panel. The clearances beyond which contact occurs

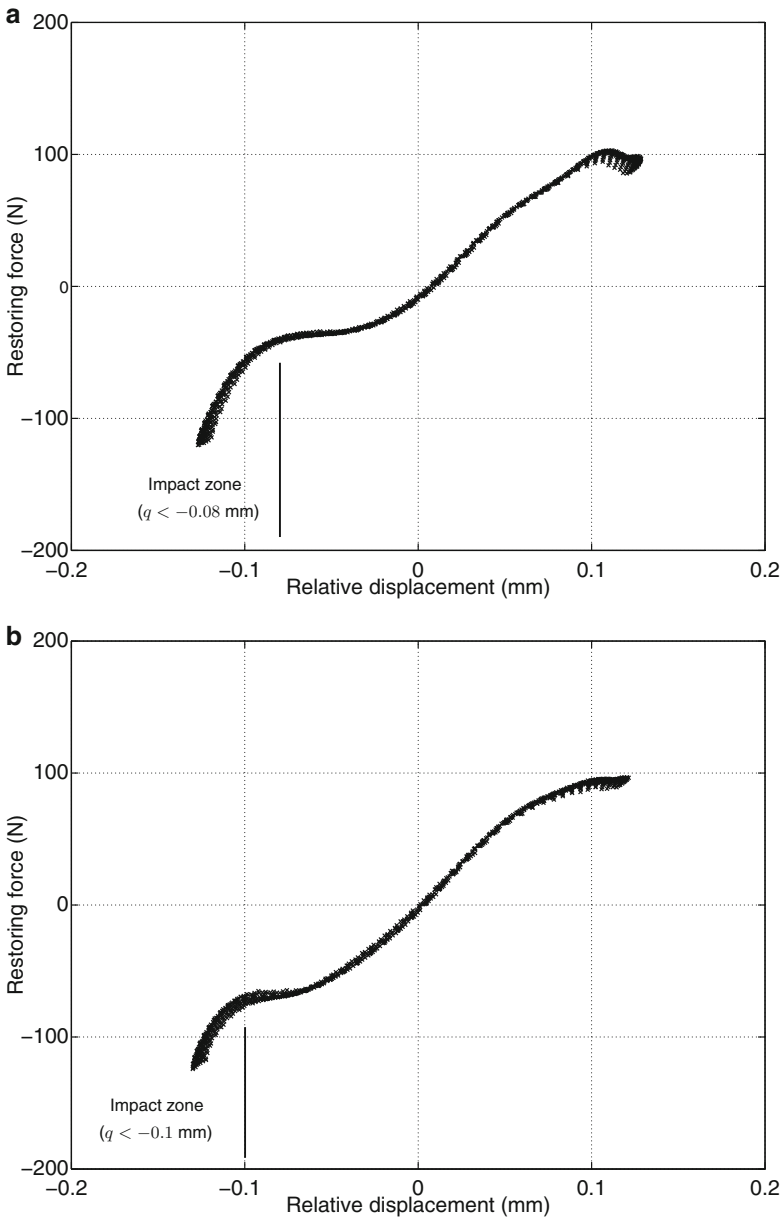

Fig. 8.7 RFS-based stiffness curves computed in the neighbourhood of mode 10 (190–191 Hz). The excitation is a 4-N sine signal sweeping the 5–350 Hz band at 172.5 Hz/min. (**a**) NL 1; (**b**) NL 2

can be estimated at 0.08 and 0.1 mm in NL 1 and NL 2, respectively. A global softening of stiffness in the system is also observed in Fig. 8.7 and is probably due to bolt loosening in the stacking points. This latter effect will be modelled as a negative cubic describing function.

The FNSI method can eventually be applied to the 3.82 NRMS random data set considering four nonlinearities as input forces, i.e. two bilinear and two negative cubic forces. For instance, Fig. 8.8 shows the describing function chosen in NL 2, consisting of a bilinear stiffness curve whose discontinuity is located in -0.1 mm superimposed to a negative cubic stiffness curve. The real parts of the four identified nonlinear coefficients μ_j are displayed in Fig. 8.9 and are found to be stable against frequency, as expected from good-quality estimates. Note that measured frequency samples were exclusively processed in the interval 185–200 Hz. This demonstrates one of the major assets of the FNSI method, namely its capability to discriminate frequencies in terms of information content. In particular, the focus of the analysis on the neighbourhood of the 190.60 Hz mode would merely be impossible in the time domain, thus considerably complicating the identification.

The averaged values of the coefficients are given in Table 8.2 and a good agreement is observed between the two nonlinear connections. Table 8.2 also lists the ratios, in logarithmic scale, between the real and imaginary parts of the coefficients. They are found to be meaningful quality indicators since the more stable a coefficient, the larger the corresponding ratio. Besides, the FNSI method can be exploited to reconstruct the FRFs of the underlying linear system. Figure 8.10 shows the

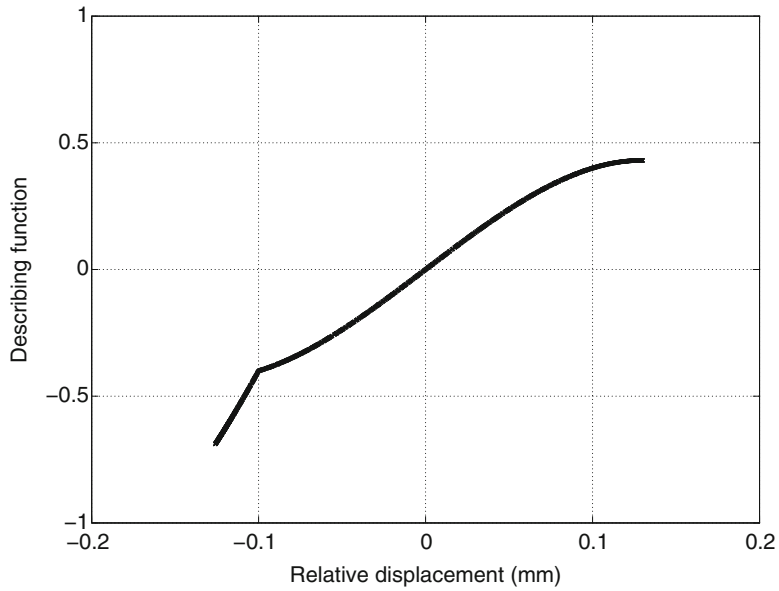

Fig. 8.8 Describing function chosen to model the nonlinearity observed in NL 2 in Fig. 8.7b. It consists of a bilinear function whose discontinuity is located in −0.1 mm superimposed to a negative cubic function

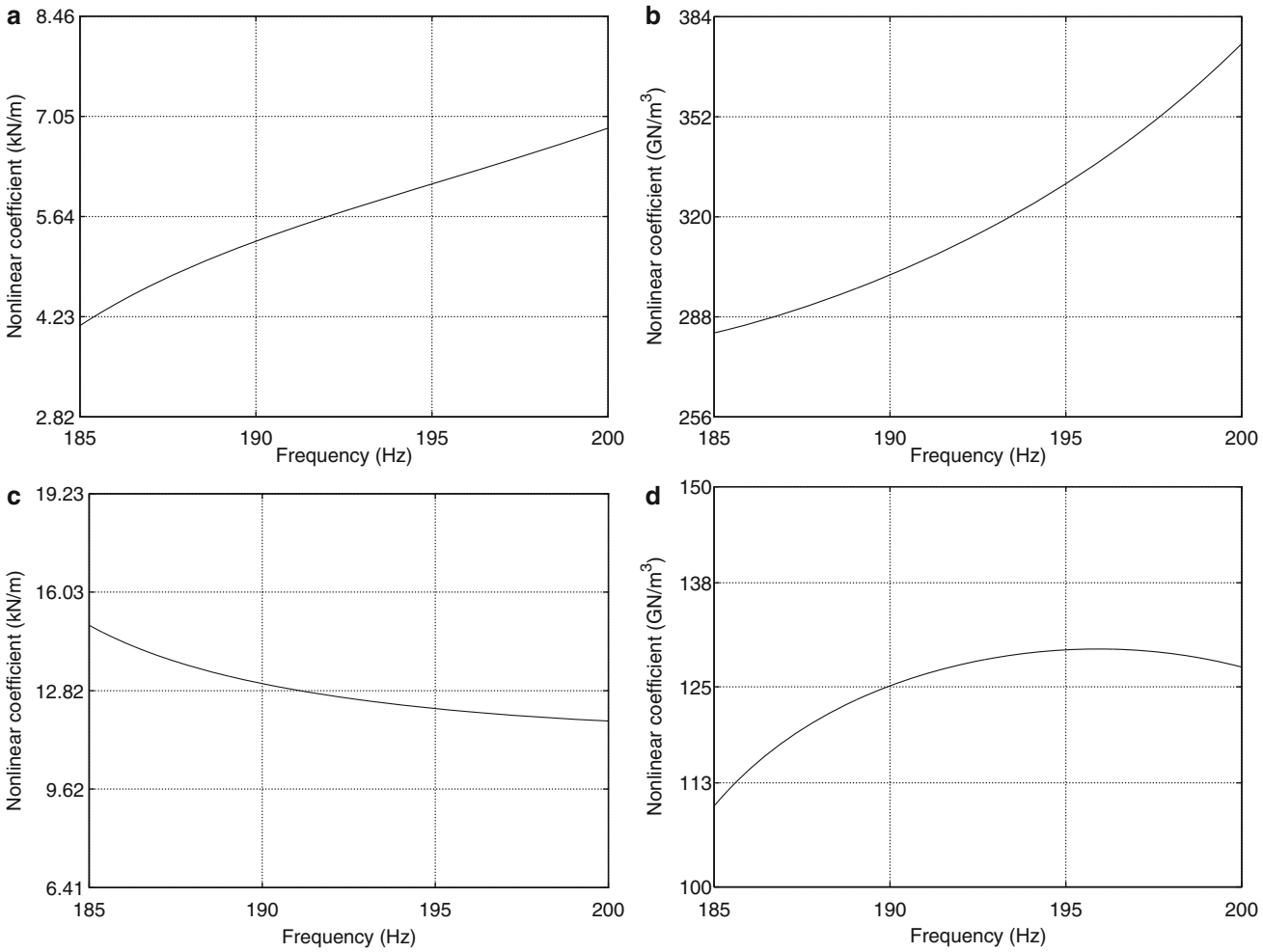

Fig. 8.9 Real parts of the four nonlinear coefficients estimated by the FNSI method. (**a,b**) NL 1; (**c,d**) NL 2. *Left column*: bilinear coefficients displayed in 50% bounds around their mean values; *right column*: cubic coefficients displayed in 20% bounds around their mean values

Table 8.2 Estimated nonlinear coefficients (real parts) and ratios in logarithmic scale between their real and imaginary parts

Nonlinear connection	Describing function	Real part	$\log_{10}$ (real/imag.)
NL 1	$q < -0.08$ mm	5.6 kN/m	0.46
	$-q^3$	319 MN/m^3	0.67
NL 2	$q < -0.1$ mm	12.8 kN/m	0.43
	$-q^3$	125 MN/m^3	2.39

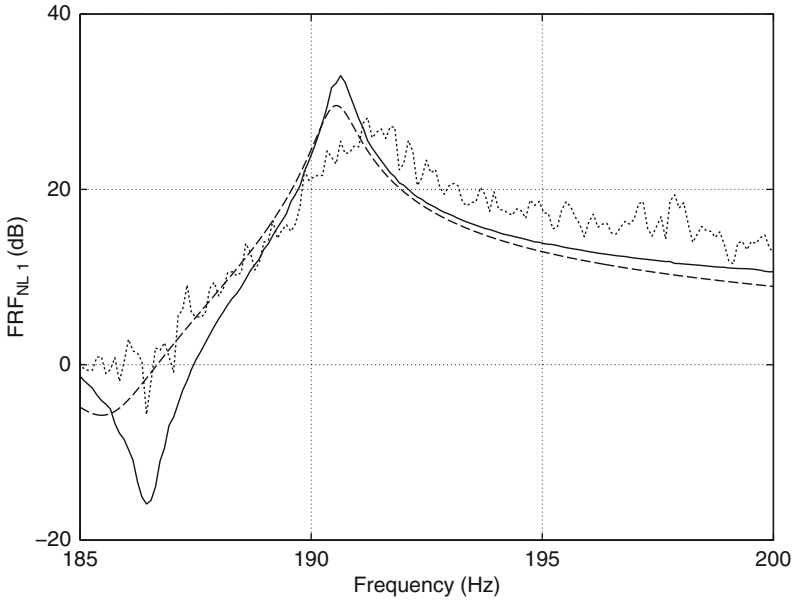

Fig. 8.10 FNSI reconstruction of the FRF in NL 1 from nonlinear data. *Solid line*: linear estimation at low level (0.16 NRMS); *dotted line*: linear estimation at high level (3.82 NRMS); *dashed line*: FNSI estimation at high level (3.82 NRMS)

improvement brought by the FNSI estimate with respect to the result of a classical linear estimator. The associated natural frequency closely matches the low-level property with a relative error of 0.04%. The damping ratio is also satisfactorily estimated at 0.21%, though suffering from a larger relative error (51%).

8.5 Conclusions

This paper intended to carry out the identification of simplified solar array structure based on experimental data. To this end, a frequency-domain nonlinear generalisation of subspace methods, referred to as the FNSI method, was exploited. The focus was put onto a single mode of vibration involving both impact and material nonlinearities. The corresponding nonlinear stiffness coefficients were estimated, and the FNSI method was also shown to accurately reconstruct the FRFs of the underlying linear structure. However, additional investigations are needed to further understand the dynamics of the structure so as to improve the predictive capabilities of an identified model. In particular, attention should now be devoted to the study of bolt loosening within the stacking points.

Acknowledgements The author J.P. Noël would like to acknowledge the Belgian National Fund for Scientific Research (FRIA fellowship) for its financial support.

References

1. Van Overschee P, De Moor B (1996) Subspace identification for linear systems. Kluwer Academic, Norwell, MA, USA
2. McKelvey T, Akcay H, Ljung L (1996) Subspace-based multivariable system identification from frequency response data. IEEE Trans Autom Control 41:960–979
3. Reynders E, De Roeck G (2008) Reference-based combined deterministic-stochastic subspace identification for experimental and operational modal analysis. Mech Syst Signal Process 22:617–637
4. Mevel L, Hermans L, Van Der Auweraer H (1999) Application of a subspace-based fault detection method to industrial structures. Mech Syst Signal Process 13:823–838

5. Noël JP, Kerschen G (2012) A new subspace-based approach to identify nonlinear mechanical structures in the frequency domain. In: 16th IFAC symposium on system identification, Brussels, Belgium
6. Noël JP, Marchesiello S, Kerschen G (2012) Time- and frequency-domain subspace identification of a nonlinear spacecraft. In: 25th ISMA international conference on noise and vibration engineering, Leuven, Belgium
7. Kerschen G, Soula L, Vergniaud JB, Newerla A (2011) Assessment of nonlinear system identification methods using the smallsat spacecraft structure. In: 29th international modal analysis conference, Jacksonville, FL, USA
8. Hot A (2011) Experimental validation of locally non-linear structures in a space context, PhD thesis, FEMTO-ST Institute, LMARC
9. Kerschen G, Worden K, Vakakis AF, Golinval JC (2006) Past, present and future of nonlinear system identification in structural dynamics. Mech Syst Signal Process 20:505–592
10. Adams DE, Allemang RJ (2000) A frequency domain method for estimating the parameters of a non-linear structural dynamic model through feedback. Mech Syst Signal Process 14(4):637–656
11. Pintelon R, Schoukens J (2001) System identification: a frequency domain approach. Wiley-IEEE, Piscataway, NJ, USA
12. Van Overschee P, De Moor B (1996) Continuous-time frequency domain subspace system identification. Signal Process 52:179–194
13. Marchesiello S, Garibaldi L (2008) A time domain approach for identifying nonlinear vibrating structures by subspace methods. Mech Syst Signal Process 22:81–101

Chapter 9
Localization and Identification of Structural Nonlinearities Using Neural Networks

A. Koyuncu, E. Cigeroglu, M.E. Yumer, and H.N. Özgüven

Abstract In this study, a new approach is proposed for identification of structural nonlinearities by employing neural networks. Linear finite element model of the system and frequency response functions measured at arbitrary locations of the system are used in this approach. Using the finite element model, a training data set is created, which appropriately spans the possible nonlinear configurations space of the system. A classification neural network trained on these data sets then localizes and determines the type of nonlinearity associated with the corresponding degree of freedom in the system. A new training data set spanning the parametric space associated with the determined nonlinearities is created to facilitate parametric identification. Utilizing this data set, a feed forward regression neural network is trained, which parametrically identifies the related nonlinearity. The application of the proposed approach is demonstrated on an example system with nonlinear elements. The proposed approach does not require data collection from the degrees of freedoms related with nonlinear elements, and furthermore, the proposed approach is sufficiently accurate even in the presence of measurement noise.

Keywords Neural networks • Nonlinearity identification • Nonlinearity classification • Nonlinear vibrations • Harmonic balance method

9.1 Introduction

Identification of structural nonlinearities in dynamic structures has become the interest of researchers in the past four decades [1]. Studies on this subject focused on two parts: localizing and characterizing the nonlinearity, and estimating the parameters of the nonlinearity based on experimentally measured data [2–6].

One of the main problems of nonlinearity identification is the determination of the location and the type of nonlinearity; in other words, classification of the nonlinear system from system responses. For this problem, frequency domain methods are mostly preferred. He and Ewins [7] used frequency response functions (FRFs) obtained at different forcing levels in order to detect nonlinearities in a system. Similarly, the method developed by Özer and Özgüven [4] determines possible locations of nonlinearities and identifies their types and parameters by using describing functions, which is as well a frequency domain method. Major restrictions of this method are the requirements of measurements collected from all degrees of freedoms (DOFs) and complete FRFs of the system for localization purposes. However, in a later study, Aykan et al. [5] improved

A. Koyuncu (✉)
Middle East Technical University, Ankara 06800, Turkey

Defense Systems Technologies Division, ASELSAN A.Ş, Ankara 06172, Turkey
e-mail: anlkoyuncu@hotmail.com

E. Cigeroglu • H.N. Özgüven
Middle East Technical University, Ankara 06800, Turkey
e-mail: ender@metu.edu.tr; ozguven@metu.edu.tr

M.E. Yumer
Middle East Technical University, Ankara 06800, Turkey

Carnegie Mellon University, Pittsburgh, PA, USA
e-mail: meyumer@cmu.edu

G. Kerschen et al. (eds.), *Topics in Nonlinear Dynamics, Volume 1: Proceedings of the 31st IMAC, A Conference on Structural Dynamics, 2013*, Conference Proceedings of the Society for Experimental Mechanics Series 35,
DOI 10.1007/978-1-4614-6570-6_9,

the method using incomplete FRFs for localization purposes. A common feature of most of the methods in literature is the identification of types of nonlinearities by observing system responses or nonlinear restoring forces, which is a time consuming process and it is not suitable for nonlinearity identification in a series of products due to manufacturing errors and assembly differences.

Parameter estimation of nonlinearities in a classified system is an easily handled problem. There exist time domain and frequency domain methods targeting parameter identification in literature [1, 8, 9]. Although these methods have their own handicaps, they are promising in specific application areas. Masri and Caughey [10] developed a method named as *Restoring Force Surface* (RFS) method to estimate parameters of nonlinearities using least squares approach in time domain. *Conditioned Reverse Path* (CRP) proposed by Richards and Singh [11] uses spectral analysis in frequency domain to compute the coefficients of nonlinearity matrix.

The method proposed in this study, classifies and identifies nonlinearities associated with the system utilizing neural networks. Neural network classifiers have been used for parameter identification of structural nonlinearities [12,13]; however, nonlinearity classification using neural networks is a new application in structural dynamics. Constructed networks are to be trained with sample data sets which are frequency response functions of selected points on the system. Nonlinear frequency responses of the system are obtained by analyzing possible nonlinear system configurations. It should be noted that in order to perform these analyses, a mathematical model of the system is required. After training the networks, location and type of the nonlinearity is determined by running trained networks with measured systems responses as the input. Parameters of the classified nonlinearities are identified by means of a regression network utilizing the same input data used for classification. The proposed method does not require taking measurements from the nonlinear DOFs; hence, system responses measured from arbitrary locations can be used for identification purposes. Moreover, with the proposed method, it is as well possible to handle measurement noise by injecting noise into data during the training process. Once networks are trained, identification is very fast; hence, the method proposed is very suitable for identification of nonlinearities in a series of products due to manufacturing errors and assembly differences.

9.2 Theory

The proposed method is composed of two parts: in the first part, a classification network is used to identify the locations and the types of the nonlinear elements, whereas in the second part, a regression network is utilized to determine the parameters associated with the identified nonlinearities. For training of the networks, forced response function of an arbitrary degree of freedom is used; therefore, a mathematical model of the system is required. There is no restriction on the mathematical model; hence finite element models (FEMs) can as well be used with the proposed method. Using the mathematical model together with the nonlinear elements and their possible configurations, simulations are performed to generate the training data by using harmonic balance method (HBM), which is a frequency domain method. Details of the neural network models and the nonlinear mathematical modeling are explained in the following sections.

9.2.1 Neural Network Models

A typical neural network model is characterized by four items: number of neurons, number of layers, transfer functions and training algorithm. The fundamental element of a neural network is *a single neuron* mathematically represented below:

$$o_j = f_j\left(\sum_{i=1}^{R} w_{ji} y_i + b_j\right) = f_j\left(\{w_j\}^T \{y\} + b_j\right) = f_j(n_j) \tag{9.1}$$

$\{y\}$ is the input vector with R number of elements, $\{w_j\}^T$ is the jth row of the weight matrix $[W]$, b_j is the bias term, o_j is the output of the jth neuron, n_j is the net input and $f_j(n_j)$ is the transfer function used. Combination of multiple neurons is named as *a layer* and it can be written in matrix form as:

$$\{o\} = \{f([W]\{y\} + \{b\})\} = \{f(\{n\})\}. \tag{9.2}$$

Weight matrix [W] is a $S \times R$ matrix where S is number of neurons in a layer. As a result, dimension of the output vector $\{o\}$ is $S \times 1$. A network can be extended by increasing the number of hidden layers used, which are referred as multilayer networks. A two-layer network is given as an example in Fig. 9.1. It can be observed that output of each layer becomes the input of the

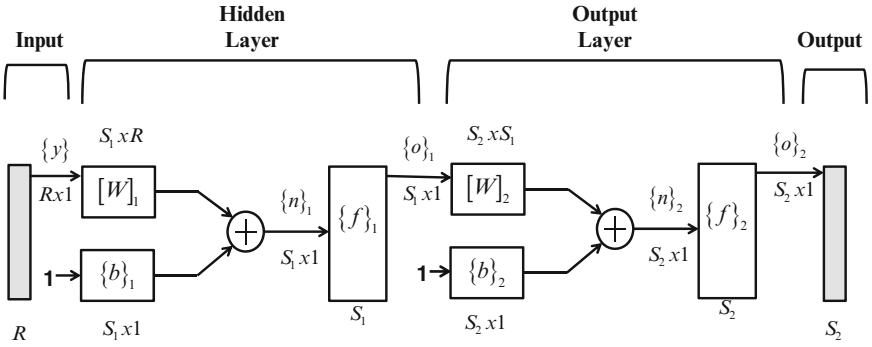

Fig. 9.1 A two-layer network

Table 9.1 Commonly used transfer functions

Name	Input/output relation	Name	Input/output relation
Hard limit	$a=0 \quad n<0$	Symmetrical saturated linear	$a=-1 \quad n<-1$
	$a=1 \quad n\geq 0$		$a=n \quad -1\leq n\leq 1$
			$a=1 \quad n>1$
Symmetrical hard limit	$a=-1 \quad n<0$	Log-sigmoid	$a=\frac{1}{1+e^n}$
	$a=+1 \quad n\geq 0$		
Linear	$a=n$	Hyperbolic-tangent sigmoid	$a=\frac{e^n-e^{-n}}{e^n+e^{-n}}$
Saturated linear	$a=0 \quad n<0$	Positive linear	$a=0 \quad n<0$
	$a=n \quad 0\leq n\leq 1$		$a=n \quad 0\leq n$
	$a=1 \quad n>1$		

next layer. Dimensions of weight matrices and bias vectors can be adjusted according to the problem requirements except R and S_2 values which are determined by length of input and target vectors. In this study, a two-layer network is used for both classification and identification purposes.

Transfer functions play an important role in the structures of neural networks. Selection of a transfer function depends on input and output vectors and training algorithm. Commonly used transfer functions in neural network models are given in Table 9.1. In the classification network used in this study, transfer functions of Layer 1 and Layer 2 are both Hyperbolic-Tangent Sigmoid function; whereas, Hyperbolic-Tangent Sigmoid and Linear transfer functions are used in parameter identification networks for Layer 1 and Layer 2, respectively.

Performance of a network is quantified through mean squared error (MSE) between the network output vector, $\{o\}$, and target vector, $\{t\}$ as:

$$MSE = \frac{1}{N}\int_{i=1}^{N}(e_i)^2 = \frac{1}{N}\int_{i=1}^{N}(o_i - t_i)^2. \tag{9.3}$$

Objective of a neural network problem is to minimize MSE via tuning the elements of weight matrices and bias vectors. The tuning process is called as training, where weight matrices and bias vectors are updated according to "*the training algorithm*". In this study, Scaled Conjugate Gradient Backpropogation algorithm is used for nonlinearity localization and classification; whereas, Levenberg-Marquardt algorithm is used for identification of parameters of the nonlinear elements [14]. Before starting to the training process, collected data is required to be divided into three subsets as: *training*, *validation* and *test* data sets. Weight matrices and bias vectors are updated based on the training data set; whereas, network error based on the validation data set is used as the stopping criteria in order to prevent over fitting. Although the test data set is not used in training, errors based on the test data set are useful in post processing. In this study, 75% of samples are allocated as training data set, 15% of samples are allocated as the validation data set and the rest is used as the test data set.

9.2.2 Mathematical Modeling

Before starting the training process, training data should be generated first. Training data consists of input vectors and corresponding target vectors. Input vectors are outputs of the physical system in both classification and identification problems; whereas, target vectors are the location and type of the nonlinearity in the classification problem, and parameters of

the nonlinearity in the identification problem. A simulated data set which covers full range of possible input space is required as input data. In order to obtain this, nonlinear frequency responses of all selected system configurations are required to be determined. Equation of motion of a nonlinear system can be written as follows

$$[M]\{\ddot{x}\} + [C]\{\dot{x}\} + i[H]\{x\} + [K]\{x\} + \{f_{NL}(\{x\},\{\dot{x}\},\ldots)\} = \{f(t)\}, \tag{9.4}$$

where $[M]$, $[C]$, $[H]$ and $[K]$ are mass, viscous damping, structural damping and stiffness matrices of linear system, respectively. In this equation, $\{x(t)\}$, $\{f_{NL}(t)\}$ and $\{f(t)\}$ are response, nonlinear force and excitation force vectors of the system, respectively. For harmonic forcing, excitation force vector can be written as:

$$\{f(t)\} = \{F\}e^{i\omega t}. \tag{9.5}$$

For harmonic input, it can be assumed that system response is also harmonic, which can be written as follows

$$\{x(t)\} = \{X\}e^{i\omega t}, \tag{9.6}$$

using a single harmonic term. Substituting Eqs. (9.5) and (9.6) into Eq. (9.4), the following equation is obtained:

$$\left([K] - \omega^2[M] + i\omega[C] + i[H]\right)\{X\} + \{F_{NL}(\{X\})\} = \{F\}. \tag{9.7}$$

The nonlinear forcing can be written using a single term Fourier series as follows

$$\{F_{NL}(\omega)\} = \frac{i}{\pi}\int_0^{2\pi} f_{NL}(\psi)e^{i\psi}d\psi, \tag{9.8}$$

where $\psi = \omega t$.

Equation (9.7) can be divided into linear and nonlinear parts, which decreases the total number of nonlinear equations to be solved, by using the receptance method developed by Menq et al. [15]. Receptance method employed in this study decreases the computational time required for the solution of nonlinear equations obtained, which makes the proposed method suitable for realistic finite element models. The resulting nonlinear equations can be solved by a nonlinear equation solver. In this study, Newton's method with Arc-Length Continuation [16, 17] is used to solve the resulting system of nonlinear equations.

Training process is to be performed using the frequency response of one of the coordinates, which does not need to be measured from the nonlinear DOFs. In order to include the effect of measurement noise, input vectors are polluted by addition of random numbers having Gaussian distribution with zero mean and realistic standard deviation. Input training data is generated from frequency response of the nonlinear system as follows:

$$\{y\} = \{\mathrm{Re}\{X(\omega_1) \quad X(\omega_2)\cdots X(\omega_n)\} \,|\, \mathrm{Im}\{X(\omega_1) \quad X(\omega_2)\cdots X(\omega_n)\}\}^T. \tag{9.9}$$

Target vectors define the configurations of the nonlinear system and the parameter values of the nonlinear elements in classification and identification problems, respectively. For classification networks, length of the target vectors are determined from the total number of possible nonlinear system configurations; therefore, orthogonality of target vectors can be achieved easily.

After obtaining the input and target vectors, the classification and identification networks are ready to train. In Fig. 9.2, flowchart of the proposed method is explained schematically.

9.3 Case Study: 4-DOF Nonlinear System

In this section, application of the proposed approach is presented on a simple 4-DOF system with local nonlinearities. From the physics of the problem or experiences it is possible to localize nonlinearities; hence, in this case study, the possible locations of the nonlinear elements are identified as between the ground and the first mass and between the third and the fourth masses as shown in Fig. 9.3. Moreover, from the physics of the problem or experience it is known that hardening type cubic stiffness nonlinearity and symmetric gap nonlinearity are the possible nonlinearities that can be encountered (Fig. 9.4). This yields eight possible nonlinear system configurations as indicated in Table 9.2 with their corresponding classification network targets.

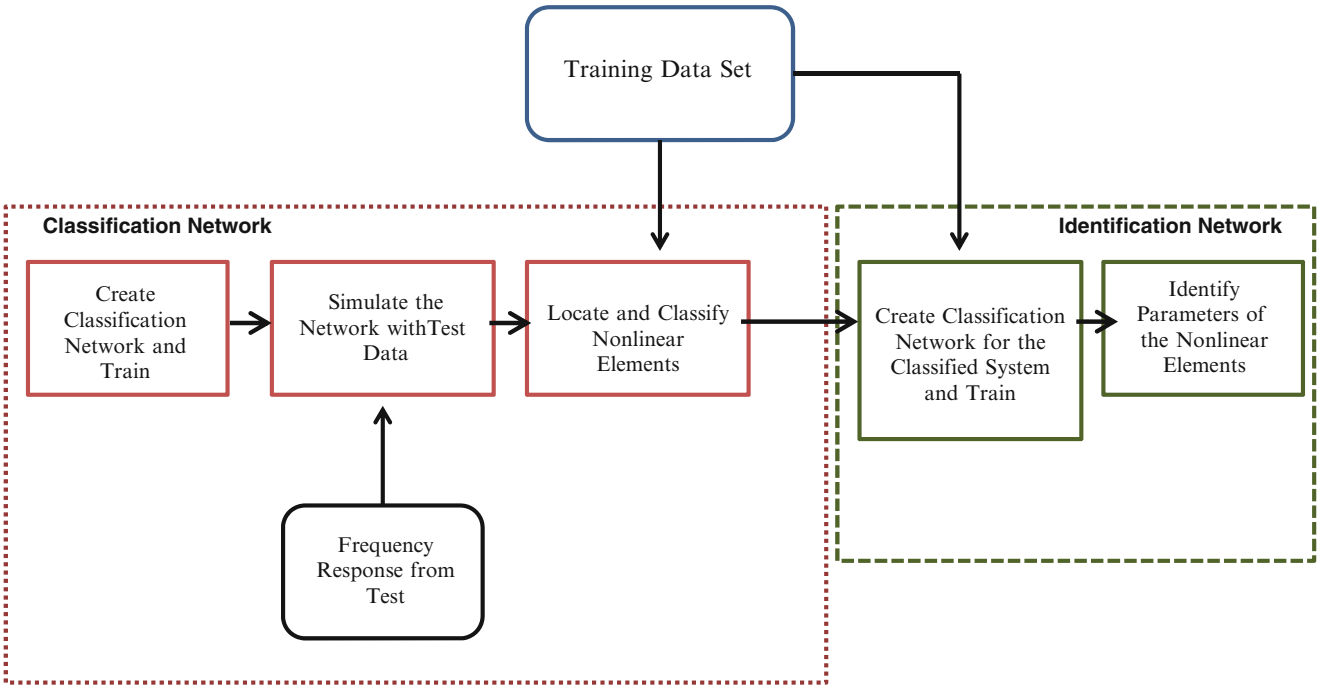

Fig. 9.2 Flowcharts of nonlinearity classification and parametric identification

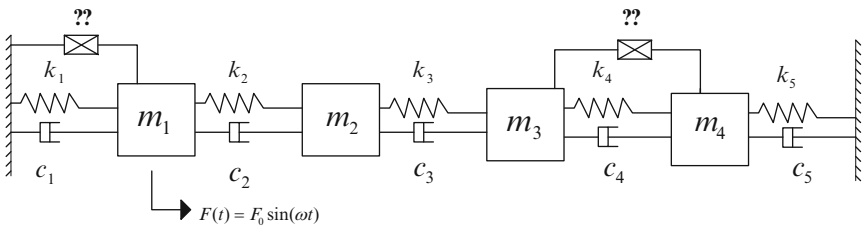

Fig. 9.3 4-DOF non-linear system schematic view

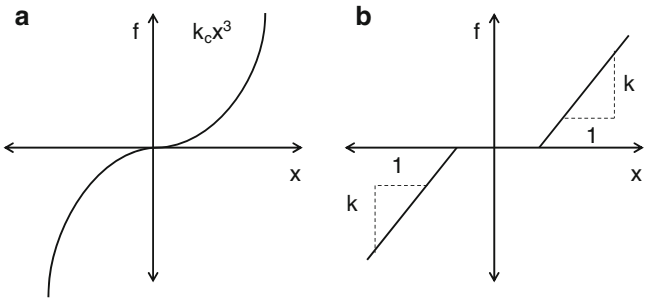

Fig. 9.4 Restoring force diagram of possible nonlinearities (**a**) Cubic stiffness, (**b**) Symmetric gap nonlinearity

Table 9.2 Possible nonlinear system configurations and corresponding classification network targets

Conf no	DOF 1 and ground	DOF 3 and DOF 4	Binary network targets
1	Hardening cubic stiffness	Linear stiffness with backlash	$\{1,0,0,0,0,0,0,0\}^T$
2	Linear stiffness with backlash	Hardening cubic stiffness	$\{0,1,0,0,0,0,0,0\}^T$
3	Hardening cubic stiffness	Hardening cubic stiffness	$\{0,0,1,0,0,0,0,0\}^T$
4	Linear stiffness with backlash	Linear stiffness with backlash	$\{0,0,0,1,0,0,0,0\}^T$
5	Hardening cubic stiffness	Linear	$\{0,0,0,0,1,0,0,0\}^T$
6	Linear	Hardening cubic stiffness	$\{0,0,0,0,0,1,0,0\}^T$
7	Linear stiffness with backlash	Linear	$\{0,0,0,0,0,0,1,0\}^T$
8	Linear	Linear stiffness with backlash	$\{0,0,0,0,0,0,0,1\}^T$

A two-layered classification network is created to determine the location(s) and type(s) of the nonlinearities. Numbers of neurons used in the hidden and the output layers are 50 and 8 respectively. At this stage input and target data sets are generated for training purposes. Nonlinear frequency response of the second DOF, which is not connected to any nonlinear DOF, is calculated under a 10 N harmonic excitation force applied at the first DOF in order to generate the input training data. Frequency range of interest is considered as 0–8 Hz with increments of 0.01 Hz. For the simulations, the ranges of parameter values are selected as: 5×10^4–$2 \times 10^6 \mathrm{N/m^3}$ for cubic stiffness coefficient, and 2.5×10^{-4}–0.01 m gap for the symmetric gap nonlinearity with a known linear stiffness of 500 N/m. For each nonlinear system configuration about 1,600 samples a total of 12,708 data sets are created. Training input vectors are polluted by normally distributed random numbers with zero mean and 0.5 mm standard deviation, representing measurement noise. After dividing the samples into training, validation and test data; training operation is performed, which is completed after 198 epochs. Confusion matrix presented in Fig. 9.5 shows that 100% classification of nonlinearities in the system is achieved as indicated by the last column or row of the confusion matrix for training, validation and test sets.

After determining location(s) and type(s) of the nonlinearities, parameters of the nonlinear elements are identified by means of a regression network. Eight regression networks are created for all nonlinear system configurations. For all nonlinear system configurations, 50 neurons are used in the hidden layer; whereas for the output layers 2 and 1 neuron are used for configurations 1–4 and 5–8, respectively, since there is only one parameter identified in configurations 5–8. Input data sets generated for the classification network can as well be used in the regression network. However, in this case, target vectors are the unknown parameters of the nonlinear elements corresponding to each input data vector. Using these data and the identified configuration, regression networks are trained similar to the classification network. Correlation coefficients of the resulted regression networks are presented in Table 9.3.

As an example, a system with a hardening cubic stiffness with a coefficient of $10^6 \mathrm{N/m}$ attached between the first DOF and ground and a symmetric gap element with a stiffness of 500 N/m and a backlash of 0.005 m between the third and the fourth DOFs is considered. In order to simulate the experimentally measured frequency response from the second DOF, time domain solution of the nonlinear system is obtained by using ODE45 solver of MATLAB increasing frequency from 0 to 8 Hz with 0.01 Hz increments. Steady state oscillation amplitudes are collected as the frequency response values at the corresponding frequency. In order to represent the effect of measurement noise, data obtained from time marching is polluted by adding random numbers having a normal distribution with 0 mean and 0.5 mm standard deviation. The resulting frequency response is given in Fig. 9.6, which is used as the input to the trained networks. Classification and identification process is also repeated by considering noise free response data and. The results obtained for noisy and noise free cases are presented in Table 9.4. Comparison of identified and actual system responses are presented for noisy and noise free measurement cases in Figs. 9.7 and 9.8, respectively. It should be noted that, in the identification process a single harmonic HBM is used; whereas, in the simulated measurement data, time marching method is utilized. Therefore, even though identification is done by using a single harmonic, identified time domain simulation of the system shows that the identified system response is very close to the actual system for both noisy and noise free measurement cases. However, it should be noted that since networks are trained with noisy data, there is a slight increase in the error for parameter identification of coefficient of cubic stiffness if noisy free measurement is used. On the other hand, the error obtained for gap parameter decreases if noise free measurement is used.

9.4 Conclusion

In this study, artificial neural networks are used for nonlinearity classification and parameter identification. Proposed method has three main steps: generation of training data, training of the neural network and identification by using the trained networks. Application of the method is demonstrated on a simple case study. Most of the effort is required in order to generate training data sets, which are frequency response sets of the system for all possible nonlinearity configurations and possible ranges of parameter values. Therefore, application of the proposed method to realistic finite element models requires reduction methods in order to decrease the computational time required for data generation process. A nonlinear solution method utilizing harmonic balance method with a single harmonic is used to obtain the required training data, which are employed in the training of the classification and identification networks. It should be noted that in order to increase the applicability of the proposed method, the generated data sets are polluted with random data in order to have a method that is prone to measurement noise.

In this study, two-layered networks give considerably accurate results; however, the number of neurons used in hidden layers should be optimized in order to achieve this accuracy. Using the measured system responses as the inputs of the

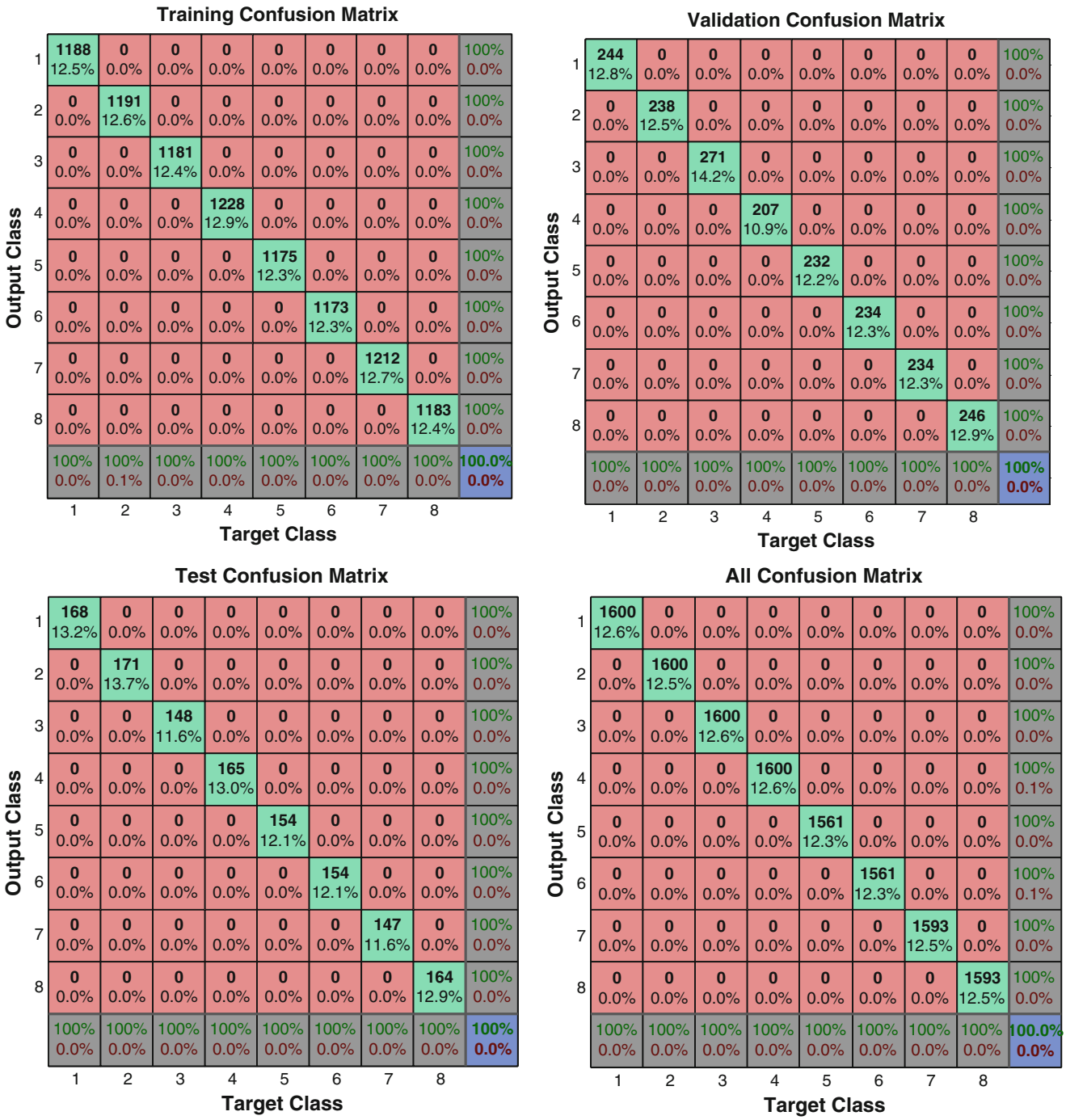

Fig. 9.5 Confusion matrices of classification network

Table 9.3 Correlation coefficients for each regression network

	Training data set	Validation data set	Test data set
Configuration 1	0.999	0.998	0.998
Configuration 2	0.998	0.997	0.997
Configuration 3	0.997	0.992	0.992
Configuration 4	0.997	0.994	0.993
Configuration 5	0.997	0.995	0.995
Configuration 6	0.990	0.992	0.991
Configuration 7	0.999	0.996	0.996
Configuration 8	0.996	0.996	0.996

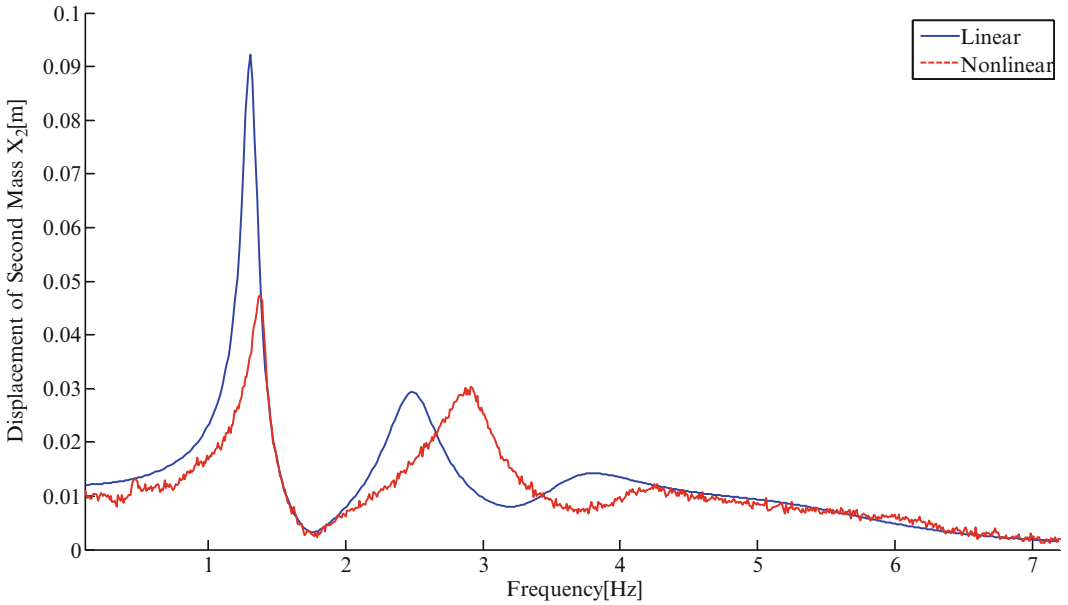

Fig. 9.6 Displacement of the second DOF

Table 9.4 Classification and parameter identification results

	Simulation with noise free measurement			Simulation with noisy measurement		
	Target vector	Cubic stiffness N/m^3	Backlash (m)	Target vector	Cubic stiffness N/m^3	Backlash (m)
Actual system	$\{1,0,0,0,0,0,0,0\}^T$	100,0000	0.005	$\{1,0,0,0,0,0,0,0\}^T$	100,0000	0.005
Identified system	$\{0.999,0,0,0.005,0,0,0,0\}^T$	1,015,500	0.004935	$\{1,0,0,0.013,0,0,0,0\}^T$	998,930	0.0047514
Error	$\boldsymbol{MSE = 3 \times 10^{-6}}$	**1.2%**	**1.3%**	$\boldsymbol{MSE = 1.7 \times 10^{-4}}$	**0.1%**	**4.9%**

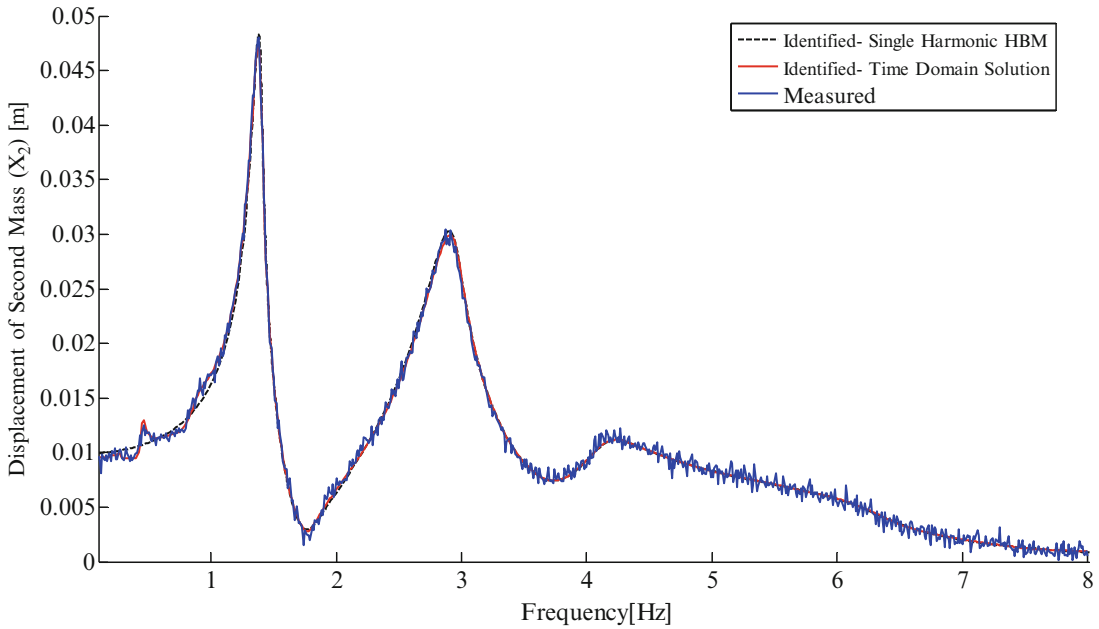

Fig. 9.7 Comparisons of actual and identified system responses for noisy measurement case

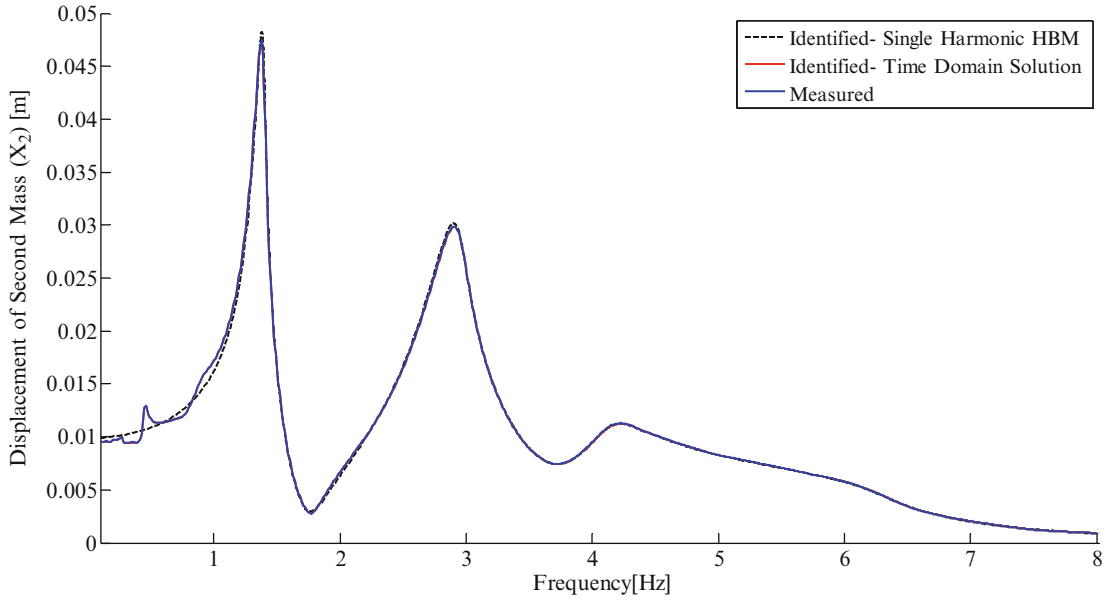

Fig. 9.8 Comparisons of actual and identified system responses for noise free measurement case

trained networks, nonlinearities in a 4-DOF system are classified and the parameters associated with them are identified. The results obtained show that the proposed method is capable of identifying the locations and types of the nonlinearities and the parameters associated with them even in the presence of measurement noise.

Number of nonlinear system configurations and size of the training data generated depend on the number possible nonlinearities in the system. Number of nonlinear equations solved for generating training data also depends on the number of nonlinear elements used in the analysis. Therefore, for realistic finite element models, data generation process is a time consuming one, which can be overcome by employing reduction methods. In this study, the number of nonlinear equations is reduced by employing receptance method, which is a very effective method, especially if the nonlinearities are local.

Proposed method is capable to perform identification even the measurements are taken from linear DOFs. This is especially important, since before the classification process, locations of the nonlinearities are unknown. Moreover, by employing a noise injection to the training data, proposed method can handle measurement noise successfully. Even though training data generation step is computationally demanding, once the networks are trained identification is very fast. Therefore, it is very good candidate for online identification purposes.

References

1. Kerschen G, Worden K, Vakakis AF, Golinval JC (2006) Past, present and future of nonlinear system identification in structural dynamisc. Mech Syst Signal Process 20:505–592
2. Adams DE, Allemang RJ (1988) Survey of nonlinear detection and identification techniques for experimental vibrations. In: International seminar on modal analysis (ISMA 23), Leuven, Belgium
3. Kerschen G, Worden K, Vakakis AF, Golinval JC (1986) Nonlinear system identification in structural dynamics: current status and future directions. In: 4th International modal analysis conference, vol 1, pp 712–719, Los Angeles, CA,USA
4. Özer MB, Özgüven HN, Royston TJ (2009) Identification of structural non-linearities using describing functions and the Sherman–Morrison method. Mech Syst Signal Process 23(1):30–44
5. Aykan M, Özgüven HN (2012) Parametric identification of nonlinearity from incomplete FRF data using describing function inversion. In: Proceedings of SEM IMAC XXX conference, pp 323–334, Jacksonville, FL USA
6. Göge D, Sinapius M, Füllekrug U, Link M (2005) Detection and description of non-linear phenomena in experimental modal analysis via linearity plots. Int J Nonlinear Mech 40(1):27–48
7. He J, Ewins DJ (1987) A simple method of interpretation for the modal analysis of non-linear systems. In: 5th international modal analysis conference, pp 626–634, London, England
8. Adams DE, Allemang RJ (2000) A frequency domain method for estimating the parameters of a non-linear structural dynamic model through feedback. Mech Syst Signal Process 14(4):637–656
9. Chatterjee A, Vyas NS (2004) Non-linear parameter estimation in multi-degree-of-freedom systems using multi-input Volterra series. Mech Syst Signal Process 18(3):457–489

10. Masri SF, Caughey TK (1979) A nonparametric identification technique for nonlinear dynamic problems. J Appl Mech 46:433–447 (Introduction Section 3; Sections 3.2, 5.1, 6.1, 6.2)
11. Richards CM, Singh R (1998) identification of multi-degree-of-freedom non-linear systems under random excitations by the reverse-path spectral method. J Sound Vib 213 673–708 (Sections 3.3, 6.6, 7.1)
12. Masrit SF, Chassiakosl AG, Caugheys TK (1992) Structure-unknown non-linear dynamic systems: identification through neural networks. 1:45–56
13. Xie SL, Zhang YH, Chen CH, Zhang XN (2012) Identification of nonlinear hysteretic systems by artificial neural network. Mech Syst Signal Process, 34(1–2) 76–87
14. Beale MH, Hagan MT, Demuth HB (2012) Neural network toolbox TM user's guide, The MathWorks, Inc., pp 18–84
15. Menq C.-H, Griffin JH, Bielak J (1986) The influence of microslip on vibratory response, Part II: a comparison with experimental results. J Sound Vib 107(2) 295–307
16. Cigeroglu E, Samandari H (2012) Nonlinear free vibration of double walled carbon nanotubes by using describing function method with multiple trial functions. Physica E: Low-dimensional Syst Nanostruct 46:160–173
17. Yümer ME, Ciğeroğlu E, Özgüven HN (2010) Non-linear forced response analysis of mistuned bladed disk assemblies. ASME turbo expo 2010: power for land, sea, and air (GT2010), pp 757–766, Glasgow, Scotland

Chapter 10
Locally Non-linear Model Calibration Using Multi Harmonic Responses: Applied on Ecole de Lyon Non-linear Benchmark Structure

Vahid Yaghoubi, Yousheng Chen, Andreas Linderholt, and Thomas Abrahamsson

Abstract In industry, linear FE-models commonly serve to represent global structural behavior. However, when test data are available they may show evidence of nonlinear dynamic characteristics. In such a case, an initial linear model may be judged being insufficient in representing the dynamics of the structure. The causes of the non-linear characteristics may be local in nature whereas the major part of the structure is satisfactorily represented by linear descriptions. Although the initial model then can serve as a good foundation, the parameters needed to substantially increase the model's capability of representing the real structure are most likely not included in the initial model. Therefore, a set of candidate parameters controlling nonlinear effects, opposite to what is used within the vast majority of model calibration exercises, have to be added. The selection of the candidates is a delicate task which must be based on engineering insight into the structure at hand.

The focus here is on the selection of the model parameters and the data forming the objective function for calibration. An over parameterized model for calibration render in indefinite parameter value estimates. This is coupled to the test data that should be chosen such that the expected estimate variancesof the chosen parameters are made small. Since the amount of information depends on the raw data available and the usage of them, one possibility to increase the estimate precision is to process the test data differently before calibration. A tempting solution may be to simply add more test data but, as shown in this paper, the opposite could be an alternative; disregarding low excessive data may make the remaining data better to discriminate between different parameter settings.

Since pure mono-harmonic excitation during test is an abnormality, the excitation force is here designed to contain sub and super harmonics besides the fundamental one. Further, the steady-state responses at the side frequencies are here shown to contain most valuable information for the calibration process of models of locally nonlinear structures.

Here, synthetic test data stemming from a model representing the Ecole Centrale de Lyon (ECL) nonlinear benchmark are used for illustration. The nonlinear steady state solutions are found using iterative linear reverse path state space calculations. The model calibration is here based on nonlinear programming utilizing several parametric starting points. Candidates for starting points are found by the Latin Hypercube sampling method. The best candidates are selected as starting points for optimization.

Keywords Nonlinear • Calibration • Multi-harmonic • Identifiability • Fisher

10.1 Introduction

Although nonlinear systems have caught much attention both from faculty and industry, linear finite element models are still dominating the representation of global structural dynamics of complex mechanical systems. This is due to that linear models are computationally efficient and have simple input-output relationships which offer good insight into the models' dynamics. If significant nonlinear characteristics are found within the test data, when available, a linear model may be judged

V. Yaghoubi • T. Abrahamsson
Department of Applied Mechanics, Chalmers University of Technology, 41296 Göteborg, Sweden
e-mail: yaghoubi@chalmers.se; thomas.abrahamsson@chalmers.se

Y. Chen • A. Linderholt (✉)
Department of Mechanical Engineering, Linnaeus University, 35195 Växjö, Sweden
e-mail: Yousheng.chen@lnu.se; Andreas.linderholt@lnu.se

G. Kerschen et al. (eds.), *Topics in Nonlinear Dynamics, Volume 1: Proceedings of the 31st IMAC, A Conference on Structural Dynamics, 2013*, Conference Proceedings of the Society for Experimental Mechanics Series 35,
DOI 10.1007/978-1-4614-6570-6_10,

being insufficient in representing the structural behavior whereby a nonlinear model has to be utilized. For many mechanical systems, causes of nonlinear behavior are local in nature; joints introducing gaps or dry friction and structural parts subjected to large displacements are examples of such. An initial linear model can then form a good foundation for model calibration. However, the parameters needed to substantially increase the model's capability of representing the real structure are most likely not included in the initial model. Therefore, a set of candidate parameters controlling nonlinear effects, opposite to what is used within the vast majority of model calibration exercises, have to be added. The selection of the candidates is a delicate task which solution must be based on engineering insight into the structure at hand.

The selection of data to be used in model calibration is vital; the data selection is coupled to the model parameterization chosen. Using an over parameterized model for calibration makes the estimated parameter values indeterminate. When there is a lack of information to discriminate between different parameters, or groups of linearly combined parameters, a re-parameterization or a modification of the data used has to be made, see Linderholt [1]. The Cramer-Rao lower bound quantifies a limit to the accuracy of parameter estimates from the information in the test data. The inverse of the Cramer-Rao lower bound is known as the Fisher information (FIM), see Udwadia [2]. The Cramer-Rao lower bound and the FIM are useful quantities to assess test data informativeness and parameter identifiability and they can be estimated a priori using a calculation model. The test data should be chosen such that the expected variances of the estimated parameters are small. Since the amount of information depends on the raw data available and the usage of them, one possibility is to process the test data differently before calibration. A tempting solution may be to simply add more test data but, as shown in this paper, the opposite could be an alternative; disregarding low excessive data may make the remaining data better to discriminate between different parameter settings.

The excitation force fed into a structure during a vibrational test is dependent on the signal sent to the exciter but also to the interaction between the exciter and the structure itself. When nonlinearities are present, an intended pure mono-harmonic excitation therefore often becomes a multi-harmonic excitation consisting of the fundamental frequency together with sub and super harmonics of this. Here, the excitation force is designed to contain sub and super harmonics together with the fundamental one; the magnitudes of these side harmonics are made small compared to the fundamental harmonic but large compared to the expected noise. If the structure were linear, the responses at the sub and super harmonics would be given by its frequency response function in combination with the excitation. The deviation from linear response is therefore stemming from the nonlinearities within the structure. By using a multiple harmonic excitation, the responses at the multiple frequencies can be compared with known non zero values stemming from a linear model. The response deviations, between test and analyses, at the side frequencies contain most valuable information for calibration of models of locally nonlinear structures.

In this paper, the model calibration is made by use of synthetic test data stemming from a finite element model representing the Ecole Centrale de Lyon (ECL) nonlinear benchmark structure, see Thouverez [3]. This structure consists of one long robust beam segment connected to another short and flexible membrane like, beam segment. The beam assembly is fixed at its ends and subjected to superimposed pre-tensile loading. The static loading represents pretension due to misalignment during assembly. The nonlinearity is localized to the short beam that is subjected to large deflection even at low load levels. This is a simple nonlinear structure that permits a good understanding of the underlying nonlinear phenomena. To increase the identifiability complexity, a nonlinear spring is added between ground and the beam-membrane intersection.

10.2 Theoretical Background

In general, the forced vibration response of a nonlinear deterministic system can be expressed by the state-space system of ordinary differential equations as

$$\dot{x} = f(x,u), \quad y = g(x,u) \tag{10.1a,b}$$

Here $\boldsymbol{u}$ is the excitation vector, $\boldsymbol{x}$ the state vector and $\boldsymbol{y}$ the response vector. For steady-state periodic excitation it is well-known that a linear system reacts to such stimulus by a periodic steady-state response with same periodicity when the initial transients have settled. It is also well-known that this is not generally the situation for nonlinear systems. The steady state-response of a nonlinear system may be periodic with stimulus periodicity or with another periodicity, or there will be no periodic response at all, see Nayfeh and Mook [4]. For stationary harmonic excitation with excitation frequency Ω, corresponding to period $T = 2\pi/\Omega$, the non-linear system may respond in a periodic steady-state with the periodicity $nT, n \in Z^+$ which will be referred to as being n-cycle periodic. Here, the study is confined to n-cycle periodic steady-state conditions and thereby response solutions that are chaotic, non-periodic or periodic with any other periodicity are rejected.

For a linear system with periodic excitation

$$u(t) = \Re\left\{\boldsymbol{u}_1 \exp(i\Omega t) + \boldsymbol{u}_2 \exp(2i\Omega t) + \cdots + \boldsymbol{u}_\upsilon \exp(\upsilon i\Omega t) + \boldsymbol{u}_{1/2} \exp(i\Omega t/2) + \cdots + \boldsymbol{u}_{1/\upsilon} \exp(i\Omega t/\upsilon)\right\} \tag{10.2}$$

where the harmonic order is $\upsilon \in Z^+$, the response may be written as

$$\boldsymbol{y}(t) = \Re\left\{\boldsymbol{y}_1 \exp(i\Omega t) + \boldsymbol{y}_2 \exp(2i\Omega t) + \cdots + \boldsymbol{y}_\upsilon \exp(\upsilon i\Omega t) + \boldsymbol{y}_{1/2} \exp(i\Omega t/2) + \cdots + \boldsymbol{y}_{1/\upsilon} \exp(i\Omega t/\upsilon)\right\} \tag{10.3}$$

or

$$\boldsymbol{y}(t) = \Re\left\{\boldsymbol{H}(\Omega)\boldsymbol{u}_1 \exp(i\Omega t) + \boldsymbol{H}(2\Omega)\boldsymbol{u}_2 \exp(2i\Omega t) + \cdots + \boldsymbol{H}(\Omega/\upsilon)\boldsymbol{u}_{1/\upsilon} \exp(i\Omega t/\upsilon)\right\} \tag{10.4}$$

Where $\boldsymbol{H}(\Omega)$ is the system's complex-valued frequency dependent transfer function at frequency Ω. Hence, for the mono-frequency excitation

$$\boldsymbol{u}(t) = \Re\left\{\boldsymbol{u}_1 \exp(i\Omega t)\right\} \tag{10.5}$$

and the stationary response of a linear system is

$$\boldsymbol{y}(t) = \Re\left\{\boldsymbol{H}(\Omega)\boldsymbol{u}_1 \exp(i\Omega t)\right\} \tag{10.6}$$

However, for a nonlinear system in n-cycle periodic steady-state exposed to a mono-frequency loading, the response is generally not mono-frequency. Its response can be written as

$$\boldsymbol{y}(t) = \Re\left\{\bar{\boldsymbol{y}}_1 \exp(i\Omega t) + \sum_{\upsilon=2}^{\upsilon_{\max}} \bar{\boldsymbol{y}}_\nu \exp(i\nu\Omega t) + \underline{\boldsymbol{y}}_\upsilon \exp(i\Omega t/\nu)\right\} \tag{10.7}$$

Where $\bar{\boldsymbol{y}}_\nu$ and $\boldsymbol{y}_\upsilon$ are the superharmonic and subharmonic distortion amplitudes of order υ respectively. The magnitudes of these generally depend on the stimulus magnitude $\boldsymbol{u}_1$ together with the excitation frequency Ω. It is convenient for the sequel to denote the stimulus and response magnitudes by load, order and frequency indices such that $u_{\lambda\upsilon k}$ denotes the excitation level λ of harmonic order υ at the k : th discrete frequency Ω_k and $y_{\lambda\upsilon k}$ denotes the υ : th order response due to that excitation.

10.2.1 δ-Level Multi-harmonics Frequency Response Functions

In testing, the mono-frequency excitation is an abnormality and harmonic distortion is always present due to imperfections in the test setup and exciter-structure interaction. Instead of trying to achieve a pure sinusoidal excitation, one may have a better chance to enforce a multi-harmonic stimulus with a distortion level that overshadows the intrinsic test setup distortion. Let the δ-level multi-harmonic excitation of load level λ at the fundamental frequency Ω_k be defined as

$$\boldsymbol{u}_{k\lambda}(t) = \Re\left\{\boldsymbol{u}_\lambda \exp(i\Omega_k t) + \delta u_\lambda \sum_{\upsilon=2}^{\upsilon_{\max}} \left(\exp(i\nu\Omega_k t) + \exp(i\Omega_k t/\nu)\right)\right\} \tag{10.8}$$

By letting $\delta \ll 1$, a harmonic function including a small distortion to the fundamental harmonic at Ω_k is built up. That stimulus signal can be used in testing or simulation. After initial transients have settled, under n-periodic steady-state conditions, the system response will eventually become periodic and before the pureperiodic condition arise;

$$\boldsymbol{y}_{k\lambda}(t) = \Re\left\{\bar{\boldsymbol{y}}_{\lambda 1} \exp(i\Omega_k t) + \sum_{\upsilon=2}^{\upsilon_{\max}} \left(\bar{\boldsymbol{y}}_{\lambda\nu} \exp(i\nu\Omega_k t) + \underline{\boldsymbol{y}}_{\lambda\upsilon} \exp(i\Omega_k t/\nu)\right)\right\} + \text{residual} \tag{10.9}$$

The complex-valued amplitudes of $\bar{\boldsymbol{y}}_\nu$ and $\underline{\boldsymbol{y}}_\upsilon$ can be found by regression. Theδ-level multi-harmonic frequency response function that relates the output (response) at the i : th dof to the input (excitation) at the j : th dof is defined as the complex-valued quantities

$$\bar{\boldsymbol{H}}_{\lambda\upsilon ij}(\Omega_k) = \bar{\boldsymbol{y}}_{\lambda\nu i}(\Omega_k)/u_{\lambda j} \quad \text{and} \quad \underline{\boldsymbol{H}}_{\lambda\upsilon ij}(\Omega_k) = \underline{\boldsymbol{y}}_{\lambda\upsilon i}(\Omega_k)/u_{\lambda j} \tag{10.10a,b}$$

for the first together with the superharmonic orders and subharmonic orders respectively. Particularly, for a linear system:

$$\bar{\boldsymbol{H}}_{\lambda\upsilon ij}(\Omega_k) = \delta\bar{\boldsymbol{H}}_{\lambda 1ij}(\nu\Omega_k) \quad \text{and} \quad \underline{\boldsymbol{H}}_{\lambda\upsilon ij}(\Omega_k) = \delta\underline{\boldsymbol{H}}_{\lambda 1ij}(\Omega_k/\upsilon)\upsilon \neq 1 \tag{10.11a,b}$$

i.e. the superharmonic and subharmonic frequency response function can be obtained from the frequency response function of the fundamental harmonics by a scaling with the level parameter δ.

For a nonlinear system, relations as those of Eq. (10.11a,b) do not hold and the δ-level frequency response functions will depend on the excitation level λ. A quantity of the difference between these functions of the nonlinear system and the corresponding functions of the linearized system may the give an insight into the nonlinear behavior of the system. A slight adjustment of the notation is made here; the δ-level frequency response function $H_{\lambda\nu kij}$ from now on means the function value that pertain to the excitation level of index $\lambda(\lambda = 1,2,\ldots,\lambda_{\max})$, of indexed order ν ($\nu = 1,2,\ldots,\nu_{\max}$) that includes both superharmonic and subharmonic orders, at indexed fundamental frequencies Ω_k ($k = 1,2,\ldots,k_{\max}$). The frequency response function $H_{\lambda\nu kij}$ relates the output at dof i with the input at dof j. Furthermore, the Matlab colon notation is used; the vector $H_{:\nu kij}$ is defined as the vector with elements being function values $H_{\lambda\nu kij}$ for indices λ of all available loads as

$$\boldsymbol{H}_{:\nu kij} = \overset{vect}{\forall\lambda}(\boldsymbol{H}_{\lambda\nu kij}) \tag{10.12}$$

with fixed order index, frequency index and dof index. Similarly, the vectors $H_{\lambda:kij}$ and $H_{\lambda\nu:ij}$ are defined as

$$\boldsymbol{H}_{\lambda:kij} = \overset{vect}{\forall\nu}(\boldsymbol{H}_{\lambda\nu kij}) \quad \text{and} \quad \boldsymbol{H}_{\lambda\nu:ij} = \overset{vect}{\forall k}(\boldsymbol{H}_{\lambda\nu kij}) \tag{10.13}$$

Also, the vector operator for defined subsets of loads λ_s is defined as

$$\boldsymbol{H}_{\lambda_s\nu kij} = \lambda \overset{vect}{\in} \lambda_s(\boldsymbol{H}_{\lambda\nu kij}) \tag{10.14}$$

with similar notation for subsets of order indices and frequency indices. The vectorization concept is generalized, e.g.

$$\boldsymbol{H}_{::kij} = \overset{vect}{\forall(\lambda,\nu)}(\boldsymbol{H}_{\lambda\nu kij}) \tag{10.15}$$

is the vector of data for all available load levels and orders and

$$\boldsymbol{H}_{:\nu_s kij} = \forall\lambda, \nu \overset{vect}{\in} \upsilon_s(\boldsymbol{H}_{\lambda\nu kij}) \tag{10.16}$$

is the vector of data for all available load levels for orders from the subset ν_s. Other combinations should now be obvious.

10.2.2 A Deviation from Linearity criterion Function

For a linear system, the frequency response function, here denoted $H^{lin}_{\upsilon kij}$, is independent of the load level, λ. In the sequel the focus is on the difference between the nonlinear system's frequency response behavior and the linearized systems counterpart. Here, the deviation from linearity is defined as

$$e_{\lambda\nu kij} = \boldsymbol{H}_{\lambda\nu kij} - \boldsymbol{H}^{\text{lin}}_{\upsilon kij} \tag{10.17}$$

where the same vector notation is used as previously for H. In short the vector of elements $e_{\lambda\upsilon kij}$ is denoted the vector $\boldsymbol{e}$, with proper indexing when needed for clarity. The deviation from linearity is a complex-valued number and consequently $\boldsymbol{e}$ is a complex-valued vector. A real-valued scalar deviation criterion function E is defined as

$$E = \bar{\boldsymbol{e}}^{\mathrm{T}}\boldsymbol{e} \tag{10.18}$$

where overbar denotes the complex conjugate. For identifiability purpose, the gradient,∇E, of this function with respect to model parameters, p_m, $m = 1,2,\ldots$ is studied.

$$\nabla E = [\partial E/\partial p_1 \partial E/\partial p_2 \cdots] \tag{10.19}$$

The m : th component can be expressed as

$$\partial E/\partial p_m = 2\Re\left\{\bar{\boldsymbol{e}}^{\mathrm{T}}\partial\boldsymbol{e}/\partial p_m\right\} = \sum\nolimits_k \Re\left\{2\bar{\boldsymbol{e}}^{\mathrm{T}}_{::::k::::}\partial e_{::::k::::}/\partial p_m\right\} = \text{def} = \sum\nolimits_k \varepsilon_{k,m} \tag{10.20}$$

The gradient components $\varepsilon_{k,m}$ are functions of discrete frequencies Ω_k and they are here used to evaluate the parameter identifiability.

10.2.3 Ranking Identifiability of Parameters

The requirements for a test design are that the resulting test data should be informative with respect to the parameters and that the parameters should be identifiable. The first means that a change of the value of any parameter should change the observed response in a noticeable way. The latter is to say that test data should differentiate changes of different parameter values. In computational model calibration, these requirements are coupled to the usefulness of the test data in estimating model parameter values accurately. The two requirements can jointly be stated as; regardless of which parameters that are estimated, precise estimates require a small parameter covariance matrix. This should ultimately be examined prior to a final model calibration.

The Fisher information, which is a scalar, is a measure of the information an observable variable, i.e. test data, X carries with respect to a single unknown parameter that the probability of X depends on. The probability function of X is also the likelihood function for X given a certain parameter value$p$. That function is denoted $f(X:p)$. The partial derivative of the natural logarithm of$f$ with respect to p is denoted the score. An unbiased estimator is an estimator having a mean that converges to the correct parameter setting as the number of test data tends towards infinity. That means that the first moment of the score vanishes. Further, the second moment of the score is known as the Fisher information. The corresponding measure for a multi parameter problem is the Fisher information matrix (FIM) having size $p \times p$. When it comes to estimating parameter values, p_{est}, the Fisher information matrix, here denoted $J(p)$, plays an important role, see Walter and Pronzato [5] and Spall [6]. The reason for this is the Cramer-Rao theoretical lower bound which establishes a limit on the expectation of the covariance matrix of the estimate of the parameter values. This limit is coupled to the FIM according to;

$$\Xi[p_{est-}p][p_{est-}p]^{\mathrm{T}} \geq J^{-1} \tag{10.21}$$

in which Ξ denotes the expectation. The Cramer-Rao bound implies that, irrespective of the method used to quantify the parameters from the data, there is a bound on the estimation precision that can not be overcome. Similar to the single parameter situation, the Fisher information matrix is determined by the joint probability density function, f;

$$J(p) = \Xi\left[\frac{\partial}{\partial p}\log f\right]^{\mathrm{T}}\left[\frac{\partial}{\partial p}\log f\right] \tag{10.22}$$

Here, the measurement noise is assumed to be of the simplest kind, from an analytical point of view. It consists of independent Gaussian sequences having zero mean values. Further, it is assumed that the noise is uncorrelated and statistically equivalent for all measured quantities; the noise variance equals σ^2. Then, the FIM expression simplifies into:

$$J(p) = \frac{1}{\sigma^2}\sum_{k=1}^{N}\nabla E_k^{\mathrm{T}}\nabla E_k \tag{10.23}$$

The gradient ∇E is a $1 \times m$ vector. Each of its columns is formed as a summation, see Eq. (10.20). Let all, N, possible components contributing in the summation be stacked on top of each other to form an $N \times m$ matrix, here denoted $\nabla\tilde{E}$. The FIM can now be calculated as

$$J(p) = \frac{1}{\sigma^2}\nabla\tilde{E}^T\nabla\tilde{E} \tag{10.24}$$

with unchanged result. However, the formation of $\nabla\tilde{E}$ is useful in the study of data informativeness and parameter identifiability which are complementary. When the value of a model parameter is changed, the measurement data should change noticeable in order to the data to be informative with respect to the parameters involved in the model calibration. Complementary, changing the values of two parameters should change the measurement data differently. A combination of a parameter selection and a test design rendering in that all pairs of columns of $\nabla\tilde{E}$ are orthogonal is the ultimate. The angle between two columns is easily calculated; using the definition of the modal assurance criterion gives a good, normalized, measure of the linear dependencies. When two columns associated with parameters p_i and p_j are orthogonal, the element of the i : th row and the j : th column of the Fisher information matrix is zero.

If the ideal situation for which the columns are orthogonal is not fulfilled, the linear relationship between groups of columns has to be examined since changing one parameter (or a group of parameters) may change the dynamics of the model in the same way as a change of another parameter (or another group of parameters). When this happens, the parameters are not identifiable from test data, which means that a model calibration will be unreliable. Proper measures have to be taken, possibly involving re-parameterization or a change of the test design, see Linderholt and Abrahamsson [7]. The conclusion is that it is not enough to examine only relations between pairs of parameters and this is where the FIM and its inverse is a more useful measure.

A number of criteria ranking the goodness of the FIM or its inverse have been proposed. The A-optimality focus on minimizing the trace of the inverse of the Fisher information matrix. The D-optimality aims at maximizing the determinant of the FIM. E-optimality, maximizes the minimum eigenvalue of the FIM. Further, the T-optimality maximizes the trace of the FIM. Finally, the G-optimality seeks to minimize the maximum expected variance estimated parameter values. These are just examples of frequently used matrix criteria. In this study, yet another criterion is chosen; that is the condition number of the FIM. A low condition number indicated a well-conditioned matrix which in turn is necessary for small parameter estimate variances given by the inverse of the FIM.

The FIM and its inverse, and thereby the data informativeness and the parameter identifiability, varies with the response data used. It is therefore important to include all available data that carries information that differentiate parameter settings. This is partly controlled by the selection of excitation and response measurement during test; that is the actuator and sensor placement together with the excitation time history. Another part is the choice of the perspective on which the test data are looked upon. Sometimes, processing the data may hide or destroy pieces of information that are in the original data. Some test data simply destroys or decreases the goodness of the overall test data; such data should be excluded before the updating is made.

With each column in $\nabla\tilde{E}$ being partitioned into information contributions stemming from different combinations of sensors, excitation frequencies, load levels, response orders etc., also the FIM is built up by a summation of FIM:s stemming from each such combination, here denoted with the index s.

$$J(p) = \sum_{s=1}^{S} {}^{s}J(p) \tag{10.25}$$

It is not known a priori how many and which of the contributing data that should be taken into account to get a low condition number of the FIM. Examining all possible combinations of reductions is time consuming since the number of combinations grows rapidly as a function of the number of possible sensors etc. Using a sub-set selection technique is an inexpensive choice to achieve a good, although not guaranteed to be optimal, solution, see Miller [8].

10.2.4 Parameter Estimation

Having an identifiable parameter setting, the following step is to calibrate the model, using test data as well as model response data. The model calibration is an optimization task; many strategies have been proposed during the last decades. It is common to use several starting points for optimization studies to increase the likelihood of finding the global optimum. It is computationally inexpensive to evaluate the value of the objective function at one point within the parametric space compared to the cost of a complete optimization starting at such parametric point. With a limitation in computational time it may be wise to trade complete optimization runs in favor for examination of more staring point candidates; then using the ones for which the objective function have the smallest values as starting points for calibration. Indeed studying an infinite number of starting points spanning the parametric space would constitute an optimization with a global optimum guaranty. Since also the affordable number of starting points to evaluate is limited, the parameter settings of these points should be chosen so that the parametric space is represented satisfactorily. Here, the Latin Hypercube sampling method is used for that, see McKay, Beckman and Conover [9].

10.3 Numerical Example

Here, the identifiability properties of the parameters with respect to the criterion based on the deviation from linearity is illustrated by studying an FE-model representing the ECL Benchmark setup. The ECL Benchmark, which was designed with the parameter identification of localized nonlinear systems in mind, consists of two assembled parts; a cantilever beam connected with a thin membrane like beam [3]. The thin beam mostly acting like a membrane gives a nonlinear restoring force at the beam end. Here, it is assumed that the axial force within the membrane is constant and equal to the pretension force R. This assumption makes the vertical force, acting on the beam end, stemming from the membrane equal to $R\sin\phi$. Hence, the restoring force is built up by a linear part and a cubic part together with higher order terms. The structure, clamped at its two ends, is excited by a transversal force, $u(t)$ at the intersection between the beam and the membrane, see Fig. 10.1.

Twelve linear Euler-Bernoulli finite elements of equal lengths are used to model the beam element using CBAR in MSC Nastran [10]. Likewise, the membrane is modeled by four planar linear Euler-Bernoulli finite elements. The stiffness and

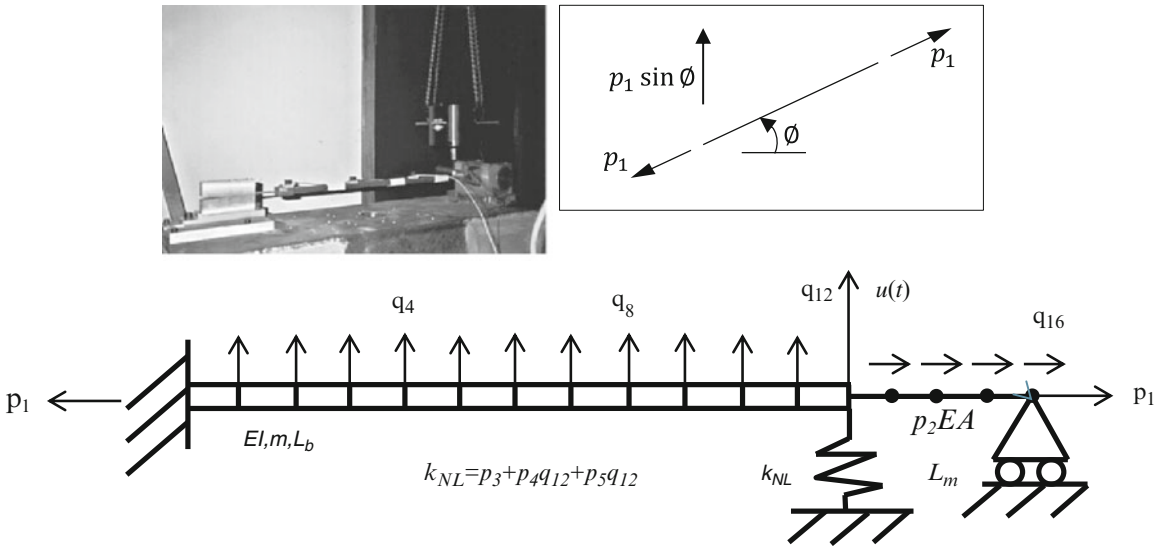

Fig. 10.1 Thirty six-degrees-of-freedom numerical model of ECL Benchmark setup. Photo of test bed from (Thouverez). The beam, to the *left* of the discrete spring, has bending stiffness, mass per unit length and total length equal to EI, m and L_b respectively. The taut membrane, to the *right* of the discrete spring, has tensional stiffness EA and free length L_m. The system pretension is R and the periodic loading is $u(t)$. Responses at dofs $q_1, \cdots, q_{16}$; 12 vertical and 4 horizontal, are used. The loading of displaced membrane is shown in insert. The restoring force from the membrane $p_1 \sin(\emptyset)$ acting at the beam end is a nonlinear function of the displacements because the membrane rotation ϕ is not small. Numerical data: $EI = 672\,\mathrm{Nm}^2, m = 3.36\,\mathrm{kg/m}, EA = 3150\,\mathrm{kN}, L_\mathrm{b} = 593\,\mathrm{mm}, L_\mathrm{m} = 57\,\mathrm{mm}$

mass matrices are then exported from Nastran into Matlab in which also the restoring force representing the taut membrane is added. The taut force of the membrane in its neutral position and the Young's modulus of both the beams, are here denoted parameter one (p_1) and parameter (p_2) respectively. To increase the identifiability complexity, beyond that of the original ECL-structure, a nonlinear spring is added between the beam/membrane intersection and ground. The constant, linear and quadratic spring stiffness coefficients here constitute parameters three (p_3), four (p_4) and five (p_5) respectively. The nominal parameter setting for which, SI-units is used is:$10, 2.1 \cdot 10^{11}, 10^3, 10^5, 10^8$. Within the preceding calculations normalized parameter are used; the normalization is made such that the normalized nominal values all equals one.

$$p_i^{\mathrm{norm}} = p_i / p_i^{nominal}, \quad \mathrm{i} = 1,2,3 \quad \text{and} \quad p_i^{norm} = log_{10}\left(10 \cdot p_i / p_i^{nominal}\right), \quad \mathrm{i} = 4,5 \tag{10.26}$$

In the simulation a periodic force $u(t)$ having two possible magnitudes ($u_\lambda = 2\,\mathrm{N}$ and $u_\lambda = 10\,\mathrm{N}$ for $\lambda = 1,2$) is applied and the responses at 16 dofs during each full period are evaluated. A stationary check is made by comparing the response for one period with its preceding period and it is assumed that stationarity is achieved when the responses for two consecutive periods are the same, i.e. when the norm of the difference of responses between the periods is small. All cases here studied settled to periodic solutions. The multi-level FRF:s of the last simulated period for the given condition are evaluated.

Figure 10.2 shows the δ-level multi-harmonics frequency response functions with $\delta = 0.01$. It can be noted that the frequency response functions deviates from the linearized system's frequency response functions mainly in the vicinity of structural resonances where the deviation is significant for the larger (10 N) load level. A vectorizing operation such that

$$\varepsilon_{,m} = \overset{\mathrm{vect}}{\forall k}\, \varepsilon_{k,m} \tag{10.27}$$

is used for the study of the correlation of these vector functions for the five parameters, $m = 1,2,\ldots,5$. A correlation index, C_{mn}, being the cosine-square of the angle between the vectors (similar to the well-known MAC index for eigenvectors) is used.

$$C_{mn} = \cos^2\left(\angle(\varepsilon_{,m}\varepsilon_{,n})\right) \tag{10.28}$$

Figure 10.3 shows the gradient components $\varepsilon_{k,m}$, see Eq. (10.20), for two load levels $u_{\lambda=1} = 2\,\mathrm{N}$ and $u_{\lambda=2} = 10\,\mathrm{N}$. The gradients were evaluated by finite differentiation of the parameters p_i with $\Delta p_i = 10^{-4}$. It is clear that the gradients related to different parameters are highly correlated. Since changes of different parameter values change the data, intended to be used for model calibration, indifferently the opposite holds. Thus a successful model calibration using this data is not likely.

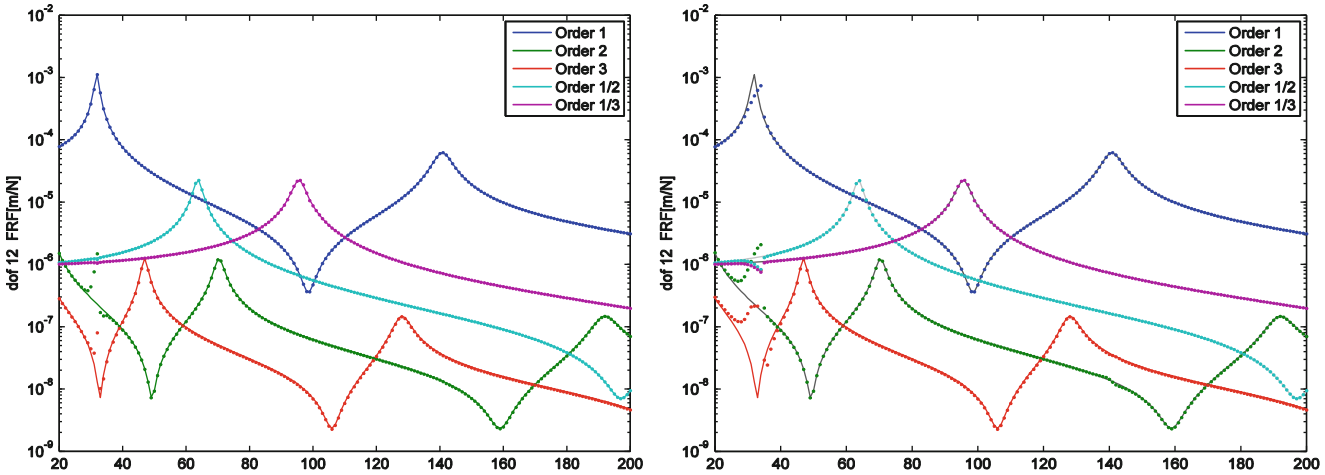

Fig. 10.2 δ-level multi-harmonics frequency response functions at load amplitudes $F_\lambda = 2$ (*left figure*) and 10 N (*right figure*) for $\lambda = 1, 2$

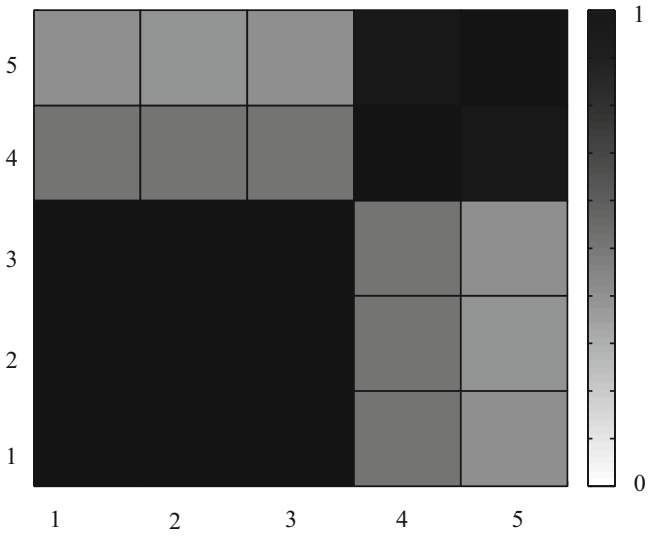

Fig. 10.3 The correlation index C_{mn} for gradient data associated with the full data set and the five parameters. The correlations between parameters one, two and three as well as between parameters four and five parameters are clear

Therefore, either the parameterization or the data set has to be modified. The 16 degrees of freedom together with the 2 load levels (2 and 10 N) and the 5 orders (1, 2, 3, 1/2 and 1/3), form 160 sets each contributing to the FIM. By using a backward sub-set selection technique, one contribution at the time is removed. The selection is made such that the condition number of the remaining FIM is kept as low as possible within each reduction step. The result shows that by reducing the set of combinations by up to 40, the condition number of the FIM is lowered considerably, see Fig. 10.4. Using all data sets results in a condition number, of the Fisher's information matrix, equal to $7.7 \cdot 10^{13}$. The twenty first data sets to be de-selected are shown in Table 10.1.

The data stemming from degree-of-freedom no.11, a load level equal to 2 N and order 1 is the first to be removed according to the reduction criterion. The Auto MAC of the part of $\nabla \tilde{E}$ gradient stemming from that combination is shown in Table 10.2. It is obvious that the column vectors are highly correlated. Thus, it is understandable that excluding such data strengthens the information which results in a decrease of the condition number of the Fisher information matrix.

The backward subset selection process mainly deselects data sets associated with order one frequency response data, see Table 10.2. Although the condition number can be improved it is not possible to make parameters one, two and three uncorrelated. Parameters two (Young's modulus) and three (constant stiffness coefficient for the discrete spring) are causing restoring forces that are linear in the displacement. The restoring force from the taut membrane is here equal to $p_1 \cdot \sin(\emptyset)$ which is dominated by its linear component, which can be seen by a Taylor series expansion, for small angles. Hence, it is not surprisingly that these three parameters are correlated. In this situation, a re-parameterization or a re-design of the test setup is necessary. Here, parameters two and three are from now on considered as constant having their nominal values. This decision renders in a re-parameterized model consisting of three parameters p_1, p_4 and p_5.

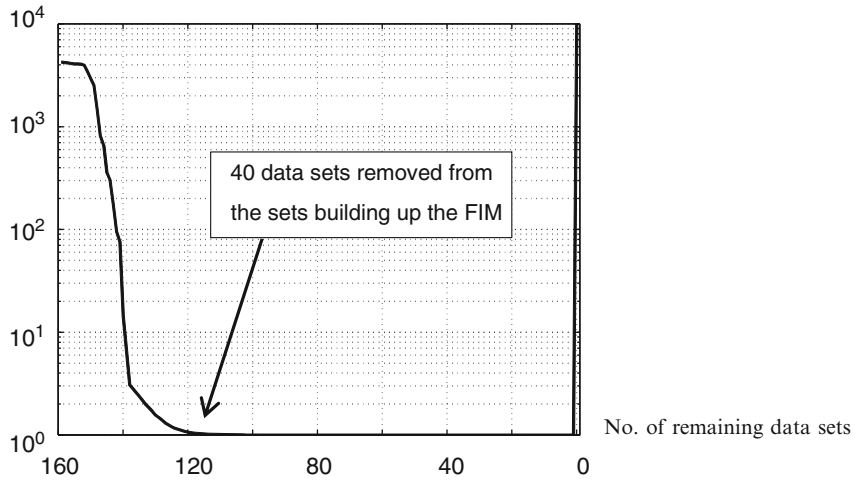

Fig. 10.4 The condition number, normalized such that the smallest value equals one, of the Fisher's information matrix as a function of the remaining number of data sets

Table 10.1 The first 20 data sets that are de-selected within the backward sub-set selection process

Deselection	Dof	Load (N)	Order	Deselection	Dof	Load (N)	Order
1	11	2	1	11	7	2	1
2	10	2	1	12	6	2	1
3	11	10	1	13	5	2	1
4	9	2	1	14	7	10	1
5	8	10	1	15	6	10	1
6	9	10	1	16	4	2	1
7	12	2	1	17	5	10	1
8	12	10	1	18	4	10	1
9	8	2	1	19	3	2	1
10	10	10	1	20	3	10	1

Table 10.2 The AutoMAC matrix associated with the data that should be excluded first among the 160 candidate sets. The data stem from degree of freedom no. 11, load level 2 N and order 1

1.00	1.00	1.00	0.62	0.50
1.00	1.00	1.00	0.61	0.49
1.00	1.00	1.00	0.62	0.50
0.62	0.61	0.62	1.00	0.99
0.50	0.49	0.50	0.99	1.00

Table 10.3 The first 20 data sets that are de-selected within the backward sub-set selection process for the re-parameterized model having three parameters

Deselection	Dof	Load (N)	Order	Deselection	Dof	Load (N)	Order
1	12	2	1	11	2	2	1
2	11	2	1	12	1	2	1
3	10	2	1	13	1	2	3
4	8	2	1	14	13	2	1
5	7	2	1	15	13	2	2
6	11	10	1	16	13	2	3
7	6	2	1	17	13	2	1/2
8	5	2	1	18	13	2	1/3
9	4	2	1	19	13	10	1
10	3	2	1	20	13	10	2

Naturally, parameters p_4 and p_5 are still correlated. The condition number of the 3×3 Fisher's information matrix is studied. The condition number using all data sets now equals $1.5 \cdot 10^7$. The backward subset selection process ones again picks several data sets associated with order one to be de-selected, see Table 10.3. The gradient components for two sets are shown in Fig. 10.5. Here, all order one data sets are chosen to be de-selected. All other sets now constitute the reduced data set for which the condition number becomes equal to 36. Although the condition number could be reduced slightly more,

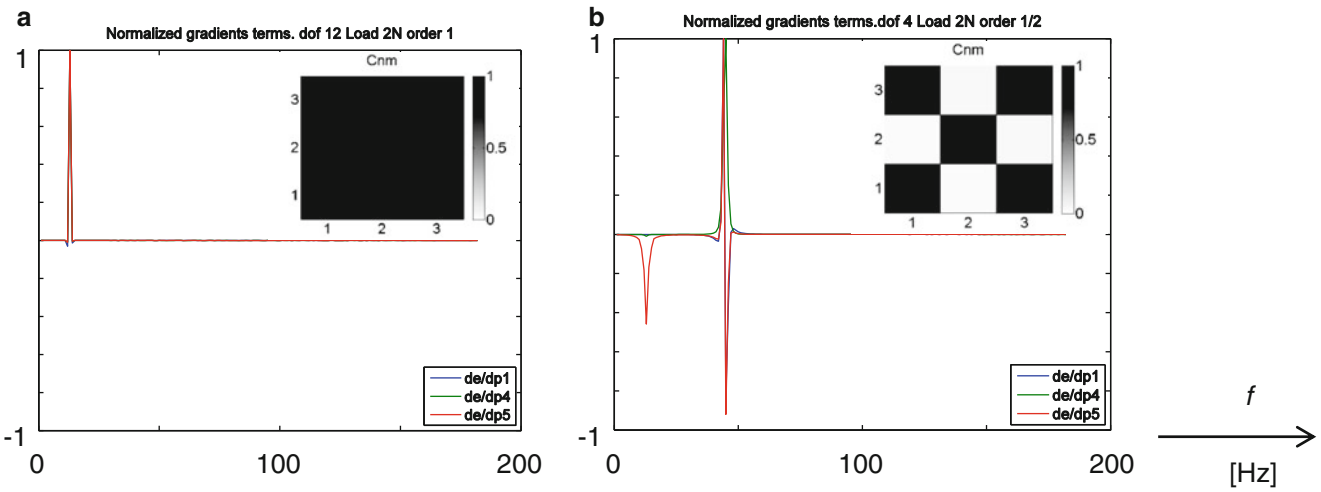

Fig. 10.5 Functions $\varepsilon_{k,m}$ evaluated for $\mu_1 = 2\,\mathrm{N}$ together with correlation indices C_{nm} for corresponding gradient vectors. (**a**) dof 12, load 2 N and order 1 for which the vectors are highly correlated, (**b**) dof 4, load 2 N and order $1/2$ for which parameter two has low correlation with the other whereas parameters one and three are correlated

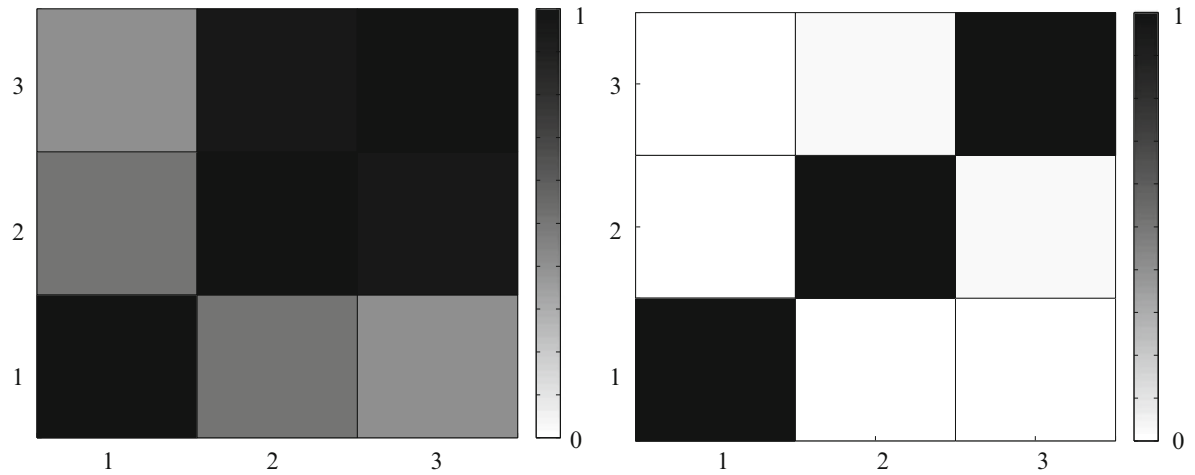

Fig. 10.6 The correlation gradient data associated with the full data set (*left figure*) and the reduced data set (*right figure*) for which all data associated with order one data are de-selected

the hereby chosen reduced set gives almost uncorrelated parameters, see Fig. 10.6. It is worth mentioning that no single data set gives that small condition number. The data set associated with dof 14, load 2 N and order 2 is the set having the lowest condition number, equal to 119, when used alone.

10.3.1 Parameter Estimation

Negative values are not physical for the parameters used. Instead of the normal distributions, a Beta-distribution is used for the pretension force parameter,p_1. The mean value is equal to the value of the nominal model (10 N) and the standard deviation is equal to 20% of the mean value. For the nonlinear parameters; the linear and quadratic stiffness coefficient, it is assumed that their natural logarithm follows a uniform distribution; $p_4 \in [10^4, 10^6]$ and $p_5 \in [10^7, 10^9]$. One hundred parameter realizations were sampled by the Latin hypercube sampling method. The multi harmonic frequency response functions of these realizations were compared with the frequency response functions from the nominal model, here mimicking test data. Among the 100 candidate starting points the 10, for which deviation metrics are the smallest, are used as starting points for complete optimizations. The Levenberg-Marquardt method was used for optimization, see Nash and Sofer [11]. The selection

Table 10.4 The estimated parameter values, p_1, p_4 and p_5, for the case where all data sets are used and the case where order one data sets are de-selected are shown together with the parameter values at the starting points. The starting points were, selected among 100 candidates; the ones having smallest deviations were used as starting points for the optimizations. NI is the number of iterations for convergence. Deviation is the frobenius norm of $(H(p_{estimated}) - H(p_{nominal}))/H(p_{nominal})$

		All data sets			Order one data excluded		
No	Starting points	Parameter estimates parameters	Deviation	NI	Parameter estimates parameters	Deviation (%)	NI
1	[1.002 1.025 1.094]	Did not converge within 100 iterations			[1.004 0.998 0.998]	0.048	2
2	[0.998 1.148 0.795]	[1.000 1.000 1.000]	0.000 %	9	[1.005 1.005 0.996]	0.104	5
3	[1.104 0.973 0.581]	[1.000 1.002 1.000]	0.001 %	12	[1.000 0.996 0.995]	0.162	3
4	[0.958 0.165 0.541]	[0.962 0.004 0.542]	48.29 %	20	[1.005 0.998 0.998]	0.102	3
5	[0.964 1.683 0.663]	[1.000 1.007 1.000]	0.003 %	5	[1.001 1.002 1.000]	0.001	3
6	[1.188 0.463 0.994]	Did not convergewithin 100 iterations			[1.001 0.998 0.997]	0.091	2
7	[1.087 0.483 0.333]	[1.124 0.000 0.343]	52.66 %	25	[1.001 0.994 0.992]	0.253	3
8	[0.970 0.188 0.375]	[0.970 0.000 0.375]	51.66 %	16	[1.001 0.996 0.995]	0.156	3
9	[1.054 2.227 0.856]	Did not converge within 100 iterations			[1.053 2.225 0.859]	5.372	11
10	[1.001 0.103 1.904]	[1.011 0.000 1.905]	43.48 %	11	[0.952 1.234 1.848]	43.43	18

and the following calibrations are made using all data sets as well as using the reduced set for which all order one data are de-selected. It is clear that the reduced set, having superior parameter identifiability indices, makes the calibration process more reliable (Table 10.4).

10.4 Conclusions

It is shown that test data should be looked upon from different perspectives; processing data may hide or destroy information. Here, information from sub and superharmonic components found from steady state oscillation of nonlinear systems assist the information within the fundamental harmonic response; it is shown that they contain most valuable information for calibration of locally nonlinear systems. Instead of trying to get a pure mono-harmonic excitation, which is hard in practice, it is here proposed to include a few sub and superharmonics having amplitudes that are low compared to the amplitude of the fundamental harmonic but still large enough to dominate over the excitation noise. Furthermore, the condition number of the Fisher information matrix, associated with the physical parameters selected, is chosen as the optimization objective. Finally it is shown that disregarding data that have low information value can actually increase the parameter identifiability and data informativity.

Acknowledgements We gratefully acknowledge the Swedish National Aviation Engineering Program (NFFP) for their kind support of this work.

References

1. Linderholt A (2003) Test design for finite element model updating, identifiable parameters and informative test data, Department of Applied Mechanics, Chalmers University of Technology, Göteborg
2. Udwadia FE (1997) A finite element model updating formulation using frequency responses and eigenfrequencies. In: NAFEMS international conference on structural dynamics modelling, pp. 293–305
3. Thouverez F (2003) Presentation of the ECL benchmark. Mech Syst Signal Process, Elsevier 17(1):195–202
4. Nayfeh AH, Mook DT (1979) Nonlinear oscillations. Wiley, New York
5. Walter E, Pronzato L (1997) Identification of parametric models from experimental data. Springer, Great Britain
6. Spall C (1999) The information matrix in control, computation and some applications. In: 38th conference on decision and control, Arizona, pp. 2367–2372
7. Linderholt A, Abrahamsson T (2003) Parameter identifiability in finite element model error localization. Mech Syst Signal Process 17(3):579–588
8. Miller AJ (1990) Subset selection in regression. Chapman and Hall, London
9. McKay MD, Beckman RJ, Conover WJ (1979) A comparison of three methods for selecting values of input variables in the analysis of output from a computer code. Technometrics 21(2):239–245
10. MSC Nastran version 2012, MSC Software
11. Nash SG, Sofer A (1996) Linear and nonlinear programming. McGraw-Hill, New York

Chapter 11
Fatigue Dynamics Under Statistically and Spectrally Similar Deterministic and Stochastic Excitations

Son Hai Nguyen, Michael Falco, Ming Liu, and David Chelidze

Abstract Estimating and tracking crack growth dynamics is essential for fatigue failure prediction. A new experimental system—coupling structural and crack growth dynamics—is used to show fatigue damage accumulation is different under chaotic and stochastic loading, even when both excitations possess same spectral and statistical signatures. Furthermore, the conventional rain-flow counting method considerably overestimates damage in case of chaotic forcing. Important nonlinear loading characteristics, which can explain the observed discrepancies, are identified and suggested to be included as loading parameters in new fatigue models.

Keywords Material fatigue • Chaotic forcing • Stochastic forcing • Damage accumulation • Nonlinear characteristics

11.1 Introduction

The fatigue life prediction in variable amplitude loading conditions has received considerable attention. This is due to the fact that many structures in service are not subject to constant amplitude loadings. It is currently understood that load factors are nonlinearly coupled with the fatigue life [12,13]. The most widely used method, Miner rule, which is based on a superposition principle, is inadequate in practice. Thus, it is important to identify essential load factors that contribute to fatigue life.

In the next section, a novel fatigue testing rig based on inertial forces is described. The new testing rig has three major advantages over traditional apparatuses. In particular, it has ability to: (1) mimic complicated real-world load histories, such as chaotic and random excitations; (2) conduct fatigue tests at various R-ratios[1] (including zero or negative), which is controlled accurately and can be adjusted during a test; and (3) conduct high frequency tests (going higher than 30 Hz based on current design).

In our experiment, fatigue tests are conducted using chaotic and random loading, which have the similar power spectral densities and the probability distribution functions. The mean and variance of the excitation will be kept constant throughout the experiment. Thus, superposition based cycle counting methods should be applicable. Then the rain-flow counting method and Palmgren-Miner rule are applied to quantify the damage variables. Nonlinear loading characteristics are proposed to explain the differences in the results, followed by a conclusion.

[1] $R = \sigma_{\min}/\sigma_{\max}$, where $\sigma_{\min}$ is the minimum peak stress and $\sigma_{\max}$ is the maximum peak stress

S.H. Nguyen • M. Liu • D. Chelidze (✉)
Department of Mechanical, Industrial and Systems Engineering, University of Rhode Island, Kingston, RI 02881, USA
e-mail: haisonbk@gmail.com; liumingmech@gmail.com; chelidze@egr.uri.edu

M. Falco
Sensata Technologies, 529 Pleasant Street, Attleboro, MA 02703, USA
e-mail: mfalco27@gmail.com

G. Kerschen et al. (eds.), *Topics in Nonlinear Dynamics, Volume 1: Proceedings of the 31st IMAC, A Conference on Structural Dynamics, 2013*, Conference Proceedings of the Society for Experimental Mechanics Series 35,
DOI 10.1007/978-1-4614-6570-6_11,

11.2 New Fatigue Testing Apparatus

11.2.1 Mechanical Setup

The experimental system was first introduced in [4]. A schematic of the test rig is shown in Fig. 11.1. The mechanical backbone of the system is a slip table guided by four linear bearings on two parallel rails mounted to a granite base. An LDS V722 electromagnetic shaker is used to drive the slip table under various loading conditions. The specimen is a single edge notched beam which is simply supported by pins on each end. Two inertial masses, guided by linear bearings mounted to the slip table provide dynamic loads. The masses are kept in contact with the specimen with the use of two pneumatic cylinders. Different R-ratios can be obtained by adjusting the pressure in each cylinder and the amplitude of the signal supplied to the shaker. Pressures within the cylinders, however, must be large enough to keep the masses in contact with the specimen at all times. This requirement allows for the transfer of inertial forces to the specimen. When the slip table moves, the specimen drives the masses to follow the motion of the slip table.

The specimens are designed to follow the fracture toughness test standard ASTM E1820-08a [1] and one is shown in Fig. 11.2. The specimen is made of 6,061 aluminum bar stock, with dimensions $314.70 \times 20.32 \times 6.35$ mm (length $\times$ height $\times$ width), and the fatigue is initiated by a machined 'V' notch. In order to get rid of residual and machining stresses, the specimens are fully annealed prior to testing.

11.2.2 Instrumentation

The structural response is measured using accelerometers and an eddy current displacement sensor. Two single-axis accelerometers from PCB Piezoelectronics, model number 333B42, are used. A sensitive axis of each accelerometer is always kept parallel with the horizontal x-axis. One eddy current sensor from Lion Precision, model number U5 with an ECL202 driver, is used to measure the relative displacement between one mass and the slip table.

Drive signals of the testing rig are generated by a program controlled function generator (Tektronix AFG 30222), which can generate different types of excitation signals based on either internal functions (such as random and harmonic) or stored arbitrary time histories (such as chaotic). The function generator is connected to a PC using a USB cable, so we can have full control of the excitation signals. The preload is measured by two pressure sensors which are directly connected to the pneumatic cylinders. The dynamical forces between the pneumatic cylinders and the masses are measured by two

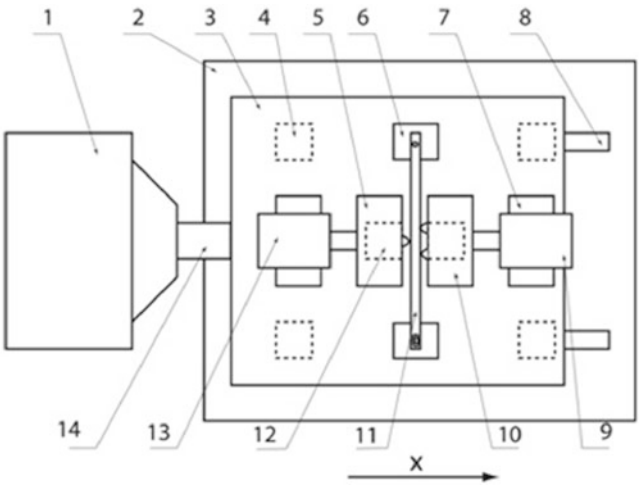

Fig. 11.1 Schematic of the apparatus. *1.* shaker; *2.* granite base; *3.* slip table; *4.*linear bearing; *5.* back mass; *6.* specimen supports; *7.* pneumatic cylinder supports; *8.* rails; *9.* front cylinder; *10.* front mass; *11.* the specimen; *12.* bearing blocks; *13.* back cylinder; and *14.* flexible axial coupling

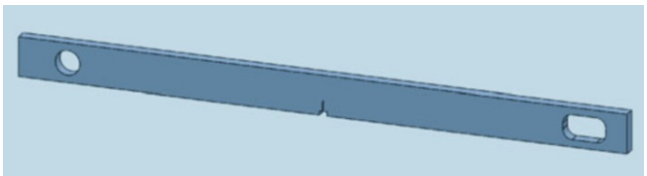

Fig. 11.2 Model of the specimen. the machined notch can be seen in the *center*, the round hole is on the *left* and the oblong slot on the *right*

piezoelectric force sensors (Model 208C02 from PCB Piezoelectronics). All data from the sensors are recorded using a data acquisition (DAQ) card from National Instrument on a PC; and all control and DAQ tasks are implemented through a LabView program.

The new design has two major advantages over a similar inertial force based fatigue apparatus described in [2, 6]. Firstly, the horizontal setup reduces the excitation force necessary to drive the system. Therefore, a similar load capacity can be achieved by using a smaller, and lower cost electromagnetic shaker. Secondly, the slip table is built using a standard mounting surface, which allows for simple modifications to accommodate various types of specimens and configurations.

11.3 Description of Experiment and Results

In our experiment, chaotically and stochastically excited fatigue tests are conducted. For chaotic loading, a chaotic signal generated from a double-well Duffing oscillator is utilized. In particular, we have used a steady state response of the following equation as the chaotic excitation signal supplied to the shaker,

$$\ddot{x} + 0.25\dot{x} - 0.6x + x^3 = 0.2\cos t\,, \tag{11.1}$$

sampled uniformly using $\Delta t = 0.2$. For the stochastic excitation, the chaotic signal is modified using the method of surrogate time series described in [11]. In this procedure, the chaotic signal is randomized and the power spectrum and the probability distribution function of the stochastic driving signal is matched with the chaotic driving signal. Figure 11.3 shows the comparison of histograms and the power spectrums of the original chaotic and stochastic signals. The delay coordinate reconstruction of both signal is also shown in Fig. 11.4, using a delay determined for the chaotic signal. This figure shows the clear difference in time evolution of the trajectories: chaotic signal has an attractor, while surrogate data does not. The two signals supplied to the shaker are henceforth called Chaotic and Random. The experimental design is very straightforward. The excitation amplitude is set to keep the test time manageably short for quick turnaround time. This results in a total of ten sets of data for analysis shown in Table 11.1. It should be noted that all names are indicative of the order run and no further inference should be made.

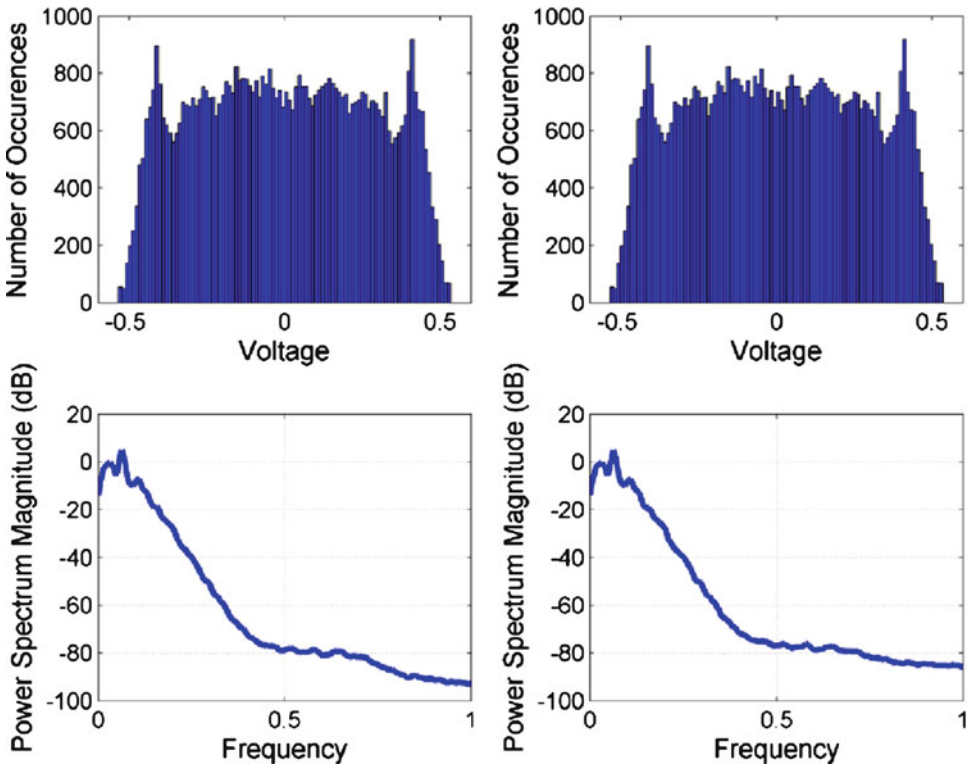

Fig. 11.3 Histogram and power spectrum of the original chaotic (*left*) and stochastic (*right*) signals

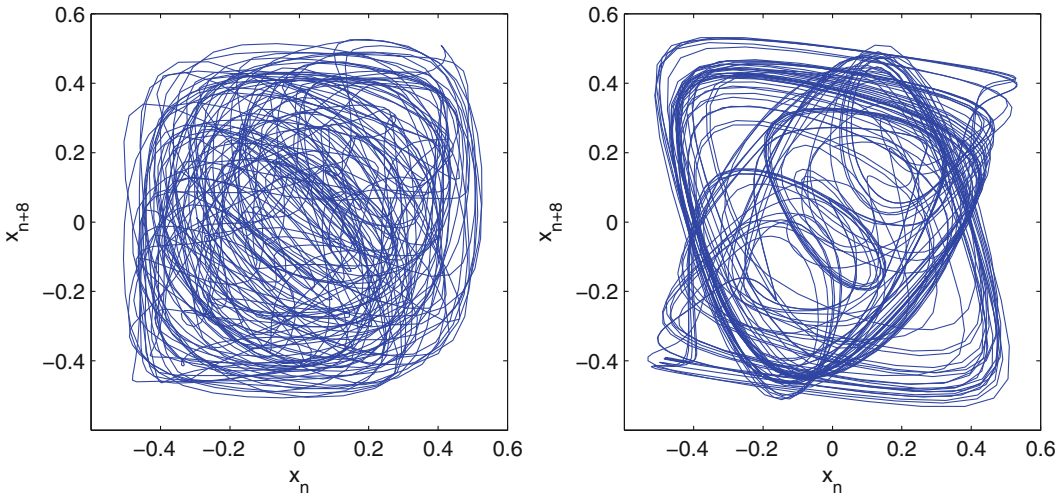

Fig. 11.4 Delay coordinate reconstruction of phase portraits for the stochastic (*left*) and original chaotic (*right*) signals

Table 11.1 Test results. Mean, variance, skewness and kurtosis are calculated from base acceleration data over 20 min. Damage is estimated based on rain-flow counting and the Palmgren-Miner rule

Random signal	TTF hrs:min	Damage	Mean V	Variance V^2	Skewness	Kurtosis
1 – A	0:53	0.97	−0.0036	0.0754	0.0045	2.5897
2 – A	1:07	1.06	−0.0036	0.0724	0.0079	2.5822
3 – A	0:44	1.00	−0.0035	0.0758	0.0104	2.6032
4 – A	0:52	1.07	−0.0036	0.0763	0.0136	2.5963
5 – A	0:45	0.86	−0.0040	0.0735	0.0051	2.5957
Average	0:52	0.99	−0.0037	0.0747	0.0083	2.5934
Chaotic signal	TTF hrs:min	Damage	Mean V	Variance V^2	Skewness	Kurtosis
1 – B	1:44	1.48	−0.0030	0.0728	−0.0091	2.6602
2 – B	1:50	2.08	−0.0038	0.0725	−0.0115	2.6466
3 – B	1:46	1.51	−0.0034	0.0735	−0.0041	2.6001
4 – B	1:42	1.39	−0.0037	0.0729	−0.0068	2.6715
5 – B	1:13	1.03	−0.0039	0.0725	−0.0078	2.6494
Average	1:39	1.50	−0.0036	0.0728	−0.0079	2.6456

The load statistics are included in Table 11.1 to show that the basic statistical qualities of both signals match well and do not show any significant deviation from experiment to experiment. Any drift in these statistics, from test to test, is due to the differences between specimens and/or the lack of a sophisticated shaker output controller. However, these tests have proven very repeatable and the variations in the statistics of the excitation signals are negligible at this amplitude level.

The histograms and power spectral densities from the actual random and chaotic experiments ($1-A$ and $1-B$, respectively) can be seen in Fig. 11.5. The figures use the base acceleration signals collected over 10 min. The probability distributions for the voltage signals supplied to the shaker match identically (Fig. 11.3). However, these signals then pass through the shaker and couplings to reach the base. The base acceleration probability distributions are not then entirely identical as seen in Fig. 11.5, while the power spectral densities remain fairly similar for both stochastic and chaotic loads. Furthermore, the differences in the histograms are only observed for small amplitudes. The corresponding reconstructed phase portraits are shown in Fig. 11.6, where again we see the characteristics observed for the original input signals. It would be a very difficult task to build input surrogate data which would match the base acceleration properties of the chaotic signal. As long as the main factors such as mean, and minimum and maximum acceleration are preserved, the differences are deemed acceptable.

The first and most obvious piece of data that gives an indication of a fracture process is the *time to failure* (TTF). A clear trend emerges in the TTF data shown in Table 11.1. It is obvious that the random excitation is much more damaging to the specimen than the chaotic excitation. These test results show that the system under chaotic excitation outlasts the system under Random excitation by nearly a factor of two in all accounts. The question then is if these differences can be explained

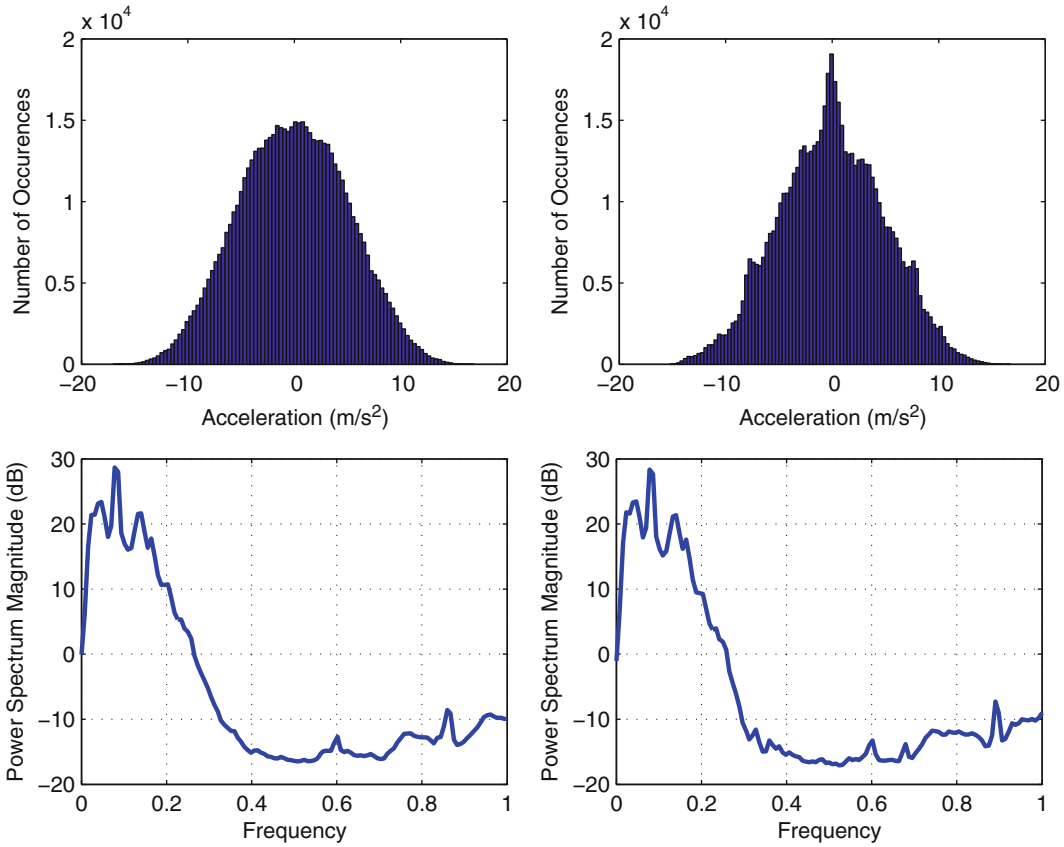

Fig. 11.5 Histogram and power spectrum of the base acceleration data of the random (*left*) and chaotic (*right*) signals

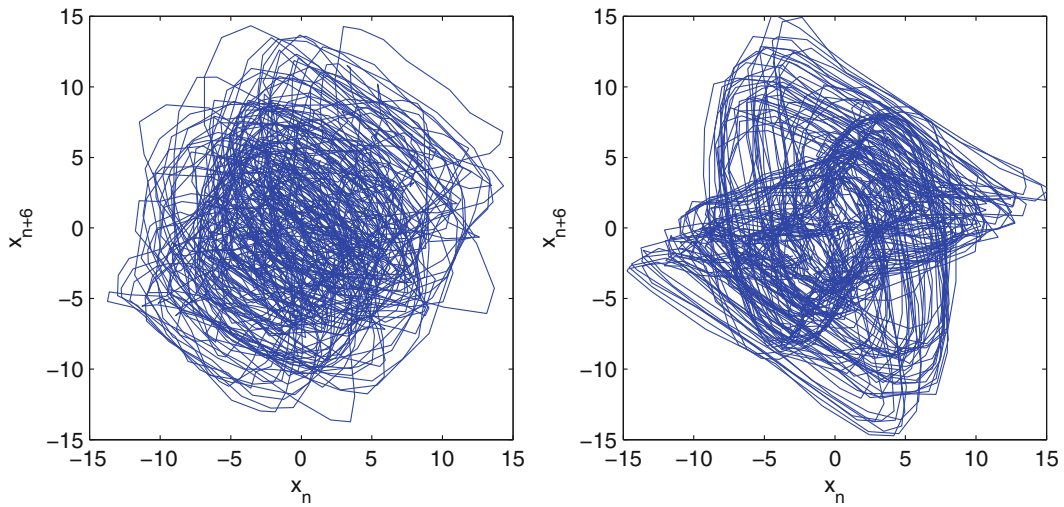

Fig. 11.6 Reconstructed phase portrait of the base acceleration data for the random (*left*) and chaotic (*right*) signals

solely by the differences observed in the base excitation histograms shown in Fig. 11.5. Since the mean, variance, skewness and kurtosis of the excitation do not vary significantly during the experiment, superposition principle based cycle counting methods should account for the differences in histograms.

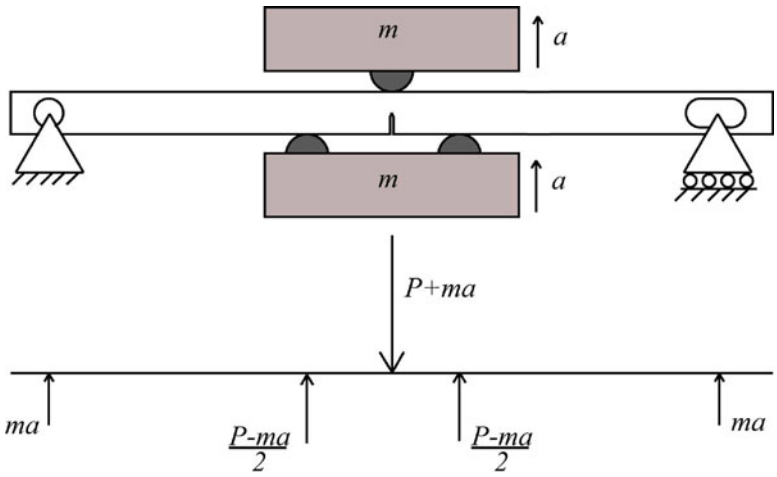

Fig. 11.7 Beam diagram with applied forces

11.4 Cumulative Fatigue Damage

Rain-flow counting and the Palmgren-Miner rule are used here to quantify the damage based on stress cycles. An S-N curve is necessary to evaluate the Miner rule and find the damage variable. Theoretically, the criteria for failure would occur when the damage variable [9], D, reaches one. Since D is simply a ratio, its exact value depends on the S-N curve used and is inherently nondescript. For the comparison of chaotic and random loadings, the S-N curve is chosen to yield $D \approx 1$ for all random loadings.

The cycles of the entire fatigue tests are counted. The stress at the crack tip is approximated by simple beam theory. The specimen is regarded as a simply supported beam with an applied load, P, on each side in three point bending (Fig. 11.7). P is the static mean force due to the pressure within the cylinders. In this testing, both cylinders have equal pressure. The rainflow cycle counting method [3] is applied to the time series of the maximum stress at the notch of the beam. Then the damage variable is calculated for each test. The results are shown in Table 11.1.

Typically, the Miner rule would be used to predict the failure by characterizing a typical stress history over some time, and approximating the stress history over the expected lifetime of the fatiguing structure. The failure criteria would be met once the damage variable $D \geq 1$. In our analysis the damage criteria is calculated over the actual stress history of the entire load time history. Therefore, since the failure criteria is equivalent for all tests it can be expected that for all tests D would be approximately equal if the linear damage law is applicable. This is true across tests of the same type, chaotic or random. However, in comparison between the two, the linear damage law does not reflect the observed effects of the time history on TTF. In particular, it significantly overestimates damage for the chaotic signal.

The fatigue testing using random and chaotic excitation that have nearly identical statistical and spectral properties showed that specimens failed twice as fast during chaotic forcing (Table 11.1). The actual stress loads at the crack had almost exact spectral characteristics, but histograms showed that chaotic forcing has more low amplitude loads, while maintaining approximately the same loading for larger amplitudes (Fig. 11.5). Everything being equal and keeping excitation amplitude constant over all experiments, the linear Palmgren-Miner damage law, which is independent of the loading history, should have accounted for the differences in histograms. However, while it was adequate to estimate damage during random excitation, it significantly overestimated the damage variable for the chaotic excitation. This implies that the excitation time history is very important in fatigue accumulation, even when main statistical moments of the load at the crack do not change significantly, and both linear statistics and spectral properties of both signals are very similar. Thus, we need to look at nonlinear characteristics of the excitation time series.

11.5 Nonlinear Characterization of Loading

The two main features of dissipative nonlinear dynamical systems are Lyapunov exponents and fractal dimensions. Lyapunov exponents are the average exponential rates of separation of infinitesimally close orbits. Fractal dimensions relate to the complexity of the system, and the degrees-of-freedom in the dynamical system. These quantities are characteristics of a deterministic dynamical system, and are not defined or appropriate for the stochastic systems. Here we will not focus on

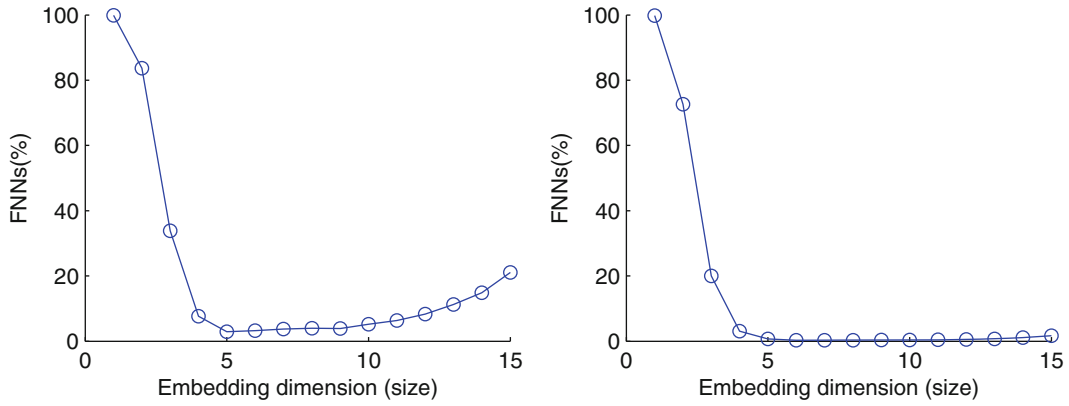

Fig. 11.8 Estimation of embedding dimension for the random (*left*) and chaotic (*right*) signals

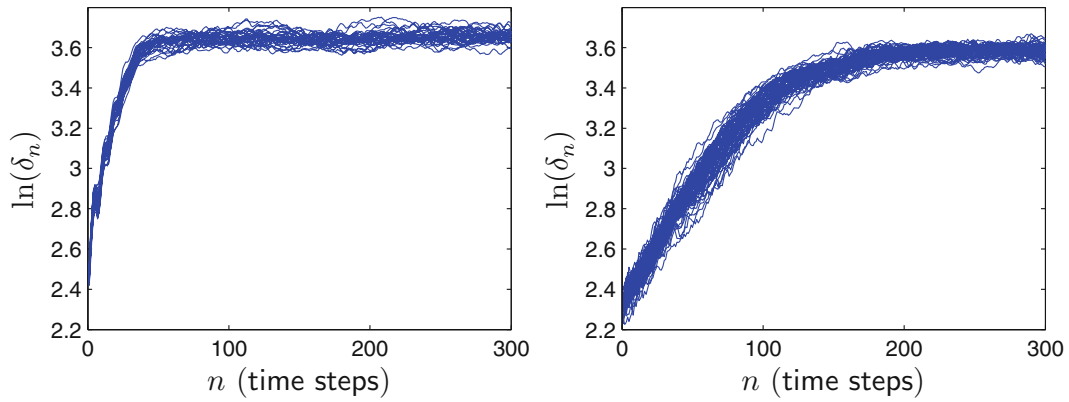

Fig. 11.9 Average trajectory divergence rates for all records in random loading (*left*) and chaotic loading (*right*)

estimating actual Lyapunov exponents or fractal dimensions, but instead look at features extracted by applying the appropriate algorithms to the load time histories. The hope is that these features will capture the differences that can be used to explain the discrepancies in the observed TTF.

We use the algorithm used to calculate the maximal Lyapunov exponent [7, 10] to obtain feature curves that describe average divergence of nearby trajectories in the phase space over finite time. Since crack propagation can make the system structurally unstable, stress data is divided into data records of 100,000 points in each. A delay time of 7 time steps [5] is used for the delay coordinate embedding of the time series. Embedding dimension is determined for the random signal using the first minimum of false nearest neighbors (FNNs) curve [8]. Figure 11.8 shows that an embedding dimension of 5 is sufficient. The average trajectory divergence is estimated in each data records. The results for test 1 – A and 1 – B are shown in Fig. 11.9. As expected, there is a clear difference between the divergence rates observed for the chaotic and random excitations for small time scales, while these features are fairly consistent during each experiment. This divergence rate at small scale for the random signal is much higher than for the chaotic, which could also explain differences observed in histograms for the small amplitudes (larger divergence will cause fewer small distance scales in the data).

Figure 11.10 shows the average trajectory divergence rates for all ten tests in the first data record. These results are consistent for each test type and again show clear difference in the random and chaotic divergence, which is smaller for the chaotic excitation.

The correlation integral is usually used to estimate the fractal dimension of an attractor. However, since random signal does not have a finite-dimensional attractor, we use the correlation integral as a feature differentiating our signals. It is estimated using the method described in [14], and results are shown in Fig. 11.11. Again we see that for small length scales there are clear differences. For the chaotic signal there are considerably more smaller distances than for the random signal. However, both signals have identical correlation integral for the large amplitudes or distances, which again correlates well with the similarity of the histograms for large amplitudes.

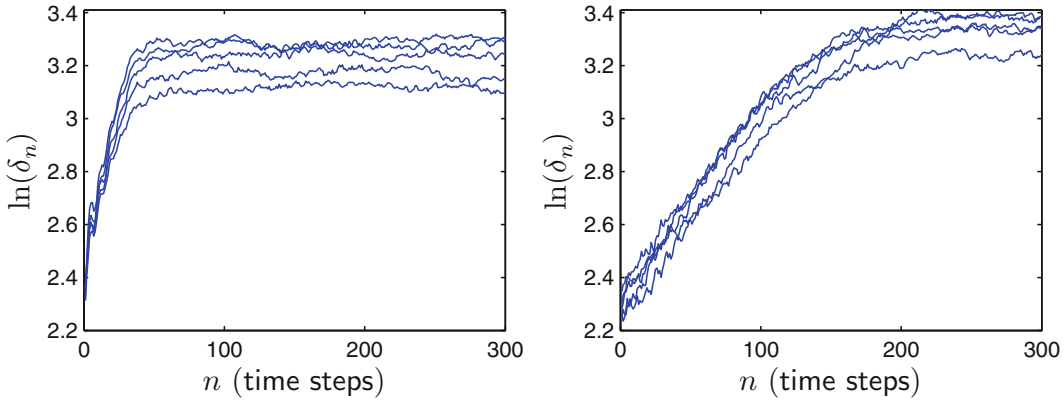

Fig. 11.10 Average trajectory divergence rates for all tests using random loading (*left*) and chaotic loading (*right*)

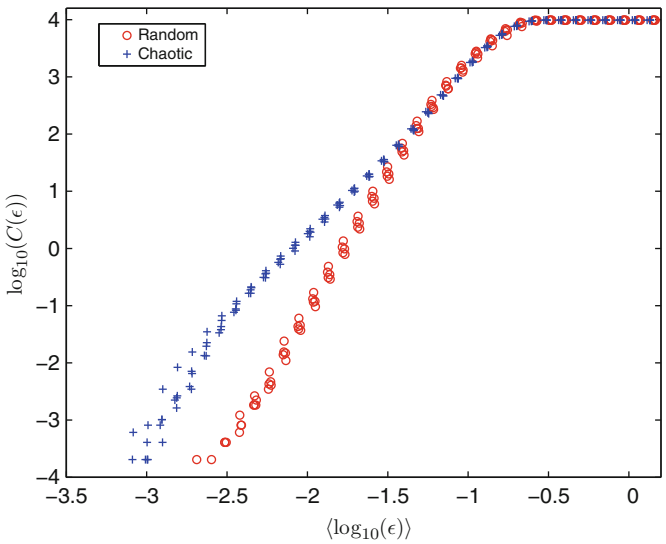

Fig. 11.11 Correlation integral for all ten tests

11.6 Discussion

Differences in excitation observed in histograms did not prove sufficient to provide consistent estimates of TTF using Palmgren-Miner and Rain-Flow counting method. Additional nonlinear characteristics (trajectory divergence rates and correlation integral) showed more drastic differences in the small time- and length-scale dynamics that can explain the differences in TTF. Larger divergence rates for small scales in the random signal clearly correlate well with shortened TTF in the random tests. For small length- and time-scales, this causes the load on the crack to change faster for the random signal than for the chaotic. Therefore, the crack under random load experiences fewer low stress cycles when compared to the chaotic load which can explain the differences in the TTF. In particular, this suggests that fatigue life depends not only on the cycles of maximum stress experienced, but also on the rate at which this maximum stress is achieved. The observed differences in divergence rates are also reflected in the deviations observed in the correlation integrals at small scale. Therefore, both of these features correlate well with the observed TTF and may be used as loading parameters for a new damage model that could account for the observed differences.

11.7 Conclusion

In this paper, we reported on the experimental results from fatigue testing in which chaotic and random loading tests were conducted using a novel fatigue testing apparatus. Both loadings shared the same statistical and spectral properties. However, experimental results showed that random loading was more damaging than chaotic. Standard linear damage Palmgren-Miner

law and Rainflow-counting method grossly overestimated damage for the chaotically excited system, while they where adequate to describe damage in randomly excited system. Nonlinear dynamical characteristics of the excitation time series were considered to explain the differences. These metrics clearly showed that while the signals had similar characteristics at large scale, for a small scale trajectory divergence rates were much higher for the random signal. In addition, there was more finer detail in the chaotic signal as shown by the correlation integral. This stipulated that crack was experiencing fewer low stress cycles for the random excitation, which is also reflected in excitation histograms. This also suggested that fatigue life depends on rate at which maximum stress is reached at the crack tip. Therefore, both of the considered nonlinear characteristics correlate well with the observed differences in the TTF, and may be used as loading parameters for the new damage laws providing more consistent TTF estimates.

Acknowledgements This paper is based upon work supported by the National Science Foundation under Grant No. 1100031.

References

1. ASTM E1820-08a (2008) Standard test methods for measurement of fracture toughness. In: Annual book of ASTM standards. American Society for Testing and Materials, Philadelphia
2. Chee-Hoe Foong, Wiercigroch M, Deans WF (2006) Novel dynamic fatigue-testing device: design and measurements. Meas Sci Technol 17:2218–2226
3. Downing SD, Socie DF (1982) Simple rainflow counting algorithms. Int J Fatigue 4(1):31–40
4. Falco M, Liu M, Chelidze D (2010) A new fatigue testing apparatus model and parameter identification. In: ASME 2010 international design engineering technical conferences and computers and information in engineering conference, Montreal, vol 5(44137), pp 1007–1012
5. Fraser AM, Swinney HL (1986) Independent coordinates for strange attractors from mutual information. Phys Rev A 33:1134–1140
6. Jakšič N, Chee-Hoe Foong, Wiercigroch M, Boltežar M (2008) Parameter identification and modelling of the fatigue-testing rig. Int J Mech Sci 50(7):1142–1152
7. Kantz H, Schreiber S (2004) Nonlinear time series analysis. Cambridge University Press, Cambridge
8. Kennel MB, Brown R, Abarbanel HDI (1992) Determining embedding dimension for phase-space reconstruction using a geometrical construction. Phys Rev A 45:3403–3411
9. Miner M (1945) Cumulative damage in fatigue. J Appl Mech 67:A159–A164
10. Rosenstein MT, Collins JJ, De Luca CJ (1993) A practical method for calculating largest lyapunov exponents from small data sets. Phys D 65:117–134
11. Schreiber T, Schmitz A (1996) Improved surrogate data for nonlinearity tests. Phys Rev Lett 77:635–638
12. Skorupa M (1999) Load interaction effects during fatigue crack growth under variable amplitude loading – a literature review. part i: Empirical trends. Fatigue Fract Eng Mater Struct 21:987–1006
13. Skorupa M (1999) Load interaction effects during fatigue crack growth under variable amplitude loading – a literature review. part ii: Qualitative interpretations. Fatigue Fract Eng Mater Struct 22:905–926
14. Theiler J (1986) Spurious dimension from correlation algorithms applied to limited time-series data. Phys Rev A 34:2427–2432

Chapter 12
Forced Response of a Nonlinear Translating Brake Band in the Presence of Friction Guides

Osman Taha Sen, Jason T. Dreyer, and Rajendra Singh

Abstract The goal of this article is to investigate the response of a nonlinear translating brake band system under different external loading and constraint conditions. A friction bench experiment is designed, built, and instrumented accordingly. In this experiment, an actuation body (supported by the friction guides) is pushed against a translating brake band over a prescribed actuation cycle. Therefore, two friction regimes are generated; one between the actuation body and brake band, and another one between the actuation body and friction guide(s). Locations of the friction guides and external load application points are varied and all possible cases are experimentally and computationally studied. First, the effect of the center of contact force shift on the forced response is investigated, and conditions that lead to this shift are examined. Second, a nonlinear mathematical model is utilized to explain the relationship between the center of contact force location and the forced system response, as well as to observe certain trends. Finally, such trends are confirmed by measurements, and a better understanding of the effect of external load and constraint locations on a variation in the friction force is obtained. Some of the findings are briefly linked to the vehicle brake judder problem.

Keywords Friction-induced vibration • Experimental dynamics • Leading and trailing edge dynamics in translating media • Brake judder • Frictional guides

12.1 Introduction

The effect of the center of contact force location on the generation of brake squeal noise was first studied by Spurr [1], where the so-called squeal mechanism, "sprag-slip", is first proposed. Spurr [1] illustrated this mechanism with a rigid strut that was loaded against a rotating surface with an angle α, and calculated the friction force (F_f) at the interface as $F_f = \mu_b F_N/(1-\mu_b \tan(\alpha))$, where μ_b and F_N are the friction coefficient at the contact interface and normal load, respectively. This expression shows that F_f is boundless when the condition $\alpha = \cot^{-1}(\mu_b)$ is satisfied; hence the strut will lock and will not permit any motion. As initiated by Spurr [1], the sprag-slip concept has been subsequently studied using pin-on-disc models [2–4] with experimental and analytical techniques, and the system stability is related to the sprag angle, though other mechanisms of the brake squeal problem have been extensively studied [5, 6]. Fieldhouse and Steel [7] and Fieldhouse et al. [8] expand the Spurr model with an additional friction regime, which locates between the brake pad and the abutment (support) bracket. Fieldhouse et al. [8] calculate the distance between the center of contact force and the supported edge (ρ) with the following expression: $\rho = \mu_b w + (1 \pm \mu_b \mu_g) l/2$, where μ_g, w and l are the friction coefficient at the supported edge,

O.T. Sen (✉)
Research Associate, Department of Mechanical Engineering, Istanbul Technical University, Istanbul, 34437, Turkey
e-mail: senos@itu.edu.tr

J.T. Dreyer
Research Scientist, Department of Mechanical and Aerospace Engineering, The Ohio State University, Columbus, OH, 43210, USA
e-mail: dreyer.24@osu.edu

R. Singh
Professor, Department of Mechanical and Aerospace Engineering, The Ohio State University, Columbus, OH, 43210, USA
e-mail: singh.3@osu.edu

G. Kerschen et al. (eds.), *Topics in Nonlinear Dynamics, Volume 1: Proceedings of the 31st IMAC, A Conference on Structural Dynamics, 2013*, Conference Proceedings of the Society for Experimental Mechanics Series 35,
DOI 10.1007/978-1-4614-6570-6_12,

thickness, and length of the pad, respectively; the $\pm$ sign corresponds to the directional behavior of the friction force at the supported edge. Note that this expression is only valid for a pad that is supported at the trailing edge.

The above mentioned concept has yet to be applied to the vehicle brake judder problem, which is a low frequency, friction-induced forced vibration problem. The primary source to this problem is assumed to be the geometric distortion of the brake rotor at single or multiple orders of the excitation frequency that is proportional to the vehicle speed [9–13]. Brake judder is typically quantified in terms of the brake torque variation $(T(t))$ [9–12], though it is also observed as steering wheel nibble [13]. Disturbances generated at the source are usually amplified at the path, e.g. the dynamic amplification in the angular displacement of the vehicle steering wheel has been related to the rotor imperfections and to the resonances of structural paths [13]. Additionally, experimental studies suggest that the frictional torque amplitudes at higher speeds are influenced by the caliper dynamics, though the available judder models do not seem to include the actuation system [9–13]. Accordingly, the chief goal of this article is to experimentally and numerically investigate the effect of actuation system dynamics on the brake judder response by examining the dynamic interactions between the brake pad and the caliper (including the guide pins). Due to a large number of different caliper designs, it is extremely difficult to construct an experiment to evaluate alternate designs under controlled conditions. Therefore, investigations are carried out with a simplified yet controlled translating brake band experiment, and the effects of the frictional guide and normal load application locations on the shift of the center of contact force location are conceptually examined. Further, the effect of the center of contact force location shift on the brake judder response is explained with lower dimensional models.

12.2 Problem Formulation

Schematics of the proposed physical system are shown in Fig. 12.1 where a friction material (simulates the brake pad) is pushed against a translating band (simulates the brake rotor). In the study, the friction material is supported either from leading (superscript l) or trailing (superscript t) edge with a frictional guide (simulates the guide pin). Therefore, two different caliper designs known as "push" and "pull" type calipers in automotive brake applications are examined [14]. The second frictional regime that emerges at one of these edges is represented with F_{fg}, where the preceding $\pm$ sign stands for the positive and negative velocity conditions at the supported edge. In addition, the normal loads and contact forces at the first frictional regime (between the friction material and band) are given with F_N^l, F_N^t, F_p^l and F_p^t, respectively. Besides different constraint location cases (cases A and B), the normal load (F_N^l and F_N^t) application locations are also varied as shown in Fig. 12.2: Close to the edges (1), center with a narrow gap (2), leading edge (3), and trailing edge (4). Accordingly, eight different cases are investigated in total (Fig. 12.2).

The main objectives of the current article are as follows: (1) Calculate and compare the center of contact force locations for all the configurations of Fig. 12.2 based on the static equilibria. (2) Develop a simplified nonlinear model of the system of Fig. 12.1, and obtain numerical solutions for all cases. (3) Design a simple laboratory experiment to simulate the system of Fig. 12.1, perform experiments, and validate the nonlinear model solutions.

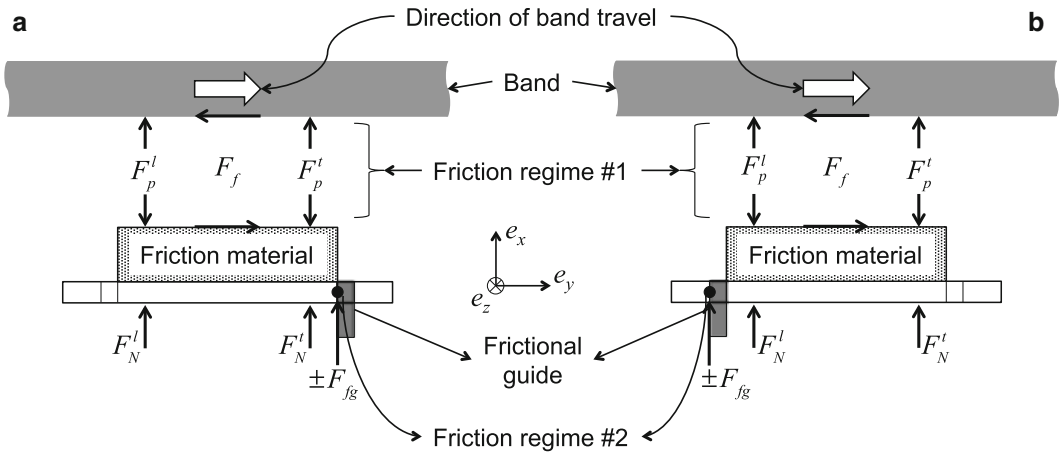

Fig. 12.1 Illustration of the problem statement; (**a**) case A with the frictional guide located at the trailing edge; (**b**) case B with the frictional guide at the leading edge

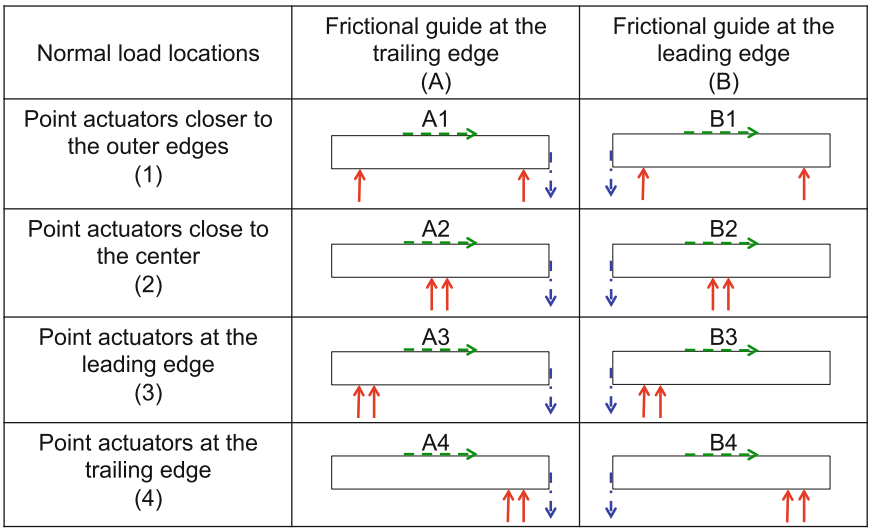

Fig. 12.2 Illustration of all configurations. Letters *A* and *B* describe the different constraint location cases. Numbers *1–4* designate the different normal load configurations. *Arrows* represent the forces acting on the friction material. Key: $\longrightarrow, F_N^l$ and F_N^t; $--\!>, F_f, -\cdot\!>, F_{fg}$

12.3 Calculation of Center of Contact Force Location

The distance from the center of contact force to the frictional guide (ρ) is calculated for all cases by using force and moment equilibria, which are derived from the free body diagram in Fig. 12.3. As seen in the figure, the total friction force $F_f = \mu_b F_p$, where μ_b and F_p are the friction coefficient and the total contact force at the friction material/band interface, respectively. Obviously, F_f is transmitted to the frictional constraint as a normal load, and thus the friction force at this supported edge is $F_{fg} = \mu_g F_f$, where μ_g is the friction coefficient at the friction material and guide interface. Since the direction of F_{fg} changes for the positive and negative velocity of the constrained edge, equilibrium equations must be solved for these two sliding cases. Since $-\mu_b\mu_g F_p \le F_{fg} \le \mu_b\mu_g F_p$, the center of contact force location for the pure sticking condition should be between these two sliding conditions. First, the equations of force Eq. (12.1a,b) and moment Eq. (12.2) equilibria (about point O in Fig. 12.3) are given below for case A.

$$F_N^l + F_N^t - F_p - \mu_b\mu_g F_p = 0 \qquad for \qquad \dot{x} - 0.5l\dot{\theta} > 0, \tag{12.1a}$$

$$F_N^l + F_N^t - F_p + \mu_b\mu_g F_p = 0 \qquad for \qquad \dot{x} - 0.5l\dot{\theta} < 0, \tag{12.1b}$$

$$F_N^l\left(0.5l + l^l\right) + F_N^t\left(0.5l - l^t\right) - F_p\rho + \mu_b w F_p = 0. \tag{12.2}$$

The unknowns F_p and ρ are solved with Eqs. (12.1a,b) and (12.2), and ρ is obtained for the two sliding cases as:

$$\rho^+ = (1+\mu_b\mu_g)\left[\frac{l}{2} + \frac{\mu_b w}{1+\mu_b\mu_g} + \frac{F_N^l l^l - F_N^t l^t}{F_N^l + F_N^t}\right] \qquad for \qquad \dot{x} - 0.5l\dot{\theta} > 0, \tag{12.3a}$$

$$\rho^- = (1-\mu_b\mu_g)\left[\frac{l}{2} + \frac{\mu_b w}{1-\mu_b\mu_g} + \frac{F_N^l l^l - F_N^t l^t}{F_N^l + F_N^t}\right] \qquad for \qquad \dot{x} - 0.5l\dot{\theta} < 0, \tag{12.3b}$$

where the superscripts + and - correspond to the positive and negative sliding velocities, respectively. For the special case of $F_N^l l^l = F_N^t l^t$, Eq. (12.3a,b) simplifies to Fieldhouse et al.'s expression [8]. Similarly, ρ^+ and ρ^- for case B are obtained as:

$$\rho^+ = (1+\mu_b\mu_g)\left[\frac{l}{2} - \frac{\mu_b w}{1+\mu_b\mu_g} - \frac{F_N^l l^l - F_N^t l^t}{F_N^l + F_N^t}\right] \qquad for \qquad \dot{x} + 0.5l\dot{\theta} > 0, \tag{12.4a}$$

$$\rho^- = (1-\mu_b\mu_g)\left[\frac{l}{2} - \frac{\mu_b w}{1-\mu_b\mu_g} - \frac{F_N^l l^l - F_N^t l^t}{F_N^l + F_N^t}\right] \qquad for \qquad \dot{x} + 0.5l\dot{\theta} < 0. \tag{12.4b}$$

Based on Eqs. (12.3a,b) and (12.4a,b), the center of contact force locations can be estimated for various conditions. These conditions and the center of contact force locations are tabulated in Table 12.1 for both positive and negative sliding velocity cases. As seen in the table, μ_g is the key parameter that affects ρ^+ and ρ^-. Moreover $\rho^+ = \rho^-$ as $\mu_b\mu_g = 0$. For $\mu_b = 0$,

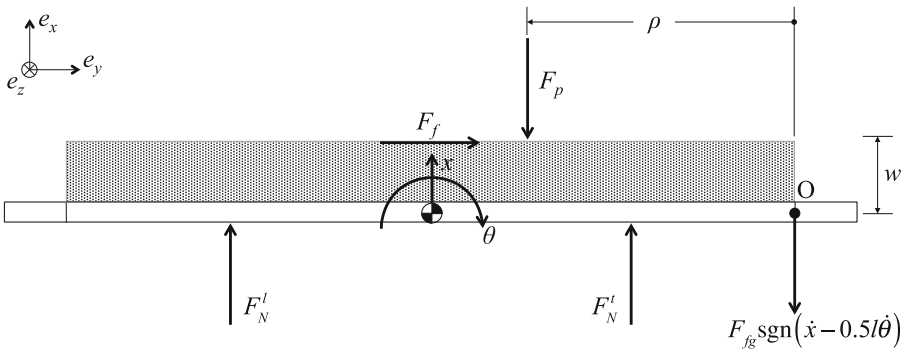

Fig. 12.3 Forces acting on the friction material for case A with the frictional guide located at the trailing edge

Table 12.1 Summary of the conditions and corresponding center of contact force locations for both positive and negative sliding conditions

	Positive sliding velocity		Negative sliding velocity	
Case	Condition	Center of contact force location	Condition	Center of contact force location
A1: $(l^l - l^t = 0)$	Always	$\rho^+ > 0.5l$	$\mu_g > 2w/l$	$\rho^- < 0.5l$
			$\mu_g < 2w/l$	$\rho^- > 0.5l$
A2: $(l - l^t = 0)$	Always	$\rho^+ > 0.5l$	$\mu_g > 2w/l$	$\rho^- < 0.5l$
			$\mu_g < 2w/l$	$\rho^- > 0.5l$
A3: $(l^l - l^t > 0)$	Always	$\rho^+ > 0.5l$	$\mu_g > \frac{2\mu_b w + l^l - l^t}{\mu_b(l + l^l - l^t)}$	$\rho^- < 0.5l$
			$\mu_g < \frac{2\mu_b w + l^l - l^t}{\mu_b(l + l^l - l^t)}$	$\rho^- > 0.5l$
A4: $(l^l - l^t < 0)$	$\mu_g > -\frac{2\mu_b w + l^l - l^t}{\mu_b(l + l^l - l^t)}$	$\rho^+ > 0.5l$	$\mu_g > \frac{2\mu_b w + l^l - l^t}{\mu_b(l + l^l - l^t)}$	$\rho^- < 0.5l$
	$\mu_g < -\frac{2\mu_b w + l^l - l^t}{\mu_b(l + l^l - l^t)}$	$\rho^+ < 0.5l$	$\mu_g < \frac{2\mu_b w + l^l - l^t}{\mu_b(l + l^l - l^t)}$	$\rho^- > 0.5l$
B1: $(l^l - l^t = 0)$	$\mu_g > 2w/l$	$\rho^+ > 0.5l$	Always	$\rho^- < 0.5l$
	$\mu_g < 2w/l$	$\rho^+ < 0.5l$		
B2: $(l^l - l^t = 0)$	$\mu_g > 2w/l$	$\rho^+ > 0.5l$	Always	$\rho^- < 0.5l$
	$\mu_g < 2w/l$	$\rho^+ < 0.5l$		
B3: $(l^l - l^t > 0)$	$\mu_g > \frac{2\mu_b w + l^l - l^t}{\mu_b(l - l^l + l^t)}$	$\rho^+ > 0.5l$	Always	$\rho^- < 0.5l$
	$\mu_g < \frac{2\mu_b w + l^l - l^t}{\mu_b(l - l^l + l^t)}$	$\rho^+ < 0.5l$		
B4: $(l^l - l^t < 0)$	$\mu_g > \frac{2\mu_b w + l^l - l^t}{\mu_b(l - l^l + l^t)}$	$\rho^+ > 0.5l$	$\mu_g > -\frac{2\mu_b w + l^l - l^t}{\mu_b(l - l^l + l^t)}$	$\rho^- < 0.5l$
	$\mu_g < \frac{2\mu_b w + l^l - l^t}{\mu_b(l - l^l + l^t)}$	$\rho^+ < 0.5l$	$\mu_g < -\frac{2\mu_b w + l^l - l^t}{\mu_b(l - l^l + l^t)}$	$\rho^- > 0.5l$

Table 12.2 Normalized center of contact force locations. Normalization is done by the geometric center of the body $(0.5l)$

	Friction guide at trailing edge (Case A)		Friction guide at leading edge (Case B)	
Normal load locations	$\bar{\rho}^+$	$\bar{\rho}^-$	$\bar{\rho}^+$	$\bar{\rho}^-$
(1)	1.64	0.50	1.45	0.28
(2)	1.77	0.53	1.43	0.27
(3)	2.29	0.66	0.80	0.12
(4)	1.00	0.34	2.09	0.44

$F_f = F_{fg} = 0$; hence, both friction regimes are inactive. However for $\mu_g = 0$, $F_f \neq 0$, but $F_{fg} = 0$, though $\rho^+ = \rho^-$ is still valid. This concludes that the friction regime at the friction material and frictional guide interface has a significant effect on the center of contact force location.

By using Eqs. (12.3a,b) and (12.4a,b), numerical values for ρ^+ and ρ^- are calculated and listed in Table 12.2 in a normalized way, where the normalization is done with: $\bar{\rho} = \rho/0.5l$.

First, observe the following rank orders: $\bar{\rho}^{A4} < \bar{\rho}^{A1} < \bar{\rho}^{A2} < \bar{\rho}^{A3}$ for case A and $\bar{\rho}^{B3} < \bar{\rho}^{B2} < \bar{\rho}^{B1} < \bar{\rho}^{B4}$ for case B. Second, it is seen that $\bar{\rho}^+ > \bar{\rho}^-$ for all cases. This means that the motion in the $+e_x$ direction shifts ρ further away from the supporting guide than the motion in the $-e_x$ direction. Third, for symmetrically loaded cases (A1, A2, B1, B2), the motion of the band in the $+e_y$ direction causes the center of contact forces to shift closer to the leading edge. Therefore, $\bar{\rho}^A > \bar{\rho}^B$ for these cases. Fourth, for the asymmetrically loaded cases (A3, A4, B3, B4), the center of contact forces moves towards the loaded edge.

12.4 Nonlinear Mathematical Model of the Translating Brake Band Problem

As a further investigation, a two degree of freedom nonlinear model of the translating brake band problem is developed and shown in Fig. 12.4. The model assumes only the translation (x) in the e_x direction and rotation (θ) about the e_z direction. The contact between the band and the friction material is modeled with point contact models at two different locations, which are described with linear springs (k_p^l and k_p^t) and viscous dampers (c_p^l and c_p^t).

Governing equations for case A (Fig. 12.4) are obtained as:

$$m\ddot{x}+\left(c_p^l+c_p^t\right)\dot{x}+\left(c_p^l l_p^l-c_p^t l_p^t\right)\dot{\theta}+\left(k_p^l+k_p^t\right)x+\left(k_p^l l_p^l-k_p^t l_p^t\right)\theta+F_{fg}\mathrm{sgn}\left(\dot{x}-0.5l\dot{\theta}\right)=F_N^l+F_N^t, \tag{12.5}$$

$$I\ddot{\theta}+\left(c_p^l l_p^l-c_p^t l_p^t\right)\dot{x}+\left(c_p^l\left(l_p^l\right)^2+c_p^t\left(l_p^t\right)^2\right)\dot{\theta}+\left(k_p^l l_p^l-k_p^t l_p^t\right)x+\left(k_p^l\left(l_p^l\right)^2+k_p^t\left(l_p^t\right)^2\right)\theta-F_f w$$
$$-0.5F_{fg}l\,\mathrm{sgn}\left(\dot{x}-0.5l\dot{\theta}\right)=F_N^l l^l-F_N^t l^t, \tag{12.6}$$

where m and I are the mass and the inertia of the friction material. Distances l^l, l^t, l_p^l and l_p^t are between the center of mass and the leading edge point actuator, trailing edge point actuator, leading edge point contact location, and trailing edge point contact location, respectively. The friction force F_f between the friction material and band is calculated as:

$$F_f=\mu_b\left\{c_p^l\left(\dot{x}+l_p^l\dot{\theta}\right)+c_p^t\left(\dot{x}-l_p^t\dot{\theta}\right)+k_p^l\left(x+l_p^l\theta\right)+k_p^t\left(x-l_p^t\theta\right)\right\}. \tag{12.7}$$

Obviously, F_{fg} changes direction due to the direction of the friction material velocity at the supported edge. Therefore, the three valued "sgn" function is used to represent the directionality of F_{fg}. However, for the numerical simulations "sgn" function is approximated as $\mathrm{sgn}(z)=\tanh(\sigma z)$, where z is the argument of the "sgn" function and σ is the regularizing factor [9, 10]. Similar to case A, the governing equations for case B are derived as follows, where Eq. (12.7) still applies:

$$m\ddot{x}+\left(c_p^l+c_p^t\right)\dot{x}+\left(c_p^l l_p^l-c_p^t l_p^t\right)\dot{\theta}+\left(k_p^l+k_p^t\right)x+\left(k_p^l l_p^l-k_p^t l_p^t\right)\theta+F_{fg}\mathrm{sgn}\left(\dot{x}+0.5l\dot{\theta}\right)=F_N^l+F_N^t, \tag{12.8}$$

$$I\ddot{\theta}+\left(c_p^l l_p^l-c_p^t l_p^t\right)\dot{x}+\left(c_p^l\left(l_p^l\right)^2+c_p^t\left(l_p^t\right)^2\right)\dot{\theta}+\left(k_p^l l_p^l-k_p^t l_p^t\right)x+\left(k_p^l\left(l_p^l\right)^2+k_p^t\left(l_p^t\right)^2\right)\theta-F_f w$$
$$+0.5F_{fg}l\,\mathrm{sgn}\left(\dot{x}+0.5l\dot{\theta}\right)=F_N^l l^l-F_N^t l^t. \tag{12.9}$$

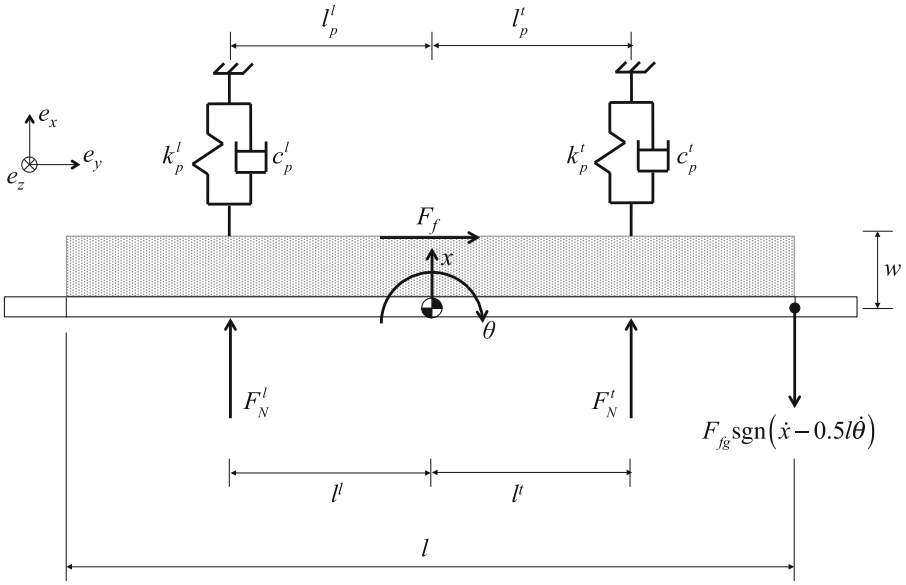

Fig. 12.4 Two degree of freedom nonlinear mathematical model for case A with the frictional guide located at the trailing edge

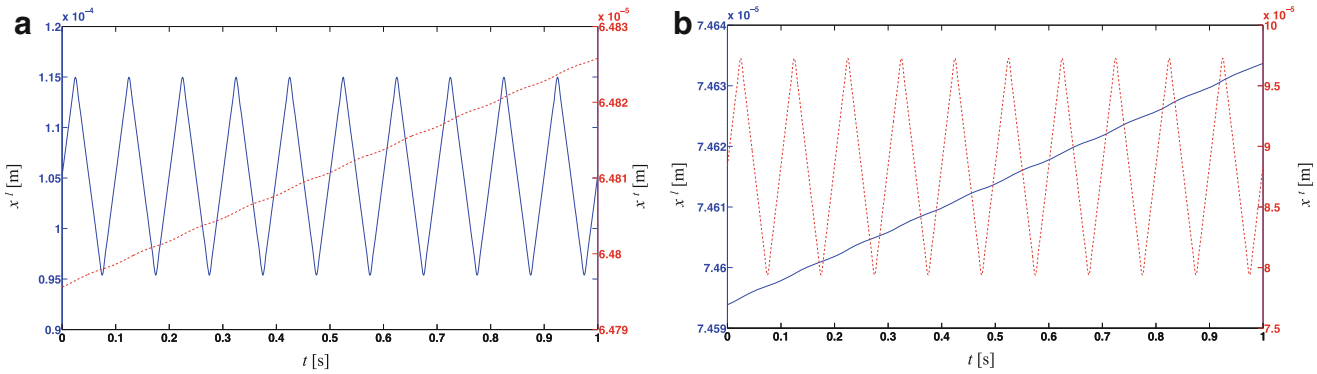

Fig. 12.5 Numerically calculated leading and trailing edge displacements; (**a**) case A1; (**b**) case B1. Key: ____ , x^l; – – –·, x^t

External loads F_N^l and F_N^t are described as a combination of mean (F_{Nm}^l and F_{Nm}^t) and sinusoidal loads with constant amplitudes (F_{Na}^l and F_{Na}^t) as given below.

$$F_N^l = F_{Nm}^l + F_{Na}^l \sum_{n=0}^{\infty} \frac{(-1)^n}{(2n+1)^2} \sin((2n+1)\omega t), \tag{12.10a}$$

$$F_N^t = F_{Nm}^t + F_{Na}^t \sum_{n=0}^{\infty} \frac{(-1)^n}{(2n+1)^2} \sin((2n+1)\omega t), \tag{12.10b}$$

where the fundamental excitation frequency ω is assumed to be $20\pi\,\mathrm{rad/s}$ $(10\,\mathrm{Hz})$ due to experimental limitations as explained in Sect. 12.5. Since it is aimed to explain the effect of center of contact force location on the judder response, a periodic type excitation is preferred. Note that the chief excitation in the judder problem is the rotor surface distortion profiles. In the translating brake band problem, the undulated surface effect is generated with modulated normal forces as given with Eq. (12.10a,b), where the time-variant parts are essentially the representation of a triangular wave. This waveform is chosen due to the experimental limitations, and is explained in Sect. 12.5. Moreover, the numerical simulations are run with constant μ_b and μ_g values, and the locations of point contacts are assumed to be at the edges of the friction material, i.e. $l_p^l = l_p^t = 0.5l$.

Results of numerical solutions are given in Fig. 12.5 for cases A1 and B1, in terms of displacements at the leading ($x^l = x + 0.5l\theta$) and trailing edges ($x^t = x - 0.5l\theta$). Observe that the supported edge is almost stationary compared to the other edge for both cases; supported edges move a total displacement of about 30 nm (x^t for Case A1) and 40 nm (x^l for case B1). These small amounts of motion at the supported edges arise due to the approximation of the "sgn" function, and these edges should stick to the frictional guide. This can be explained with the sticking condition, which is $|F_N^l + F_N^t - F_c| \le \mu_b \mu_g F_c$. The term F_c in this condition stands for the total contact force at the friction material/band interface and is calculated with the expression inside the brackets of Eq. (12.7). Rewrite this condition after some algebraic manipulations:

$$\frac{F_N^l + F_N^t}{1 + \mu_b \mu_g} \le F_c \le \frac{F_N^l + F_N^t}{1 - \mu_b \mu_g}. \tag{12.11}$$

The satisfaction of the condition given with Eq. (12.11) causes the friction material to stick to the frictional guide. Since it is always satisfied during numerical simulations, it is concluded that the motion of friction material at the supported edge is due to numerical approximation; hence a pure sticking condition cannot be numerically achieved by approximating "sgn" function.

Since the frictional material should not move at the supported edge, the two degree of freedom nonlinear model can be simplified to a single degree of freedom linear one, which does a pivoting motion about the contact point at the frictional guide. Calculated mean ($\bar{F}_{fm}$) and peak-to-peak ($\bar{F}_{fpp}$) friction force values using this linear system are listed in Table 12.3 for all cases. Note that the results are presented in a normalized way where the normalization is done with the corresponding value of case A1; i.e. $\bar{F}_{fm} = F_{fm}/F_{fm}^{A1}$ and $\bar{F}_{fpp} = F_{fpp}/F_{fpp}^{A1}$. First, observe that $\bar{F}_{fm}$ and $\bar{F}_{fpp}$ show the same rank orders as in ρ; $\bar{F}_f^{A4} < \bar{F}_f^{A1} < \bar{F}_f^{A2} < \bar{F}_f^{A3}$, $\bar{F}_f^{B3} < \bar{F}_f^{B2} < \bar{F}_f^{B1} < \bar{F}_f^{B4}$. This shows that as the center of contact force location moves further away from the supported edge, a higher F_f is obtained. Second, it is seen that in all cases except (4), $\bar{F}_f^A > \bar{F}_f^B$ for both mean and peak-to-peak values. This can be explained with the sprag-slip model of Spurr [1]. For cases A1 and A2, the center of

Table 12.3 Predicted mean and peak-to-peak friction force. Data is normalized with the corresponding values of case A1

	Friction guide at trailing edge (A)		Friction guide at leading edge (B)	
Normal load locations	$\bar{F}_{fm}$	$\bar{F}_{fpp}$	$\bar{F}_{fm}$	$\bar{F}_{fpp}$
(1)	1.00	1.00	0.91	0.91
(2)	1.08	1.08	0.90	0.90
(3)	1.42	1.42	0.54	0.54
(4)	0.58	0.58	1.29	1.29

contact force locations are at the leading edge half of the friction material (Table 12.2). Hence the total reaction force has a lateral component, which is in $-e_y$ direction (opposite to the direction of band motion). Therefore, the friction material digs in to the band surface, and higher contact forces are generated. However, for cases B1 and B2, the center of contact force locations are at the trailing edge, and thus the directions of the lateral component of the reaction force and band motion are both in $+e_y$ direction. For cases (3) and (4), normal load locations dominate the response; i.e. the moment arm between the external loads and frictional guide location is longer in cases A3 and B4. Hence, higher contact forces are generated in these cases compared to A4 and B3. Third, observe that exact same values are obtained for both normalized mean and peak-to-peak values. This is expected since it is a linear system and the response should not have any frequency dependency.

12.5 Translating Friction Band Experiment

In order to validate the numerical solution of the nonlinear model, a translating friction band experiment is designed and built as depicted in Fig. 12.6. In the experiment, a custom-built stationary friction material is pushed towards a translating friction band by two point actuators; hence the band is compressed between the two surfaces of the actuation system. On one side of the actuation system, Teflon is preferred due to its low friction characteristics. Thus the friction force generated at this side of the band is minimal. The following sensors are utilized on the setup: (a) Load cell to measure the force ($F_f(t)$) that pulls the band; (b) pressure transducer to measure the pressure ($p_N(t)$) at the air inlets of the point actuators; (c) linear potentiometer to measure the displacement of the band ($y(t)$); and (d) uniaxial piezoelectric accelerometers to measure the accelerations of the custom-built friction material ($\ddot{x}^l$ and $\ddot{x}^t$) and actuation system ($\ddot{x}^l_a$ and $\ddot{x}^t_a$) at the leading and trailing edges.

The experiment is specifically designed to run all cases of Fig. 12.2. The design of the custom-built friction material allows obtaining the friction regime between the friction material and leading or trailing edge frictional guides separately. In addition, point actuators can slide in the slot located on the actuation system; hence the different loading conditions of Fig. 12.2 can also be achieved. During the tests, $p_N(t)$ is modulated with a solenoid valve, and thus a triangular wave shaped normal force is obtained as defined earlier. The modulation frequency is chosen as 10 Hz due to the physical limitations of the solenoid valve.

Experimentally, it is observed that the band displacement (y) exhibits an almost constant velocity behavior for all cases of Fig. 12.2. Therefore, the band has almost no acceleration; the measured pulling force should be equal to the friction force F_f. This measured friction force F_f and total normal force F_N ($F_N = F_N^l + F_N^t$) are displayed in Fig. 12.7, again for cases A1 and B1. Note that F_N is calculated by multiplying the measured $p_N(t)$ with the internal areas of the point actuators A^l and A^t. Figures show that both F_f and F_N have triangular shaped waveforms with almost constant mean and peak-to-peak values. In addition, case B1 (Fig. 12.7b) shows less mean and peak-to-peak values compared to case A1 (Fig. 12.7a), even for the almost same F_N values. This was explained with the sprag-slip concept in the previous section.

Measured normalized mean and peak-to-peak values of F_f are tabulated in Table 12.4, and the normalization is again done by the corresponding value of case A1, i.e. $\bar{F}_f = F_f/F_f^{A1}$. Similar to the numerical simulations, measurements present the same rank orders for the peak-to-peak values where $\bar{F}_{fpp}^{A4} < \bar{F}_{fpp}^{A1} < \bar{F}_{fpp}^{A2} < \bar{F}_{fpp}^{A3}$ and $\bar{F}_{fpp}^{B3} < \bar{F}_{fpp}^{B2} < \bar{F}_{fpp}^{B1} < \bar{F}_{fpp}^{B4}$ for cases A and B, respectively. In terms of F_{fm}, the same rank ordering is still valid for B cases. However, for A cases the orders of A1 and A4 are switched.

Furthermore, the motion of the friction material on leading and trailing edges is checked with the measured acceleration data $\ddot{x}^l$, $\ddot{x}^t$, $\ddot{x}^l_a$ and $\ddot{x}^t_a$. The relative accelerations at the edges of the friction material with respect to the actuation system are calculated as $\ddot{x}^l_{rel}(t) = \ddot{x}^l(t) - \ddot{x}^l_a(t)$ and $\ddot{x}^t_{rel}(t) = \ddot{x}^t(t) - \ddot{x}^t_a(t)$. Finally, calculated relative accelerations are transformed to the frequency domain, and the acceleration response ratio from trailing edge to leading edge is calculated with:

$$\bar{a}_{tl}(\omega) = \frac{\ddot{x}^t_{rel}(\omega)\ddot{x}^l_{rel}(\omega)^*}{\ddot{x}^l_{rel}(\omega)\ddot{x}^l_{rel}(\omega)^*}, \tag{12.12}$$

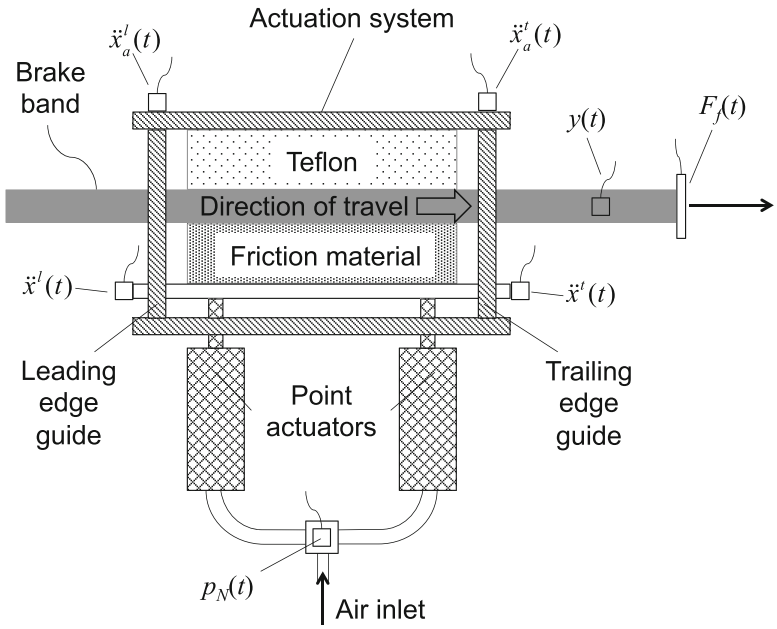

Fig. 12.6 Translating friction band experiment and the actuation system including the sensors utilized

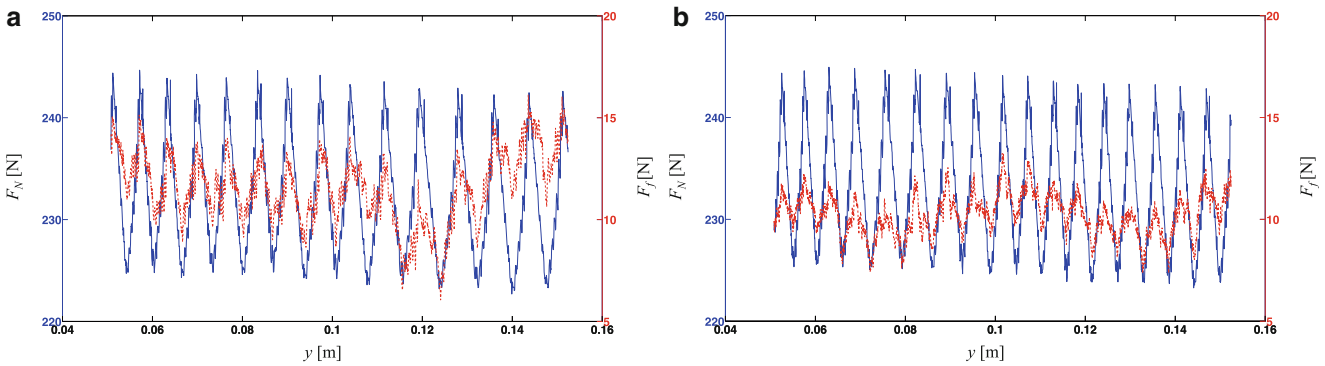

Fig. 12.7 Measured normal (F_N) and friction (F_f) forces; (**a**) case A1; (**b**) case B1. Key: ——, F_N; – – –, F_f

Table 12.4 Measured mean and peak-to-peak friction force. Data is normalized with the corresponding values of case A1

	Friction guide at trailing edge (A)		Friction guide at leading edge (B)	
	$\bar{F}_{fm}$	$\bar{F}_{fpp}$	$\bar{F}_{fm}$	$\bar{F}_{fpp}$
(1)	1.00	1.00	0.88	0.67
(2)	1.04	1.07	0.81	0.63
(3)	1.19	1.38	0.56	0.56
(4)	1.03	0.78	1.05	1.16

where * denotes the conjugate operator. Using Eq. (12.12), $\bar{a}_{tl}$ is calculated at $\omega = 20\pi$ rad/s which is the fundamental excitation frequency, and it is observed that the acceleration response ratios at the unconstrained edge of the friction material are at least an order of magnitude higher than the constrained edge, i.e. $\bar{a}_{tl} < 1$ and $\bar{a}_{tl} > 1$ for cases (A) and (B), respectively.

12.6 Conclusion

The current article investigates the shift of contact force center location and its effect on the system response due to different loading and constraint combinations. It is successfully shown that the location of the center of contact force alters the generated friction force response; hence the judder response of the system changes. The main contributions of this article are summarized as follows. First, the location of the center of contact force is calculated with force and moment equilibria, and the main factors that affect this location are investigated. Second, a two degree of freedom nonlinear mathematical

model of the problem is developed, and numerical solutions are obtained for eight different cases where specific trends are observed. Third, a simple yet controlled translating friction band experiment is designed and built. The same cases of numerical investigation are run on the setup, and data is successfully collected. Similar trends are observed experimentally; hence the numerical solutions are conceptually validated.

References

1. Spurr RT (1961) A theory of brake squeal. Proc Inst Mech Eng 15:33–52
2. Jarvis RP, Mills B (1963) Vibrations induced by dry friction. Proc Inst Mech Eng 178:847–857
3. Earles SWE, Chambers PW (1987) Disc brake squeal noise generation: predicting its dependency on system parameters including damping. Int J Veh Des 8:538–552
4. Earles SWE, Badi MNM (1984) Oscillatory instabilities generated in a double-pin and disc undamped system: a mechanism of disc-brake squeal. Proc Inst Mech Eng C 198:43–50
5. Kinkaid NM, O'Reilly OM, Papadopoulos P (2003) Automotive disc brake squeal. J Sound Vib 267:105–166
6. Papinniemi A, Lai JCS, Zhao J, Loader L (2002) Brake squeal: a literature review. Appl Acoust 63:391–400
7. Fieldhouse JD, Steel WP (2003) A study of brake noise and the influence of the center of pressure at the disc/pad interface, the coefficient of friction and caliper mounting geometry. Proc Inst Mech Eng D 217:957–973
8. Fieldhouse JD, Bryant D, Talbot CJ (2011) The influence of pad abutment on brake noise generation. SAE Technical Paper 2011-01-1577
9. Sen OT, Dreyer JT, Singh R (2012) Order domain analysis of speed-dependent friction-induced torque in a brake experiment. J Sound Vib 331:5040–5053
10. Sen OT, Dreyer JT, Singh R (2012) Envelope and order domain analyses of a nonlinear torsional system decelerating under multiple order frictional torque. Mech Syst Signal Process 35(1–2):324–344 http://dx.doi.org/10.1016/j.ymssp.2012.09.008
11. Jacobsson H (2003) Aspects of disc brake judder. Proc Inst Mech Eng D 217:419–430
12. Jacobsson H (2003) Disc brake judder considering instantaneous disc thickness and spatial friction variation. Proc Inst Mech Eng D 217: 325–341
13. Duan C, Singh R (2010) Analysis of the vehicle brake judder problem by employing a simplified source-path-receiver model. Proc Inst Mech Eng D 225:141–149
14. Bill K, Breuer BJ (2008) Brake technology handbook, 1st edn. SAE International, Warrendale

Chapter 13
Obtaining Linear FRFs for Model Updating in Structures with Multiple Nonlinearities Including Friction

Güvenç Canbaloğlu and H. Nevzat Özgüven

Abstract Most of the model updating methods used in structural dynamics are for linear systems. However, in real life applications structures may have nonlinearity. In order to apply model updating techniques to a nonlinear structure, linear FRFs of the structure have to be obtained. The linear dynamic behavior of a nonlinear structure can be obtained experimentally by using low forcing level excitations, if friction type of nonlinearity does not exist in the structure. However when the structure has multiple nonlinearities including friction type of nonlinearity, nonlinear forces due to friction will be more pronounced at low forcing level excitations. Then it will not be possible to measure linear FRFs by using low level forcing. In this study a method is proposed to obtain linear FRFs of a nonlinear structure having multiple nonlinearities including friction type of nonlinearity by using experimental measurements made at low and high forcing levels. The motivation is to obtain FRFs of the linear part of the system that can be used in model updating of a nonlinear system. The method suggested can also be used as a nonlinear identification method for nonlinear systems. The proposed method is validated with different case studies using SDOF and lumped MDOF systems and simulated experimental data. The effect of the excitation frequency, at which experiments are carried out, on the accuracy of the proposed method, is also demonstrated.

Keywords Nonlinear identification • Nonlinearity • Friction nonlinearity • Model updating • Nonlinear structures

13.1 Introduction

Structural modeling is one of the most important stages in the design of a structure. Since design stage is iterative, the need for structural modeling has come into prominence and accurate prediction of the dynamic response of a structure has become a vital step in the design stage. With the development of computation technology, finite element (FE) method has established itself as the most common numerical method used for obtaining the dynamic response of engineering structures. However, application of FE method may yield inaccuracies arising from numerical and modeling errors. Due to these errors, there are always discrepancies between the dynamic responses obtained by FE method and experiment; therefore FE models need to be updated by using the experimental results and changing some of the parameters used in the FE model.

Over the last three decades various model updating methods have been developed in order to have correct analytical models that reflect the real dynamic responses better. However, most of the model updating methods available in the literature are for linear systems. Berman [1] updated the analytical mass matrix by using incomplete set of measured modes in order to achieve the orthogonality of the mass matrix. In order to correlate the FE model and test results of an aerospace structure, Sidhu and Ewins [2] proposed a method in which the error matrix equation was used. Caesar [3] used Berman's direct system matrix update method, suggested improvements on this method and applied the extended method to a test model.

G. Canbaloğlu (✉)
Department of Mechanical Engineering, Middle East Technical University, 06800 Ankara, Turkey

MGEO Division, ASELSAN Inc., 06800 Ankara, Turkey
e-mail: gcanbal@aselsan.com.tr

H.N. Özgüven
Department of Mechanical Engineering, Middle East Technical University, 06800 Ankara, Turkey
e-mail: ozguven@metu.edu.tr

G. Kerschen et al. (eds.), *Topics in Nonlinear Dynamics, Volume 1: Proceedings of the 31st IMAC, A Conference on Structural Dynamics, 2013*, Conference Proceedings of the Society for Experimental Mechanics Series 35,
DOI 10.1007/978-1-4614-6570-6_13,

In a later study, Caesar [4] described the methods for updating mass and stiffness matrices based on the eigendynamic behavior of linear structures. Visser and Imregun [5] investigated the use of a model updating technique by using FRFs. They discussed the requirement for minimum measured data for successful implementation of the technique and applied the updating technique to different systems in order to demonstrate the effectiveness of the method. Larsson and Sas [6] worked on model updating technique employing forced vibration testing. They proposed a set of updating equations based on force response data and investigated the limitation in the measurements and numerical aspects in the formulations. Bollinger [7] presented constrained optimization theory in order to improve FE model. Lammens et al. [8] optimized reduced analytical dynamic stiffness matrix by solving a linearized set of equations, and updated the FE model of an engine sub frame. Girard et al. [9] extended energy approach for the model updating of a rotating shaft mounted on hydrodynamic bearings. They applied the method to a simple shaft model including mass, stiffness and damping parameters. Billet et al. [10] used an updating method based on minimization of an error in constitutive relation in order to update a nuclear reactor building scale model. Mottershead et al. [11] compared the selection of different updating parameters in the model updating of an aluminum space frame. In a more recent work, Kozak et al. [12] presented a new error localization method and an updating routine and they applied the routine to different case studies.

Since most of the structures have nonlinear behavior, it is vital to have model updating techniques for nonlinear structures as well. In order to apply model updating techniques developed for linear systems to nonlinear structures and to correct linear system matrices, linear dynamic behaviors of the structure have to be experimentally obtained which may require identification of nonlinearity first. In early 1990s Benhafsi et al. [13] worked on the parametric identification of nonlinearities in structures by using describing function method. In a later study, Richards and Singh [14] studied on the identification of nonlinearities that are in the form of polynomial forms and they approximated the nonlinear elastic forces as polynomial functions. Chong and Imregun [15, 16] presented an identification procedure in terms of variable modal parameters for nonlinear systems. Adams and Allemang [17] derived a method for estimating the parameters of nonlinear models and demonstrate the implementation of this method on simulated data for SDOF and MDOF lumped parameter systems. One of most detailed nonlinear system identification literature survey was performed by Kerschen et al. [18] in which more than 400 papers are cited. Özer et al. [19] extended their previous study [20] and identified the nonlinearity in structures by using describing functions and Sherman-Morrison method. Jalali et al. [21] used the inversion of describing functions in order to identify the nonlinearities in the structure.

In a recent study by Arslan et al. [22], two different methods which are capable of identifying nonlinearities in structures are implemented on a test rig containing a nonlinear element. They used low forcing level excitations in the experiments in order to obtain the linear FRFs of the structure. However, when there are multiple nonlinearities including friction type of nonlinearity, it will not be possible to measure the linear FRFs at low level of force excitation. Since most of the model updating methods are applied to linear analytical models it is important to obtain linear FRFs of a nonlinear structure first. In the present study a method is proposed to obtain linear FRFs in order to update linear model parameters of a nonlinear structure having multiple nonlinearities including friction type of nonlinearity. The proposed method is validated with different case studies using SDOF and lumped MDOF systems. In these case studies simulated experimental data is used. The effect of the excitation frequency, at which experiments are carried out, on the accuracy of the proposed method, is also demonstrated with a case study. The method suggested can also be used as a nonlinear identification method.

13.2 Theory

The proposed method in this study is based on the theory developed by Budak and Özgüven [23, 24] for expressing the nonlinear forcing vector in a nonlinear structure as a matrix multiplication form for harmonically excited nonlinear MDOF systems. They expressed the nonlinear internal force vector in a nonlinear MDOF system as

$$\{N(x,\dot{x})\} = [\Delta(x,\dot{x})]\{X\}e^{i\omega t} \tag{13.1}$$

where $\{N(x,\dot{x})\}$ stands for the nonlinear internal forcing vector, $\{X\}$ is a complex response amplitude vector and $[\Delta(x,\dot{x})]$ is the "nonlinearity matrix" which was first presented by Budak and Özgüven [23, 24] for certain types of nonlinearities, and later by Tanrıkulu et al. [25] for any type of nonlinearity by using describing functions. The elements of nonlinearity matrix are written in terms of describing functions, such that the describing function ν_{rj} represents the nonlinearity in the system by giving the best average restoring force between coordinates r and j.

The elements of $[\Delta(x,\dot{x})]$ are given as follows [25]:

$$\Delta_{rr} = v_{rr} + \sum_{\substack{j=1 \\ j\neq r}} v_{rj}, \quad r = 1, 2, \ldots, n \tag{13.2}$$

$$\Delta_{rj} = -v_{rj}, \quad r \neq j, \quad r = 1, 2, \ldots, n \tag{13.3}$$

The response level dependent nonlinear FRF matrix (in the form of receptances) for a nonlinear system can be written as follows:

$$\left[H^{NL}\right] = \left[-\omega^2[M] + i\omega[C] + i[D] + [K] + \Delta\right]^{-1} \tag{13.4}$$

where $[M]$, $[C]$, $[D]$, $[K]$ represent the mass, viscous damping, structural damping and stiffness matrices, respectively. Considering the linear part of this nonlinear system, the linear FRF matrix (in the form of receptances) can be written as follows:

$$\left[H^{L}\right] = \left[-\omega^2[M] + i\omega[C] + i[D] + [K]\right]^{-1} \tag{13.5}$$

Taking the inverses of $\left[H^{NL}\right]$ and $\left[H^{L}\right]$ matrices given in Eqs. (13.4) and (13.5), and then subtracting the second from the first, the following equation is obtained:

$$[\Delta] = \left[H^{NL}\right]^{-1} - \left[H^{L}\right]^{-1} \tag{13.6}$$

After some matrix manipulations, the linear FRF matrix can be obtained as

$$\left[H^{L}\right] = \left[\left[H^{NL}\right]^{-1} - [\Delta]\right]^{-1} \tag{13.7}$$

For a nonlinear MDOF system with multiple nonlinearities including friction type of nonlinearity, nonlinearity matrix $[\Delta]$ can be partitioned as

$$[\Delta] = \left[\Delta_f\right] + [\Delta_{HF}] \tag{13.8}$$

where $[\Delta_f]$ is the nonlinearity matrix due to friction and $[\Delta_{HF}]$ is the nonlinearity matrix due to remaining nonlinearities that are dominant at high forcing levels of excitation. Substituting equation (13.8) into Eq. (13.6), the following equation can be obtained:

$$\left[\Delta_f\right] + [\Delta_{HF}] = \left[H^{NL}\right]^{-1} - \left[H^{L}\right]^{-1} \tag{13.9}$$

When the structure is excited at low forcing levels, $[\Delta_f]$ will be dominant and $[\Delta_{HF}]$ will have negligible terms. Then, at low forcing levels Eq. (13.9) can be approximated as

$$\left[\Delta_f\right] \cong \left[H^{NL}\right]^{-1} - \left[H^{L}\right]^{-1} \tag{13.10}$$

On the other hand, for high forcing levels, $[\Delta_{HF}]$ will be more pronounced compared to frictional nonlinear forces, therefore Eq. (13.9) can be approximated at high forcing levels as

$$[\Delta_{HF}] \cong \left[H^{NL}\right]^{-1} - \left[H^{L}\right]^{-1} \tag{13.11}$$

Then, by using Eqs. (13.10) and (13.11), and measuring FRFs experimentally several times at the same frequency but at different forcing levels, the linear FRFs can be obtained and the nonlinearities can be identified as explained below.

Let us assume that a certain set of experiments are performed at a constant frequency ω, at different forcing levels. Firstly, let the system be excited at a low forcing level, and then $(n-1)$ times at different high forcing levels. Using Eqs. (13.10) and (13.11), the following equations can be written:

$$\left[\Delta_f\right]_1 = \left[H^{NL}\right]_1^{-1} - \left[H^{L}\right]_1^{-1} \tag{13.12}$$

$$[\Delta_{HF}]_2 = \left[H^{NL}\right]_2^{-1} - \left[H^{L}\right]_2^{-1} \tag{13.13}$$

$$[\Delta_{HF}]_3 = [H^{NL}]_3^{-1} - [H^L]_3^{-1} \tag{13.14}$$

$$[\Delta_{HF}]_4 = [H^{NL}]_4^{-1} - [H^L]_4^{-1} \tag{13.15}$$

$$[\Delta_{HF}]_n = [H^{NL}]_n^{-1} - [H^L]_n^{-1} \tag{13.16}$$

where subscript 1, 2, 3, … n indicates forcing cases. If the equation at low forcing level (Eq. 13.12) is subtracted from each of the following ones, a new set of equations will be obtained:

$$[\Delta_{HF}]_2 - [\Delta_f]_1 = [H^{NL}]_2^{-1} - [H^{NL}]_1^{-1} \tag{13.17}$$

$$[\Delta_{HF}]_3 - [\Delta_f]_1 = [H^{NL}]_3^{-1} - [H^{NL}]_1^{-1} \tag{13.18}$$

$$[\Delta_{HF}]_4 - [\Delta_f]_1 = [H^{NL}]_4^{-1} - [H^{NL}]_1^{-1} \tag{13.19}$$

$$[\Delta_{HF}]_n - [\Delta_f]_1 = [H^{NL}]_n^{-1} - [H^{NL}]_1^{-1} \tag{13.20}$$

Since the linear FRF matrix is not forcing level dependent, then these terms will be canceled out and they will not appear in the resulting equations as can be seen above. There are both zero and nonzero elements in the nonlinearity matrices at the left hand sides of the equations, and nonzero elements are related to nonlinear coordinates. These nonzero elements which can be written as polynomial functions of response amplitudes with unknown coefficients are the describing functions of the corresponding nonlinearities. Since it is always possible to take data points more than the unknown coefficients, least square fit can be used for obtaining the unknown coefficients. In order to find the unknown coefficients, polynomial fit for $(n-1)$ data points is applied in a least square sense and the equation of the corresponding regression curve is obtained. For more complex nonlinearities where polynomial fit may be insufficient, nonlinear fit can also be used. Once the unknown coefficients are obtained, by comparing the terms of the regression equation with the corresponding describing functions, nonlinearities are identified and then linear FRFs can easily be calculated by using one of the equations from (13.12) to (13.16), one of which is given below.

$$[H^L]_1 = \left[[H^{NL}]_1^{-1} - [\Delta_f]_1 \right]^{-1} \tag{13.21}$$

The Eqs. (13.17), (13.18), (13.19), and (13.20) will be reduced to very simple algebraic equations for a SDOF system:

$$\Delta_{HF_2} - \Delta_{f_1} = \frac{1}{H_2^{NL}} - \frac{1}{H_1^{NL}} \tag{13.22}$$

$$\Delta_{HF_3} - \Delta_{f_1} = \frac{1}{H_3^{NL}} - \frac{1}{H_1^{NL}} \tag{13.23}$$

$$\Delta_{HF_4} - \Delta_{f_1} = \frac{1}{H_4^{NL}} - \frac{1}{H_1^{NL}} \tag{13.24}$$

$$\Delta_{HF_n} - \Delta_{f_1} = \frac{1}{H_n^{NL}} - \frac{1}{H_1^{NL}} \tag{13.25}$$

For a SDOF system, since all the matrix inversions simplify to inversions of a scalar, it is much easier to obtain the right hand sides of the above equations by using experimental measurements. Then linear FRFs of the system can be calculated by using the following equation:

$$\frac{1}{H_1^L} = \frac{1}{H_1^{NL}} - \Delta_{f_1} \tag{13.26}$$

Equation (13.26) is valid for low forcing level at any frequency; therefore it is possible to obtain the linear FRFs over the desired frequency range. It should be noted that, although the above equations are valid for a harmonic excitation and therefore harmonic vibration of the system at any frequency, the difference between linear and nonlinear FRFs at an arbitrary frequency may be negligible, making it very difficult to identify the nonlinearity accurately. Hence, the identification can be made most accurately at frequencies where the nonlinearity has the maximum effect on the system response.

13.3 Case Studies

In this section, applications of the proposed method to SDOF and MDOF nonlinear systems are presented. The first case study is purely a theoretical one and it illustrates the identification of nonlinearities and calculation of the linear frequency response of a nonlinear system from nonlinear FRF measurements. The second case study is an extension of the first one, in which polluted data is used in the analysis in order to simulate the experimental measurements more realistically. In the third case study, the proposed approach is applied to a MDOF system with multiple nonlinearities including friction. In this case study, again simulated experimental data is used. Finally, in order to study the effect of the excitation frequency at which measurements are made, on the accuracy of the proposed method, the same MDOF system is considered. The nonlinear parameters are identified by using simulated experimental FRF values obtained at different excitation frequency each time and the identified values are compared with each other. In obtaining all simulated experimental results, harmonic balance approach is used.

13.3.1 Application of the Approach to a SDOF System

In this case study, the proposed method is applied to a SDOF system with cubic stiffness and dry friction nonlinearities. The system and the dry friction model used in the case study are given in Fig. 13.1.

The parameters of these nonlinear elements and the properties of the system are given as follows:

$$m_1 = 0.1kg, k_1 = 2 \times 10^6 N/m and\, \gamma(loss factor) = 0.01$$
$$k^* = 1 \times 10^{10} N/m^3$$
$$\mu = 0.1, Normal\, Force = 10N and\, k_f = 3 \times 10^5 N/m.$$

Firstly, the system is excited harmonically with a low forcing amplitude (F = 0.01 N). The harmonic response of the system at this forcing level is compared with the linear frequency response of the system obtained disregarding both friction and cubic stiffness nonlinearity (Fig. 13.2).

As can be seen in Fig. 13.2, since at low forcing level nonlinear internal forces due to cubic stiffness are negligible, the only nonlinear effect is due to friction. Frictional internal force causes a shift in the resonance frequency due to its stiffness component. Afterwards, 11 different higher excitation cases are considered by taking the amplitude of the harmonic excitation force between 100 and 300 N and the responses of the system are obtained. In Fig. 13.3, nonlinear harmonic responses at only the forcing levels of F = 130 N and F = 280 N are shown.

Since frictional nonlinearity is negligible at high forcing levels, as can be seen from the Fig. 13.3, only the cubic stiffness nonlinearity will be effective, and it will change the frequency response of the system around resonance causing a jump, which is a typical response behavior of cubic stiffness element. All above computations are based on the nonlinear identification made by using 11 different FRFs obtained at the excitation frequency of 710 Hz. By using "polyfit" function

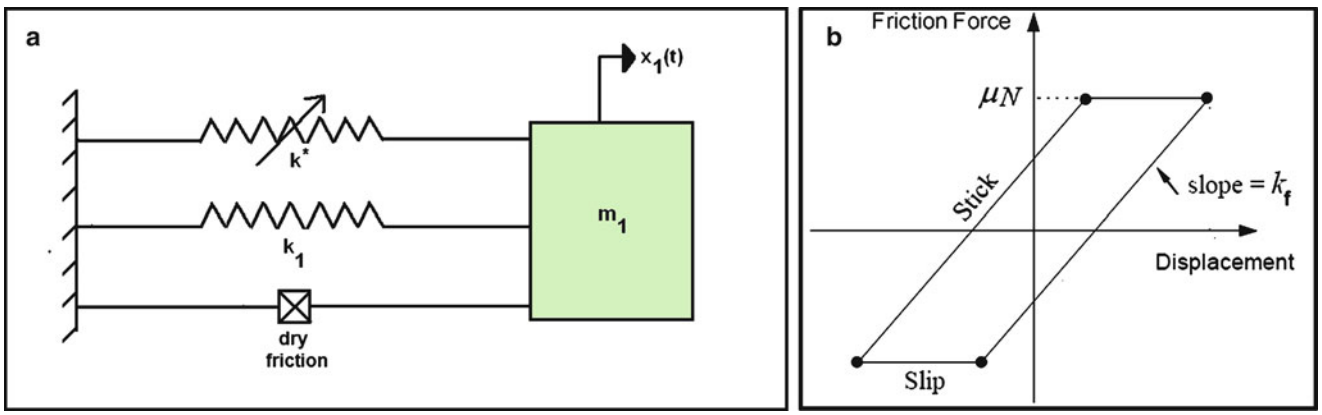

Fig. 13.1 (**a**) SDOF nonlinear system, (**b**) dry friction model

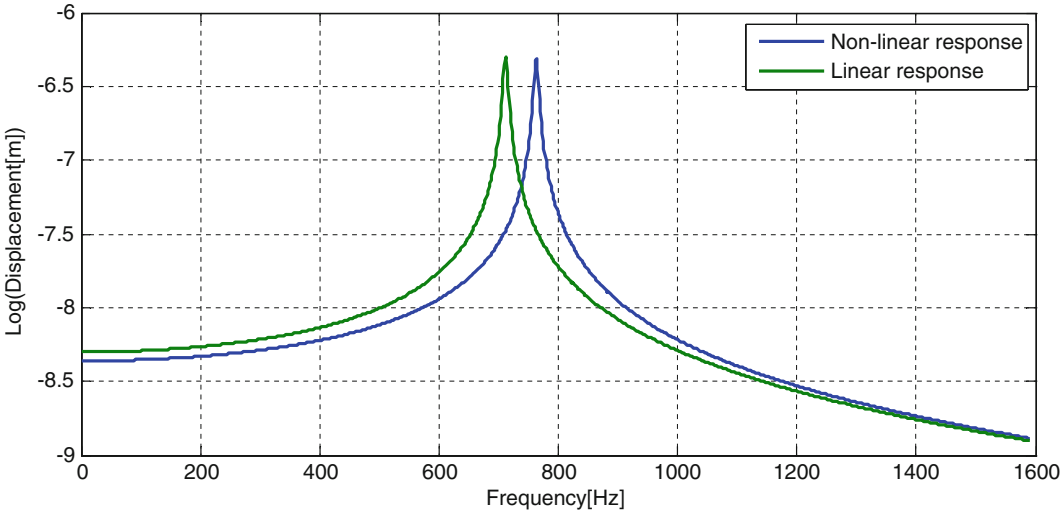

Fig. 13.2 Harmonic response of the system for F = 0.01 N

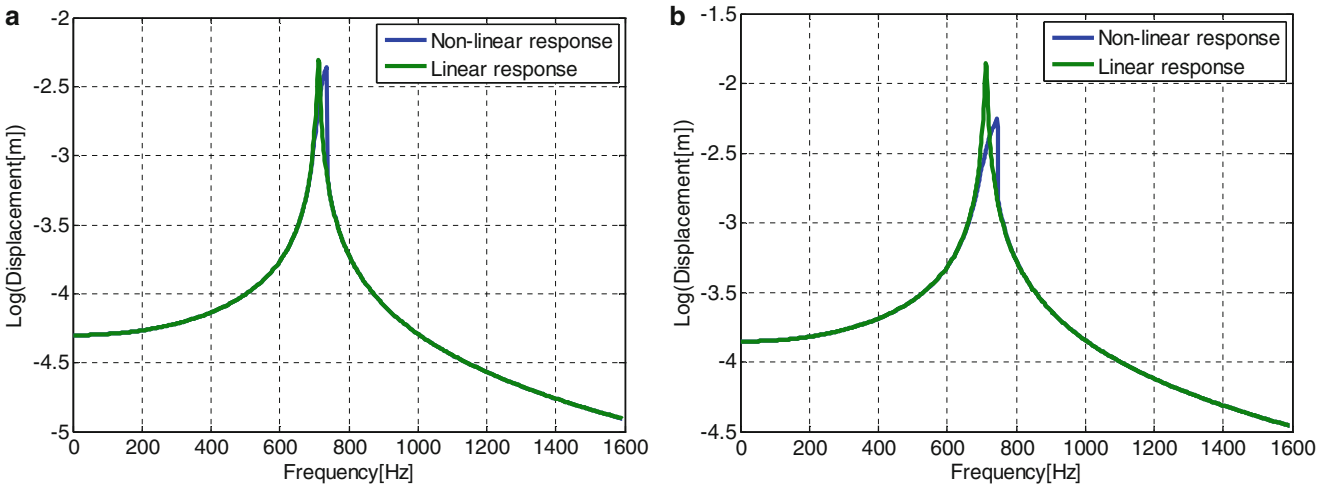

Fig. 13.3 Harmonic response of the system for (**a**) F = 130 = N, (**b**) F = 280 N

of MATLAB, equation of the regression curve is obtained and nonlinear parameters are identified by comparing the terms of the regression equation with the corresponding describing functions. The regression curve obtained can be seen in Fig. 13.4

The nonlinear parameters estimated are given below:

$$k^* = 9.9 \times 10^9 N/m^3 \quad and \quad k_f = 3 \times 10^5 \quad N/m$$

It can be seen that the estimated parameters perfectly match with the actual values. The linear FRF of the system now can be calculated by using Eq. (13.26). The comparison of the estimated and actual linear frequency response is given in Fig. 13.5. As expected, there is a perfect match between estimated and actual linear frequency responses of the system.

13.3.2 Application of the Approach to a SDOF System with Polluted Data

In the second case study, in order to simulate the experimental data, theoretical data is polluted with 5% noise. The noise has normal distribution and standard deviation of 5% of the amplitude of the original response. In the analysis, SDOF nonlinear system with the same parameters as in the first case study is used. The system is excited with a low forcing amplitude and

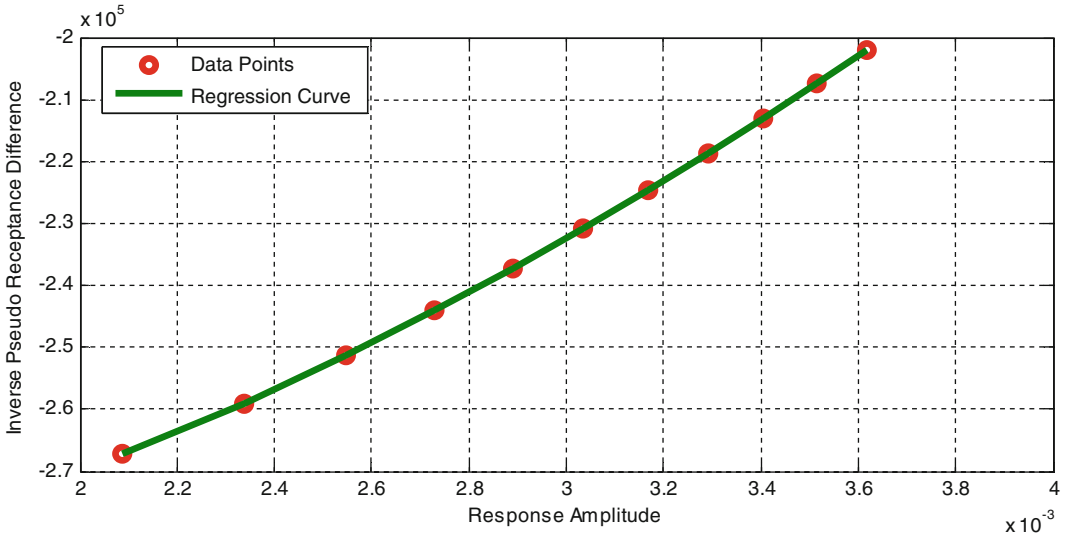

Fig. 13.4 Polynomial regression curve for the available data points

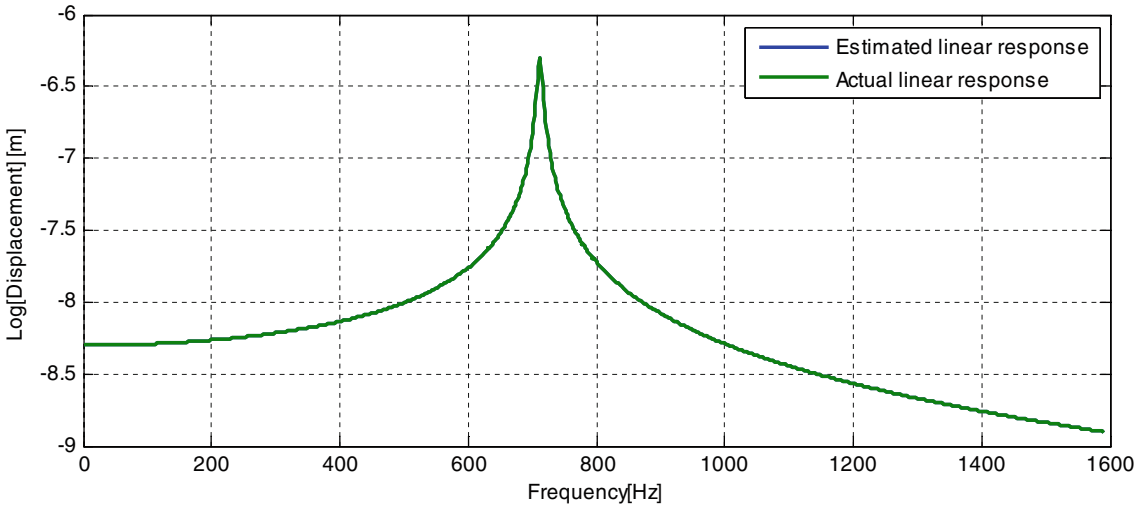

Fig. 13.5 Comparison of the estimated and actual linear frequency responses of the system

then with 11 different high forcing amplitudes. In Fig. 13.6, the FRF of the nonlinear system for F = 0.01 N is compared with the linear frequency response of the system obtained disregarding both friction and cubic stiffness nonlinearity. The frequency responses of the system for F = 130 N and F = 280 N are given in Fig. 13.7.

At the excitation frequency of 710 Hz, 11 different data points are generated and the polynomial regression curve given in Fig. 13.8 is obtained.

Identified nonlinear parameters and comparison of these values with the actual ones are given in Table 13.1.

As can be seen in Table 13.1, there is a slight difference between the estimated and actual nonlinear parameters, mainly due to addition of noise to the theoretical data. Comparison of the estimated and actual linear frequency responses is given in Fig. 13.9. As expected, estimated linear frequency response matches perfectly with the actual one.

13.3.3 Application of the Approach to a MDOF System with Polluted Data

In the third case study, application of the proposed approach to a nonlinear MDOF system with polluted data is illustrated (Fig. 13.10). The same dry friction model given in previous case study is used here as well.

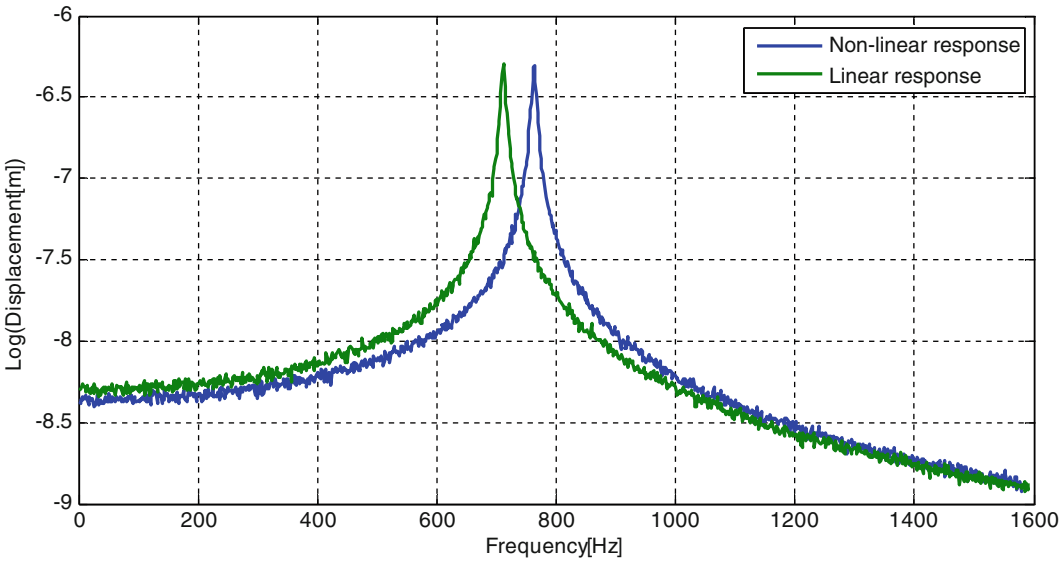

Fig. 13.6 Frequency response of the system at F = 0.01 N with 5% noise

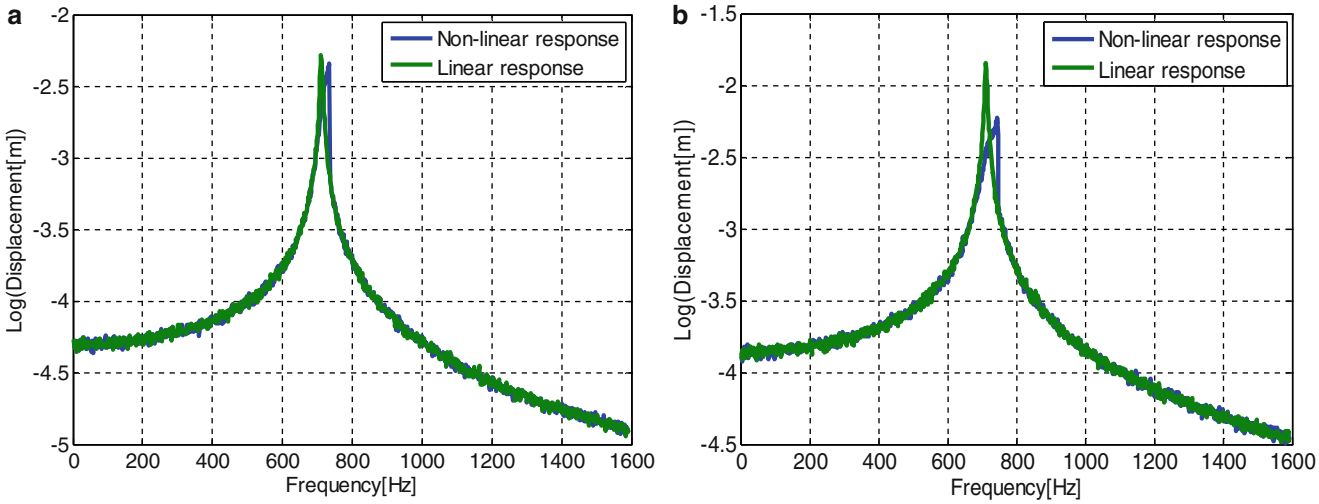

Fig. 13.7 Frequency response of the system with 5% noise for (**a**) F = 130 N, (**b**) F = 280 N

Parameters of the nonlinear element and the properties of the other system elements are given as follows:

$$m_1 = 0.1, m_2 = 0.5\,kg, k_1 = k_2 = k_3 = 1 \times 10^6 N/m \, and \, \gamma(loss\,factor) = 0.005$$
$$\mu = 0.1, Normal\,Force = 10N \, and \, k_f = 8 \times 10^4 N/m$$
$$k^* = 1 \times 10^{10} N/m^3$$

In order to simulate the experimental data, theoretical data is polluted with 5% noise. The noise has normal distribution and standard deviation of 5% of the amplitude of the original response. The system is excited with a low forcing level and then with 11 different high forcing levels. The frequency responses of the system at forcing levels of F = 0.01 N and F = 100 N are given in Figs. 13.11 and 13.12, respectively.

As can be seen in Fig. 13.11, for low forcing amplitudes, the only nonlinear effect is due to friction and frictional internal force causes a shift in the resonance frequency. The frictional nonlinearity is much more effective in the second mode.

In Fig. 13.12, it can be seen that, since frictional nonlinear internal forces are negligible for high forcing level, the nonlinearity changes the response of the system around second resonance considerably by causing a jump, which is mainly

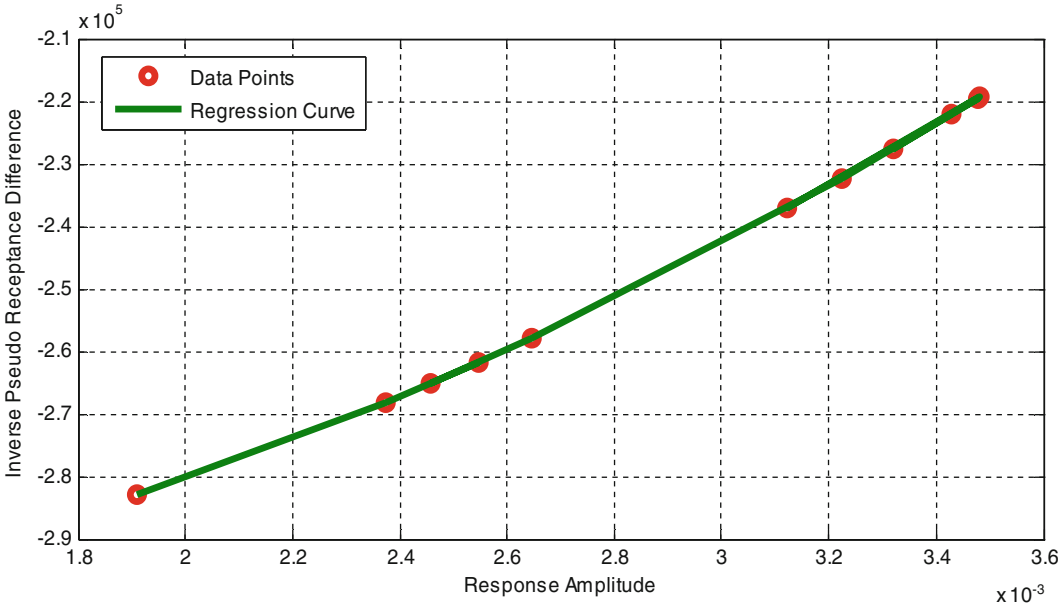

Fig. 13.8 Polynomial regression curve for the available data points

Table 13.1 Comparison of nonlinear parameters

Nonlinear parameters	Estimated	Actual	% error
$k^* \, (N/m^3)$	9.9×10^9	1×10^{10}	1
$k_f \, (N/m)$	3.1×10^5	3×10^5	3.3

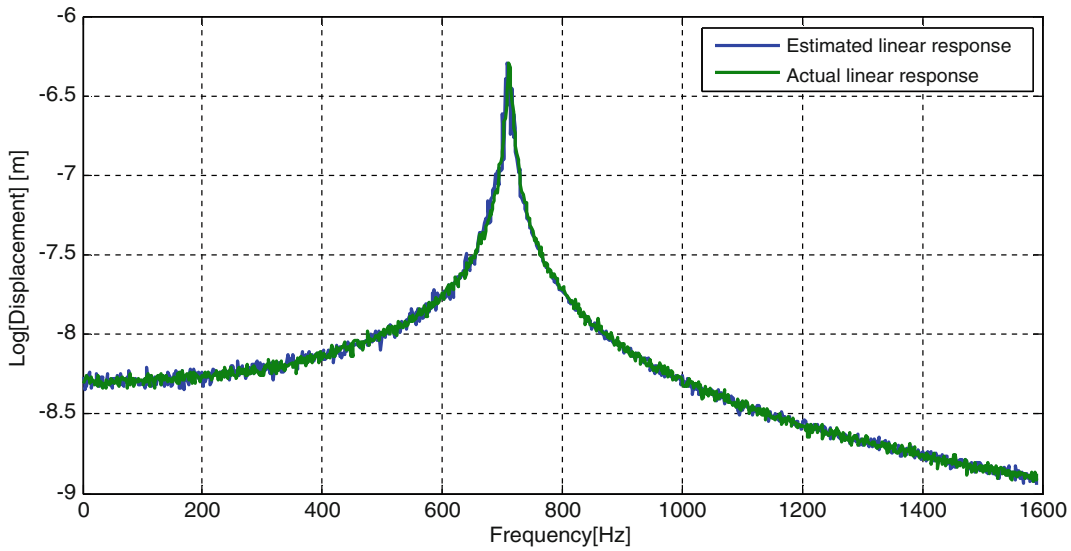

Fig. 13.9 Comparison of the estimated and actual linear frequency response of the system with 5% noise

due to cubic stiffness. As in the low forcing level case, first mode is not much affected from the existence of the stiffness nonlinearity in the system. The nonlinear parameters given in Table 13.2 are estimated as explained in the first case study (Fig. 13.13).

As can be seen from the values in Table 13.2, estimated and actual nonlinear parameters are in perfect match. However, since in the proposed approach, excitation frequency is a free parameter (i.e., the equations are valid for any forcing level and therefore vibration at any frequency), the effect of the excitation frequency used in the experiments on the performance of the method should be analyzed.

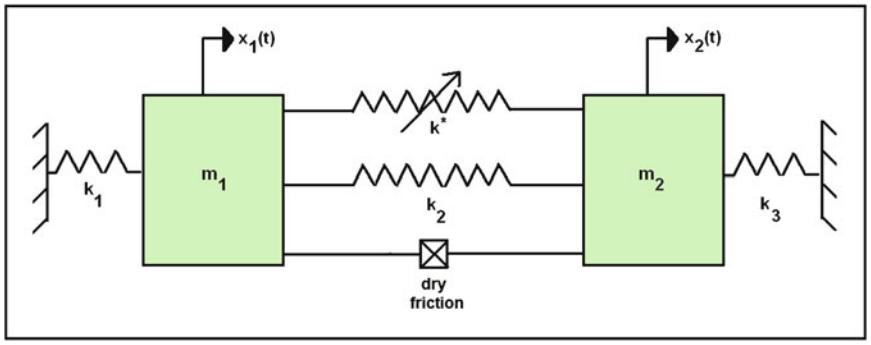

Fig. 13.10 MDOF nonlinear system used in Case Study 3

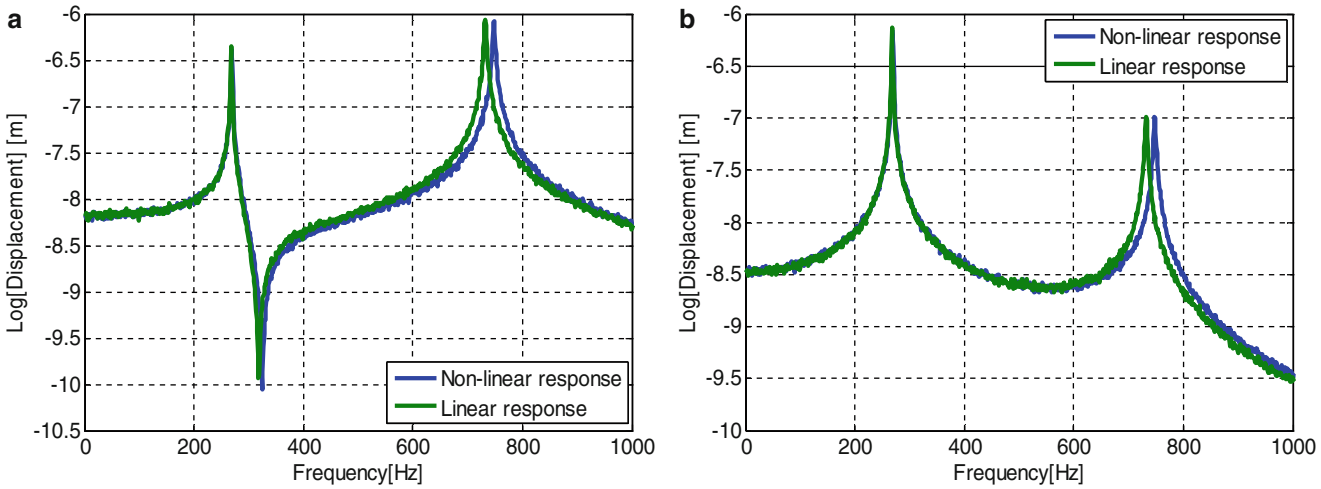

Fig. 13.11 Frequency responses of the system with 5% noise for F = 0.01 N. (**a**) First coordinate, (**b**) second coordinate

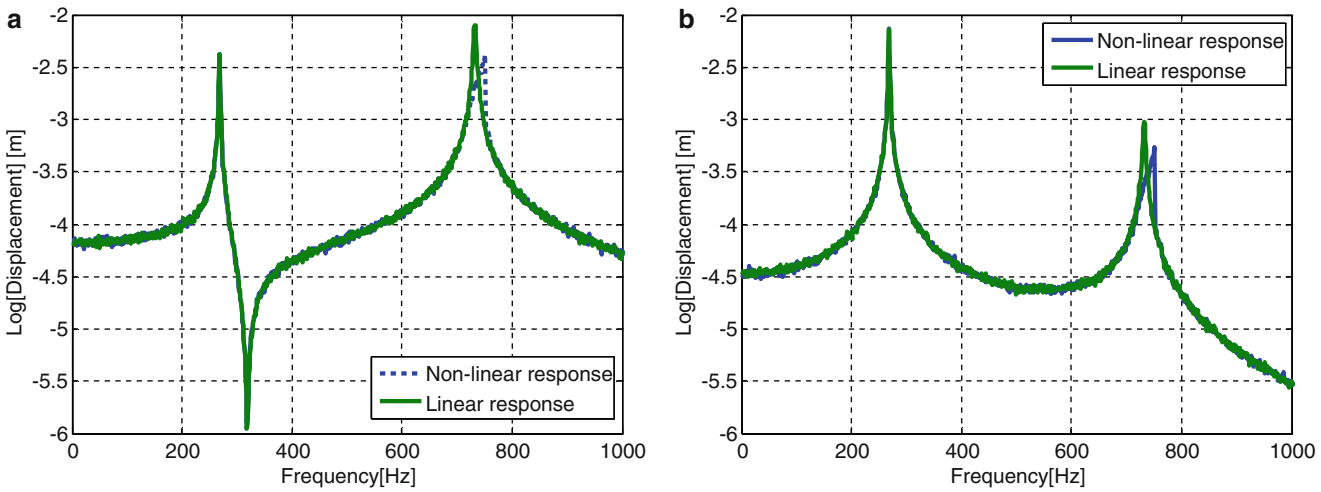

Fig. 13.12 Frequency responses of the system with 5% noise for F = 100 N. (**a**) First coordinate, (**b**) second coordinate

Table 13.2 Comparison of nonlinear parameters

Nonlinear parameters	Estimated	Actual	% error
k^* (N/m^3)	9.9×10^9	1×10^{10}	1
$k_f(N/m)$	8.03×10^4	8×10^4	0.4

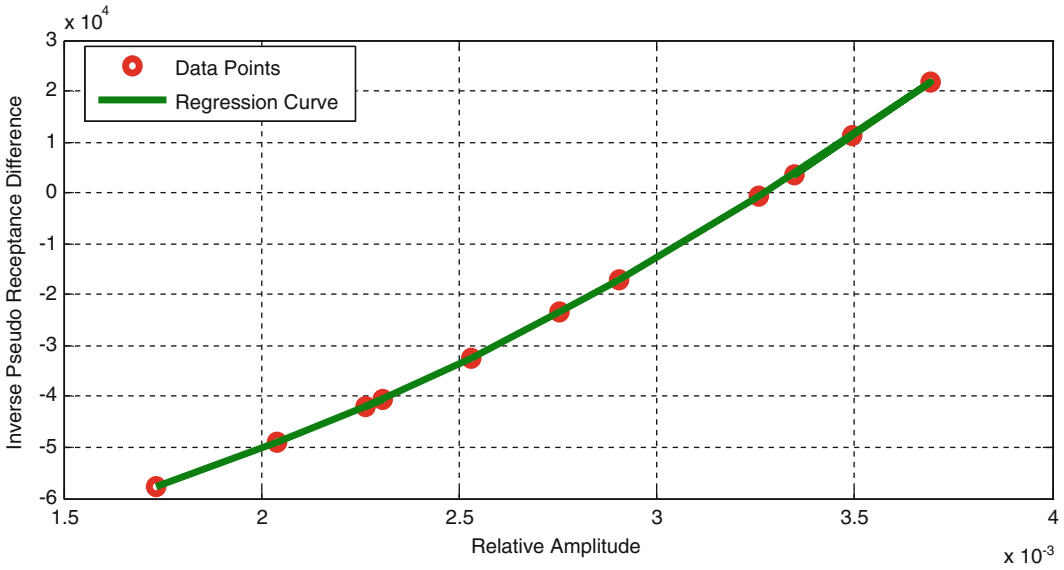

Fig. 13.13 Polynomial regression curve for the available data points

Table 13.3 Comparison of nonlinear parameters identified by using different excitation frequencies

Excitation frequency (Hz)	Estimated $k^*(N/m^3)$	Actual $k(N/m^3)$	% error for k^*	Estimated $k_f(N/m)$	Actual $k_f(N/m)$	% error for k_f
725	9.9×10^9	1×10^{10}	1.0	8.03×10^4	8×10^4	0.4
730	9.9×10^9		1.0	7.67×10^4		4.1
745	9.9×10^9		1.0	16.3×10^4		103.8

13.3.4 Performance of the Method at Different Excitation Frequencies

As the last case study, in order to see the effect of excitation frequency on the proposed method, different simulated tests at various frequencies are performed for the MDOF nonlinear system given in the previous case study. For each test case, nonlinearities are identified and they are compared with the actual nonlinear parameters. Comparison of the results is given in Table 13.3.

Since the nonlinear forces affect the second mode more, excitation frequencies are selected around the second resonance of the system. As can be seen from Table 13.3, for all the excitation frequencies used, cubic stiffness values are successfully estimated. However, the frictional stiffness value is highly affected from the selection of excitation frequency, even though all frequencies are around the resonance region. It is observed that when the excitation frequency is closer to the second resonance of the linear frequency response, estimated values become more accurate.

13.4 Discussion and Conclusions

When there are multiple nonlinearities including friction in a system, it is not possible to obtain the linear frequency response of the system by using low forcing levels in the experiments. In this paper, an approach for obtaining the linear FRFs of a nonlinear system with multiple nonlinearities including friction is proposed. The basic motivation is to have FRFs of the linear part of a nonlinear structure, so that they can be used in model updating.

In the method proposed, FRF values are measured at all coordinates that we are interested in, but at a constant frequency ω and at different forcing levels. First, the system is excited at a low forcing level, and then several times at different high forcing levels. By using the measured nonlinear FRFs, first the nonlinearities are identified and then linear FRFs are obtained in order to use them in model updating of nonlinear systems.

The method is validated with different case studies using SDOF and MDOF systems and simulated experimental data. In the first and second case studies, application of the approach is demonstrated on a SDOF nonlinear system. It is shown that the approach is very successful in identifying multiple nonlinearities in the system, as well as in determining the linear FRF. In simulated experimental case study it is observed that, the noise added to the data affects the values of the identified nonlinear parameters and linear frequency response. In the third case study, the method is applied to a MDOF nonlinear system by using simulated experimental data again. The results obtained show that nonlinearities can be identified very accurately by using nonlinear FRFs measured at low and high forcing levels. In the last case study, the effect of the excitation frequency used in the experiments on the performance of the method is investigated. From the results obtained it is concluded that excitation frequency should be close to the resonance frequency, otherwise the accuracy of the identified friction nonlinearity can be deteriorated considerably.

Consequently, it can be said that the method can successfully be used for the identification of nonlinearity and calculation of the linear FRFs of a nonlinear structure with multiple nonlinearities including friction. The applicability and accuracy of the approach proposed is demonstrated only on simple SDOF and MDOF systems. The method needs to be tested on real structures, in order to apply it to obtain FRFs of the linear part of a nonlinear structure that can be used in model updating of the nonlinear structure.

References

1. Berman A (1979) Mass matrix correction using an incomplete set of measured modes. AAIA J 17(1):1147–1148
2. Sidhu J, Ewins DJ (1984) Correlation of finite element and modal test studies of a practical structure. In: Proceedings of the 2nd international modal analysis conference, Orlando, FL, pp 756–762
3. Caesar B (1986) Update and identification of dynamic mathematical models. In: Proceedings of the 4th international modal analysis conference, Los Angeles, CA, pp 394–401
4. Caesar B (1987) Updating system matrices using modal test data. In: Proceedings of the 5th international modal analysis conference, London, England, pp 453–459
5. Visser WJ, Imregun M (1991) A technique to update finite element models using frequency response data. In: Proceedings of the 9th international modal analysis conference, Florence, Italy, pp 462–469
6. Larsson PO, Sas P (1992) Model updating based on forced vibration testing using numerically stable formulations. In: Proceedings of the 10th international modal analysis conference, San Diego, CA, pp 966–974
7. Bollinger AT (1994) Finite element model updating for FEA/EMA modal correlation via constrained optimization theory. In: Proceedings of the 12th international modal analysis conference, Honolulu, Hawaii, pp 882–888
8. Lammens S, Brughmans M, Leuridan J, Sas P (1996) Application of a FRF based model updating technique for the validation of the finite element model of an engine subframe. In: Proceedings of the 14th international modal analysis conference, Dearborn, MI, pp 1063–1070
9. Girard A, Chatelain J, Bugeat LP (1997) Model updating by energy approach for rotating shafts. In: Proceedings of the 15th international modal analysis conference, Orlando, FL, pp 1419–1425
10. Billet L, Moine P, Lebailly P (1997) Updating a finite element model of the Hualien nuclear reactor building. In: Proceedings of the 15th international modal analysis conference, Orlando, FL, pp 1924–1930
11. Mottershead JE, Mares C, Friswell MI, James S (2000) Model updating of an aluminium space-frame using different parameter sets. In: Proceedings of the 18th international modal analysis conference, San Antonio, TX, pp 576–583
12. Kozak MT, Cömert MD, Özgüven HN (2007) Model updating routine based on the minimization of a new frequency response based index for error localization. In: Proceedings of the 25th international modal analysis conference, Orlando, FL, USA, pp 84–95
13. Benhafsi Y, Penny JET, Friswell MI (1992) A parameter identification method for discrete nonlinear systems incorporating cubic stiffness elements. Int J Anal Exp Modal Anal 7(3):179–196
14. Richard CM, Singh R (2000) Feasibility of identifying nonlinear multi-degree-of-freedom systems with unknown polynomial forms. In: Proceedings of the 18th international modal analysis conference, San Antonio, TX, pp 496–502
15. Chong YH, mregün M (2000) Variable modal parameter identification for nonlinear MDOF systems – parts I: formulation and numerical validation. J Shock Vib 7(4):217–227
16. Chong YH, mregün M (2000) Variable modal parameter identification for nonlinear MDOF systems – parts II: experimental validation and advanced case study. J Shock Vib 7(4):229–240
17. Adams DE, Allemang RJ (2000) A frequency domain method for estimating the parameters of a non-linear structural dynamic model through feedback. Mech Syst Signal Process 14(4):637–656
18. Kerschen G, Worden K, Vakakis AF, Golinval JC (2006) Past, present and future of nonlinear system identification in structural dynamics. Mech Syst Signal Process 20:505–592
19. Özer MB, Özgüven HN, Royston TJ (2009) Identification of structural non-linearities using describing functions and the Sherman–Morrison method. Mech Syst Signal Process 23:30–44
20. Özer MB, Özgüven HN (2002) A new method for localization and identification of nonlinearities in structures. In: 6th biennial conference on engineering systems design and analysis, stanbul, Turkey
21. Jalali H, Bonab BT, Ahmadian H (2011) Identification of weakly nonlinear systems using describing function inversion. Exp Mech 51:739–747
22. Arslan Ö, Aykan M, Özgüven HN (2011) Parametric identification of structural nonlinearities from measured frequency response data. Mech Syst Signal Process 25:1112–1125

23. Budak E, Özgüven HN (1990) A method for harmonic responses of structures with symmetrical nonlinearities. In: Proceedings of the 15th international seminar on modal analysis and structural dynamics, Leuven, Belgium, 17–21 September 1990, vol 2, pp 901–915
24. Budak E, Özgüven HN (1993) Iterative receptance method for determining harmonic response of structures with symmetrical non-linearities. Mech Syst Signal Process 7(1):75–87
25. Tanrikulu Ö, Kuran B, Özgüven HN, mregün M (1993) Forced harmonic response analysis of non-linear structures using describing functions. AIAA J 31(7):1313–1320

Chapter 14
LDV Measurement of Local Nonlinear Contact Conditions of Flange Joint

V. Ruffini, C.W. Schwingshackl, and J.S. Green

Abstract The traditional approach to evaluating the linear dynamic behavior of structures for modal validation is based on the acquisition of frequency response functions and their modal analysis. With small modifications, a similar technique can be used to validate nonlinear response predictions. The use of nonlinear dynamic analysis of flange joints for sealing and wear predictions makes it necessary to also provide validation information for the localised nonlinear mechanisms at the contact surface. For this purpose, a technique based on two Laser Doppler Vibrometers has been developed. The experimental set-up can provide data of the relative out-of-plane displacement of the bolted flange joint during a vibration cycle, which indicates contact separation and permanent gap locations. The observed influence of different excitation levels and bolt torques on the global and local dynamic response led to an understanding of the nonlinear behaviour of the flange and of the local contact conditions.

Keywords Scanning LDV • Full field measurement • Flange joint • Nonlinear contact behaviour • Model validation

14.1 Introduction

The trend in industry today is to use as much simulation as possible during product development to optimise the design at an early stage, avoid costly design mistakes, and minimise the amount of testing required once the hardware becomes available. This process is well established for linear dynamic analysis, and very accurate predictions can be obtained via finite element methods. The effect of this accurate analysis is that previously neglected nonlinear effects suddenly become more prominent, and must be included in the consideration if good agreement with measured response is required. To accommodate this need, nonlinear dynamic analysis tools that allow the inclusion of different types of nonlinearity in the results have been developed.

Of particular interest is the nonlinear behaviour of friction joints, which can have a significant effect on the response [1–4], and are actively used in the aircraft engine industry to design the required damping behaviour into a structure (e.g. underplatform dampers [4–6], blade root damping [7, 8], shroud contacts [9, 10], ...). The validation of these nonlinear models is currently attracting a large amount of interest [11], with different approaches being investigated to ensure an accurate prediction. Most of these approaches focus on the validation of the global nonlinear response of a structure since it has the biggest influence on the development of the product [12, 13]. The issue with this validation approach is that it focuses on the global response, but does not really consider the underlying nonlinear mechanism at the contact itself. A model update based on the global response of the system can be effective in predicting how the assembled structure will behave during operations, but it may reach these results with the wrong mechanism at its core.

With advances in nonlinear analysis, new applications are being considered, which use the local information at the contact interface to predict additional features, such as wear on the contact surface [14]. One such application is the behaviour of aircraft engine flange joints [15], which have to ensure gas tightness and provide structural stiffness to the engine. A nonlinear behaviour of such a structure can lead to changes in the global response of the engine, but it can also affect the gas tightness and possible wear behaviour of the joint. In the latter case, a local prediction of the joint behaviour is required to understand how much separation will occur, and where on the flange slip or stick is present. Recent research on underplatform dampers

V. Ruffini (✉) • C.W. Schwingshackl • J.S. Green
Mechanical Engineering, Imperial College London, Exhibition Road, SW7 2AZ London, UK
e-mail: valentina.ruffini@imperial.ac.uk; c.schwingshackl@imperial.ac.uk

G. Kerschen et al. (eds.), *Topics in Nonlinear Dynamics, Volume 1: Proceedings of the 31st IMAC, A Conference on Structural Dynamics, 2013*, Conference Proceedings of the Society for Experimental Mechanics Series 35,
DOI 10.1007/978-1-4614-6570-6_14,

has focused successfully on local relative motion of the damper [16], and an ultrasonic approach has been used to measure the contact condition for static bolted flange joints [17]. The correlation between gap opening behaviour and global nonlinear dynamic response of a flanged structure has also been investigated [18], but the study was limited to only two points along the joint.

This work introduces a new measurement system that allows full-field measurement of the out-of-plane motion of a bolted flange joint during a vibration cycle, providing information of contact separation and permanent gaps at the contact interface, which can then be used for the validation of local effects.

14.2 Bolted Flange Joint Design

A vibrating flange joint can undergo two types of global motion (Fig. 14.1): an in-plane transverse displacement u_y, and an out-of-plane oscillation u_x. Due to the discontinuity at the flange interface, local displacements will in general be superposed over the global ones during a vibration cycle, including stick or slip in the interface plane, separation of the two flange members, or free motion due to permanent gaps in the out-of-plane direction. The nonlinear behaviour at the flange interface leads to relative motion between opposite points on the contact interface, in-plane due to slip, and out-of-plane due to separation. The out-of-plane motion can be monitored with two laser Doppler vibrometers (LDVs) that are pointed onto the flange from opposite sides: it is thus possible to simultaneously record the out-of-plane displacement components $u_{1,x}$ and $u_{2,x}$of the two members of the flange and then work out the relative displacement between them. The contact separation and gap opening will be the main objective of the present study, as it can be a root cause of gas flow leakage and nonlinearity in aero-engine casings.

A test piece was designed to maximise the separation at the flange interface. It consists of two straight L-shaped beams, joined by two bolts. This simple geometry is easy to model and manufacture for an experimental set-up, while still being able to reproduce the desired separation in the flange. A fully parametric FE model was used to optimise the global dynamic performance of the test piece, and maximise the flange opening behaviour: beam and flange length, width and height were all varied during the optimisation procedure. A small annular area around the bolt holes was fully constrained between the two members of the flange to simulate stuck conditions due to high pressure under the bolts. The boundary conditions were set as free-free, as this was meant to be the experimental configuration. The model was composed of around 10,000 10-node tetrahedral elements, and the commercial software Ansys v12.1 used for the analyses.

The second bending mode of the piece (Fig. 14.2a) was the most suitable for the experimental investigations: the linear FE analyses showed good levels of separation between the two members of the flange, while at the same time the presence of an anti-node very close to the flange interface helped minimise the global out-of-plane oscillation. The global transverse displacement was also minimised, because it is a potential source of measurement errors. The FE simulations showed that this component of the motion would dominate the global response of the structure, as it is one to two orders of magnitude larger than the out-of-plane local displacement of the flange. Such a significant displacement in a direction perpendicular to the one under investigation can interfere with the output signal from the measurement devices, and an accurate alignment of the experimental set-up is therefore of the utmost importance.

A test piece was manufactured based on the design from the FE optimisation (Fig. 14.2b). To obtain satisfactory contact conditions at the flange interface, strict geometrical tolerances were imposed. The flat beams were cut from an annealed steel sheet, while the flange members were milled from two solid blocks of the same material into two L-shaped parts, which were welded to the beams. The manufacturing technique was chosen to provide good planarity at the flange interface, but the welding procedure introduced residual thermal stresses in the thin flange surfaces, giving them a concave shape: once

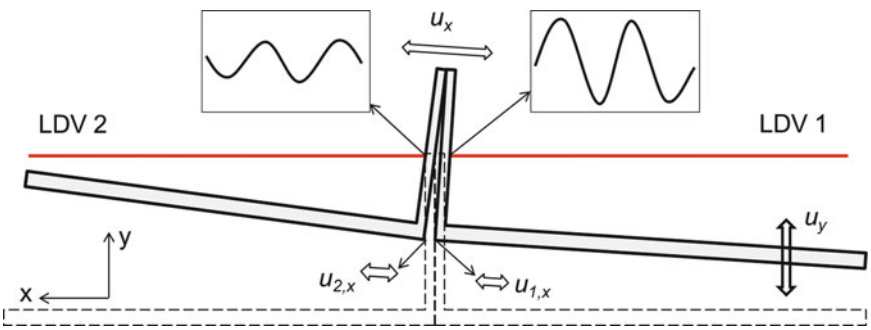

Fig. 14.1 Global and local displacements of a typical flange joint and basic measurement principle

Fig. 14.2 Second bending mode of the flange model (**a**), and manufactured test piece (**b**)

bolted together, a gap was visible, leading to an undetermined contact condition at the flange. To improve contact, the inner surfaces were manually sanded after manufacturing to make them planar. The gap was strongly reduced, but full planarity could not be reached with this approach. A bolt torque of 20 Nm was selected for the flange, and locknuts used in place of regular nuts to avoid relaxation of the bolt pre-stress, while no washers were added, in order to minimise the areas of contact in the system, and hence dissipation by friction.

14.3 Experimental Test Rig

A test rig had to be developed to allow precise alignment between the flange and the LDVs, and the attachment of an excitation source to the flange. The rig was further required to have a minimum influence on the dynamic response at high excitation levels. Several test set-ups were investigated, and the final one can be seen in Fig. 14.3: the test piece is suspended horizontally by four thin nylon wires, each passing through a small hole drilled into the beams at the nodal lines of the second bending mode. The horizontal orientation of the flange allowed good alignment with the LDVs, and was therefore chosen for the final design. Due to this set-up, the shaker excitation direction becomes parallel to the supporting wires, leading to translational and rotational rigid body motions in the vertical direction with frequencies larger than zero. However, since the second bending mode, which was the mode of interest, has a natural frequency around three times larger than the highest rigid body mode, and the wires were mounted in the nodal lines, it was assumed that the influence of the supports was minimal.

Precise alignment between the flange and lasers was required to optimise the measurement accuracy. Since it is nearly impossible to verify the perpendicularity of the laser beams to the flange directly, a global reference frame needs to be established. The lasers and the flange positions can then be determined relative to it, resulting in an indirect alignment of the different components. A flat steel table was used for the global reference: the laser heads were placed directly on its surface, and aligned so that each laser beam pointed at the centre of the other's lens. The alignment procedure of the two LDVs proved to be very time-consuming, so it was decided to move the target flange during a scan, instead of having to realign the LDVs each time for a new location on the flange surface.

The test piece was mounted on a frame that could be moved horizontally on wheels, allowing scanning along the width of the flange. The nylon wire supports were fixed to four threaded rods, which allow accurate vertical positioning of the flange. With this procedure, the lengthy laser alignment had to be carried out only at the beginning of the tests, whereas the shorter process of the flange positioning was repeated every time another pair of points on the flange surface had to be measured. The measurement grid in Fig. 14.4 was used for the scans, to keep the test time reasonably short, while at the same time providing an acceptable grid density.

The measurement system was setup for two complementary purposes: (i) the recording of the local behaviour of the flange, through two Polytec OFV-503 single-point sensor heads, and (ii) the global response of the structure, through a PCB Piezotronics 352B10 ICP accelerometer at the base of the flange. The LDVs, accelerometer, and shaker force gauge were connected to Data Physics' QUATTRO DAQ system to record all inputs simultaneously. The velocity signals from the lasers were integrated in Matlab to obtain the corresponding displacements.

The acceleration signal was also used to allow an amplitude-controlled measurement: the absolute acceleration was thereby kept constant to ensure that the amplitude-dependent nonlinear behaviour at the flange interface would be activated at the same level throughout the narrow frequency range around resonance. This approach leads to the same nonlinear energy dissipation for each frequency step, and provides a linearised measurement for a given response amplitude [13].

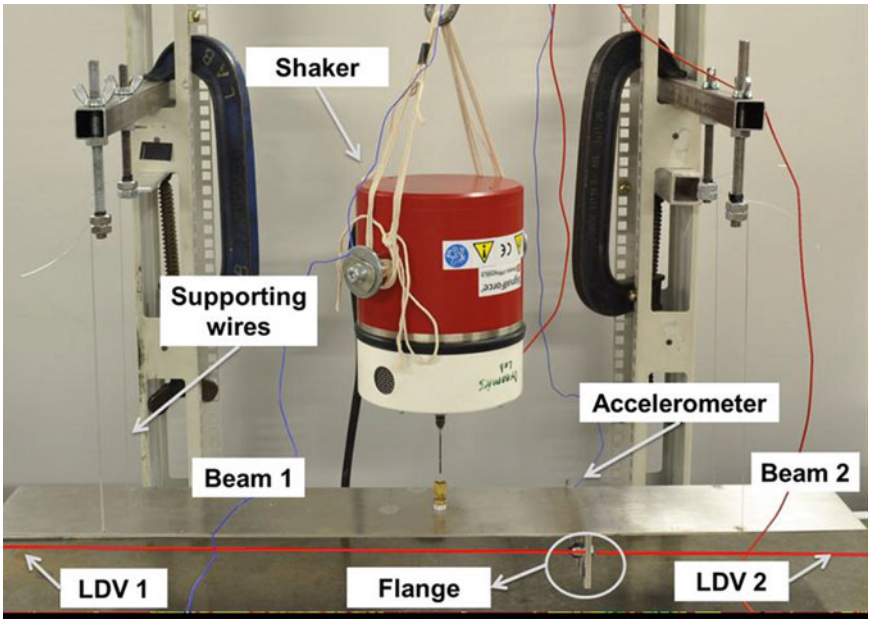

Fig. 14.3 Experimental set-up

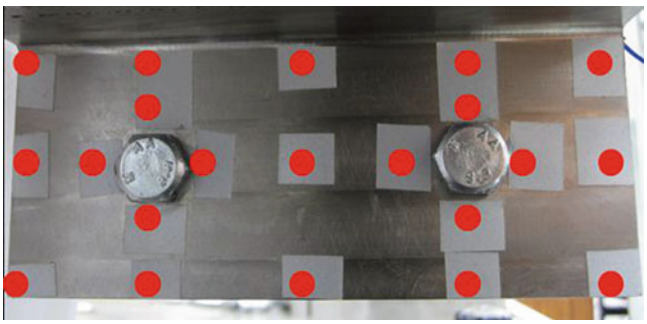

Fig. 14.4 Measurement grid

14.4 Measurement Simulation and Alignment

As previously described, the out-of-plane flange motion under study is one to two orders of magnitude lower than the transverse in-plane displacement due to the bending deformation of the beam. This implies that misalignment between the laser beams and the structure can distort the output signal by adding the unwanted in-plane components to the line-of-sight of the LDVs. The influence of alignment on the output data needed therefore to be evaluated [19, 20].

The laser beams can be misaligned both with respect to the flange, and to each other. It is necessary to consider two distinct pairs of alignment angles for each laser, so two Cartesian frames $O_i x_i y_i z_i (I = 1,\ 2)$, centred at the laser heads' positions, and corresponding to perfect alignment, are used as reference: ϑ_i is the angle formed with the x_i-axis by the projection of laser beam i onto the $x_i - z_i$ plane, and represents misalignment in the horizontal direction; φ_i is the angle formed by laser beam i with its projection onto the $x_i - z_i$ plane, thus representing the vertical misalignment parameter (Fig. 14.5).

The two angle pairs define two new Cartesian reference frames $Ox'_i y'_i z'_i$, in which the x'_i-axes coincide with the actual directions of the laser beams. Their orientations can be described by the multiplication of two pairs of rotation matrices, $R_{i\vartheta}$ and $R_{i\phi}$, defined as following:

$$R_{i\vartheta} = \begin{vmatrix} \cos\vartheta_i & 0 & -\sin\vartheta_i \\ 0 & 1 & 0 \\ \sin\vartheta_i & 0 & \cos\vartheta_i \end{vmatrix},$$

$$R_{i\phi} = \begin{vmatrix} \cos\phi_i & -\sin\phi_i & 0 \\ \sin\phi_i & \cos\phi_i & 0 \\ 0 & 0 & 1 \end{vmatrix}.$$

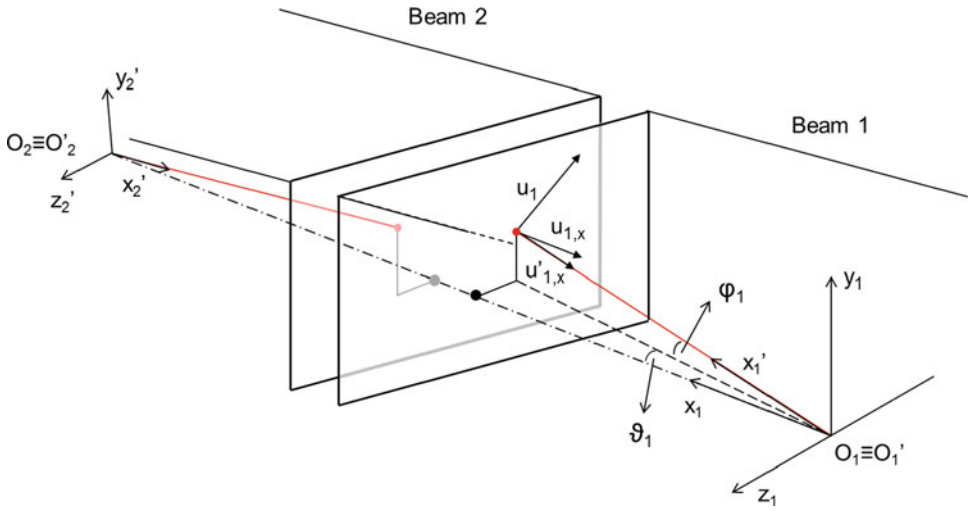

Fig. 14.5 Misalignment model

The projection $\boldsymbol{u}_i'$ of the total displacement vector $\boldsymbol{u}_i$ onto the $Ox_i'y_i'z_i'$ frame can then be obtained via the following equation, which can be further simplified making the assumption of small misalignment angles:

$$\boldsymbol{u}_i' = \boldsymbol{R}_{i\vartheta}\boldsymbol{R}_{i\phi}\boldsymbol{u}_i = \begin{vmatrix} \cos\vartheta_i\cos\phi_i & -\cos\vartheta_i\sin\phi_i & -\sin\vartheta_i \\ \sin\phi_i & \cos\phi_i & 0 \\ \sin\vartheta_i\cos\phi_i & -\sin\vartheta_i\sin\phi_i & \cos\vartheta_i \end{vmatrix} \boldsymbol{u}_i \approx \begin{vmatrix} 1 & -\phi_i & -\vartheta_i \\ \phi_i & 1 & 0 \\ \vartheta_i & 0 & 1 \end{vmatrix} \begin{vmatrix} u_{i,x} \\ u_{i,y} \\ u_{i,z} \end{vmatrix} = \begin{vmatrix} u_{i,x} - \phi_i u_{i,y} - \vartheta_i u_{i,z} \\ \phi_i u_{i,x} + u_{i,y} \\ \vartheta_i u_{i,x} + u_{i,z} \end{vmatrix}$$

Since the lasers can only record the component $u_{i,x}'$, the output signal is affected by the error component $-\phi_i u_{i,y} - \vartheta_i u_{i,z}$.

To evaluate the influence of the $u_{i,y}$ and $u_{i,z}$ on the measured response, a measurement simulation was carried out. The displacements obtained by a harmonic analysis of the FE model were used as input data, and different misalignment angles were imposed at the start of the simulation, thus fixing the measurement direction and the position of the effective measurement point in the global reference system. The transverse displacement of the flange adds another uncertainty, because the laser spot stays in the same position, while its corresponding point on the flange changes due to the vertical motion. During the simulation, this effect was also taken into account to ensure accurate results, and the associated error resulted to be less than 1 %. An error of 1° in φ_i can cause a difference between the true and measured value of the relative displacement of 50 %, because of the large displacement component $u_{i,y}$.The contribution from ϑ_i is practically negligible in the case of small misalignment errors, due to the limited lateral displacement $u_{i,z}$. The alignment of the system, and the reliability of the final results, therefore depends strongly on the minimisation of the vertical error φ_i, and in turn on an accurate parallel alignment of the flange to the reference table.

14.5 Measurement Results

The global and local response of the flange under varying excitation levels has been investigated. Global frequency response functions (FRFs) of the flange before and after the sanding process were obtained for the second bending mode. Different constant acceleration levels ranging from 2 to 100 $\mathrm{m/s^2}$ were used for the frequency sweeps. The constant amplitude control led to constant activation of the nonlinear mechanism in the flange, and in turn to linearised FRFs. Fig. 14.6a shows the transverse accelerance for the original and sanded flange. The original response increases by 9 % between 2 and 20 $\mathrm{m/s^2}$, and then decreases by 15 % from 20 to 100 $\mathrm{m/s^2}$. The peak frequency shows a very weak softening behaviour. The FRFs for the sanded flange at the same torque level follow a similar trend, except that the accelerance curves are shifted by 0.7 % relatively to the original frequency and the maximum amplitude is slightly lower.

Due to the linearization of the system via amplitude control, the linear modal analysis software ICATS could be used to extract the damping values for different acceleration levels. The maximum step adopted for the frequency sweeps was 0.05 Hz, which provided enough data for the damping extraction with the line-fit method [21]. The resulting loss factor curve of the original flange, shown in Fig. 14.6b, has a nearly parabolic trend, decreasing from a value of $\eta = 0.079\,\%$ at 2 $\mathrm{m/s^2}$ to a

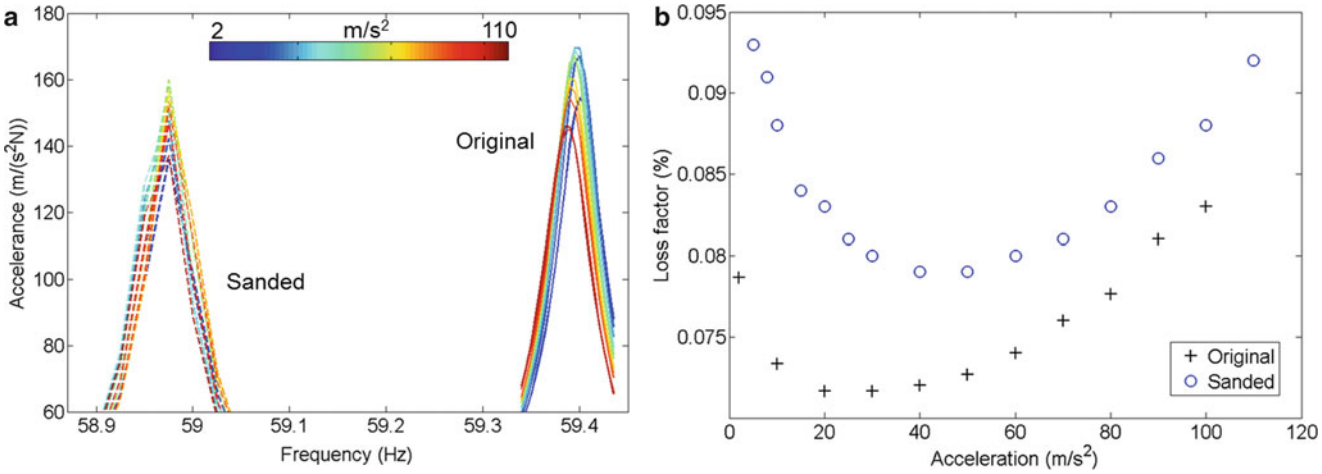

Fig. 14.6 FRFs of the original and sanded flange at different acceleration levels (**a**), and corresponding damping values (**b**)

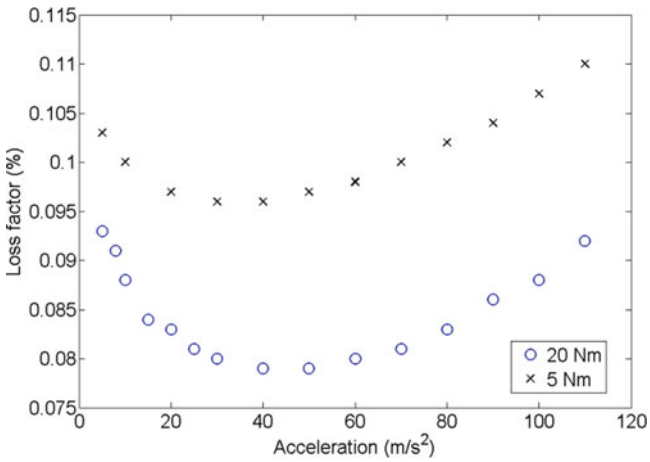

Fig. 14.7 Damping values for the sanded flange at 20 and 5 Nm of bolting torque

minimum of $\eta = 0.072\,\%$ between 20 and $30\,\mathrm{m/s^2}$, and rising back up to 0.085 % for higher accelerations. The loss factor curve for the sanded flange follows a similar trend, but with higher overall values.

The sanded flange was bolted at two torque levels—5 and 20 Nm—to investigate its influence on the nonlinear behaviour, due to the expected increase in friction at lower levels. The flange was torqued initially to 5 Nm, and the corresponding FRF measurements conducted before the torque was increased to 20 Nm without reassembly: the resulting difference in flange behaviour seen in Fig. 14.7 was thus only due to the different torque levels. The loss factors display the same trend as observed in Fig. 14.6b, but the lower torque value increases the minimum damping by 19 %, from $\eta = 0.079\,\%$ at 20 Nm to $\eta = 0.096\,\%$ at 5 Nm.

The local behaviour of the flange was monitored at the same time as the global, in order to obtain the displacement distribution on the flange. The displacements were obtained via software integration of the velocity signal from the lasers. The velocity signal was heavily affected by speckle noise, due to the significant motion in the direction perpendicular to the laser beams, but the very high frequency noise peaks were averaged out during integration. Any remaining spikes in the output displacements were eliminated by a Fourier low-pass filter implemented in Matlab.

Figure 14.8a shows the global response of the original flange, torqued at 20 Nm, and driven at $100\,\mathrm{m/s^2}$, at the maximum transverse displacement position, where the global motion is an oscillation in the direction arbitrarily chosen as negative. In Fig. 14.8b, after half a period, the flange pivots towards the positive one. The distance between the two outer flange surfaces (which is 5 mm) is not to scale, so that the micrometric displacements due to vibration can be visualised. A displacement gradient is clearly present in both cases, with minimum global out-of-plane motion at the base of the flange, where the flange is attached to the beams, and maximum at the free end.

More details can be seen by plotting the displacements of a horizontal cross-section of the flange. Figure 14.9 shows the displacements at the middle line of the flange, which passes through the bolt centres. Figure 14.9a corresponds to the point

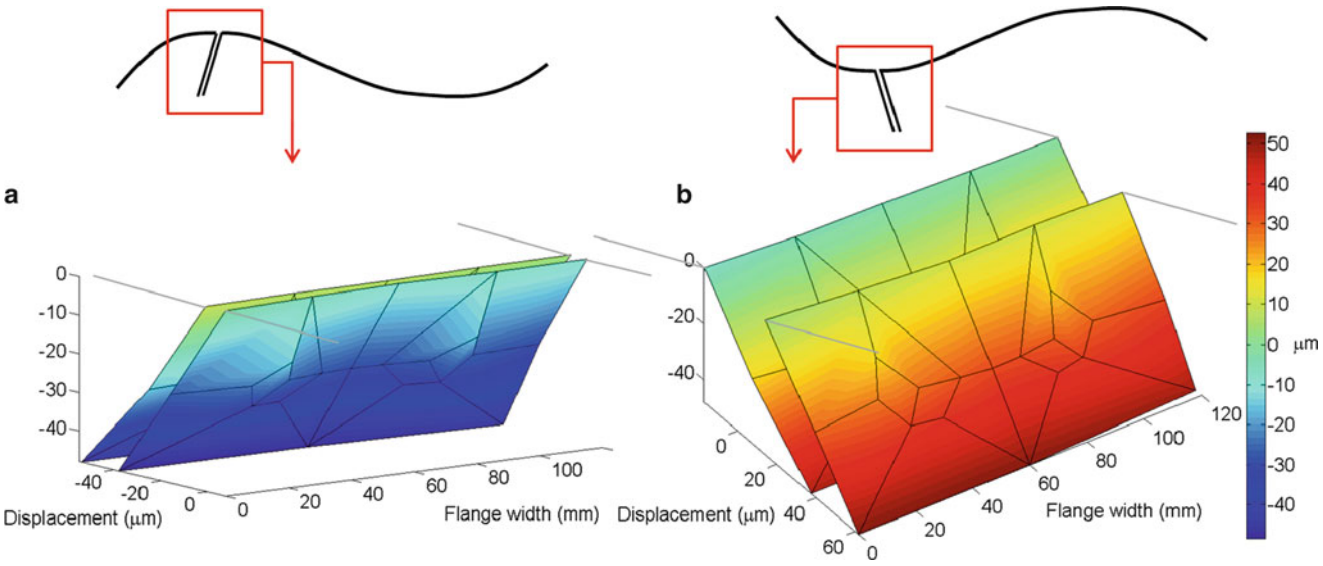

Fig. 14.8 Displacement map of the two flange members at two different points of the transverse global motion: maximum (**a**), and minimum (**b**)

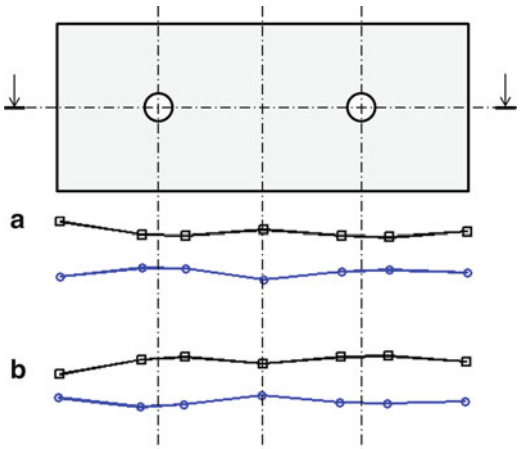

Fig. 14.9 Local displacements at the middle cross-section of the flange at the point of minimum (a) and maximum (b) transverse displacement

of maximum transverse displacement, Fig. 14.9b to its minimum. In both cases, it can be seen that the absolute displacement varies also along the width of the flange: the free ends and the middle point clearly display a cyclic vibration superposed onto the overall oscillation of the flange previously discussed, while the displacements at the points closer to the bolts are lower. It must be added that, since the initial position of each point on the flange interface was not known accurately due to the uncertainty in the interface geometry, all the displacements were plotted from the same zero baseline instead of their actual unknown position. In the case of Fig. 14.9b, this seems to lead to a penetration of the two contact surfaces at the edges and in the middle, where in reality most likely an initial gap conditions allows the free vibration of the points without closing the gap during the vibration cycle.

The relative displacements measured with the new technique can be used to visualize the conditions of separating and closing interfaces. To distinguish between the two, the relative displacements for all the grid points were multiplied by the sign of the relative velocity to take the direction of the relative displacement into account. The results were then interpolated and plotted on a meshed surface, as shown in Fig. 14.10: the negative displacement corresponds to a closing of the interface, while the positive to a separation.

Figure 14.10a displays the relative motion of the original flange. The maximum/minimum relative displacement is reached at the centre of the flange base, and it can be seen that there is a displacement gradient from the base to the top of the flange. Zones of low relative motion are located around the bolts: this non-zero displacement depends on the fact that the measurement points around the bolts were outside of the bolt pressure cones, so that a small relative displacements can be expected, especially considering the planarity errors due to manufacturing.

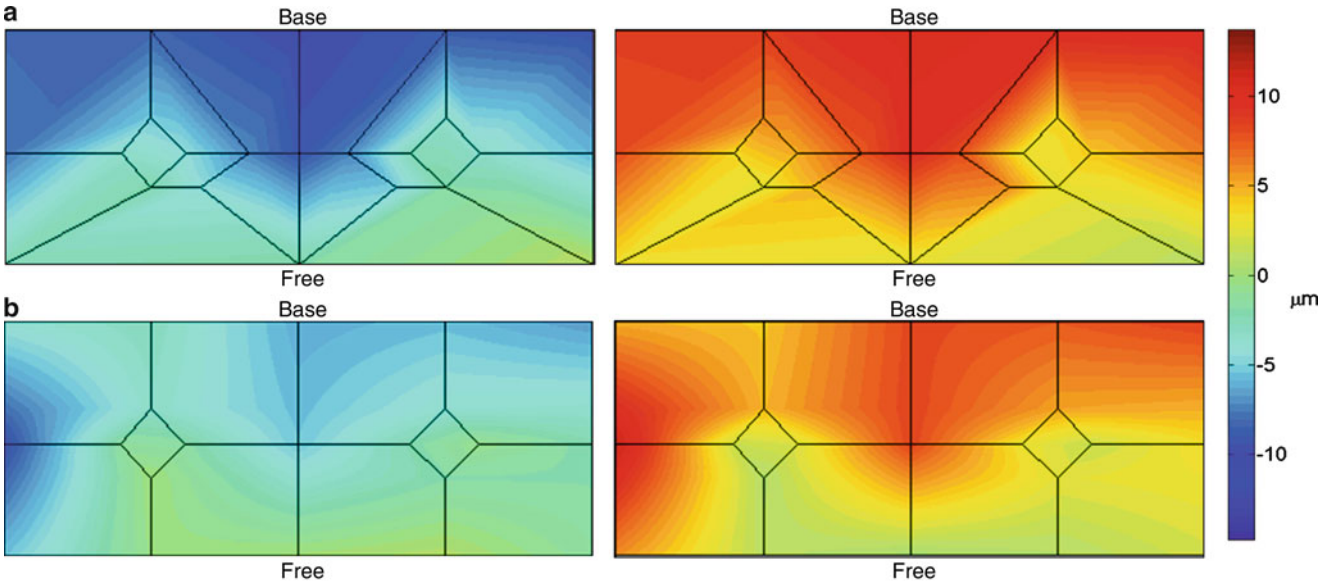

Fig. 14.10 Relative displacement maps of the original (**a**), and sanded (**b**) flange

The relative displacement maps for the sanded flange are reported in Fig. 14.10b. The overall level of motion appears lower than in the previous case: in particular, the relative displacements in the lower part of the flange look more uniformly close to zero. The main characteristics seen in the original flange are still present, with separation in the middle of the flange between the bolts, and maximum level of relative displacement at the base of the flange. A new feature is a localised spot of high relative motion on the left side of the flange.

14.6 Discussion

The global frequency response functions of the flange shows some consistent nonlinear behaviour for the investigated cases. On one hand, nearly no frequency shift could be observed for the two different contact conditions, the low and high torque level, and the different excitation amplitudes, indicating that the contact condition has only a minor influence on the stiffness of the investigated second bending mode. The amplitude behaviour and the directly related damping values, on the other hand, show some nonlinearity, which in turn indicates a change in the nonlinear contact conditions for different test cases.

A higher initial damping at low amplitudes, which may be due to some slip in areas of low contact pressure, is being reduced at increasing amplitude levels. This may indicate that initially slipping low-pressure contact areas start to separate at higher amplitudes, thereby reducing the amount of dissipated energy. At larger response amplitudes, previously stuck areas, close to the bolts or at the top and bottom of the flange, start to slip as well, increasing the level of energy dissipation once more, and leading to an increase in damping. The flattened flange shows more damping, which is an indication of a larger contact area on the flange, since more of the surfaces are now able to slip. A reduction in bolt torque leads to a reduced static contact pressure, and in turn to more slip of the contact zones and more damping in the system.

The novel measurement technique for the local nonlinear out-of-plane behaviour of the flange contact has led to the acquisition of the very small out-of-plane motion displacements, so that some clear indication about the flange vibration could be obtained. The absolute response of the two flanges in the out-of-plane direction highlighted the major motion of the flange, which was dictated by the global mode shape of the beams. Underlying this global motion was the relative local displacement between the two contact surfaces (see Fig. 14.10), which provided a good understanding of contact, separation and gap conditions.

Due to the originally convex shape of the flange, and the uncertainty in the flange geometry after sanding, the main detected motion was a free vibration of the flange surface due to the starting gaps at the contact interface. The largest relative motion occurred at the top of the flange about 10 mm below to the flange base. The relative vibration levels were significantly reduced at the free end of the flange, where a smaller bending moment caused limited relative displacement. High contact pressures close to the bolts also prevented the flange from separating, and led to more or less continuous contact in that area.

The area between the two bolts showed separation, meaning that the contact pressure underneath the bolts did not extend into this area. The symmetry of the relative displacement also suggests that some permanent gap was present.

A significant change in the nonlinear mechanism could also be observed between the strongly convex original and the flatter sanded flange. An increase in the area of very low relative vibration indicates the improved flatness of the flange, and supports the earlier explanation of larger possible slip areas for an increase in damping. The measurement results of the relative displacement also give an indication of the quality of the sanding procedure, since it shows some asymmetry in the local relative displacement. The left side has significantly more motion than the right, which means that the right side must have a flatter surface.

Based on these observations, it can be concluded that the developed measurement technique is able to pick up the relative out-of-plane motion of the two flange surfaces, and it can therefore be used to provide local data for nonlinear model validation. A nonlinear analysis is currently being conducted to validate the developed approach: the initial results seem to be confirming some of the findings of this research, but a detailed discussion is outside the scope of this work, and will be presented in the future.

14.7 Conclusions

The validation of the local nonlinear contact behaviour of bolted flange joints during a vibration cycle requires information about contact, contact separation, and permanent gaps in the out-of-plane direction. For this purpose a novel measurement technique has been developed. Two accurately aligned LDVs monitor the flange behaviour during vibration, and from the measured data the local relative out-of-plane contact motion of the flange can be derived. Global FRF measurements of two flange geometries at different excitation levels and bolt torques have shown a nonlinear response and an interesting change in damping behaviour. Full field scans of the flange surface highlighted the underlying change in the nonlinear mechanism between the original convex and modified flatter flange. An observed increase in contact area at the flange and a transition to more localised relative motion was identified as the main source of an increase in the damping of the flattened flange. Low levels of relative motion around the flange holes, and a clear distinction of gaps on the surface, showed the overall flange motion, and can provide validation data for future nonlinear analysis.

Acknowledgements The authors are grateful to Rolls-Royce Plc. and Campusworld/Università Politecnica delle Marche for providing the financial support for this work.

References

1. Petrov EP, Ewins DJ (2004) Generic friction models for time-domain vibration analysis of bladed disks. Trans ASME J Turbomach 126(1):184–92
2. Petrov EP, Ewins DJ (2002) Analytical formulation of friction interface elements for analysis of nonlinear multiharmonic vibrations of bladed discs. ASME J Turbomach 125:364–371.
3. Zucca S, Firrone CM, Gola MM (2012) Numerical assessment of friction damping at turbine blade root joints by simultaneous calculation of the static and dynamic contact loads. Nonlinear Dyn 67(3):1943–1955.
4. Firrone CM, Zucca S, Gola M (2009) Effect of static/dynamic coupling on the forced response of turbine bladed disks with underplatform dampers. In: Proceedings of the ASME turbo expo, 8–12 June 2009, Orlando, FL, USA, GT2009–59905
5. Cigeroglu E, An N, Menq CH (2007) Wedge damper modeling and forced response prediction of frictionally constrained blades. In: Proceedings of the ASME turbo expo, 14–17 May 2007, Montreal, Canada, GT2007–27963
6. Petrov EP (2008) Explicit finite element models of friction dampers in forced response analysis of bladed disks. J Eng Gas Turbines Power 130(2):022502
7. Charleux D, Gibert C, Thouverez F, Dupeux J (2006) Numerical and experimental study of friction damping in blade attachments of rotating bladed disks. Int J Rotat Mach Article ID 71302: 1–13
8. Petrov EP, Ewins DJ (2006) Effects of damping and varying contact area at blade-disc joints in forced response analysis of bladed disc assemblies. ASME J Turbomach 128:403–410
9. Chen JJ, Menq CH (2001) Prediction of periodic response of blades having 3D nonlinear shroud constraints. ASME J Eng Gas Turbines Power 123:901–909
10. Petrov EP (2004) A method for use of cyclic symmetry properties in analysis of nonlinear multiharmonic vibrations of bladed discs. Trans ASME J of Turbomach 126:175–183.
11. Kerschen G, Worden K, Vakakis AF, Golinval JC (2006) Past, present and future of nonlinear system identification in structural dynamics. Mech Syst Signal Process 20(3):505–592
12. Ma X, Bergman L, Vakakis A (2001) Identification of bolted joints through laser vibrometry. J Sound Vib 246(3):441–460

13. Perinpanayagam S, Robb D, Ewins DJ, Barragan JM (2004) Non-linearities in an aero-engine structure: from test to design. In: Proceedings of the 2004 international conference on noise and vibration engineering, ISMA, Leuven, Belgium, pp 3167–3181
14. Salles L, Blanc L, Thouverez F, Gouskov AM (2011) Dynamic analysis of fretting-wear in friction contact interfaces. Int J Solids Struct 48(10):1513–24
15. Schwingshackl CW, Petrov EP (2012) Modelling of flange joints for the nonlinear dynamic analysis of gas turbine engine casings. In: Proceedings of the ASME turbo expo, Copenhagen, Denmark, 11–15 June 2012, GT2012–69281
16. Gola MM, Braga dos Santos M, Tong L (2012) Measurement of the scatter of underplatform damper hysteresis cycle: experimental approach. In: Proceedings of the ASME 2012 international design engineering technical conferences & computers and information in engineering conference, Chicago, IL, USA, 12–15 August 2012
17. Pau M, Baldi A, Leban B (2008) Visualization of contact areas in bolted joints using ultrasonic waves. Exp Tech 32(4):49–53
18. Boeswald M, Link M (2003) Experimental and analytical investigations of non-linear cylindrical casing joints using base excitation testing. In: Proceedings of international modal analysis conference 2003, IMAC XXI, Kissimmee, FL
19. Schwingshackl CW, Massei L, Zang C, Ewins DJ (2010) A constant scanning LDV technique for cylindrical structures: simulation and measurement. Mech Syst Signal Process 24(2):394–405
20. Halkon BJ, Rothberg SJ (2006) Vibration measurements using continuous scanning laser vibrometry: Advanced aspects in rotor applications. Mech Syst Signal Process 20(6):1286–99
21. Ewins DJ (2000) Modal testing: theory, practice, and application, 2nd edn. Research Studies Press, Baldock, Hertfordshire/Philadelphia

Chapter 15
Experimental Study of Joint Linearity

Brandon R. Zwink and Laura D. Jacobs-Omalley

Abstract Joints in finite element models (FEMs) are often either ignored or simplified using linear assumptions. When experimental modal analysis is performed to validate the accuracy of FEMs, the experiments are usually performed at low excitation energies to minimize excitation of nonlinear properties within a structure. When finite element models are calibrated to low excitation level modal tests, they may not be suited for predicting high excitation level environments. This study was conducted to determine, for a particular set of hardware, how results from a low excitation level modal test compare to results for a high excitation level modal test. A set of simplified hardware, in which cones are connected through a threaded joint, was developed for this study and was subjected to random excitations as well as controlled-force step-sine testing to investigate the effects of joint linearity across different excitation levels. The goal of this work is to obtain a point of reference for how much error would be associated with a FEM, calibrated to low excitation level modal data, if the FEM was used to predict responses at a higher excitation level. Using this information, it can be determined if a linear FEM is appropriate for predicting responses or if nonlinearities need to be incorporated into the model.

Keywords Nonlinear • Joint • Experimental • Step-sine • Modal

15.1 Introduction

Typical modal parameter estimation for experimental systems involves the assumption that the system behaves as a linear system. Most structural dynamic finite element models (FEMs) are limited to linear properties. Therefore, in modal analysis, the system being studied is typically assumed to behave in a linear fashion or measures are taken to reduce nonlinearity by reducing rattling, tightening joints, re-designing the test setup, or reducing the excitation energy. One such method of obtaining a good linear estimate of a nonlinear system is to excite the system using a low-level random excitation spectrum. For a random excitation, the nonlinear component of the response is treated as noise and mitigated by averaging. As systems are excited to higher energy levels, the nonlinear effects of the system usually become more pronounced. Therefore, very low-level excitations are typically utilized when performing a modal test to obtain a linear estimate of the system. This linear estimate of the experimental system is then used to validate a linear finite element model. The validated finite element model is then used to predict system responses at much higher energy levels than what was used in modal testing. This assumption would be valid for systems that continue to behave linearly at large excitation energies, however for systems with significant joints, this assumption is questionable. The purpose of this paper is to investigate the validity of these assumptions for a single mode in a real system with multiple joints. The purpose of this paper is to perform a high level test that represents the in-use environment for a structure and compare to results from a low level modal test to this "truth" data for the purpose of FEM validation.

B.R. Zwink (✉) • L.D. Jacobs-Omalley, PhD
Sandia National Laboratories, P.O. Box 5800 MS 0557, Albuquerque, NM 87185-0557, USA
e-mail: bzwink@sandia.gov; ldjacob@sandia.gov

G. Kerschen et al. (eds.), *Topics in Nonlinear Dynamics, Volume 1: Proceedings of the 31st IMAC, A Conference on Structural Dynamics, 2013*, Conference Proceedings of the Society for Experimental Mechanics Series 35,
DOI 10.1007/978-1-4614-6570-6_15,

15.2 Test Setup

The hardware selected for this study was a subset of the MACE hardware, which was developed to facilitate dynamics studies on a simple structure that can be considered representative of more complex systems. The hardware consisted of three aluminum pieces, the body, the case, and the collar. Depictions of the three pieces of hardware along with measurement locations on the hardware are shown in Fig. 15.1.

When assembled, the system used for this study comprises three joints, a threaded joint between the collar and body, a preloaded joint between the collar and case, and a preloaded joint between the case and body. A depiction of the three assembled components with labeled joints is shown in Fig. 15.2. The hardware was assembled by applying a torque of 20 ftlbf, using a spanner wrench, to the collar while applying a reaction force on the case using a strap wrench. During preliminary testing, it was discovered that the joint dynamics were not repeatable do to the properties of the joint changing throughout the test sequences. To overcome these difficulties, the system was lightly tapped with a rubber mallet while the torque was applied to ensure the joints didn't bind up prematurely due to misalignment of the three components.

Instrumentation locations on the hardware were chosen to clearly show the dynamics of the joints in question and allow for extraction of mode shapes that exercise the dynamics of the joint most effectively. The instrumentation consisted of both uni-axial and bi-axial accelerometer configurations as shown in Fig. 15.1.

The hardware was hung from bungee cords to approximate free-free boundary conditions as shown in Fig. 15.3. A MB Dynamics Modal 50 modal shaker was attached to the system using a 1" stinger to provide excitation forces without transmitting significant moment through the force gauge measuring the excitation force.

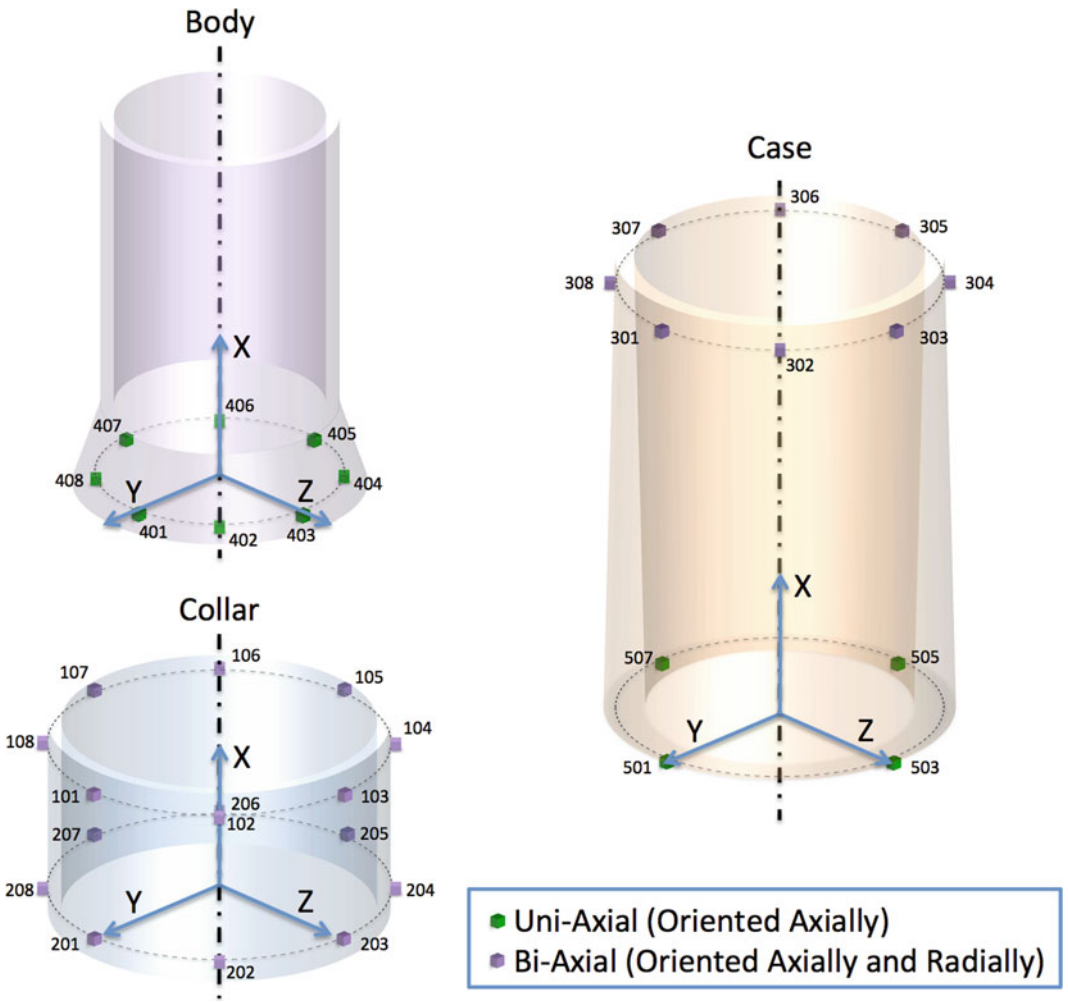

Fig. 15.1 Hardware and instrumentation for joint study

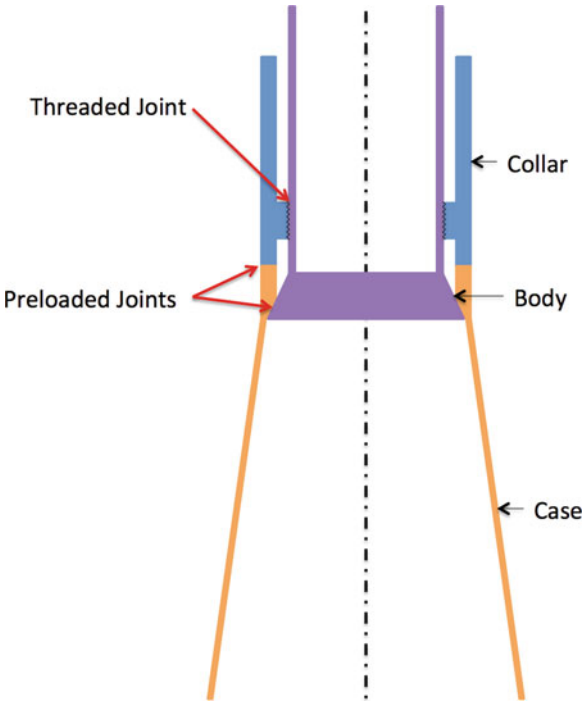

Fig. 15.2 Assembled joint study hardware

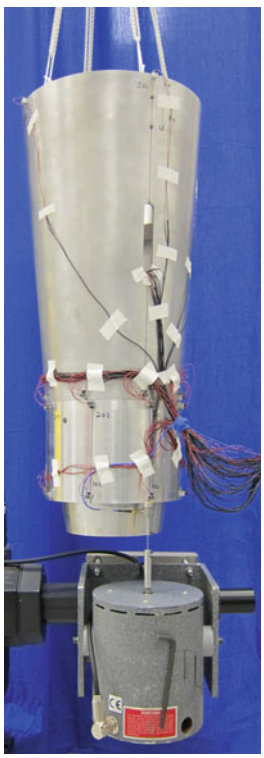

Fig. 15.3 Joint study hardware with instrumentation and shaker

15.3 Excitation Methods

The system was first studied using a low level random excitation. The low level random excitation was representative of the test that would typically be performed on this structure to validate a linear finite element model. After analyzing the mode shapes, a single mode shape was selected for study to limit the scope of this study to fit the constraints of the project. The mode shape that was selected for investigation was one of the first bending modes of the system because it was relatively isolated from other modes in the system and because it exercised the joints in the system effectively. A depiction of the

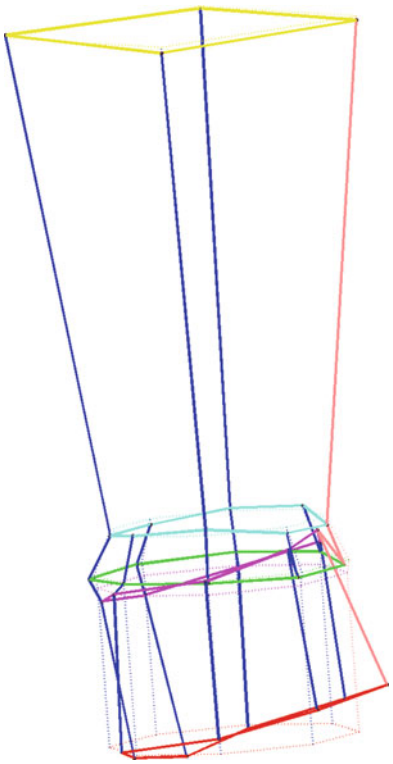

Fig. 15.4 Selected mode shape for investigation

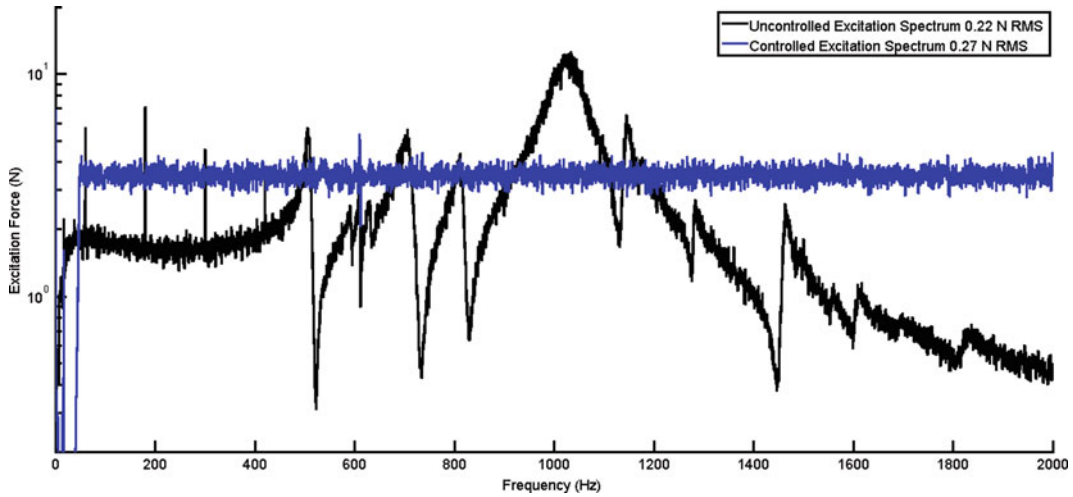

Fig. 15.5 Force spectra for uncontrolled white noise and controlled white noise excitation

mode shape is given in Fig. 15.4. The mode shape appears to be the first bending mode of the full system. The majority of the mode shape movement stems from the preloaded joint between the collar and case compressing on one side while decompressing on the opposite side of the structure. This mode shape is ideal for this study because it is often important for FEMs to accurately predict the first bending mode of a system and this system has considerable joint effects present in it's first bending mode.

In order to experimentally test how well the hardware in question maintains linear properties at different excitation energies, the system was excited at different excitation energies using a variety of excitation techniques. One excitation technique was to excite the system with a random spectrum generated by creating a white noise signal with a specified root-mean-squared (RMS) force level over the desired frequency range. Because the resulting force spectrum is dependent on properties of the system, the shaker, and the amplifier, the system was also excited using a closed loop feedback controller to provide an excitation voltage that resulted in a flat force excitation spectrum. Both the controlled and uncontrolled excitation spectra for similar excitation levels are shown in Fig. 15.5. Because an uncontrolled force spectrum produces very little

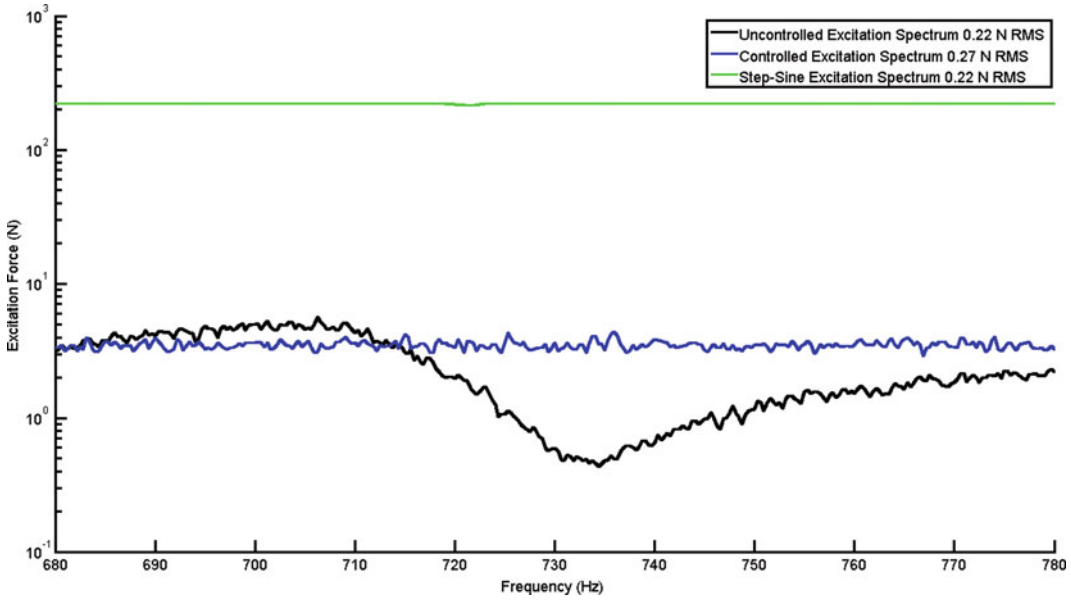

Fig. 15.6 Force spectra for uncontrolled white noise, controlled white noise, and step sine excitation

excitation at resonances it was thought that a controlled excitation would provide a much more accurate means of comparing different excitation levels at resonance.

The third excitation method used was a closed-loop feedback controller to provide a constant force step-sine excitation. The step sine excitation method was chosen because it provided the means to put a relatively large amount of excitation energy into each spectral line, one at a time. The excitation spectrum for step-sine testing is shown along with the two white noise excitation methods, over the frequency range of the mode of vibration chosen for investigation in Fig. 15.6. Even though all three RMS levels are similar, the force spectra are quite different. The step sine testing provides a much higher overall excitation level due to the fact that all excitation energy is concentrated into one spectral line at a time.

15.4 Results

The system was first excited using an uncontrolled force spectrum, similar to the one shown in Fig. 15.5, at six different force levels. The lowest excitation was chosen to be slightly above the noise level observed on the measurements. It was observed, through previous testing, that the characteristics of the joint were changing as the joint was tested. For this reason, the testing started with the lowest excitation level, stepped up to the highest excitation level, and then stepped back down to the lowest excitation level to ensure the system did not significantly change during testing. The driving point FRFs for the uncontrolled excitations are shown in Fig. 15.7.

Similarly, a set of data was collected on the same system using a flat force excitation spectrum similar to the one shown in Fig. 15.5. Again, the testing started with the lowest excitation level, stepped up to the highest excitation level, and then stepped back down to the lowest excitation level to ensure the system did not significantly change during testing. The driving point FRFs for the uncontrolled excitations are shown in Fig. 15.8.

It was observed in the data for both the uncontrolled and controlled excitation FRFs that as the excitation level increased, the natural frequency of the bending mode decreased and the damping increased. This result indicates that the stiffness of the joint decreases as it is exercised more. The apparent increase in damping was typical as this is often observed for nonlinear systems. As the joint was excited to higher energy levels, more energy was dissipated through joint friction causing an increase in damping. Additionally, it was observed by comparing Figs. 15.7 and 15.8 that the result was not greatly affected by using a controlled excitation spectrum as opposed to an uncontrolled excitation spectrum. Using a controlled excitation spectrum did not result in larger observable effects of nonlinearities as compared to an uncontrolled excitation spectrum for this set of data.

In addition to comparing FRFs for the test data, the coherence functions were also compared and are shown in Fig. 15.9 for the controlled white noise excitation. It was observed that an increase in excitation level resulted in a drop in coherence.

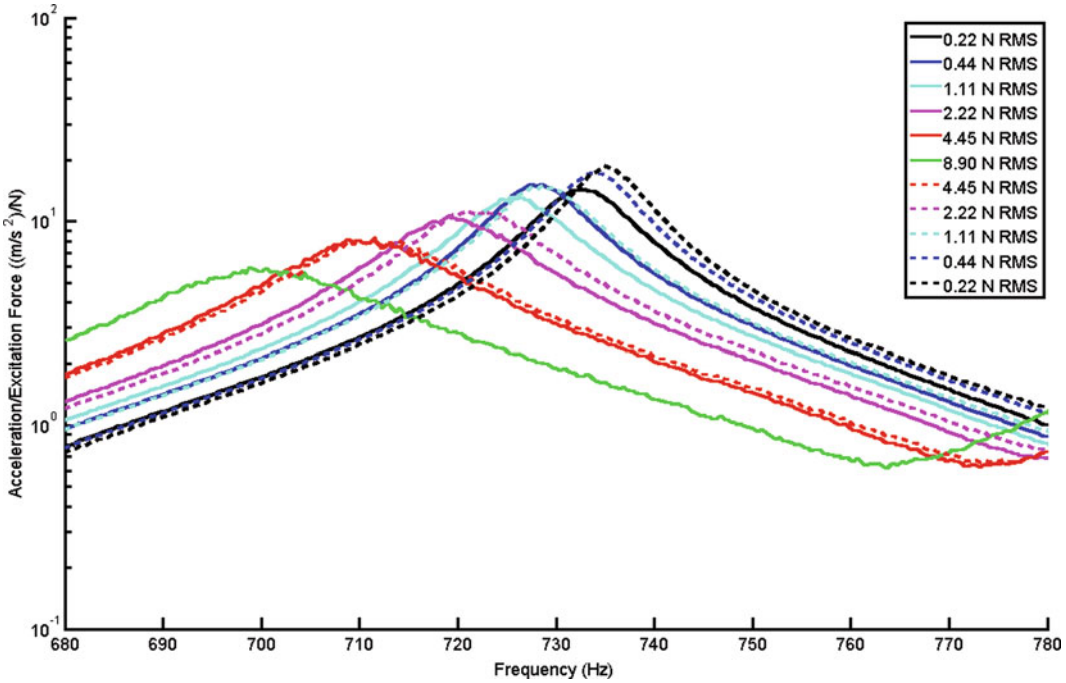

Fig. 15.7 Driving point FRFs uncontrolled white noise excitation

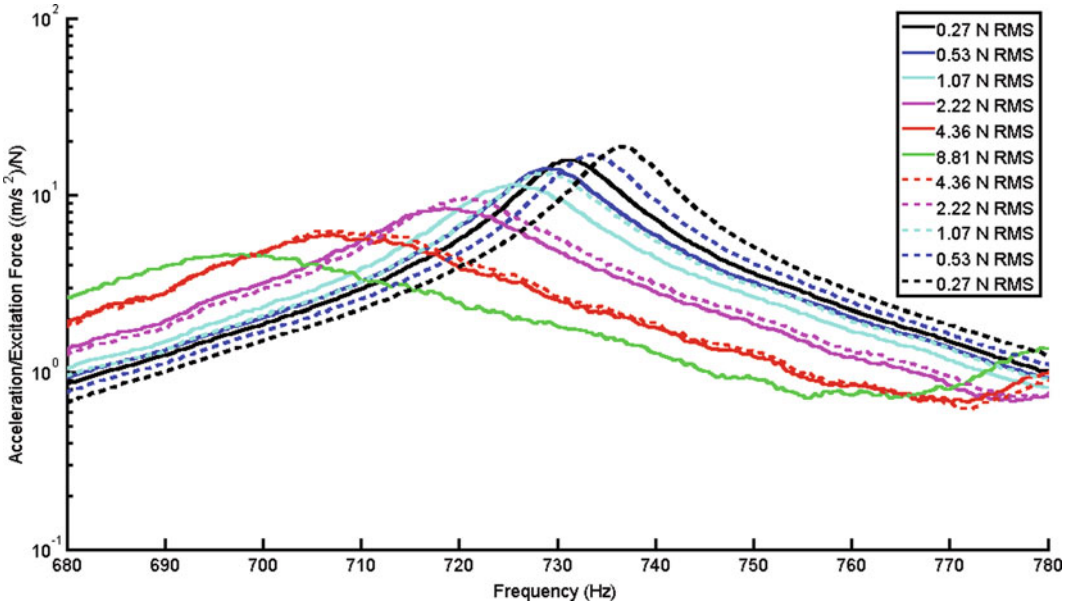

Fig. 15.8 Driving point FRF for controlled white noise excitation

This result was expected because coherence is, as described by Davies [1], is "the fraction of output power attributed to linear operations on the input". Because the nonlinear properties of the system are more prevalent for larger excitation forces, the coherence drops when the system is excited to higher energy levels.

The random excitation spectra, result in a low level "linear estimate" of the characteristics of the nonlinear system. It was therefore desirable to estimate FRFs from experimental data that is more representative of the high level environments that the system will be subjected to in order to determine how different the FRFs were from the "linear estimates" obtained through random testing. The excitation method selected for this testing was a controlled force step-sine test method. For this testing, the system was excited at one frequency at a time, allowing at least two seconds for the transient response to decay, then data was collected, the system would then step to the next excitation frequency, and the same process would then be

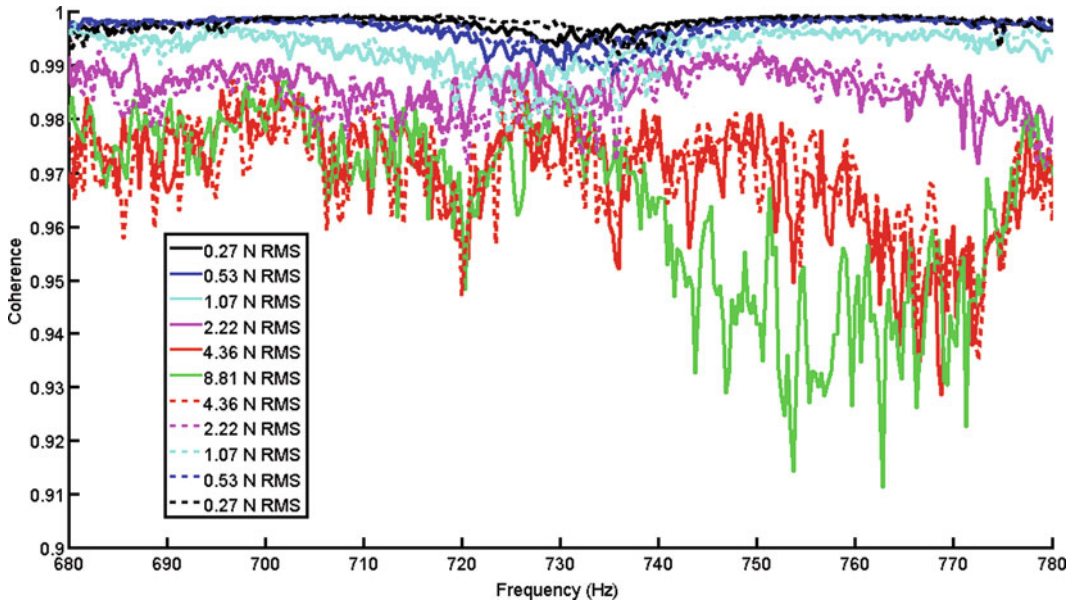

Fig. 15.9 Driving point coherence for controlled white noise excitation

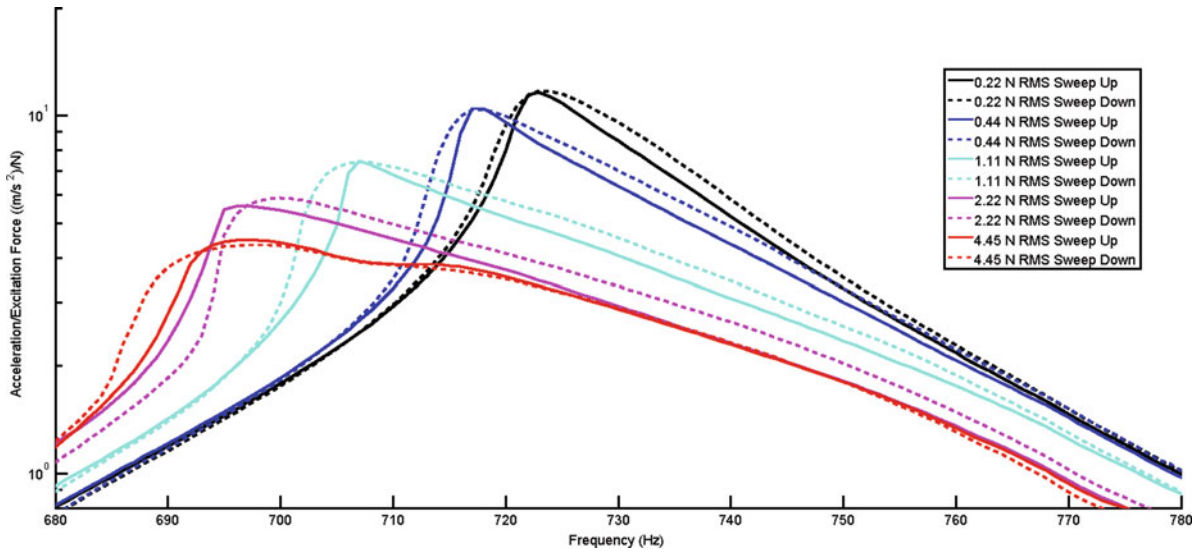

Fig. 15.10 Driving point FRFs for step-sine excitation

repeated. Unlike linear systems, nonlinear systems can have multiple points of equilibrium for a given frequency of response based on the original state of the system. For this reason, the step-sine excitation was executed both going up in frequency and going down in frequency to observe if there would be a difference in the two FRFs, which would indicate nonlinearity. The driving point FRFs for this test method are shown in Fig. 15.10.

It was observed that there was a difference in FRFs between stepping up in frequency and stepping down in frequency. This difference is likely due to the nonlinear system creating multiple equilibrium conditions for each frequency based on the past state of the system. The data showed that as force increased, the FRF began to lean to the left to an increasing degree. This is indicative of a nonlinear softening stiffness. Additionally, because damping increases as excitation level increases, there must also be nonlinear damping properties present in the joints as well.

The relationship between excitation force and estimated natural frequency of the first bending mode being studied is shown in Fig. 15.11. The parameter estimation for the random excitation data was completed using a real normal modes approximation, which fit the data well. The step-sine data was fit using both a real normal modes as well as a complex modes approximation. Because the high-level step sine data was more affected by nonlinearities present in the system, the linear fits to the data were poor.

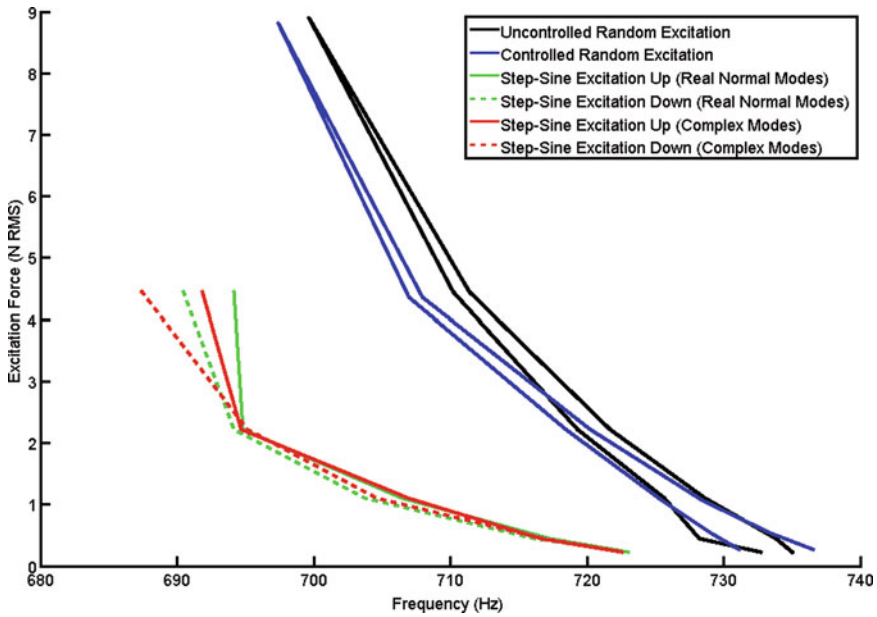

Fig. 15.11 Frequency vs. excitation force

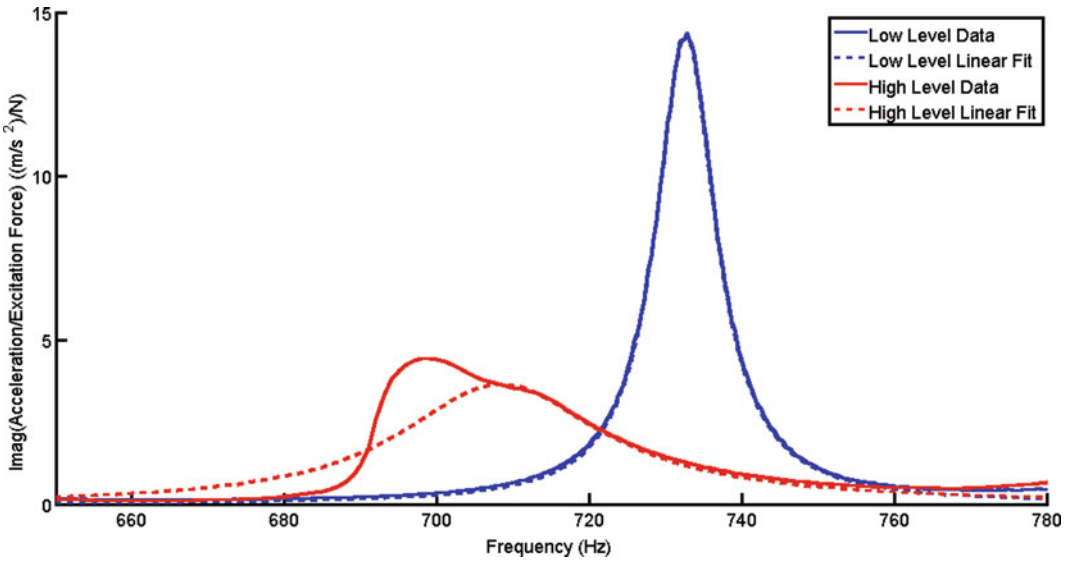

Fig. 15.12 Imaginary driving point FRF for low level and high level data with real normal modes fit

There are many methods that have been studied to attempt to determine how to model the nonlinearities in a system as reviewed by Adams and Allemang [2]. However, if the goal of the fit is to produce a correlated linear FEM, it is the author's opinion that the best approach, when possible, is to obtain the best real normal modes approximation to the nonlinear data because the FEM typically can only model real normal modes. For this reason, a comparison was done between the best real normal modes fit of the low level random excitation data and the best real normal modes fit of the highest level step-sine data to determine how much potential error would be incorporated into a FEM.

The imaginary part of the driving point FRFs are shown in Fig. 15.12 along with the re-synthesized FRFs from the real normal modes fits of the data. Similarly, the real part of the driving point FRFs are shown in Fig. 15.13 also with the re-synthesized FRFs from the real normal modes fits of the data. The real normal modes fit of the low level data was a good approximation. This is because for low-level excitations, the nonlinear effects of the joint are not excited well. The real normal modes approximation of the step-sine data was much worse, but if the goal is to use a linear FEM, it is the most representative response that the model will be able to predict at those particular excitation levels.

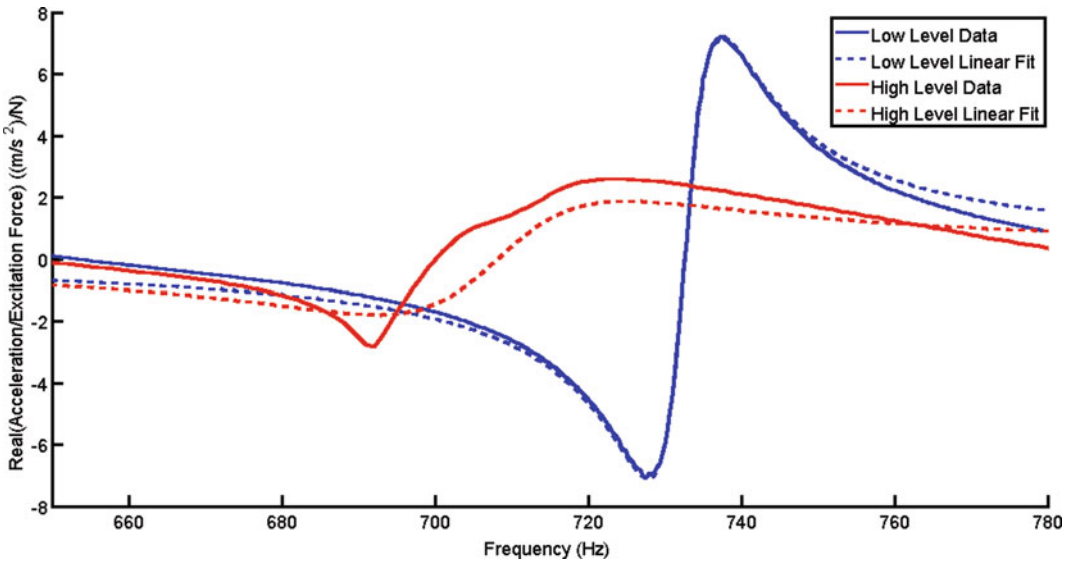

Fig. 15.13 Real driving point FRF for low level and high level data with real normal modes fit

Table 15.1 Low level and high level frequency and damping estimates

–	Frequency (Hz)	Damping (% Crit)
Low excitation level fit	732.6	0.66
High excitation level fit (truth)	708.2	2.30
Error (%)	3.5	−71.5

The frequency error between the best real normal modes fit of the lowest level random data and the best real normal modes fit of the highest level excitation data was 3.5% and the damping error was -71.5% as shown in Table 15.1. Because there is often more than 3.5% error in the frequency predictions of a FEM and a modal test, the error between the high level modal test frequency predictions and the low level modal test frequency predictions is relatively small. However the error in the damping estimate was significant. Because of the error in the damping estimate, the magnitude of the response prediction for this mode, of a FEM calibrated to the low excitation level data, would have been about 3.2 times higher than the response that was actually observed when the structure was excited at the higher excitation level.

15.5 Conclusions

Typically in FEM validation, modal frequencies of the FEM are considered adequate if they are within 5% of the experimental modal frequencies. It was observed that for the spectrum of excitation levels studied in this test, the error in modal frequency estimation was less than typical acceptance criteria at only 3.5%. Therefore, if the FEM for this system were calibrated using typical modal testing methods, the estimated frequency predicted by the FEM for this particular mode of vibration, would still be reasonably accurate even when trying to predict large excitation responses. However, it was observed that the damping estimate that would have been associated with this mode of vibration was 71.5% different at low excitation levels when compared to high excitation levels and would have resulted in a FEM response prediction 3.2 times higher than what was observed at high excitation levels.

The method for validating a model of a system depends on a variety of factors such as how accurate the model needs to be, what resources are available to develop the model, what resources are available to validate the model, and the range of excitation levels and frequencies for which the model will be used. Due to the very large cost of developing nonlinear models for complex systems and validating those models at multiple excitation energies, linear models and linear assumptions can produce fairly accurate estimates even for nonlinear systems as long as the assumptions involved are understood and accounted for. For systems such as this one, if the conservatism of, underestimating damping values, is acceptable, a FEM correlated to low-level modal parameters is useful. If the conservatism needs to be reduced, one may attempt higher-level

excitation experiments and obtain less conservative damping estimates. If the accuracy of the previous method is still not high enough, a nonlinear model must be developed and other parameter estimation methods, such as those discussed by Adams and Allemang [2], for nonlinear systems will need to be applied to identify how to best model the particular nonlinearity in question.

References

1. Davies P (2008) Course notes for ME 597, Purdue University, Fall
2. Adams DE, Allemang RJ (1998) Survey of nonlinear detection and identification techniques for experimental vibrations. In: 23rd conference of the international society of modal analysis, Belgium, Sept 1998

Chapter 16
Nonlinear Modal Decomposition Using Normal Form Transformations

Simon A. Neild, Andrea Cammarano, and David J. Wagg

Abstract In this paper we discuss a technique for decomposing multi-degree-of-freedom weakly nonlinear systems into a simpler form. This type of decomposition technique is an established cornerstone of linear modal analysis. Extending this type of technique to nonlinear multi-degree-of-freedom systems has been an important area of research in recent years. The key result in this work is that a theoretical transformation process is used to reveal both the linear and nonlinear system resonances. For each resonance, the parameters which characterise the backbone curves and higher harmonic components of the response, can be obtained. The underlying mathematical technique is based on a near identity normal form transformation for systems of equations written in second-order form. This is a natural approach for structural dynamics where the governing equations of motion are written in this form as standard practice. The example is a system with cubic nonlinearities, and shows how the transformed equations can be used to obtain a time independent representation of the system response. It is shown that when the natural frequencies are close to an integer multiple of each other, the backbone curve bifurcates. Examples of the predicted responses are compared to time-stepping simulations to demonstrate the accuracy of the technique.

Keywords Normal form • Resonances • Backbone curves • Nonlinear • Multi-degree-of-freedom

16.1 Introduction

The concept of normal modes of vibration is fundamental to the analysis of linear multi degree-of-freedom systems, with each mode relating to a physical configuration of the system and a natural frequency. For linear systems, the governing equations of motion can be decomposed into a modal model by applying a linear modal transform. This results in a modal model of the system consisting of a series of independent oscillators that capture the complete system behaviour via superposition of the modal responses. The ability to create a modal from a structural model is key to the experimental identification of dynamic properties known as modal testing [1] and model updating [2]. While a linear model can capture the key characteristics of many systems, nonlinear behaviour is encountered in a large number of applications, such as structures that exhibit large deflections resulting in geometric nonlinearities.

The idea of using a modal approach to analysing the behaviour of nonlinear systems has many challenges. The concept of nonlinear normal modes was introduced in the 1960s by Rosenberg [3] and many researchers have pursued this idea—see for example [4–6, 17, 18] and references therein.

In this paper we consider a different approach, in that rather than looking to define modes, we attempt to decompose the nonlinear system into its simplest (aka normal) form. In the context of multi degree-of-freedom nonlinear structural systems, "simplest form" means elimination of as many cross-coupling and nonlinear terms as possible. In fact the method we use will find this simplified form and also includes expressions for the modeshapes as a by product of the process as well.

The method of normal forms has a long history (see [7] for example), and involves applying transformations to the governing equations of motion with the aim of finding a simplified form. Detailed discussions on the theory of normal forms are given in [8, 9] among others. Of particular interest here is the application of normal forms to find periodic steady-state

S.A. Neild (✉) • A. Cammarano • D.J. Wagg
Department of Mechanical Engineering, University of Bristol, Queens Building,
University Walk, Bristol, BS8 1TR, UK
e-mail: simon.neild@bristol.ac.uk; Andrea.cammarano@bristol.ac.uk; david.wagg@bristol.ac.uk

G. Kerschen et al. (eds.), *Topics in Nonlinear Dynamics, Volume 1: Proceedings of the 31st IMAC, A Conference on Structural Dynamics, 2013*, Conference Proceedings of the Society for Experimental Mechanics Series 35,
DOI 10.1007/978-1-4614-6570-6_16,

system response solutions, as considered by Jézéquel and Lamarque [10] and Nayfeh [11]. Potential advantages of using normal forms over other perturbation techniques for this type of problem include the ease in which it can be extended to consider multi-degree-of-freedom systems and non-autonomous systems [12] and its suitability for analysis using symbolic manipulation programs [13]. Relating to nonlinear normal modes, Jézéquel and Lamarque [10] considered a multi-mode system using normal forms. Touzé et al. [14] linked the near-identity transform, which provides an asymptotic non-linear change of coordinates for the system, to the normal modes of the system.

The normal form transformation is normally applied to dynamic equations expressed in their state-space, or first-order differential equation, form. Recently a method of applying the normal form technique directly to second-order nonlinear oscillators has been reported [15, 16, 20]. As linear modal analysis is based on second-order differential equation representation of the equations of motion, this second-order normal form technique has potential to provide a more natural nonlinear extension to the linear problem. Here, we use the second-order normal form technique to find the backbone curves for a two degree-of-freedom system.

We present results for a two degree-of-freedom system with cubic spring nonlinearities. The backbone curves are found using the second-order normal form technique and it is shown that when the natural frequencies are close to an integer multiple of each other, one of the backbone curves bifurcates. The curves are obtained by considering the initial conditions which results in one of four types of modeshape for the system. Examples of the resulting motion from a selection of the initial conditions are also shown. These predicted responses are compared to time-stepping simulations to demonstrate the accuracy of the technique.

16.2 Modal Decomposition for a Nonlinear System

The normal forms technique as defined by [19] involves applying a series of transformations resulting in an equation of motion using the following steps:

- Apply a linear transform to decouple the linear terms,
- Apply a forcing transformation,
- Apply a nonlinear near-identity transform.

The aim of the forcing and the near-identity transforms is to remove the non-resonant terms for each mode. The non-resonant terms are defined as those in the equation of motion that result in harmonics of the natural frequency (in the case of the unforced system) or of the dominant response frequency (in the case of forced systems). The forcing transformation targets the non-resonant forcing terms, and the near-identity transform removes the nonlinear non-resonant terms. Note that the response due to the non-resonant terms is not lost, instead it is captured in the transform equations. Transforming these non-resonant terms out of the equations of motion, for, say, the nth mode, allows the use of a trial solution of the form $U_n\cos(\omega_{rn}t-\phi_n)$ to solve the equation exactly, thereby removing the need for a harmonic balance type approximation.

Full details of the method can be found in [16, 19], here we consider a two mass oscillator with three springs, one connecting each mass to ground and one between the masses. The springs connecting the masses to ground have a force-deflection relationship $F=k\Delta+\kappa\Delta^3$ and the spring between the masses has the relationship $F=k_2\Delta+\kappa_2\Delta^3$, where Δ is the length change of the spring. Linear viscous dampers are also connected between the masses and ground (damping c) and between the masses (damping c_2). The configuration of the system is such that the resulting system has symmetric mass, damping and stiffness matrices. Single frequency forcing $P_1\cos(\Omega t)$ and $P_2\cos(\Omega t)$ is applied to the two masses. The resulting equation of motion is

$$\begin{bmatrix} m & 0 \\ 0 & m \end{bmatrix}\begin{pmatrix} \ddot{x}_1 \\ \ddot{x}_2 \end{pmatrix}+\begin{bmatrix} c+c_2 & -c_2 \\ -c_2 & c+c_2 \end{bmatrix}\begin{pmatrix} \dot{x}_1 \\ \dot{x}_2 \end{pmatrix}+\begin{bmatrix} k+k_2 & -k_2 \\ -k_2 & k+k_2 \end{bmatrix}\begin{pmatrix} x_1 \\ x_2 \end{pmatrix}+\begin{pmatrix} \kappa x_1^3+\kappa_2(x_1-x_2)^3 \\ \kappa x_2^3+\kappa_2(x_2-x_1)^3 \end{pmatrix}=\tfrac{1}{2}\begin{bmatrix} P_1 & P_1 \\ P_2 & P_2 \end{bmatrix}\mathbf{r} \quad (16.1)$$

where $\mathbf{r}=\{r_p,r_m\}^T=\{e^{\mathrm{i}\Omega t},e^{-\mathrm{i}\Omega t}\}^T$ is used to represent the harmonic forcing.

Applying the linear modal transform $\mathbf{x}=\Phi\mathbf{q}$, where Φ is a matrix of eigenvectors of $M^{-1}K$ results in

$$\ddot{\mathbf{q}}+\Lambda\mathbf{q}+\mathbf{N}_q(\mathbf{q})=\mathbf{P}_q\mathbf{r}, \quad (16.2)$$

where,

$$\Phi = \begin{bmatrix} 1 & 1 \\ 1 & -1 \end{bmatrix}, \quad \Lambda = \begin{bmatrix} k/m & 0 \\ 0 & (k+2k_2)/m \end{bmatrix},$$
$$N_q(\mathbf{q}) = \frac{\kappa}{m}\begin{pmatrix} q_1^3 + 3q_1q_2^2 \\ 3q_1^2q_2 + \gamma q_2^3 \end{pmatrix} + \begin{bmatrix} 2\zeta_1\omega_{n1} & 0 \\ 0 & 2\zeta_2\omega_{n2} \end{bmatrix}\dot{\mathbf{q}},$$
$$\mathbf{P}_q = \frac{1}{4m}\begin{bmatrix} P_1+P_2 & P_1+P_2 \\ P_1-P_2 & P_1-P_2 \end{bmatrix}. \tag{16.3}$$

Also $\gamma = 1 + (8\kappa_2/\kappa)$, the linearized natural frequencies $\omega_{n1} = k/m$ and $\omega_{n2} = (k+2k_2)/m$ and damping relationships $2\zeta_1\omega_{n1} = c/m$ and $2\zeta_2\omega_{n2} = (c+2c_2)/m$.

The forcing transform $\mathbf{q} = \mathbf{v} + [e]\mathbf{r}$ is now applied and considering each mode in turn, this transform removes forcing terms that are away from resonance while retaining those that are near-resonant. In this paper we will not consider forced equations of motion in detail, and as a result we write $\mathbf{q} = \mathbf{v}$ and $\mathbf{P}_q = \mathbf{0}$. For the case where $\mathbf{q} = \mathbf{v}$, the resulting equation of motion is

$$\ddot{\mathbf{v}} + \Lambda\mathbf{v} + \mathbf{N}_v(\mathbf{v}, \dot{\mathbf{v}}, \mathbf{r}) = \mathbf{P}_v\mathbf{r} \tag{16.4}$$

where $\mathbf{P}_v = \mathbf{P}_q = \mathbf{0}$. The resulting nonlinear term, without damping, can written as

$$\mathbf{N}_v(\mathbf{v}) = \mathbf{N}_q(\mathbf{v}) = \frac{\kappa}{m}\begin{pmatrix} v_1^3 + 3v_1v_2^2 \\ 3v_1^2v_2 + \gamma v_2^3 \end{pmatrix} \tag{16.5}$$

Now the equation of motion is in a form in which the near-identity nonlinear transform can be applied. This transform is written as

$$\mathbf{v} = \mathbf{u} + \mathbf{h}(\mathbf{u}, \dot{\mathbf{u}}, \mathbf{r}) \tag{16.6}$$

The aim of the transform is to simplify the dynamic equation, Eq. (16.4), into a form that can be solved exactly using a single frequency trial solution for each mode. The resulting transformed (i.e. simplified) normal form equation is expressed as

$$\ddot{\mathbf{u}} + \Lambda\mathbf{u} + \mathbf{N}_u(\mathbf{u}, \dot{\mathbf{u}}, \mathbf{r}) = \mathbf{P}_u\mathbf{r} \tag{16.7}$$

where currently $\mathbf{N}_u$, and the transform $\mathbf{h}$, are the unknown.

To keep track of the relative sizes of terms we introduce ε, a small parameter, which can be viewed as a bookkeeping aid. Using this bookkeeping notation, the nonlinear vectors and the transform vectors are expressed as a power series in ε

$$\begin{aligned} \mathbf{N}_v(\mathbf{v}, \dot{\mathbf{v}}, \mathbf{r}) &= \varepsilon\mathbf{n}_{v1}(\mathbf{v}, \dot{\mathbf{v}}, \mathbf{r}) + \varepsilon^2\mathbf{n}_{v2}(\mathbf{v}, \dot{\mathbf{v}}, \mathbf{r}) + \cdots \\ \mathbf{N}_u(\mathbf{u}, \dot{\mathbf{u}}, \mathbf{r}) &= \varepsilon\mathbf{n}_{u1}(\mathbf{u}, \dot{\mathbf{u}}, \mathbf{r}) + \varepsilon^2\mathbf{n}_{u2}(\mathbf{u}, \dot{\mathbf{u}}, \mathbf{r}) + \cdots \\ \mathbf{h}(\mathbf{u}, \dot{\mathbf{u}}, \mathbf{r}) &= \varepsilon\mathbf{h}_1(\mathbf{u}, \dot{\mathbf{u}}, \mathbf{r}) + \varepsilon^2\mathbf{h}_2(\mathbf{u}, \dot{\mathbf{u}}, \mathbf{r}) + \cdots \end{aligned} \tag{16.8}$$

Note that there are no ε^0 terms as $\mathbf{N}_v$, $\mathbf{N}_u$ and $\mathbf{h}$ are all small compared to the linear terms.

Using the method described in [16, 19] ε^2 and higher terms are assumed to be zero, and the coefficients of the ε^1 terms can be written as

$$\begin{aligned} \mathbf{n}_{v1}(\mathbf{u}, \dot{\mathbf{u}}, \mathbf{r}) &= [n_v]\mathbf{u}^*(\mathbf{u}_p, \mathbf{u}_m, \mathbf{r}) \\ \mathbf{n}_{u1}(\mathbf{u}, \dot{\mathbf{u}}, \mathbf{r}) &= [n_u]\mathbf{u}^*(\mathbf{u}_p, \mathbf{u}_m, \mathbf{r}) \\ \mathbf{h}_1(\mathbf{u}, \dot{\mathbf{u}}, \mathbf{r}) &= [h]\mathbf{u}^*(\mathbf{u}_p, \mathbf{u}_m, \mathbf{r}) \end{aligned} \tag{16.9}$$

where the $[\bullet]$ matrices are $N \times L$ where N is the number of degrees-of-freedom and L is the length of $\mathbf{u}^*$ which contains all the nonlinear terms. The expressions in (16.9) can be used to obtain a relationship for the coefficients of the form

$$[\tilde{h}] = [n_v] - [n_u] \tag{16.10}$$

where the (n,ℓ)th element in $[\tilde{h}]$, $\tilde{h}_{n,l}$, is related to the corresponding element in $[h]$, $h_{n,l}$, using

$$\begin{aligned}\tilde{h}_{n,\ell} &= \left(\left[(m_{\ell p}-m_{\ell m})\Omega+\sum_{n=1}^{N}(s_{\ell np}-s_{\ell nm})\omega_{rn}\right]^2-\omega_{rn}^2\right)h_{n,\ell}\\ &= \beta_{n,\ell}h_{n,\ell}.\end{aligned} \tag{16.11}$$

Here we use the matrix $[\beta]$ in which the (n,ℓ)th element is $\beta_{n,\ell}$—see [15] or [16] for full details of this derivation.

For the near-identity transform, $\mathbf{v}\to\mathbf{u}$, the nonlinear term is rewritten in terms of $\mathbf{u}$, the substitution $\mathbf{u}=\mathbf{u}_p+\mathbf{u}_m$ is made and nonlinear term is written in matrix form

$$N_v(\mathbf{u}_p+\mathbf{u}_m)=\varepsilon[n_v]\mathbf{u}^*, \tag{16.12}$$

using Eqs. (16.9) and (16.8), where for each element u_n in $\mathbf{u}$ we have

$$u_n=u_{np}+u_{nm}:\quad u_{np}=\frac{U_n}{2}e^{-\mathrm{i}\phi_n}e^{\mathrm{i}\omega_{rn}t},\ \ u_{nm}=\frac{U_n}{2}e^{\mathrm{i}\phi_n}e^{-\mathrm{i}\omega_{rn}t}. \tag{16.13}$$

Using these relationships for our current example we obtain

$$\mathbf{u}^*=\begin{bmatrix}u_{1p}^3\\ u_{1p}^2u_{1m}\\ u_{1p}u_{1m}^2\\ u_{1m}^3\\ u_{1p}u_{2p}^2\\ u_{1p}u_{2p}u_{2m}\\ u_{1p}u_{2m}^2\\ u_{1m}u_{2p}^2\\ u_{1m}u_{2p}u_{2m}\\ u_{1m}u_{2m}^2\\ u_{1p}^2u_{2p}\\ u_{1p}^2u_{2m}\\ u_{1p}u_{1m}u_{2p}\\ u_{1p}u_{1m}u_{2m}\\ u_{1m}^2u_{2p}\\ u_{1m}^2u_{2m}\\ u_{2p}^3\\ u_{2p}^2u_{2m}\\ u_{2p}u_{2m}^2\\ u_{2m}^3\end{bmatrix},\quad [n_u]^T=\frac{\hat{\kappa}}{m}\begin{bmatrix}1&0\\3&0\\3&0\\1&0\\3&0\\6&0\\3&0\\3&0\\6&0\\3&0\\0&3\\0&3\\0&6\\0&6\\0&3\\0&3\\0&\gamma\\0&3\gamma\\0&3\gamma\\0&\gamma\end{bmatrix}[\beta]^T=\omega_{r1}^2\begin{bmatrix}8&-\\0&-\\0&-\\8&-\\4(n^2+n)&-\\0&-\\4(n^2-n)&-\\4(n^2-n)&-\\0&-\\4(n^2+n)&-\\-&4(1+n)\\-&4(1-n)\\-&0\\-&0\\-&4(1-n)\\-&4(1+n)\\-&8n^2\\-&0\\-&0\\-&8n^2\end{bmatrix} \tag{16.14}$$

where $\omega_{r2}=n\omega_{r1}$ and, in $[\beta]$, a dash has been used where the corresponding value in $[n_v]$ is zero and hence the value in $[\beta]$ is of no importance. Note that as $\omega_{ri}\approx\omega_{ni}$ the linear natural frequencies must be approximately related by $\omega_{n2}\approx n\omega_{n1}$.

We are now in a position to select both the transform terms and the nonlinear terms in the dynamic equation for $\mathbf{u}$. Considering element (n,ℓ), if possible we wish to remove the nonlinear term from the dynamic equation and place it in the transform equation. However this is not possible for all terms. From Eq. (16.11) it can be seen that $h_{n,\ell}$ can be large compared to $\tilde{h}_{n,\ell}$ if $\beta_{n,\ell}$ is close to zero. Also from Eq. (16.10), it can be seen that $[\tilde{h}]$ is of a similar size to $[n_u]$ and $[n_v]$. Hence for the terms where $\beta_{n,\ell}$ is close to zero, this would suggest that if the element in the nonlinear term in matrix $[n_v]$ is placed in the transform matrix $[h]$, the transform can not be said to be near-identity. This results in two options for the (n,ℓ) element, that satisfy Eq. (16.10) and ensure the near-identity condition it met. These are the preferred option in which the term is removed from the equation of motion

$$\text{Preferred Option:}\quad n_{u,n,\ell}=0,\ \ h_{n,\ell}=n_{v,n,\ell}/\beta_{n,\ell} \tag{16.15}$$

and, to ensure that the transform is near-identity, the near-resonant option in which the nonlinear term is kept in the equation of motion

$$\text{Near-resonant Option:} \quad n_{u,n,\ell} = n_{v,n,\ell}, \;\; h_{n,\ell} = 0 \tag{16.16}$$

Using these transforms the equation of motion can be solved, for each mode in turn, using a trial solution in the form $u_n = \frac{U_n}{2} e^{-\mathrm{i}\phi_n} e^{\mathrm{i}\omega_{rn}t} + \frac{U_n}{2} e^{\mathrm{i}\phi_n} e^{-\mathrm{i}\omega_{rn}t}$ (for the nth mode) without the need for a harmonic balance approximation. Information regarding the harmonics of the response are captured in the transform equation

$$\mathbf{v} = \mathbf{u} + \varepsilon[h]\mathbf{u}^* + \cdots \tag{16.17}$$

This equation can also be used to identify the nonlinear normal modes of a system.

From $[\beta]$ it can be seen that regardless of the value of n the following terms are resonant; $[1,2]$, $[1,3]$, $[1,6]$, $[1,9]$, $[2,13]$, $[2,14]$, $[2,18]$ and $[2,19]$. In addition if $n = 1$ the terms $[1,7],[1,8],[2,12]$ and $[2,15]$ are resonant. For the resonant terms we set the relevant terms in $[n_u]$ to equal those in $[n_v]$ and set the corresponding terms in $[h]$, the transform matrix, to equal zero. Provided $n \neq 1$, this results in the following normal form for the system

$$\ddot{u}_1 + \omega_{n1}^2 u_1 + \frac{3\kappa}{m} u_{1p} u_{1m} u_1 + \frac{6\kappa}{m} u_{2p} u_{2m} u_1 = 0 \tag{16.18}$$

$$\ddot{u}_2 + \omega_{n2}^2 u_2 + \frac{3\gamma\kappa}{m} u_{2p} u_{2m} u_2 + \frac{6\kappa}{m} u_{1p} u_{1m} u_2 = 0 \tag{16.19}$$

where $u_{ip} + u_{im} = u_i$ has been used.

16.2.1 Backbone Curves

To understand the modal response of the system using second-order normal forms we will concentrate on the underlying modal dynamics, i.e. looking at the system response when the damping and forcing are zero. Taking the $n \neq 1$ case, and making the substitutions $u_{ip} = (U_i/2)e^{\omega_{ri}t}$ and $u_{im} = (U_i/2)e^{-\omega_{ri}t}$, such that $u_i = U_i \cos(\omega_{ri}t)$, and noting that $\omega_{r2} = n\omega_{r1}$ results in the time-independent relationships

$$\left[-\omega_{r1}^2 + \omega_{n1}^2 + \frac{3\kappa}{4m}(U_1^2 + 2U_2^2)\right] U_1 = 0, \tag{16.20}$$

$$\left[-n^2\omega_{r1}^2 + \omega_{n2}^2 + \frac{3\kappa}{4m}(2U_1^2 + \gamma U_2^2)\right] U_2 = 0. \tag{16.21}$$

Note that for the case where $n = 1$, the $[1,7],[1,8],[2,12]$ and $[2,15]$ terms will be included in the normal form equations, which results in time-independent relationships

$$\left[-\omega_{r1}^2 + \omega_{n1}^2 + \frac{3\kappa}{4m}(U_1^2 + 3U_2^2)\right] U_1 = 0, \tag{16.22}$$

$$\left[-\omega_{r1}^2 + \omega_{n2}^2 + \frac{3\kappa}{4m}(3U_1^2 + \gamma U_2^2)\right] U_2 = 0. \tag{16.23}$$

From here, for clarity when deriving the equations we will concentrate on the $n = 1$ case, however the technique is the same for both. There are two straightforward solutions to Eqs. (16.20) and (16.21) and to Eqs. (16.22) and (16.23), these are

$$\text{S1:} \quad U_2 = 0, \quad \omega_{r1}^2 = \omega_{n1}^2 + \frac{3\kappa}{4m} U_1^2 \tag{16.24}$$

$$\text{S2:} \quad U_1 = 0, \quad n^2\omega_{r1}^2 = \omega_{n2}^2 + \frac{3\kappa\gamma}{4m} U_2^2 \tag{16.25}$$

These represent two backbone curves for the two degree-of-freedom system with $S1$ and $S2$ corresponding to a response in the first and second modes respectively.

In addition to these, under certain conditions there are two further solutions in which both U_1 and U_2 are non-zero. Taking Eqs. (16.22) and (16.23), and setting the terms in the square brackets of both equations to zero gives

$$\omega_{r1}^2 = \omega_{n1}^2 + \frac{3\kappa}{4m}(U_1^2 + 3U_2^2) = \omega_{n2}^2 + \frac{3\kappa}{4m}(3U_1^2 + \gamma U_2^2) \tag{16.26}$$

Rearranging this equation, and using $\gamma = 1 + (8\kappa_2/\kappa)$, gives

$$U_1^2 = \left(1 - 4\frac{\kappa_2}{\kappa}\right) U_2^2 - \frac{2m}{3\kappa}(\omega_{n2}^2 - \omega_{n1}^2). \tag{16.27}$$

It can be seen that for a real solution to U_1 two conditions must be met

$$\kappa \geq 4\kappa_2 \quad \text{and} \quad U_2^2 \geq \frac{2m}{3(\kappa - 4\kappa_2)}(\omega_{n2}^2 - \omega_{n1}^2). \tag{16.28}$$

This indicates that unless $\omega_{n2} = \omega_{n1}$, for this solution to be valid U_2 cannot be zero. However, $U_1 = 0$ is a valid solution, and in this case comparing Eqs. (16.25) and (16.26) we can see that the solution lies on the S2 backbone curve, and in fact these two solutions branch out of the S2 backbone.

If we eliminate U_1 from Eq. (16.26) we obtain the response frequency equation

$$\omega_{r1}^2 = \omega_{r2}^2 = \frac{3\omega_{n1}^2 + \omega_{n2}^2}{2} + \frac{3(\kappa - \kappa_2)}{m} U_2^2 \tag{16.29}$$

Taking Eqs. (16.27) and (16.29) we can summarise the two further solution as

$$\begin{aligned}
\text{S3:}\quad & U_1 = \sqrt{(1 - 4\frac{\kappa_2}{\kappa})U_2^2 - \frac{2m}{3\kappa}(\omega_{n2}^2 - \omega_{n1}^2)}, \\
& \omega_{r2}^2 = \frac{3\omega_{n1}^2 + \omega_{n2}^2}{2} + \frac{3(\kappa - \kappa_2)}{m} U_2^2, \\
\text{S4:}\quad & U_1 = -\sqrt{(1 - 4\frac{\kappa_2}{\kappa})U_2^2 - \frac{2m}{3\kappa}(\omega_{n2}^2 - \omega_{n1}^2)}, \\
& \omega_{r2}^2 = \frac{3\omega_{n1}^2 + \omega_{n2}^2}{2} + \frac{3(\kappa - \kappa_2)}{m} U_2^2.
\end{aligned} \tag{16.30}$$

These two solutions indicate that four modal solutions exist despite the system just having two degree-of-freedom.

16.2.2 Modeshapes

Using these backbone solutions we can generate the modeshapes for the system. Here, for the unforced, undamped system we will plot the initial displacement conditions (assuming zero initial velocities) at which a mode is observed in the x_1–x_2 plane. Then we consider the resulting modeshapes from these initial conditions. The forced response is computed in [22] using the numerical continuation software AUTO [21].

Firstly we must consider the near-identity transform, Eq. (16.17), to calculate the response in x

$$\mathbf{x} = \Phi\mathbf{q} = \Phi\mathbf{v} = \Phi(\mathbf{u} + \varepsilon[h]\mathbf{u}^*) \tag{16.31}$$

Again considering the $n = 1$ case, using Eqs. (16.14) and (16.15) we can write

$$\begin{aligned}
x_1 &= (U_1 + U_2)\cos(\omega_{r1}t) + \frac{\kappa}{m}\frac{U_1^3 + 3U_1^2U_2 + 3U_1U_2^2 + \gamma U_2^3}{32\omega_{r1}^2}\cos(3\omega_{r1}t) \\
x_2 &= (U_1 - U_2)\cos(\omega_{r1}t) + \frac{\kappa}{m}\frac{U_1^3 - 3U_1^2U_2 + 3U_1U_2^2 - \gamma U_2^3}{32\omega_{r1}^2}\cos(3\omega_{r1}t).
\end{aligned} \tag{16.32}$$

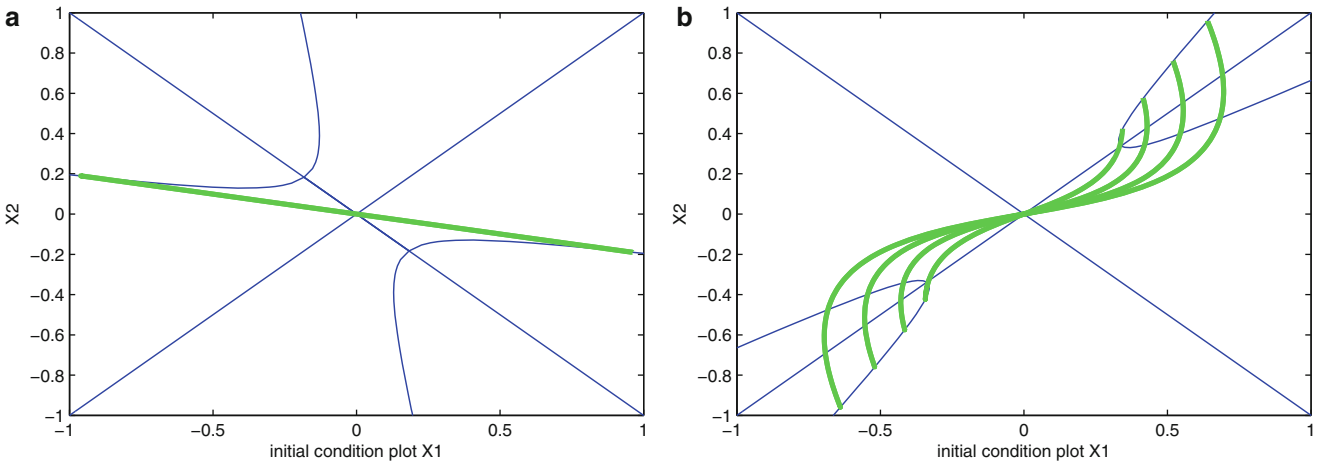

Fig. 16.1 Initial displacement conditions at which a modal response is observed, assuming the initial velocities are zero (shown as *thin lines*), for (**a**) n=1 system and (**b**) n=3 system. The *thick line* gives an example of the resultant oscillatory motion from a point on the S3 solution branch

For backbone solutions S1 and S2, where $U_2 = 0$ and $U_1 = 0$ respectively, these equations show that the corresponding modeshapes ($x_1 = x_2$ and $x_1 = -x_2$ respectively) are independent of amplitude and response frequency ω_{r1}. For solutions S3 and S4 the modeshapes are more complex. For these solutions the ratio x_2/x_1 is a function of amplitude and hence response frequency. The initial displacements that result in a modal response may be written as

$$\begin{aligned} x_1|_{initial} &= \omega_{r1}^2(U_1+U_2)+(\kappa/32m)(U_1^3+3U_1^2U_2+3U_1U_2^2+\gamma U_2^3) \\ x_2|_{initial} &= \omega_{r1}^2(U_1-U_2)+(\kappa/32m)(U_1^3-3U_1^2U_2+3U_1U_2^2-\gamma U_2^3) \end{aligned} \tag{16.33}$$

with ω_{r1} and the relationship between U_1 and U_2 are defined by Eq. (16.30) (noting $\omega_{r1} = \omega_{r2}$ as $n = 1$).

16.2.3 Simulation Results

Consider the two degree-of-freedom system with parameters; $m = 1$, $k = 1$, $k_2 = 0.005$, $\kappa = 0.4$ and $\kappa_2 = 0.05$ such that $\omega_{n1} = 1$ and $\omega_{n2} = 1.005$. Using Eq. (16.33), the initial conditions which result in a modal vibration are shown as thin lines in Fig. 16.1a. The thick line shows the resulting motion if released from a point on the S3 solution branch, calculated using Eq. (16.32).

In the previous figure the oscillatory motion is almost an exact straight line, hence the mode shape is essentially fixed during the oscillation and is just a function of initial displacement conditions. However, for the case where $n \neq 1$ this is not the case, the modeshape varies during oscillations if the system is released from branches S3 or S4. To see this we consider the case where $n = 3$ using a system with parameters $m = 1$, $k = 1$, $k_2 = 4.015$, $\kappa = 0.05$ and $\kappa_2 = 10$ such that $\omega_{n1} = 1$ and $\omega_{n2} = 3.005$. Figure 16.1b shows the initial conditions which result in a modal response (thin lines). It can be seen that for this system the bifurcation occurs on the S1 solution. The thick lines show a series of responses for the system released from the S3 initial conditions. It can be seen that in this case the shape of the response varies over the oscillation.

To assess the accuracy of the normal form analysis, Fig. 16.2a shows the system response calculated using time-stepping simulation for two periods of oscillation (thick dashed line). It can be seen that it agrees well with the normal form prediction. Figure 16.2b shows the corresponding response of x_1 and x_2 over time, confirming the behaviour is a vibration in unison as defined by [3]. To further highlight the vibration-in-unison behaviour, Fig. 16.3 shows approximately two cycles of time simulation response of the system for initial conditions that do not lie on the S1-4 solution curves.

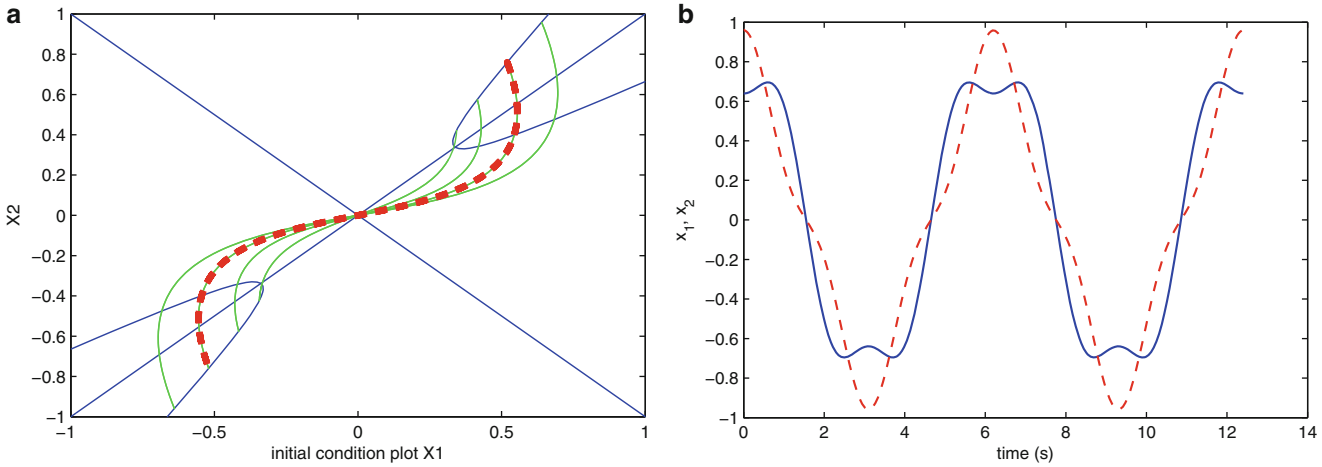

Fig. 16.2 (**a**) Comparison between time-stepping simulation (*thick dashed line*) over two periods of oscillation and the normal form predictions for an initial displacement condition lying on the S3 solution and (**b**) the corresponding response in x_1 (*solid line*) and x_2 (*dashed line*) over time

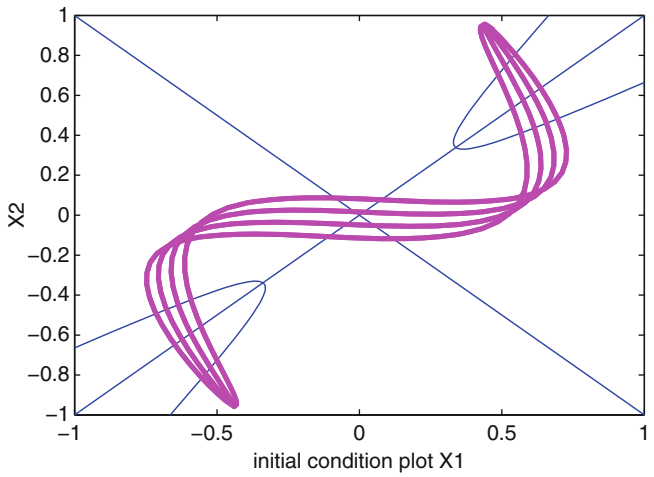

Fig. 16.3 Approximately two cycles of time-stepping simulation response for initial conditions that do not lie on the S1-S4 modal lines

16.3 Conclusion

In this paper, we demonstrate how the second-order normal form method can be used to understand the nonlinear modal response of a system. This is done by considering a two degree-of-freedom nonlinear system with closely matching linear natural frequencies. We show how the system backbone curves can be found using the second-order normal form technique. These curves are plotted in the x_1–x_2 plane as initial displacement conditions (assuming no initial velocities) from which a modal response is observed. These solutions are more complex than the expressions for the underlying linear system as for some x_1 values there are four x_2 values at which a modal response is observed due to a bifurcation in one of the backbone curves. The responses over a cycle of oscillation are also shown for a number of initial conditions, highlighting that the mode shape can vary over each cycle of oscillation. The normal form predictions are shown to have high accuracy using time-stepping simulation results.

References

1. Ewins DJ (2000) Modal testing: theory, practice and application, 2nd edn. Research Studies Press, Hertfordshire
2. Friswell MI, Mottershead JE (1995) Finite element model updating in structural dynamics. Kluwer Academic, Dordrecht/Boston
3. Rosenberg RM (1960) Normal modes of nonlinear dual-mode systems. J Appl Mech 27:263–268
4. Shaw SW, Pierre C (1991) Non-linear normal modes and invariant manifolds. J Sound Vib 150:170–173
5. Vakakis AF (ed) (2002) Normal modes and localization in nonlinear systems. Kluwer Academic, London

6. Kerschen G, Peeters M, Golinval JC, Vakakis AF (2009) Nonlinear normal modes, part I: a useful framework for the structural dynamicist. Mech Syst Signal Process 23:170–194
7. Kahn PB, Zarmi Y (2000) Nonlinear dynamics: a tutorial on the method of normal forms. Am J Phys 68(10):907–919
8. Arnold VI (1988) Geometrical methods in the theory of ordinary differential equations. Springer, New York
9. Murdock J (2002) Normal forms and unfoldings for local dynamical systems. Springer, New York
10. Jézéquel L, Lamarque CH (1991) Analysis of nonlinear dynamic systems by the normal form theory. J Sound Vib 149:429–459
11. Nayfeh AH (2000) Nonlinear interactions. Wiley series in nonlinear science. Wiley, New York
12. Kahn PB, Zarmi Y (1991) Minimal normal forms in harmonic oscillations with small nonlinear perturbations. Phys D 54:65–74
13. Rand RH, Ambruster D (1987) Perturbation methods, bifurcation theory and computer algebra. Springer, New York
14. Touzé C, Thomas O, Huberdeau A (2004) Asymptotic non-lnear normal modes for large-amplitude vibrations of continuous structures. Comput Struct 82:2671–2682
15. Neild SA, Wagg DJ (2010) Applying the method of normal forms to second-order nonlinear vibration problems. Proc R Soc A 467(2128):1141–1163
16. Neild SA (2012) Approximate methods for analysing nonlinear structures. In: Wagg DJ, Virgin LN (eds) Exploiting nonlinear behaviour in structural dynamics. Springer, New York
17. Vakakis AF, Rand RH (1992) Normal modes and global dynamics of a 2-degree-of-freedom nonlinear-system; part I: low energies. Int J Nonlinear Mech 27:861–874
18. Vakakis AF, Rand RH (1992) Normal modes and global dynamics of a 2-degree-of-freedom nonlinear-system; part II: high energies. Int J Nonlinear Mech 27:875–888
19. Wagg DJ, Neild SA (2009) Nonlinear vibration with control. Springer, New York
20. Xin Z, Neild SA, Wagg DJ (2011) The selection of the linearized natural frequency for the second-order normal form method. In: Proceedings of the ASME international design engineering technical conferences and computers and information in engineering conference IDETC/CIE 2011, Washington, DC, Paper DETC2011-47654
21. Doedel EJ, Paffenroth RC, Champneys AR, Fairgrieve TF, Kuznetsov YA, Oldeman BE, Sandstede B, Wang XJ (2007) AUTO-07P: continuation and bifurcation software for ordinary differential equations. http://indy.cs.concordia.ca/auto
22. Neild SA, Cammarano A, Wagg DJ (2012) Towards a technique for nonlinear modal analysis. In: Proceedings of IDETC/CIE ASME international design engineering technical conferences, Chicago, Paper DETC2012-70322

Chapter 17
Nonlinear Normal Modes of Nonconservative Systems

L. Renson and G. Kerschen

Abstract Linear modal analysis is a mature tool enjoying various applications ranging from bridges to satellites. Nevertheless, modal analysis fails in the presence of nonlinear dynamical phenomena and the development of a practical nonlinear analog of modal analysis is a current research topic. Recently, numerical techniques (e.g., harmonic balance, continuation of periodic solutions) were developed for the computation of nonlinear normal modes (NNMs). Because these methods are limited to conservative systems, the present study targets the computation of NNMs for nonconservative systems. Their definition as invariant manifolds in phase space is considered. Specifically, a new finite element technique is proposed to solve the set of partial differential equations governing the manifold geometry.

Keywords Nonlinear normal modes • Invariant manifold • Nonconservative systems • Nonlinear modal analysis

17.1 Introduction

In many engineering applications, the efficiency of the system is critical. For structures it usually results in reducing weight, increasing flexibility, or pushing the operating range limits. As a consequence, structural dynamicists are facing new challenges in their design. One of those are nonlinearities introduced, for instance, by large displacements, nonlinear materials, damping, or gaps and joints. In this context, linear modal analysis (LMA) can still provide a useful framework to design and model the structure as long as nonlinear phenomena are negligible. In the case of essentially nonlinear systems or in the case where strong nonlinear phenomena are present, LMA fails to explain the system dynamics and results, at best, in a suboptimal design. To overcome this issue, new theoretical and numerical tools have to be developed. Among many, a specific one has drawn the attention of the structural dynamics community, namely: the Nonlinear Normal Modes (NNMs).

NNMs are mathematical tools that offers a new framework to understand nonlinear phenomena. They are a rigorous extension of the linear normal modes (LNMs) to nonlinear systems (see Sect. 17.2) and were pioneered in the 1960s by Rosenberg [1, 2]. He defined an NNM as a *vibration in unison* of the system. Shaw and Pierre proposed a generalization of Rosenberg's definition that provides an elegant extension of the NNM concept to damped systems. Based on geometric arguments and inspired by the center manifold theory, they defined an NNM as a two-dimensional invariant manifold in phase space [3, 4].

If a large body of literature has addressed the computation of NNMs using analytical techniques (see, e.g., [4–8]), there have been relatively few attempts to compute NNMs using numerical methods. Most of these latter methods compute undamped NNMs, which are considered as periodic solutions of the underlying Hamiltonian system [9–13]. On the one hand, this is particularly attractive when targeting a numerical computation of the NNMs; it paves the way for the application of the NNM theory to large-scale, complex structures [14]. On the other hand, the influence of (linear and nonlinear) damping cannot be studied, which may be an important limitation in practice.

The first attempt to carry out numerical computation of damped NNMs is that of Pesheck et al. [15, 16]. The manifold-governing partial differential equations (PDEs) are solved in modal space using a Galerkin projection with the NNM motion

L. Renson (✉) • G. Kerschen
Space Structures and Systems Laboratory (S3L), Structural Dynamics Research Group,
Department of Aerospace and Mechanical Engineering, University of Lige, Liege, Belgium
e-mail: l.renson@ulg.ac.be; g.kerschen@ulg.ac.be

G. Kerschen et al. (eds.), *Topics in Nonlinear Dynamics, Volume 1: Proceedings of the 31st IMAC, A Conference on Structural Dynamics, 2013*, Conference Proceedings of the Society for Experimental Mechanics Series 35,
DOI 10.1007/978-1-4614-6570-6_17,

parametrized by amplitude and phase variables. This method eliminates a number of problems associated with the local polynomial approximation of the manifold [4]. Probably the most significant advantage is that the computation of NNMs in large-amplitude regimes can be handled. In a recent contribution, Touzé and co-workers [17] also tackle the PDEs in modal space. They show that these PDEs can be interpreted as a transport equation, which, in turn, can be discretized using finite differences. In the study by Noreland et al. [18], the manifold is described by partial differential algebraic equations, which are also solved by finite differences. Another interesting approach uses a Fourier-Galerkin procedure and relies on the concept of complex nonlinear modes [19]. It does not solve the governing equations of the manifold, but it is able to compute it a posteriori.

The present study introduces a new method for the computation of NNMs defined as invariant manifolds in phase space. The transformation of the manifold-governing PDEs to modal space is not necessary, which means that an NNM motion is parametrized by master displacement and velocity, as in [4].

The approach developed in [16] uses global shape functions to discretize the NNM PDEs, i.e. shape functions defined over the entire computational domain. The discretization ended up with a set of highly-coupled and highly-nonlinear algebraic equations to solve. As a consequence, the computational burden was dramatically increased as the number of degree of freedom of the mechanical system increases and a "shift in tactics" was needed [16]. A semi-discrete approach was then introduced by dividing the amplitude domain into several sub-domains in order to reduce the complexity of the shape functions in amplitude. As we are targeting the computation of NNMs for high-dimensional systems such as those met in the industry, we propose to solve the set of PDEs using the finite element (FE) method, which employs local shape functions. Thus, despite we consider physical rather than modal coordinates, our developments fits into the continuity of the work of [16]. The FE method renders the algorithm general and systematic.

The present paper is organized as follows. Section 17.2 briefly introduces the theoretical concepts about NNMs. Section 17.3 presents the details of the algorithm we developed. The FE method is presented as well as our specific treatment of boundary conditions. Section 17.4 validates our algorithm on a 5 degrees of freedom (DOF) system composed of multiple nonlinearities. The validation procedure involves comparison with a continuation of periodic solution algorithm. Section 17.5 presents the computation of NNMs for a nonlinear system including linear and/or nonlinear damping. Finally, Sect. 17.6 concludes about the key developments and findings of this paper.

17.2 Review of Normal Modes for Nonlinear Systems

A detailed description of NNMs and of their fundamental properties (e.g., frequency-energy dependence, bifurcations, and stability) is given in [7, 20] and is beyond the scope of this paper. For completeness, the two main definitions of an NNM are briefly reviewed in this section.

The free response of discrete mechanical systems with N degrees of freedom (DOF) is considered, assuming that continuous systems (e.g., beams, shells, or plates) have been spatially discretized using the FE method. The equations of motion are

$$\mathbf{M}\ddot{\mathbf{x}}(t) + \mathbf{G}_{\text{gyr}}\dot{\mathbf{x}} + \mathbf{C}\dot{\mathbf{x}}(t) + \mathbf{K}\mathbf{x}(t) + \mathbf{f}_{\text{nl}}\{\mathbf{x}(t), \dot{\mathbf{x}}(t)\} = 0 \tag{17.1}$$

where $\mathbf{M}$, $\mathbf{G}_{\text{gyr}}$, $\mathbf{C}$, and $\mathbf{K}$ are the mass, gyroscopic coupling, damping, and stiffness matrices, respectively; $\mathbf{x}$, $\dot{\mathbf{x}}$, and $\ddot{\mathbf{x}}$ are the displacement, velocity, and acceleration vectors, respectively; $\mathbf{f}_{\text{nl}}$ is the nonlinear restoring force vector.

Targeting a straightforward nonlinear extension of the concept of LNMs, Rosenberg defined an NNM motion as a synchronous periodic oscillation. This definition requires that all material points of the system reach their extreme values and pass through zero simultaneously and allows all displacements to be expressed in terms of a single reference displacement. At first glance, Rosenberg's definition may appear restrictive in two cases:

1. In the presence of internal resonances, an NNM motion is no longer synchronous, but it is still periodic. This is why an extended definition was considered in [10, 20]; an NNM motion was defined as a *(non-necessarily synchronous) periodic motion* of the undamped mechanical system.
2. The definition cannot be easily extended to nonconservative systems. However, as shown in [20], the damped dynamics can be interpreted based on the topological structure of the NNMs of the underlying conservative system, provided that damping has a purely parasitic effect.

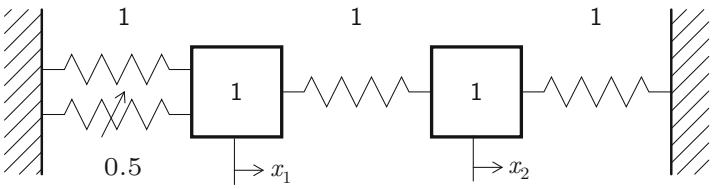

Fig. 17.1 Schematic representation of the 2DOF system example

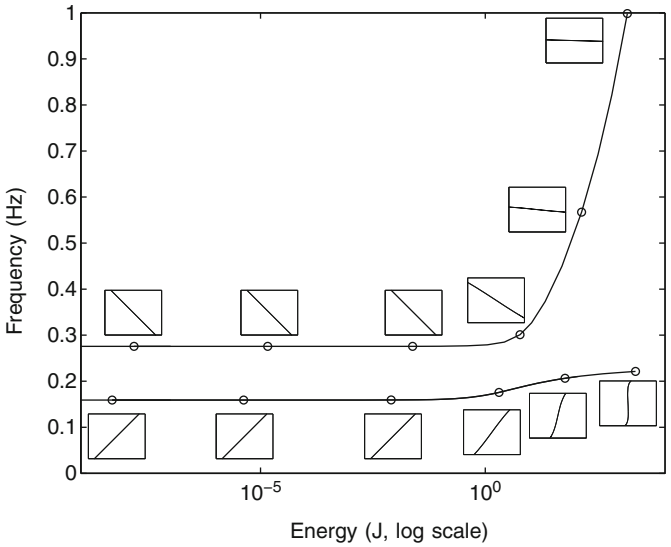

Fig. 17.2 Frequency-energy plot of system (17.2). NNM motions depicted in the configuration space are inset

For illustration, the system depicted in Fig. 17.1 and governed by the equations

$$\begin{aligned} \ddot{x}_1 + (2x_1 - x_2) + 0.5x_1^3 &= 0, \\ \ddot{x}_2 + (2x_2 - x_1) &= 0, \end{aligned} \tag{17.2}$$

is considered. The NNMs corresponding to in-phase and out-of-phase motions are represented in the frequency-energy plot (FEP) of Fig. 17.2. An NNM motion is represented by a point in the FEP, which is drawn at a frequency corresponding to the minimal period of the periodic motion and at an energy equal to the conserved total energy during the motion. A branch, represented by a solid line, is a family of NNM motions possessing the same qualitative features (e.g., in-phase NNM motion).

To provide a rigorous extension of the NNM concept to damped systems, Shaw and Pierre defined an NNM as a two-dimensional invariant manifold in phase space [3]. Such a manifold is invariant under the flow (i.e., orbits that start out in the manifold remain in it for all time), which generalizes the invariance property of LNMs to nonlinear systems. In order to parametrize the manifold, a single pair of state variables (i.e., both the displacement and the velocity) are chosen as master coordinates, the remaining variables being functionally related to the chosen pair. Therefore, the system behaves like a nonlinear single-DOF system on the manifold.

Geometrically, LNMs are represented by planes in phase space, and NNMs are two-dimensional surfaces that are tangent to them at the equilibrium point. The bending and contortion of a NNM surface is purely due to nonlinear effects. The invariant manifolds corresponding to in-phase and out-of-phase NNM motions of system (17.2) are given in Fig. 17.3.

17.2.1 Manifold-Governing Partial Differential Equations

To derive the equations governing the geometry of the manifold, Eq. (17.1) are recast into state-space form:

$$\begin{aligned} \dot{x}_i &= y_i, \\ \dot{y}_i &= f_i(\mathbf{x}, \mathbf{y}), \qquad i = 1, \ldots, N. \end{aligned} \tag{17.3}$$

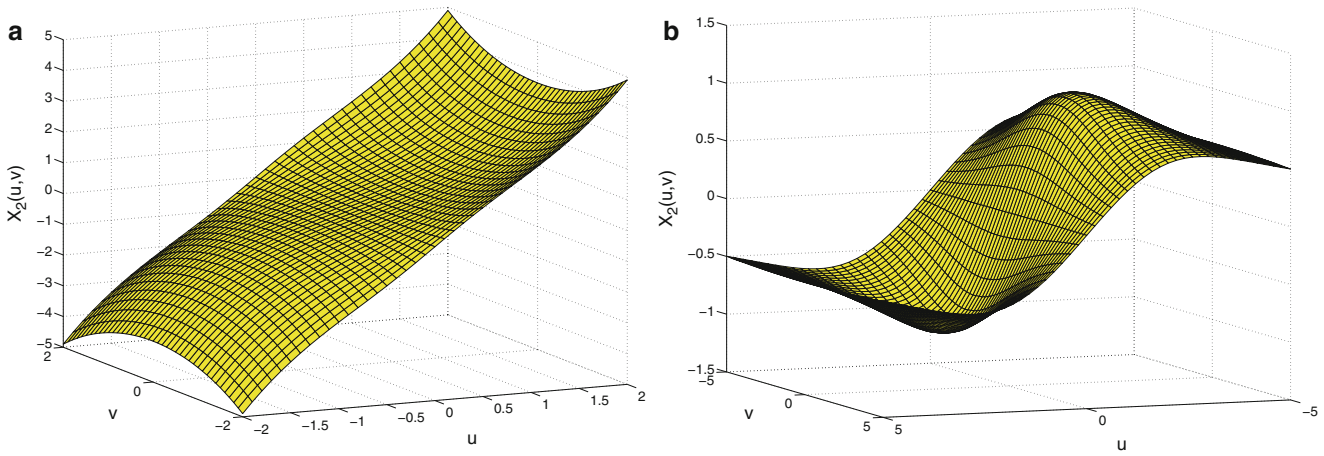

Fig. 17.3 Two-dimensional invariant manifolds of system (17.2) computed with an algorithm for the continuation of periodic solutions. The different periodic solutions computed form orbits in the phase space that paves the manifold. (**a**) In-phase NNM; and (**b**) out-of-phase NNM

The formulation and notations presented here closely follow those used in reference [4]. The $f_i(\mathbf{x},\mathbf{y})$ accounts for all the forcing terms presented in the equations of motion: linear stiffness terms, linear gyroscopic coupling terms, linear damping terms, and nonlinear stiffness and damping terms.

During an NNM motion, there is a functional dependence between all degrees of freedom, and the motion can be parametrized by a single displacement-velocity pair. The selection of the master coordinates $(u,v) = (x_k, y_k)$, i.e., the nonlinear modal coordinates, is arbitrary. The $2N-2$ constraint equations governing the slave coordinates are:

$$\begin{aligned} x_i &= X_i(u,v), \\ y_i &= Y_i(u,v), \qquad i = 1,\ldots,N;\ i \neq k. \end{aligned} \tag{17.4}$$

To obtain a set of equations governing the manifold geometry, i.e., the X_i's and Y_i's, the time dependence in the equations is eliminated. Taking the time derivative of the constraint Eq. (17.4) and using the chain rule for differentiation yields:

$$\begin{aligned} \dot{x}_i &= \frac{\partial X_i}{\partial u}\dot{u} + \frac{\partial X_i}{\partial v}\dot{v}, \\ \dot{y}_i &= \frac{\partial Y_i}{\partial u}\dot{u} + \frac{\partial Y_i}{\partial v}\dot{v}, \qquad i = 1,\ldots,N;\ i \neq k. \end{aligned} \tag{17.5}$$

Plugging Eqs. (17.3) and (17.4) into Eq. (17.5) leads to a set of 2N-2 partial differential equations (PDEs) that can be solved for the X_i's and Y_i's:

$$\begin{aligned} Y_i(u,v) &= \frac{\partial X_i(u,v)}{\partial u} v + \frac{\partial X_i(u,v)}{\partial v} f_k(u,\mathbf{X}(u,v),v,\mathbf{Y}(u,v)), \\ f_i(u,\mathbf{X}(u,v),v,\mathbf{Y}(u,v)) &= \frac{\partial Y_i(u,v)}{\partial u} v + \frac{\partial Y_i(u,v)}{\partial v} f_k(u,\mathbf{X}(u,v),v,\mathbf{Y}(u,v)), \\ i &= 1,\ldots,N;\ i \neq k, \end{aligned} \tag{17.6}$$

where $\mathbf{X} = \{X_j : j = 1,\ldots,N\,; j \neq k\}$ and $\mathbf{Y} = \{Y_j : j = 1,\ldots,N\,; j \neq k\}$. Equations for $i = k$ are trivially satisfied.

Once the manifold-governing PDEs are solved, constraint Eq. (17.4) represent the geometrical description of the NNM. Around the equilibrium point, Eq. (17.6) admit N solutions, i.e., one for each mode. The nonlinear modal dynamics is then generated by substituting the X_i's and Y_i's in the pair of equations of motion governing the master coordinates x_k and y_k. This results in a single-DOF nonlinear motion:

$$\begin{aligned} \dot{u} &= v, \\ \dot{v} &= f_k(u,\mathbf{X}(u,v),v,\mathbf{Y}(u,v)), \qquad i = 1,\ldots,N;\ i \neq k. \end{aligned} \tag{17.7}$$

Here, we mention that the approach followed to derive NNMs PDEs relies on the assumption of a two-dimensional description of the dynamics. For some regime of motion, often away from the equilibrium point, this assumption is not true. It results in a failure of the PDE description and in an inability to compute the NNMs in these regions. This limitation influences the selection of the master coordinates that are, in fact, not arbitrary. The observation of reference solutions show that the maximum computational domain is (strongly) influenced by this choice. Thus, taking the appropriate master coordinates ensure results with a large validity range. Unfortunately, there is not yet good practices to identify the most appropriate set of coordinates.

17.3 Finite Element Computation of Nonlinear Normal Modes

To fit into a formulation more convenient to the FEM, Eq. (17.6) are recast into Eq. (17.8) where ∇ is the gradient vector, and $\partial\Omega$ the domain boundary. This boundary comprises an inflow boundary $\partial\Omega^- = \{\mathbf{u} \in \partial\Omega : \mathbf{V}(\mathbf{u}).\mathbf{n}(\mathbf{u}) < 0\}$ and an outflow boundary $\partial\Omega^+ = \{\mathbf{u} \in \partial\Omega : \mathbf{V}(\mathbf{u}).\mathbf{n}(\mathbf{u}) > 0\}$. The 2N-2 equations are quasilinear first order partial differential equations that are similar to flow equations encountered in fluid dynamics. This interpretation of the PDEs is identical to the interpretation made by Touzé and its co-workers [17] who interpreted the PDEs as a transport problem. The vector $\mathbf{V}$ can therefore be interpreted as the velocity vector of the master coordinates flow. Transforming the PDEs in Eqs. (17.8) into (17.9), a new matrix $\mathbf{A}$ is bring out where $\mathbf{I}$ is the identity matrix and $\mathbf{F}^T = \{f_j : j = 1,\ldots,N\,;\, j \neq k\}$. It is a diagonal matrix which has a single real eigenvalue $\lambda = f_k/v$ of multiplicity 2N − 2. The eigenvalues of $\mathbf{A}$ can be interpreted as the flow speed. Here, the velocity amplitude and direction is identical for every unknown field X_i or Y_i. The flow direction is called the characteristic direction and illustrates the propagation of the information into the domain [21–23].

$$\begin{cases} \mathbf{V}\cdot\nabla X_i - Y_i = 0, \\ \mathbf{V}\cdot\nabla Y_i - f_i = 0, \\ X_i|_{\partial\Omega^-} = X_i^-, \\ Y_i|_{\partial\Omega^-} = Y_i^-, \qquad i = 1,\ldots,N;\ i \neq k, \qquad \mathbf{V}^T = \{f_k \;\; v\} \end{cases} \tag{17.8}$$

$$\mathbf{I}.\partial_u\{\mathbf{Z}\} + \mathbf{A}(\mathbf{u},\mathbf{Z}).\partial_v\{\mathbf{Z}\} - (1/v)\{\tilde{\mathbf{Z}}\} = \mathbf{0}, \qquad \text{where} \quad \mathbf{Z}^T = \{\mathbf{X} \;\; \mathbf{Y}\} \qquad \text{and} \quad \tilde{\mathbf{Z}}^T = \{\mathbf{Y} \;\; \mathbf{F}\} \tag{17.9}$$

Figure 17.4a shows the flow of a 2DOF nonlinear conservative system. In the domain Ω, characteristic directions form curves called characteristic curves (or characteristics). In the present case, the conservation of the energy induces closed characteristics. Since information travels through out the domain along these curves, we conclude in a clear distinction between the dynamics of different energies. Indeed, the "information" related to a given energy is limited to the corresponding characteristic. This illustrates there are no mixing between different energy dynamics; high and low energy dynamics do not influence each other. In the non-conservative case, characteristics spiral toward the equilibrium point of the system (here, the origin) (see Fig. 17.4b).

Solving hyperbolic PDEs requires boundary conditions at inflow ($\partial\Omega^-$), i.e. where the velocity vector $\mathbf{V}$ points inward the domain. In our first order problem, it requires to set the unknown field values (X_i^-, Y_i^-) at this boundary. However, the domain boundary is away from the equilibrium point and corresponds to a region of high-energy where no theoretical information about the manifold is available. A first classical strategy would use an extrapolation techniques to estimate the unknown values at the boundary using the solution computed inside the domain. According to the above interpretation in terms of characteristics, this will involve a mixing between different energy dynamics. Extrapolation was therefore neglected. Nevertheless, we note that a domain with an iso-energy curve for boundary remains everywhere tangent to the flow and boundary conditions become obsolete. Assuming two different iso-energy curves, they form the inner and outer boundaries of an annular domain. Since a clear partition of the dynamics exists, one can solve the PDEs in this region disregarding the solution computed outside it. This strategy is key to our algorithm. It avoids to set disruptive boundary conditions and reduces the computational burden. This is particularly interesting as the number of degree of freedom of the mechanical system becomes large.

For noncoservative systems, there is no partition of the dynamics and the flow points inward the domain boundary. However, the methodology suggested remains applicable. Indeed, let's take an annular domain whose inner and outer boundaries correspond to iso-energy curves. Generally speaking, the flow points in and out at the outer and inner boundaries; respectively. However, from a pure mathematical point of view, characteristics only specify directions. It means that the flow can be "inverted" and spiral in and out at the inner and outer boundary; respectively. According to this observation, we can solve an "inverse" problem where boundary conditions have to be specified at the inner boundary. A recursive strategy can

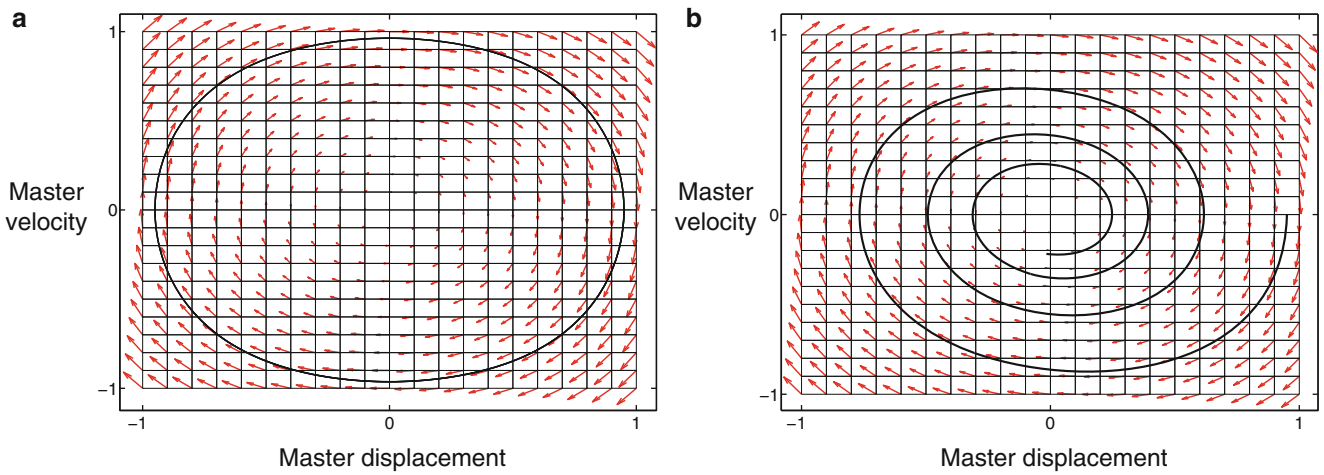

Fig. 17.4 PDEs are interpreted as flow equations where **V** describes the velocity field (→). (**a**) For a conservative system, the flow is tangent to iso-energy curves. (**b**) For a nonconservative system, the flow spirals to the equilibrium point

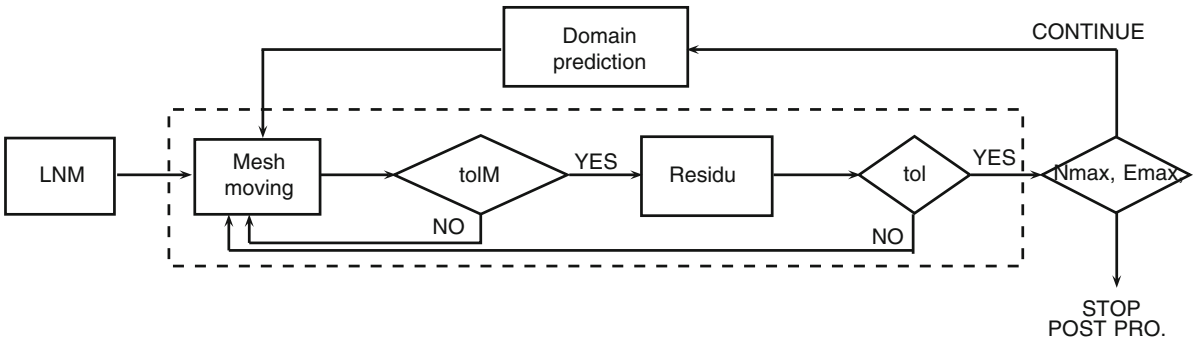

Fig. 17.5 Schematics of the algorithm resolution strategy

then be applied to progressively solve the PDEs using previously computed solution as boundary conditions for the next domain.

The proposed strategy suffers from a single limitation that is: iso-energy curves are only known at the solution. To circumvent this issue, a first guess of the iso-energy curve is computed using the previous domain boundary and solution. Then the shape of the new computational domain is iteratively modified as the new solution is computed. At the solution, the domain boundary fits the actual iso-energy.

17.3.1 Resolution Strategy Overview

The resolution strategy is illustrated in Fig. 17.5. The computation starts in a small domain around the origin where the system behaves almost linearly. The domain boundary is established for a given initial energy and computed using LNM. The LNM selected corresponds to the targeted NNM. The LNM is also considered as a first guess for the solution. To compute the actual solution, the domain boundary is corrected in order to fit the iso-energy corresponding to the current estimation of the solution. The correction is performed thanks to a mesh moving technique. It is applied a user-defined number of times and until some criteria are fulfilled (see Sect. 17.3.4). Domain corrections precedes each correction of the PDE solution in order to satisfy the boundary conditions. Once the solution is computed within a given accuracy *tol*, a new annular domain can be predicted. The prediction of the next iso-energy is performed using the previously computed solution. The new curve is considered as the new outer boundary whereas the old outer boundary becomes the inner one. Both boundaries define the new computational domain. The solution on this new annular region can be computed following a similar sequence of domain-correction and solution-correction. The NNM computation stops when the number of domain to compute or a maximum energy has been reached. Post-processing is performed in order to merge the different annular domains computed.

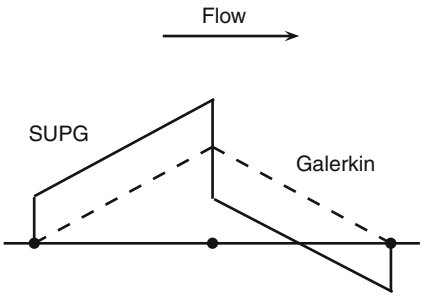

Fig. 17.6 Comparison between test functions in a classical Galerkin formulation (– –) and the discontinuous test functions in the SUPG formulation (—)

17.3.2 Streamline Upwinded Petrov-Galerkin

In order to solve hyperbolic PDEs using the FEM, specific numerical techniques are employed. Indeed, classical Galerkin finite element formulations using similar shape and test function spaces have demonstrated poor results, for instance, in the context of fluid dynamics[23, 24]. In the Finite Difference (FD) framework, off-centered schemes in the upwind direction are used in order to account for the "transport" phenomenon. In a similar way, several finite element formulations deal with this transport phenomenon using alternative test functions. The SUPG method is used herein and consists in over-weighting the shape functions that are upstream. This method falls within the general category of Petrov-Galerkin formulations where test and shape functions are taken in different spaces. The approach is rather standard and out of the scope of our paper. We briefly present the major points of our formulation and the interested reader can refer to [23–25] for practical details about SUPG.

To derive our finite element formulation, a weighted residual approach is applied to Eq. (17.8). The formulation is presented in Eq. (17.10) where $i = 1, \ldots, N$ with $i \neq k$ and where shape functions are considered as simple first order Lagrange shape functions: $N^b \in \mathbb{P}^1$. The test functions are $\tilde{N}^b = N^b + \tau \mathbf{V}.\nabla \mathbf{N^b}$. As already mentioned, test functions differ from classical Galerkin test functions via an upstream overweighting ($\tau \mathbf{V}.\nabla \mathbf{N^b}$). As a consequence, discontinuous test functions are employed [25]. Such test functions are illustrated in Fig. 17.6 and naturally account for the upstream origin of the information transported throughout the domain.

$$\begin{aligned} \int\int_{\Omega} [\mathbf{V}(u,v,\mathbf{X},\mathbf{Y}) \cdot \nabla X_i(u,v) - Y_i(u,v)]\, \delta \tilde{Y}_i \, du dv = 0 \\ \int\int_{\Omega} [\mathbf{V}(u,v,\mathbf{X},\mathbf{Y}) \cdot \nabla Y_i(u,v) - f_i(u,v,\mathbf{X},\mathbf{Y})]\, \delta \tilde{X}_i \, du dv = 0 \end{aligned} \tag{17.10}$$

The parameter τ is a problem dependent parameter. In fluid dynamics, it is often determined using Eq. (17.11) which is a function of the Peclet element number Pe^h, i.e. the ratio between diffusion and advection over the element, and h is the characteristic size of the elements. In the present case, our problem does not involve any diffusion and the limit for $\mathrm{Pe}^h \to \infty$ is $\tau = \frac{h}{2||V||_2}$. The estimation of the parameter τ is an important topic which still gives rise to recent publications [26]. Indeed, various other possible definitions for τ are presented in the literature [27–29]. According to this literature, the value of τ has a strong influence on the quality of the results. In our preliminary tests, the accuracy of the algorithm for NNM computation is not critically influenced by τ. However, the speed of convergence is. Further investigations on this parameter have to be performed.

$$\tau = \frac{h}{2||V||_2} \left(\coth(\mathrm{Pe}^h) - \frac{1}{\mathrm{Pe}^h} \right) \tag{17.11}$$

After the FE discretization, the set of PDEs is transformed to a set of coupled nonlinear algebraic equations. These equations are solved using a Newton-Raphson procedure where the Jacobian matrix is provided analytically. An important feature of our problem is that equations to solve remains nonlinear despite the mechanical system considered is linear.

In practice, master displacement and velocity frequently have different scales as it is commonly encountered in mechanical systems. This difference results in a domain with a poor aspect-ratio which, in turn, requires an excessive number of mesh elements. Two different scalings are applied to overcome this issue. The first one scales the time in order to retrieve similar displacement and velocity scales. The second scaling modifies both displacements and velocities in order to make them of order unity. Since such scalings are standard, they are not further discussed.

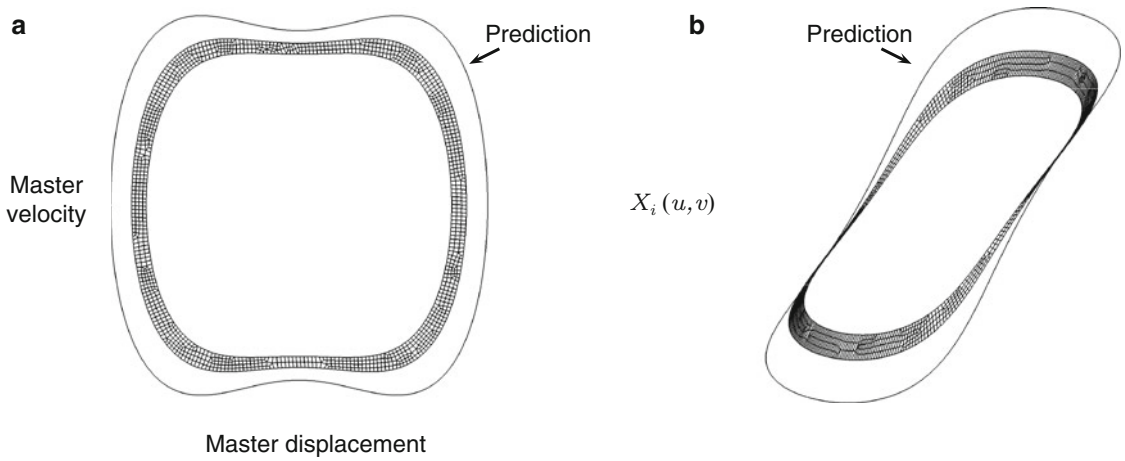

Fig. 17.7 From the solution computed for the annular domain, we predict the next domain boundary (**a**) and the values of the different unknown fields (**b**)

17.3.3 Domain Prediction

The prediction of the domain $d+1$ is performed using an approach similar to continuation. We first assume that the solution computed on the domain d is accurate. The outer boundary is therefore an iso-energy curve of energy E^d. This outer boundary becomes the inner boundary of the next domain $d+1$. To compute the new outer boundary, we apply an energy increment ΔE^d and look for an estimation of the iso-energy curve at $E^{d+1} = E^d + \Delta E^d$. Linearizing the energy around each point i of the boundary d, we obtain Eq. (17.12). Solving Eq. (17.13) transforms the energy increment in terms of displacements $(\Delta u_i, \Delta v_i)$ to apply to the boundary nodes. Figure 17.7a illustrates the result of this procedure.

$$E^{d+1} = E^d + \tfrac{dE}{du}|^{d,i}\Delta u_i + \tfrac{dE}{dv}|^{d,i}\Delta v_i, \quad \forall i, \tag{17.12}$$

$$\Rightarrow \Delta E^d = \tfrac{dE}{du}|^{d,i}\Delta u_i + \tfrac{dE}{dv}|^{d,i}\Delta v_i, \quad \forall i. \tag{17.13}$$

Solving for $(\Delta u, \Delta v)$ requires the use of the "Moore-Penrose" pseudo-inverse since the system is under determined. The sensitivity of the energy with respect to u and v is presented in Eqs. (17.14) and (17.15) where the constraint relations between slave and master coordinates are considered. The sensitivity of the energy with respect to master or slave coordinates has a clear link with the equations of motion (17.1) and is provided analytically. The sensitivity of the constraint relations (i.e. $\partial_u X, \ldots$) are provided by the FEM. Note that linear and nonlinear nonconservative terms are disregarded in the equations. Finally, an estimation of the unknown field j is provided thanks to the local tangent-plane at each node i (Eq. (17.16)). The result is illustrated in Fig. 17.7b.

$$E_i = E_i(u,v) = E_i(u,v,\mathbf{X}(u,v),\mathbf{Y}(u,v)) = \frac{1}{2}\left(\mathbf{q}^T\mathbf{K}\mathbf{q} + \dot{\mathbf{q}}^T\mathbf{M}\dot{\mathbf{q}} + \dot{\mathbf{q}}^T\mathbf{G}_{\text{gyr}}\dot{\mathbf{q}} + E_{\text{NL}}\right). \tag{17.14}$$

$$\begin{aligned}
\frac{dE_i}{du} &= \left.\frac{\partial E}{\partial u}\right|_i + \left.\frac{\partial E}{\partial \mathbf{X}}\right|_i \left.\frac{\partial \mathbf{X}}{\partial u}\right|_i + \left.\frac{\partial E}{\partial \mathbf{Y}}\right|_i \left.\frac{\partial \mathbf{Y}}{\partial u}\right|_i, \\
\frac{dE_i}{dv} &= \left.\frac{\partial E}{\partial v}\right|_i + \left.\frac{\partial E}{\partial \mathbf{X}}\right|_i \left.\frac{\partial \mathbf{X}}{\partial v}\right|_i + \left.\frac{\partial E}{\partial \mathbf{Y}}\right|_i \left.\frac{\partial \mathbf{Y}}{\partial v}\right|_i.
\end{aligned} \tag{17.15}$$

$$\begin{aligned}
X_j^{d+1}(u_i^{d+1}, v_i^{d+1}) &= X_j^i(u_i^d, v_i^d) + \left.\frac{\partial X_j}{\partial u}\right|_i \Delta u_i + \left.\frac{\partial X_j}{\partial v}\right|_i \Delta v_i \\
Y_j^{d+1}(u_i^{d+1}, v_i^{d+1}) &= Y_j^i(u_i^d, v_i^d) + \left.\frac{\partial Y_j}{\partial u}\right|_i \Delta u_i + \left.\frac{\partial Y_j}{\partial v}\right|_i \Delta v_i, \\
\forall i, \qquad & j = 1, \ldots, N;\ j \neq k.
\end{aligned} \tag{17.16}$$

17.3.4 Domain Correction Using a Mesh Moving Technique

As introduced, the shape of the computational domain is chosen in order to avoid to impose boundary conditions. Such a domain needs to be everywhere tangent to the flow $\mathbf{V}$. In the particular case of a conservative system, the flow is everywhere tangent to iso-energy curves. An iso-energetic domain boundary would therefore meet our requirement. Unfortunately, such curves are known at the solution and only a prediction of it can be performed. In order to satisfy the need of boundary conditions to solve the hyperbolic problem, the domain is modified at each iteration such that it is an iso-energy curve for the current estimation of the solution. At each iteration, BCs are thus satisfied and the hyperbolic problem is well posed.

In order to modify the domain's shape so that it fits closely an iso-energy curve, the mesh is considered as a pseudo-elastic medium and a linear elasticity problem is solved. The inner boundary is considered as clamped (displacements are set to zero) while the outer boundary is moved in order to equal a reference energy. For simplicity reasons, the reference energy is considered to be the energy of the node with $u_{max} = max(u)$. This reference energy evolves with the computation of the solution. The formula used to compute the displacements imposed to the boundary nodes are similar to formula used for domain prediction (Eqs. (17.12)–(17.15)). The only difference is the energy increment ΔE that is now determined to equal the reference energy.

Mesh moving techniques have the advantage to properly deform the domain so that elements remain well-shaped and that (almost) no remeshing operations are needed. Without going into the details of mesh moving techniques, the equations governing the displacements are:

$$\begin{aligned} &\nabla.\sigma = \mathbf{0}, \sigma = \mathbf{D} : \varepsilon, \varepsilon = \frac{1}{2}(\nabla\mathbf{q} + \nabla\mathbf{q}^{\mathrm{T}}), \\ &\mathbf{D}_{ijkl} = \frac{E\nu}{(1+\nu)(1-2\nu)}\delta_{ij}\delta_{kl} + \frac{E}{1+\nu}\left(\frac{1}{2}\delta_{ik}\delta_{jl} + \frac{1}{2}\delta_{il}\delta_{jk}\right), \end{aligned} \tag{17.17}$$

where $\nabla.(\,)$ denotes the divergence operator, σ the Cauchy stress tensor, $\mathbf{D}$ the Hooke tensor, ε the strain tensor, E Young's modulus, ν Poisson's ratio, and δ_{ij} the Kronecker delta. After discretization using the finite element method, a linear algebraic problem is obtained (Eq. (17.18)) where $\mathbf{K}^{elast}$ denotes the stiffness matrix of the discretized domain considered as a pseudo-elastic medium. This matrix should not be confused with the stiffness matrix $\mathbf{K}$ of the mechanical system.

$$\mathbf{K}^{\text{elast}}\mathbf{q} = \mathbf{0} \tag{17.18}$$

The displacements $\mathbf{q}$ are split into three different sets, namely: clamped nodes whose displacements equal zero ($\mathbf{q}_0 = \mathbf{0}$), outer nodes whose displacements are non-zero and follow the energy corrections ($\mathbf{q}_d$), and finally internal nodes whose displacements are unknown ($\mathbf{q}_i$). This partition provides a straight forward expression for the unknown displacements $\mathbf{q}_i$ (Eq. (17.19)). Additional information about mesh moving techniques can be found in [30, 31].

$$\begin{bmatrix} \mathbf{K}_{ii} & \mathbf{K}_{id} & \mathbf{K}_{i0} \\ \mathbf{K}_{di} & \mathbf{K}_{dd} & \mathbf{K}_{di} \\ \mathbf{K}_{0i} & \mathbf{K}_{0d} & \mathbf{K}_{00} \end{bmatrix}^{\text{elast}} \begin{bmatrix} \mathbf{q}_i \\ \mathbf{q}_d \\ \mathbf{q}_0 \end{bmatrix} = \mathbf{0} \Rightarrow \mathbf{q}_i = -\mathbf{K}_{ii}^{-1}\mathbf{K}_{id}\mathbf{q}_d \tag{17.19}$$

Mesh modification according to iso-energy curves is critical and can lead to divergence if not performed. Indeed, the correction should be applied enough times in order to have a domain which is consistent with the current estimation of the solution. Without proper boundary conditions, the problem to solve is not well posed and the PDE resolution will fail. The mesh-moving algorithm is applied, at least, a user-defined number of times. It is stopped if the mean energy of all boundary points is sufficiently close to the reference energy. An additional criteria can be set on the standard deviation of the energy to ensure that boundary points have indeed an energy close to the reference one.

17.4 Algorithm Demonstration on Conservative Examples

In this section, the NNMs of a five DOF conservative system are discussed and used to assess our resolution method. The system considered includes a cubic spring between the second and third masses. It also includes a quadratic and quintic spring between the third and fifth masses. The system is illustrated in Fig. 17.8 with its numerical parameters.

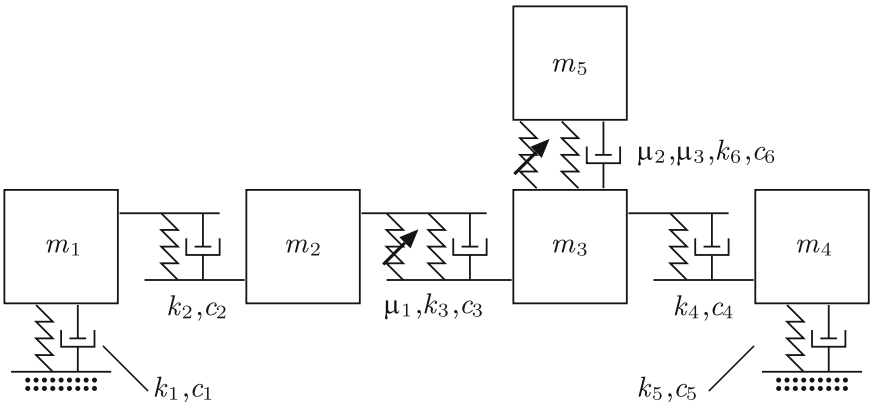

Fig. 17.8 Schematic view of the 5 DOF system. A cubic nonlinearity with coefficient μ_1 is introduced between the second and the third masses. A quadratic and quintic nonlinearity is introduced between the third and the fifth masses (μ_2, μ_3). $m_{1-6} = 1$ [Kg], $k_{1-5} = 50e3$ [N/m], $k_6 = 35e3$ [N/m], $c_{1-6} = 0$ [Ns/m], $\mu_1 = 500e6$ [N/m^3], $\mu_2 = -500e3$ [N/m^2], $\mu_3 = 10e9$ [N/m^5]

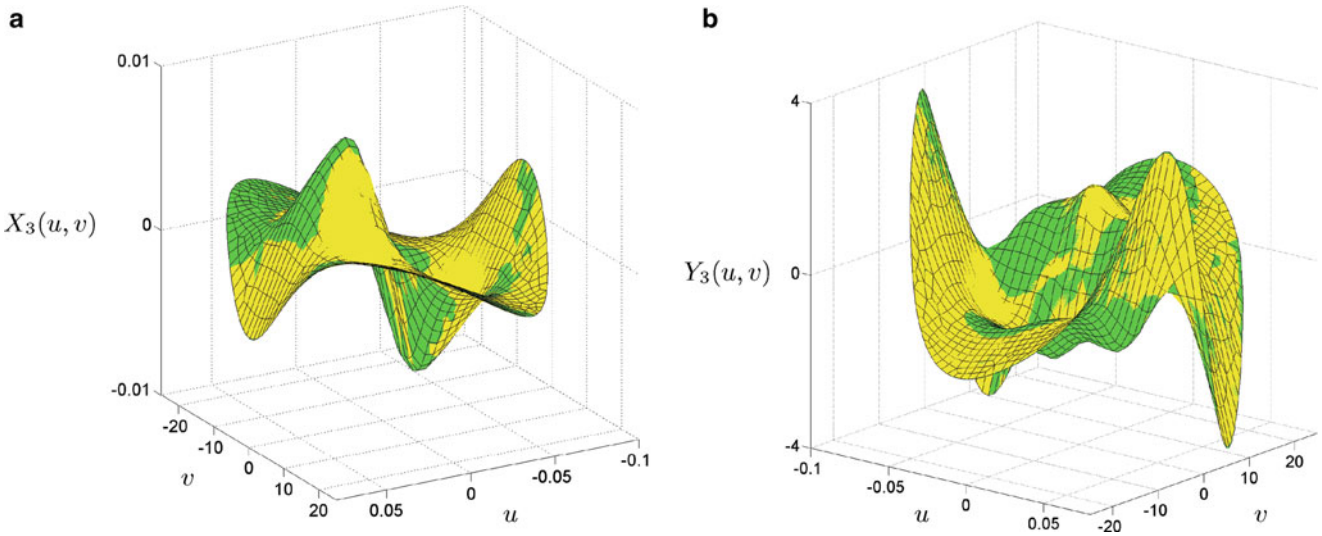

Fig. 17.9 Second NNM for the 5 DOF system. The results from the invariant manifold approach (*green*) are in excellent agreement with the reference (*yellow*). (**a**) Slave displacement X_3. (**b**) Slave velocity Y_3 (color figure online)

For conservative systems, different reference algorithms to compute NNMs exist [11, 13, 32]. For instance, the "exact" manifolds can be computed using the technique developed in [13], which combines shooting and pseudo-arclength continuation. For each NNM, the graphical depiction in phase space of the periodic orbits at different energy levels provides a reference solution to which we can compare the solution computed using the invariant manifold approach.

Figure 17.9 presents the second NNM of the 5DOF system for the slave displacement and velocity of the third mass (X_3 and Y_3). The results coming from the invariant manifold approach are depicted in green whereas the reference solutions are in yellow. A very good agreement between computed and reference surfaces is observed (green and yellow are "intimately mixed").

A more quantitative comparison of the results is now carried out. The initial conditions in the modal space (u, v) of the second mode are transformed back to physical space $(\mathbf{x}, \mathbf{y})$ using Eq. (17.4). Both the equations of motion in physical space (17.1) and in modal space (17.7) are numerically integrated for these initial conditions using a fifth order Runge-Kutta method. The resulting time series in modal space are then transformed back to physical space and compared to the time series generated directly in physical space. The comparison is achieved using the normalized mean-square error (NMSE):

$$\text{NMSE}(\hat{f}) = \frac{100}{N\sigma_f^2} \sum_{i=1}^{N} (f(i) - \hat{f}(i))^2 \tag{17.20}$$

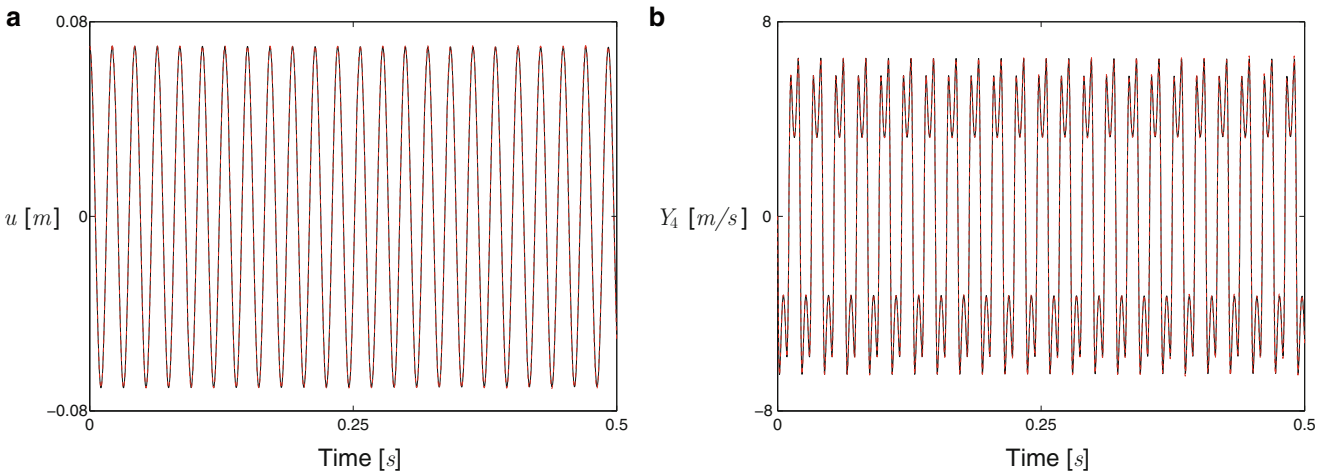

Fig. 17.10 Comparison between the dynamics reduced on the manifold (—) and the full-system dynamics (– –). Both time series are superimposed and the NMSE value of 7e −2% confirms the perfect matching. (**a**) Master displacement. (**b**) Slave velocity of the fourth mass (color figure online)

where $\hat{f}$ is the time series to be compared to the reference series f, N is the number of samples and σ_f^2 is the variance of the reference time series. A NMSE value of 1% is commonly assumed to reflect excellent concordance between the time series.

Figure 17.10 compares the dynamics reduced on the invariant manifold and the full-system dynamics. A excellent agreement between the different time series is observed. Despite the complexity of the time series (cf. Fig. 17.10b), the matching is conserved over more than 20 periods. It especially indicates a very accurate capture of the motion frequency (in addition to the motion amplitude capture). The NMSE of 7e − 2% confirms our observations.

17.5 Two Nonlinear Nonconservative Systems

In this section, we first consider a simple nonlinear system with weak linear non-proportional damping. This system is the system already presented in Fig. 17.1 where we have introduced damping. The equations of motion are presented in Eq. (17.21).

$$\begin{aligned} \ddot{x}_1 + 2x_1 - x_2 + 0.5x_1^3 + c_1\dot{x}_1 - c_2\dot{x}_2 &= 0, \\ \ddot{x}_2 + 2x_2 - x_1 - c_2\dot{x}_1 + c_3\dot{x}_2 &= 0. \end{aligned} \tag{17.21}$$

Figure 17.11 presents the second NNM of the system. This mode corresponds to an out-of-phase motion of the two masses. In the nonconservative case, reference solutions do not exist and the solution accuracy assessment is performed through the dynamics. The computation of the dynamics for various initial conditions shows NMSE values around 1e − 3%. This very good accuracy is illustrated in Fig. 17.12a where we observe a perfect matching between the dynamics reduced on the NNM and the full-system dynamics.

In Fig. 17.11a, we observe a "hill" in the surface describing the slave displacement $X_2(u,v)$. This hill illustrates the localization phenomenon. Indeed, as the energy increases, both master coordinates increase whereas the slave coordinates decreases, all the energy is localized into the first mass. The localization phenomenon was already observed for the conservative system and it is now preserved in the presence of weak linear damping. The integration of the dynamics over a very long period (the system is weakly damped) and for "high-energy" initial conditions illustrates the particular behavior of X_2 (see Fig. 17.12b). Thus, despite the presence of damping, X_2 first increases and then decreases. On the surface $X_2(u,v)$, the time series of Fig. 17.12b corresponds to a motion that starts out close to the domain boundary and that spirals toward the origin. Each passage through the hill happens closer to the origin and first increases then decreases the motion amplitude. Exponential decay is observed for the master DOF.

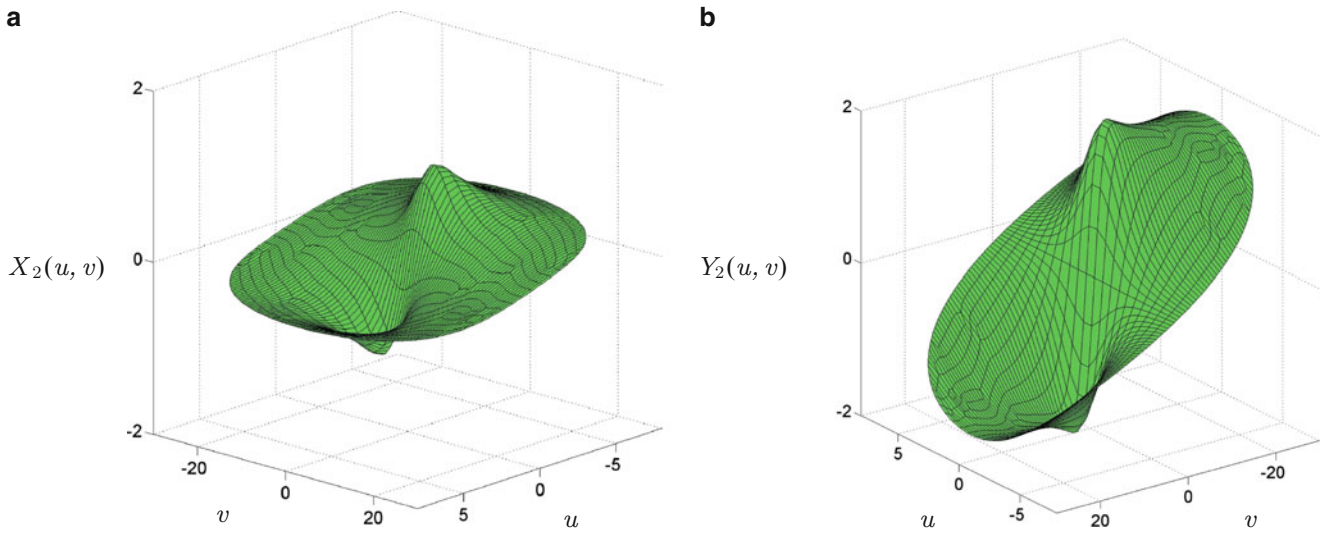

Fig. 17.11 Second NNM for the 2DOF system with weak non-proportional linear damping. (**a**) Slave displacement X_3. (**b**) Slave velocity Y_3

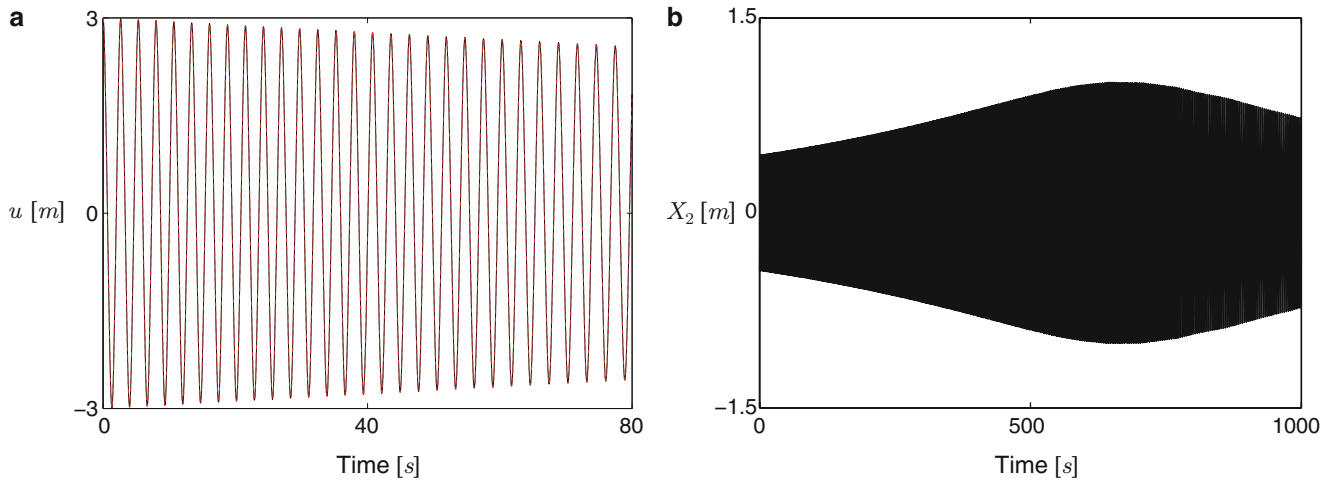

Fig. 17.12 (**a**) Comparison between the dynamics reduced on the manifold (—) and the full-system dynamics (– –). Both figures represents the master displacement $u(t)$. Initial conditions are taken as $(u, v) = (4.0, 0)$. The NMSE equals $1e-3\%$. (**b**) Localization phenomenon observed for high-energy initial conditions ($(u, v) = (6.0, 0)$) (color figure online)

We now consider a more complicated system with 2DOF and including a cubic stiffness, negative linear damping, and cubic positive damping. The equations of motion of these coupled-Rayleigh oscillators are presented in Eq. (17.22) where $a = 0.1$ and $b = 0.75$.

$$\begin{aligned} \ddot{x}_1 + 2x_1 - x_2 + 0.5x_1^3 + b\dot{x}_1^3 + b(\dot{x}_1 - \dot{x}_2)^3 - 2a\dot{x}_1 + a\dot{x}_2 = 0 \\ \ddot{x}_2 + 2x_2 - x_1 + b\dot{x}_2^3 - b(\dot{x}_1 - \dot{x}_2)^3 - 2a\dot{x}_2 + a\dot{x}_1 = 0 \end{aligned} \tag{17.22}$$

Figure 17.13a displays the invariant manifold computed from the first LNM. Results validation are performed using the dynamics. Figure 17.14 presents the dynamics computed for two different initial conditions. An excellent agreement is again observed and NMSE values do not exceed $3e-3\%$. For both initial conditions, we can observe that oscillations amplitude are conserved after some transient response. The representation of time series in the (u, v) plane highlights the presence of a limit cycle. We note that to properly simulate the dynamics, a fine mesh is needed around this limit cycle.

In this example, we went beyond the theoretical framework of NNMs. However, we show that the algorithm is still capable of reducing accurately the dynamics on a two-dimensional invariant manifold.

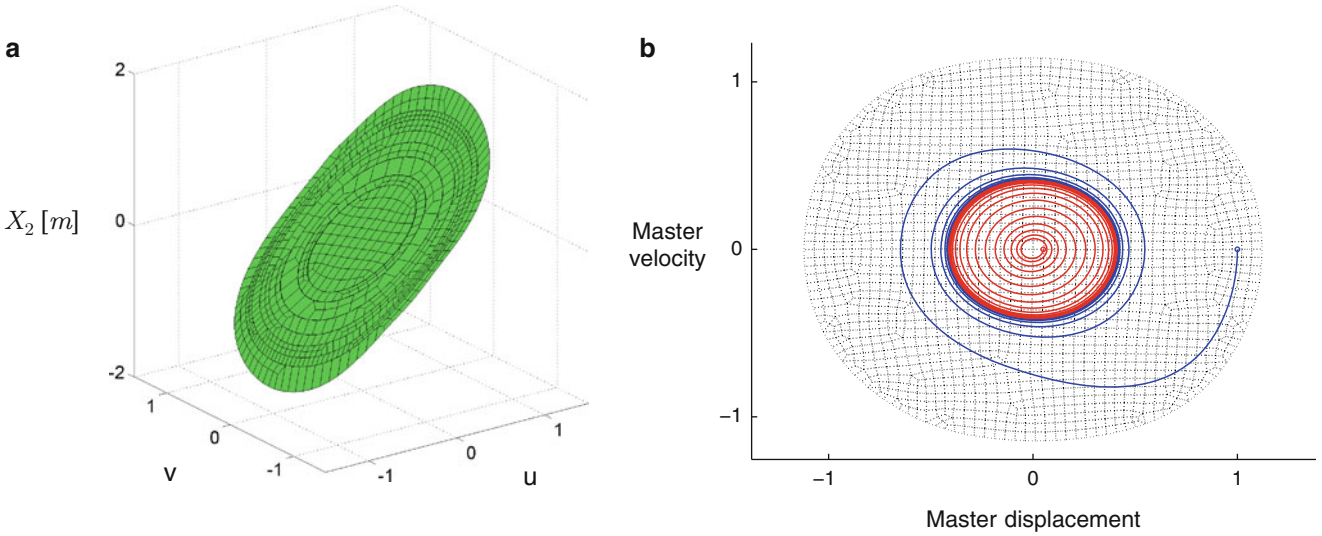

Fig. 17.13 Invariant manifold computed from the first LNM. (**a**) Slave displacement of the second mass (X_2) (**b**) Dynamics in the 2D phase plane. Two different initial conditions are considered: $(u,v) = (0.1,0)$ and $(u,v) = (0.94,0)$ and both are denoted by a *circle*. A limit-cycle is observed

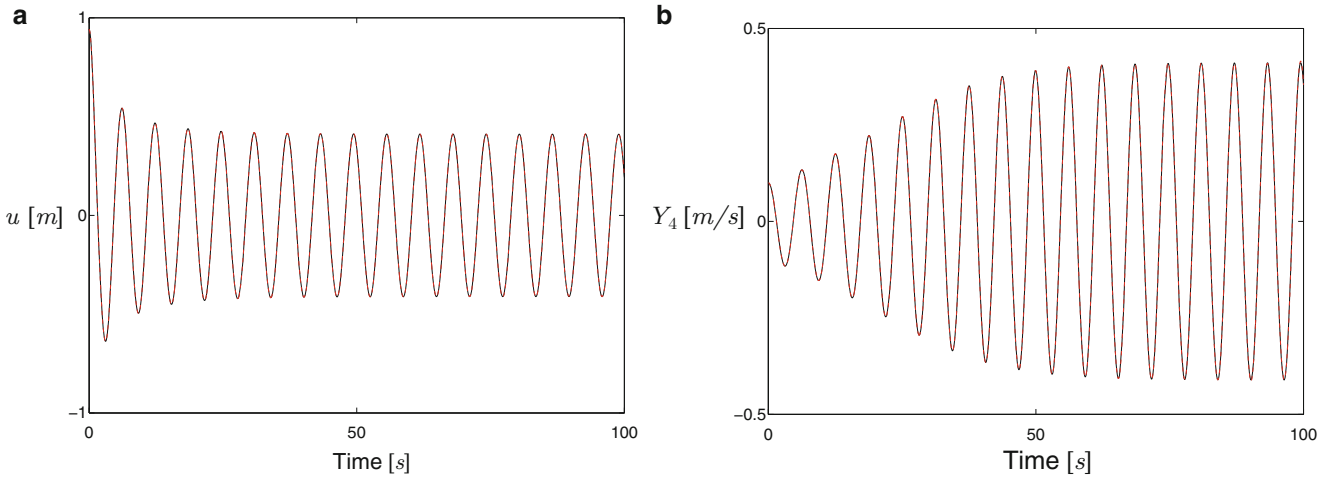

Fig. 17.14 Comparison between the dynamics reduced on the manifold (—) and the full-system dynamics (– –). *Both figures* represents the master displacement $u(t)$. (**a**) Initial conditions are taken as $(u,v) = (0.94,0)$. The NMSE equals 1e −3%. (**b**) Initial conditions are taken as $(u,v) = (0.1,0)$. The NMSE equals 3e − 3%

17.6 Conclusions

After a brief review of the key concepts about NNMs (Sect. 17.2), we introduced the PDEs governing the NNMs defined as an invariant manifold in phase space. Alike [4], our formulation uses physical rather than modal coordinates. In Sect. 17.3, we presented a novel algorithm to solve NNMs equations. We especially highlighted the hyperbolic nature of the PDEs (transport phenomenon) and, based on this observation, we proposed specific numerical treatments. The FE formulation (SUPG) is properly suited to our equations and the resolution strategy accounts for the boundary conditions using annular-ring domains with iso-energy boundaries. A mesh moving technique is employed to correct the shape of the domain. Section 17.4 demonstrated the algorithm on a MDOF conservative system with multiple nonlinearities. The computation of the NNM and the resulting dynamics were both very accurate. Finally, Sect. 17.5 demonstrated that the developed algorithm was applicable to nonconservative system including either linear or nonlinear damping.

Despite our algorithm can already deal with a large variety of systems, additional investigations are still needed. In particular, we note the influence of the SUPG parameter τ that is crucial to the method. Another feature of the invariant

manifold approach is that the notion of time is lost and the access to the motion frequency is not straightforward. Next developments will include the computation of this frequency.

Acknowledgements The author L. Renson would like to acknowledge the Belgian National Fund for Scientific Research (FRIA fellowship) for its financial support.

References

1. Rosenberg RM (1966) On nonlinear vibrations of systems with many degrees of freedom. Adv Appl Mech 9:155–242
2. Rosenberg RM (1962) The normal modes of nonlinear n-degree-of-freedom systems. J Appl Mech 29(1):7–14
3. Shaw SW, Pierre C (1991) Non-linear normal modes and invariant manifolds. J Sound Vib 150(1):170–173
4. Shaw SW, Pierre C (1993) Normal modes for non-linear vibratory systems. J Sound Vib 164:40
5. Jezequel L, Lamarque CH (1991) Analysis of non-linear dynamical systems by the normal form theory. J Sound Vib 149(3):429–459
6. King ME, Vakakis AF (1994) An energy-based formulation for computing nonlinear normal modes in undamped continuous systems. J Vib Acoust 116(3):332–340
7. Mikhlin YV, Pilipchuk VN, Zevin AA, Vakakis AF, Manevitch LI (1996) Normal modes and localization in nonlinear systems. Wiley, New York
8. Touz C, Thomas O, Huberdeau A (2004) Asymptotic non-linear normal modes for large-amplitude vibrations of continuous structures. Comput Struct 82:2671–2682
9. Slater J (1996) A numerical method for determining nonlinear normal modes. Nonlinear Dyn 10(1):19–30
10. Lee YS, Kerschen G, Vakakis AF, Panagopoulos P, Bergman L, McFarland DM (2005) Complicated dynamics of a linear oscillator with a light, essentially nonlinear attachment. Phys Nonlinear Phenom 204:41–69
11. Arquier R, Bellizzi S, Bouc R, Cochelin B (2006) Two methods for the computation of nonlinear modes of vibrating systems at large amplitudes. Comput Struct 84:1565–1576
12. Wang F, Bajaj A (2007) Nonlinear normal modes in multi-mode models of an inertially coupled elastic structure. Nonlinear Dyn 47(1):25–47
13. Peeters M, Vigui R, Srandour G, Kerschen G, Golinval JC (2009) Nonlinear normal modes, part II: toward a practical computation using numerical continuation techniques. Mech Syst Signal Process 23(1):195–216
14. Peeters M, Kerschen G, Golinval JC, Stephan C (2011) Nonlinear normal modes of real-world structures: application to a full-scale aircraft. ASME Conf Proc 2011(54785):475–492
15. Pesheck E (2000) Reduced order modeling of nonlinear structural systems using nonlinear normal modes and invariant manifolds. PhD thesis, University of Michigan
16. Pesheck E, Pierre C, Shaw SW (2002) A new Galerkin-based approach for accurate non-linear normal modes through invariant manifolds. J Sound Vib 249(5):971–993
17. Blanc F, Touzé C, et al. (2013) On the numerical computation of nonlinear normal modes for reduced-order modelling of conservative vibratory systems. Mech Syst Signal Process 36(2):520–539
18. Noreland D, Bellizzi S, Vergez C, Bouc R (2009) Nonlinear modes of clarinet-like musical instruments. J Sound Vib 324:983–1002
19. Laxalde D, Legrand D (2011) Nonlinear modal analysis of mechanical systems with frictionless contact interfaces. Comput Mech 47(4):469–478
20. Kerschen G, Peeters M, Golinval JC, Vakakis AF (2009) Nonlinear normal modes, part I: a useful framework for the structural dynamicist. Mech Syst Signal Process 23(1):170–194
21. Larsson S, Thome V (2003) Partial differential equations with numerical methods, vol 45. Springer, Berlin/Heidelberg
22. Renardy M, Rogers R (2004) An introduction to partial differential equations, vol 13. Springer, Berlin/Heidelberg
23. Donea J, Huerta A (2005) Finite element methods for flow problems. Wiley, Chichester
24. Brooks AN, Hughes TJR (1982) Streamline upwind/Petrov-Galerkin formulations for convection dominated flows with particular emphasis on the incompressible Navier-Stokes equations. Comput Methods Appl Mech Eng 32:199–259
25. Hughes TJR, Tezduyar TE (1984) Finite element methods for first-order hyperbolic systems with particular emphasis on the compressible euler equations. Comput Methods Appl Mech Eng 45(1–3):217–284
26. Knobloch P (2008) On the definition of the SUPG parameter. Electron Trans Numer Anal 32:76–89
27. Tezduyar TE, Osawa Y (2000) Finite element stabilization parameters computed from element matrices and vectors. Comput Methods Appl Mech Eng 190:411–430
28. Akin JE, Tezduyar TE (2004) Calculation of the advective limit of the SUPG stabilization parameter for linear and higher-order elements. Comput Methods Appl Mech Eng 193:1909–1922
29. Codina R, Oate E, Cervera M (1992) The intrinsic time for the streamline upwind/Petrov-Galerkin formulation using quadratic elements. Comput Methods Appl Mech Eng 94(2):239–262
30. Stein K, Tezduyar TE, Benney R (2004) Automatic mesh update with the solid-extension mesh moving technique. Comput Methods Appl Mech Eng 193:2019–2032
31. Xu Z, Accorsi M (2004) Finite element mesh update methods for fluid-structure interaction simulations. Finite Elem Anal Des 40:1259–1269
32. Cochelin B, Vergez C (2009) A high order purely frequency-based harmonic balance formulation for continuation of periodic solutions. J Sound Vib 324:243–262

Chapter 18
Discrete Empirical Interpolation Method for Finite Element Structural Dynamics

Paolo Tiso and Daniel J. Rixen

Abstract Model Order Reduction (MOR) in nonlinear structural analysis problems in usually carried out by a Galerkin projection of the primary variables on a sensibly smaller space. However, the cost of computing the nonlinear terms is still of the order of the full system. The Discrete Empirical Interpolation Method is an effective algorithm to reduce the computational of the nonlinear term. However, its efficiency is diminished when applied to a Finite Element (FE) framework. We present here an alternative formulation of the DEIM that suits an FE formulation and preserves the efficiency of the method.

Keywords Model order reduction • Nonlinear dynamics • DEIM • Finite elements • Reduction basis

18.1 Introduction

Several advanced structural systems often exploit nonlinear geometrical effects rather than avoiding them. Large displacements are unavoidable for aeronautics and aerospace structures for which the minimum weight is a key design factor. It is therefore important to consider nonlinearity even in the early design stage by appropriate modeling practice. However, the nonlinear dynamic analysis of large finite element (FE) structural models is an onerous task, and effective Model Order Reduction (MOR) techniques are widely welcomed.

An well known MOR technique is the Galerkin projection. The solution is projected onto a subspace of much smaller dimension, spanned by a set of appropriate modes, otherwise called Reduction Basis (RB). In this work, we refer to RBs formed by Proper Orthogonal Decomposition (POD) [3]. However, other choices are possible when dealing with geometrical nonlinearities [4, 5].

When the discretized equations of motion are projected onto the displacement RB, the cost of the evaluation of the nonlinear term (in our case, the nonlinear internal elastic forces) still scales with the dimension of the original problem. Recently, the Discrete Empirical Interpolation Method (DEIM) has been proposed [2] to drastically reduce the computational cost of the evaluation of the discretized nonlinear term in a Galerkin framework. The main idea is to project the nonlinear vector onto a RB. The unknown amplitudes of the modes contained in the RB are obtained by collocating the approximation at specific components which are selected by a greedy procedure. The component values at other locations are approximated through the RB by an interpolation matrix that can be pre-computed offline.

The direct application of DEIM on FE discretized problems is rather inefficient. The problem lays in the fact that each component of the nonlinear force depends on the nodal displacements of all the neighbouring elements (in other words, it depends on the sparsity of the problem). Depending on the type of element and the mesh, this would require a relative large number of element function call for the evaluation of just a single component of the nonlinear term.

P. Tiso (✉)
Delft University of Technology, Mekelweg 2, 2628CD, Delft, The Netherlands
e-mail: p.tiso@tudelft.nl

D.J. Rixen
Technischen Universität Mnchen, Fakultät für Maschinenwesen, Boltzmannstraße 15 85748 Garching, Deutschland
e-mail: rixen@tum.de

G. Kerschen et al. (eds.), *Topics in Nonlinear Dynamics, Volume 1: Proceedings of the 31st IMAC, A Conference on Structural Dynamics, 2013*, Conference Proceedings of the Society for Experimental Mechanics Series 35,
DOI 10.1007/978-1-4614-6570-6_18,

We propose a simple modification of the original DEIM algorithm that minimizes the number of element function calls, thus preserving the high sparsity nature of the algorithm. Essentially, the idea is to operate with unassembled vectors in order for each DEIM selected point to be linked with just one element. We call this modification UDEIM (Unassembled DEIM).

We will show through some preliminary numerical experiments that the UDEIM variant produces similar accuracy of the original DEIM but reduces the number of element calls. Possible difficulties and improvements are then indicated.

18.2 Preliminaries

In this section, we first introduce the governing equations for geometrically nonlinear structural dynamics. Subsequently, we present the general Galerkin technique for model order reduction (MOR) and briefly summarize the Proper Orthogonal Decomposition (POD) approach to obtain a suitable reduction basis.

18.2.1 Governing Equations

We consider here the discretized N FE nonlinear dynamic equations of motion of a general tridimensional structure. For this study, we do not consider damping. The governing FE system of equations, together with the boundary conditions, writes:

$$\begin{cases} \mathbf{M}\ddot{\mathbf{y}} + \mathbf{K}\mathbf{y} + \mathbf{f}(\mathbf{y}) = \mathbf{p} \\ \mathbf{y}(0) = \mathbf{y}_0 \\ \dot{\mathbf{y}}(0) = \dot{\mathbf{y}}_0 \end{cases} \tag{18.1}$$

where $\mathbf{y}(t) \in \mathbb{R}^n$ is the generalized displacement vector, $\mathbf{M} \in \mathbb{R}^{n\times n}$ and $\mathbf{K} \in \mathbb{R}^{n\times n}$ are the mass and the linear stiffness matrices, respectively, $\mathbf{f}(\mathbf{y}) : \mathbb{R}^n \mapsto \mathbb{R}^n$ is the nonlinear force vector (in general, vector valued) and $\mathbf{p} \in \mathbb{R}^n$ is the time dependent applied load vector. The initial conditions for the displacement and the velocity vector are indicated with $\mathbf{y}_0$ and $\dot{\mathbf{y}}_0$, respectively. We further assume that the nonlinearity of $\mathbf{f}(\mathbf{y})$ is caused by geometrical effects only, i.e. when the displacements are so large that a linear kinematic model does not hold. This is typically the case of thin-walled structures, which can undergo large displacements while staying in the elastic range of the material. We adopt here the Von-Karman kinematic model, which is valid for moderate rotation and small strains [1].

18.2.2 Galerkin Projection

In practical applications, the system of n equations (18.1) is usually large. The number of unknowns can be reduced to k, with $k \ll n$, by projecting the displacement field $\mathbf{y}$ on a suitable basis $\boldsymbol{\Phi} \in \mathbb{R}^{n\times k}$ of time-independent vectors, as:

$$\mathbf{y} \approx \boldsymbol{\Phi}\mathbf{q} \tag{18.2}$$

where $\mathbf{q}(t) \in \mathbb{R}^k$ is the vector of modal amplitudes. The governing equations can then be projected on the chosen basis $\boldsymbol{\Phi}$ in order to make the residual orthogonal to the subspace in which the solution $\mathbf{q}$ is sought. This results in a reduced system of k non-linear equations:

$$\boldsymbol{\Phi}^T\mathbf{M}\boldsymbol{\Phi}\ddot{\mathbf{q}}(t) + \boldsymbol{\Phi}^T\mathbf{K}\boldsymbol{\Phi}\mathbf{q} + \boldsymbol{\Phi}^T\mathbf{f}(\boldsymbol{\Phi}\mathbf{q}) = \boldsymbol{\Phi}^T\mathbf{p} \tag{18.3}$$

or, equivalently,

$$\hat{\mathbf{M}}\ddot{\mathbf{q}} + \hat{\mathbf{K}}\mathbf{q} + \hat{\mathbf{f}}(\boldsymbol{\Phi}\mathbf{q}) = \hat{\mathbf{p}} \tag{18.4}$$

where the time dependency of $\mathbf{q}$ has been dropped for clarity. We refer to the numerical solution $\mathbf{y}$ of the full model (18.1) as the *full* solution, while the solution of the reduced model (18.4) will be called *reduced* solution, indicated as $\tilde{\mathbf{y}} = \boldsymbol{\Phi}\tilde{\mathbf{q}}$. The key of a good reduction method is to find a suitable basis $\boldsymbol{\Phi}$ that is able to reproduce the full solution with a good, hopefully controlled, accuracy.

18.2.3 Proper Orthogonal Decomposition

Among other choices, the Proper Orthogonal Decomposition (POD) is an effective method to construct a low-dimensional approximation of a subspace. The outline of the method is briefly recapped here.

Let us suppose to collect an ensemble of snapshots $\mathbf{Y} = [\mathbf{y}_1, \ldots, \mathbf{y}_{n_s}] \in \mathbb{R}^{n \times n_s}$ of a full solution, and $r = span(\mathbf{Y})$. A POD basis of dimension $k < r$ is a set of orthonormal vectors $\{\boldsymbol{\Phi}_i\}_{i=1}^{k}$ which solves the following minimization problem:

$$\min_{\{\boldsymbol{\Phi}_i\}_{i=1}^{k}} \sum_{j=1}^{n_s} ||\mathbf{y}_j - \sum_{i=1}^{k} (\mathbf{y}_j^T \boldsymbol{\Phi}_i)\boldsymbol{\Phi}_i||_2^2 \tag{18.5}$$

It is well known that the solution to (18.5) is the set of singular vectors of $\mathbf{Y}$. These are obtained by the Singular Value Decomposition (SVD) as:

$$\text{SVD}(\mathbf{Y}) : \ \mathbf{Y} = \mathbf{W}\Sigma\mathbf{V}^T \tag{18.6}$$

where $\mathbf{W} = [\mathbf{w}_1, \ldots, \mathbf{w}_r] \in \mathbb{R}^{n \times r}$, $\mathbf{V} = [\mathbf{v}_1, \ldots, \mathbf{v}_r] \in \mathbb{R}^{r \times n_s}$ are orthogonal and $\Sigma = \text{diag}(\sigma_1, \ldots \sigma_r) \in \mathbb{R}^{r \times r}$ with $\sigma_1 > \sigma_2 > \cdots > \sigma_r > 0$. The error on the minimum 2-norm for approximating the snapshots using the POD base is given by:

$$\sum_{j=1}^{n_s} ||\mathbf{y}_j - \sum_{i=1}^{k} (\mathbf{y}_j^T \mathbf{w}_i)\mathbf{w}_i||_2^2 = \sum_{i=k+1}^{r} \sigma_i^2 \tag{18.7}$$

We choose for our application a reduced basis formed by the first most meaningful left singular vectors of a matrix of displacements snapshots sampled from a full solution.

18.3 Discrete Empirical Interpolation Method

18.3.1 Computational Complexity in Evaluating the Nonlinear Term

As clearly indicated by [2], the Galerkin projection of the nonlinear term $\mathbf{f}(\mathbf{y})$ poses a fundamental inefficiency. In fact, the evaluation of

$$\underbrace{\hat{\mathbf{f}}}_{m \times 1} := \underbrace{\boldsymbol{\Phi}^T}_{m \times n} \underbrace{\mathbf{f}(\boldsymbol{\Phi}\mathbf{q})}_{n \times 1} \tag{18.8}$$

involves two distinct steps. First, the computation of $\mathbf{f}(\boldsymbol{\Phi}\mathbf{q})$, which requires n vector-valued evaluations. Second, the projection on the reduction basis $\boldsymbol{\Phi}$, which involves nk operations. In other words, the nonlinear term still needs to be computed as function of the physical, rather than the modal coordinates, and therefore the computational burden is even higher as compared to the full model (evaluation of the physical dofs *and* matrix basis projection). As for the nonlinear Jacobian of the system, which is in our case the tangential stiffness matrix:

$$\mathbf{K}_t(\mathbf{y}) = \frac{\partial \mathbf{f}}{\partial \mathbf{y}} \tag{18.9}$$

the same shortcoming holds:

$$\hat{\mathbf{K}}_t(\mathbf{q}) := \boldsymbol{\Phi}^T \mathbf{K}_t(\boldsymbol{\Phi}\mathbf{q})\boldsymbol{\Phi}^T \tag{18.10}$$

The Discrete Empirical Interpolation Method (DEIM) as proposed by [2] is an effective way to reduce the computational effort associated to the approximation (18.8). The main features of the method are outlined in the following section.

Algorithm 1 DEIM points selection

Require: $\{\mathbf{u}_i\}_{i=1}^m \subset \mathbb{R}^n$ linearly independent
Ensure: $\wp = [\wp_1, \ldots, \wp_m]^T \in \mathbb{R}^m$
1: $[|\rho|\ \wp_1] = \max |\mathbf{u}_1|$
2: $\mathbf{U} = [\mathbf{v}_1]$, $\mathbf{P} = [\mathbf{e}_{\wp 1}]$, $\wp = [\wp_1]$
3: **for** $i = 2$ to m **do**
4: Solve $(\mathbf{P}^T\mathbf{U})\mathbf{c} = \mathbf{P}^T\mathbf{u}_i$ for $\mathbf{c}$
5: $\mathbf{r} = \mathbf{u}_i - \mathbf{U}\mathbf{c}$
6: $[|\rho|\ \wp_i] = \max |\mathbf{r}|$
7: $\mathbf{U} \leftarrow [\mathbf{U}\ \mathbf{u}_i]$, $\mathbf{P} \leftarrow [\mathbf{P}\ \mathbf{e}_{\wp_i}]$, $\wp \leftarrow \begin{bmatrix} \wp \\ \wp_i \end{bmatrix}$
8: **end for**

18.3.2 The DEIM Algorithm

The main idea behind DEIM is to provide and approximation for the nonlinear forces $\mathbf{f}(\mathbf{y})$ by a projection on a smaller subspace of dimension $m < n$ spanned by the basis $\mathbf{U} = [\mathbf{u}_1, \ldots, \mathbf{u}_m] \in \mathbb{R}^{n \times m}$ as:

$$\mathbf{f} \approx \mathbf{U}\mathbf{c} \tag{18.11}$$

where $\mathbf{c} \in \mathbb{R}^{m \times 1}$ is the vector of unknown amplitudes. the system of Eq. 18.11 is overdetermined. In order to solve it, we can choose m distinct rows by premultiplying by the transpose of the boolean matrix $\mathbf{P} \in \mathbb{R}^{n \times m}$:

$$\mathbf{P}^T\mathbf{f} = \mathbf{P}^T\mathbf{U}\mathbf{c} \tag{18.12}$$

if $\mathbf{P}^T\mathbf{U}$ is non-singular, we can determine the amplitudes $\mathbf{c}$ by solving (18.12):

$$\mathbf{c} = (\mathbf{P}^T\mathbf{U})^{-1}\mathbf{P}^T\mathbf{f} \tag{18.13}$$

and therefore the force approximation (18.11) becomes:

$$\mathbf{f} \approx \mathbf{U}(\mathbf{P}^T\mathbf{U})^{-1}\mathbf{P}^T\mathbf{f} \tag{18.14}$$

In other words, the term $\mathbf{P}^T\mathbf{f}$ specifies that the nonlinear term $\mathbf{f}$ needs to be calculated only at the entries specified by $\mathbf{P}^T$. The precomputed term $\mathbf{U}(\mathbf{P}^T\mathbf{U})^{-1}$ provides the interpolation onto the other locations. The projection basis $\mathbf{U}$ is provided by a POD of an appropriate set of snapshots of the nonlinear forces $\mathbf{f} = [\mathbf{f}(\mathbf{y}_1), \ldots, \mathbf{f}(\mathbf{y}_{n_s})]$. The selection points are determined from the Algorithm 1. Details are given in [2].

18.3.3 Inefficiency of DEIM Applied to FEM

The DEIM algorithm requires the evaluation of the nonlinear vector only at few selected locations. This approach is particularly efficient when $\mathbf{f}(\mathbf{y})$ is scalar-valued. In other works, when each component of the nonlinear force vector depends on the corresponding entry of the displacement vector: $f_i = f_i(y_i)$. In this case, the cost of the DEIM evaluation of $\mathbf{f}$ is the cost of m scalar valued functions $f_{\wp_i}(\boldsymbol{\Phi}_{\wp_i}\mathbf{q})$. Formally, the selection matrix $\mathbf{P}$ can be brought inside the function evaluation:

$$\mathbf{P}^T\mathbf{f}(\boldsymbol{\Phi}\mathbf{q}) = \mathbf{f}(\mathbf{P}^T\boldsymbol{\Phi}\mathbf{q}) \tag{18.15}$$

Unfortunately, this does not hold when $\mathbf{f}$ results from a FEM discretization. In a FE framework, each component f_i represents the generalized force component at one specific node. This entry depends on the generalized displacements of all the nodes belonging to the neighbouring elements. Formally, the selection matrix $\mathbf{P}$ cannot be brought inside the function:

$$\mathbf{P}^T\mathbf{f}(\boldsymbol{\Phi}\mathbf{q}) \neq \mathbf{f}(\mathbf{P}^T\boldsymbol{\Phi}\mathbf{q}) \tag{18.16}$$

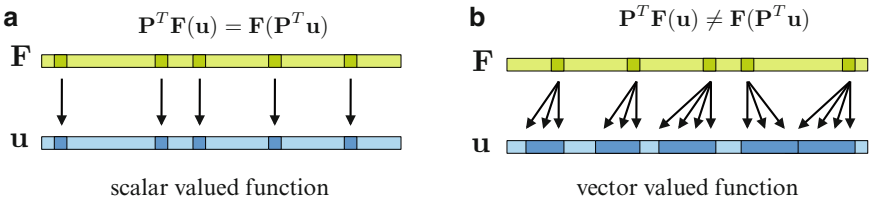

Fig. 18.1 Scalar valued function (*left*) and vector valued function (*right*). In the first case, each component F_i of $\mathbf{F}$ depends on only one component u_j of $\mathbf{u}$. In the second case, F_i depends on several components of $\mathbf{u}$. This case is representative of the FE framework. (**a**) Scalar valued function. (**b**) Vector valued function

Algorithm 2 UDEIM

Require: unassembled snapshots matrix $\mathbb{F}_u = [\mathbf{f}_u^1, \ldots, \mathbf{f}_u^{n_s}] \in \mathbb{R}^{n_u \times n_s}$
Ensure: selection indeces: $\wp^{\mathbf{u}} = [\wp_1^u, \ldots, \wp_m^u]^T \in \mathbb{R}^m$
interpolation matrix: $\mathbf{U}_a(\mathbf{P}_u^T\mathbf{U}_u)^{-1}$
1: SVD$(\mathbb{F}_u)$: $\mathbb{F}_u = \tilde{\mathbf{U}}_u\boldsymbol{\Sigma}_u\mathbf{V}_u^T$
2: select first m columns of $\tilde{\mathbf{U}}_u$: $\mathbf{U}_u = \tilde{\mathbf{U}}_u(:, 1:m)$, with $m < n_s$
3: `DEIM`$(\mathbf{U}_u) \rightarrow \mathbf{P}_u$
4: compute $(\mathbf{P}_u^T\mathbf{U}_u)^{-1}$
5: assemble $\mathbf{U}_a \in \mathbb{R}^{n \times m}$: $\mathbf{U}_a :=$ `assemble`$(\mathbf{U}_u)$
6: $\mathbf{f} \approx \mathbf{U}_a(\mathbf{P}_u^T\mathbf{U}_u)^{-1}(\mathbf{P}_u^T\mathbf{f}_u)$

This situation is better illustrated in Fig. 18.1 and highlights the inefficiency of DEIM on FE schemes. In general, a generic component $f_{\wp_i}$ depends on a subset of the displacements $\bar{\mathbf{y}}_{\wp_i} \in \mathbb{R}^p$, where p depends on the type of element and the mesh connectivity. More specifically, for a FE discretization, the evaluation of a single component of the nonlinear force vector f_i requires a call to the element functions relative to all the neighbouring elements. In the next section, we will introduce an alternative formulation of DEIM that mitigates this difficulty related to FE discretization.

18.4 Alternative Deim Formulation

The inefficiency of DEIM for FE discretizations is essentially due to the relatively large number of element calls that needs to be performed for the evaluation of a single force component selected by $\mathbf{P}$. A possible workaround is to operate the DEIM on the unassembled force vector. In this way, the evaluation of a single entry of such vector will require just one element call. The concept is illustrated in Fig. 18.2. The proposed modification is called UDEIM (Unassembled DEIM).

Essentially, one has to form a collection of snapshots $\mathbf{f}_u = [\mathbf{f}(\mathbf{y}_1), \ldots, \mathbf{f}(\mathbf{y}_{n_s})]$ of the unassembled forces. Formally, we can write:

$$\mathbf{f}_u^T = \left[\mathbf{f}_{e_1}^T(\mathbf{y}_{e_1}), \ldots, \mathbf{f}_{e_{ne}}^T(\mathbf{y}_{e_{ne}})\right] \tag{18.17}$$

where $\mathbf{f}_{e_i}^T(\mathbf{y}_{e_i})$ is the element force vector relative to the element i, $i = 1, \ldots, n_e$. The unassembled force vector $\mathbf{f}_u$ is projected onto a basis $\mathbf{U}_u$ obtained by a SVD of the unassembled snapshots. The DEIM algorithm is then applied to $\mathbf{U}_u$ and the obtained indeces will point to elemental degrees of freedom. Once the amplitudes $\mathbf{c}_u$ have been obtained, an assembled approximation of $\mathbf{f}$ can be formed by:

$$\mathbf{f} \approx \mathbf{U}_a(\mathbf{P}_u^T\mathbf{U}_u)^{-1}(\mathbf{P}_u^T\mathbf{f}_u) \tag{18.18}$$

where $\mathbf{U}_a$ is obtained by a regular FE assembly of the element contribution. The details of the algorithm are shown in Algorithm 2.

18.5 Results

We present some preliminary results that highlight the DEIM performance for geometrically nonlinear structural dynamics problems. We show how the proposed modification to the DEIM algorithm increases the sparsity of the element function call and therefore improves the efficiency of the algorithm.

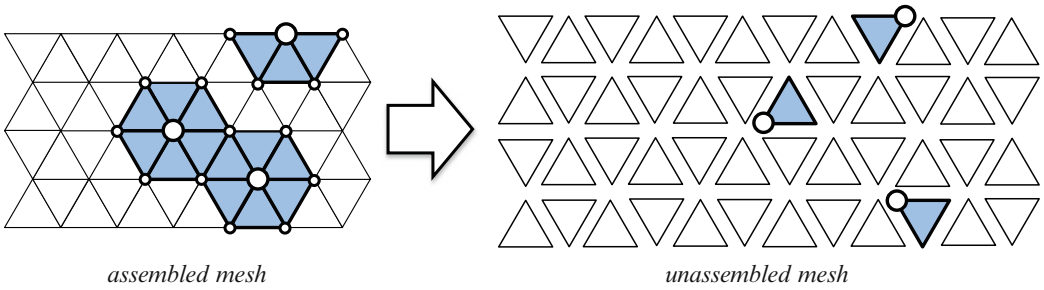

Fig. 18.2 Sparsity comparison for the evaluation of **f** at the DEIM points. In the case of assembled meshes (*left*) one evaluation implies a element function call for all the neighbouring elements. If the mesh is treated as unassembled (*left*) only one element per DEIM point needs to be processed

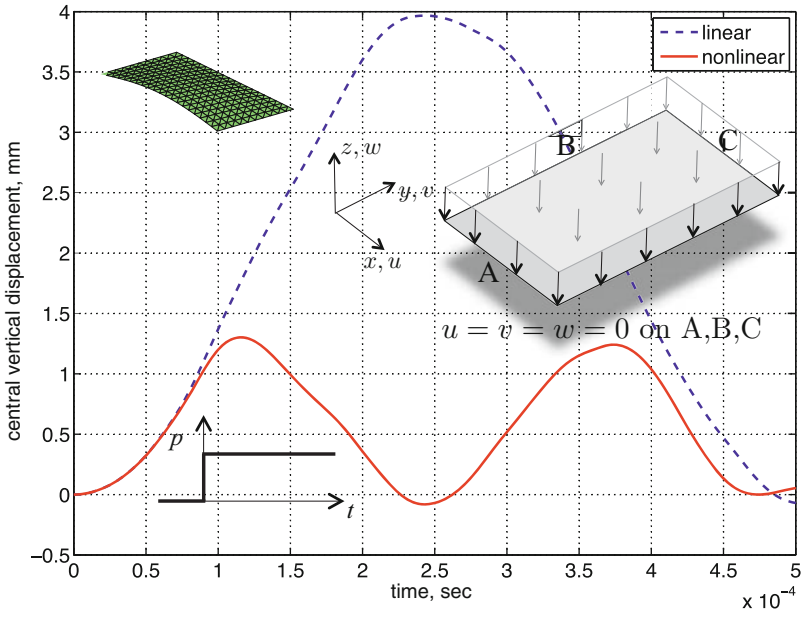

Fig. 18.3 Dynamic analysis of a flat plate subjected to a uniform pressure applied as a step load. The vertical displacement of the middle point of the free edge in shown

We consider here a rectangular flat plate (40×20 mm) which is simply supported on three sides and subjected to a uniform pressure field applied as a temporal step function. The material is elastic isotropic, with $E = 70$ GPa, $\rho = 2{,}700$ Kg/m^{-3}, $\nu = 0.3$, and the thickness is 0.8 mm. The pressure magnitude is 34 N/mm^{-2}. The plate is modelled with 400 triangular shell elements with 18 degrees of freedom per node. The total number of degrees of freedom n is 1,263. The geometrical nonlinearity is modelled here with the von-Karman kinematic model, which is valid when the out-of-plane displacement is in the order of the shell thickness [1]. A comparison between a linear and a full nonlinear analysis is shown in Fig. 18.3. The markedly stiffer behavior of the nonlinear case is due to the stretching induced by the finite out-of-plane displacement.

The accuracy of the DEIM method for the proposed problem and the proposed modification (UDEIM) is shown in Fig. 18.4. Both the DEIM and the UDEIM approximations yield good results already for a small number of points ($m = 10$). The accuracy of the DEIM approximation is shown also in Figs. 18.5 and 18.6, where the displacement error:

$$\varepsilon_{\mathbf{y}} = \frac{1}{n} \frac{||\mathbf{y} - \tilde{\mathbf{y}}||}{||\mathbf{y}||} \tag{18.19}$$

and the force error:

$$\varepsilon_{\mathbf{r}} = \frac{1}{n} \frac{|\mathbf{r}||}{||\mathbf{M}\ddot{\tilde{\mathbf{y}}}|| + ||\mathbf{p}||} \tag{18.20}$$

are shown. The residual **r** is the force unbalance due to the approximated solution $\tilde{\mathbf{y}}$:

$$\mathbf{r} = \mathbf{M}\ddot{\tilde{\mathbf{y}}} + \mathbf{K}\tilde{\mathbf{y}} + \mathbf{f}(\tilde{\mathbf{y}}) - \mathbf{p} \tag{18.21}$$

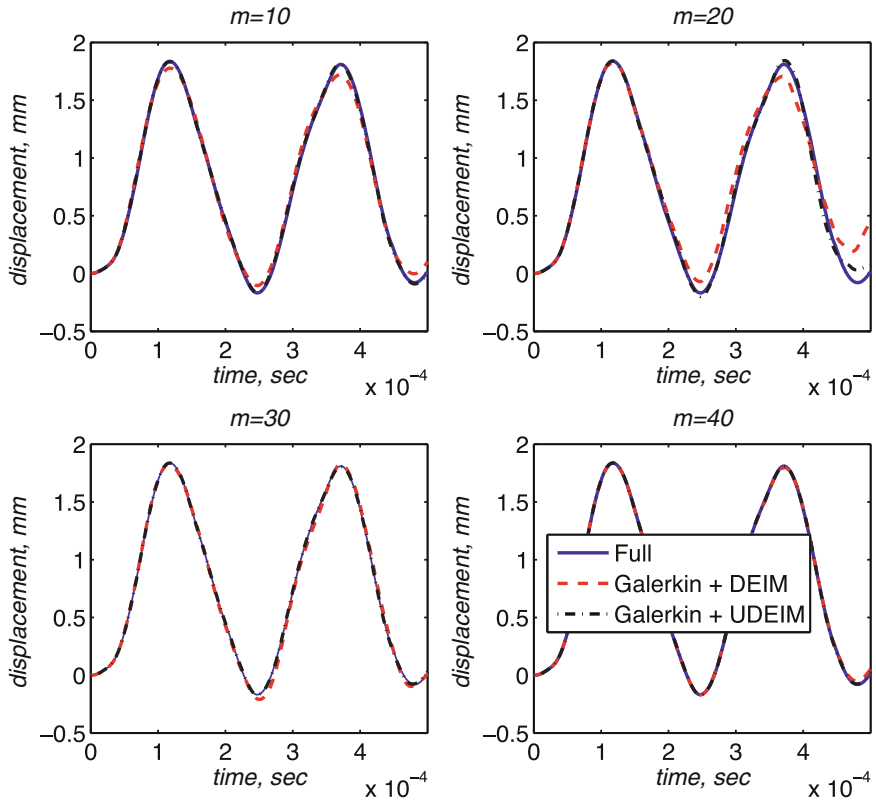

Fig. 18.4 Comparison of the DEIM and UDEIM solution. The vertical displacement of the middle point of the free edge in shown. Both methods deliver very good accuracy

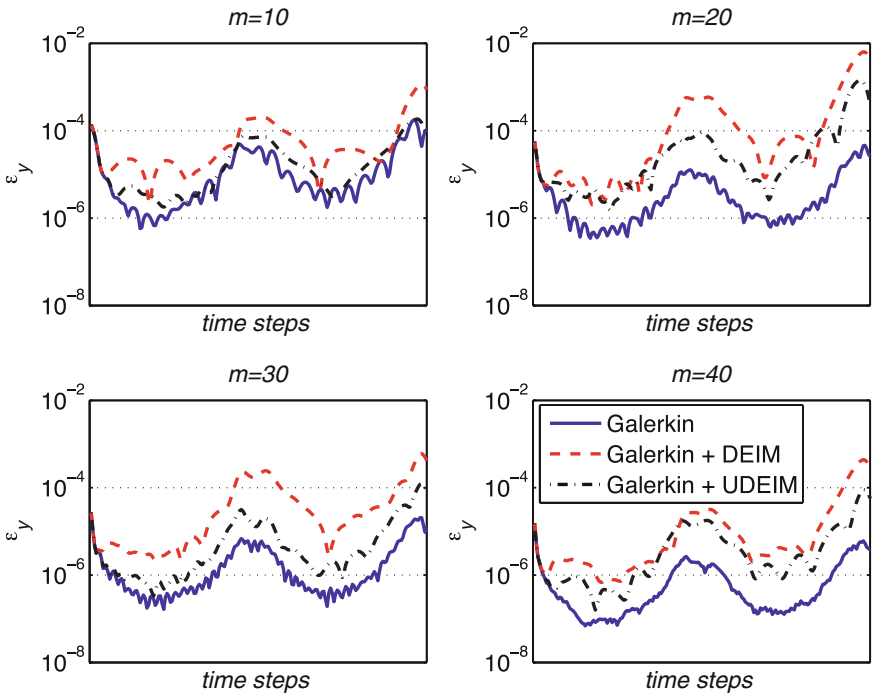

Fig. 18.5 Relative displacement error (18.19) associated to the reduced cases of Fig. 18.4

The benefits of the UDEIM modification are highlighted in Figs. 18.7 and 18.8. For the same number of evaluation points, UDEIM requires approximatively 4.5 times less element call as compared to DEIM. This result is of course relative to the mesh and the element type considered. However, similar savings are expected also for problems discretized with different element types and different meshes.

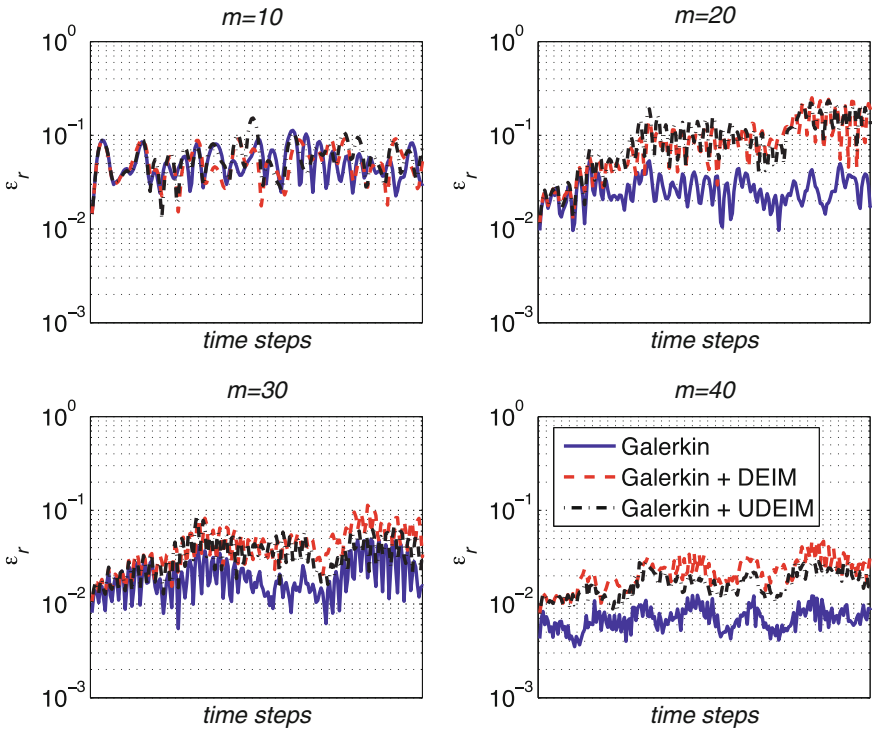

Fig. 18.6 Relative residual error (18.20) associated to the reduced cases of Fig. 18.4

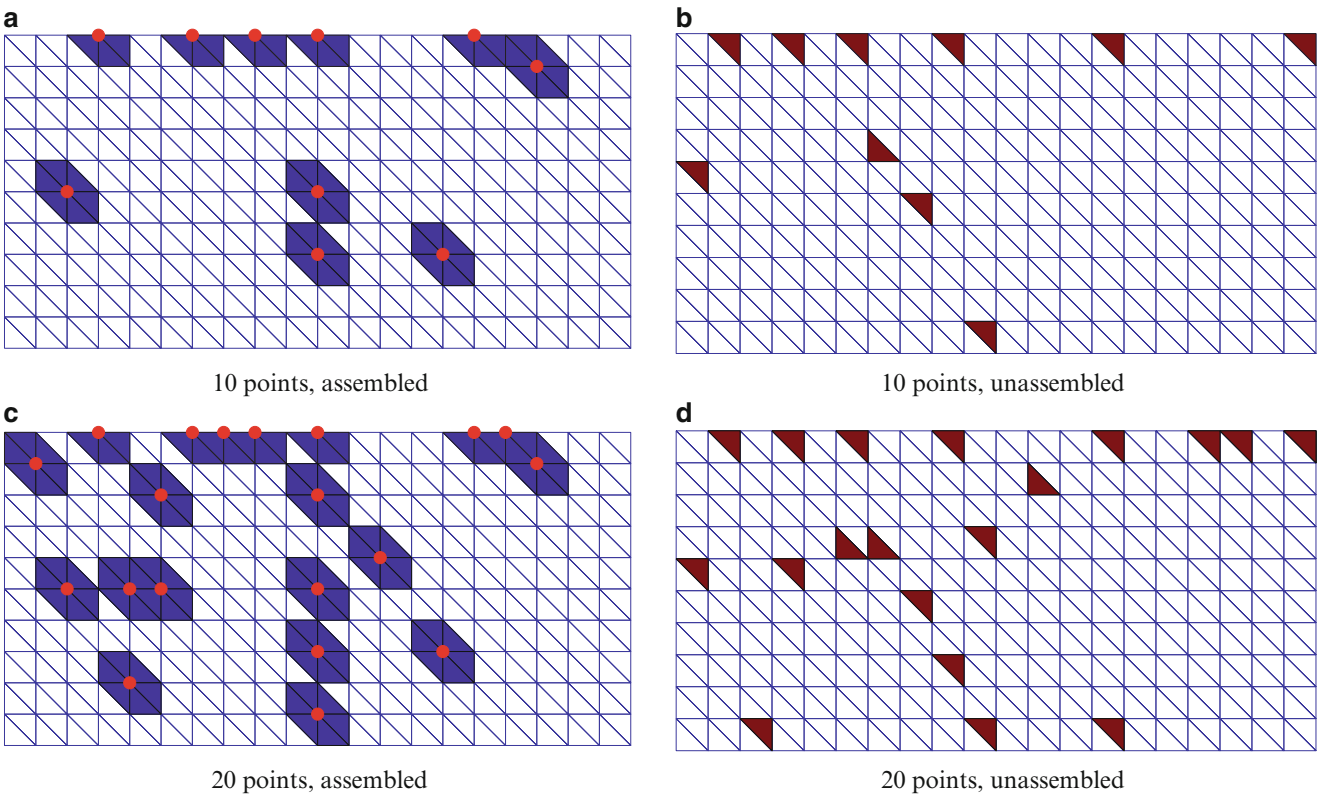

Fig. 18.7 (continued)

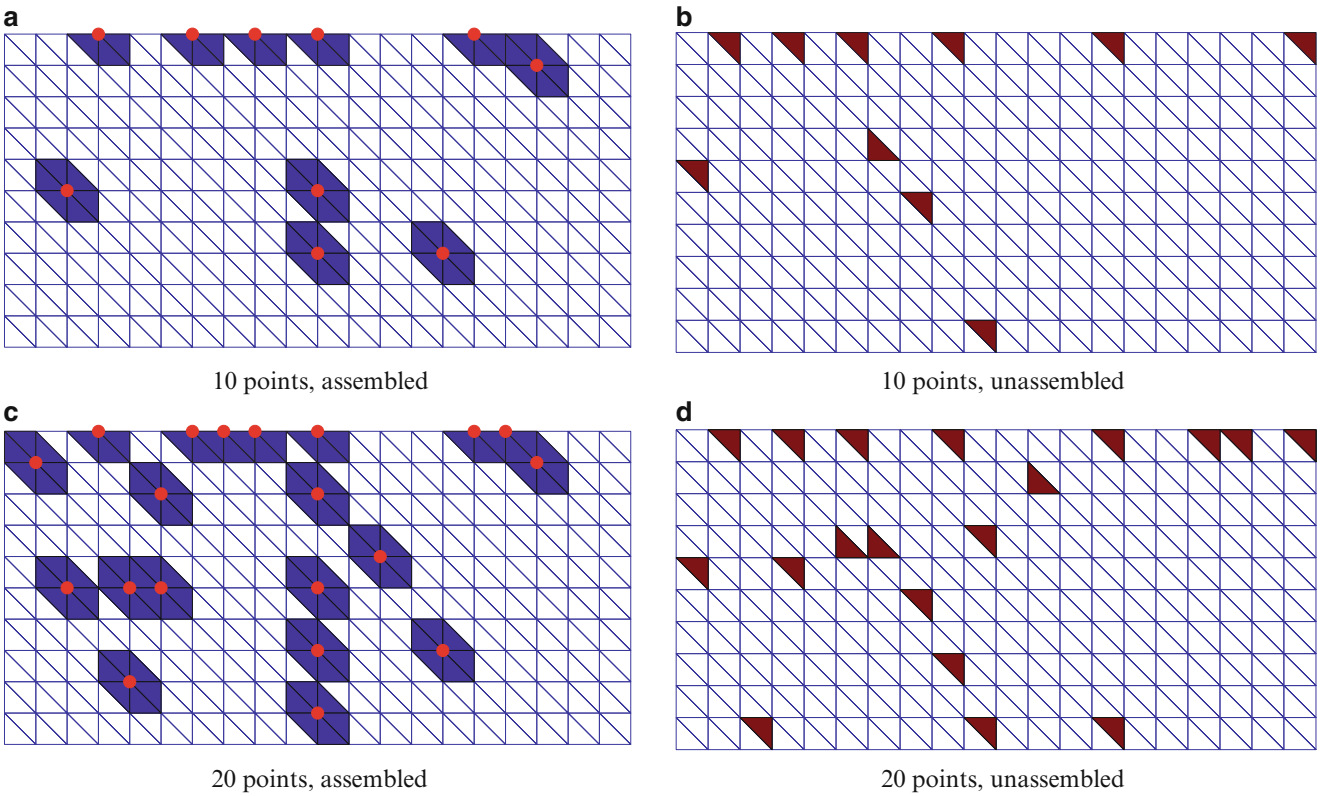

Fig. 18.7 Comparison between the sparsity pattern between DEIM and UDEIM. In the UDEIM case, the selection is performed on degrees of freedom relative to the unassembled mesh. At most one element per selected point needs to be involved in the calculation. (**a**) 10 points, assembled. (**b**) 10 points, unassembled. (**c**) 20 points, assembled. (**d**) 20 points, unassembled. (**e**) 30 points, assembled. (**f**) 30 points, unassembled. (**g**) 40 points, assembled. (**h**) 40 points, unassembled

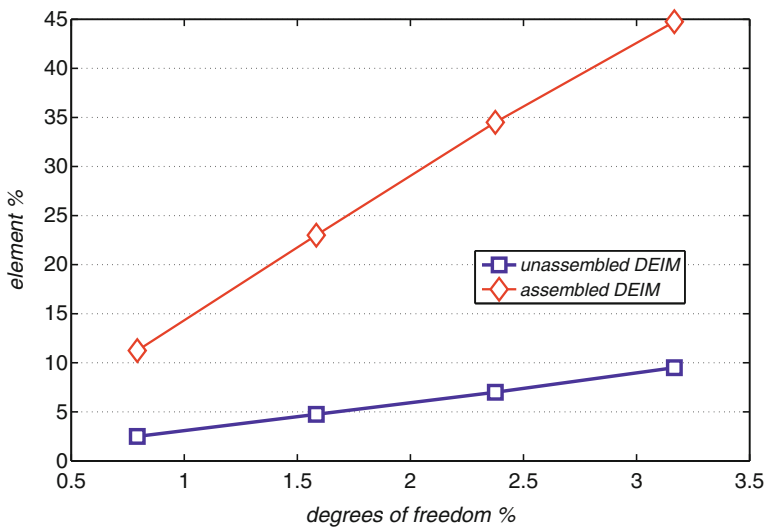

Fig. 18.8 Evaluation cost comparison between DEIM and UDEIM. For the same amount of points, the UDEIM requires roughly 4.5 times less element function calls. This result is relative to the example problem shown. Different meshes and different elements will of course lead to different results

18.6 Discussion and Conclusions

We have shown that DEIM algorithm can be an effective tool to further reduce the computational effort when resorting to a Galerking model order reduction technique. As the direct application of DEIM onto a FE discretized problem does not fully exploit the sparsity of the DEIM itself, we proposed a simple modification of DEIM that implies operations on unassembled FE nonlinear internal forces (UDEIM). This strategy preserves the accuracy of the DEIM while minimizing the element function calls required to calculate each DEIM selected collocation point.

The UDEIM procedure requires an SVD on the snapshots of the unassembled nonlinear forces, which is of a larger size than the corresponding assembled vector. This increases the offline computational cost. A possible remedy is to form a surrogate vector of a much smaller size that will contain the essential informations at the element level. Work in this direction is currently in progress.

References

1. Antman SS (1977) Bifurcation problems in non-linearly elastic structures. Academic Press, New York
2. Chaturantabut S, Sorensen D (2010) Nonlinear model reduction via discrete empirical interpolation. SIAM J Sci Comput 32(5):2737–2764
3. Krysl P, Lall S, Marsden JE (2001) Dimensional model reduction in non-linear finite element dynamics of solids and structures. Int J Numer Methods Eng 51:479–504, 4
4. Tiso P, Jansen E, Abdalla M (2011) Reduction method for finite element nonlinear dynamic analysis of shells. AIAA J 49(10):2295–2304, 2012/11/01
5. Tiso P, Rixen DJ (2011) Optimal second order reduction basis selection for nonlinear transient analysis. In: 29th IMAC, Jacksonville

Chapter 19
Nonlinear Forced Dynamics of Planar Arches

R. Alaggio, F. Benedettini, and D. Zulli

Abstract The nonlinear dynamics of planar elastic arches, under resonant vertical harmonic tip force and different sag-to-span ratios, are considered. An analytical model based on the polar continuum, curved rod theory, is formulated. Different values of initial curvature are considered, ranging from non-shallow to shallow conditions. The nonlinear change in curvature is expressed in terms of displacement components. The hypothesis of vanishing axial strain is assumed when dealing with non-shallow cases, while the Mettler theory, based on a constant strain, is usually used for shallow arches. The PDEs of the motion obtained through the extended Hamilton principle, are projected on the reduced basis constituted by the two first linear modes or analogous meaningful functions. Regions of instability of the one-mode solution are numerically detected, and coupled regular and non-regular motions are described using standard complexity indicators. Experimental tests are realized on two companion laboratory steel prototypes of arches, in order to compare and validate the results of the prevision of the analytical model. The behavior charts of the analytical and experimental problems and the nonlinear frequency-response curves show good agreement in a wide range of amplitude and frequency of the external excitation. The 2D model recently proposed by the authors seems to be the only adequate when dealing with real arches.

Keywords Arches • Nonlinear dynamics • Bifurcation • Modal identification • Experiment

19.1 Introduction

The correct modeling of planar arch-structures is addressed in this paper with the aim of verifying the accuracy of reduced order nonlinear models (proposed by the authors and existing in literature) in reproducing different and various phenomena exhibited by experimental prototypes constructed and tested under a vertical sinusoidal tip excitation, in the Nonlinear Dynamics Lab of Civil, Architectural and Environmental Engineering Department (DICEAA) at University of L'Aquila. The finite periodically-forced dynamics of elastic structures having initial curvature (arches, cables, shells ...) are particularly rich and varied because of the presence, in the restoring force, of both even and odd nonlinearities linked respectively to the curved initial shape and to the stretching of the axis, during finite oscillations. Such a circumstance generates, differently than in the linear case, a series of critical frequencies corresponding to primary and secondary external resonance conditions. Moreover, such resonance conditions linked to critical values of elasto-geometric parameters and/or to the location and entity of possibly applied concentrated masses, could exalt the classical modal-coupling characteristic of multi dof nonlinear systems and could affect the quality of the response. In the case of the planar dynamics of circular arches excited by harmonic vertical loads applied on the tip, the directly excited one-mode symmetric solution, stable for low excitation levels, loses stability when critical forcing amplitude and frequency are reached around meaningful resonance conditions and coupled solutions appear. A series of consecutive bifurcations generates more complex, periodic and not periodic coupled responses, characterized by the presence of both symmetric and anti-symmetric components. When particular values of system parameters give rise to a nearly-integer ratio between the natural frequencies of first anti-symmetric and symmetric

R. Alaggio • F. Benedettini • D. Zulli (✉)
Civil, Architectural and Environmental Engineering Department, University of L'Aquila, L'Aquila, Italy
e-mail: rocco.alaggio@univaq.it; daniele.zulli@univaq.it; francesco.benedettini@univaq.it

G. Kerschen et al. (eds.), *Topics in Nonlinear Dynamics, Volume 1: Proceedings of the 31st IMAC, A Conference on Structural Dynamics, 2013*, Conference Proceedings of the Society for Experimental Mechanics Series 35,
DOI 10.1007/978-1-4614-6570-6_19,

modes, the dynamic instability is magnified even if, in such cases, the coupled solutions are periodic in wider zones of the parameters space; on the contrary, when the ratio between the linear frequencies of symmetric and not symmetric modes is far away from those *particular tuning zones*, the coupled solutions emanating after the bifurcation, are more easily, characterized by non periodicity.

The problem of the dynamic instability of the one-mode solution in planar arches is already known for a long time, since the 1962 work by Bolotin [1] and has been recently revisited in the case of non shallow (Thomsen [2], Alaggio et al. [3], Benedettini [4, 5]) and shallow (Win-Min Tien et al. [6, 7]) arches.

The aim of this paper is to discuss, for different arches characterized by different sag to span ratios, the accuracy of available analytical models in the study of the dynamical behavior.

Results of experimental tests conducted in the Nonlinear Dynamics Lab at the University of L'Aquila on two different prototypes having a sag to span ratio (shallowness parameter) of about 1:2 and 1:10, are also discussed.

Because the nonlinear discrete models are generally based on a Galerkin approximation based on a truncated series of shape functions, the paper discusses also the alternative use of linear eigenfunctions and proper orthogonal modes (*POMs*), in the spatial discretization.

In fact, analyzing the response of the laboratory prototypes, it was possible to verify, by using the Karunen-Loeve decomposition, *the spatial shapes more visited during the dynamic evolution (POMs)* and validate, in such a way, the spatial shapes that should be used in a correct analytical, truncated approximation. In the discussed cases, the *POMs* are evaluated by processing synchronous time series corresponding to the accelerations of eight equally-spaced points on the arches, acquired by using radial and tangential accelerometrs.

When the coupled solution loses the periodicity, quasi-periodic and chaotic motion are activated and in such cases the *complexity of the motion* and the *strangeness of underlying attractors* are *measured* by using classical indicators evaluated in the pseudo phase-space, reconstructed, according to the Takens theorem [8], from the measure of a scalar component of the motion.

19.2 Theoretical and Experimental Models

In the following a discussion concerning the different assumptions usually done during the modeling of the nonlinear behavior of planar arches is presented. To this end two different analytical models are considered: an original model of a *2D curved beam* recently proposed by the authors (Benedettini et al. [5]) and the Mettler model [9], often assumed to study the dynamics of shallow arches. Being one of the objective of the paper the discussion on the applicability of such analytical nonlinear models in the study of real cases, the results of experiments on two different steel prototypes of planar arches having respectively a sag-to-span ratio of 1/2 and 1/10, are presented. The two models constructed in the Nonlinear Dynamics Lab of DICEAA (Civil Architectural and Environmental Department) at University of L'Aquila, Italy, are shown in Fig. 19.1 in which is also reported the electrical counter-rotating-mass exciter used to furnish the harmonic force on the tip of the arches.

The analytical models previously cited should be useful to analyze the finite dynamics of planar arches belonging, respectively, to two different classes: a general arch in which a nonlinear change in curvature during the motion is the source of the nonlinear behavior (general 2D model [5]) and a model (Mettler [9]), valid only for arches having very low sag-to-span ratios and for buckled beams, in which the source of nonlinearities is the stretching of the arch axis.

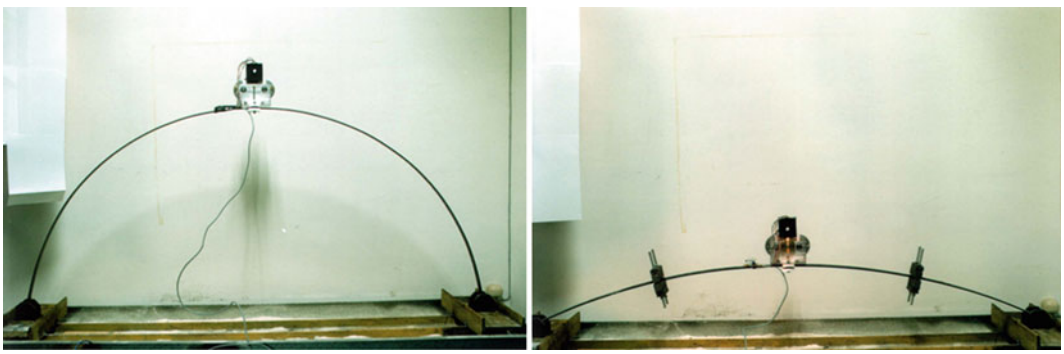

Fig. 19.1 The two experimental prototypes of planar circular arches having a sag-to-span ratio of 1/2 (*left*) and 1/10 (*right*)

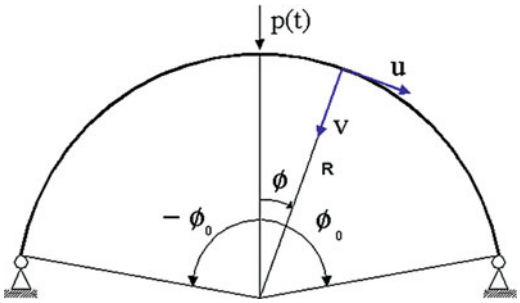

Fig. 19.2 The planar displacement field of arch axis

19.2.1 General 2D Model Based on the Assumption of Negligible Stretching and Finite Change in Curvature of Arch Axis

In this case the kinematics description of the displacement field is based on both the radial v and the tangential u, planar displacement components having the same order of magnitude during the motion (Fig. 19.2).

In this case, valid in the general condition of large initial curvature, a simplification of the kinematic description is based on the assumption (confirmed by the experiments) of negligible elongation of axis-fibers ($\varepsilon = 0$) (see Henrich [10]). Such an internal constraint, as we will see later, will be introduced in the analytical modeling by using a Lagrange multiplier in the expression of the potential energy.

The nonlinear change in curvature and the nonlinear stretching of the axis-fibers are expressed by the following kinematic relations (Benedettini et al. [5]):

$$\Delta\chi(s,t) = v'' + \bar{k}u' + 2\bar{k}^3(2v^2 - u^2 + 2\bar{k}(v'^2 - 2u'^2) + ; \\ +2u'v'' - u''v' + \bar{k}(2vv'' - uu'') \qquad \varepsilon(s,t) = u' - \bar{k}v + \frac{1}{2}\left(\bar{k}u + v'\right) \tag{19.1}$$

The kinetic and potential energy, written to allow the presence of a concentrated mass M and a vertical force on the tip are:

$$T = \sum_{J=1}^{2}\left(\frac{1}{2}\int_{D_j} m(\dot{u}_j^2 + \dot{v}_j^2)ds + \frac{1}{4}M(\dot{u}_{j0}^2 + \dot{v}_{j0}^2)\right); \; U = \sum_{j=1}^{2}\int_{D_j}\left(\frac{1}{2}EI\Delta\chi_j^2 + \tau_j\varepsilon_j\right)ds \tag{19.2}$$

in which τ is the Lagrange multiplier previously mentioned.

The extended Hamilton principle allows the determination of the *PDEs* of dynamic equilibrium:

$$\delta\int_{t_1}^{t_2}(T-U)\,dt + \int_{t_1}^{t_2}\delta W_{nc}\,dt = 0 \tag{19.3}$$

$\forall\delta u_j = \delta v_j = \delta\tau_j = 0$ in $t = t_1, t_2$ and $j = j_1, j_2$ and:

$$\delta W_{nc} = \sum_{j=1}^{2}\left(\int_{D_j}(c\dot{u}_j\delta u_j + c\dot{v}_j\delta v_j)ds + \frac{1}{2}f(t)\delta v_{j0}\right) \tag{19.4}$$

The *PDEs*, very cumbersome in this case, are omitted for the sake of brevity.

Searching for a minimal, discrete, reduced order model of the arch, a Galerkin approximation of the displacement field based on suitable two-components shape functions, is proposed:

$$u(\varphi,t) = f_1(\varphi)\cdot q_1(t) + f_2(\varphi)\cdot q_2(t) \\ v(\varphi,t) = g_1(\varphi)\cdot q_1(t) + g_2(\varphi)\cdot q_2(t) \tag{19.5}$$

To describe in a correct, even if reduced way, the dynamic evolution, the tangential and radial components of the first two eigenfunctions of the linearized problem are assumed as spatial shapes $f_1(\varphi), g_1(\varphi)$ and $f_2(\varphi),\ g_2(\varphi)$.

Using the first two eigenfunctions of the linearized problem, a quite good agreement between experimental and analytical results was found even in fully developed nonlinear regimes. While in the case of periodic evolutions the comparison was done on the base of modal components present in the motion, in non-periodic cases the comparison was done on the base of *POMs* evaluated by the Karhunen-Loeve decomposition of experimental time series.

Substituting the approximation (19.5) in the *PDEs* of the motion a 2 dof reduced order model is obtained and, in the case of a circular arch carrying a concentrated tip mass and excited by a sinusoidal vertical force on the tip, the relevant discrete 2 dof equations read:

$$\begin{aligned}
&\ddot{q}_1 + \mu_1 \dot{q}_1 + c_{10} q_1 + c_{20} q_1^2 + c_{02} q_2^2 + c_{30} q_1^3 + c_{12} q_1 q_2^2 = P sin(\Omega \tau) \\
&\ddot{q}_2 + \mu_2 \dot{q}_2 + q_2 + c_{11} q_1 q_2 + c_{02} q_2^2 + c_{03} q_2^3 + c_{21} q_1^2 q_2 = 0
\end{aligned} \tag{19.6}$$

19.2.2 Mettler Model Based on the Assumption of Constant Stretching of Arch Axis and Small Change in Curvature

In this case, pertaining to shallow arches, the reference model is the model derived by Mettler [9] for the dynamic analysis of buckled beams whose validity is usually extended, by many authors, to the analysis of shallow arches. The model is based on an approximated description of the displacement of the arch-axis: accordingly, from the *PDEs* of the motion obtained by assuming a small change in curvature and a large extensional strain and neglecting the longitudinal inertia and damping forces, a static condensation of the tangential displacement component u is gotten by means of an integral relation obtained by assuming a constant elongation along the axis (19.7).

Accordingly, the resulting partial integro-differential equation of the motion (19.8), contains only the radial displacement component $v(x,t)$ while the tangential component $u(x,t)$, can be evaluated by means of the integral relation (19.9):

$$\varepsilon(t) = \frac{1}{l} \int_0^l \left(\frac{1}{2} v'^2 + v' v_0' \right) dx \tag{19.7}$$

$$EI v'''' + \frac{EA}{l} \left[\int_0^l \left(\frac{1}{2} v'^2 + v' v_0' \right) dx \right] \left(v'' + v_0'' \right) + M^* \ddot{v} + \mu \dot{v} = p \tag{19.8}$$

$$u(x,t) = \varepsilon(t) \cdot x - \int_0^x \left(\frac{1}{2} v'^2 + v' \cdot v_0' \right) dx \tag{19.9}$$

It is worth noticing how, in this case, because of the shallowness of the arch, the curvilinear abscissa s is replaced by the abscissa x of its projection on the horizontal axis.

Using again a two-function approximation of the displacement field according to:

$$v(x,t) = v_1(x) \cdot q_1(t) + v_2(x) \cdot q_2(t) \tag{19.10}$$

two ode's of the motion are obtained:

$$\begin{aligned}
&\ddot{q}_1 + \mu_1 \dot{q}_1 + \frac{\omega_s}{\omega_a} q_1 + d_{20} q_1^2 + d_{02} q_2^2 + d_{30} q_1^3 + d_{12} q_1 q_2^2 = P sin(\Omega \tau) \\
&\ddot{q}_2 + \mu_2 \dot{q}_2 + q_2 + d_{11} q_1 q_2 + d_{02} q_2^2 + d_{03} q_2^3 + d_{21} q_1^2 q_2 = 0
\end{aligned} \tag{19.11}$$

Despite the formal equality of Eqs. (19.6) and (19.11), the two models are deeply different in the nonlinear terms being the coefficients c_{ij} of Eq. (19.6) and d_{ij} of Eq. (19.11) linked, respectively, to the nonlinear change in curvature (19.1-left) and to the nonlinear axis-elongation (19.7).

While the use of Eq. (19.6) was considered as necessary to correctly describe the dynamical evolution of the prototype in Fig. 19.1, left, Eq.(19.11) were first used to describe the dynamics of the shallow arch (Fig. 19.1, right): even a preliminary analysis of the analytical response of Eq. (19.11) with parameters corresponding to the model of Fig. 19.1, right enlightened a great discrepancy between experimental and analytical results. Anyway, in the original work by Mettler, the proposed theory was always related to buckled beams and never to arches (even shallow). On the basis of the preceding comments it could be observed how such a model (Mettler), probably is correct to describe, besides buckled beams, only shallow arches

not exceeding the first crossover point (first mode symmetric and second one, anti-symmetric) and accordingly exhibiting a symmetric first mode having only one half wave on the span with planar displacements prevalently involving the extensional strain. Using on the contrary Eq. (19.6) with the corresponding parameters, a quite good agreement was found permitting to infer how, for arches to be used in structural engineering, for every sag to span ratio, the only utilizable model is the *general* model described in the preceding paragraph, despite the large and *improper* use of the Mettler approximation.

19.3 An Experimentally Validated Correct Modeling

As stated before, the nonlinear *PDEs* of the motion are usually discretized to obtain more treatable discrete *reduced order* models. In the approximation linked to the space truncation (Galerkin procedure) a crucial role is played by the shape functions used in the procedure. The ability of the truncated model to reproduce and synthesize the real more complex behavior mainly depends by the correct choice of meaningful shape functions, able to interpolate the actual displacement field. The classical choice is the assumption, as shape functions, of the eigenfunctions of the linearized problem. Depending on how many eigenfunctions are considered, different reduced order models of increasing complexity could be developed. However, in many real problems, the actually analyzed systems could be quite *different* from the simple systems whose eigenfunctions are usually used in the approximation. In fact, the boundary conditions and/or the presence of extra masses on the continuous system (secondary structural components carried by the principal structure) generally affect the modal shapes. Moreover, in this cases, the eigensolutions are generally no longer analytically expressible. In this situation, the discretization should be based on the use, as shape functions, of an analytical, truncated series of eigenfunctions belonging to the simple archetypal system, respecting the boundary condition and interpolating the numerical eigenfunctions obtained by using a finite element model of the real structure. Afterwards the assumed shape functions could be verified by a comparison with the modal shapes of an experimental prototype.

As example, the case of the non-shallow arch carrying two concentrated masses and reported in Fig. 19.1, right, is presented. The comparison between the assumed shape functions obtained by a three-terms series of the simple arch and the identified modes of the experimental prototype (radial component v) is reported in Fig. 19.3. After the assumption of suitable shape functions, the reduced order analytical model could be developed and the analytical frequencies could be coherently evaluated and compared with the experimental ones.

The frequency comparison is reported, in the analyzed case, again for the shallow arch, in Table 19.1.

Eventually, for what is concerned with the damping estimation, the logarithmic decrement method or the transfer function evaluation could be used to infer the right modal dampings to be used in the equations of the motion (Fig. 19.4).

After developing a reliable analytical model based on the modal identification of the companion experimental prototype, the prediction of strongly developed nonlinear regimes could be started.

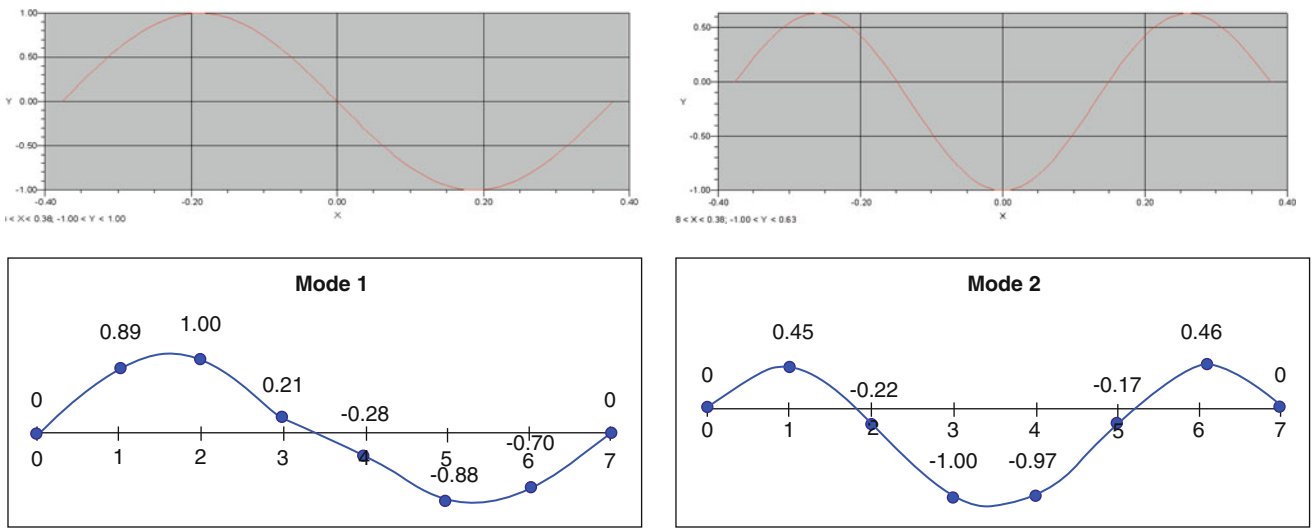

Fig. 19.3 Analytical (*top*) and experimental (*bottom*) anti-symmetric (*left*) and symmetric (*right*) modal shapes

Table 19.1 Natural frequencies, shallow arch

	Numerical	Analytical	Experimental
$\omega_{anti-symm}$	5.67	5.66	5.46
ω_{symm}	9.51	9.53	9.89

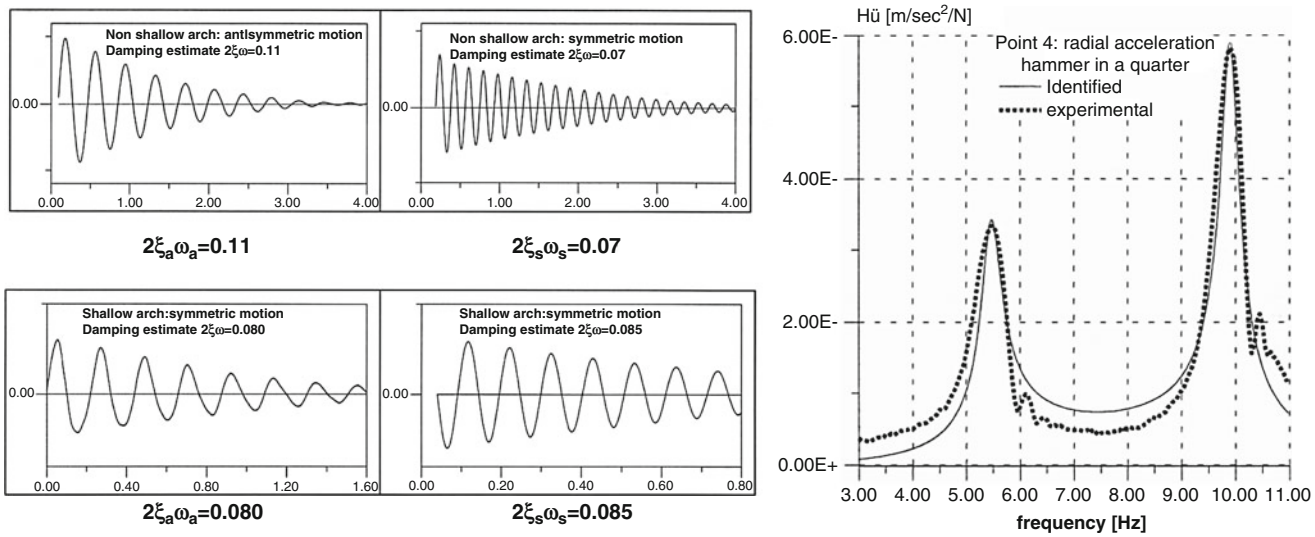

Fig. 19.4 Random decrement (*left*, non shallow arch *top*, shallow *bottom*) and transfer function (*right*) damping estimate

19.4 Analytical Prediction and Experimental Validation

The main objective of the analysis is the study of the excitation parameters conditions (amplitude and frequency of the tip sinusoidal excitation), giving rise to the instability of the simple one-mode, directly excited, symmetric solution and to the developing of a quite complex nonlinear coupled (symmetric-anti-symmetric) dynamic regime. In particular, to assess the capability of the analytical 2 dof nonlinear model to reproduce the main characteristics of the experimental response, a comparison between the analytical prediction and the experimental observation has been done for what is concerned to frequency-response curves and behavior charts in the control-parameters plane of external excitation. As mentioned, the principal dynamical phenomenon exhibited by the arch-models is the instability of the one-mode, directly excited, symmetric solution and the activation, after a bifurcation, of coupled symmetric-antisymmetric solutions.

Moreover, inside the instability regions, sub-regions of instability of every periodic solutions bounded by Hopf-limits, have been also found. As expected, within those inner limits, further bifurcations activate complex responses which complexity can be analyzed by classical indicators like the *Lyapunov exponents* and the *correlation dimension* (Benedettini [11]).

In the case of the analyzed arches, such response could be classified alternatively as a QP-motions on a two-torus or as chaotic motions. When chaotic motions arise, it is possible, in principle, that couples of points on the arch lose the mutual synchrony in a kind of structural turbulence. Such a circumstance could completely invalidate the analytical predictions based on an assumed shape model. Because of the Galerkin approximation, the analytical models are constrained to evolve with fixed spatial shapes also during non-periodic evolutions. Because of such a circumstance, it appears important to verify, on the experimental prototypes, the spatial coherence between couples of points, using the Karhunen-Loeve decomposition. After the decomposition, eigenvectors (*POMs*) and eigenvalues of the spatial coherence matrix represent, respectively, the shapes more visited in average during non-periodic evolutions and a measure of the probability characterizing the occurrence in average of the corresponding shape (Cusumano [12]). Following the proposed approach, the *POMs* represent the experimental reference terms for the shape functions of the analytical approximation during a complex non periodic evolution, as the linear eigenfunctions do, during regular motions.

To verify the theoretical models, the analytical prediction in the cases of the non-shallow arch model (Fig. 19.1, left) has been verified: when particular geometric-elastic-inertial conditions come true, the arch reaches an internal 1:2 resonance condition between the first antisymmetric and the first symmetric modes. Such internal resonance condition further enlarges the instability zones. In this case the experimental (left) and analytical (right) frequency-response curves are reported, respectively, in Fig. 19.5.

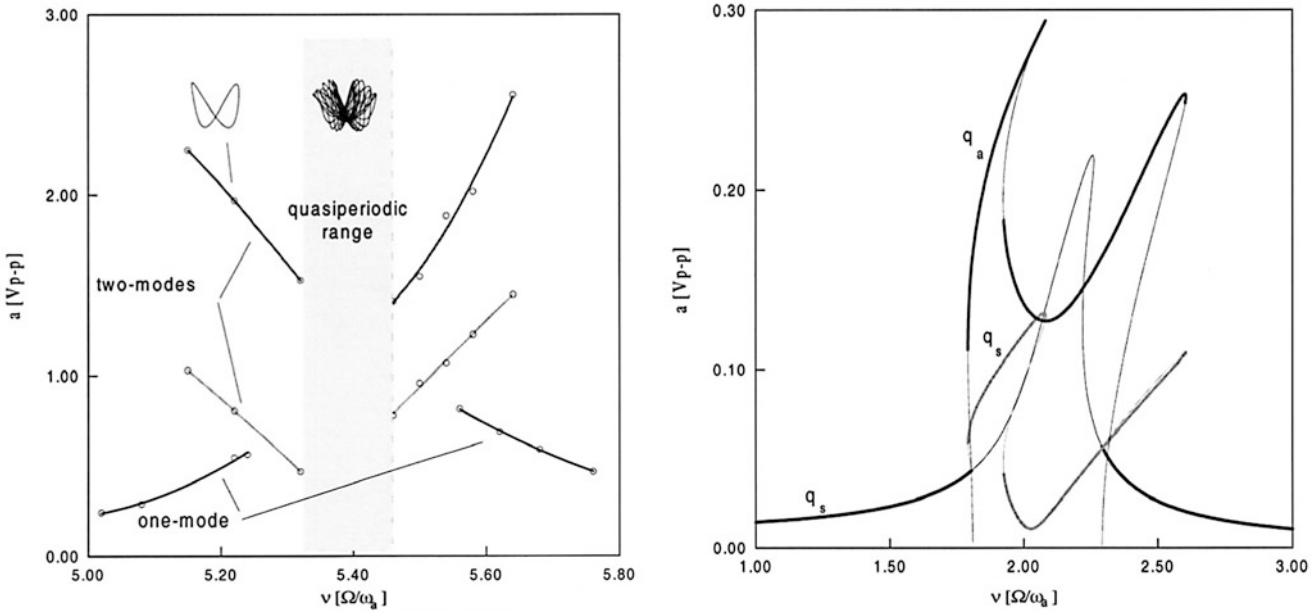

Fig. 19.5 Internally resonant, non shallow arch: experim response curves (*left*) and analytical (*right*, thick-stable, thin-unstable)

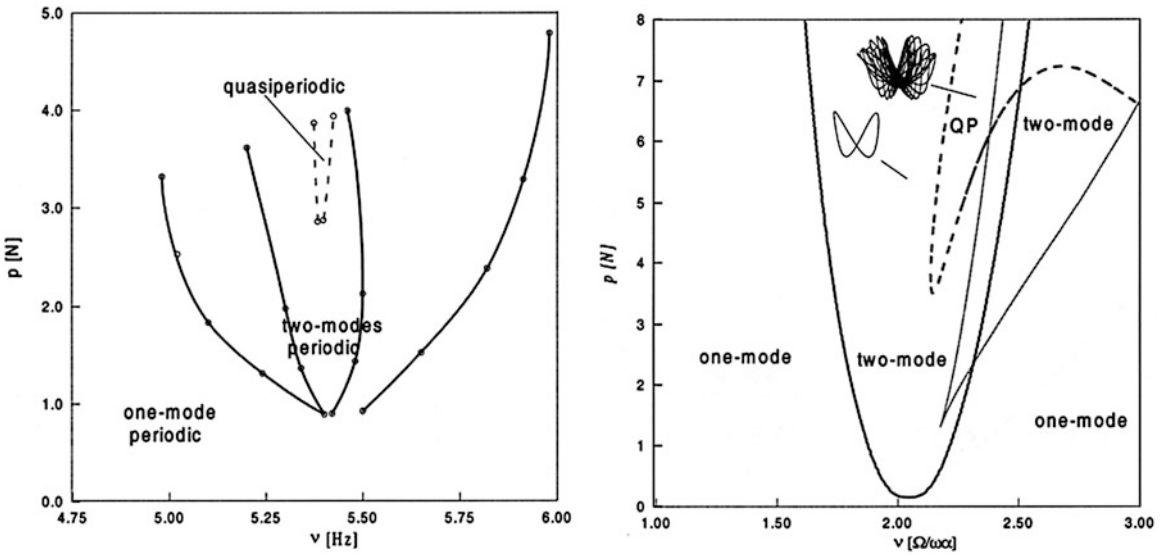

Fig. 19.6 Internally resonant, non shallow arch: experimental (*left*) and analytical (*right*) behavior charts

The experimental-analytical agreement for the one-mode as well as the coupled responses appears to be quite good. Both figures clearly show the instability phenomenon of the 1 mode solution and the excitation, around an adimensionalized frequency of 2, of a coupled solution. Such frequency value corresponds to the primary external resonance condition for the symmetric mode and the $1/2$ subharmonic resonance condition for the antisymmetric one.

However, it is worth noticing how the analytical model shows a more pronounced hardening behavior certainly due to an over-estimation of cubic nonlinearities. Repeating the analysis for different excitation levels, it is possible to draw experimental and analytical behavior charts (Fig. 19.6) evidencing, in the excitation control parameter plane, the bifurcation phenomenon previously described. Both experimental and analytical charts show a similar scenario: the one-mode, directly excited symmetric solution, stable in the whole analyzed frequency-range for low excitation levels, when a critical forcing value is reached, loses stability around the nominal external resonance condition. The bigger is the excitation level, the bigger is the frequency range in which the coupled solution appears. The V-shaped instability zone is further divided in different sub-regions: the external parts of the plot correspond to multiple solutions zones in which, depending on the initial

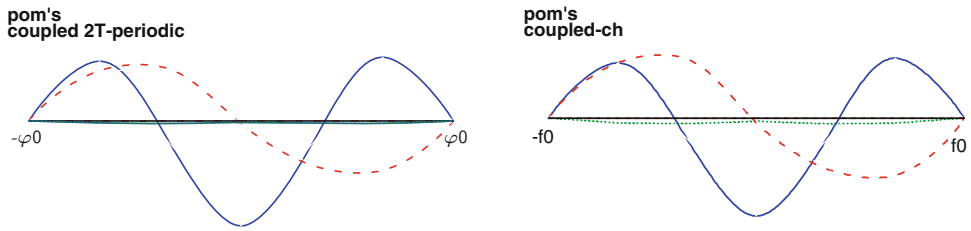

Fig. 19.7 Non-shallow arch: first (red) and second (blue) POMs, periodic (*left*) and chaotic (*right*) evolutions (color figure online)

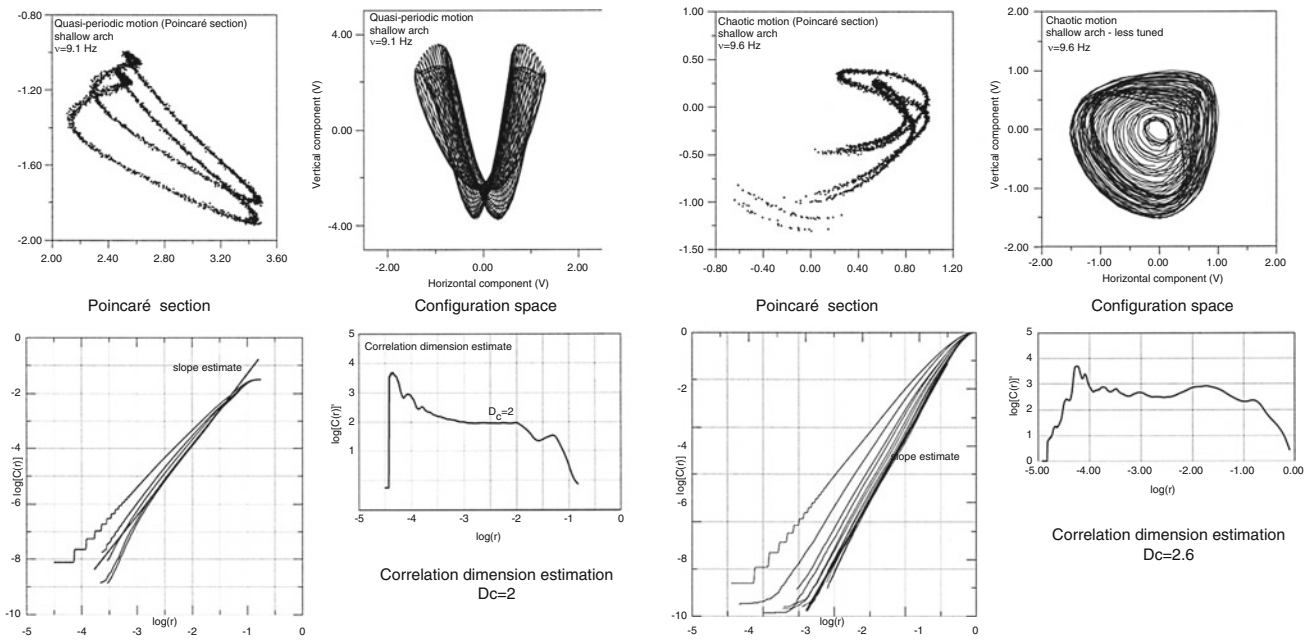

Fig. 19.8 QP (*left*) and chaotic (*right*) characterization of experimental motions

conditions, the one-mode or the coupled solution is alternatively reached; on the contrary, entering the core of the diagram, coupled solutions arise for every choice of initial conditions. Inside this inner area, a further inner sub-region bounded by Hopf boundary limits is found: inside this area there are not periodic solutions at all and quasi periodic and/or chaotic motions arise. Such non periodic zones appear in the experimental chart for lower excitation levels in comparison with the same limit-level in the analytical chart because of the inherently non-perfectly symmetric excitation achieved during the experiments.

To establish whether or not the reduced order model could be used in the forecasting of complex dynamic evolutions, synchronous time series on eight equally spaced points on the arch were acquired. The spatial correlation matrix was formed and the Karunen-Loeve decomposition was applied to determine the *POMs*. The obtained *POMs* are reported in Fig. 19.7. It is easy to observe how, in both cases, the *POMs* are similar and practically coincident with the analytical eigenvectors reported, for the same case, in the upper part of Fig. 19.3. Such a circumstance guarantees a certain level of accuracy in the prediction of even non-periodic evolutions, by using the analytical, experimentally validated, model.

When describing the experimental response, a reference was done to the non-periodic character of the motion; the relevant classification was performed by using the delay-map technique (Takens [8]) allowing the estimation of global complexity indicators like the correlation dimension and the maximum Lyapunov exponent, starting even from a single scalar component of the acquired motion. In Fig. 19.8 the results of a characterization of a QP (left) and a chaotic (right) states within the instability region of Fig. 19.6, is reported. On the left series of diagrams, the QP character is recognized by the double period two-torus Poincaré section (left-top left) and the integer correlation dimension of 2 (left-bottom right), while the chaotic character is recognized, in the diagrams on the right, by the strange attractor in the Poincaré section (right-top left) and the non-integer correlation dimension of 2.6 (right- bottom right).

19.5 Conclusions and Future Developments

The phase of analytical modeling of systems characterized by a finite dynamics is often developed without any caution about the ability to catch real physical behavior. In such situations all the analytically observed phenomena, mainly when complex motions arise, could be linked more to the nonlinear structure of underlying equations than to a real mechanical behavior.

The use of experimental tests to support and validate the analytical formulation is suggested as the correct way to establish a nonlinear reduced order model of analyzed systems. The case study is concerned with the nonlinear dynamics of circular arches having different sag to span ratios.

In the discussed case study, the use of different available analytical models based on different kinematic approximations, is also proposed.

The model proposed by Mettler and largely used in the literature to treat dynamic arch problems, seems to be adequate, besides the analysis of buckled beams, only for arches having a shallowness ratio of about 1/100 and, in any case, when the first mode of the linearized system is symmetric (as in beams).

The instability conditions of the directly excited one-mode symmetric solution were analyzed and different classes of coupled motions were coherently analyzed and discussed.

Moreover, along all the paper, a lay-out of interacting phases of analytical formulation and experimental validation has been drawn: such an interaction seems to be a suitable way to deal with the analysis of even simple structures evolving in strongly developed nonlinear regimes.

References

1. Bolotin VV (1962) The dynamic stability of elastic systems (trans: Weingarten VI et al). Holden-Day, San Francisco
2. Thomsen JJ (1992) Chaotic vibrations of non-shallow arches. J Sound Vib 153(2):239–258.
3. Alaggio R, Benedettini F (2001) The use of experimental tests in the formulation of analytical models for the finite forced dynamics of planar arches. In: Proceedings of the 2001 ASME DETC, Pittsburg, VIB-21613
4. Benedettini F (2000) Theoretical and experimental evidence of symmetric-response instability in the finite, planar dynamics of a circular arch. In: Kreuzer E, van Dao N (eds) IUTAM symposium on recent development in nonlinear oscillations of mechanical systems
5. Benedettini F, Alaggio R, Zulli D (2012) Nonlinear coupling and instability in the forced dynamics of a non-shallow arch: theory and experiments. Nonlinear Dyn 68(4):505–517. doi:10.1007/s11071-011-0232-y
6. Tien W-M, Sri Namachchivaya N, Bajaj A (1994) Non-linear dynamics of a shallow arch under periodic excitation—1. 1:2 internal resonance. Int J Nonlinear Mech 29:349–366
7. Tien W-M, Sri Namachchivaya N, Bajaj A (1994) Non-linear dynamics of a shallow arch under periodic excitation—1. 1:1 internal resonance. Int J Nonlinear Mech 29:367–396
8. Takens F (1981) Detecting strange attractors in turbulence. In: Rand DA, Yang LS (eds) Dynamical systems and turbulence. Springer lecture notes in mathematics, vol 898. Springer, New York, pp 266–281
9. Mettler E (1962) Dynamic buckling. In: Flügge W (ed) Handbook of engineering mechanics. McGraw Hill, New York
10. Henrych J (1981) The dynamics of arches and frames (trans: Major R). Elsevier, Amsterdam
11. Benedettini F (1996) An experimental time series analysis approach in the classification of non periodic motions in nonlinear structural dynamics. In: Augusti G, Borri C, Spinelli P (eds) Proceedings of the third European conference on structural dynamics: EURODYN 96. A.A. Baklema, Rotterdam/Brookfield, pp 415–421
12. Cusumano JP, Bai BY (1993) Period-infinity periodic motions, chaos, and spatial coherence in a 10 degree of freedom impact sscillator. Chaos Solitons Fractals 3(5):515–535

Chapter 20
Investigation of Jointed Structures Using the Multiharmonic Balance Method

Dominik Süß, Martin Jerschl, and Kai Willner

Abstract This paper deals with the investigation of a jointed structure in the frequency domain. Because of the nonlinearity of most jointed systems the steady state response shall be calculated utilizing the Multiharmonic Balance Method (MHBM). In the framework of this method the response displacements of the system are assumed to be periodic and are approximated by a Fourier-type series expansion considering a limited number of harmonic parts. The MHBM is presented for a system containing a bolted lap joint. For the contacting bodies small deformations and linear elastic material behavior are assumed. The system will be modeled with the Finite Element Method (FEM) using so called Zero Thickness (ZT) elements for discretizing the contact plane. Since this contact area is known and only small relative displacements occur, the suggested contact element is well suited for the present problem. The ZT elements contain a three-dimensional nonlinear contact law considering dry friction effects. A model updating process is used to fit the calculation results with respect to the measured data of a real system.

Keywords Structural dynamics • Jointed structure • Harmonic balance • FEM • Contact element

20.1 Introduction

The jointed structure investigated here is the friction oscillator sketched in Fig. 20.1.

The design of this structure made of steel is based on an idea of Gaul, see e.g. [3], and consists of two cylindrical main masses (I and II). Because of a flexure spring located between these two masses the first resonance frequencies lie in a quite low frequency range smaller than 1 kHz. The oscillator usually has its operating point around the resonance frequency which corresponds to the first bending eigenform of the flexure spring. This means a counter-wise translational motion of the two main masses.

The main advantage of the structure is that the bolted lap joint lying between the left mass (II) and the bending spring is the only joint in the system and can be investigated isolated. The typical form of the equations of motion for such a system reads

$$\mathbf{M}\ddot{\mathbf{x}}(t) + \mathbf{D}\dot{x}(t) + \mathbf{K}\mathbf{x}(t) + \mathbf{f}_{nl}(\mathbf{x}, \dot{\mathbf{x}}, t) = \mathbf{f}_e(t), \tag{20.1}$$

containing not only the mass, damping and stiffness matrices $\mathbf{M}$, $\mathbf{D}$, $\mathbf{K}$ and the excitation forces $\mathbf{f}_e$ but also a vector of nonlinear forces $\mathbf{f}_{nl}$ which may depend on the time as well as on the displacement vector $\mathbf{x}$ and its derivative with respect to the time. The structure shall be investigated in the frequency domain but because of $\mathbf{f}_{nl}$ it is not possible to directly transform the system equations analytically into the frequency domain, where steady state calculations can be performed with low effort. Because of that the MHBM shall be utilized.

D. Süß (✉) • M. Jerschl • K. Willner
Chair of Applied Mechanics, University of Erlangen-Nuremberg, Egerlandstr. 5, 91058 Erlangen, Germany
e-mail: dominik.suess@ltm.uni-erlangen.de; martin.jerschl@ltm.uni-erlangen.de; kai.willner@ltm.uni-erlangen.de

G. Kerschen et al. (eds.), *Topics in Nonlinear Dynamics, Volume 1: Proceedings of the 31st IMAC, A Conference on Structural Dynamics, 2013*, Conference Proceedings of the Society for Experimental Mechanics Series 35,
DOI 10.1007/978-1-4614-6570-6_20,

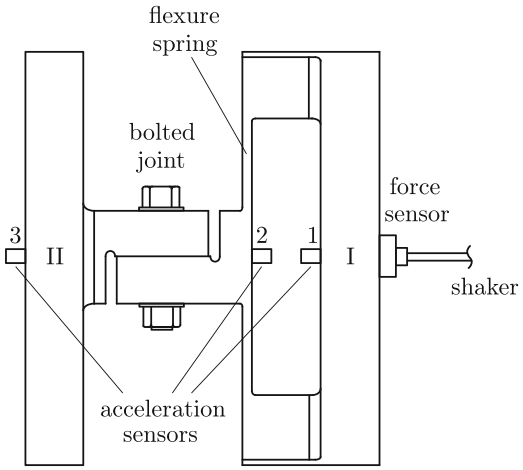

Fig. 20.1 Sketch of the friction oscillator

20.2 Multiharmonic Balance Method

The basic assumption using the MHBM is that the response displacements $\mathbf{x}(t)$ of the system are expected to be periodically and are approximated by the ansatz

$$\mathbf{x}(t) = \mathbf{X}_{(0)} + \sum_{k=1}^{n_h} \left(\tilde{\mathbf{X}}_{(k)} e^{i \cdot k\omega t} + \bar{\tilde{\mathbf{X}}}_{(k)} e^{-i \cdot k\omega t} \right), \tag{20.2}$$

considering n_h harmonic parts. The same ansatz is used for the nonlinear forces $\mathbf{f}_{nl}$ and can be utilized for $\mathbf{f}_e$ as well, if the excitation is not chosen harmonic or periodic with less or equal than n_h harmonics. Since containing no further information the conjugate complex parts can be omitted. So the equations of motion can be written as

$$\sum_{k=0}^{n_h} \left(\left(-k^2\omega^2 \mathbf{M} + i \cdot k\omega \mathbf{D} + \mathbf{K} \right) \tilde{\mathbf{X}}_{(k)} e^{i \cdot k\omega t} + \tilde{\mathbf{F}}_{nl,(k)} e^{i \cdot k\omega t} \right) = \sum_{k=0}^{n_h} \left(\tilde{\mathbf{F}}_{e,(k)} e^{i \cdot k\omega t} \right). \tag{20.3}$$

This system of equations is first split into its different harmonics and then into its real and imaginary parts, in order to get a real valued problem. As an example the real form of the displacement vector reads

$$\mathbf{X} = \left[\mathbf{X}_{(0)},\, \Re\{\tilde{\mathbf{X}}_{(1)}\},\, \Re\{\tilde{\mathbf{X}}_{(2)}\},\, \ldots,\, \Re\{\tilde{\mathbf{X}}_{(n_h)}\},\, \Im\{\tilde{\mathbf{X}}_{(1)}\},\, \Im\{\tilde{\mathbf{X}}_{(2)}\},\, \ldots,\, \Im\{\tilde{\mathbf{X}}_{(n_h)}\} \right]^T. \tag{20.4}$$

Then the real valued system of equations of motion can be written in the form

$$\mathbf{S}(\omega)\mathbf{X}(\omega) + \mathbf{F}_{nl}(\mathbf{X}(\omega)) = \mathbf{F}_e(\omega), \tag{20.5}$$

where $\mathbf{S}$ denotes the diagonal block matrix of the real valued dynamic stiffness matrices

$$\mathbf{S}(\omega) = \begin{bmatrix} \mathbf{K} & \mathbf{0} & \mathbf{0} \\ \mathbf{0} & \operatorname{diag}(-k^2\omega^2\mathbf{M} + \mathbf{K}) & \operatorname{diag}(-k\omega\mathbf{D}) \\ \mathbf{0} & \operatorname{diag}(k\omega\mathbf{D}) & \operatorname{diag}(-k^2\omega^2\mathbf{M} + \mathbf{K}) \end{bmatrix}, \quad \text{with} \quad k = 1, \ldots, n_h. \tag{20.6}$$

Equations (20.5) are solved using the Alternating Frequency Time Domain Method (AFT), see e.g. [1, 12]. In the framework of this method the frequency domain representation of $\mathbf{F}_{nl}$ is calculated by a Fast Fourier Transform (FFT) of the nonlinear forces $\mathbf{f}_{nl}$ in the time domain. These forces may in turn be derived from an iterative solution for $\mathbf{x}$, if an explicit dependency $\mathbf{f}_{nl}(\mathbf{x})$ exists. For solving system (20.5) iteratively a residual

$$\mathbf{R}(\omega, \mathbf{X}(\omega)) = \mathbf{S}(\omega)\mathbf{X}(\omega) + \mathbf{F}_{nl}(\mathbf{X}(\omega)) - \mathbf{F}_e(\omega) \stackrel{!}{=} \mathbf{0} \tag{20.7}$$

is formulated and a Newton-Raphson type solver is applied. The needed partial derivatives of the residual with respect to the displacements have the form

$$\frac{\partial \mathbf{R}}{\partial \mathbf{X}} = \mathbf{S} + \frac{\partial \mathbf{F}_{nl}}{\partial \mathbf{X}}, \tag{20.8}$$

at which the partial derivatives of the nonlinear forces $\mathbf{F}_{nl}$ with respect to the response displacements $\mathbf{X}$ can (like $\mathbf{F}_{nl}$ itself) be evaluated in the time domain and are transformed into the frequency domain afterwards,

$$\frac{\partial \tilde{\mathbf{F}}_{nl}}{\partial \tilde{\mathbf{X}}} = \frac{\partial \mathfrak{F}\{\mathbf{f}_{nl}(\mathbf{x})\}}{\partial \tilde{\mathbf{X}}} = \frac{\partial \mathfrak{F}\{\mathbf{f}_{nl}(\mathfrak{F}^{-1}\{\tilde{\mathbf{X}}\})\}}{\partial \tilde{\mathbf{X}}} = \mathfrak{F}\left\{\frac{\partial \mathbf{f}_{nl}(\mathfrak{F}^{-1}\{\tilde{\mathbf{X}}\})}{\partial \tilde{\mathbf{X}}}\right\}, \tag{20.9}$$

see e.g. [2, 11]. For simplicity they are given here in complex form. Replacing the inverse Fourier transform in Eq. (20.9) by a Fourier series and setting in the (explicit) law for the nonlinear forces, the partial derivatives of these forces as a function of the response displacement harmonics can be calculated analytically. Hence all needed values for solving problem (20.7) are given.

20.3 FEM Model

In [14] the system investigated here was modeled by a simple 3-DOF model. Because of the special design of the structure this works very well. But in order to get a way of predicting the stationary dynamic behavior of jointed structures in general, here the Finite Element Method shall be applied. The mesh of the chosen FEM model is pictured in Fig. 20.2.

The two parts of the system are discretized using hexahedral elements. Because only small deformations are assumed the material behavior shall be modeled linear elastic. The corresponding material parameters like Young's modulus may be determined by either a tension test or an experimental modal analysis on one of the parts of the system. Material damping shall be modeled using the ansatz of proportional damping. Because of the symmetry of the structure, symmetry boundary conditions can be applied. The support of the structure is modeled with the help of linear elastic springs.

20.3.1 ZT Elements

The contact plane is discretized using so called Zero Thickness elements, see e.g. [6, 8] or [5, 13]. These isoparametric eight-node elements consist of two linear quadrilateral elements with the thickness of zero, see Fig. 20.3.

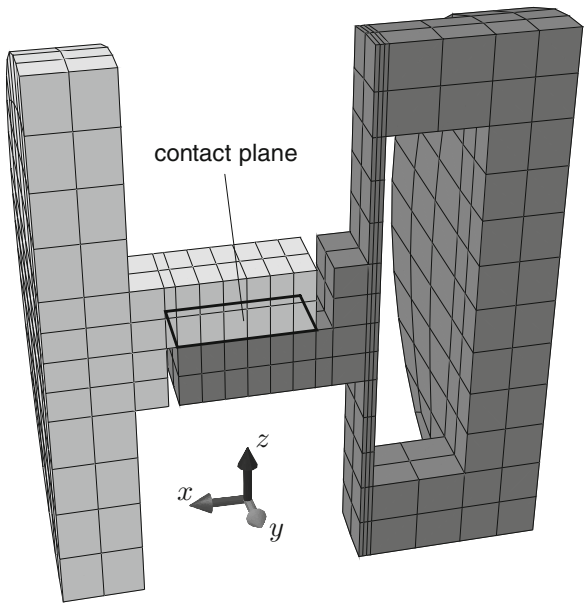

Fig. 20.2 Mesh of the friction oscillator FEM model

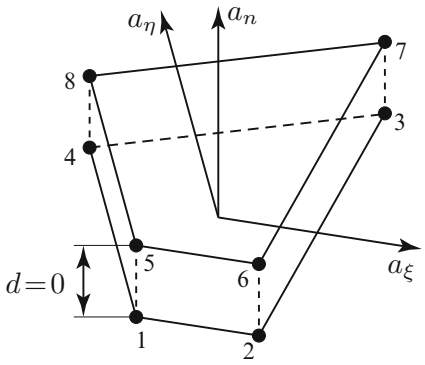

Fig. 20.3 Sketch of a 8-node ZT element

Using the local coordinate system $[\mathbf{a}_n, \mathbf{a}_\xi, \mathbf{a}_\eta]$ the local relative displacements of the two layers and the contact stresses read

$$\mathbf{g} = [g_n, g_\xi, g_\eta]^T = [g_n, \mathbf{g}_t]^T \qquad \text{and} \qquad \mathbf{t} = [t_n, t_\xi, t_\eta]^T = [t_n, \mathbf{t}_t]^T, \tag{20.10}$$

respectively. For details concerning the formulation of these elements, see e.g. [9]. Between the two segments nearly arbitrary constitutive laws may be applied.

20.3.2 Three-Dimensional Contact Law

The constitutive law in normal direction for the case of contact is linear elastic. For the case of separation, the local normal stress t_n is set to zero. So the contact stresses in normal direction for the ℓ-th time step read

$$t_n(\ell) = \begin{cases} 0 & \text{separation} \\ c_n g_n(\ell) & \text{contact} \end{cases}, \tag{20.11}$$

with the normal stiffness coefficient c_n and the normal displacements g_n. In tangential direction so called Masing elements are applied accounting for dry friction effects, see e.g. [10]. Then the tangential contact stresses can be written as

$$\mathbf{t}_t(\ell) = \begin{cases} \mathbf{0} & \text{separation} \\ {}^{tr}\mathbf{t}_t(\ell) & \text{stick} \\ {}^{m}t_t(\ell)\dfrac{{}^{tr}\mathbf{t}_t(\ell)}{\|{}^{tr}\mathbf{t}_t(\ell)\|} & \text{slip} \end{cases}. \tag{20.12}$$

For the correct calculation of these stresses a radial return mapping algorithm is applied, calculating the trial stresses

$${}^{tr}\mathbf{t}_t(\ell) = c_t \overline{\mathbf{m}}\,(\mathbf{g}_t(\ell) - \mathbf{g}_t(\ell-1)) + \mathbf{t}_t(\ell-1), \tag{20.13}$$

with the tangential stiffness coefficient c_t and the contra-variant metric $\overline{\mathbf{m}}$, transforming the covariant displacements into contravariant coordinates. In the case of slip, the norm of the trial stresses is bigger than the maximal stiction stress

$${}^{m}t_t(\ell) = -\mu t_n(\ell), \tag{20.14}$$

with the friction coefficient μ. Then the tangential stresses have to be limited to this value.

For the MHBM procedure the partial derivatives of the q-th harmonic of the contact stresses with respect to the p-th harmonic of the relative displacements,

$$\frac{\partial \mathbf{T}}{\partial \mathbf{G}} = \begin{bmatrix} \dfrac{\partial \Re\{\tilde{\mathbf{T}}_{(q)}\}}{\partial \Re\{\tilde{\mathbf{G}}_{(p)}\}} & \dfrac{\partial \Re\{\tilde{\mathbf{T}}_{(q)}\}}{\partial \Im\{\tilde{\mathbf{G}}_{(p)}\}} \\ \dfrac{\partial \Im\{\tilde{\mathbf{T}}_{(q)}\}}{\partial \Re\{\tilde{\mathbf{G}}_{(p)}\}} & \dfrac{\partial \Im\{\tilde{\mathbf{T}}_{(q)}\}}{\partial \Im\{\tilde{\mathbf{G}}_{(p)}\}} \end{bmatrix}, \tag{20.15}$$

have to be computed. As mentioned above, these partial derivatives are calculated in the time domain. A consistent derivation of the constitutive laws (20.11) and (20.12), analogously to e.g. [4], is possible. As an example, the partial derivatives of the tangential contact stresses with respect to the real parts of the normal relative displacements can be written as

$$\frac{\partial \mathbf{T}_{t,(q)}}{\partial \Re\{G_{n,(p)}\}} = \frac{\partial \Re\{\mathbf{T}_{t,(q)}\}}{\partial \Re\{G_{n,(p)}\}} + \frac{\partial \Im\{\mathbf{T}_{t,(q)}\}}{\partial \Re\{G_{n,(p)}\}} = \mathfrak{F}^{(q,\ell)} \left\{ \frac{\partial \mathbf{t}_t(\ell)}{\partial \Re\{G_{n,(p)}\}} \right\}, \tag{20.16}$$

with

$$\frac{\partial \mathbf{t}_t(\ell)}{\partial \Re\{G_{n,(p)}\}} = \begin{cases} \mathbf{0} \\ \dfrac{\partial \mathbf{t}_t(\ell-1)}{\partial \Re\{G_{n,(p)}\}} \\ \dfrac{1}{\|{}^{tr}\mathbf{t}_t(\ell)\|} \left({}^{m}t_t(\ell) \dfrac{\partial \mathbf{t}_t(\ell-1)}{\partial \Re\{G_{n,(p)}\}} - \mu c_n \cos\left(\ell p \dfrac{2\pi}{N}\right) {}^{tr}\mathbf{t}_t(\ell) \right) - \dfrac{{}^{m}t_t(\ell)\,{}^{tr}\mathbf{t}_t(\ell)}{\|{}^{tr}\mathbf{t}_t(\ell)\|^3} \left({}^{tr}\mathbf{t}_t(\ell)\,\overline{\mathbf{m}}\, \dfrac{\partial \mathbf{t}_t(\ell-1)}{\partial \Re\{G_{n,(p)}\}} \right) \end{cases} \tag{20.17}$$

for the three cases separation, stick and slip respectively. After numerical integration and assembly the global nonlinear contact forces $\mathbf{f}_{nl}$ as well as their partial derivatives are transformed back into the frequency domain using the discrete Fourier transform $\mathfrak{F}$. Using the partial derivatives computed this way, Frequency Response Functions (FRFs) of the system can be calculated. A parameter identification can be applied using measured FRFs to identify the three unknown contact parameters c_n, c_t and μ.

20.4 Numerical Results

The measurements for getting reference FRFs of the real system are recorded using a shaker, see Fig. 20.1, and performing a swept sine excitation of the structure. For the calculation this excitation is assumed to be harmonic, with a constant excitation amplitude $\tilde{F}_{e,(1)} = 100\,\mathrm{N}$. Using a least squares model updating algorithm the calculation results are fitted with respect to the measured curves to identify the contact parameters. Figure 20.4 shows the comparison of the FRFs evaluated for acceleration sensor 3.

It can be seen that there is a very good correlation between measured and calculated data. The biggest difference between the two curves occurs at approximately 307 Hz because of an overshoot of the measured FRF due to the inertia of the closed loop shaker control. Due to the strong response of the structure in this region neither the excitation amplitude is constant nor the function itself is harmonic. This of course can not be modeled with the assumptions for the excitation force made above. The corresponding contact parameters

$$c_n = 1.0 \cdot 10^6\,\mathrm{N/mm^3}, \qquad c_t = 2.2 \cdot 10^2\,\mathrm{N/mm^3}, \qquad \mu = 0.8 \tag{20.18}$$

were identified under consideration of 11 harmonics. Especially the value for μ is quite high for dry contact of steel on steel. There are two possible reasons for this:

Firstly, the rather coarse discretization has an influence on the identified parameters – a refinement of the mesh has to be done. Secondly, when the structure was in operation for some time, after disassembling it is possible to see strong signs of wear and beginning cold welding, so an increasing μ-value during the operation is very probable.

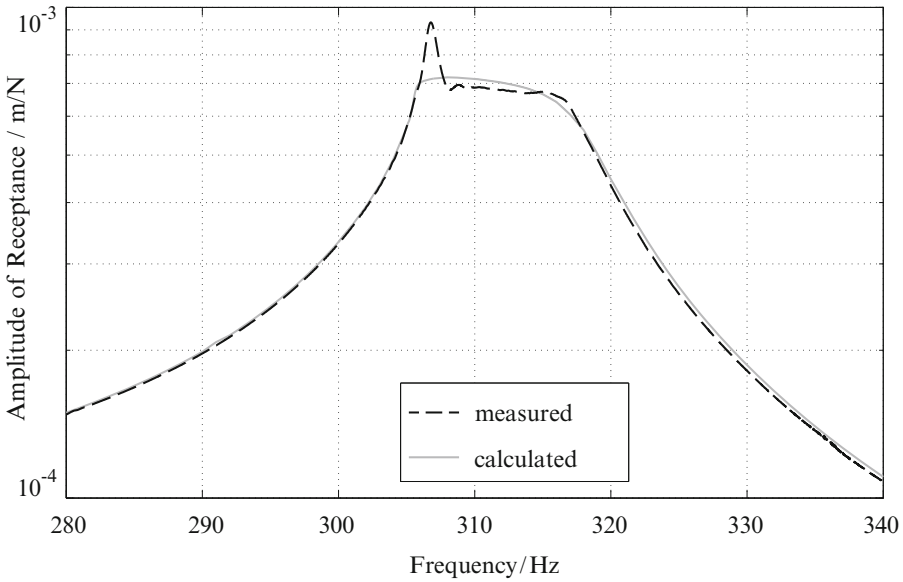

Fig. 20.4 Comparison of measured and calculated FRFs

20.5 Conclusion

The friction oscillator analyzed here is an academic structure but offers the chance of an isolated investigation of a bolted lap joint. The presented FEM model for this system is a much more general alternative to the rheological models known from literature, see [7] or [14]. Using the MBHM/AFT method it is possible to calculate realistic FRFs.

References

1. Cameron T M, Griffin JH (1989) An alternating frequency/time domain method for calculating the steady-state response of nonlinear systems. J Appl Mech 56:149–154
2. Cardona A, Coune T, Lerusse A, Geradin M (1994) A multiharmonic method for non-linear vibration analysis. Int J Numer Methods Eng 37:1593–1608
3. Gaul L, Lenz J (1997) Nonlinear dynamics of structures assembled by bolted joints. Acta Mech 125:169–181
4. Geisler J (2010) Numerische und experimentelle Untersuchungen zum dynamischen Verhalten von Strukturen mit Fügestellen. PhD thesis, LTM Erlangen
5. Geisler J, Willner K (2007) Modeling of jointed structures using zero thickness interface elements. PAMM 7(1):4050009–4050010
6. Goodman RE, Taylor RL, Brekke TL (1968) A model for the mechanics of jointed rock. J Soil Mech Found Div 94:637–660
7. Lenz J.: Strukturdynamik unter dem Einfluss von Mikro- und Makroschlupf. PhD thesis, IAM Stuttgart, 1997.
8. Mayer M (2007) Zum Einfluss von Fügestellen auf das dynamische Verhalten zusammengesetzter Strukturen. PhD thesis, IAM Stuttgart
9. Mayer M, Gaul L (2007) Segment-to-segment contact elements for modelling joint interfaces in finite element analysis. Mech Syst Sig Process 21:724–734
10. Ottl D (1981) Schwingungen mechanischer Systeme mit Strukturdämpfung. VDI Forschungsheft, 603
11. Petrov EP, Ewins D J (2003) Analytical formulation of friction interface elements for analysis of nonlinear multi-harmonic vibrations of bladed disks. Trans ASME 125:364–371
12. Poudou O., Pierre C (2003) Hybrid frequency-time domain methods for the analysis of complex structural systems with dry friction damping. Collection of technical papers – AIAA/ASME/ASCE/AHS/ASC structures. Struct Dyn Mater Conf 1:111–124
13. Süß D, Geisler J, Willner K (2010) Numerical and experimental investigations on dynamic contact phenomena of jointed structures. PAMM 10:263–264
14. Süß D, Willner K (2010) Multiharmonic balance analysis of a jointed friction oscillator. Proceedings of the ECCOMAS, Vienna, CD-ROM

Chapter 21
The Nonlinear Tuned Vibration Absorber

R. Viguié and G. Kerschen

Abstract The objective of this paper is to introduce a new nonlinear dynamical absorber, the nonlinear tuned vibration absorber, through a rigorous nonlinear extension of the tuning rule for the linear tuned vibration absorber. This nonlinear tuning methodology combined with the increased suppression bandwidth brought by the intentional use of nonlinearity leads to the development of an absorber that is effective in wide ranges of frequencies and motion amplitudes. The results are illustrated using a one-degree-of-freedom primary system.

Keywords Vibration mitigation • Tuned absorber • Nonlinear dynamics • Numerical continuation and bifurcation analysis

21.1 Introduction

Nonlinear vibration absorbers, first introduced by Roberson [1], Pipes [2] and Arnold [3], offer an interesting alternative to linear vibration absorbers, because they are effective in a wider frequency range. More recent developments in passive nonlinear vibration absorbers include the autoparametric vibration absorber, which exploits the saturation phenomenon [4], and the nonlinear energy sink (NES) relying on the concept of essential nonlinearity [5]. However, due to the frequency-energy dependence of nonlinear oscillations, these nonlinear absorbers are characterized by the lack of amplitude robustness, which makes their design challenging.

In this study, a nonlinear primary structure is considered, and a nonlinear vibration absorber that enables an effective mitigation of the vibrations of one specific nonlinear mode in a wide range of forcing amplitudes is developed. The proposed methodology relies on a frequency-energy based approach followed by bifurcation analysis. The first step considers the underlying Hamiltonian system and selects an appropriate functional form for the absorber by imposing its backbone to possess a qualitatively similar dependence on energy as that of the backbone of the primary system [6]. Based upon this result, the second step considers the forced system and determines appropriate stiffness and damping coefficients for the absorber by tracking bifurcation points in parameter space [7].

21.2 Problem Statement

The response of a single-degree-of-freedom nonlinear oscillator with cubic stiffness to harmonic excitation is considered:

$$m_1\ddot{x}_1 + c_1\dot{x}_1 + k_{lin_1}x_1 + k_{nl_1}x_1^3 = F\cos\omega t \tag{21.1}$$

R. Viguié • G. Kerschen (✉)
Space Structures and Systems Laboratory (S3L), Structural Dynamics Research Group,
Department of Aerospace and Mechanical Engineering, University of Liège, Liège, Belgium
e-mail: regis.viguie@techspace-aero.be; g.kerschen@ulg.ac.be

G. Kerschen et al. (eds.), *Topics in Nonlinear Dynamics, Volume 1: Proceedings of the 31st IMAC, A Conference on Structural Dynamics, 2013*, Conference Proceedings of the Society for Experimental Mechanics Series 35,
DOI 10.1007/978-1-4614-6570-6_21,

This system, termed the primary system, can also represent the vibration of a specific mode of a multi-degree-of-freedom structure.

The objective of this study is to design a nonlinear vibration absorber that can mitigate the vibrations of system (21.1) in a wide range of forcing amplitudes, and this despite the frequency-energy dependence of nonlinear oscillations. Specifically, an appropriate functional form for the absorber, together with adequate stiffness and damping coefficients, will be determined through a two-step procedure.

21.3 First Step of the Tuning Methodology: Frequency-Energy Based Approach

An undamped, unforced two-degree-of-freedom system, comprising an essential nonlinear oscillator coupled to an essential nonlinear vibration absorber with unknown functional form α is first considered to illustrate the tuning methodology:

$$\begin{aligned} m_1\ddot{x}_1 + k_{nl_1}x_1^3 + k_{nl_2}(x_1 - x_2)^3 &= 0 \\ m_2\ddot{x}_2 + k_{nl_2}(x_2 - x_1)^\alpha &= 0 \end{aligned} \tag{21.2}$$

A nonlinear extension of the tuning of the classical tuned mass damper (TMD) is proposed herein. According to the TMD theory, the stiffness and mass of a linear absorber should be chosen so that its resonant frequency is equal to the resonant frequency of the linear primary oscillator [8]. In view of the frequency-energy dependence of nonlinear oscillations, the selection of the exponent of the absorber nonlinear spring should therefore be selected so that *the backbone curve of the absorber possesses the same dependence on energy as that of the primary system* [6,7].

According to this rule, the absorber should possess a cubic nonlinearity, i.e., $\alpha = 3$. The absorber parameters are then computed by considering the two oscillators separately

$$\begin{aligned} m_1\ddot{x}_1 + k_{nl_1}x_1^3 &= 0 \\ m_2\ddot{x}_2 + k_{nl_2}x_2^3 &= 0 \end{aligned} \tag{21.3}$$

and by calculating their backbone curves in a frequency-energy plane. Using, e.g., a one-term harmonic balance expansion, it follows:

$$E_1(\omega) = \frac{4m_1^2}{9k_{nl_1}}\omega^4 \quad \text{and} \quad E_2(\omega) = \frac{4m_2^2}{9k_{nl_2}}\omega^4 \tag{21.4}$$

and

$$E_1(\omega) = E_2(\omega) \rightarrow k_{nl_2} = \frac{m_2^2 k_{nl_1}}{m_1^2} \tag{21.5}$$

where E_1 and E_2 correspond to the energy of the first and second oscillators, respectively. Further details about these developments can be found in [6].

The impulsive response of the coupled, dissipative system is now analyzed:

$$\begin{aligned} m_1\ddot{x}_1 + c_1\dot{x}_1 + c_2(\dot{x}_1 - \dot{x}_2) + k_{nl_1}x_1^3 + k_{nl_2}(x_1 - x_2)^3 &= 0 \\ m_2\ddot{x}_2 + c_2(\dot{x}_2 - \dot{x}_1) + k_{nl_2}(x_2 - x_1)^3 &= 0 \end{aligned} \tag{21.6}$$

with $\dot{x}_1(0) \neq 0$ and $x_1(0) = x_2(0) = \dot{x}_2(0) = 0$. The parameters of the primary system are $m_1 = 1\,(\text{kg})$ and $k_{nl_1} = 1\,(\text{N/m}^3)$. For obvious practical reasons, a light-weight absorber is adopted, $m_2 = 0.05\,(\text{kg})$. The nonlinear stiffness of the absorber is computed according to relation (21.5), and $k_{nl_2} = 0.0025\,(\text{N/m}^3)$. Weak damping $c_1 = c_2 = 0.002\,(\text{Ns/m})$ is introduced to induce dissipation.

The performance of the nonlinear tuned absorber is examined in Fig. 21.1a through a three-dimensional plot showing the energy dissipated in the absorber against the nonlinear stiffness k_{nl_1} and the impulse magnitude $\dot{x}_1(0)$. For $k_{nl_1} \approx 0.3\,(\text{N/m}^3)$ and regardless of the value of $\dot{x}_1(0)$, the tuned nonlinear absorber can dissipate a major portion of the input energy (i.e., 95%). In addition, the region of high energy dissipation is not localized to a particular value of k_{nl_1}, but it extends over the interval $k_{nl_1} = [0.1 - 0.35]\ (\text{N/m}^3)$.

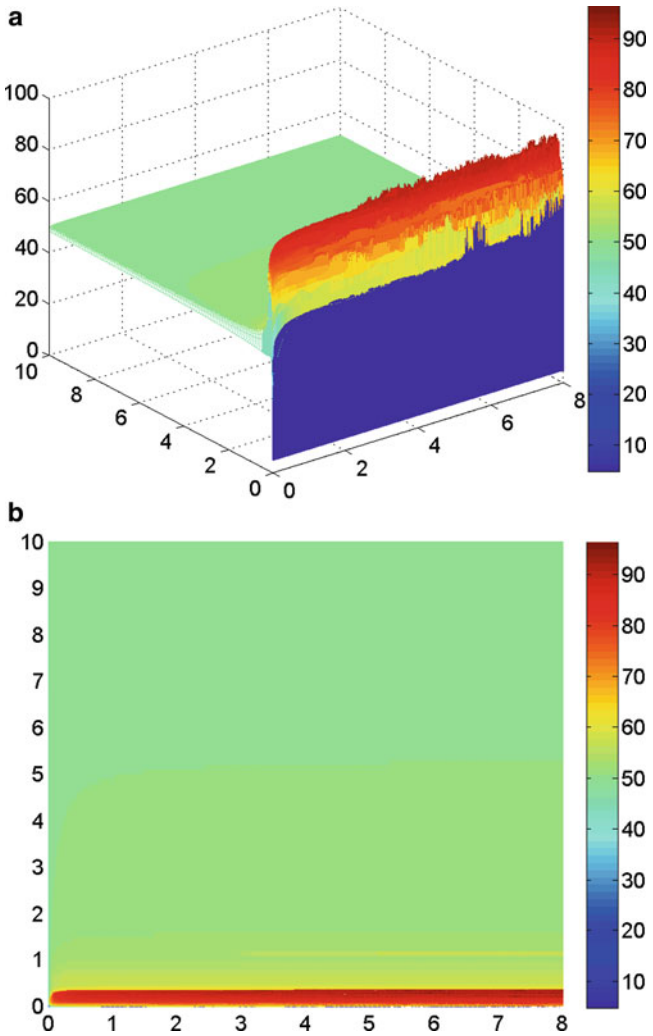

Fig. 21.1 Energy dissipated in the nonlinear absorber (with $k_{nl_2} = 0.0025\,(\mathrm{N/m^3})$) against the nonlinear stiffness of the primary system and the impulse magnitude. (**a**) Three-dimensional graph; (**b**) contour plot

These results seem to validate the proposed tuning procedure, at least qualitatively: a nonlinear absorber that can mitigate the vibrations of a nonlinear primary system in a wide range of impulse magnitudes has been obtained. The quantitative agreement is less satisfactory, because high energy dissipation appears around $k_{nl_1} = 0.3\,(\mathrm{N/m^3})$ and not around $k_{nl_1} = 1\,(\mathrm{N/m^3})$. The nonlinear stiffness should in fact be $k_{nl_2} = 0.0075\,(\mathrm{N/m^3})$ so that the high dissipation appears around $k_{nl_1} = 1\,(\mathrm{N/m^3})$. This is one limitation of the procedure, because the coupling between the oscillators was neglected. This limitation is addressed in what follows.

21.4 Second Step of the Tuning Methodology: Bifurcation Analysis

The forced system is now considered

$$\begin{aligned} m_1\ddot{x}_1 + c_1\dot{x}_1 + c_2(\dot{x}_1 - \dot{x}_2) + k_{nl_1}x_1^3 + k_{nl_2}(x_1 - x_2)^3 &= F\cos\omega t \\ m_2\ddot{x}_2 + c_2(\dot{x}_2 - \dot{x}_1) + k_{nl_2}(x_2 - x_1)^3 &= 0 \end{aligned} \tag{21.7}$$

with $F = 0.1\,(\mathrm{N})$ and $m_1 = 1\,(\mathrm{kg})$, $k_{nl_1} = 1\,(\mathrm{N/m^3})$, $m_2 = 0.05\,(\mathrm{kg})$, $k_{nl_2} = 0.0025\,(\mathrm{N/m^3})$, and $c_1 = c_2 = 0.002\,(\mathrm{Ns/m})$. Its frequency response (NLFRF) is computed using the MATCONT software [9] and is represented in Fig. 21.2b. The frequency response of the uncontrolled case (i.e., without the nonlinear absorber) is depicted in Fig. 21.2a and shows that (i) more complex dynamics is introduced by the absorber nonlinearity, which is evidenced by the increased number of bifurcations in Fig. 21.2b, and (ii) a 31% peak reduction is achieved thanks to the nonlinear vibration absorber.

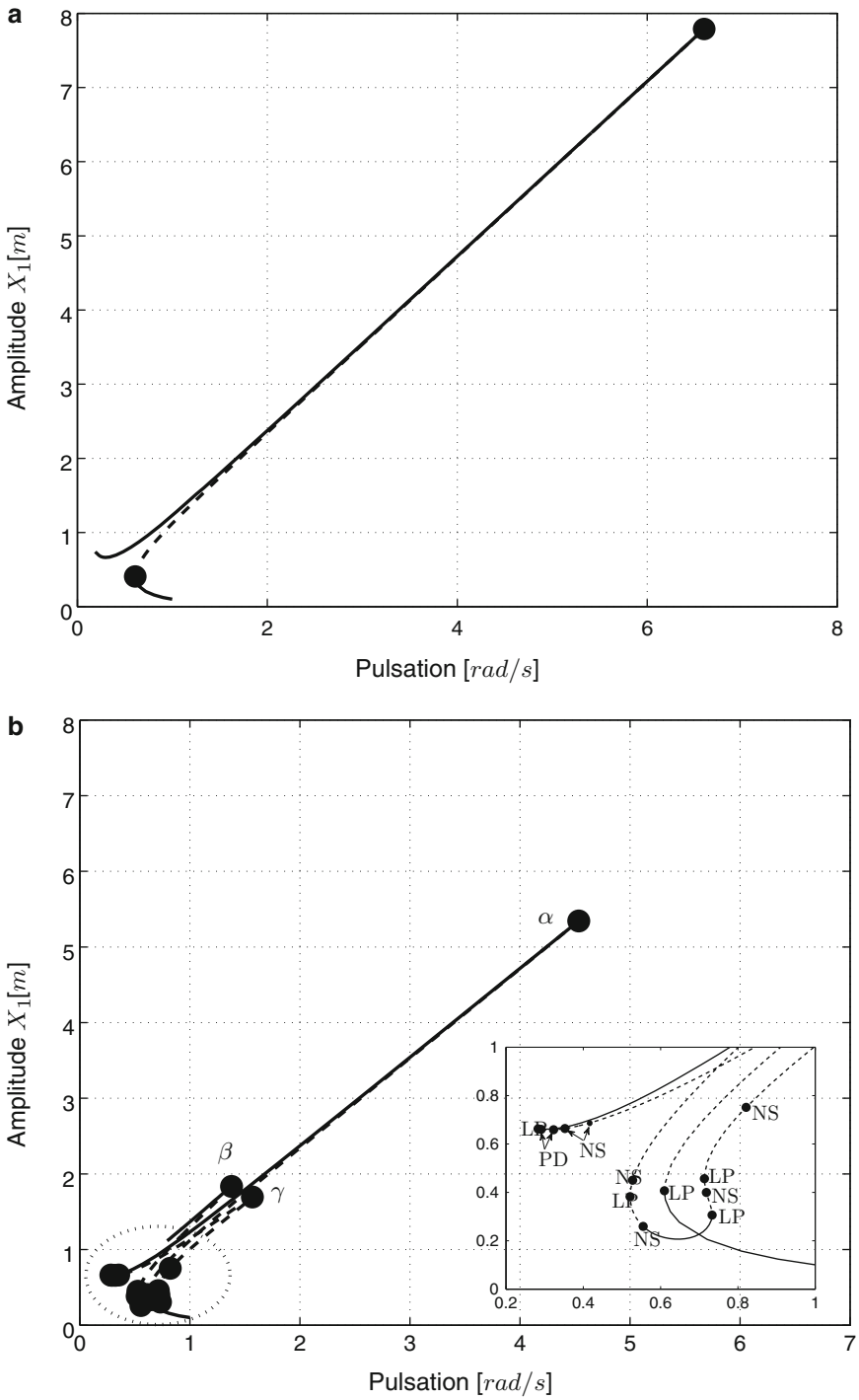

Fig. 21.2 Frequency response for F = 0.1 N. (**a**) Uncontrolled response; (**b**) controlled response with $k_{nl_2} = 0.0025\,\mathrm{N/m^3}$. *Solid* and *dashed lines* correspond to stable and unstable periodic solutions, respectively; *dots* are related to bifurcation points

The second step of the tuning methodology determines appropriate stiffness and damping coefficients for the absorber through bifurcation analysis. Specifically, Fig. 21.2b illustrates that the points of maximum amplitude α, β and γ correspond to bifurcations (limit point, LP). Tracking such bifurcation in parameter space (k_{nl_2},c_2) is therefore a possible means of adjusting the design of a nonlinear absorber.

However, because the excitation frequency is also a necessary parameter during numerical continuation, a codimension three continuation problem is to be solved, which is beyond the current capability of MATCONT. The proposed solution is to first optimize the absorber performance with respect to the nonlinear stiffness, which is a codimension two problem. The same procedure can then be carried out for damping, and the whole process can be repeated until convergence is reached.

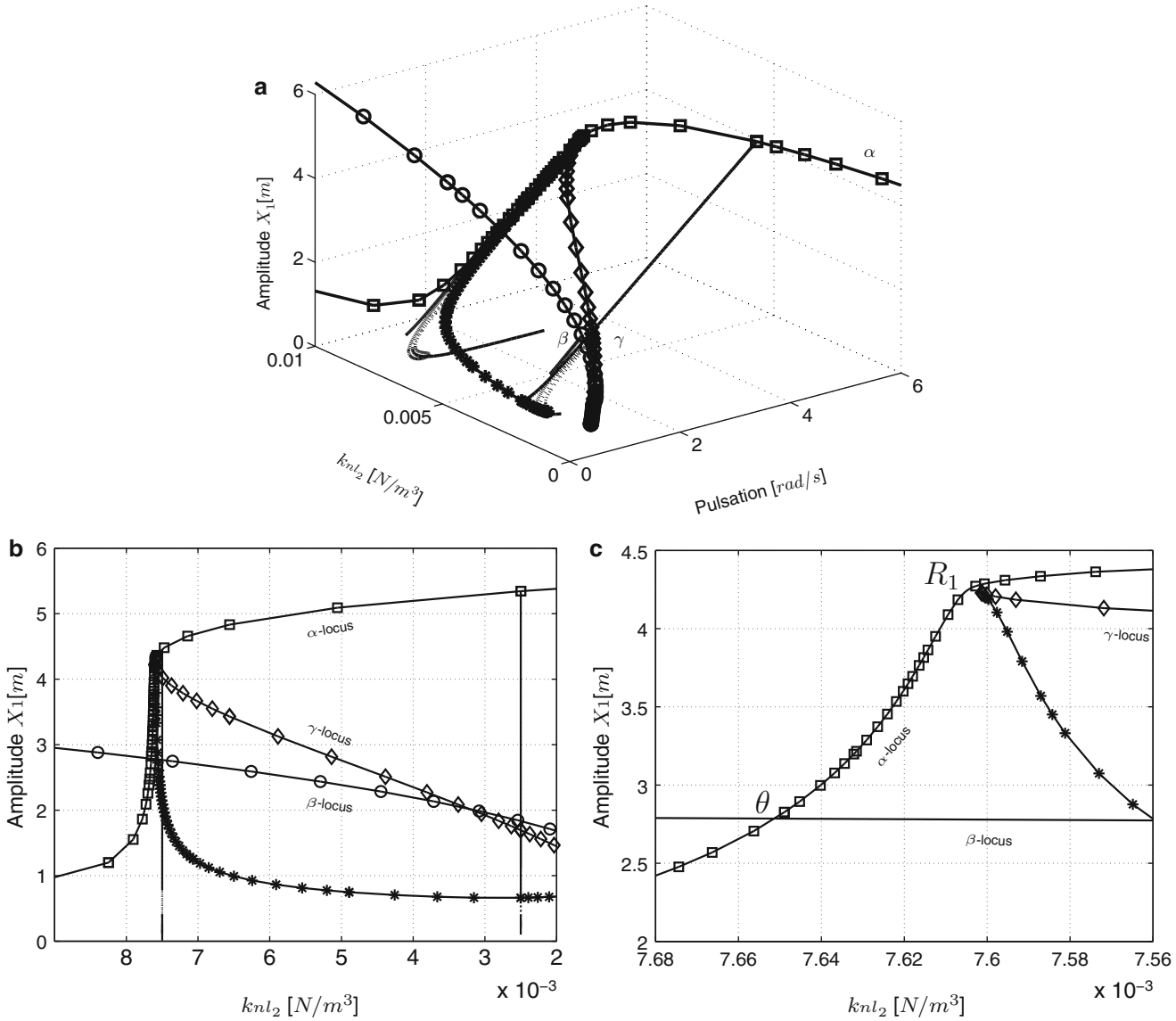

Fig. 21.3 Bifurcation tracking versus k_{nl_2}. *Solid* and *dotted lines* without symbols are related to the stable and unstable parts of the NLFRFs, respectively. *Solid lines* with *squares*, *circles* and *diamonds* are related to bifurcation loci. (**a**) Three dimensional plot; (**b**) two-dimensional projection in the plane (k_{nl_2},X_1); (**c**) close-up of the 2D projection around the optimal region

21.4.1 Continuation of Bifurcations: Absorber Stiffness

The continuation of bifurcations α, β and γ of Fig. 21.2b with respect to nonlinear stiffness k_{nl_2} and pulsation ω is shown in Fig. 21.3. Figure 21.3a shows the three-dimensional space whereas two-dimensional projections are depicted in Fig. 21.3b, c.

The first interesting feature is that there exists a value of the nonlinear coefficient, $k_{nl_2} = 0.007601\,\mathrm{N/m^3}$, above which the bifurcation point γ is eliminated. At point R_1, the locus of bifurcation γ meets the locus of another bifurcation point (different from α and β), which eventually leads to the elimination of the two bifurcations. In addition, for $k_{nl_2} = 0.0076515\,\mathrm{N/m^3}$ denoted by θ, the two remaining bifurcations α and β are such that the corresponding resonance peaks have the same amplitude, which is a possible tuning condition (the TMD is often designed such that the two FRF peaks have the same amplitude). The NLFRF for $k_{nl_2} = 0.0076515\,\mathrm{N/m^3}$ and $c_2 = 0.002\,(\mathrm{Ns/m})$ is represented in Fig. 21.4a and confirms these findings. Comparing Figs. 21.2b, and 21.4a indicates that the peak amplitude is reduced by approximately 50% after this first iteration.

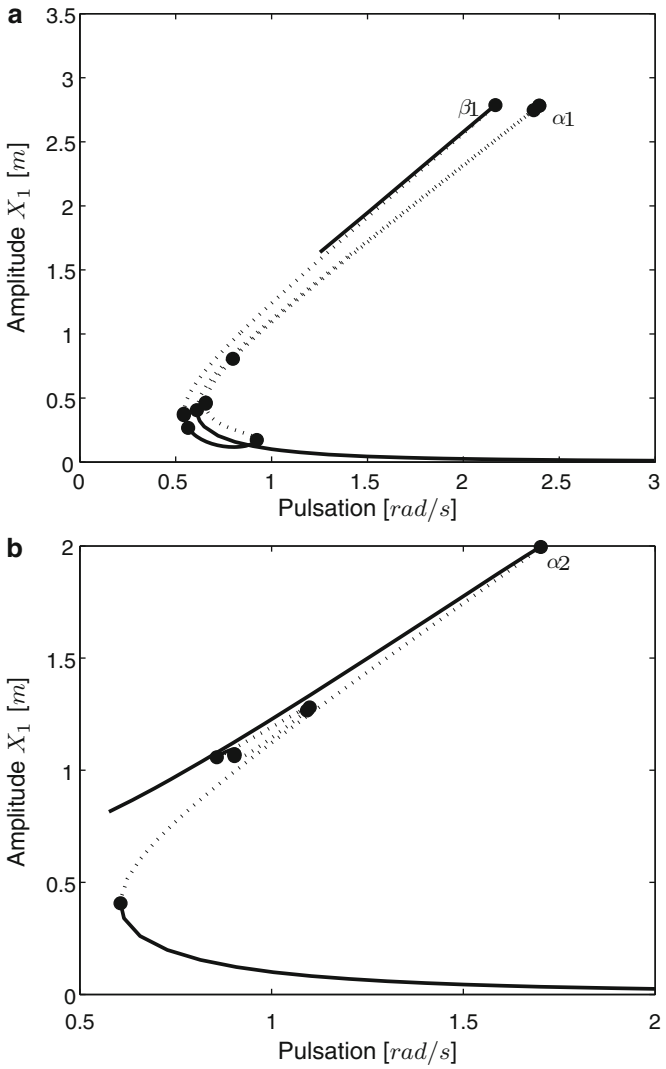

Fig. 21.4 NLFRF of the primary system. (**a**) After the first iteration: $k_{nl_2} = 0.0076515\,(\mathrm{N/m^3})$, $c_2 = 0.002\,(\mathrm{Ns/m})$; (**b**) after the second iteration: $k_{nl_2} = 0.0076515\,(\mathrm{N/m^3})$, $c_2 = 0.016973\,(\mathrm{Ns/m})$. *Solid* and *dotted lines* refer to stable and unstable periodic solutions with bifurcations represented by *dots*

21.4.2 Continuation of Bifurcations: Absorber Damping

The optimization of the damping coefficient is the next step of the procedure, and the initial guess is the point computed by the previous iteration, i.e., $k_{nl_2} = 0.0076515\,(\mathrm{N/m^3})$ and $c_2 = 0.002\,(\mathrm{Ns/m})$. One important remark is that another tuning condition is considered for damping optimization. Going back to the TMD, it is well-known that, for the optimal damping value, two resonance peaks still coexist. Beyond this value, the two peaks tend to merge, resulting in higher peak amplitude and, hence, in less effective vibration mitigation. By analogy, we propose to select the damping coefficient of the nonlinear absorber when the NLFRF starts presenting a single resonance. The details of this procedure are explained in [7], and only the end result in terms of NLFRF is depicted here; see Fig. 21.4b, which corresponds to $k_{nl_2} = 0.0076515\,(\mathrm{N/m^3})$ and $c_2 = 0.016973\,(\mathrm{Ns/m})$. Comparing Fig. 21.4a,b indicates that the peak amplitude is again reduced by approximately 50% after this second iteration. We also notice that due to a higher damping coefficient the dynamics tends to be less complicated (e.g., smaller number of bifurcation points).

21.4.3 Subsequent Iterations

The sequential optimization of the absorber nonlinear stiffness and damping coefficients can be continued until one tuning condition can no longer be satisfied; convergence is then reached. Table 21.1 shows that the process stops after three

Table 21.1 Iterative procedure for k_{nl_2} and c_2 optimization

Iteration	Variable	k_{nl_2}	c_2	% of X_1 reduction
0	/	0.0025	0.002	31
1	k_{nl_2}	0.0076515	0.002	65
2	c_2	0.0076515	0.016973	74
3	k_{nl_2}	0.01025	0.016973	85

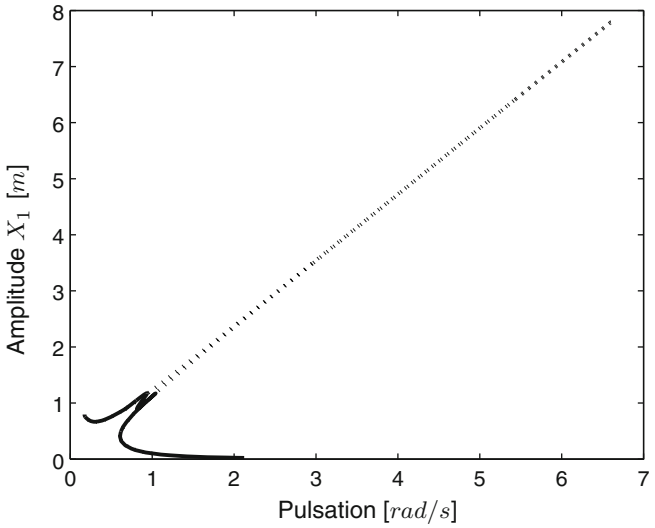

Fig. 21.5 Comparison of the NLFRF of the uncontrolled (*dotted line*) and the controlled (*solid line*) primary system after optimization

Table 21.2 Optimal absorber configuration for different forcing amplitudes F

Set	Force	Iteration	k_{nl_2}	c_2	% of X_1 reduction
1	0.01	3	0.01035	0.007915	78
2	0.1	3	0.01025	0.016973	85
3	1	3	0.01025	0.036500	90

iterations and that the computed absorber coefficients give rise to 85% amplitude reduction with respect to the uncontrolled case. Figure 21.5 compares the NLFRFs of the uncontrolled and controlled primary system and confirms that the nonlinear absorber indeed performs large peak reduction.

21.4.4 Influence of the Forcing Amplitude: Performance-Robustness Analysis

Rather arbitrarily, forcing amplitude of 0.1 N was considered in the previous sections. Because the objective is to design a nonlinear absorber which is effective in a wide range of amplitudes, the entire process was repeated for lower, $F = 0.01$ N, and higher, $F = 1$ N, excitation amplitudes.

Table 21.2 compares the results for the three forcing amplitudes. Convergence is always reached after three iterations, resulting in a computationally efficient tuning procedure. An interesting observation is that the nonlinear stiffness does not seem to be affected by the input energy in the system. However, there is a significant change in damping and peak reduction. Figure 21.6 depicts the performance of the three parameter sets of Table 21.2 for varying amplitudes. It turns out that, while the nonlinear stiffness seems to be intrinsic to the system, the choice of damping is to be made according to the trade-off which exists between performance (i.e., peak reduction maximization) and robustness (i.e., sensitivity to forcing amplitude). Small damping results in lower performance, but the absorber is effective in a larger range of forcing amplitudes. Conversely, large damping results in increased performance, but the absorber is effective in a narrower range of forcing amplitudes. Interestingly, the same trade-off exists for the TMD, but, for this linear absorber, the performance is to be balanced against the frequency range of interest.

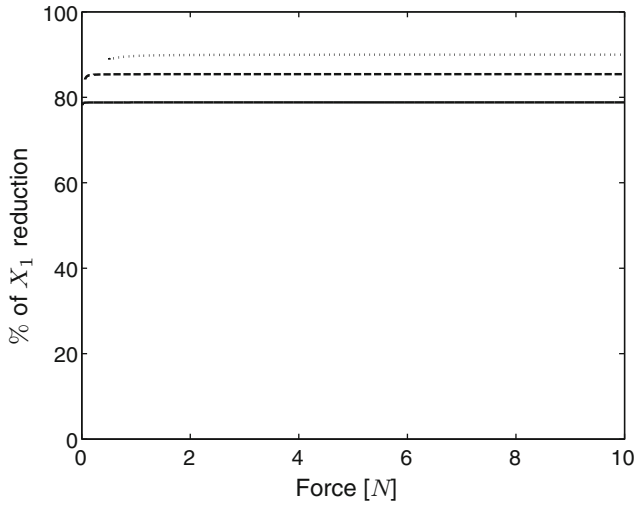

Fig. 21.6 Performance – robustness curves of the nonlinear absorber. *Solid line*: $k_{nl_2} = 0.01035$ (N/m^3), $c_2 = 0.007915$ (Ns/m); *dashed line*: $k_{nl_2} = 0.01025$ (N/m^3), $c_2 = 0.016973$ (Ns/m); *dotted line*: $k_{nl_2} = 0.01025$ (N/m^3), $c_2 = 0.036500$ (Ns/m)

Table 21.3 Parameters of the 2DOF nonlinear system

Parameter	Units	Value
m_1	(kg)	1
m_2	(kg)	0.05
c_1	(Ns/m)	0.002
c_2	(Ns/m)	0.016973
k_1	(N/m)	1
k_2	(N/m)	0.05
k_{nl_1}	(N/m^3)	1
k_{nl_2}	(N/m^3)	0.01025

21.5 General Nonlinear Primary System

Now that the methodology is validated for a primary system possessing essential nonlinearity, a more general oscillator comprising, e.g., a linear and a cubic stiffness, can be considered; i.e., as in Eq. 21.1.

According to the first step of the tuning methodology, the nonlinear absorber should also possess a linear and a cubic stiffness. Realizing that the dynamics of the primary oscillator for low (high) input energies will resemble that of a linear oscillator (essentially nonlinear oscillator), the values of the linear and cubic springs k_2 and k_{nl_2} are determined independently thanks to the TMD theory and the methodology described in this paper, respectively. The resulting parameters are listed in Table 21.3 for a forcing level $F = 0.1$ (N).

The performance-robustness curve is depicted in Fig. 21.7 and highlights that excellent results in terms of performance and robustness are achieved thanks to the nonlinear vibration absorber. Peak amplitude reduction of at least 85% is achieved for all considered excitation levels.

21.6 Concluding Remarks

Nonlinear mechanical systems are characterized by the frequency-energy dependence of their oscillations. This renders their vibration control and, hence, the design of nonlinear vibration absorbers challenging.

The objective of this paper is to develop an absorber which can mitigate the vibrations of a nonlinear system in a wide range of input energies. We showed that the backbone of the absorber should possess a qualitatively similar dependence on energy as that of the backbone of the primary system. To fulfill this frequency-energy-based tuning condition, the functional form of the absorber nonlinearity is to be carefully selected.

In addition to the qualitative tuning procedure, a quantitative methodology was also developed, which targets the computation of adequate values for the absorber nonlinear coefficient and damping. To this end, the forced response was

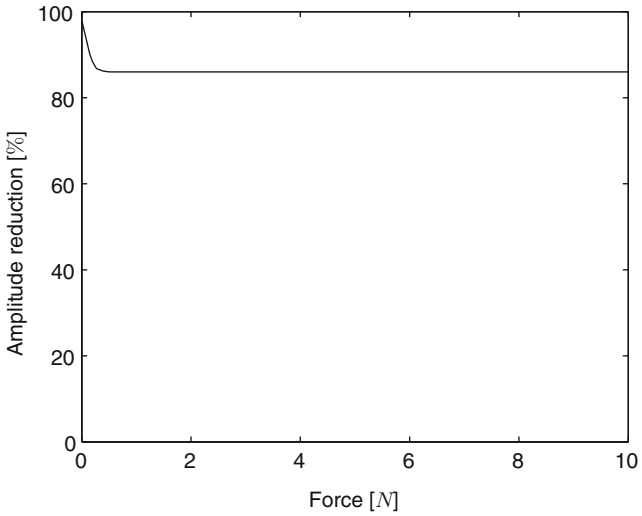

Fig. 21.7 Amplitude reduction for varying forcing amplitudes F

considered, and bifurcation analysis was exploited. Specifically, bifurcation tracking in parameter space was shown to be an effective alternative to computationally intensive parametric studies, and its use for absorber tuning seems particularly meaningful.

Acknowledgements The author G. Kerschen would like to acknowledge the financial support of the European Union (ERC Starting Grant NoVib-307265).

References

1. Roberson RE (1952) Synthesis of a nonlinear dynamic vibration absorber. J Franklin Inst 254:205–220
2. Pipes LA (1953) Analysis of a nonlinear dynamic vibration absorber. J Appl Mech 20:515–518
3. Arnold FR (1955) Steady-state behavior of systems provided with nonlinear dynamic vibration absorbers. J Appl Mech 22:487–492
4. Haxton RS, Barr ADS (1972) The autoparametric vibration absorber. ASME J Eng Ind 94:199–125
5. Vakakis AF, Gendelman LA, Bergman LA, McFarland DM, Kerschen G, Lee YS (2009) Nonlinear targeted energy transfer in mechanical and structural systems. Springer, Dordrecht
6. Viguié R,Kerschen G, (2009) Nonlinear vibration absorber coupled to a nonlinear primary system: a tuning methodology. J Sound Vib 326:780–793
7. Viguié R(2010) Tuning methodology of nonlinear vibration absorbers coupled to nonlinear mechanical systems. Ph.D. thesis, University of Liège. Available online at: http://www.ltas-vis.ulg.ac.be/cmsms/index.php?page=kerschen.
8. Den Hartog JP(1985) Mechanical vibrations. Dover books on engineering, 4th edn. Dover, New York
9. Govaerts W, Gazhiani R, Kuznetsov Y, Meijer H (2007) Matcont: a toolbox for continuation and bifurcation of cycles of maps, Universiteit Gent – Utrecht University, 2007.

Chapter 22
Response of a Pendulum TMD with Large Displacements

P.M. López-Reyes, A. Lorenzana, A.V. Belver, and C.E. Lavín

Abstract The behavior of a nonlinear pendulum working as a tuned mass damper (TMD) for slender structures is analyzed in this paper. The influence of the inherent nonlinearity of the oscillations of the pendulum, together with the dry friction damping, in its vibration control behavior is modeled as a 2 DOF system with the usual linear elements together with nonlinear spring and damping elements between the equivalent mass of the structure and the mass of the TMD. Due to the frequency-energy dependence of the oscillations of the system, the frequency response functions (FRFs) are no longer invariant and the displacement response is dependent on the level of excitation, so the nonlinear normal modes (NNMs) are computed using numerical computations. The comparison of the results with the behavior of the underlying linear normal modes (LNMs) is shown and discussed and well as the influence of the nonlinear elastic, damping and force coefficients.

Keywords Nonlinear • Pendulum • TMD • Chimney • Normal modes

22.1 Introduction

Industrial chimneys and other slender structures like towers, masts, cables of bridge-decks are very sensitive to the dynamic effects of wind. The flow behind this quasi cylindrical object becomes irregular and Karman vortices appear in alternately clockwise and anticlockwise directions, descending the cylinder regularly and inducing vibrations that generally do not entail any danger of damage to the structure. However, when the frequency of detaching vortices overlaps the natural frequency of the structure, a resonance effect may occur, resulting in the rise of a force that affects the cylinder in a direction perpendicular to the direction of the stream flow. Due to the properties of the stream, the descent of the vortices is a self-excited process. The practical significance of vortex-induced vibrations has led to a considerable amount of research work, both experimental and theoretical. Fundamental results and discoveries concerning vortex-induced vibrations are widely discussed in the review of Williamson and Govardhan [1]. However, although numerous studies dealing with these vibrations have been carried out, the problem of vertical excitation is not fully solved: despite engineering design calculations comply with current standards, vortex-induced vibrations may still cause considerable displacements of an industrial chimney top.

One of the solutions for controlling these vibrations of the abovementioned slender structures is the introduction of a tuned mass damper (TMD), a device attached to a structure whose main purpose is to reduce its dynamic response by resonating out of phase with the structural motion. The frequency of this damper has to be tuned to a particular frequency to achieve that goal. The TMD concept was first applied by Frahm in 1909 [2] to reduce the rolling motion of ships as well as ship hull vibrations. A theory for the TMD, applicable for an undamped single-degree-of-freedom (SDOF) system subjected to a sinusoidal force excitation, was presented later [3].

P.M. López-Reyes (✉) • A.V. Belver • C.E. Lavín
CARTIF Centro Tecnológico, Parque Tecnológico de Boecillo, 47151 Valladolid, Spain
e-mail: pablop@cartif.es

A. Lorenzana
ITAP, EII University of Valladolid, 47011, Valladolid, Spain

G. Kerschen et al. (eds.), *Topics in Nonlinear Dynamics, Volume 1: Proceedings of the 31st IMAC, A Conference on Structural Dynamics, 2013*, Conference Proceedings of the Society for Experimental Mechanics Series 35,
DOI 10.1007/978-1-4614-6570-6_22,

22.2 Pendulum TMD

Among all types of possible TMD for slender structures (spring and damper, double mass, ball pendulum, etc.) a simple pendulum appears to be a simple yet effective solution. It consists of a weight, suspended from a pivot so that it can swing freely, that, when displaced sideways from its resting equilibrium position, it is subjected to a restoring force due to gravity that will accelerate it back towards the equilibrium position, causing it to oscillate. Although the equations of motion of a pendulum are very simple when a small-angle approximation is considered, for arbitrary-amplitude period pendulums (as the one needed to work properly as a TMD of a chimney) the period of motion (T) is defined in terms of the complete elliptic integral of the first kind K(k) as follows:

$$T = 4\sqrt{\frac{l}{g}}K\left(\sin\frac{\theta_0}{2}\right) \tag{22.1}$$

where l is the length of the pendulum, g the value of gravity and θ_0 the semi-amplitude of the oscillation.

There are many ways of computing the elliptical integral, (for example, using the arithmetic-geometric mean solution [4] or Taylor series), but for numerical purposes, the Maclaurin series used in the Legendre polynomial solution has been found satisfactory, resulting in the following power series [5]:

$$T = 2\pi\sqrt{\frac{l}{g}}\left(1 + \frac{1}{16}\theta_0^2 + \frac{11}{3072}\theta_0^4 + \frac{173}{737280}\theta_0^6 + \frac{22931}{1321205760}\theta_0^8 + \cdots\right) \tag{22.2}$$

The difference between the exact solution and the Taylor and Maclaurin series approximations can be observed in Fig. 22.1, where the normalized period of movement is plotted versus the amplitude of the movement. While for small amplitudes the three solutions are indistinguishable, for amplitudes increasingly closer to π the Maclaurin-Legendre solution behaves better. The relative errors for amplitudes $0.33 \cdot \pi$ and $0.99 \cdot \pi$ are 0.0013 and 53.98% respectively for Taylor solution and 0.00018 and 31.35% respectively for Maclaurin-Legendre solution.

The equations of movement of a large amplitude pendulum involve Jacobi elliptical functions SN to express the angle, resulting in the following equation:

$$\theta(t) = 2\sin^{-1}\left(SN(\tau)\cdot\sin\frac{\theta_0}{2}\right) \tag{22.3}$$

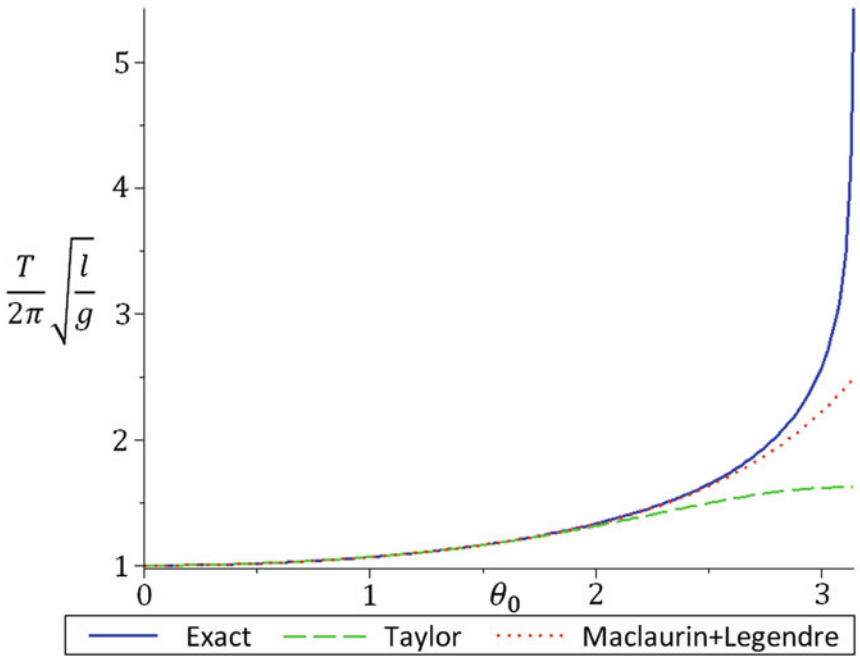

Fig. 22.1 Normalized period of a pendulum for small and large amplitudes

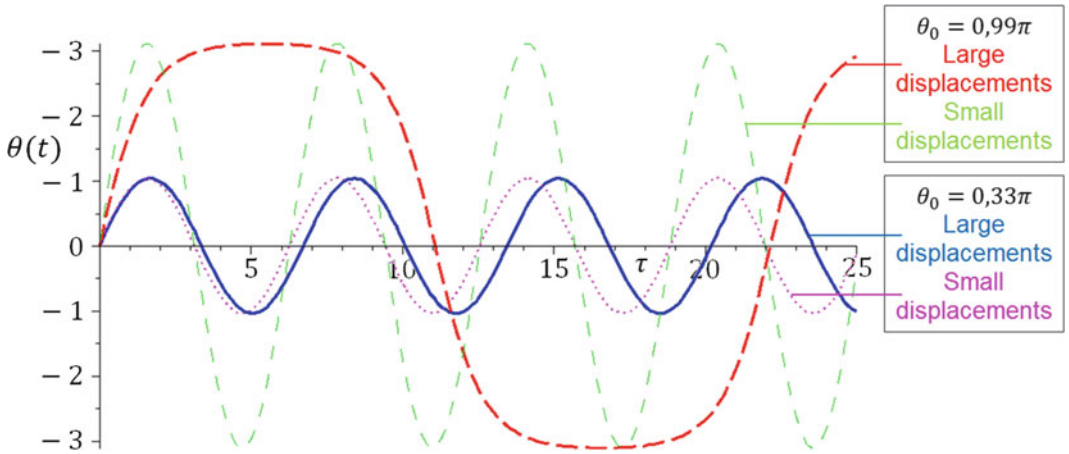

Fig. 22.2 Equations of movement for a nonlinear pendulum with amplitudes $0.33 \cdot \pi$ and $0.99 \cdot \pi$

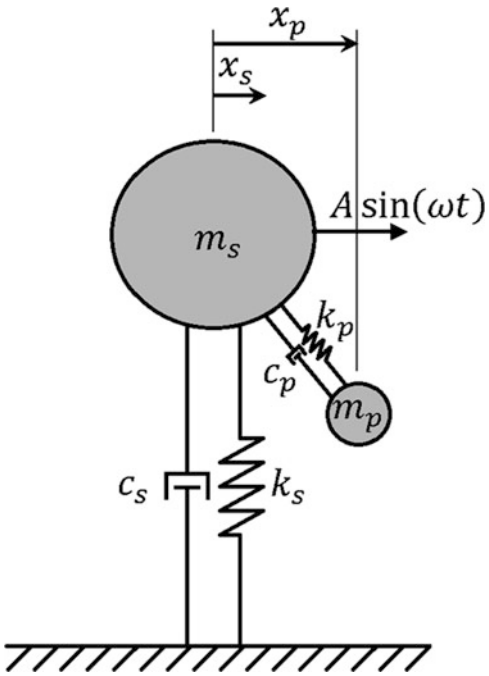

Fig. 22.3 Model of a SDOF structure with a TMD pendulum

where $\tau = \sqrt{\frac{g}{l}}t$ is the normalized time. It can be observed in Fig. 22.2 that, for small amplitudes, the movement is almost a sine, while for large amplitudes it behaves completely different.

A large pendulum TMD can be modeled as a SDOF TMD attached to the structure, as shown in Fig. 22.3 with a SDOF structure model in turn. In this case, the pendulum, excited by the motion of the structure to which the external force is applied, would move with a phase shift, leading to a reduction of the structure's vibrations.

The governing dynamic equations of motion of the resultant system are:

$$\begin{cases} m_s\ddot{x}_s + (c_s + c_p)\dot{x}_s - c_p\dot{x}_p + (k_s + k_p(t))x_s - k_p(t)x_p = A\sin(\omega t) \\ m_p\ddot{x}_p - c_p\dot{x}_s + c_p\dot{x}_p - k_p(t)x_s + k_p(t)x_p = 0 \end{cases} \tag{22.4}$$

and can be summarized in the following matrix equation:

$$M\ddot{x} + C\dot{x} + K(t)x = F\ \sin(\omega t) \tag{22.6}$$

where

$$M = \begin{bmatrix} m_s & 0 \\ 0 & m_p \end{bmatrix}, C = \begin{bmatrix} c_s + c_p & -c_p \\ -c_p & c_p \end{bmatrix}, K(t) = \begin{bmatrix} k_s + k_p(t) & -k_p(t) \\ -k_p(t) & k_p(t) \end{bmatrix}, F = \begin{bmatrix} A \\ 0 \end{bmatrix} \tag{22.7}$$

In the above equation, $\ddot{x}_s$, $\dot{x}_s$ and x_s are the horizontal acceleration, velocity and displacement and k_s, c_s and m_s the stiffness coefficient, damping coefficient and mass of the structure (respectively for the pendulum TMD with subscript p).

The nonlinearity of the system can be found in the definition of the pendulum stiffness matrix, taking the following expression [6]:

$$k_p(t) = \frac{m_p g}{l^2}\sqrt{l^2 - (x_p - x_s)^2} \tag{22.8}$$

22.3 Chimney

The specimen under study in this article is a chimney from the Rugeley Power Station, located in Staffordshire, England, that was constructed around 1968 and substituted by a new chimney recently. However, during the period of construction of the new chimney, some evidences [7–9] suggested that the security of the old chimney could be compromised, due to the interferences between them (see Fig. 22.4). The solution for these 2 years of coexistence of both chimneys was the installation of a pendulum TMD to increase the structural damping of the system, reducing the displacements and stress caused by the wind.

The chimney consists of a 183 m high reinforced concrete windshield that tapers from a an external diameter of 9.4 m at the top to 15.7 m at the base, with a variable thickness from 0.191 to 0.864 m respectively, having a mass of $1.281 \cdot 10^6$ kg. A monitoring system was installed and the measured structural damping was 0.7%. A TMD was designed for achieving the necessary damping 2.5%. It consisted of a 42,000 kg concrete ring, hanged from the top of the chimney with 2.357 m cables, with 5 dampers with a coefficient of c = 2,016.6 Ns/m and 0.450 m of effective length, as it can be seen in Fig. 22.5.

The resulting system can be modeled as a SDOF element for the chimney and a SDOF element for the pendulum TMD, obtaining a model like the one depicted in Fig. 22.3. The equivalent mass of the chimney lumped at the top can be obtained from the following formula [10]:

$$m_s = 0.23\,M \tag{22.9}$$

Fig. 22.4 Old (*left*) and new (*right*) chimney of the Rugeley Power Station

Fig. 22.5 Pendulum TMD in the chimney

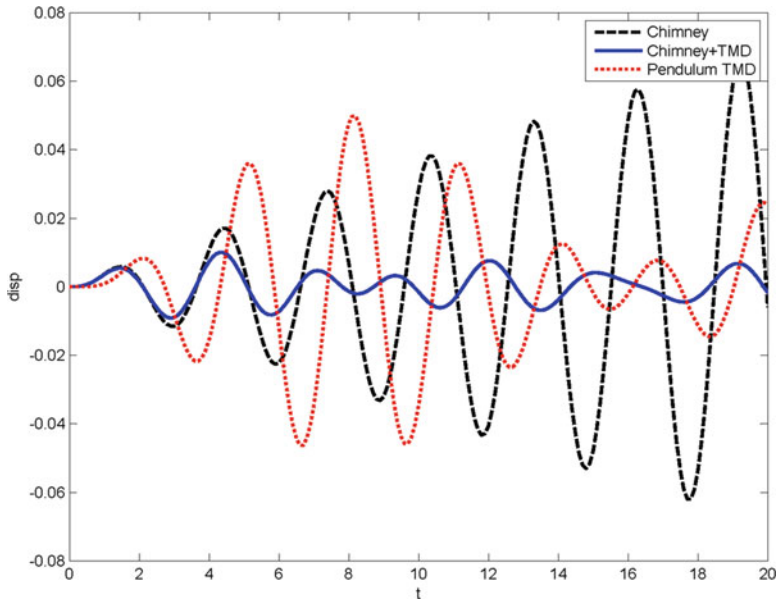

Fig. 22.6 Comparison of the behaviour of the chimney with and without the pendulum TMD (time)

where M is the total mass of the chimney. The values of the stiffness and damping coefficients can be obtained with the following formulas [11]:

$$k_s = m_s \left(\frac{2\pi}{T}\right)^2 \tag{22.10}$$

$$c_s = 2\varepsilon\sqrt{m_s k_s} \tag{22.11}$$

The values of the natural period and damping were determined with the monitoring system (T = 2.957s and $\varepsilon = 0.7\%$).

For excitation force amplitude of 5,000 N, the behaviour of the system can be observed in Fig. 22.6. While the amplitude of the chimney movement is increasingly higher, the action of the TMD can decrease this maximum amplitude to a value of 0.01 m.

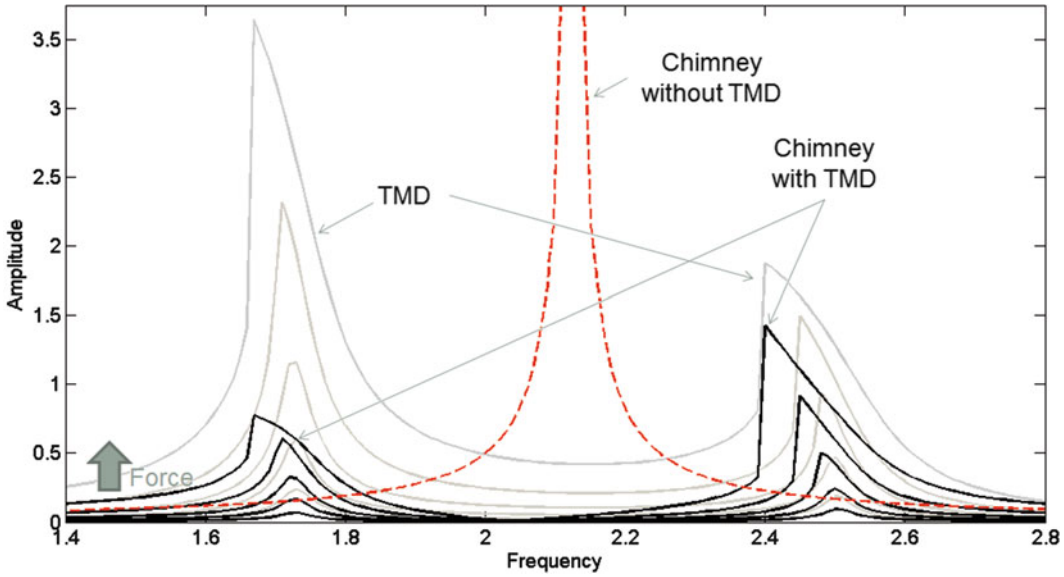

Fig. 22.7 Comparison of the behaviour of the chimney with and without the pendulum TMD (frequency)

22.4 NNM

Shaw and Pierre [12] generalized Rosenberg's definition [13] of a nonlinear normal mode (NNM) for damped systems. They defined it as a two-dimensional invariant manifold in phase space, invariant under the flow. This concept extends the invariance property of linear normal modes (LNM) to nonlinear systems as the one depicted in this article, where some usual hypothesis of linear systems (as the orthogonality between modes) are no longer applicable. It is more, NNMs have intrinsic properties that are fundamentally different from those of LNMs, as the frequency-energy dependence, the modal interaction (internally resonant NNMs) or mode bifurcations and stability [14, 15].

The numerical computing technique developed for the analysis of the NNM of the 2-DOF chimney-pendulum TMD system is based on an asymptotic approach, and its results can be observed in Fig. 22.7. The relationship between the horizontal displacements of the structure (x_s) and the pendulum TMD (x_p) is clearly nonlinear through the definition of the stiffness coefficient of the TMD $k_p(t)$. For the small angles of vibration of the TMD the difference between the NNM and the modes of the underlying linear system are virtually negligible but for large excitation forces the nonlinearity of the system emerges, obtaining different frequencies for different amplitudes.

However, the contribution of the pendulum TMD can also be analyzed with this method, comparing the results of the chimney in the amplitude-frequency plot versus the results obtained with the action of the TMD.

22.5 Conclusions

In this paper we present the general behavior of a pendulum without considering the small angle simplification, obtaining more complex equations of its movement. This behavior is used to model a pendulum TMD designed to counteract the wind vortex-induced vibrations of the top of a slender concrete chimney. For this purpose, a 2-DOF model was developed to take into account the relation between the structure and the TMD. It has been show that this simple model is accurate enough to simulate the behavior of the problem. The techniques developed allowed us to reduce the vibration of the chimney to an acceptable level, demonstrating that the use of a pendulum TMD damper leads to significant reduction in the structural vibrations when it is correctly tuned.

A numerical study of the NNM of the behavior of the 2DOF system was also conducted. Despite the nonlinearity of the system, the small angles of vibration of the pendulum TMD make the NNM of the response of the system indistinguishable from the linear approach. However, the contribution of the pendulum TMD to the reduction of the amplitude of the response of the system was also analyzed with this method.

References

1. Williamson CHK, Govardhan R (2008) A brief review of recent results in vortex induced vibrations. J Wind Eng Ind Aerodyn 96(6–7):713–735
2. Frahm H (1909) Device for damping vibrations of bodies. U.S. Patent No. 989958, 30 Oct 1909
3. Ormondroyd J, Den Hartog JP (1928) The theory of the dynamic vibration absorber. Trans ASME, APM-50-7:9–22
4. Carvalhaes C, Suppes P (2008) Approximations for the period of the simple pendulum based on the arithmetic-geometric mean. Am J Phys 76(12):1150–1154
5. Nelson R, Olsson MG (1986) The pendulum – Rich physics from a simple system. Am J Phys 54(2):112–121
6. Jankowski R, Kujawa M, Szymczak C (2004) Reduction of steel chimney vibrations with a pendulum damper. Task Q 8(1):71–78
7. Brownjohn JMW, Carden EP, Goddard RC, Oudin G, Koo K (2009) Real-time performance tracking on a 183 m concrete chimney and tuned mass damper system. In: 3rd International Operational Modal Analysis Conference (IOMAC), Ancona (Italy)
8. Friswell MI, Mottershead JE (1995) Finite element model updating in structural dynamics. Kluwer Academic, Dorcdrecht
9. García-Diéguez M, Koo KY, Middleton CM, Brownjohn JMW, Goddard C (2010) Model updating for a 183 m of reinforced concrete chimney. In: 3rd International Operational Modal Analysis Conference (IOMAC), Ancona (Italy)
10. Harris CM (1988) Shock and vibration handbook. McGraw-Hill, New York
11. Clough RW, Penzien J (1993) Dynamics of structures. McGraw-Hill, New York. International edition
12. Shaw SW, Pierre C (1991) Non-linear normal modes and invariant manifolds. J Sound Vib 150:170–173
13. Rosenberg RM (1960) Normal modes of nonlinear dual-mode systems. J Appl Mech 27:263–268
14. Kerschen G, Peeters M, Golinval JC, Vakakis AF (2009) Nonlinear normal modes, part I: a useful frame work for the structural dynamicist. Mech Syst Signal Process 23:170–194
15. Peeters M, Viguié R, Sérandour G, Kerschen G, Golinval JC (2009) Nonlinear normal modes, part II: toward a practical computation using numerical continuation techniques. Mech Syst Signal Process 23:195–216

Chapter 23
The Experimental Performance of a Nonlinear Dynamic Vibration Absorber

Yung-Sheng Hsu, Neil S. Ferguson, and Michael J. Brennan

Abstract This paper investigates the physical behaviour and effectiveness of a nonlinear dynamic vibration absorber (NDVA). The nonlinear absorber considered involves a nonlinear hardening spring which was designed and attached to a cantilever beam excited by a shaker. The cantilever beam can be considered at low frequencies as a linear single degree-of-freedom system. The nonlinear attachment is designed to behave as a hardening Duffing oscillator. The nonlinearity of the attachment is due to the particular geometrical configuration undergoing a large amplitude response. The experiment investigated the potential for vibration reduction of the system Analytical and numerical results are presented and compared. From the measured results it was observed that the NDVA had a much wider effective bandwidth compared to a linear absorber. The frequency response curve of the NDVA has the effect of moving the second resonant peak to a higher frequency away from the tuned frequency so that the device is robust to mistuning.

Keywords Nonlinear vibration • Vibration absorber • Vibration reduction • Passive vibration control • Duffing oscillator

23.1 Introduction

The passive vibration absorber is an important device used for vibration reduction in structures. The linear vibration absorber is limited in that it reduces vibration over a very narrow frequency range. This range is not enough to correspond to changes in speed for a rotating unbalanced source due to load, motor power supply or source variations. A technical benefit of the NDVA has been hypothesized that they can operate efficiently over a broader range of forcing frequencies.

The bandwidth problem was first identified by Roberson [1] who considered the impractical case of an undamped absorber comprising a linear plus cubic spring acting in parallel. Hunt and Nissen [2] presented a NDVA with a softening spring composed of a stack of Belleville washers to overcome the previous design feasibility. Nissen et al. [3] studied the optimal parameters of a NDVA and considered the technical aspects for realization. Soom [4] and Jordanov [5] have investigated both the optimal parameter design of linear and nonlinear dynamic vibration absorbers for damped primary systems. They investigated optimization criteria other than traditional measures and obtained a small improvement in the steady state response by using nonlinear springs. Zhu et al. [6] studied the system with nonlinear damping and nonlinear springs, they found that a reduction of the vibration amplitude can be obtained by adjusting the parameters of the nonlinear dampers, nonlinear spring stiffness and excitation frequency. It has also been demonstrated [7–10] that the primary phenomena behind the energy pumping produced is due to resonant interactions between coupled linear and nonlinear components.

From the review of the existing literature, it can be seen that experimental results for the nonlinear absorber have not been widely published. The aim of this paper is to partially fill this gap. The problem is first studied here analytically, to determine the most important features, before an experimental design is presented, implemented and its behavior is discussed.

Y.-S. Hsu (✉) • N.S. Ferguson
Institute of Sound and Vibration Research, University of Southampton, Southampton, SO17 1BJ, United Kingdom
e-mail: yh1a08@soton.ac.uk; nsf@isvr.soton.ac.uk

M.J. Brennan
Departamento de EngenhariaMecanica, Universida de Estadual Paulista, Ilha Solteira, 15385-000 Sao Paulo, Brazil
e-mail: mjbrennan@dem.feis.unesp

G. Kerschen et al. (eds.), *Topics in Nonlinear Dynamics, Volume 1: Proceedings of the 31st IMAC, A Conference on Structural Dynamics, 2013*, Conference Proceedings of the Society for Experimental Mechanics Series 35,
DOI 10.1007/978-1-4614-6570-6_23,

23.2 Equations of Motion of a Single Degree of Freedom System with an Attached Nonlinear Absorber

As shown in Fig. 23.1, a NDVA is attached to a linear single degree-of-freedom main structural system. In the figure, k_s, c_s and m_s are the spring constant, viscous damping coefficient and mass of the main structural system respectively. For the NDVA, it has a mass m, a viscous damper c and a nonlinear spring with a nonlinear restoring force given by the function $f(x) = k1x + k3x^3$, where x is the static displacement across the spring, which has linear and nonlinear stiffness terms k_1 and k_3, respectively. The sign of k_3 denotes the nonlinear stiffness behaviour; a positive value means that the system is hardening $x_s, x, \dot{x}_s, \dot{x}, \ddot{x}_s$ and $\ddot{x}$ are the displacement, velocity and acceleration of the main structural system and NDVA, respectively. The equations of motion for this system are given by

$$m_s\ddot{x}_s + c_s\dot{x}_s + k_s x_s + c(\dot{x}_s - \dot{x}) + k_1(x_s - x) + k_3(x_s - x)^3 = F\cos(\omega t)$$

$$m\ddot{x} - c(\dot{x}_s - \dot{x}) - k_1(x_s - x) - k_3(x_s - x)^3 = 0 \tag{23.1a,b}$$

where F is the amplitude of the excitation, which is periodic in time t with frequency ω.

It is convenient to write Eq. (23.1a,b) in non-dimensional form as

$$(1+\mu)y_s'' + 2\zeta_s y_s' + y_s - \mu w'' = \cos(\Omega\tau) \tag{23.2a,b}$$

$$w'' + 2\zeta\omega_0 w' + \omega_0^2 w + \gamma w^3 = y_s''$$

where the non-dimensional parameters are given by $y_s'' = \ddot{x}_s/\omega_s^2 x_0$, $y_s' = \dot{x}_s/\omega_s x_0$, $y_s = x_s/x_0$; $w'' = \ddot{z}\omega_s^2 x_0$, $w' = \dot{z}/\omega_s x_0$, $w = z/x_0\mu = m/m_s$, $\gamma = (k_3/\mu k_s)x_0^2$, $\zeta_S = c_s/2m_s\omega_s$, $\zeta = c/2m\omega_1$, $\omega_0 = \omega_1/\omega_s$ and $\Omega = \omega/\omega_s$ where $\omega_s^2 = k_s/m_s$, $\omega_1^2 = k_1/m$ and x_0 is the static extension of the linear spring due to a static force of amplitude F, $z = xx - x$ is the extension of the spring (equivalent to the relative displacement of the primary mass to the NDVA mass) and $(\bullet)' = \mathrm{d}(\bullet)/d\tau$ in which $\tau = \omega_s t$ is non-dimensional time.

The fundamental assumption in the Harmonic Balance method (HBM) approach used for the first order solution is that the response of the main system and the absorber is predominantly harmonic at the excitation frequency. Applying the HBM, it is assumed that a solution is of the form

$$y_s = Y_s\cos(\Omega\tau + \varphi_s) \tag{23.3a, b}$$

$$w = W\cos(\Omega\tau + \varphi)$$

Substituting Eq. (23.3a, b) into Eq. (23.2a,b) gives two expressions involving the amplitudes of the responses of the two masses, namely

$$Y_s^2 = \frac{1}{\Omega^4}\left(\begin{array}{l}\frac{9}{16}\gamma^2 W^6 + \frac{3}{2}\gamma(\omega_0^2 - \Omega^2)W^4 \\ +(\Omega^4 + 4\zeta^2\Omega^2\omega_0^2 + \omega_0^4 - 2\Omega^2\omega_0^2)W^2\end{array}\right) \tag{23.4a, b}$$

$$aW^6 + bW^4 + cW^2 + d = 0$$

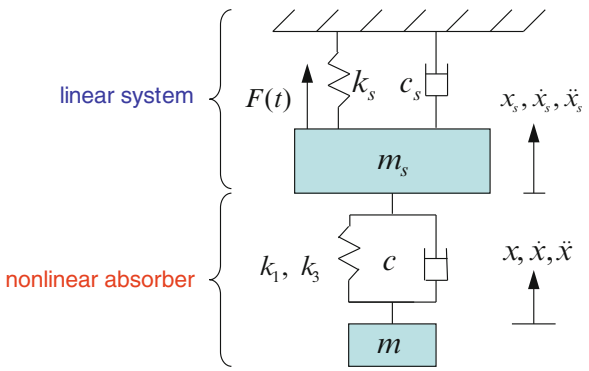

Fig. 23.1 A nonlinear dynamic vibration absorber (NDVA) attached to a single degree-of-freedom main system

where

$$a = \frac{9}{16}\gamma^2,\ b = \frac{3}{2}\gamma(\omega_0^2 - \Omega^2) + \Omega^4\frac{g}{e},$$

$$c = (\omega_0^2 - \Omega^2)^2 + 4\zeta^2\omega_0^2\Omega^2 + \Omega^4\frac{h}{e},\quad d = -\frac{\Omega^4}{e},$$

$$e = \left(1 - \Omega^2(1+\mu)\right)^2 + 4\zeta_s^2\Omega^2,\ g = -\frac{3}{2}\gamma\mu(1 - \Omega^2(1+\mu)),\ h = \Omega^4\mu^2 - 2\mu(1 - \Omega^2(1+\mu))(\omega_0^2 - \Omega^2) + 8\zeta_s\zeta\mu\,\omega_0\Omega^2$$

Once the parameters for the system and the excitation frequency have been specified, then the solutions of Eq. (23.4a, b) in W^2 give the three numerical solutions, which should be checked for physical interpretation and existence. It is noted that only real solutions for W^2 are physical responses. When the normalised relative displacement W has been determined it can be substituted into Eq (23.4a, b) to obtain the amplitude of the main system Y_s
Three steady-state solutions of Eq (23.4a, b) are given by

$$W_1^2 = s + t - \frac{b}{3a},$$

$$W_{2,3}^2 = -\frac{1}{2}(s+t) - \frac{b}{3a} \pm j\frac{\sqrt{3}}{2}(s-t) \tag{23.5a–c}$$

where

$$s = \sqrt[3]{r + \sqrt{\frac{-\Delta}{108a^4}}},\ t = \sqrt[3]{r - \sqrt{\frac{-\Delta}{108a^4}}},\ r = \frac{9abc - 27a^2d - 2b^3}{54a^3},\ \Delta = 18abcd - 27a^2d^2 - 4b^3d + b^2c^2 - 4c^3a$$

Depending on the degree of nonlinearity in the NDVA system, there are combinations of the parameters which produce a multivalued response. To find the conditions for such a response, Δ, the discriminant of the cubic polynomial in W^2 in Eq (23.4a, b) can be examined [11]. If $\Delta > 0$ there are three distinct real roots, if $\Delta < 0$ there is one real root and a pair of complex conjugate roots and if $\Delta = 0$ then there are at least two real coincident roots.

23.3 Vibration Reduction of a NDVA

The influence of the nonlinear stiffness parameter (γ) and the damping ratio (ζ) on the reduction of vibration can now be investigated analytically. These were also checked by direct numerical integration (using the MATLAB ode45 function) of the equations of motion. The combined system response is nonlinear and is compared in terms of the relative response to the amplitude of the static response of the primary system on its own when an equal static force is applied

23.3.1 Influence of the Nonlinear Parameter (γ)

In Fig. 23.2a, b, the effect on the normalized primary system displacement Y_s can be seen. It is to shift the first resonance peak Ω_{r_1} and bend the second resonance peak Ω_{r_2} to the right. An unstable branch appears in between the two stable branches of the first resonance peak at the frequency Ω_{r_1}. For low values of the nonlinearity, the unstable branch may appear at a response level above the stable branches of the second resonance peak. For higher values of the nonlinearity, the two stable branches intersect each other and the amplitude of the unstable branch is above the two stable branches.

The suppression band can be observed in Fig. 23.2a, b, i.e., bandwidth where $Y_s = X_s/X_0 \leq 1$, which contains the effective tuned frequency. The difference is apparent between the vibration reduction of the linear and the nonlinear absorbers; the nonlinear device has a much wider effective bandwidth. It is increased by about 6 and 211% compared to the linear case for values of the nonlinear stiffness parameter of $\gamma = 10^{-5}$ and $\gamma = 10^{-4}$ respectively. These were also checked by numerical integration of the equations of motion. Equation (23.1a,b) were solved numerically and the Fourier coefficients extracted from the time histories. The amplitude of the first of these coefficients is depicted by circles in the frequency response curves shown here. It is noted that in order to find the stable multivalued responses the initial conditions for the displacement and velocity need to be adjusted.

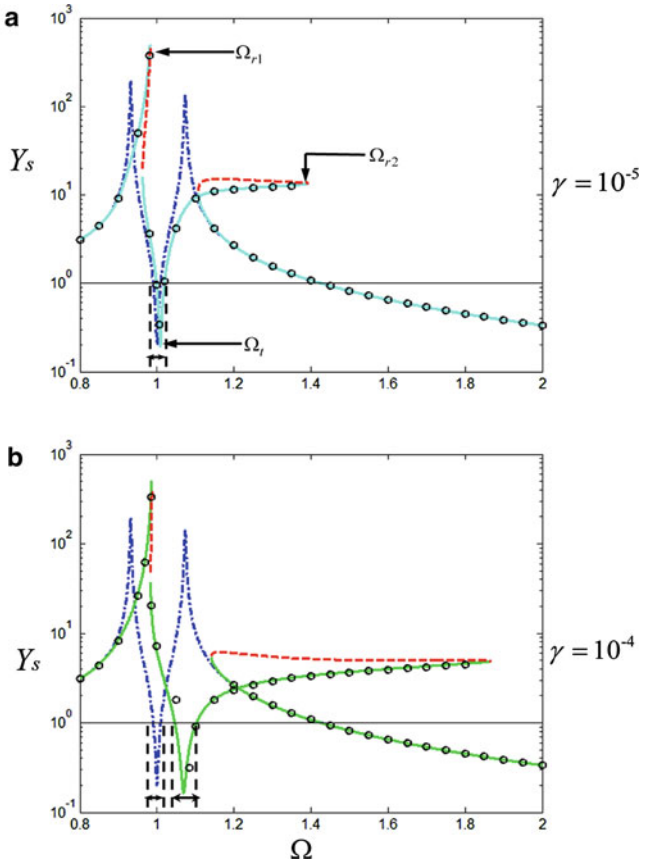

Fig. 23.2 Plots showing the effect of the nonlinear absorber stiffness on the primary system frequency response curves Y_s as a function of Ω The 'tuned' frequency $\omega_0 = \omega_1/\omega_s = 1$, mass ratio $\mu = 0.02$ and damping ($\zeta_s = 0.001$, $\zeta = 0.002$). The response for the system with the linear absorber is given by *the dashed-dotted line*, the solid line is the stable solution and the *dashed line* gives the unstable solution. Direct numerical solutions are shown by the symbol ('∘'). (**a**) $\gamma = 10^{-5}$ low absorber stiffness and (**b**) $\gamma = 10^{-4}$ high absorber stiffness

Figure 23.2a, b also shows that the first resonance frequency of the system with the nonlinear absorber Ω_{r_1} moves to a slightly higher frequency as it is affected by the nonlinearity. The peak response of the primary mass at the first resonance frequency is also higher than that for the linear absorber case.

23.3.2 The Effect of Damping (ζ) in the Nonlinear Absorber

In Fig. 23.3a, b the linear damping ratio for the attached system is increased from $\zeta = 2 \times 10^{-3}$ to $\zeta = 8 \times 10^{-3}$. The difference between the vibration response due to the linear and the nonlinear absorber in Fig. 23.3a, b is again that the nonlinear absorber has a much wider bandwidth. It is increased by about 211 and 255% compared to the linear case for a value of $\zeta = 2 \times 10^{-3}$ and $\zeta = 8 \times 10^{-3}$, respectively. It is noted that for a larger damping ratio (ζ), the wider the reduction bandwidth of the nonlinear absorber compared to the linear case and the reduction at the effective tuned frequency is less. As ζ is increased in the nonlinear absorber case, the vibration reduction bandwidth decreases. In addition, in the response curves of the system corresponding to larger damping, at the second resonance frequency Ω_{r_2} of the system with the nonlinear absorber will shift to a lower frequency. The amplitude of the first resonance frequency Ω_{r_1} of the system slightly reduces.

By adding damping, the displacement of the primary system can be made to be single valued for all frequencies, so that no jumps can occur in the response. A disadvantage though is that higher damping results in less vibration reduction at the tuned frequency Ω_t. For the case of high damping, one might expect that the nonlinear absorber will dissipate more vibration energy at some frequencies when the relative velocity is high. Thus, the 'resonance' peaks might be expected to be significantly reduced with increased damping. This is apparent in the reduction in the peak response amplitude at the resonance frequencies Ω_{r1}, Ω_{r2} for the linear absorber, but it does not appear to be the case for the nonlinear absorber.

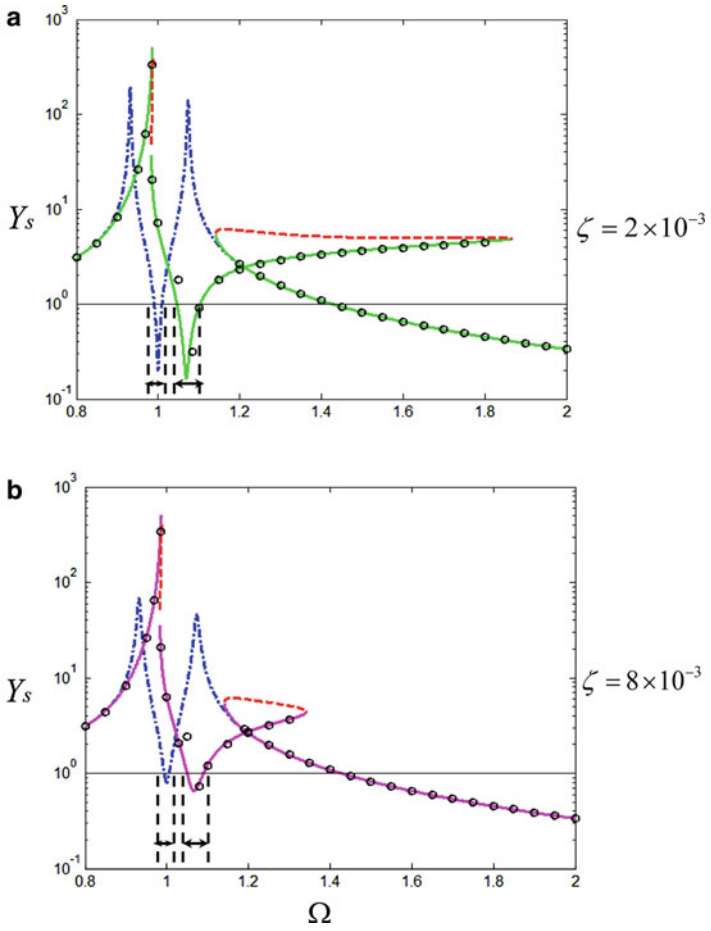

Fig. 23.3 Plots showing the effect of the damping in the nonlinear absorber on the primary system frequency response curves Y_s as a function of Ω The 'tuned' frequency $\omega_0 = \omega_1/\omega_s = 1$, nonlinear absorber stiffness $\gamma = 10^{-4}$, mass ratio $\mu = 0.02$ and damping $\zeta_s = 0.001$). The response for the system with the linear absorber is given by the *dashed-dotted line*, the *solid line* is the stable solution and the *dashed line* gives the unstable solution. Direct numerical solutions are shown by the symbol ('$\circ$'). (**a**) $\zeta = 2 \times 10^{-3}$ low absorber damping and (**b**) $\zeta = 8 \times 10^{-3}$ high absorber damping

23.4 Experimental Validation

A nonlinear absorber was designed and attached to a cantilever beam which was excited by a shaker. The overall system is modelled as a nonlinear hardening Duffing oscillator coupled to a linear system. The aim of the experimental investigation is to demonstrate the corresponding vibration reduction of the configuration using this particular nonlinear vibration absorber.

23.4.1 Nonlinear Dynamic Vibration Absorber Design and Experimental Investigation

The phenomenon of nonlinear stiffness was reproduced using a thin clamped circular plate undergoing large flexural deflection [12]. The absorber mass was attached at the centre of the thin circular plate. The plate is clamped by a frame on its edges as illustrated in Fig. 23.4. The circular plate has a radius r, thickness h, Poisson's ratio ν and Young's modulus E. When the mass moves in the vertical direction, the plate bends with a large deflection producing axial strain and a change in length of the midplane axis. This large deflection, producing geometric nonlinearity, is the cause of the nonlinearity in the restoring force and hence effective stiffness of the absorber. The static relationship between applied static force f at the centre of the circular plate and the deflection at that point has been obtained when ν is equal to 0.3 [12].

$$0.217\frac{fr^2}{Eh^4} = \frac{y}{h} + 0.443\left(\frac{y}{h}\right)^3 \tag{23.6}$$

It can be written as

$$f = k_1 y + k_3 y^3 \tag{23.7}$$

where $k_1 = \frac{Eh^3}{0.217r^2}$ and $k_3 = \frac{0.443Eh}{0.217r^2}$ are the corresponding stiffness coefficients.

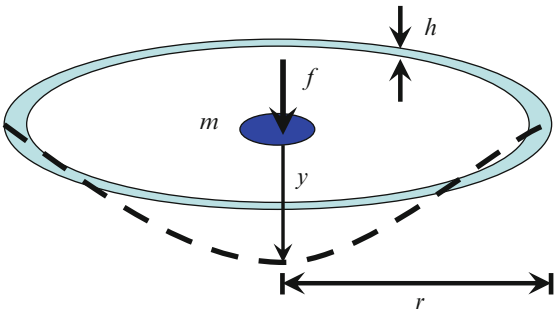

Fig. 23.4 Schematic representation of a nonlinear vibration absorber using a thin circular plate

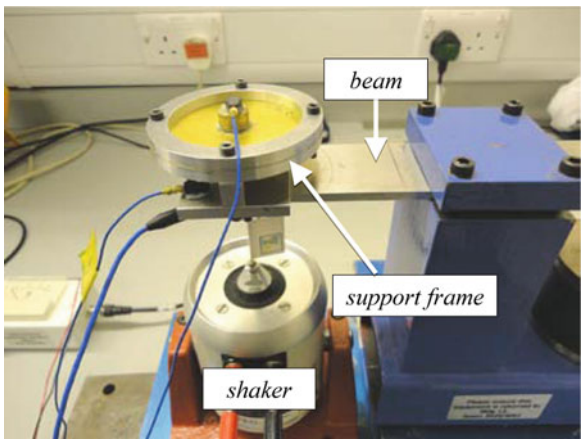

Fig. 23.5 Photograph of the actual experimental system consisting of a nonlinear absorber attached to a cantilever beam excited by an electro-dynamic shaker

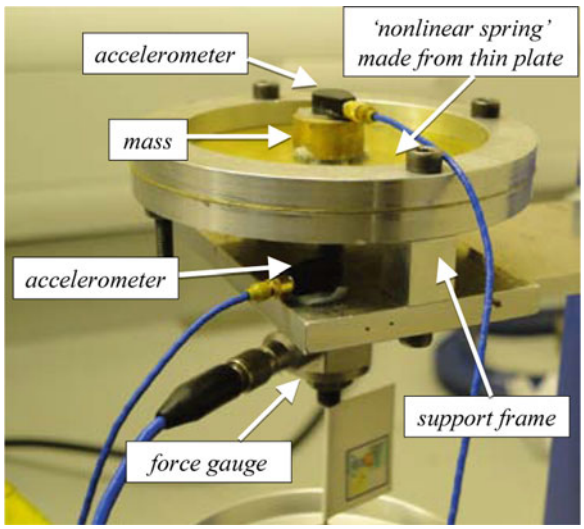

Fig. 23.6 Photograph showing the details of the nonlinear system

The practical implementation of the nonlinear vibration absorber is shown in Figs. 23.5, 23.6, 23.7. Photographs are shown in Figs. 23.5 and 23.6 and a schematic representation is shown in Fig. 23.7. A mass m was attached to the thin plate, which is itself bolted to a cantilever beam by a support frame. The spring characteristics between the absorber mass and the support frame are due to the thin circular plate, which can be modelled as a nonlinear stiffness k_1, k_3 and for small dissipation effects a viscous damper c was introduced. The thickness of the plate or shim and the attached mass can be altered and these have a large effect on the nonlinear attachment system characteristics. In addition, the length of the cantilever beam can also be altered, so it is possible to consider different natural frequencies. For large dynamic deformations it was hypothesized that the absorber would be nonlinear. The cantilever beam was excited by an electro-dynamic shaker. The support frame and beam structure without the absorber can be modelled as a linear system comprising of a spring k_s, a viscous damper c_s and a mass m_s Applying a constant amplitude force at each frequency to the shaker the excitation can be modelled as a constant amplitude harmonic force, as shown in Fig. 23.7.

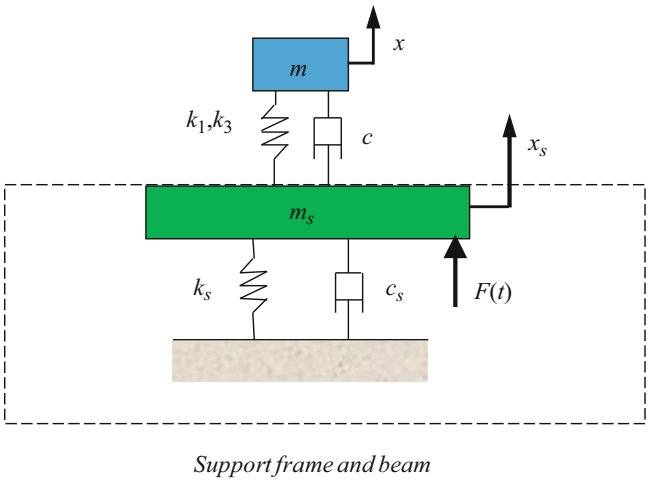

Fig. 23.7 Schematic representation of a nonlinear absorber attached to a cantilever beam system excited by a shaker

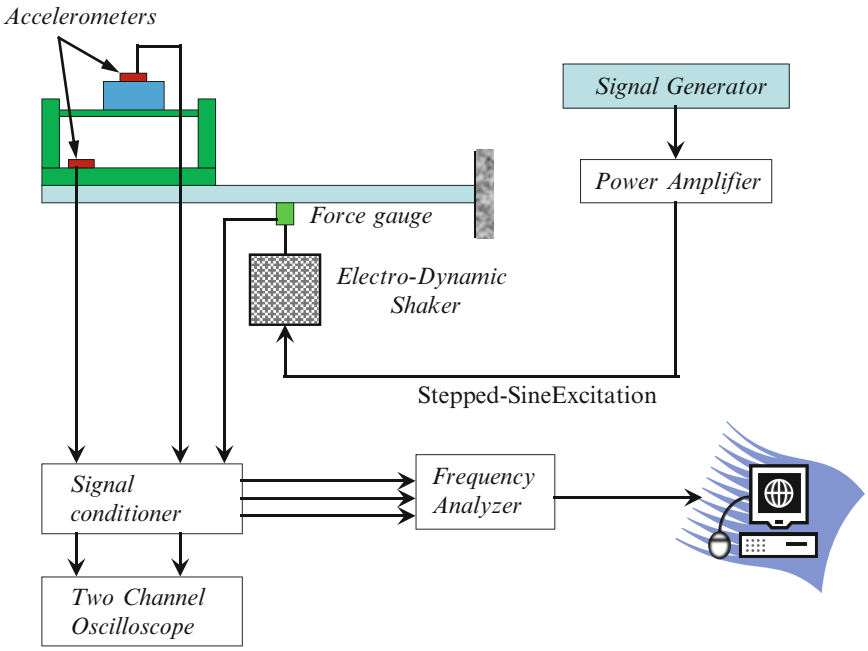

Fig. 23.8 Schematic diagram of the instrumentation setup used for the laboratory tests under harmonic excitation

23.4.2 Experimental Procedure and Results

The schematic diagram of the experimental setup is shown in Fig. 23.8. The electro-dynamic shaker was driven by a signal generator producing a stepped-sine signal. The accelerometers (PCB type 352C22) were attached to the support structure and to the mass of the absorber, while the oscilloscope was used to observe the system response.

A preliminary test was implemented to broadly investigate the dynamic behaviour of the system. For each test, the shaker had a different force amplitude. In the high force amplitude test, a slow frequency sweep (where the force gauge recorded a constant voltage and hence force amplitude) was applied from 100 Hz to about 225 Hz and the response of the system was observed using the oscilloscope. The first resonance was monitored at around 123 Hz, with large vibrational amplitudes in both systems. In addition, the first resonance peak was difficult to measure because of the light damping in the cantilever beam. When the frequency was increased beyond this, the tuned frequency was observed at about 183 Hz. In this frequency region the vibration of the support frame was a minima. However, a second resonance occurred at about 213 Hz, where only the vibration of the absorber mass was large. This was followed by a sudden decrease in the motion of the mass of absorber; a jump-down in the response. The frequency was then slowly swept down from this high frequency back to the low frequency. A sudden increase in the amplitude was observed at a frequency of about 199 Hz, again only for the mass of the absorber (a jump-up). At 123 Hz, the resonance response, for which there was large motion of both the support structure and the mass

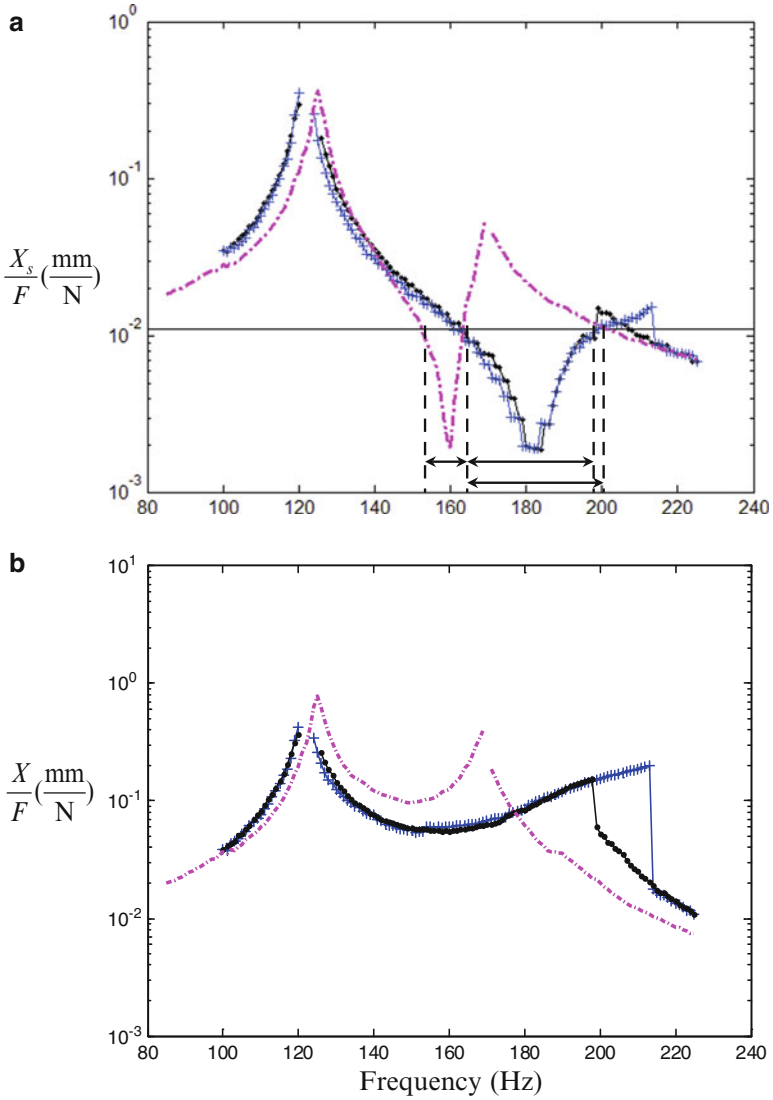

Fig. 23.9 Comparison of the measured frequency response curves for the system in Table 23.2. Plate thickness 0.2 (mm): (**a**) Absolute displacement of the beam structure, (**b**) Absolute displacement of the absorber. Low force amplitude for $F = 0.11$N (*dashed-dotted line*). High force amplitude for $F = 1.12$N: increasing frequency ('+'), decreasing frequency ('•') $\left(\frac{\text{mm}}{\text{N}}\right)$ $\left(\frac{\mathbf{mm}}{\text{N}}\right)$

of absorber, was observable. In the low force amplitude test, the response behaviour was observed that is approximately similar to the a linear system. The first resonance, tuned frequency and second resonance were found to occur at around 125, 160 and 172 Hz respectively. The jump-up and jump-down frequencies did not occur.

For the measured data presented, the shaker was driven at discrete frequencies for the system with the thin plate, corresponding to the cases described above. The excitation frequency was increased from 100 to 225 Hz, in 1 Hz increments, and then decreased to 100 Hz with the same frequency decrements. The amplitude of the excitation force was maintained at a constant level for all excitation frequencies, by manually adjusting the power amplifier so that the output voltage of the force gauge was 127 and 12.7 mV respectively. This corresponded to an equivalent force of 1.12 and 0.11 N respectively. At each frequency, once the system was at steady-state, 5 s of acceleration time histories were captured using a DataPhysics frequency analyser connected to a PC. Subsequently, the acceleration of the support frame and beam structure and the absorber were measured, and then this data was processed to give the displacement. The data is presented in terms of the absolute displacement x_s of the support frame and beam structure and the absolute displacement x of absorber. The Fourier series coefficients were extracted from these time histories and the amplitude of the first harmonic of each data set is plotted at the corresponding excitation frequency. This can be seen in Fig. 23.9 for the system for which the forces have low and high amplitudes respectively. At low force amplitude, the data points in each graph are dashed-dotted line. At high force amplitude, the data points in each graph are denoted by '+' for increasing frequency and '•' for decreasing frequency respectively.

The response of the support frame and beam structure X_s is plotted in Fig. 23.9a. It can be seen that the first resonance frequency and tuned frequency occur at about 125, 160 and 123 Hz, 183 Hz for the low and high force amplitude cases, respectively. The nonlinear system attached to the cantilever beam structure has a great effect on its response. In addition,

Table 23.1 The estimated system parameters from the experimental tests

	m_s(kg)	c_s(N· s/m)	k_s(N/m)	F(N)
Low force amplitude	126×10^{-3}	1.26	8.93×10^4	0.11
High force amplitude				1.12
	m(kg)	c (N·s/m)	k_1(N/m)	k_3(N/m^3)
Low force amplitude	6.44×10^{-3}	0.15	5.69×10^3	6.90×10^{10}
High force amplitude				

Table 23.2 Equivalent non-dimensional system parameters for the model predictions

	μ	ω_0	γ	ζ_s	ζ
Low force amplitude	5.11×10^{-2}	1.17	2.29×10^{-5}	5.95×10^{-3}	1.18×10^{-2}
High force amplitude			2.73×10^{-3}		

the jump-down frequency occurs at approximately 213 Hz and the corresponding jump-up frequency at about 199 Hz for the high force amplitude. However, the jump-up and jump-down frequencies did not occur for the low force amplitude. In Fig. 23.9b, which shows the response of the absorber X, in addition to the peak associated with the first resonance frequency of the support frame and beam structure, a jump-down and a jump-up frequency can also be observed for the high force amplitude.

23.4.3 Parameter Estimation and Model Validation

The cantilever beam was made of aluminium with a total length $L = 0.09$m, cross-sectional area $A = 0.04\text{m} \times 0.004\text{m}$, density $\rho = 2{,}700\text{kg/m}^3$, and Young's modulus$E = 70\text{GN/m}^2$. In addition, the circular plate was made of brass with thickness 0.2×10^{-3}m, area $A = \pi\,(0.026)^2\,\text{m}^2$, density $\rho = 8{,}500\,\text{kg/m}^3$, and Young's modulus $E = 110\text{GN/m}^2$. The parameters for the systems tested were required in order to compare the experimental results with the model predictions. These parameters (m_s, c_s, k_s, m, c, k_1, k_3) were measured independently and were estimated as follows.

The Frequency Response Function (FRF) of the support frame attached to the cantilever beam without the absorber was measured using pseudo random force measurements. The system parameters (mass m_s, damping c_s and stiffness k_s) were estimated by fitting a theoretical single degree of freedom FRF to the experimental FRF. In addition, the mass of the absorber m was measured directly. The viscous damping coefficient c of the nonlinear attachment was estimated on it separately through the half power points method at low amplitude [13]. Moreover, the stiffnesses k_1 and k_3 of the nonlinear attachment were estimated using the measurements of the static displacement for applied static loads. Above these parameters are listed in Table 23.1. The equivalent system parameters for the equation of motion written in the non-dimensional form of Eq (23.2a,b) are listed in Table 23.2 It is noted that the system was designed such that by simply adjusting the thickness of the plate, in the vibration absorber, the nonlinear stiffness and natural frequency of the absorber could be varied.

The frequency bandwidth was determined such that $X_s \leq X_0$ in that frequency range, where X_0 is the corresponding static extension of the linear spring represented by the cantilever beam for the same magnitude of the static load. The response $X_s = X_0$ is the thin solid horizontal line shown in Figs. 23.9 and 23.10a. Examining Figs. 23.9 and 23.10a, the high force amplitude applied for nonlinear absorber has a much wider vibration reduction bandwidth. The numerical parameters for the system are given in Table 23.2. The frequency response curves described by Eq (23.4a, b) are shown in Fig. 23.10. In Table 23.3, for the approximate HBM solution, the bandwidth for vibration reduction is increased by about 311 and 188% for the increasing and decreasing frequency cases, respectively. For the measurement, it is increased by about 280 and 240% for the increasing and decreasing frequency cases, respectively.

23.5 Conclusions

This paper has investigated the influence of the NDVA parameters on the vibration reduction. The nonlinearity resulted in a much wider effective bandwidth compared to that for a linear absorber with similar mass and damping. It was found that the frequency response curve of the NDVA has the effect of moving the second resonant peak to a higher frequency away from the tuned frequency so that the device is robust to mistuning. Experimental results have been presented to compare with the model derived.

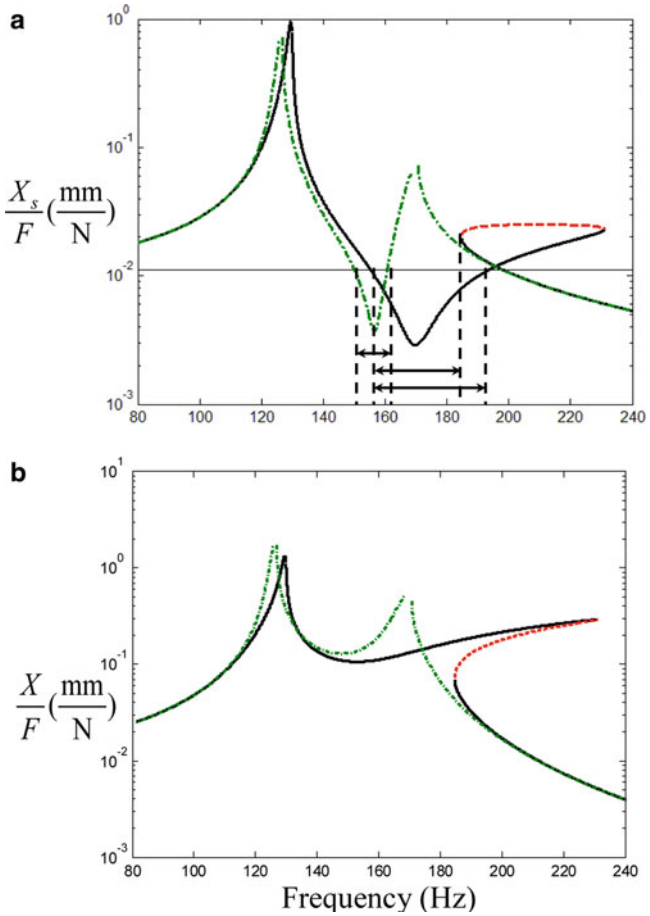

Fig. 23.10 Comparison of the predicted frequency response curves (HBM solution) for the system in Table 23.2. Plate thickness 0.2 (mm): (**a**) Absolute displacement of the beam structure, (**b**) Absolute displacement of the absorber. Low force amplitude for $F = 0.11$N (*dashed-dotted line*). High force amplitude for $F = 1.12$N: stable solution (*solid line*), unstable solution (*dashed line*) $\left(\frac{\text{mm}}{\text{N}}\right)$ $\left(\frac{\text{mm}}{\text{N}}\right)$

Table 23.3 The bandwidth frequency of NDVA on the primary system frequency response curves

HBM solution	Low force amplitude	High force amplitude
Bandwidth for increasing frequency	9	37
Bandwidth improvement (%)		311
Bandwidth for decreasing frequency	9	28
Bandwidth improvement (%)		188
Measurements	**Low force amplitude**	**High force amplitude**
Bandwidth for increasing frequency	10	38
Bandwidth improvement (%)		280
Bandwidth for decreasing frequency	10	34
Bandwidth improvement (%)		240

References

1. Roberson RE (1952) Synthesis of a nonlinear dynamic vibration absorber. J Frankl Inst 254(3):205–220
2. Hunt JB Nissen JC (1982) The broadband dynamic vibration absorber. J Sound Vib 83(4):573–578
3. Nissen JC, Popp K et al (1985) Optimization of a non-linear dynamic vibration absorber. J Sound Vib 99(1):149–154
4. Soom A Lee M (1983) Optimal design of linear and non-linear vibration absorbers for damped systems. Trans ASME 105:112–119
5. Jordanov IN Cheshankov BI (1988) Optimal design of linear and non-linear dynamic vibration absorbers. J Sound Vib 123(1):157–170
6. Zhu SJ, Zheng YF et al (2004) Analysis of non-linear dynamics of a two-degree-of-freedom vibration system with non-linear damping and non-linear spring. J Sound Vib 271(1–2):15–24
7. Gendelman OV, Gourdon E et al (2006) Quasiperiodic energy pumping in coupled oscillators under periodic forcing. J Sound Vib 294(4–5):651–662
8. Gourdon E, Alexander NA et al (2007) Nonlinear energy pumping under transient forcing with strongly nonlinear coupling: theoretical and experimental results. J Sound Vib 300(3–5):522–551
9. Gendelman O, Starosvetsky Y et al (2008) Attractors of harmonically forced linear oscillator with attached nonlinear energy sink I: description of response regimes. Nonlinear Dyn 51(1):31–46

10. Starosvetsky Y, Gendelman O (2008) Attractors of harmonically forced linear oscillator with attached nonlinear energy sink. II: optimization of a nonlinear vibration absorber. Nonlinear Dyn 51(1):47–57
11. http://en.wikipedia.org/wiki/Cubic_equation.htm(2008)
12. Timoshenko S, Woinowsky-Krieger S (1959) Theory of plates and shells. McGraw-Hill, New York, p 580
13. Mead DJ (1998) Passive vibration control Wiley, New York

Chapter 24
The Effects of Clutch Damper in Idling Driveline Rattle

Nobutaka Tsujiuchi, Takayuki Koizumi, Naoki Hara, Yoshihiro Yamakaji, and Kazuhiro Yamashita

Abstract In recent years, measures have been implemented to improve automotive environmental performance, such as increasing engine torque at low speeds and reducing idling speed. These measures tend to increase the engine's torque fluctuation, which adversely affects the noise and vibration (NV) phenomena of the powertrain. Demand continues to increase for NV measures in powertrains.

Gear rattle, which is a general NV problem of powertrains, strongly influences the torsional stiffness and the hysteresis torque of the clutch damper, which is an absorption element of a powertrain, and the inertia of the transmission or the flywheel. In this paper, we built a mechanism analysis model of a powertrain that can predict gear rattle and examined the relevance of the first stage hysteresis torque of a clutch damper and the gear rattle behavior.

Keywords Gear rattle • Clutch damper • Transmission • Mechanism analysis • Hysteresis torque

24.1 Introduction

Engine torque fluctuations, which are the excitation sources of noise and vibration in powertrains, are transmitted to the transmission through the clutch and the torque converter. The transmission consists of a number of gear pairs, and the rattle is caused by the backlash among them. This rattle is the main factor of powertrain noise and vibration. The clutch, which is used to start device in manual transmissions, not only transmits and disconnects the engine power but also functions as a powertrain damper since the clutch disc has a torsional spring and a friction plate. A clutch's schematic diagram is shown in Fig. 24.1. The components of a common clutch disc are shown in Fig. 24.2. Engine power, which is transmitted to a clutch disc through a flywheel and a clutch cover, is transmitted to the transmission after the torsional vibration is damped in a clutch disc.

Presently, in some vehicles with low-price strategies, the main reason for decreasing the engine torque fluctuation by a clutch disc is to increase the longevity of the powertrain parts. Therefore, the torsional characteristics of the clutch disc are installed for high loads, and a clutch disc with a single torsional characteristic is used. However, high quality silence is required in many vehicles. In recent years, the following NV problems must be measured by a clutch disc: rattling noise during idling, driving and coasting; booming noise during driving.

To measure these problems with one clutch disc, a multi-stage spring and variable hysteresis characteristics are needed. The torsional characteristics of these clutch discs are shown in Fig. 24.3. A clutch disc with the torsional characteristics of the single stage shown in (a) is called a normal disc. A clutch disc with a multi-stage spring has variable hysteresis torques,

N. Tsujiuchi • T. Koizumi • N. Hara (✉)
Department of Mechanical Engineering, Doshisha University, 1-3 Tataramiyakodani, Kyotanabe-City, Kyoto, 610-0321, Japan
e-mail: dtl0313@mail4.doshisha.ac.jp

Y. Yamakaji • K. Yamashita
EXEDY Corporation, 1-1-1 Kidamotomiya, Neyagawa-City, Osaka, 572-8570, Japan

G. Kerschen et al. (eds.), *Topics in Nonlinear Dynamics, Volume 1: Proceedings of the 31st IMAC, A Conference on Structural Dynamics, 2013*, Conference Proceedings of the Society for Experimental Mechanics Series 35,
DOI 10.1007/978-1-4614-6570-6_24,

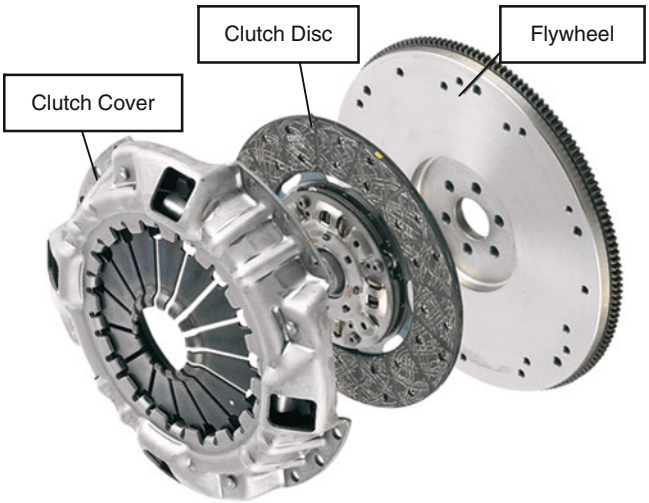

Fig. 24.1 Clutch componentry

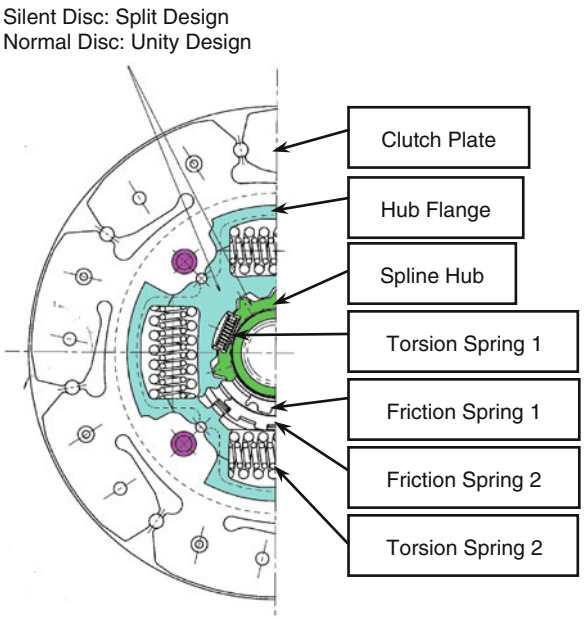

Fig. 24.2 Clutch disc componentry

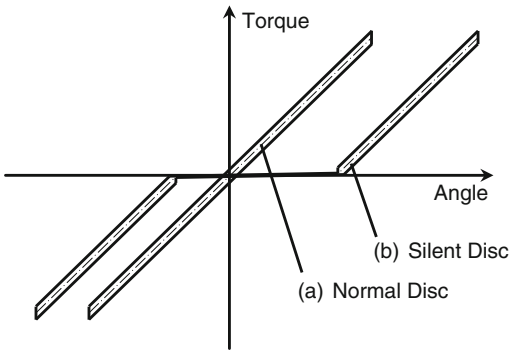

Fig. 24.3 Torsional characteristic

and the wide angle torsional characteristic shown in (b) is called a silent disc. Each NV phenomena can be taken measure by individual clutch discs. Because each NV phenomena occur at different load torques like positive, negative, high-load or low-load. In other words, the optimum torsional characteristics of the clutch disc are installed for each torque ranges. The parameter for the torsional characteristic is the torsional stiffness of the torsion spring constant and the hysteresis torque of the torsional resisting torque by dry friction.

However, since engine torque fluctuations have increased in recent years, the torque inputted into a clutch damper goes beyond the allowable torque in the first stage, into the operating range at driving, then a possibility of a non-linear vibration would be generated. Since the non-linear vibration of a clutch damper increases the noise and the vibration in the powertrain, we must expand the allowable torque in the first stage, where there is high torsional stiffness; however, since such a countermeasure would increase the resonance frequency of the powertrain during idling, we are concerned about generating powertrain resonance. Changing the structure is another way of expanding the torsional angle in the first stage. However, increasing cost, increasing impact, and response delays resulted from acceleration/deceleration. We have to increase the torsional stiffness and optimize the hysteresis torque to find compromise between control of the powertrain resonance and damping.

Although many analysis results have been published about the rattle phenomenon, few papers have discussed the relevance of a gear pair's behavior and a clutch damper's hysteresis torque in the first stage. In this paper, we built a mechanism-analysis model of the powertrain that can predict the rattle phenomenon and examined the relevance of hysteresis torque and rattling behavior in the first stage.

24.2 The Rattle During Idling

The rattle during idling is a noise that is caused by the gear tooth surface of the input and counter gears of the transmission strikes, since engine rotational fluctuations are excessive when the clutch is released in neutral due to waiting for signals; this is generally called idle rattle. We performed the countermeasures by reducing the amount of transmission gear rotational fluctuations to the amount of rotational fluctuations that aren't produced gear separation. Sufficient angle to absorb the rotational fluctuation and sufficiently low torsional stiffness and low hysteresis torque are needed to reduce the shock of the gear rattle for a clutch damper.

24.3 Modeling Powertrain

With ADAMS mechanism analysis software, we built a simulation model of a powertrain that can duplicate the gear rattle of a manual transmission.

Since this study's purpose is phenomenon analysis that concentrates on the relevance of the first stage hysteresis torque of the clutch damper and gear rattle behavior, the modeling scope is the damper function parts of a clutch disc and a transmission's gear pair that produces a rattle. We built a clutch disc model with three components: a clutch plate, a hub flange, and a spline hub. We also built a transmission model with a gear pair of a drive gear on an input shaft and a counter gear, which is floating on the output shaft. The simulation model's outline is shown in Fig. 24.4. The model's parameters and the simulation conditions are shown in Tables 24.1 and 24.2.

The input torque is a sine wave that has the amplitude of the measured value of the engine speed fluctuation and the engine combustion primary frequency. The drag torque changes with different temperatures and amounts of transmission oil. However, in this simulation, as a constant value, we adopted the measured value's drag torque of a compact car in high temperature. Because the hysteresis torque is a parameter that greatly contributes to a clutch damper's attenuation performance, we obtained the relevance of the static and kinetic friction al forces by measuring the frictional characteristics of actual equipment based on the simulation model's hysteresis torque.

24.4 Simulation

We examined the consistency of the simulation models with actual clutches and ran simulations with the hysteresis torque parameter. We also confirmed whether the adherence phenomenon between the component parts of a clutch are reproducible in the simulation model, since the adherence phenomenon that occurs when the hysteresis torque is too large greatly influences the idle rattle.

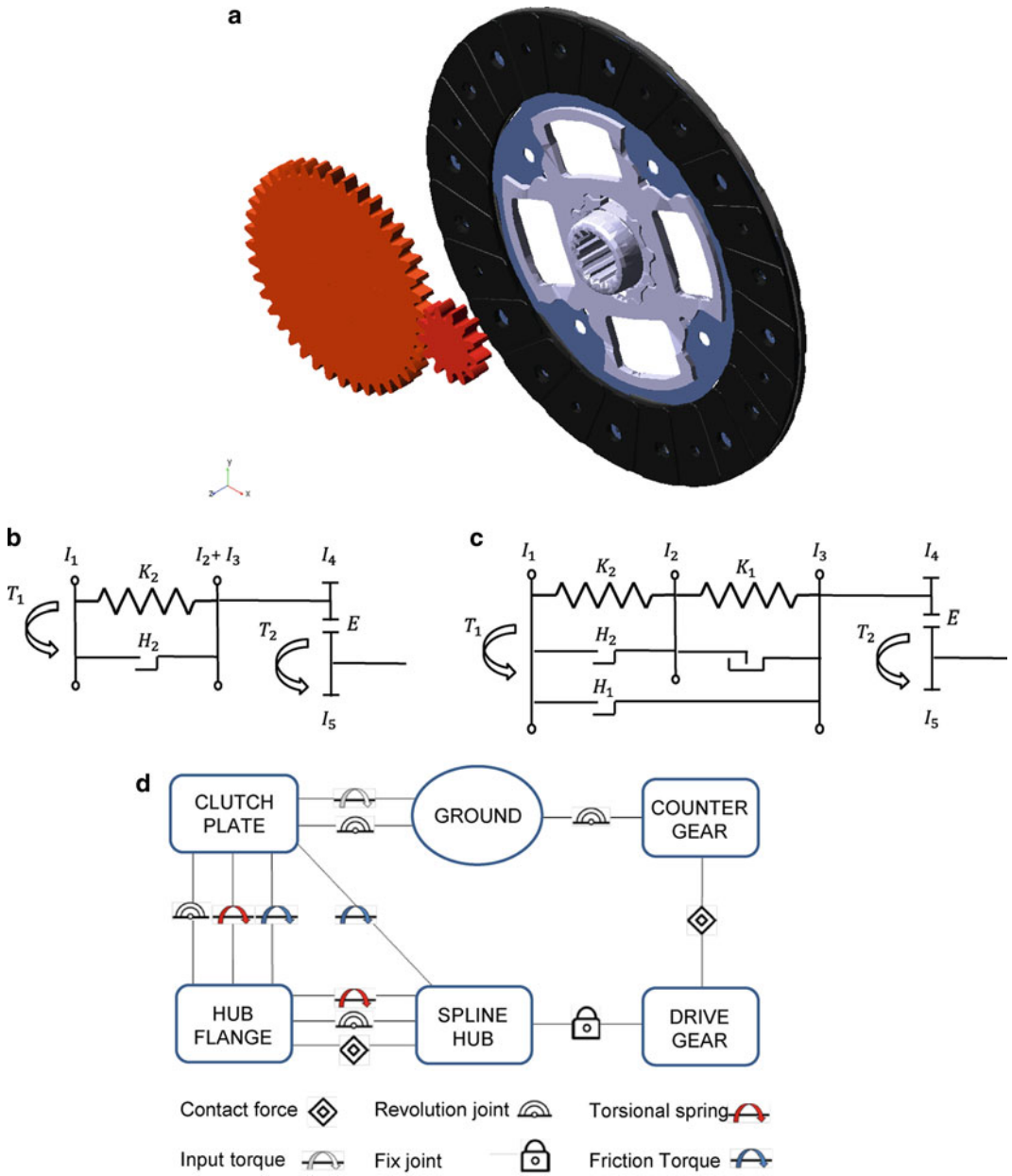

Fig. 24.4 Powertrain model for idle rattling analysis in ADAMS. (**a**) Powertrain model. (**b**) Normal disc. (**c**) Silent disc. (**d**) Topology of stimulation model

24.4.1 Evaluation of the Model Consistency

We ran simulations that used the specifications of a compact car and compared transmissibility of a clutch damper calculated by following equation with a measured value and the result calculated with existing two-dimensional analysis software:

$$\tau = \frac{N_{CP}}{N_{SH}}$$

where N_{CP}: Angular velocity amplitude of clutch plate, N_{SH}: Angular velocity amplitude of Spline hub.

The analysis result of the three conditions is shown in Fig. 24.5. The transmissibility of the clutch damper calculated by this simulation substantially matches the measured values and the results of the existing analysis software. We verified that our simulation model can reproduce the damper function of an actual clutch with sufficient accuracy.

Table 24.1 Parameter on simulation model

Symbol	Parameter
T_1	Engine torque
A_1	First order amplitude of engine firing
f	Frequency of excitation
T_2	Drag torque on idling gear
I_1	Inertia of clutch plate
I_2	Inertia of hub flange
I_3	Inertia of spline hub
I_4	Inertia of drive gear
I_5	Inertia of counter gear
K_1	Torsional stiffness on first stage
K_2	Torsional stiffness on second stage
H_1	Hysteresis torque on first stage
H_2	Hysteresis torque on second stage
E	Backlash between the gear pair

Table 24.2 Analysis condition

Item	Unit	
T_1	Nm	$A_1\cos(2\pi ft)$
A_1	Nm	61.6
f	Hz	21.3
T_2	Nm	0.204
I_1	kg m^2	7.12E-02
I_2	kg m^2	4.04E-04
I_3	kg m^2	3.99E-05
I_4	kg m^2	6.16E-04
I_5	kg m^2	2.56E-03
K_1	Nm/deg	0.081
K_2	Nm/deg	9.7
H_1	Nm	0.2–1.6
H_2	Nm	8.92
E	m	5.40E-06

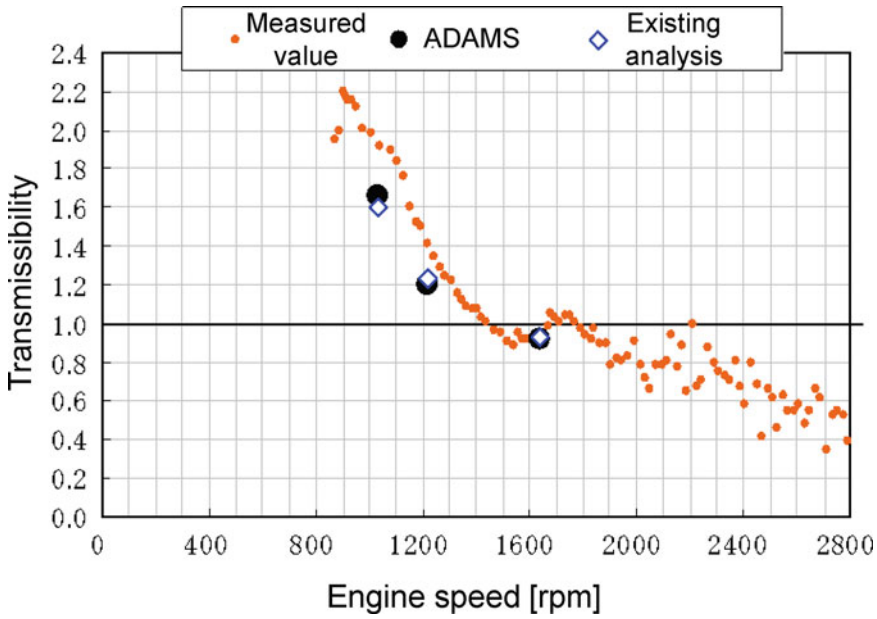

Fig. 24.5 Transmissibility of clutch damper model

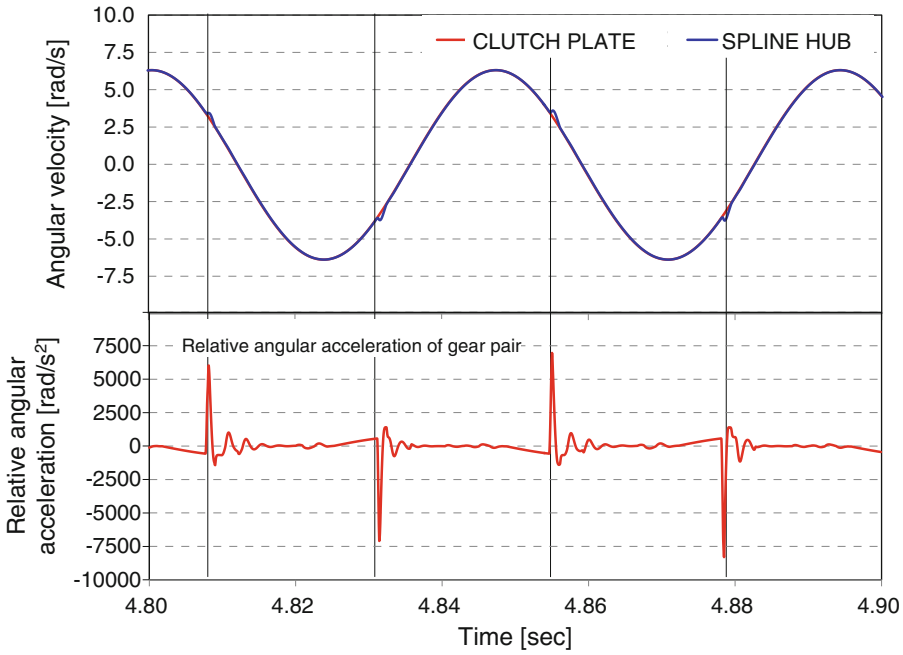

Fig. 24.6 Angular velocity of clutch plate and spline hub

24.4.2 Adherence Simulation

When the hysteresis torque exceeds the input torque, the clutch damper binds. Depending on the driving conditions, this phenomenon may also happen in actual vehicles. To verify whether the binding phenomenon among clutch disc components is reproducible by our simulation model, we performed a simulation with enough enlarged hysteresis torque of the idle stage.

The angular velocities of a clutch plate and a spline hub are shown in Fig. 24.6. They have overlapped, indicating fixing of them. However, when we focus on the angular velocity of a spline hub, the periodic minute peak of the angular velocity indicates that a spline hub slips slightly with a clutch plate because the gear rattle impact, which rises due to a pair of drive and counter gears. The relative angular acceleration of drive and counter gears is shown in Fig. 24.6. The gear rattle's impact causes the slip phenomenon of a clutch plate and a spline hub. We confirmed whether our simulation model can reproduce the adherence phenomenon that occurs when the hysteresis torque of a clutch is increased.

24.4.3 Idle Rattling Simulation

To grasp the relevance of the hysteresis torque and the idle rattle, we changed the hysteresis torque in the first stage by 0.2 units from 0.2 to 1.6 Nm and performed the simulation. The angular velocities of a clutch plate and the drive gear and the counter gear angular velocity in each hysteresis torque are shown in Fig. 24.7a, b. The gear pairs relative angular velocity and acceleration are shown in Fig. 24.7c, d. Since the angular velocity amplitude decreases as the hysteresis torque becomes small, a clutch damper's damping performance improves. Since the angular velocity amplitude decreases as the hysteresis torque becomes small, a clutch damper's damping performance also improves with decreasing hysteresis torque. For a hysteresis torque domain of 1.0–1.6, the adherence of a spline hub and a clutch plate occurred, since the change of the angular velocity amplitude is small.

We computed the envelope curve from the relative angular acceleration of the drive and counter gears, and its average absolute value is shown in Fig. 24.8. An example of envelope processing is shown in Fig. 24.9. Figure 24.8 shows that the gear pair relative angular acceleration in a 1.0–1.6-Nm adherence domain resembles a normal disc, whose clutch damper transmissibility is about 1, since it has excessive torsional stiffness to the input torque amplitude and the input excitation frequency during idling. In a domain of 1.0 Nm or less, the result of the relative angular acceleration decreases and becomes minimum at 0.6 Nm. Figures 24.7 and 24.8 show the domain of the hysteresis torque around 0.6 Nm with rattle noise in the analysis that is smaller than what occurs at 0.2 Nm with the highest damping performance.

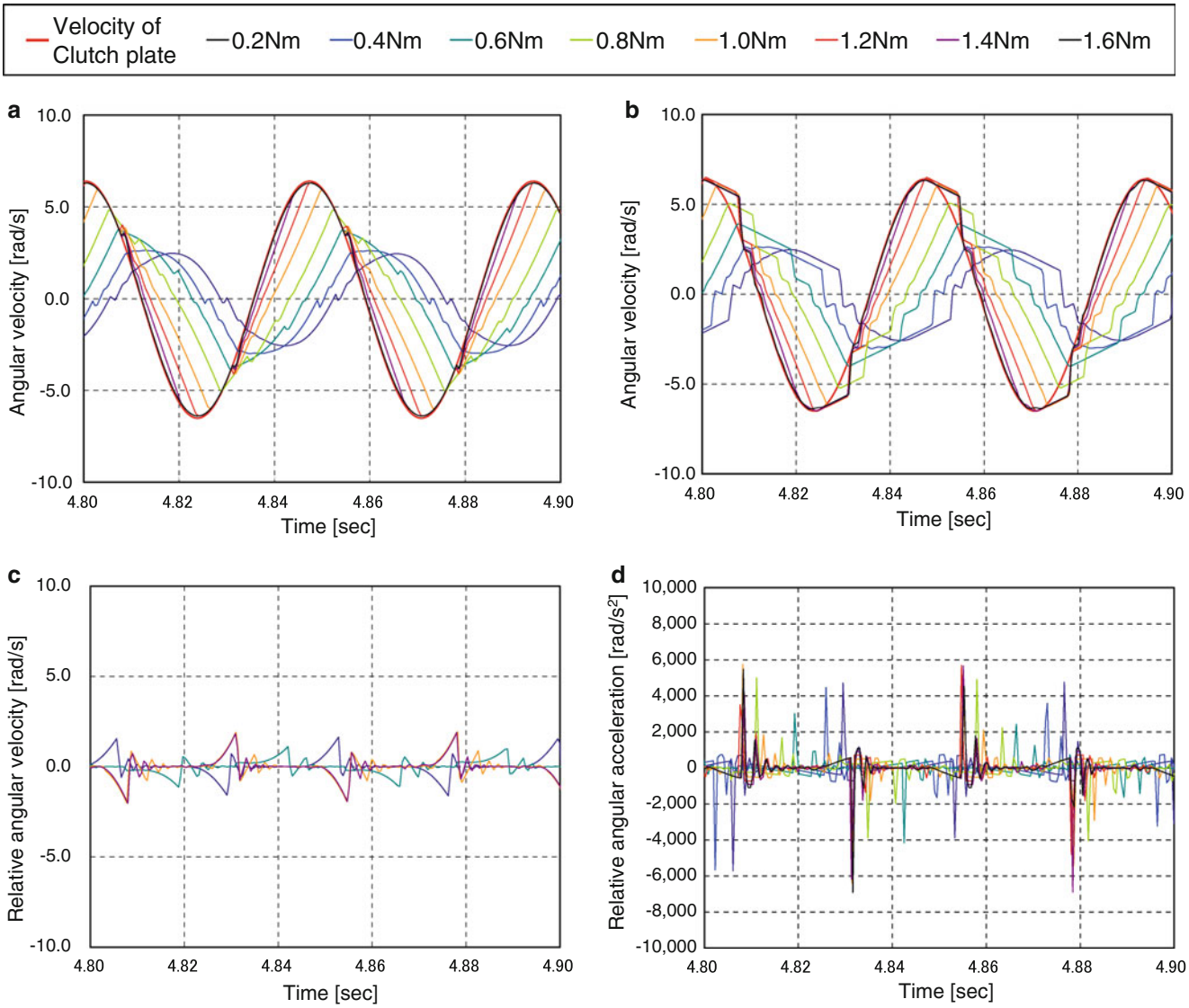

Fig. 24.7 The dynamic behavior of gear pair. (**a**) Angular velocity of drive gear. (**b**) Angular velocity of counter gear. (**c**) Relative angular velocity of gear pair. (**d**) Relative angular acceleration of gear pair

The angular velocity results of the drive and counter gears and the relative angular velocity are shown in Fig. 24.10. If the gear pair relative angular velocity during tooth flank contact is large, the gear pair's relative angular acceleration will increase. The reason that the hysteresis torque and the relative angular velocity of the gear do not necessarily have the same tendency is because the corrugated shape of the angular velocity at the drive and counter gears contributed to relative angular acceleration. The corrugated shape of the drive gear angular velocity is dependent on the frictional resistance torque that occurs under the influence of the hysteresis torque when a relative slip occurs between a clutch plate and a spline hub. The angular velocity of a counter gear constantly decreases due to the drag torque, while the tooth flank of the gear pair dissociated. At 0.6 Nm, since each corrugated shape after the tooth flank separation is alike, the relative angular acceleration became minimum. At 0.6 Nm or less, since the drive gear angular velocity after the tooth flank separation is falling steeply, the relative angular velocity to counter gear increases.

As explained above, not only the damping performance of a clutch damper but also the angular velocity waveform of a gear pair, which depends on the hysteresis torque, the drag torque, or the adherence phenomenon between the clutch disc components, contributed to the rattle level. In addition, the hysteresis torque produced by the minimum rattle in our analysis was about 0.6 Nm. This value will be changed by the elements that contribute to the corrugated shape of the angular velocity, for example, the drag torque and the transmission inertia.

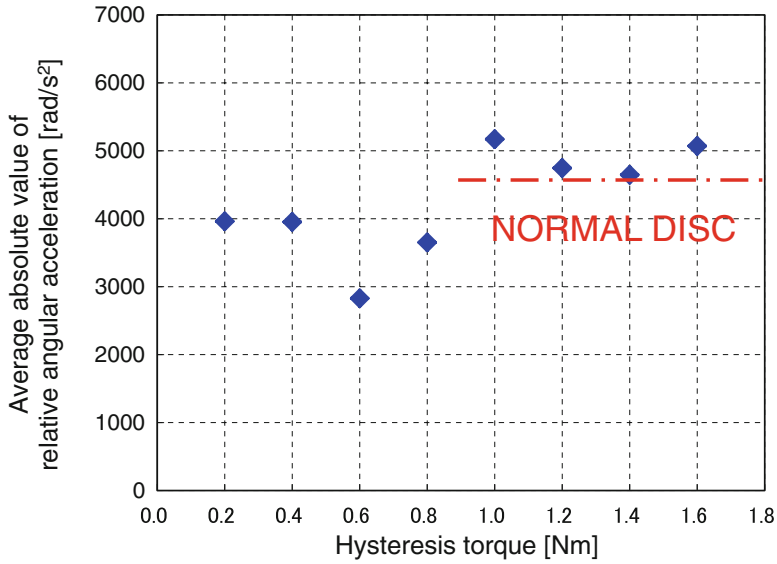

Fig. 24.8 Average of relative angular acceleration of gear pair

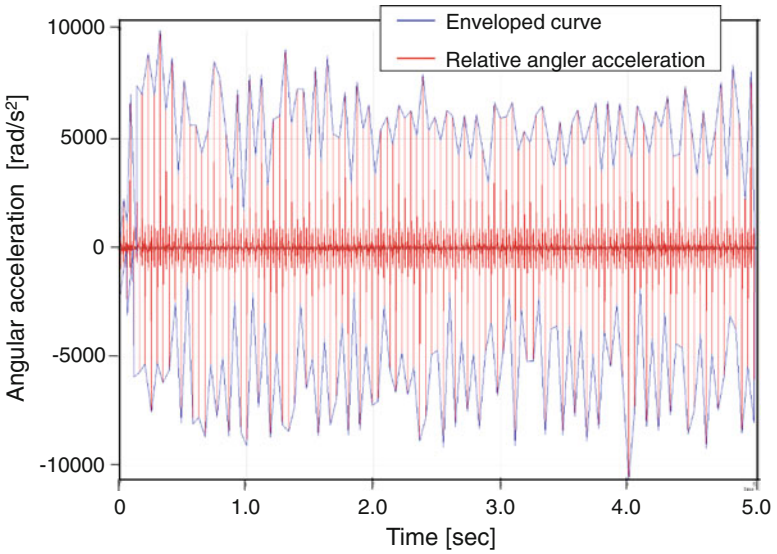

Fig. 24.9 Enveloped processing

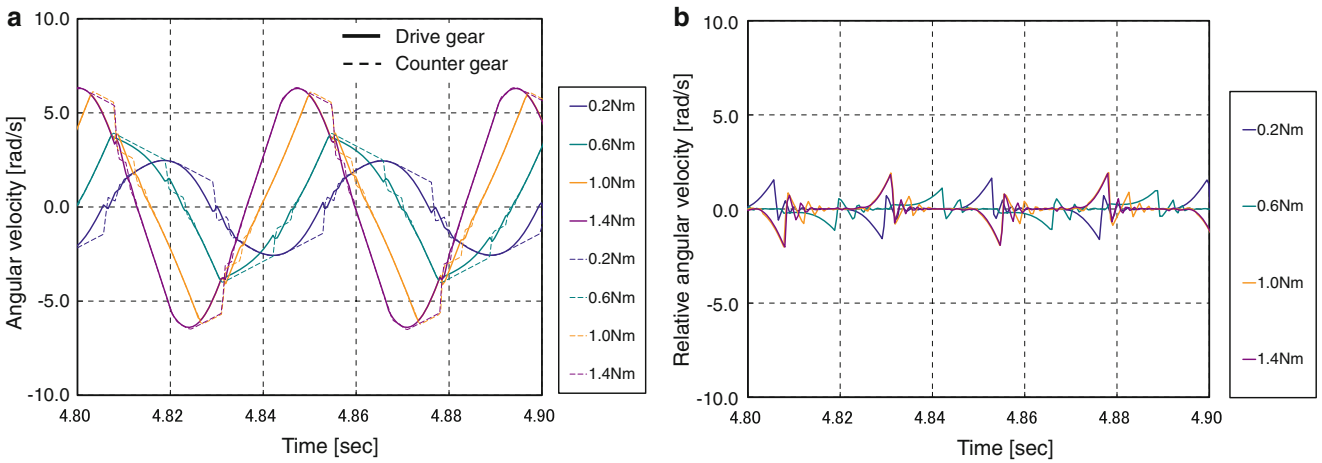

Fig. 24.10 The dynamic behavior of gear pair at 0.2, 0.6, 1.0, and 1.4 Nm. (**a**) Angular velocity. (**b**) Relative angular velocity

24.5 Conclusion

We obtained the following results from analysis of our powertrain mechanism model.

1. We built an analytical model that accurately reproduces the actual damper performance of a clutch.
2. Despite conditions with a high damping performance, our analysis confirmed the domain of the hysteresis torque that generated a large rattle noise.
3. The relative acceleration of the gear pairs is contributed to the hysteresis torque and the corrugated shape of the gear angular velocity that depends on the drag torque and the adherence phenomenon between the component parts of the clutch disc.

References

1. Kamo M, Yamamoto H (1996) The contribution analysis to drive rattle of a gear pair in powertrain. Isuzu technical report, Isuzu Motors, vol 96, pp 101–107 (in Japanese)
2. Hirai M, Nakamura M (2007) Prediction technology of the rattle excitation force in an engine timing gear. Isuzu technical report, Isuzu Motors, vol 118, pp 45–50 (in Japanese)
3. Hanai E, Mitani S, Nakamura H (2004) Research of prediction technology of gear rattle. Honda R&D technical review, vol 16(1), pp 139–144 (in Japanese)
4. Kaneko H, Hirano Y, Sakai S, Chiba R, Hojo H, Kubodera N (2003) The rattle phenomenon analysis of manual transmissions. Nissan technical report, Nissan Motor Management Council, vol 53, pp 83–87 (in Japanese)
5. Zhou C, Young S, Tang Y (2011) Two-stage gear driveline vibration and noise. In: SAE, Detroit, MI USA
6. Perera M, Theodossiades S, Rahnejat H, Kelly P (2011) Drive rattle elastodynamic response of manual automotive transmissions In: SAE, Detroit, MI USA
7. Fukushima H (1985) Noise and vibration control by an clutch disk damper. Daikin technical review, vol 16, pp 7–16 (in Japanese)
8. Fukushima H (1982) Noise and vibration of a silence disk (1). Daikin technical review, vol 6, pp 4–8 (in Japanese)
9. Fukushima H (1982) Noise and vibration of a silence disk (2). Daikin technical review, vol 6, pp 8–12 (in Japanese)

Chapter 25
Nonlinear Free Vibration of Curved Double Walled Carbon Nanotubes Using Differential Quadrature Method

Hamed Samandari and Ender Cigeroglu

Abstract Abstract In this study, nonlinear free vibration of a curved double walled carbon nanotube (DWCNT) is investigated, which are widely used in nano resonators, and sensors. Nonlinearities considered are due to large deflection of carbon nanotubes (geometric nonlinearity), initial curvature of tubes, and nonlinear interlayer van der Waals forces between inner and outer tubes. Assuming a harmonic solution in time domain, the differential quadrature method (DQM), is utilized to discretize the partial differential equations of motion in spatial domain, which resulted in a nonlinear set of algebraic equations of motion. The effect of nonlinearities, stiffness of the surrounding elastic medium, end conditions, and vibrational modes on the nonlinear free vibration of DWCNTs are investigated. The paper contribution can be divided into two main parts: in the first part, algebraic set of equation has been developed for the most general case considering different sources of nonlinearities and end conditions; hence, by selecting proper values for key parameters, the equation set can be converted into the equation of motion of desired application area. In the second part, the equations of motion are formulated using DQM in a matrix form which can be used in future modal and finite element analysis.

Keywords Carbon nanotubes • Geometric nonlinearity • Van Der Waals nonlinearity • Euler-Bernoulli theory • Differential quadrature method • Curved carbon nanotubes

25.1 Introduction

In recent years, a huge amount of attention has been devoted to Carbon nanotubes (CNTs) owing to their outstanding mechanical, electrical and thermal properties. Since their discovery by Iijima [1], the promising and diverse characteristics of CNTs have made them a remarkable candidate for new generation of materials with extensive potential applications in different fields of the nanoscience and nanotechnology [2–6].

CNTs have application areas such as resonators and sensors which require understanding of the vibrational behavior of these nanodevices. Therefore, in recent years, predicting the vibrational response of CNTs has attracted extreme interest among researchers. In early studies, the experimental methods have been often used to study the vibrational characteristic of CNTs; however, it is very difficult and also expensive to perform experiments at nanoscale levels due to limits of measurement devices. Using molecular dynamics simulations (MDS), Cao et al. [7] investigated the thermal vibration behaviors of single-walled carbon nanotubes (SWCNTs) utilizing systematic numerical studies.

Although MDS can provide a huge amount of information on the behavior of a structure in the nanoscale, they are restricted by the size of such atomic systems due to highly time consuming computational requirements. In consequence of their limitations, recently many researchers have proceeded toward continuum mechanics models to study the mechanical behavior of CNTs. For instance, elastic beam models such as Euler-Bernoulli model [8–10] and elastic shell models [11, 12] have been effectively utilized in anticipating the natural frequencies of CNTs. It is important to note that most of the current studies in literature deal with linear vibrations of CNTs.

Recent studies show that since CNTs can go through large deformations, i.e. geometric nonlinearity, they are nonlinear in nature. Fu et al. [8] explored the nonlinear free vibration of embedded multiple walled carbon nanotubes (MWCNTs) caused

H. Samandari • E. Cigeroglu (✉)
Department of Mechanical Engineering, Middle East Technical University, 06800, Ankara, Turkey
e-mail: hamed.samandari@gmail.com; ender@metu.edu.tr

G. Kerschen et al. (eds.), *Topics in Nonlinear Dynamics, Volume 1: Proceedings of the 31st IMAC, A Conference on Structural Dynamics, 2013*, Conference Proceedings of the Society for Experimental Mechanics Series 35,
DOI 10.1007/978-1-4614-6570-6_25,

by large deflections using the incremental harmonic balanced method (IHBM). Similar problem is studied by Ke et al. [13] using Timoshenko beam model. They reveal that natural frequency of CNTs increases as the vibration amplitude increases. Later studies show that in the case of MWCNTs natural frequencies of CNTs affected by another source of nonlinearity, interlayer molecular forces. The interlayer force between layers of CNTs is governed by van der Waals (vdW) forces. The vdW force estimated by Lennard-Jones potential is inherently nonlinear [14–16]; therefore, in order to accurately anticipate the vibrational behavior of MWCNTs, the nonlinear effect of vdW force should be considered [17]. The effect of vdW force on nonlinear natural frequencies of DWCNTs was investigated by Cigeroglu and Samandari [18] using describing function method with Galerkin method utilizing multiple trail functions. It is observed that utilization of multiple trial functions resulted in multiple nonlinear natural frequencies at the same amplitude of vibration. Similarly, same nonlinear natural frequency is observed for different vibration amplitudes.

Reviewing the literature on nonlinear vibrations of CNTs, authors found out that in all cases only simple linear boundary conditions are considered and solutions are restricted only to free vibration of uniform beams with hinged–hinged end conditions in consequence of limitations of approximate solutions such as Galerkin method which require knowledge on trial functions, or comparison functions, that satisfy all the boundary conditions of the system. Therefore, presenting a general formulation capable of predicting the vibrational behavior of CNTs under different boundary conditions is of high importance. It should be noted that the number of studies on vibrations of CNTs having different end conditions is rare and limited to linear systems. Recently, Ansari et al. [19] utilized finite element method (FEM) to investigate the nonlinear free vibration of DWCNTs in the presence of only geometric nonlinearity. Although classic FEMs can predict vibrational behavior of CNTs, they are disadvantaged in terms of computational time.

The differential quadrature method (DQM) is a well-developed numerical method for the quick solutions of linear and nonlinear partial differential equations. DQM developed by Bellman and Casti [20] is a discrete approach to directly solve the governing equations of various engineering problems. Different from conventional methods such as finite difference (FD) and finite element (FE) methods, DQM requires less grid points to obtain an acceptable accuracy. A comprehensive review on the DQM can be found in [21]. Owning to its efficiency and accuracy, DQM has the potential to be used in variety of application areas. Applicability of DQM for micro and nanoscale beams and tubes studied by Civalek et al. [22] for linear systems.

In this paper, nonlinear free vibrations of a curved double walled carbon nanotube (DWCNT) is investigated. A new solution approach, differential quadrature method, is proposed to discretize the partial differential equations of motion resulting in a system of nonlinear ordinary differential equations. Nonlinearities are due to large deflection of carbon nanotubes (geometric nonlinearity), and nonlinear interlayer van der Waals forces. The main advantage of DQM, in comparison to solution methods like variational approach [23], or Galerkin method, is its inherent simplicity in formulation, where different end conditions can be easily adopted. Using DQM and considering a harmonic solution in time, nonlinear differential equations of motion are converted into a set of nonlinear algebraic equations, which is solved by an iterative method. In the following section, equation of motion for DWCNTs is obtained and the basics of DQM are presented.

25.2 Modeling

Consider a DWCNT of length L, cross-sectional area A_k, area moment of inertia I_k, Young's modulus E, and density ρ embedded in an elastic medium having a stiffness per unit length of k as shown in Fig. 25.1. Assume that the transverse displacement of nanotubes is $w_k(x,t)$ where x and t are the spatial coordinate and the temporal variable. Equations of motion for free vibration of embedded curved DWCNTs considering geometric and vdW force nonlinearities is [18, 24–26].

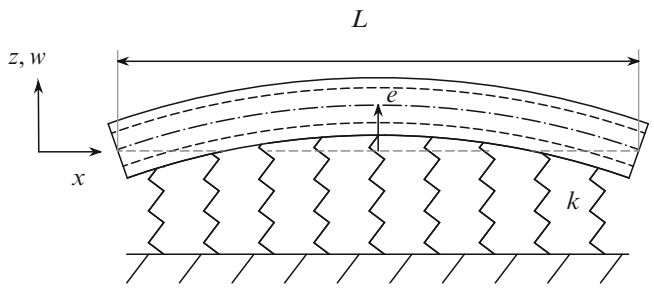

Fig. 25.1 Model of an embedded curved DWCNT

$$EI_i\frac{\partial^4 w_i}{\partial x^4}+\rho A_i\frac{\partial^2 w_i}{\partial t^2}=\frac{EA_i}{L}\int_0^L\left[\frac{\delta Z}{\delta x}\frac{\delta w_i}{\delta x}+\frac{1}{2}\left(\frac{\delta w_i}{\delta x}\right)^2\right]dx\cdot\left(\frac{\partial^2 w_i}{\partial x^2}+\frac{\partial^2 Z}{\partial x^2}\right)+p_1\left(w_o-w_i\right)+p_3\left(w_o-w_i\right)^3, \tag{25.1}$$

$$EI_o\frac{\partial^4 w_o}{\partial x^4}+\rho A_o\frac{\partial^2 w_o}{\partial t^2}+kw_o=\frac{EA_o}{L}\int_0^L\left[\frac{\delta Z}{\delta x}\frac{\delta w_o}{\delta x}+\frac{1}{2}\left(\frac{\delta w_o}{\delta x}\right)^2\right]dx\cdot\left(\frac{\partial^2 w_o}{\partial x^2}+\frac{\partial^2 Z}{\partial x^2}\right)-p_1\left(w_o-w_i\right)-p_3\left(w_o-w_i\right)^3, \tag{25.2}$$

where $Z(x)$ is the initial curvature (waviness) of cylindrical tubes. p_1 and p_3 are the coefficients of linear and nonlinear parts of vdW force, respectively. i and o refers for the inner and outer tubes, respectively. It is assumed that the waviness of tubes follow a sinusoidal initial curvature described by $Z(x)=e_0\cdot\sin(\pi x/L)$ [26], where e_0 is the amplitude of the initial waviness.

25.3 Generalized Differential Quadrature Method

The DQM estimates the derivatives of a function with respect to a spatial variable at a given discrete point by a weighted linear summation of function values at all the discrete points in the computational domain. For example, the mth derivative of a function $W_k(x)$ at the ith point, x_i, can be estimated by

$$W_k^{(m)}(x_i)=\sum_{j=1}^{N}c_{i,j}^{(m)}W_k(x_j),\quad i=1,2,\ldots,N \tag{25.3}$$

where $W_k^{(m)}(x_i)$ is the mth order derivative of $W_k(x)$ at point x_i, and N is the number of grid points utilized in discretization of the partial derivatives. $c_{i,j}^{(m)}(j=1,\ldots,N)$ are the weighting coefficients for the mth derivative estimation of the ith point, which can be pre-determined. In the generalized differential quadrature (GDQ) method [28], the global Lagrange interpolation polynomial is used to calculate the weighting coefficients, where Eq. (25.3) is considered to be exact for a test function as

$$g_i(x)=\frac{l(x)}{(x-x_j)l^{(1)}(x_j)},\quad j=1,2,\ldots,N, \tag{25.4}$$

where

$$l(x)=\prod_{k=1}^{N}(x-x_k),l^{(1)}(x_j)=\prod_{k=1,k\neq j}^{N}(x_j-x_k). \tag{25.5}$$

and $l^{(1)}(x)$ is the first derivative of Lagrange interpolating polynomial, $l(x)$. Thus, from the differentiation of Eq. (25.4) the weighting coefficients $c_{i,j}^{(1)}(i,j=1,2,\ldots,N)$ can be computed analytically as

$$c_{i,j}^{(1)}=\begin{cases}\frac{l^{(1)}(x_i)}{(x_i-x_j)l^{(1)}(x_j)} & \text{for } j\neq i\\ -\sum\limits_{j=1,j\neq i}^{N}c_{i,j}^{(1)} & \text{for } j=i\end{cases}. \tag{25.6}$$

The weighting coefficients for higher order derivatives can be found likewise. A recurrence relationship can be obtained for higher order derivatives as follows

$$c_{i,j}^{(m)}=\begin{cases}m\left(c_{i,j}^{(1)}c_{i,i}^{(m-1)}-\frac{c_{i,j}^{(m-1)}}{x_i-x_j}\right) & j\neq i\\ -\sum\limits_{j=1,j\neq i}^{N}c_{i,j}^{(m)} & j=i\end{cases}. \tag{25.7}$$

Since the positions of the sampling points plays a significant role in the accuracy of DQM, Chebyshev–Gauss–Lobatto quadrature points are used,

$$x_i=\frac{1}{2}\left[1-\cos\left(\frac{i-1}{N-1}\pi\right)\right]\quad \text{for} i=1,2,\ldots,N, \tag{25.8}$$

which results in minimum error.

25.3.1 Applying DQM

Assuming a separable solution as $w_k(x,t) = W_k(x)T(t)$ and considering a sinusoidal motion in time, the partial differential equation of motion given by Eqs. (25.1) and (25.2) can be rewritten as

$$EI_i\frac{d^4W_i}{dx^4} - \omega^2\rho A_iW_i = \frac{EA_i}{L}\int_0^L\left[\frac{dZ}{dx}\frac{dW_i}{dx} + \frac{1}{2}\left(\frac{dW_i}{dx}\right)^2\right]dx\cdot\left(\frac{d^2W_i}{dx^2} + \frac{d^2Z}{dx^2}\right) + p_1\left(W_o - W_i\right) + p_3\left(W_o - W_i\right)^3, \tag{25.9}$$

$$EI_o\frac{d^4W_o}{dx^4} - \omega^2\rho A_oW_o + kW_o = \frac{EA_o}{L}\int_0^L\left[\frac{dZ}{dx}\frac{dW_o}{dx} + \frac{1}{2}\left(\frac{dW_o}{dx}\right)^2\right]dx\cdot\left(\frac{d^2W_o}{dx^2} + \frac{\partial^2Z}{\partial x^2}\right) - p_1\left(W_o - W_i\right) - p_3\left(W_o - W_i\right)^3. \tag{25.10}$$

By applying the GDQ method, the discrete nonlinear set of equation of governing differential equations at the mth given point can be expressed as

$$EI_i\sum_{j=1}^{N}c_{m,j}{}^{(4)}{}_{m,j}W_i - \omega^2\rho A_{im}W_i = \frac{EA_i}{L}\left\{\sum_{n=1}^{N}d_n\sum_{j=1}^{N}\left.\frac{dZ}{dx}\right|_{x=x_n}c^{(1)}_{n,jn,j}W_i + \frac{1}{2}\sum_{n=1}^{N}d_n\sum_{j=1}^{N}c_{n,jn.j}W_i\right.$$
$$\left.\cdot\left(\sum_{j=1}^{N}c^{(2)}_{m,jm}W_i + \left.\frac{d^2Z}{dx^2}\right|_{x=x_n}\right) + c_1\left({}_mW_o - {}_mW_i\right) + c_3\left({}_mW_o - {}_m W_i\right)^3, \tag{25.11}$$

$$EI_o\sum_{j=1}^{N}c^{(4)}_{m,jm,j}W_o - \omega^2\rho A_{im}W_o = \frac{EA_i}{L}\left\{\sum_{n=1}^{N}d_n\sum_{j=1}^{N}\left.\frac{dZ}{dx}\right|_{x=x_n}c^{(1)}_{n,jn,j}W_o + \frac{1}{2}\sum_{n=1}^{N}d_n\sum_{j=1}^{N}c_{n,jn.j}W_o\right\}$$
$$\cdot\left(\sum_{j=1}^{N}c^{(2)}_{m,jm}W_o + \left.\frac{d^2Z}{dx^2}\right|_{x=x_n}\right) - c_1\left({}_mW_o - {}_mW_i\right) - c_3\left({}_mW_o - {}_mW_i\right)^3. \tag{25.12}$$

which can be written in matrix form as

$$(\mathbf{K_L}+\mathbf{K_{NL}})\cdot\mathbf{x} - \omega^2\mathbf{M}\cdot\mathbf{x} = \mathbf{0}, \tag{25.13}$$

where $\mathbf{x}$ denotes the unknown dynamic displacement vector defined as

$$\mathbf{x} = \{{}_1W_{i2}W_i\cdots{}_NW_i|{}_1W_{o2}W_o\cdots{}_NW_o\}^T, \tag{25.14}$$

and $\mathbf{M}, \mathbf{K_L}$ and $\mathbf{K_{NL}}$ represent mass, linear stiffness and nonlinear stiffness matrices of the system, respectively.

In the present study, three common sets of boundary conditions namely as hinged–hinged (H–H), clamped–hinged (C–H), and clamped–clamped (C–C) are investigated. Using the GDQ method, the discretized counterparts of different boundary conditions (BCs) at the end points become as
hinged ends:

$$w_k(x_{end},t) = 0 \Rightarrow_{x_{end}} W_k = 0, \tag{25.15}$$

$$\left.\frac{d^2w_k}{dx^2}\right|_{x=x_{end}} = 0 \Rightarrow \sum_{j=1}^{N}c^{(2)}_{x_{end},jj}W_k = 0. \tag{25.16}$$

clamped ends:

$$w_k(x_{end},t) = 0 \Rightarrow_{x_{end}} W_k = 0, \tag{25.17}$$

$$\left.\frac{dw_k}{dx^2}\right|_{x=x_{end}} = 0 \Rightarrow \sum_{j=1}^{N}c^{(1)}_{x_{end},jj}W_k = 0. \tag{25.18}$$

BCs can also be expressed in the matrix form as

$$\mathbf{K_B} \cdot \mathbf{x_s} + \mathbf{K_S} \cdot \mathbf{x}^* = \mathbf{0}. \tag{25.19}$$

where $\mathbf{x_s} = \{{}_1W_i, {}_2W_i, {}_{N-1}W_i, {}_NW_i, {}_1W_o, {}_2W_o, {}_{N-1}W_o, {}_NW_o\}^T$ and $\mathbf{x} = \{{}_3W_{i4}W_i \cdots {}_{N-2}W_i | {}_3W_{o4}W_o \cdots {}_{N-2}W_o\}^T$. $\mathbf{K_B}$ and $\mathbf{K_S}$ are 8×8 and $8 \times (2N-8)$ matrices, respectively. Following a similar approach Eq. (25.13) can be written as

$$\mathbf{K_D} \cdot \mathbf{x_s} + (\mathbf{K_L^*} + \mathbf{K_{NL}^*}) \cdot \mathbf{x}^* - \omega^2 \mathbf{M}^* \cdot \mathbf{x}^* = \mathbf{0}. \tag{25.20}$$

Coupling Eqs. (25.19) and (25.20), equation of motion of the system can be written as

$$\left\{(\mathbf{K_L^*} + \mathbf{K_{NL}^*}) - \mathbf{K_D}\mathbf{K_B^{-1}}\mathbf{K_S}\right\} \cdot \mathbf{x}^* = \omega^2 \mathbf{M}^* \cdot \mathbf{x}^*, \tag{25.21}$$

where $\mathbf{K_L^*}$, $\mathbf{K_{NL}^*}$, and $\mathbf{M}^*$ are $2N-8 \times 2N-8$ matrices representing the linear stiffness matrix, nonlinear stiffness matrix, and mass matrix, respectively. It is worth noting that $\mathbf{K_{NL}^*}$is a displacement dependant matrix.

25.4 Solution Method

The set of resulting nonlinear algebraic equations can be solved numerically by using Newton's method with homotopy continuation or arc-length continuation, details of which can be found in [18]. Another solution approach commonly used by a number of researchers is a direct iterative process by using eigenvalue solvers. However, based on author's knowledge [18] on similar systems, the direct iterative process cannot be applied individually and it requires modifications. For example, because of vdW force nonlinearity in-phase natural frequencies change slightly with respect to the maximum vibration amplitude; whereas, out-of-phase natural frequencies increase significantly as the maximum vibration amplitude increases [18]. Therefore, it is possible for system natural frequencies to cross each other, for instance, system can vibrate in the second mode (out-of-phase mode) with a nonlinear natural frequency higher than the nonlinear natural frequency of the third mode (in-phase mode) as vibration amplitude increases. For this reason, the modal assurance criterion is implemented.

The modal assurance criterion is outlined as a scalar constant relating the degree of consistency (linearity) between two vectors as follows:

$$MAC = \frac{\left|\{\psi_A\}^T \{\psi_x\}\right|^2}{\left|\{\psi_A\}^T \{\psi_A\}\right| \left|\{\psi_x\}^T \{\psi_x\}\right|}, \tag{25.22}$$

where $\{\psi_A\}$ and $\{\psi_x\}$ are two vectors that are compared with each other. The modal assurance criterion takes values between 0 and 1, where 0 indicates two independent vectors and 1 indicates identical vectors. Thus, if the modal vectors under investigation truly express a consistent, linear relationship, the modal assurance criterion should approach unity. This fact is utilized in finding the system eigenvalues.

The nonlinear set of equations is solved through a modified direct iterative process as given below:

- Step 1: By neglecting the nonlinear stiffness matrix, $\mathbf{K_{NL}^*}$, a linear eigenvalue problem is solved and the associated eigenvector is calculated from Eq. (25.21). The eigenvector is then appropriately scaled up such that the maximum transverse displacement of the outertube is equal to a given vibration amplitude of outertube, ${}_oW_{\max}$.
- Step 2: Calculated scaled eigenvectors are used to determine, $\mathbf{K_{NL}^*}$, and new eigenvalues and eigenvectors are calculated from the updated eigensystem. MAC is employed to select the correct eigenvalue and its related eigenvector. It is worth noting that for the first step, linear system eigenvector is considered as the reference mode shape and for higher steps eigenvector of the previous solution is considered as the reference mode shape.
- Step 3: The eigenvector is scaled up again and step 2 is repeated until the relative error between the given vibration amplitude and the maximum transverse displacement of the outertube, ${}_oW_{\max}$, is within 0.01 %.

25.5 Results

Table 25.1 compares the linear fundamental in-phase and out-of-phase natural frequencies of H–H, C–H and C–C DWCNT with different number of grid points, N in the differential quadrature method. It is worth noting that for the in-phase mode, inner and outer tubes move in the same direction; whereas for the out-of-phase mode, they vibrate in opposite directions.

Table 25.1 Effect of the number of grid points N on the linear fundamental frequencies of the DWCNTs with different boundary conditions

N	–	H–H (THz)	C–H (THz)	C–C (THz)
10	In-phase	0.46727276	0.72958103	1.05775816
	Out-of-phase	7.67867366	7.94739767	7.92494566
11	In-phase	0.46728898	0.72963714	1.05780658
	Out-of-phase	7.88518860	7.89901304	7.92495020
12	In-phase	0.46728882	0.72963963	1.05780510
	Out-of-phase	7.88518860	7.89901320	7.92495006
13	In-phase	0.46728867	0.72963869	1.05780414
	Out-of-phase	7.88518859	7.89901314	7.92494997
14	In-phase	0.46728867	0.72963868	1.05780415
	Out-of-phase	7.88518859	7.89901314	7.92494998
20	In-phase	0.46728868	0.72963869	1.05780416
	Out-of-phase	7.88518859	7.89901314	7.92494998

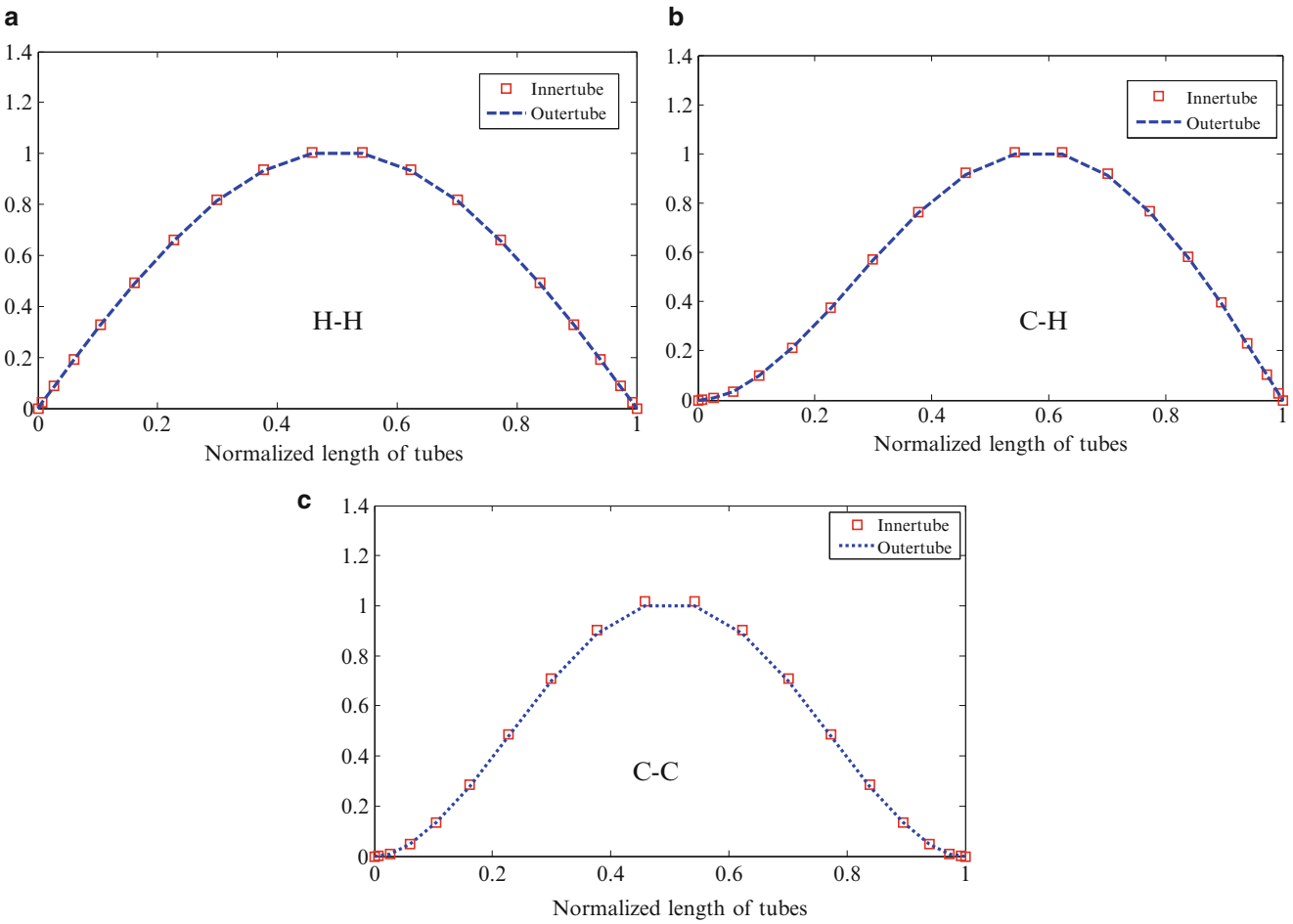

Fig. 25.2 Fundamental in-phase mode shape of a DWCNT (**a**) hinged–hinged, (**b**) clamped–hinged, and (**c**) clamped–clamped

The parameters used in this example are: innertube diameter, $d_i = 0.7\,\text{nm}$, outertube diameter, $d_0 = 1.4\,\text{nm}$, Young's modulus,$E = 1\,\text{TPa}$, Poisson's ratio, $\nu = 0.25$, and the thickness of each tube, $t = 0.34\,\text{nm}$. Table 25.1 illustrates that the accuracy of the results is improved as the number of grid points, N, increases. For $N \geq 14$, the improvement in the natural frequencies obtained is insignificant; hence, $N = 14$ is used in all of the numerical calculations. Also, the first three in-phase mode shapes of the system are given in Fig. 25.2 for different end conditions.

In Table 25.2, the fundamental natural frequency of the linear system with H–H end conditions are compared with the analytical solution obtained and the results given in literature. It can be seen that the results of DQM $(N = 14)$ and analytical solution are in agreement considering eight digits after the decimal point.

Table 25.2 Fundamental linear natural frequencies of a simply supported DWCNT

Natural frequencies	In phase	Out-of-phase
Ref. [18]	0.4673	7.8852
Ref. [17]	0.46	7.71
Analytical solution	0.46728868	7.88518860
DQM (N=14)	0.46728868	7.88518860

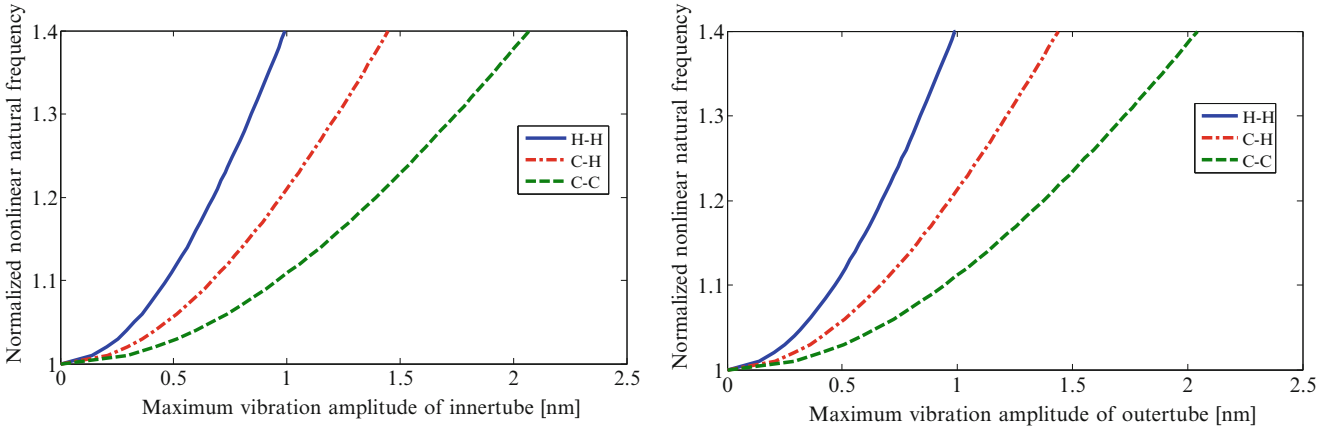

Fig. 25.3 Variation of normalized nonlinear natural frequency of inner and outer tubes vibrating in the first in-phase mode for different end conditions ($e_0 = 0$)

In the following section, the effect of nonlinearities on the first fundamental natural frequency of a curved DWCNT is investigated. First, the effect of geometric nonlinearity and initial curvature on fundamental natural frequency of the DWCNT is studied by presenting the variation of normalized nonlinear natural frequency with respect to the maximum vibration amplitude. Later, the same study is repeated considering the vdW force nonlinearity together with the geometric nonlinearity. Finally, considering both nonlinearities, the effect of length ratio (slenderness ratio) and medium stiffness on the nonlinear natural frequency of the curved DWCNTs is investigated. Meanwhile, the effects of different end conditions on natural frequencies are as well studied. In order to present the results in a proper form, the nonlinear natural frequency is normalized with respect to the corresponding linear natural frequency of the DWCNT.

25.5.1 Geometric Nonlinearity

In Fig. 25.3, the variation of the normalized nonlinear natural frequency of the first in-phase vibration mode of a DWCNT is given for different types of boundary conditions in the presence of only geometric nonlinearity. A hardening stiffness behavior is observed for different types of boundaries, i.e., the nonlinear natural frequency increases as the vibration amplitude increases. Furthermore, it is observed that although the clamped–clamped DWCNT have the highest fundamental linear natural frequencies, at the same maximum vibration amplitude, it has the lowest normalized nonlinear natural frequency. This is an expected result, because the end supports are the strongest for the clamped–clamped DWCNT and the weakest for the hinged–hinged case.

25.5.2 Effect of Initial Curvature on Fundamental Natural Frequencies of DWCNT

In Fig. 25.4, variation of fundamental nonlinear natural frequencies is given for different values of initial curvature for a hinged–hinged DWCNT. It is observed that the nonlinear natural frequency decreases as waviness increases and tends to approach to the linear one.

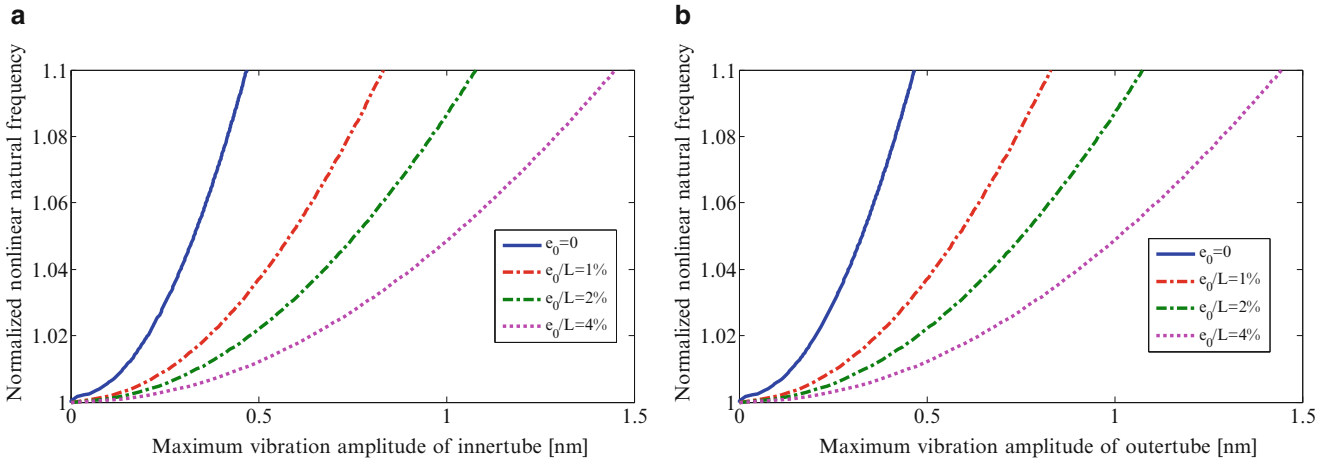

Fig. 25.4 Effect of initial curvature on variation of normalized nonlinear natural frequency of inner and outer tubes vibrating in the first in-phase mode

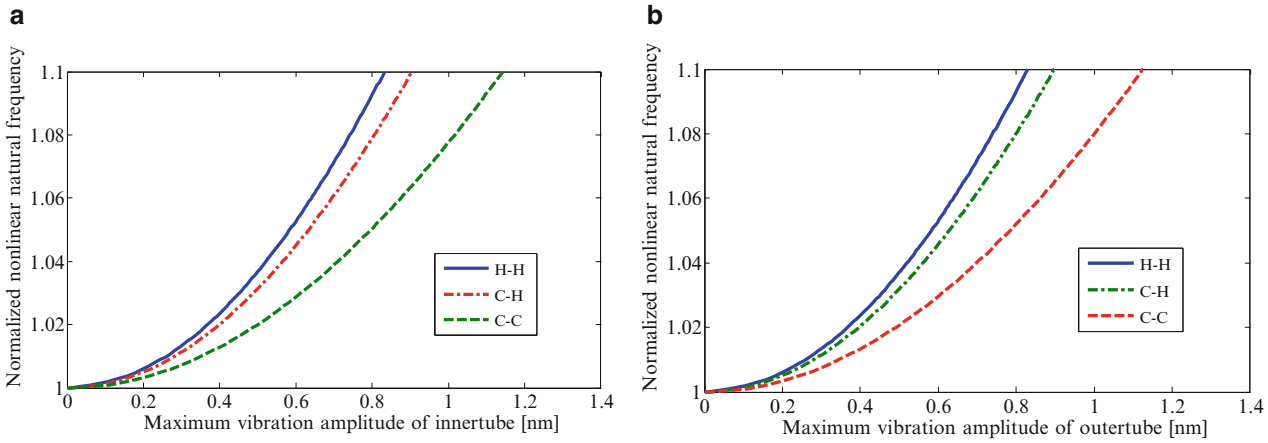

Fig. 25.5 Variation of normalized nonlinear natural frequency of inner and outer tubes vibrating in the first in-phase mode for different end conditions in the presence of both vdW force and geometric nonlinearities ($e_0 = 0$)

25.5.3 Van der Waals Force Nonlinearity Together with Geometric Nonlinearity

In Fig. 25.5, variation of normalized nonlinear natural frequency for the first in-phase vibration mode is given under the effect of different end conditions. Results show that for the first in-phase vibration mode, considering the vdW force nonlinearity in addition to geometric nonlinearity does not change the vibratory behavior of the DWCNT. Since vdW force nonlinearity depends on the relative motion between the inner and outer tubes, in case of in-phase vibration modes, this difference changes slightly during free vibration. As a result of this, the nonlinear coupling terms of vdW force are not strong enough to alter system response and the natural frequency are mainly changed by geometric nonlinearity. It should be noted if coefficients of vdW force nonlinearity are selected arbitrarily, it may be possible to see its effect in the solution. However, since these coefficients are obtained the dimension of the DWCNT under study, the resulting vdW forces are not significant compared to geometric nonlinearity.

25.5.4 Effect of Length Ratio, Slenderness Ratio

Figure 25.6 presents the effect of length ratio (slenderness ratio), L/D, on the variation of nonlinear natural frequency of DWCNT with different boundary conditions vibrating in the first in-phase vibration mode. In order to present the results in a clear form, vibration amplitudes are normalized respect to the length of the tubes. Results show that normalized

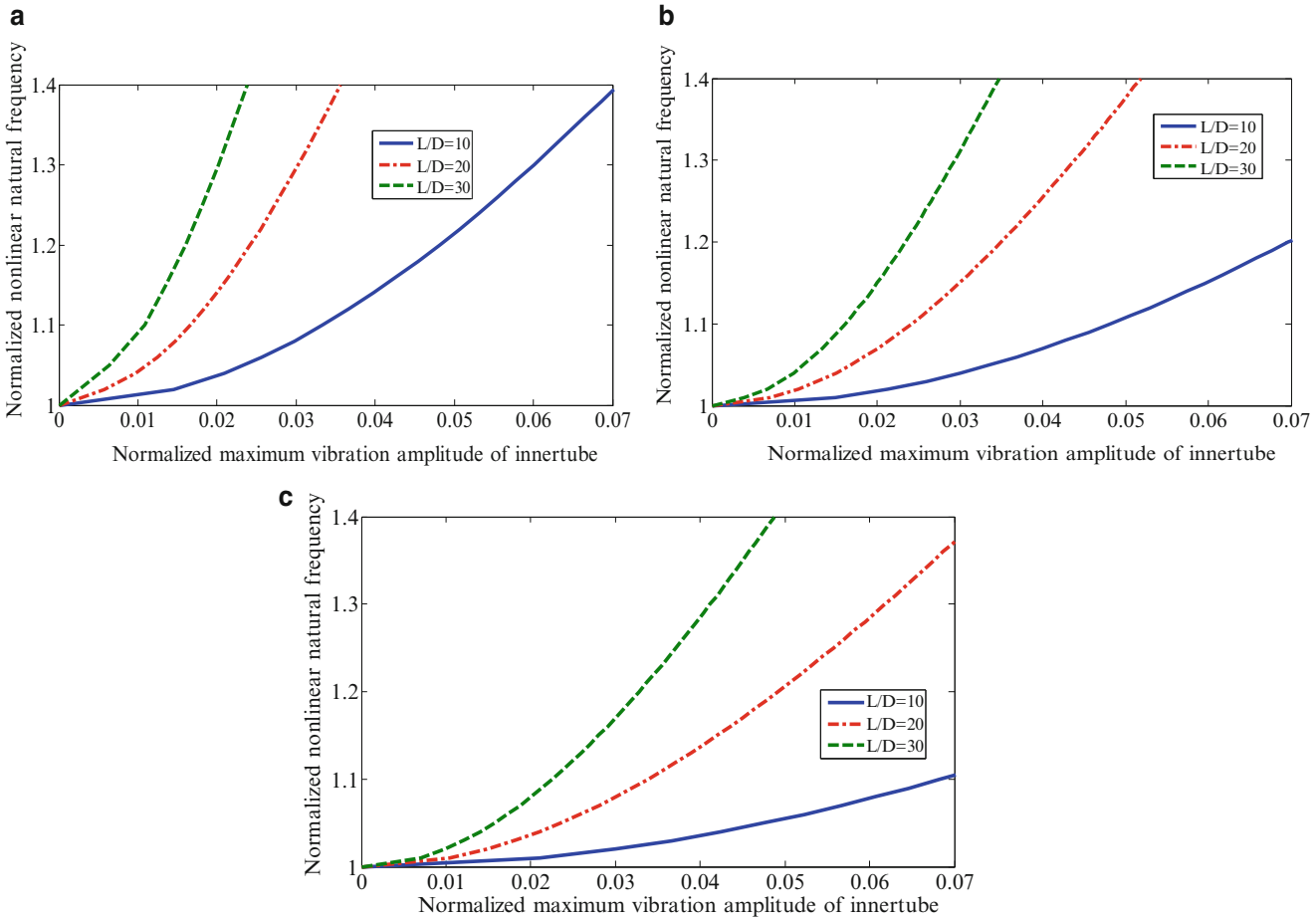

Fig. 25.6 Effect of length ratio on variation of nonlinear natural frequency: (**a**) hinged–hinged (**b**), clamped–hinged, and (**c**) clamped–clamped ($e_0 = 0$)

Table 25.3 Effect of medium stiffness on fundamental linear natural frequency of DWCNT

K	–	H–H (THz)	C–H (THz)	C–C (THz)
0	In-phase	0.46728867	0.72963868	1.05780415
	Out-of-phase	7.88518859	7.89901314	7.92494998
10^8	In-phase	0.48754131	0.74273097	1.06682286
	Out-of-phase	7.88580598	7.89963332	7.92557540
10^9	In-phase	0.64145384	0.85138957	1.14467717
	Out-of-phase	7.89137769	7.90523017	7.93121951
10^{10}	In-phase	1.45657025	1.55864030	1.73324935
	Out-of-phase	7.94861193	7.96271890	7.98918639

nonlinear frequency increases as the slenderness ratio increases, i.e. at the same normalized vibration amplitude, slender tubes have higher normalized nonlinear natural frequency. In other words, it can be seen that in order to reach the same normalized nonlinear natural frequency, clamped–hinged DWCNT should be deflected more than hinged–hinged DWCNT, while clamped–clamped DWCNT should be deflected more than both of them.

25.5.5 Effect of Medium Stiffness

Table 25.3 shows the effect of medium stiffness on fundamental linear natural frequency of DWCNT with hinged–hinged, clamped–hinged, and clamped–clamped end conditions. It can be seen that linear natural frequency of clamped–clamped DWCNT changes slightly as medium stiffness increases. Furthermore, it is observed that in-phase natural frequency is more sensitive to medium stiffness than out-of-phase natural frequency.

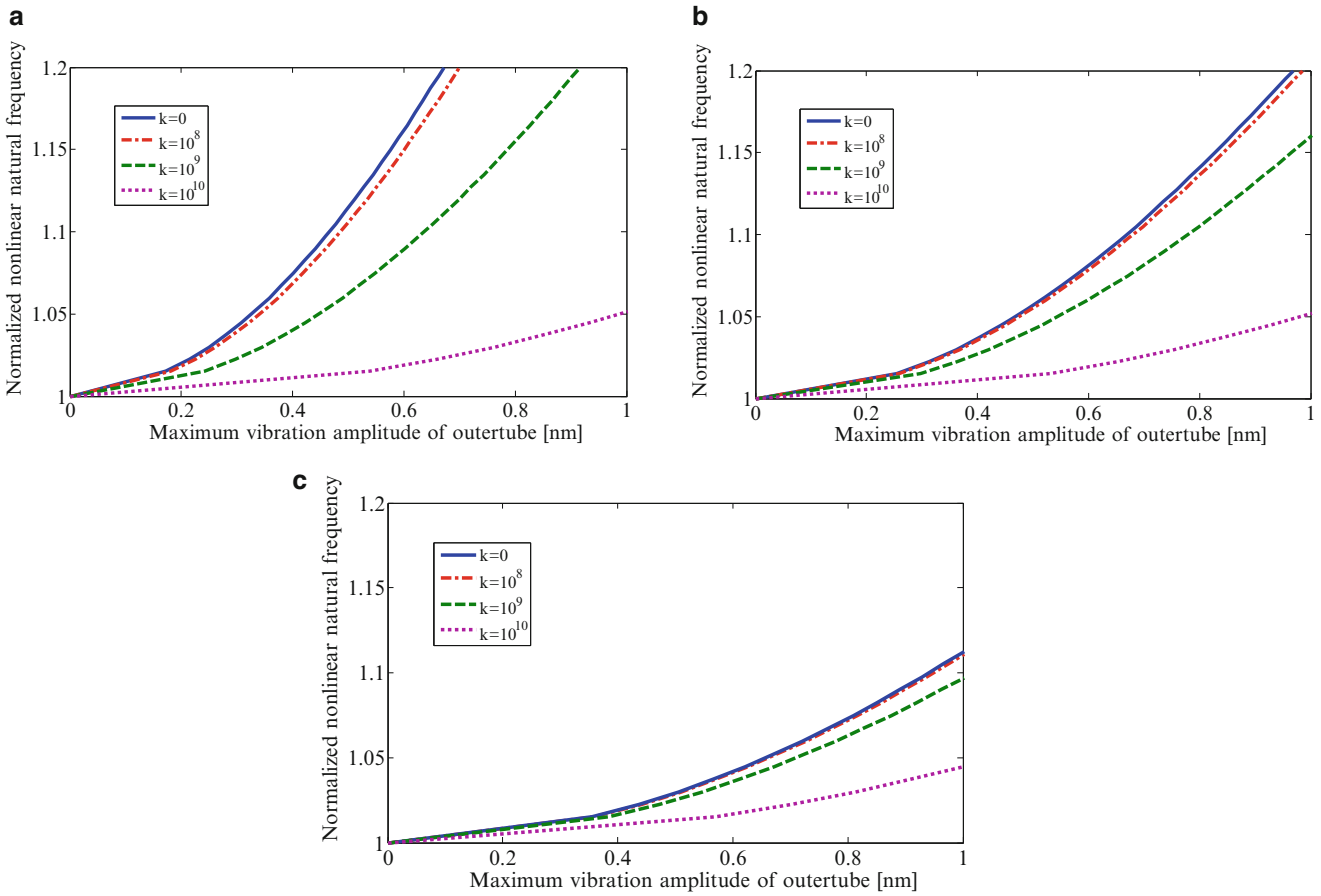

Fig. 25.7 Effect of medium stiffness on the nonlinear fundamental natural frequency of DWCNT (**a**) hinged–hinged, (**b**) clamped–hinged, and (**c**) clamped–clamped ($e_0/L = 1\,\%$)

Figure 25.7 shows the effect of the medium stiffness, k, on the variation of normalized nonlinear frequency versus maximum vibration amplitude for the curved DWCNT with three different end conditions. It is observed that with an increase in the medium stiffness, k, the normalized nonlinear frequency tends to approach to the linear one for all type of end conditions. It is seen that for relatively small value of medium stiffness ($k \leq 10^8$) variation of normalized nonlinear natural frequency slightly changes; whereas, for higher stiffness values, a small change in medium stiffness results in a remarkable changes in the normalized nonlinear natural frequency. This shows that the effect of geometric nonlinearity becomes negligible in the presence of medium with sufficiently large stiffness

25.6 Conclusion

In the present study nonlinear natural frequency of a curved DWCNT with different boundary condition is studied by using DQM, where geometric and vdW force nonlinearities are considered. Application of DQM made it possible to study the effect of different end conditions on the nonlinear natural frequencies of the curved DWCNT. It is worth noting that solution methods such as Galerkin method requires different trial functions for different end conditions; hence, they are not practical for the analysis of effect of end conditions; whereas, the DQM can be applied to any type end condition with minimal effort..

Applying DQM, a hardening behavior is observed for the curved DWCNT in the presence of geometric nonlinearity. Moreover, it is observed that as end supports of tubes become stronger, variation of the normalized nonlinear natural frequency decreases. A similar behavior is detected for the case where vdW force nonlinearity in addition to geometric nonlinearity is considered. Furthermore, the effect of initial waviness on the normalized nonlinear natural frequency of the curved DWCNT is studied. It is observed that as the initial curvature increases, normalized nonlinear natural frequency decreases. Finally, the effect of slenderness ratio and medium stiffness is as well studied. Results show that for the same

normalized vibration amplitude, slender tubes have higher normalized nonlinear natural frequency. Moreover, it is observed that as the medium stiffness increases, normalized nonlinear natural frequencies decrease and approach to the linear one for all end conditions considered in the study.

References

1. Iijima S (1991) Helical microtubules of graphitic carbon. Nature 354(6348):56–58
2. Kim DH, Kim CD, Lee HR (2004) Effects of the ion irradiation of screen-printed carbon nanotubes for use in field emission display applications. Carbon 42(8–9):1807–1812
3. Pumera M, Merkoci A, Alegret S (2006) Carbon nanotube-epoxy composites for electrochemical sensing. Sens Actuator B Chem 113(2):617–622
4. Huang YP, Tangpong XW (2010) A distributed friction model for energy dissipation in carbon nanotube-based composites. Commun Nonlinear Sci Numer Simul 15(12):4171–4180
5. Rahmat M, Hubert P (2011) Carbon nanotube-polymer interactions in nanocomposites: a review. Compos Sci Technol 72(1):72–84
6. Chen WX, Tu JP, Wang LY, Gan HY, Xu ZD, Zhang XB (2003) Tribological application of carbon nanotubes in a metal-based composite coating and composites. Carbon 41(2):215–222
7. Cao GX, Chen X, Kysar JW (2006) Thermal vibration and apparent thermal contraction of single-walled carbon nanotubes. J Mech Phys Solids 54(6):1206–1236
8. Fu YM, Hong JW, Wang XQ (2006) Analysis of nonlinear vibration for embedded carbon nanotubes. J Sound Vib 296(4–5):746–756
9. Rezaee M, Fekrmandi H (2010) Analysis of free nonlinear vibration behavior for curved embedded carbon nanotubes on elastic foundation. In: Proceedings of the ASME 10th biennial conference on engineering systems design and analysis, Istanbul, vol 5, pp 615–621
10. Yoon J, Ru CQ, Mioduchowski A (2003) Vibration of an embedded multiwall carbon nanotube. Compos Sci Technol 63(11):1533–1542
11. Li R, Kardomateas GA (2007) Vibration characteristics of multiwalled carbon nanotubes embedded in elastic media by a nonlocal elastic shell model. J Appl Mech 74(6):1087–1094
12. Yan Y, Zhang LX, Wang WQ (2008) Dynamical mode transitions of simply supported double-walled carbon nanotubes based on an elastic shell model. J Appl Phys 103(11):113523
13. Ke LL, Xiang Y, Yang J, Kitipornchai S (2009) Nonlinear free vibration of embedded double-walled carbon nanotubes based on nonlocal Timoshenko beam theory. Comput Mater Sci 47(2):409–417
14. Jiang LY, Huang Y, Jiang H, Ravichandran G, Gao H, Hwang KC, Liu B (2006) A cohesive law for carbon nanotube/polymer interfaces based on the van der Waals force. J Mech Phys Solids 54(11):2436–2452
15. Lu WB, Wu J, Jiang LY, Huang Y, Hwang KC, Liu B (2007) A cohesive law for multi-wall carbon nanotubes. Philos Mag 87(14–15):2221–2232
16. Lu WB, Wu J, Song J, Hwang KC, Jiang LY, Huang Y (2008) A cohesive law for interfaces between multi-wall carbon nanotubes and polymers due to the van der Waals interactions. Comput Method Appl M 197(41–42):3261–3267
17. Xu, K. Y., Guo, X. N., and Ru, C. Q., 2006, Vibration of a double-walled carbon nanotube aroused by nonlinear intertube van der Waals forces, Journal of Applied Physics, 99(6):1–7
18. Cigeroglu E, Samandari H (2012) Nonlinear free vibration of double walled carbon nanotubes by using describing function method with multiple trial functions. Physica E 46:160–173
19. Ansari R, Hemmatnezhad M (2012) Nonlinear finite element analysis for vibrations of double-walled carbon nanotubes. Nonlinear Dyn 67(1):373–383
20. Bellman R, Casti J (1971) Differential quadrature and long-term integration. J Math Anal Appl 34(2):235–238
21. Bert CW, Malik M (1996) Free vibration analysis of thin cylindrical shells by the differential quadrature method. J Press Vessel Technol ASME 118(1):1–12
22. Civalek O, Demir C, Akgoz B (2010) Free vibration and bending analyses of cantilever microtubules based on nonlocal continuum model. Math Comput Appl 15(2):289–298
23. Ansari R, Hemmatnezhad M (2011) Nonlinear vibrations of embedded multi-walled carbon nanotubes using a variational approach. Math Comput Model 53(5–6):927–938
24. Nayfeh AH, Balachandran B (1995) Applied nonlinear dynamics: analytical, computational, and experimental methods. Wiley, New York
25. El-Mously M (2003) A Timoshenko-beam-on-Pasternak-foundation analogy for cylindrical shells. J Sound Vib 261(4):635–652
26. Mehdipour I, Barari A, Kimiaeifar A, Domairry G (2012) Vibrational analysis of curved single-walled carbon nanotube on a Pasternak elastic foundation. Adv Eng Softw 48:1–5
27. Mayoof FN, Hawwa MA (2009) Chaotic behavior of a curved carbon nanotube under harmonic excitation. Chaos Soliton Fract 42(3):1860–1867
28. Shu C, Richards BE (1992) Application of generalized differential quadrature to solve 2-dimensional incompressible Navier-Stokes equations. Int J Numer Meth Fluids 15(7):791–798

Chapter 26
Reanalysis of Large Finite Element Models with Structural Nonlinearities

Burcu Sayin and Ender Cigeroglu

Abstract Structural modification methods are widely used for design optimization purposes, especially for systems having large number of degrees of freedoms. By the use of these methods, modifications can be adapted to the system by avoiding reevaluation of dynamic characteristics of the modified system. In this paper, a method is proposed for the reanalysis of large finite element models having structural nonlinearities in order to reflect design variations. The finite element model (FEM) of the structure is divided into two parts representing the modified and unmodified sections. The modified part characterizes the sections where design variations are executed. Harmonic balance method (HBM) with modal superposition approach is used to convert the resulting nonlinear differential equations of motion into nonlinear algebraic equations. The modal information used in the nonlinear analysis is obtained from a new structural modification method with additional degrees of freedom details of which are given in another paper. Since the proposed method uses a model superposition approach, it can be applied to systems having large number of nonlinear elements. The proposed method is demonstrated on an example cantilever beam with nonlinear elements attached and the effect of design variations on the nonlinear response of the system is studied.

Keywords Structural modification • Reanalysis of nonlinear systems • Harmonic balance method • Modal superposition • Cubic stiffness nonlinearity

26.1 Introduction

Structural modification techniques are commonly used in the design optimization of an already constructed structure. These methods are very reliable and accurate even when working with large scale finite element models (FEM). Since it is time consuming to adapt every change to the system and reanalysis for each step during design process; due to their high accuracy and time shortening capabilities, structural modification methods are widely preferred. If the modification is based on determination of the dynamic characteristics of a modified system, it is referred as reanalysis or direct structural modification. Direct structural modification is studied by Crowley et al. [1] using experimentally obtained FRFs of the original structure. On the other hand, it is called inverse structural modification when the modification on an already constructed structure is to be decided, which is mostly applied in order to eliminate vibration problems. Kyprianou et al. [2,3], Mottershead et al. [4,5] and Park et al. [6] work on inverse structural modifications. Structural modification methods can be applied either on systems having additional degrees of freedoms or not. Sherman-Morrison [7] and Woodberry [8] formulas are utilized for systems without additional degrees of freedoms. These methods find dynamic matrix of the modified system by updating the dynamic matrix of the original system. Ozguven [9] proposed a general method, matrix inversion method, for structural modification problems with or without additional degrees of freedoms in the modified structures. This method is an FRF based method which obtains FRF of the modified structure by using FRF of the original structure and dynamic structural modification matrix of the modifying structure. Sanliturk [10] presented a new method based on matrix inversion method combined with Sherman-Morrison formula and Woodberry formula for systems without additional degrees of freedoms. Matrix inversion

B. Sayin • E. Cigeroglu (✉)
Department of Mechanical Engineering, Middle East Technical University, 06800, Ankara, Turkey
e-mail: e150121@metu.edu.tr; ender@metu.edu.tr

G. Kerschen et al. (eds.), *Topics in Nonlinear Dynamics, Volume 1: Proceedings of the 31st IMAC, A Conference on Structural Dynamics, 2013*, Conference Proceedings of the Society for Experimental Mechanics Series 35,
DOI 10.1007/978-1-4614-6570-6_26,

method is also studied by Koksal et al. [11] where power series expansion is utilized in order to avoid matrix inversion. For distributed modifications, D'Ambrogio and Sestieri [12] developed a modeling approach for systems without additional degrees of freedoms.

Modifications can be applied to linear systems as well as nonlinear systems. In this paper, structures having nonlinearities either in the original or in the modifying parts are considered. In order the perform reanalysis of the structure, a new structural modification method developed by Sayin and Cigeroglu [13] is used. With the use of this method, modal information of the modified structure can be obtained by considering the modal information of the unmodified part and system matrices of the modifying part, which are later used in the nonlinear reanalysis for design optimizations.

In this study, the proposed method is first applied to a lumped mass parameter model, where the nonlinearities are considered either in the unmodified part or in the modifying part. After demonstrating the proposed method on a simple lumped parameter model, it is applied on a FEM. For this purpose, FEM of a cantilever beam with attached nonlinear elements is utilized. Effect of number of modes used in the structural modification method on the nonlinear response of the structure is studied and the accuracy of the results is investigated by utilizing the modal information obtained from a commercial FEM software, ANSYS.

26.2 Harmonic Balance Method with Modal Superposition

For the solutions of nonlinear systems, there exist time domain methods as well as frequency domain methods. Harmonic balance method (HBM) is a frequency domain method which is used in this work in order to linearize the nonlinearities. Cigeroglu et al. [14–16] proposed a model superposition method coupled with harmonic balance method, which becomes significantly useful if the number of nonlinear elements is large. Equation of motion of a nonlinear system with structural damping can be written as follows

$$[M]\{\ddot{x}(t)\} + i[H]\{x(t)\} + [K]\{x(t)\} + f_N(\{x(t)\}) = \{f(t)\}, \tag{26.1}$$

where $[M]$, $[H]$, and $[K]$ are the mass, structural damping and stiffness matrices and $\{x(t)\}$ is the response vector of the system. $f_N(\{x(t)\})$ is the nonlinear forcing matrix.

In this method, the response is written in terms of the mode shapes of the linear system as follows by assuming harmonic motion

$$\{x(t)\} = \sum_{r=1}^{N_m} a_r \{\phi_r\} e^{i\omega t} = [\phi]\{a\} e^{i\omega t}, \tag{26.2}$$

where N_m is the number of modes, $[\phi]$ is the mode shape matrix of the linear system. a_r is the complex coefficient of the r^{th} mode shape, $\{\phi_r\}$.

Substituting Eqn. (26.2) into (26.1) and pre-multiplying by $[\phi]^T$ results in

$$-\omega^2 [\phi]^T [M][\phi]\{a\} + [\phi]^T (i[H] + [K])[\phi]\{a\} + [\phi]^T \{F_N\} = [\phi]^T \{F\}. \tag{26.3}$$

Assuming proportional damping and $[\phi]$ to be mass normalized, Eq. (26.3) becomes:

$$\left[(1 + i\gamma)[\Omega] - \omega^2 [I]\right]\{a\} + [\phi]^T \{F_N\} = [\phi]^T \{F\}, \tag{26.4}$$

where γ is the loss factor, $[I]$ is the identity matrix and

$$[\Omega] = \begin{bmatrix} \omega_1^2 & 0 & 0 \\ 0 & \ddots & 0 \\ 0 & 0 & \omega_r^2 \end{bmatrix}, \tag{26.5}$$

where ω_r is the r^{th} natural frequency of the linear system.

26.2.1 Cubic Stiffness Nonlinearity

In this study, as a nonlinear element cubic stiffness is considered, for which the nonlinear force can be written as

$$F = k_c \cdot x^3, \tag{26.6}$$

where k_c is the coefficient of cubic stiffness nonlinearity. Assuming a single harmonic motion as

$$x = X_s \sin(\omega t) + X_c \cos(\omega t), \tag{26.7}$$

Nonlinear forcing can be written as follows

$$F_n = F_{ns} \sin(\omega t) + F_{nc} \cos(\omega t), \tag{26.8}$$

$$F_{ns} = \frac{1}{\pi} \int_0^{2\pi} k_c (X_s \sin(\theta) + X_c \cos(\theta))^3 \sin(\theta) d\theta = \frac{3}{4} k_c (X_s^3 + X_c^2 X_s), \tag{26.9}$$

$$F_{nc} = \frac{1}{\pi} \int_0^{2\pi} k_c (X_s \sin(\theta) + X_c \cos(\theta))^3 \cos(\theta) d\theta = \frac{3}{4} k_c (X_c^3 + X_s^2 X_c), \tag{26.10}$$

where $\theta = \omega t$. Hence, the nonlinear internal forcing becomes

$$F_n = \frac{3}{4} k_c \left(\left(X_s^3 + X_c^2 X_s \right) \sin(\omega t) + \left(X_c^3 + X_s^2 X_c \right) \cos(\omega t) \right). \tag{26.11}$$

26.3 Structural Modification Method

It is possible to consider the nonlinearities either included in the unmodified structure or in the modifying part. Structural modification method developed in [13] provides the modal data of the modified structure without employing the modal analysis to the whole (modified) structure. It uses the modal data of the original structure and mass and stiffness matrices of the modifying part as inputs. After finding the modal data of the modified structure, they are used in the modal superposition method as described in Sect. 26.2. Application of the new structural modification method, results in the following system matrices for the modified structure

$$[M_{\text{mod}}] = \begin{bmatrix} [I] & 0 \\ 0\,0\;\;0 & \end{bmatrix} + \begin{bmatrix} \begin{bmatrix} \phi_{um}^a \\ \phi_{um}^b \end{bmatrix} & 0 \\ 0 & I \end{bmatrix}^T \begin{bmatrix} 0 & 0 & 0 \\ 0 & M_m^{bb} & M_m^{bc} \\ 0 & M_m^{cb} & M_m^{cc} \end{bmatrix} \begin{bmatrix} \begin{bmatrix} \phi_{um}^a \\ \phi_{um}^b \end{bmatrix} & 0 \\ 0 & I \end{bmatrix}, \tag{26.12}$$

$$[K_{\text{mod}}] = \begin{bmatrix} [\Omega_{um}] & 0 \\ 0\,0\;\;0 & \end{bmatrix} + \begin{bmatrix} \begin{bmatrix} \phi_{um}^a \\ \phi_{um}^b \end{bmatrix} & 0 \\ 0 & I \end{bmatrix}^T \begin{bmatrix} 0 & 0 & 0 \\ 0 & K_m^{bb} & K_m^{bc} \\ 0 & K_m^{cb} & K_m^{cc} \end{bmatrix} \begin{bmatrix} \begin{bmatrix} \phi_{um}^a \\ \phi_{um}^b \end{bmatrix} & 0 \\ 0 & I \end{bmatrix}, \tag{26.13}$$

where $[M_m]$ and $[K_m]$ represent mass and stiffness matrices of the modifying part, $[\phi_{um}]$ is the mass normalized mode shape matrix of the unmodified system and $[I]$ is the identity matrix. Subscript a corresponds to DOFs which belong only to the unmodified structure, subscript b corresponds to DOFs which belong to the modified structure and subscript c corresponds to DOFs which belong only to the modifying part. $[\Omega_{um}]$ is a diagonal matrix composed of squares of natural frequencies of the unmodified structure.

Solving the eigenvalue problem defined by Eqs. (26.12) and (26.13), natural frequencies and mode shapes of the modified structure can be obtained. It should be noted that, in order to use the mode shapes obtained, they should be pre-multiplied by

$$\begin{bmatrix} \begin{bmatrix} \phi_{um}^a \\ \phi_{um}^b \end{bmatrix} & 0 \\ 0 & I \end{bmatrix}. \tag{26.14}$$

26.4 Case Studies

26.4.1 Lumped Parameter Model

A simple lumped parameter model (Fig. 26.1) is constructed representing the modified system. 3-DOF-system is added to the original (unmodified) 4-DOF system by rigid coupling resulting in a 5-DOF-system. Modal data of the modified system is obtained from directly modeling the 5-DOF system using the new structural modification method utilizing *all information* of the unmodified system. Nonlinear forced response analysis of the modified structure is performed by using these modal data and the results obtained are compared. The system parameters used for the lumped parameter model are $M_1 = M_2 = M_3 = M_4 = 1\text{kg}, K_1 = K_2 = K_3 = K_4 = 10,000\text{N/mm}$, $F = 50\text{N}$, $\gamma = 0.01$ and $M_5 = M_6 = M_7 = 2\text{kg}$, $K_5 = K_6 = K_7 = 20,000\text{N/mm}$, $F = 50\text{N}$, $\gamma = 0.01$. Lumped model including nonlinearities in the unmodified system is presented in Fig. 26.1 and corresponding response plots of the first for different k_c values are given in Fig. 26.2. Another lumped model is presented for which nonlinearities are included in the modifying system (see Fig. 26.3) and corresponding response plots of the seventh mass for different k_c values are given in Fig. 26.4.

It can be seen from Figs. 26.2 and 26.4 that results obtained the proposed method are in exact agreement with the ones obtained by utilizing the exact modal data of the modified system.

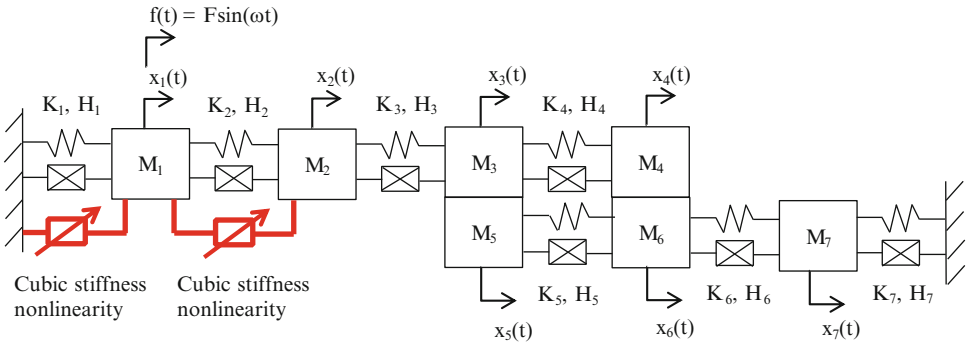

Fig. 26.1 Lumped parameter model (modified system) – Case 1

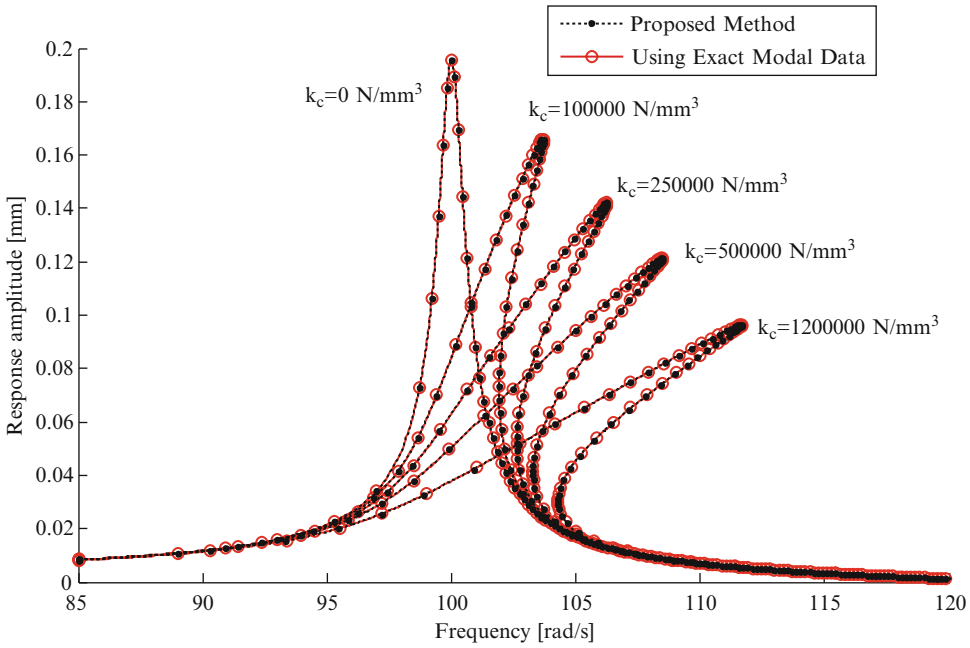

Fig. 26.2 Responses of the first mass – Case 1

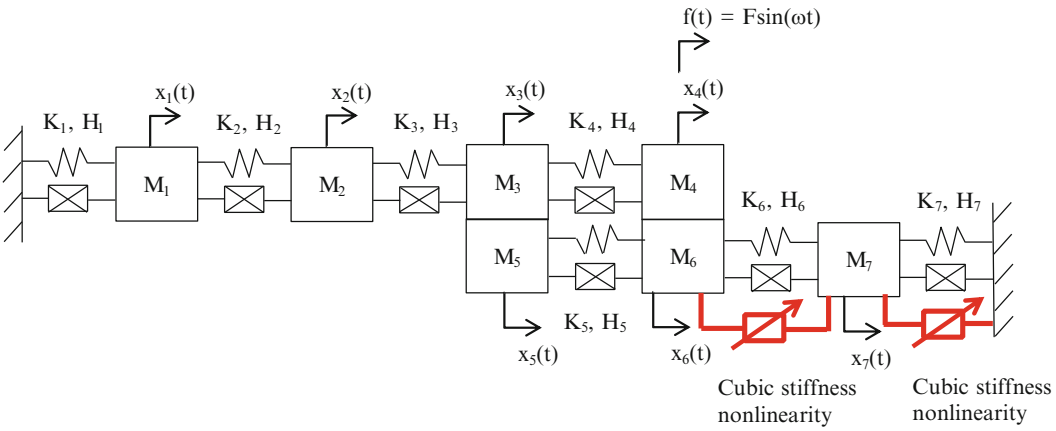

Fig. 26.3 Lumped parameter model – Case 2

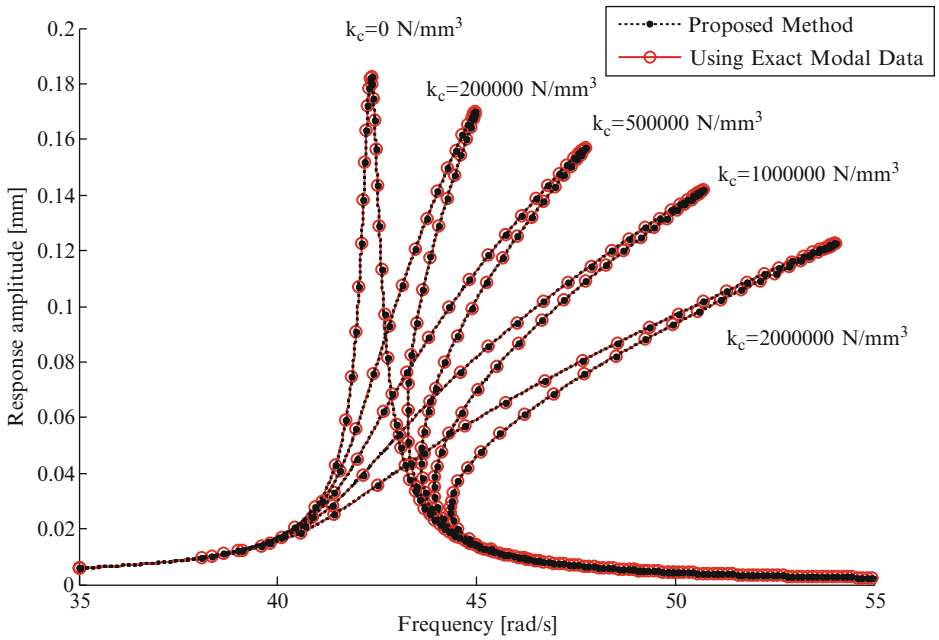

Fig. 26.4 Responses of the seventh mass – Case 2

26.4.2 Finite Element Model

Same concept as in the lumped mass parameter model is applied to a cantilever beam modeled in ANSYS. Since it is a large DOF system, all information of the original system is not included in the analysis. First, different number of modes is used for structural modification and modal data of the modified system is obtained. Then, using the obtained modal data, HBM with modal superposition is applied to obtain the nonlinear response of the modified beam. In order to obtain the exact modal data, modified beam is also modeled in ANSYS and nonlinear solution is repeated for modal data obtained from modal analysis in ANSYS. *5 modes* of the modified beam are included in all nonlinear response solutions.

Modified system can be seen in Fig. 26.5 in which modifications are shown in purple. Cubic stiffness nonlinearities are shown in the figure defined in y direction. In Case 1, they are in the original system, while in Case 2, they are in the modifying system. External loading is also shown in Fig. 26.5 in y direction. Response plots are presented in Figs. 26.6 and 26.7 for the DOF shown in Fig. 26.5 by using $k_c = 0, 10, 20, 40\,\mathrm{N/mm^3}$; $\mathrm{F} = 50\,\mathrm{N}$ and $\gamma = 0.1$.

Results in Figs. 26.6 and 26.7 show that accuracy of the method increases if more number of modes are included in the analyses. Moreover, for this particular case, the difference between the results is more visible if the nonlinearities are added to the modifying part.

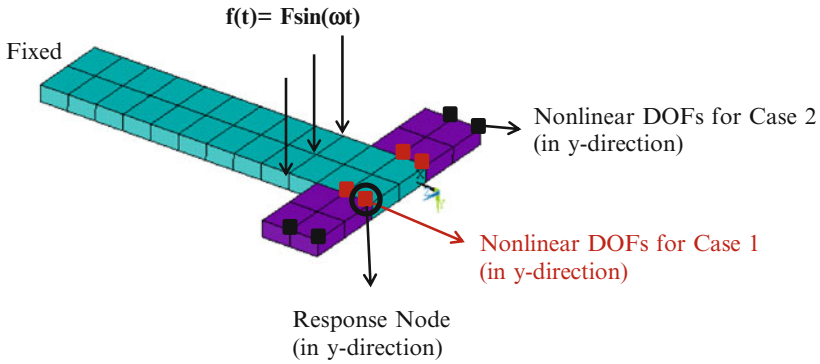

Fig. 26.5 Modified system

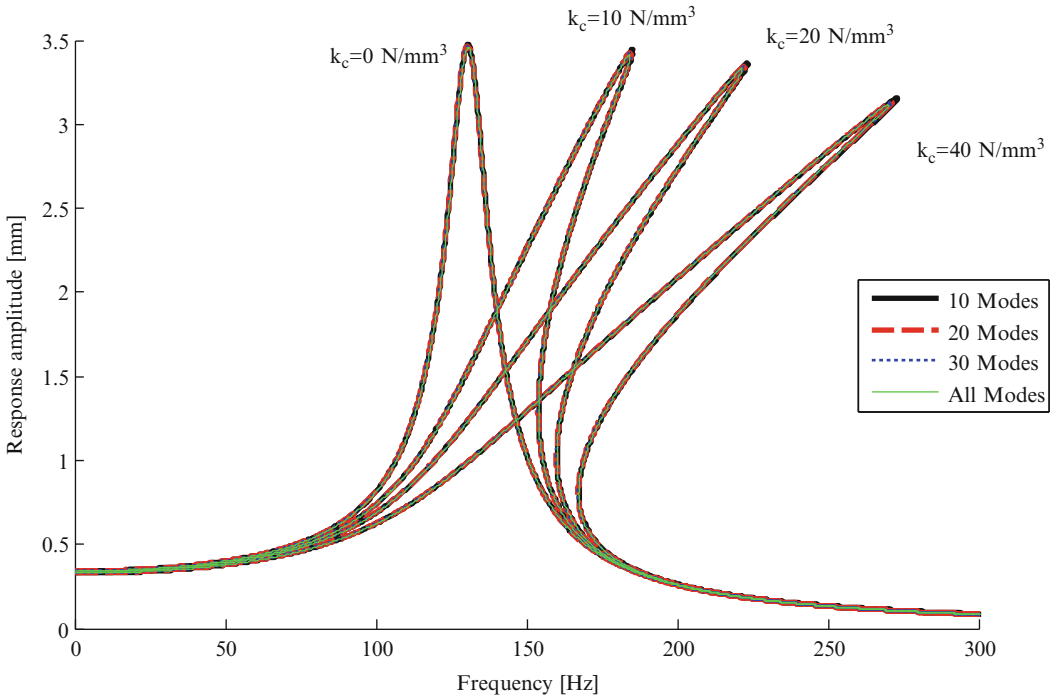

Fig. 26.6 Case 1 – nonlinear responses using 10, 20, 30 modes in formulation and exact solutions (5 modes are used in all cases)

26.5 Conclusions

In this study, a nonlinear reanalysis method is presented by using a new structural modification method developed by the authors. First, in order to verify the method, a simple lumped parameter model is considered utilizing all information of the unmodified structure. It is observed that identical results are obtained by using the proposed approach and directly solving the nonlinear system. Later, in order to show the capability of the proposed method, a FEM of a cantilever beam is considered. Instead of using all information of the unmodified system; 10, 20, and 30 modes are included in the analysis by utilizing the proposed method and response of the system is studied. It is observed from the results that increasing the number of modes used in structural modification method provides more accurate results; however, for the selected range of frequency, utilizing limited number of modes, it is possible to obtain the same results as if the exact modal information of the modified structure is employed.

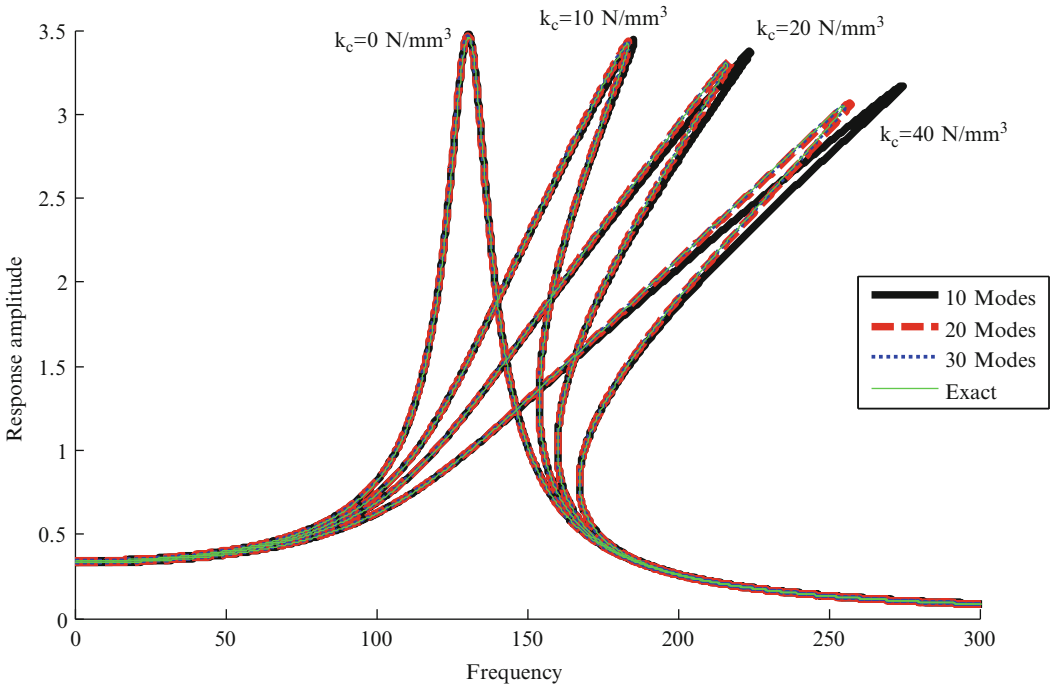

Fig. 26.7 Case 2 – nonlinear responses using 10, 20, 30 modes in formulation and exact solutions (5 modes are used in all cases)

References

1. Crowley JR, Rocklin GT, Klosterman AL, Vold H (1984) Direct structural modification using frequency response functions. In: Proceedings of international modal analysis conference, 2nd IMAC, Orlando
2. Kyprianou A, Mottershead JE, Ouyang H (2005) Structural modification. Part 2: assignment of natural frequencies and antiresonances by an added beam. J Sound Vib 284(1–2):267–281
3. Kyprianou A, Mottershead JE, Ouyang H (2004) Assignment of natural frequencies by an added mass and one or more springs. Mech Syst Signal Process 18(2):263–289
4. Mottershead JE, Kyprianou A, Ouyang H (2004) Structural modification. Part 1: rotational receptances, Mech Syst Signal Process 18(2):263–289
5. Mottershead JE, Mares C, Friswell MI (2004) An inverse method for the assignment of vibration nodes. Mech Syst Signal Process 18(2):263–289
6. Park YH, Park YS (2000) Structural modification based on measured frequency response functions: an exact eigenproperties reallocation. J Sound Vib 237(3):411–426
7. Sherman J, Morrison WJ (1949) Adjustment of an inverse matrix corresponding to changes in the elements of a given column or given row of the original matrix. Ann Math Stat 20:621
8. Woodbury M (1950) Inverting modified matrices. Memorandum Report 42, Statistical Research Group, Princeton University, Princeton
9. Özgüven HN (1990) Structural modifications using frequency response functions. Mech Syst Signal Process 4(1):53–63
10. anlıtürk KY (2002) An efficient method for linear and nonlinear structural modifications. In: Proceedings of ESDA 2002: 6th biennial conference on engineering systems design and analysis, ESDA2002/APM-028, Istanbul
11. Köksal S, Cömert MD, Özgüven HN (2006) Reanalysis of dynamic structures using successive matrix inversion method. In: Proceedings of the international modal analysis conference, 24th IMAC, St. Louis- Missouri
12. D'Ambrogio W, Sestieri A (2001) Coupling theoretical data and translational FRFs to perform distributed structural modification. Mech Syst Signal Process 15(1):157–172
13. Şayin B, Cigeroglu E (2013) A new structural modification method with additional degrees of freedom for dynamic analysis of large systems. In: Proceedings of the international modal analysis conference, 31st IMAC, Garden Grove, California
14. Cigeroglu E, An N, Menq CH (2009) Wedge Damper modeling and forced response prediction of frictionally constrained blades, transactions of ASME. J Eng Gas Turbines Power 131(5):1–11
15. Cigeroglu E, An N, Menq CH (2007) A micro-slip friction model with normal load variation induced by normal motion. Nonlinear Dyn 50:609–626
16. Cigeroglu E, An N, Menq CH (2006) Forced response prediction of constrained and unconstrained structures coupled through frictional contacts. J Eng Gas Turbines Power 131(2)

Chapter 27
Quantifying Penetration Depth of Damage in Concrete Structures Using Nonlinear Elastic Wave Spectroscopy

Anthony Chyr, Garrett W. Idler, Colton R. Lake, and T.J. Ulrich

Abstract The ubiquity of concrete as a building material necessitates the ability to inspect and evaluate its structural integrity, preferably in a nondestructive manner. Of particular interest is the ability to detect and quantify the degree to which surface damage penetrates concrete. This is especially important in the nuclear energy industry where concrete is used as a barrier protecting the primary confinement vessel, such as in dry storage casks, in which case cracks form a path for corrosion. Nondestructive evaluation techniques based on the material's nonlinear elastic parameters are orders of magnitude more sensitive to the presence of damage than linear elastic methods analogous to sonar. Two methods, both subsets of Nonlinear Elastic Wave Spectroscopy (NEWS), were used: Nonlinear Resonance Ultrasound Spectroscopy (NRUS) for evaluation of a sample's bulk nonlinear characteristics, and Time Reversal Elastic Nonlinearity Diagnostics (TREND) for evaluation of a sample's local nonlinear characteristics. These nonlinear characteristics are strong indicators of the presence of damage. Eight concrete samples were cut into two pieces, of the two piece one was thermally damaged for 3 h at 500 ˚C. Evaluations of these pieces using NRUS showed a seven times nonlinear parameter increase for the damaged pieces over the undamaged pieces. Using a minimally participating adhesive, samples were glued back together and evaluated using TREND. Results from TREND aligned closely with the expected modeled response.

Keywords Damage • Nonlinearity • Time reversal • Elastic wave spectroscopy • Concrete • Resonance ultrasound spectroscopy

27.1 Introduction

27.1.1 Motivation

As concrete structures continue to age, many structures are reaching their expected life span, and understanding the structural health of these structures is of increasing importance. In the nuclear industry, dry storage casks are used to contain spent nuclear fuel. These casks are typically made of steel with an outer layer of 1–2 m of concrete. Thermal damage resulting from heat emanating from the store material and freeze thaw damage from weather on the outside of contains are the primary causes of damage [1].

A. Chyr (✉)
Department of Mechanical Engineering, University of Utah, Salt Lake City, UT 84112, USA
e-mail: tony.chyr@gmail.com

G.W. Idler
Department of Mechanical Engineering, Colorado State University, Fort Collins, CO 80523, USA
e-mail: gidler@rams.colostate.edu

C.R. Lake
Department of Civil Engineering, New Mexico Institute of Mining and Technology, Socorro, NM 87801, USA
e-mail: dirtjumprider@msn.com

T.J. Ulrich
Solid Earth Geophysics (EES-17), Los Alamos National Laboratory, Los Alamos, NM 87545, USA
e-mail: tju@lanl.gov

G. Kerschen et al. (eds.), *Topics in Nonlinear Dynamics, Volume 1: Proceedings of the 31st IMAC, A Conference on Structural Dynamics, 2013*, Conference Proceedings of the Society for Experimental Mechanics Series 35,
DOI 10.1007/978-1-4614-6570-6_27,

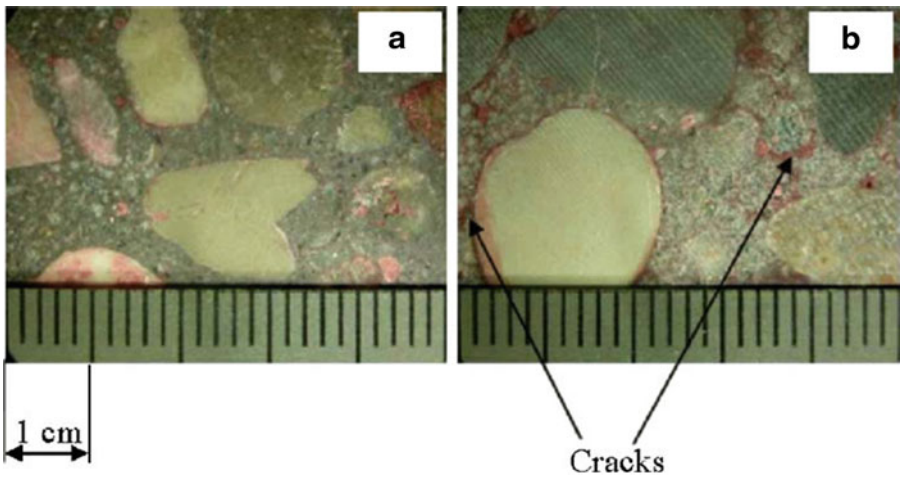

Fig. 27.1 Transition halo in **(a)** undamaged and **(b)** damaged concrete. Dye penetrant (*red*) indicates increased porosity and micro-crack in the damaged sample

Conventional ultrasonic techniques in non-destructive testing have been in use as early as 1942 with the work of F.A. Firestone [2]. While these conventional methods, analogous to sonar, have since improved; small material defects such as micro-cracks continue to evade detection. The presence of these small material defects tend to soften the host material, thus reducing its load bearing capacity, in addition to being the source of macroscopic cracks as the damage progresses. As such, direct detection through conventional methods may not be viable, as the high frequencies required to achieve the necessary spatial resolution would quickly attenuate within the host material [3]. Methods that interrogate nonlinear material characteristics within the host material on the other hand, such as the softening effect of micro-cracks, have been shown to be orders of magnitude more sensitive to the presence of damage than conventional methods [4], and will be the focus of this paper.

27.1.2 Background

27.1.2.1 Damage

In concrete, the most brittle zone is the interface between aggregate and cement paste (Fig. 27.1). This zone, called the transition halo, is the most porous and crystallized. With increasing temperature, this zone is progressively degraded due to the evaporation of free water and the difference between the thermal expansion of the aggregates and the cement paste. The degradation results in an increase in porosity and micro-cracks [5]. As the strain magnitude increases, micro-cracks are more likely to open, which results in the softening of the elastic moduli and a measurable drop in the elastic wave speed in the material. The presence of micro-cracks also leads to higher harmonics in addition to an increase in attenuation.

27.1.2.2 Methodology

Three methods were used to characterize concrete samples with known depths of damage. The first method, called Resonant Ultrasound Spectroscopy (RUS), is a nondestructive interrogation technique that allows the Elastic tensor to be characterized. The second and third method, called Nonlinear Resonance Ultrasound Spectroscopy (NRUS) and Time Reversal Elastic Nonlinearity Diagnostic (TREND), are nonlinear techniques where the strain magnitude is varied and the consequences of a drop in wave speed (i.e., elastic modulus softening) were measured.

RUS uses a transducer and receiver system and a stepped sine input to excite the sample's resonance frequencies. By determining the frequency of the resonance peaks, a stiffness matrix may be constructed given the density and geometry of the sample [5].

NRUS looks at the relationship between the peaks in the frequency response of a test specimen at increasing drive amplitudes. For example, when an ideal bell rings, it has resonant modes that dominate the response, and when the bell is hit harder, the bell rings at the same modes only louder. Now imagine the same bell, but with a series of cracks running along its side. Hitting the bell lightly results in a similar response of the bell when it was undamaged, but the harder the bell is hit, the more of an effect the cracks will have on the bell's response. Cracks have been shown to increase the damping

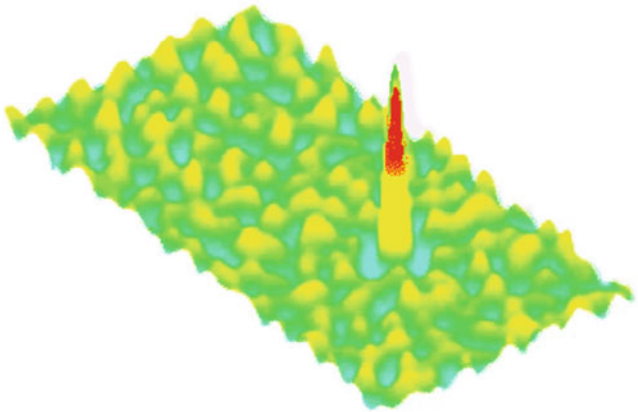

Fig. 27.2 Surface mapping of time reversed focus. *Large peak* indicates focus within an aluminum plate from previous work

of the system, shown as a reduction the amplitude and a widening of the response of the resonant peaks of a sample as a function of strain amplitude. Furthermore as the material softens, the wave speed decreases, and the resonance peaks shift toward lower frequencies. NRUS provides a quantification of the amount of damage in a specimen by looking at the shape and location of resonance peaks in the frequency response as a function of the strain magnitude [6] (Fig. 27.2).

TREND employs time reversal to focus energy to a highly localized region of a sample [7], in this region the nonlinearity is most pronounced and quantified. In time reversal, imagine dropping a rock into a pond. The rock creates a series of waves that propagate away from the point of impact. Now imagine placing an array of receiver/transducers around the point of impact, each of which set to record the pressure wave as it pass through the array. After a long period of time, the wave dissipates. If the array of receiver/transducers play the pressure wave in reverse, the back-propagating waves will simultaneously arrive at the original point of impact in phase producing a time reversed focus, a reconstruction of the original wave reversed in time [8]. Using time reversal to create a focused signal at a desired location of measurement, nonlinearity can be quantified in a focused region by comparing the frequency response of the test specimen as drive amplitude, and thus strain amplitude, increases [9].

27.1.3 Objective

This series of experiments focuses on employing nonlinear techniques to empirically quantify the amount and location of damage in concrete. Concrete test specimens with a known depth of thermally induced damage were prepared. Three steps were taken to approach the problem. In the first step, RUS was used to characterize the concrete sample used for testing. These material properties derived from RUS were used to simulate the signal's penetration depth in TREND in addition to allowing finite element models to be created and used to simulate subsequent tests. In the second step, NRUS testing was used to quantify the bulk nonlinearity in a sample. In the third step, TREND allows for nonlinearity to be characterized in a focused region, and the depth of the damaged region to be deduced.

27.2 Experimental Procedures

27.2.1 Specimen Preparation

Concrete test specimens were prepared using Portland cement with a medium aggregate mixture (Fig. 27.3). Eight blocks were produced with nominal dimensions of 100 mm wide by 100 mm tall by 50 mm deep. Variation in dimensional sizes arose because the pouring process for concrete does not result in tight tolerances and removing the concrete blocks from the mold lead to a small amount of flaking and chipping on exposed surfaces.

Five of the blocks were cut at various thicknesses to create two pieces with the 100 mm wide and 100 mm tall but with varying depths. The depths were made to be as close to evenly spaced as possible but some variation due to inaccuracies in the cutting method did occur (Table 27.1).

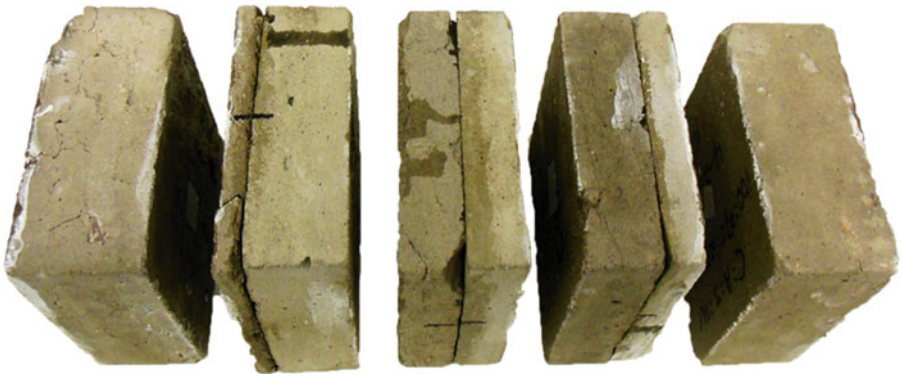

Fig. 27.3 Concrete specimen samples. From *left* to *right*: completely damaged sample, partially damaged sample, half damaged sample, mostly damaged sample, undamaged sample

Table 27.1 Sample characteristics. A denotes the damaged side of the sample. B denotes the undamaged side of a sample

		Dimensions				
Sample ID		x (cm)	y (cm)	z (cm)	Mass (g)	Density (g/cc)
	A	10.10	10.27	1.07	240.40	2.17
C1	B	10.19	10.26	4.05	871.60	2.06
	A	10.28	10.23	1.74	393.90	2.16
C2	B	10.14	10.22	3.05	694.50	2.20
	A	10.17	10.18	2.64	580.80	2.12
C3	B	10.18	10.17	2.35	507.00	2.09
	A	N/A	N/A	N/A	N/A	N/A
C4	B	10.18	10.17	5.08	1,152.40	2.20
	A	10.25	10.17	5.34	N/A	N/A
C5	B	N/A	N/A	N/A	N/A	N/A
	A	10.17	10.27	3.30	729.70	2.12
C6	B	10.14	10.16	1.64	342.90	2.03
	A	N/A	N/A	N/A	N/A	N/A
C7	B	10.11	10.13	5.16	1,142.00	2.16
	A	10.13	10.24	4.19	904.90	2.08
C8	B	10.10	10.25	0.88	176.60	1.94

One of the uncut blocks and one piece of each of the cut blocks was selected for heat treatment. The selected specimen were heated in a furnace at 500 °C for three hours with a 1 °C per min ramp during heating and cooling to encourage uniform heating and cooling in the specimen. This was used to develop uniform micro-cracks throughout the heated specimen for nonlinear testing. The heating process resulted in one fully damaged specimen and five damaged pieces. The damaged pieces were labeled "A" and undamaged pieces were labeled "B" for recognition.

27.2.2 Testing Procedures

27.2.2.1 Resonance Ultrasound Spectroscopy Sample Characterization

Resonant Ultrasound Spectroscopy (RUS) was used to characterize each piece of the eight concrete specimens. A stand for holding the block using piezoelectric transducers and a stepped sine signal were used to excite and measure the frequency response of the blocks in the 700 Hz and 20 kHz region. RUS uses the resonant response via resonant peak location in the frequency domain and the geometry of the test specimen to determine the elastic tensor for the tested material. The concrete was assumed to be isotropic and the first three peaks of the results were used to get the Elastic tensor. Many of the damaged specimens did not yield clear peaks because the cracks absorb energy of the signal and introduce small resonances the make the response less clear. Average Elastic moduli and Poisson's ratios for the damaged and undamaged states were calculated from the response.

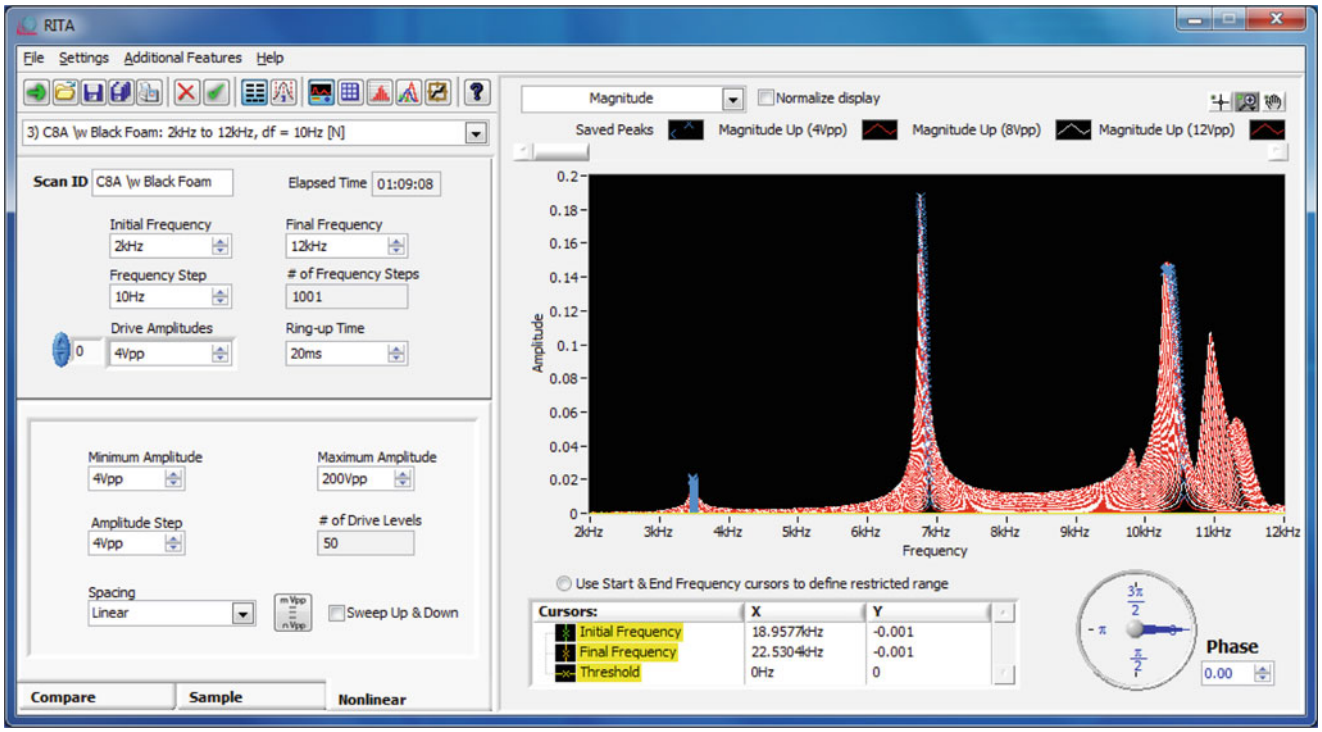

Fig. 27.4 NRUS measurement. Software interface showing the overlay of 40 scans between 4 and 200 Vpp. *Blue crosses* indicate peak locations

The theoretical frequency response for the specimen was determined using finite element modeling using Abaqus CAE. The theoretical values and the mode shapes were used to verify the peak resonance frequency values from the RUS measurements.

27.2.2.2 Nonlinear Resonance Ultrasound Spectroscopy

Once each specimen had been characterized and modeled using RUS, a large piezoelectric transducer was mounted directly on each specimen (Fig. 27.4). To mount the piezoelectric actuators, the surface of the concrete was covered in a layer of clear nail polish in order to prevent glue from entering pores in the concrete and changing its dynamic characteristics. A layer of Elmer's All-Purpose glue was then applied to base of the piezoelectric and the transducer was mounted near the corner of the large outside face of the specimen. The glue was allowed 48 h to dry before use. A small piece of reflective tape was applied to the face of the specimen to reflect light for the laser interferometer measurement system.

NRUS was performed on each specimen using a LabVIEW based software system and a National Instruments data acquisition system. An amplifier with a gain of 20 was used to amplify the input signal to the transducer and a Polytec fiber-optic interferometer was used to get displacement data for NRUS analysis. Scans were conducted on a base two log scale between voltages of 3 and 200 Vpp depending on the individual response of the specimen. The tests were always done on the first three resonant peaks to give consistency to the measurements. The software recorded the peak shift and quality factor Q (the inverse of attenuation) for each drive amplitude.

After NRUS characterization of the 13 specimens was completed, the blocks that had been cut into pieces were glued back together. This created test specimens of the uncut size with a damage layer beginning at a known depth. Once data was obtained, the peak shift due to nonlinearities in the concrete was compared to the known depth of damage so determine a correlation between peak shift and damage depth.

27.2.2.3 Time Reversal Nonlinearity Diagnostic Methods

Time Reversal Elastic Nonlinearity Diagnostic methods were used to quantify the amount of nonlinear response from a concrete specimen in the area of a time reversed focus. Two procedures were carried out. First, each specimen was tested

using a 75 kHz source signal. Time reversal focuses elastic waves that provide a measurement within one half of the wavelength of the focal point. In the concrete using a 75 kHz signal, this results in an estimated measurement depth of 2 cm. In order to get results that could be compared between specimens, the strain at the point of measurement must be similar between samples. Since the amplitude of the response varies greatly between specimens, the drive amplitudes were scaled such that maximum response amplitudes for each specimen were within 10 %. Ten drive levels of equal linear spacing between 10 and 100 % of the maximum drive level were used, and the relationship between drive amplitudes were used as metrics for nonlinearity. This method was carried out twice, measuring response from the damaged and undamaged sides. For the second test, four of the eight specimens were selected: one fully undamaged, one mostly undamaged, one mostly damaged, and one fully damaged. In these tests the signal frequency was modulated so that the penetration depth of measurement was varied. Frequencies of 37.5, 50, 75, and 150 kHz were selected to measure to a depth of 4, 3, 2, and 1 cm respectively. All measurements were taken from the damaged side of each specimen. Once again, ten linear spaced drive levels were used. The maximum strain at the point of measurement needed to remain constant between frequencies so signal frequency and maximum drive amplitude were scaled inversely in order to hold the maximum strain constant.

27.2.3 Analysis Methods

To determine the amount of nonlinearity in a test, the relationship between the responses of the specimen at varying drive amplitudes is observed. In NRUS testing, the nonlinearity is simply related to two parameters. First, the peak shift as drive amplitude increases can be recorded as a function of the strain magnitude.

$$\frac{f_i - f_0}{f_0} = \alpha\varepsilon \tag{27.1}$$

Where f_0 is the linear resonance frequency (at low amplitude), f_i is the resonance frequency when drive is at the ith amplitude, α is the nonlinear parameter, and ε is the strain amplitude. This method is based on the understanding that the material softens as damage increases which results in a lower wave speed in the material and subsequently resonance peaks move towards lower frequencies. The second parameter used to characterize nonlinearity in NRUS tests is the change in quality factor (Q) as the amplitude increases. Quality factor is a measurement of how under-damped a system is and is proportional to the inverse of damping. Two different methods were used to determine the nonlinearity of TREND tests. The highest amplitude time response of a test was analyzed to determine nonlinearity. A simple peak shift method (in the time domain) was done using a simple parabolic peak fit. A *Scaled Subtraction Method* (*SSM*) was also used, which has been shown to measure second order nonlinearity well.

$$SSM = \int_{t_0}^{t_f} \left(S_1(t) - \frac{A_2}{A_1} S_2(t) \right)^2 dt \tag{27.2}$$

Where *SSM* is the nonlinear parameter of interest, t_0 is the start of the signal, t_f is the end of the signal, S_1 is the reference signal, S_2 is the signal at the amplitude of interest, A_1 is the input amplitude at the reference signal, and A_2 is the input amplitude at the amplitude of interest. This method computes the difference between the measured response at high amplitude and low amplitude response that is scaled to reflect the ratio of the two drive amplitudes. A large number of different parameters related to and measures of nonlinearity are available. The methods that were chosen for this preliminary test were chosen based on simplicity and convenience, and future tests would benefit from a study that determine which measure of nonlinearity best measures nonlinearity for this testing method.

27.3 Results

Through the iterative process of RUS, the Young's modulus and Poisson's ratio for the concrete samples were obtained. The average Young's modulus and Poisson's ratio were 19.3 GPa and 0.13 respectively for the undamaged concrete with errors below 3 %. Due to the attenuation from the damage, RUS could not be used to get Young's modulus and Poisson's ratio for the damaged samples. Based on the resonant peaks found during NRUS tests on damaged samples, which could be done because of the higher drive amplitudes, and iteratively changing values in a finite element model, a Young's modulus between 2 and 6 GPa and a Poisson's ration around 0.1 was approximated for the damaged samples. The values for the moduli are presented in Table 27.2.

Table 27.2 Young's modulus and Poisson's ratio for undamaged samples

	C1	C2	C3	C4	C5	C6	C7	C8	μ	σ
E (GPa)	18.6	20.9	17.6	19.9	–	18.7	18.2	21.4	19.3	1.4
ν	0.089	0.107	0.105	0.168	–	0.102	0.117	0.226	0.131	0.49

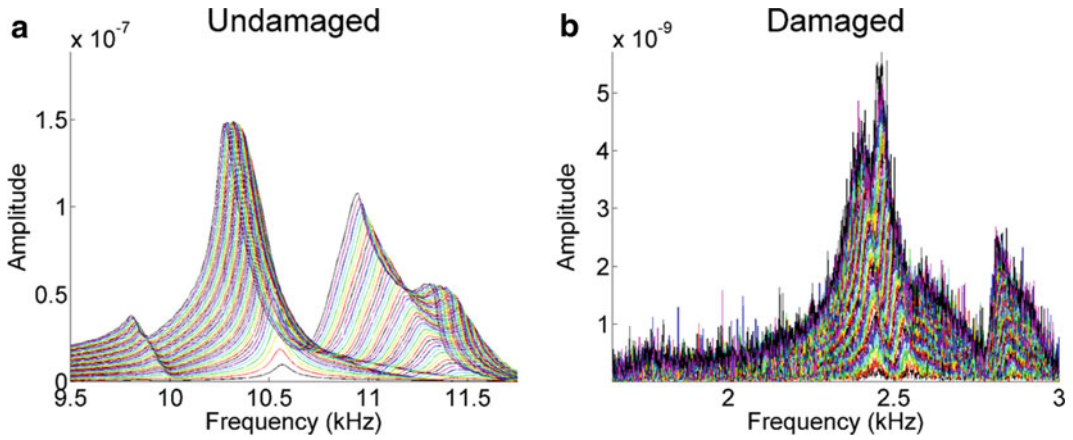

Fig. 27.5 Frequency response of damaged and undamaged sample. (**a**) Undamaged sample indicates resonance near 10.5 kHz with minimal noise. (**b**) Damaged sample indicates resonance near 2.5 kHz

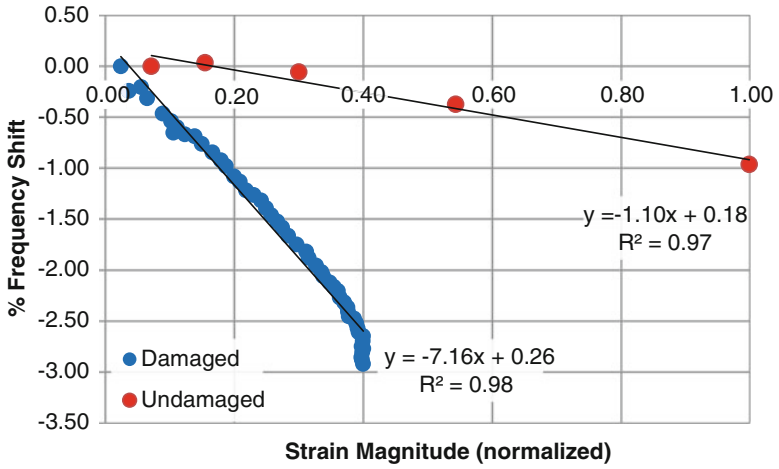

Fig. 27.6 NRUS percent frequency shift vs. normalized strain magnitude of sample C3 for the damaged and undamaged side. Linear regression of response produces the nonlinear parameter α

There were several reasons why it was difficult to obtain the Young's modulus and Poisson's ratio for the damaged samples. The frequency response modes shifted to much lower frequencies, to a range that was so low that may not have been in a linear region of our measurement system. The frequency mode peaks became distorted. In plots of the frequency response of the damaged samples, the peaks became more tightly packed and less defined, likely due to the sides of the micro and macro-cracks interacting and creating local resonances. In contrast, undamaged frequency response graphs are cleaner. The peaks are spaced further apart and are much more defined. Figure 27.5 presents a comparison of a damaged frequency response and an undamaged frequency response. Note the lower response amplitudes, less spacing between peaks, and apparent noisiness of the damaged sample compared to the undamaged sample.

When NRUS experiments were performed on the samples, it is easily seen that there is a difference between damaged and undamaged concrete in terms of strain and frequency shift. As shown in Fig. 27.6, as increasing strain is induced in the specimen by a piezoelectric transducer, a frequency shift occurs. This frequency shift depends on the concrete and the amount of damage within the concrete. The nonlinearity in the response of a sample increases as the strain increases due to higher drive amplitudes, and frequency shift will increase correspondingly. This shift is higher in damaged samples than undamaged samples due to more nonlinearity in the response.

In TREND experiments, when the signal is time reversed and then focused, it is measured as what appears to be a sine wave with a window in the time domain. In Fig. 27.7, the ten different responses from the ten drive amplitudes can be seen.

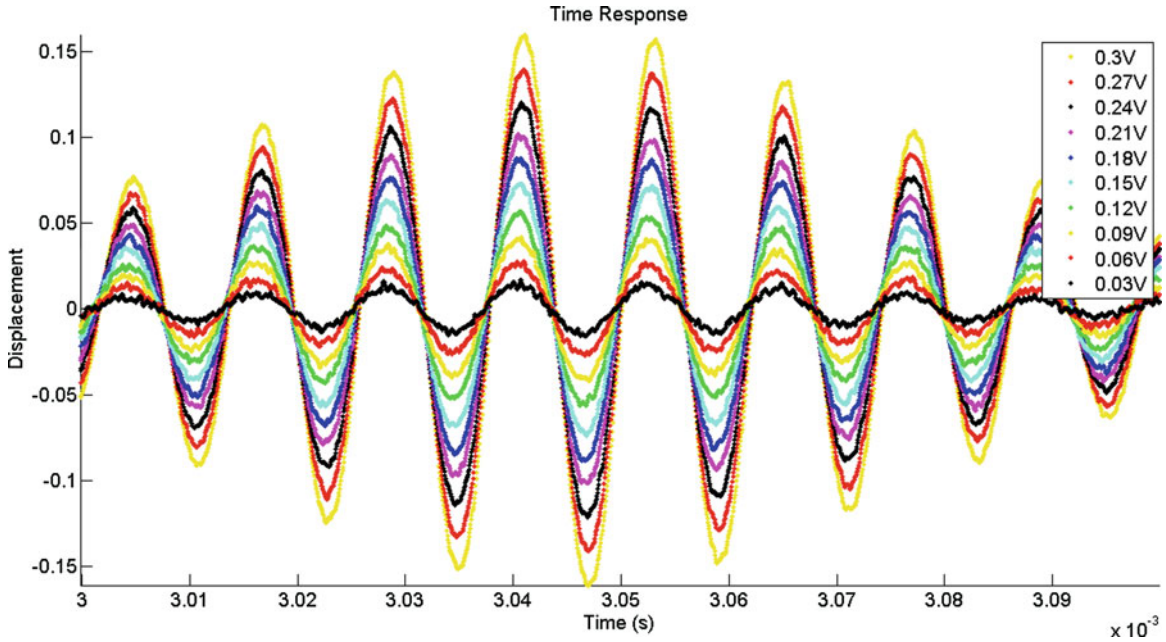

Fig. 27.7 TREND time response of a 75 kHz signal at various drive amplitudes

Fig. 27.8 *SSM* vs. excitation level and damage depth for all samples

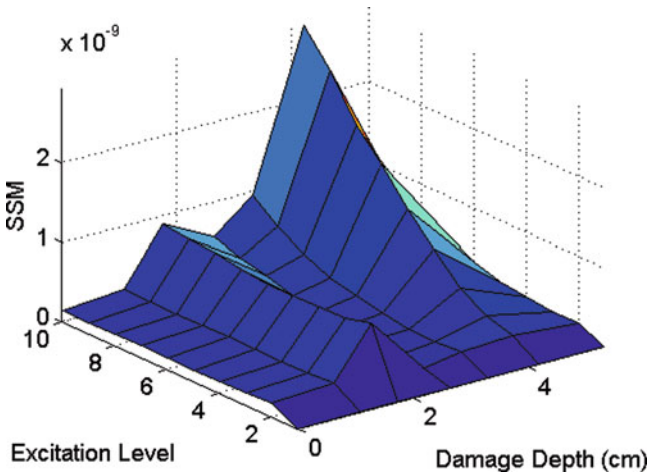

Close inspection shows a shift to the right at higher amplitudes of the peaks because the material is softening so the waves are arriving at a later time. The max peak for each drive-amplitude was found using a parabolic peak fit.

The *Scaled Subtraction Method* (*SSM*) is used as another quantifier of nonlinearity between the different drive amplitudes. The difference between two scaled signals based on their drive amplitude is quantified. The entire focused time signal is used for the characterization and its result is shown in Fig. 27.8.

To find a correlation between SSM results and damaged depth, the slope of the SSM was plotted against the damaged depth. Other than one data point which will be dismissed as an outlier due to experimental error, as explained in the discussion section, the resulting graph shows exactly what would be expected as the damaged depth is changed. When the damage depth is zero, a totally undamaged sample, the SSM changes only a small amount because there is only a small amount of nonlinearity in an undamaged sample. An increase in the SSM's slope is seen as the damage depth is increased, because an increasing amount of micro-cracks are present in the area of the time reversed focus that the SSM is quantifying. The increasing trend continues until the damage depth exceeds the depth of the focus, and then the SSM slope levels off because the amount of nonlinearity in the region is not changing. Figure 27.9 shows this result.

Error was characterized for the correlation between the slopes of the SSM as a function of strain magnitude. As expected, for the first three samples where the majority of the region influenced by the signal's focus were highly linear and the results correlation was within the noise floor (Table 27.3).

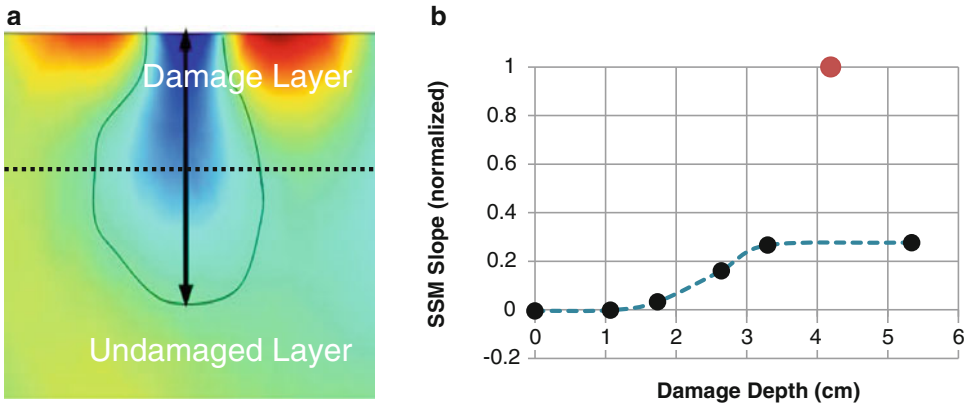

Fig. 27.9 Comparison of penetration depth and slope of SSM. **(a)** Simulated signal's penetration depth of the increase strain region for sample C2 [cf. 6]. **(b)** Slope of the SSM as a function of the excitation level vs. the depth of damage within the sample. *Red point* indicates improperly cut sample C8

Table 27.3 Characterization of error for the slope of the SSM as a function of drive level. Samples with a damage depth of 0 through 1.75 are within the noise floor

Damage Depth (cm)	SSM Slope	r	ρ @ 95 % Confidence	p-value
0	−0.0016	−0.46	[−0.86, 0.29]	0.21
1.07	0.006	−0.24	[−0.78, 0.50]	0.54
1.74	0.012	−0.55	[−0.89, 0.18]	0.12
2.64	0.057	0.96	[0.81, 0.99]	0
3.3	0.094	0.91	[0.62, 0.98]	0.0006
4.19	0.35	0.99	[0.95, 1.00]	0
5.34	0.097	0.97	[0.86, 0.78]	0

27.4 Discussion

For RUS measurements, the accuracy of the elastic tensor of a sample is based on the ability to determine and distinguish the sample's resonance peaks. The undamaged samples were easy to characterize because the frequency response had a high signal to noise ratio and peaks were well defined. A peak fitting algorithm was easily applied, which resulted in a RMS error of around 1.5 % for the majority of undamaged samples. The highest RMS error was 3 %. In the damaged samples, the increase in attenuation dramatically reduced the signal to noise ratio, making the resonance peaks difficult to characterize. The RMS error resulting for RUS measurements of damaged samples rose to unacceptable levels and the procedure was abandoned. Approximation of the elastic constants for the damaged concrete was estimated based on the higher responses attainable through the larger transducer glued to the sample used in NRUS measurements. The elastic moduli were then iteratively adjusted to fit a finite element model until rough agreement between experimental results and the model could be attained.

For NRUS measurements, the resonance peak shifts and quality factor, the inverse of attenuation, was measured as a function of strain magnitude. A comparison between damaged and undamaged samples showed that the peak shifts of the average damaged sample were seven times greater than the peak shift of the average undamaged sample. Likewise the standard deviation for the damaged sample was also roughly seven times greater than the average of the undamaged samples.

For TREND measurements, the strain amplitude at the focus of the signal had to be held constant so that the nonlinearity could be compared between tests. However, the iterative approach to scaling drive amplitudes in order to match the desire strain amplitude was slow and difficult, and it may be necessary to automate the procedure in future experiments. Two methods in TREND could be used to determine the damage in concrete structures. The first is to vary the frequency while holding the depth of damage constant. As the frequency decreases, the volumetric region encompassed by the focus increases. Thus, as the frequency decreases, more of the damaged region is encompassed by the focus. This remains the case until the frequency results in a focus that begins to encompass the undamaged region. At this point the nonlinearity levels off. While this method is ideal for real-world application, nonlinearities in the amplifiers prevent accurate measurements to be taken at high frequencies. Therefore the second method is used where the damaged depth is varied while the frequency is held constant. As the damage depth is increases, more damage is encompassed in the focus, and thus more nonlinearity is measured up until the point where the depth of the damage exceeds the focus of the signal. At this point, the nonlinearity in the damage is no longer induced by the focus. This results in a flattening of the curve between the nonlinear parameter and the damage depth. Only the second method was implemented in this set of experiments.

TREND was the most effective in quantifying the damage depth in concrete. By being able to focus the combined energy from each of the transducers to a highly localized region where the measurements were taken, the nonlinear characteristic

could be amplified and effectively characterized. Furthermore, the non-destructive and portable characteristics in TREND allow it to be a viable option in real-world application that requires a mobile device used for spot measurements in permanent structures.

27.5 Recommendations

The concrete samples that were created in this set of experiments were prepared based on the procedure used in previous tests that were used to characterize the bulk nonlinearities of single, homogenous concrete samples. Lessons were learned for improving the sample preparation. In prior tests, the epoxy that was used to combine damaged and undamaged pieces had been shown to be highly linear during TREND measurements. In this series of experiments, the glue bond appeared to have unforeseen effects that should to be characterized more deliberately in future tests. One sample, C8, came from sample prep with geometric irregularities. When the sample was cut in two pieces, the cut surface had a large shelf near one of its corners; it looked as if the saw had been backed out before a full cut through the sample was made. This does not affect the RUS and NRUS results because all tests were conducted with the pieces separated, but when the pieces were glued together, the two interfacing surfaces for sample C8 did not match. In TREND, the C8 sample had an SSM nearly an order of magnitude higher than all other samples, and was classified as an outlier.

The process used to thermally damage the concrete resulted in samples that crumbled on contact. This weakening of the material made the removal of large piezoelectric transducers glued to the sample after NRUS measurements difficult, and may have affected the latter TREND measurements in an uncontrolled manner. Furthermore, in real-world applications, micro-cracking resulting from thermal damage and freeze-thaw damage tends to produce a gradient of damage throughout the material rather than a finite boundary between damaged and undamaged portions of a structure. Therefore, developing a sample preparation procedure that creates a gradient of damage rather than piecewise damage would likely produce a better representation of the expected characteristics in real concrete structures.

For the TREND measurements, a higher signal to noise ratio would have improved the reliability and repeatability of this technique. Future tests using this method would benefit from larger amplifiers and a more transducers. These tests were approached as proof of concept. For future tests, an increase in the number of tested samples and repeated measurements would allow for a better quantification of the uncertainty in addition to characterizing the repeatability of this nonlinear testing technique.

References

1. Burton R, Hoffman D, Juzaitis R, Mtingwa S, Omberg R, Rempe J, Warin D (2011) Report of the fuel cycle subcommittee of NEAC, Washington, June 2011
2. Firestone FA (1940) Flaw detecting device and measuring instrument. Floyd A. Firestone, assignee. Patent 2280226, 27 May 1940
3. Joshi NR, Green RE (1972) Ultrasonic detection of fatigue damage. Eng Fract Mech 4.3:577–583
4. Johnson PA (1999) The new wave in acoustic testing. Materials World, the J. Inst. Materials 7, 544–546
5. Migliori A, Sarrao JL (1996) Resonant ultrasound spectroscopy: application to physics, materials measurements and nondestructive evaluation. Tech. Print
6. Payan C, Ulrich TJ, La Bas PY, Guimaraes M (2012) Quantitative linear and nonlinear resonant inspection techniques for characterizing thermal damage in concrete. Acoustics 2012:1–6
7. Fink M (1992) Time reversal of ultrasonic fields: parts I. IEEE Trans Ultrason Ferroelectr Freq Control 39.5:555–578. Web
8. Anderson BE, Griffa M, Larmat C, Ulrich TJ, Johnson PA (2008) Time reversal. Acoust Today Jan. 2008:5–16
9. Payan C, Ulrich TJ, La Bas PY, Guimaraes M (2012) Probing materials damage at different depths by use of time reversal elastic nonlinearity diagnostic: application to concrete. Acoustics 2012:1–6

Chapter 28
Investigating Cases of Jump Phenomenon in a Nonlinear Oscillatory System

Hamid A. Ardeh and Matthew S. Allen

Abstract A two degree-of-freedom (DOF) nonlinear oscillatory system is presented which exhibits jump phenomena where the period of oscillation jumps to an integer multiple of its original period when the state changes by a small amount due to damping. The jump phenomenon is investigated within the framework of Catastrophe theory where the abrupt change in the response characteristic of the system is explained by the interaction between its invariant manifolds. The authors recently presented an approach based on the concept of the Instantaneous Center Manifold (ICM), where, the center manifold of a conservative nonlinear system was replaced by an equivalent set of ICMs as two-dimensional invariant manifolds of the system that contain all of its periodic orbits. This study attempts to explain the sudden change in the response of a slightly damped oscillator as its response decays, based on the ICMs of its underlying undamped system. Such abrupt changes in the response of the system are explained based on the orientability properties of the local ICMs of the undamped system. This study also presents a bifurcation analysis of periodic orbits of the undamped system to illustrate the evolution of different types of periodic orbits, orientability of their local ICMs and their effect on the transient response of the damped system. These effects are expounded in cases of jump phenomena observed in numerical simulation of the free response of the damped system.

Keywords Jump phenomena • Instantaneous center manifold • Nonlinear mode • Orientability • Bifurcation theory • Catastrophe theory

28.1 Introduction

Mechanical systems often exhibit phenomena in which the response of the system changes character dramatically for a seemingly small change of some parameter. These phenomena are often characterized by a large amplitude discontinuity in the dynamic response of the system to small amplitude disturbances. Some examples include; sudden jumps in nonlinear torsional vibration of a power transmission system [1], vibration of nonlinear dynamic absorbers [2–4], forced vibration of a diaphragm air spring [5, 6], dynamic oscillation of a diesel generator [7], forced vibration of bladed disks (internal resonance) [8–10], roll-coupled maneuvers of airplanes [11–13] and vibration of mechanical and electrical systems described by Duffing's equation [14–17]. Standard perturbation methods such as Poincare-Linsteddt method and multiscale method, which are most suited for approximation of small amplitude nonlinear responses, can not be used to describe the large amplitude associated with such discontinuities. In these cases, catastrophe theory provides a natural synthesis between the practically observable and theoretical aspects of their sharp discontinuity when a small continuous change is made.

Catastrophe theory originated in the mid-1960s, with the ideas of French topologist Thom which were published in the book [18]. Later, Zeeman [19] suggested that the theory of catastrophes, to mean a particular mathematical model of catastrophic changes in the response of a system, should be called "Catastrophe Theory". The centerpiece of Catastrophe

H.A. Ardeh (✉)
Department of Mechanical Engineering, University of Wisconsin-Madison, Madison, WI, USA
e-mail: ansariardeh@wisc.edu

M.S. Allen
Department of Engineering Physics, University of Wisconsin-Madison, Madison, WI, USA
e-mail: msallen@engr.wisc.edu

G. Kerschen et al. (eds.), *Topics in Nonlinear Dynamics, Volume 1: Proceedings of the 31st IMAC, A Conference on Structural Dynamics, 2013*, Conference Proceedings of the Society for Experimental Mechanics Series 35,
DOI 10.1007/978-1-4614-6570-6_28,

theory is Thome's transversality theorem. This theorem asserts that two manifolds, in general position, intersects transversely where the intersection is stable in a sense that a small perturbation will not change the nature of the response significantly. However, when the intersection is non-transversal, any arbitrarily small perturbation will change the qualitative nature of the intersection dramatically. One can determine whether an intersection is transverse by checking the Jacobian of the manifolds at the intersection. What can be defined as the manifolds, in Thom's transversality theorem, depends on the response characteristic of the system being studied. If the solution of the system in state space is being investigated, one can choose the stable, unstable and center manifolds of the system as the invariant manifolds in Thom's transversality theorem.

However, for conservative oscillatory systems, the invariant manifolds of the system reduce down to only the center manifold which is, in general, defined in a high dimensional space. In a recent study, Ardeh et al. [20], using the center manifold theory, proposed an approach to replace the center manifold with an equivalent set of low dimensional invariant manifolds which were named Instantaneous Center Manifolds. Later, following the works of Rosenberg [21–25], Shaw et al. [26–28] and Kerschen et al. [29, 30], the ICM concept was used to define nonlinear modes of vibration as periodic orbits on these invariant manifolds of the system. This definition, not only extended the previously defined set of invariant manifolds of fixed points by Shaw et al. [26–28] to include the invariant manifolds of periodic obits, but was also capable of capturing the entire geometry of such manifolds (see [31] for more details).

These recently discovered invariant manifolds of periodic orbits, in a sense, are more significant than those associated with the fixed points of the system, since they intersect with the manifolds of fixed points non-transversely. That is because, at the point where they intersect the manifolds of the fixed points, the Jacobian of the center manifold is singular. This condition, i.e. singularity of the Jacobian of the center manifold, is often called the (internal) resonance condition where DOF of the system oscillate at unequal frequencies with rational ratios.

Moreover, as it will be discussed in Sect. 28.5, periodic orbits on the new interconnecting manifolds are products of bifurcations of periodic orbits on the invariant manifolds of fixed points, i.e. the manifolds of the primary nonlinear normal modes discussed in [29]. In this sense, since catastrophes are bifurcations between different equilibrium or fixed point attractors, these new interconnecting manifolds can be used to explain unexpected phenomena such as jump phenomena. In other words, one may roughly define Catastrophe theory "Bifurcation theory from the topological viewpoint" that is the study from a qualitative point of view of the ways that solutions to differential equations change [32–34]. The inverse relation has been previously studied by Arnold [35] where Thom's transversality theorem was used to locate bifurcations in versal families.[1] In this regard, this study attempts to explain catastrophes, observed in a case study, by establishing a connection between Bifurcation theory and Catastrophe theory through the concepts of ICMs and nonlinear modes of vibration.

To this end, Sect. 28.2 presents a two DOF conservative nonlinear system. The ICMs of the systems are calculated and illustrated in different views, each, emphasizing a different characteristic of the periodic orbits of the system. The concept of orientability is discussed in Sect. 28.3 to explain how it affects the evolution of the transient response of a dynamical system. Moreover, examples of orientable and non-orientable local ICMs of the conservative 2DOF system are presented. Section 28.4 discusses the stability of periodic orbits of the system in question and the relation between the stability of periodic orbits and orientability of their local ICMs. In addition, this section presents presents the upper limit of the approximation error in calculating the Floquet exponents. This limit defines a criteria that can validate the calculated Floquet exponents in stability analysis of periodic orbits, and is the key to accurately assessing the stability of the orbits studied here. This section also explains the mechanisms of losing stability, through which, some of the less trivial periodic orbits of the system bifurcate from other equilibria. In Sect. 28.5, the conservative system is modified by adding very small damping terms which are treated as perturbation terms. This is used to study the effect of changing the damping terms on the free response of the system, especially in the cases of jump phenomena. This study reveals that the jump phenomena occur as the state of the system approaches local manifolds with different orientability properties. Conclusions and directions for future work are provided in Sect. 28.6.

28.2 Case Study: The Underlying Conservative System

In this section, the two DOF conservative, nonlinear oscillatory system, shown in Fig. 28.1, is considered. The periodic orbits of the systems are calculated and illustrated in three different views; an invariant manifold (ICM) representation, an energy-frequency plane representation and a cross-section view of their Poincare map.

[1] A set of deformations that retains a special universal property under certain changes.

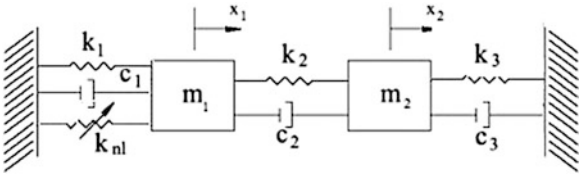

Fig. 28.1 A two DOF nonlinear oscillatory system

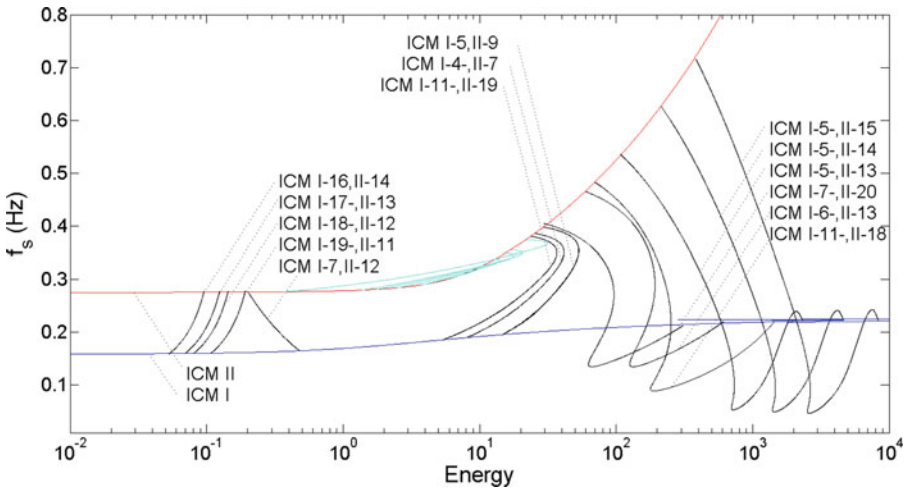

Fig. 28.2 Scaled frequencies of periodic orbits nonlinear modes on ICMs are shown as functions of their energies for the same ICMs. Scaled frequencies are calculated using Eq. (28.3). One group of ICMs, shown in *cyan*, start from the ICM II and land on ICM II while the other group of ICMs, shown in *black*, start from the ICM I (ICM II) and land on ICM II (ICM I)

Equations of motion (EOM) for the system shown in Fig. 28.1 can be obtained for the following parameters values $k_1 = k_2 = k_3 = 1$, $c_1 = c_2 = c_3 = 0$ and $k_{nl} = 0.5$ as

$$\begin{bmatrix} \ddot{x}_1 \\ \ddot{x}_2 \end{bmatrix} = -\begin{bmatrix} 2 & -1 \\ -1 & 2 \end{bmatrix} \begin{bmatrix} x_1 \\ x_2 \end{bmatrix} - \begin{bmatrix} 0.5x_1^3 \\ 0 \end{bmatrix}, \tag{28.1}$$

which can also be recast in state space defined by $(x_1, x_2, y_1, y_2) = (x_1, x_2, \dot{x}_1, \dot{x}_2)$ as

$$\begin{bmatrix} \dot{x}_1 \\ \dot{x}_2 \\ \dot{y}_1 \\ \dot{y}_2 \end{bmatrix} = \begin{bmatrix} 0 & 0 & 1 & 0 \\ 0 & 0 & 0 & 1 \\ -2 - \frac{3}{2}x_1^2 & 1 & 0 & 0 \\ 1 & -2 & 0 & 0 \end{bmatrix} \begin{bmatrix} x_1 \\ x_2 \\ y_1 \\ y_2 \end{bmatrix}. \tag{28.2}$$

28.2.1 Periodic Orbits in the Energy-Frequency Plane

One of the characteristic features of nonlinear systems is the frequency-energy dependence of their periodic orbits (nonlinear modes). As a result, the modal amplitudes and frequencies of nonlinear modes depend on the total energy of the system. Regarding this dependence, one typical representation of nonlinear modes is an energy-frequency plot. In this plot, a branch of nonlinear modes, which represents an invariant manifold (ICM), qualitatively shows how the frequencies of periodic orbits change as the total energy of the system increases. In this regard, the (scaled) frequencies of the periodic solutions of the system (28.1) are shown as functions of their energy in Fig. 28.2. The scaled frequency f_s is defined as

$$f_s = \begin{cases} f & \text{ICM I and ICM II} \\ \frac{1}{f_{max} - f_{min}} \left[m(f - f_{min}) - n(f - f_{max}) \right] f & \text{Otherwise} \end{cases} \tag{28.3}$$

where f is the fundamental frequency of periodic orbits of the system (28.1), and m and n are the positive integer factors in the terms ICM I-m, II-n referring to an invariant manifold (ICM) that intersects with the ICM I and ICM II at periodic orbits

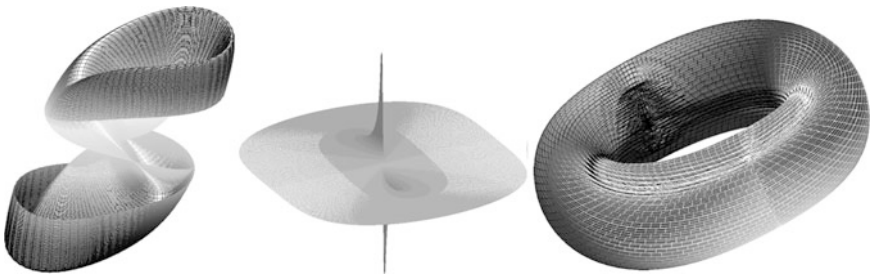

Fig. 28.3 The displacement components of some of the ICMs are shown. For each surface, x_2 of the system is plotted versus the x_1 and H_{x_1} where x_1 is the first DOF chosen as the independent variable and H_{x_1} is the Hilbert transform of x_1. *Left*: First (of two) invariant manifolds that is tangent to the vector field of the system at its fixed point, i.e. the origin. *Middle*: Second invariant manifold that is tangent at the fixed point of the system. *Right*: One of infinitely many invariant manifolds that is tangent to the vector field of the system at its periodic orbit. This manifold is an example of one that connects the other two invariant manifolds, as mentioned in Sect. 28.1

that are cases of, respectively, m:1 (m to one) and n:1 resonances, i.e. $f_1 = mf_2$ and $f_1 = nf_2$. It is important to notice that the frequency f_s represents the fundamental frequency only for the ICM I and ICM II. For all of the other ICMs, f_s represents a scaled version of their fundamental frequencies, where, the scaling factor is a positive integer only at the intersection of theses ICMs with the ICM I and ICM II. This scaling is done to show all of the branches of the nonlinear modes in a region between the two branches defined by ICM I and ICM II.

28.2.2 Periodic Orbits on the Invariant Manifolds of the System

Periodic orbits of the system (28.1) are found using the ICM approach and continuation algorithm [30, 31] and used to construct the ICMs of the system (28.1). Examples of such ICMs are shown in Fig. 28.3. Each manifold is constructed by creating a mesh in which each individual solution, i.e. a periodic orbit (limit cycle) of the system (28.1), generates a tray of the geometry of the invariant manifold.

28.2.3 Periodic Orbits as Fixed Points of a Poincare Map

Another way to illustrate the periodic orbits of this system is through a Poincare map. In this regard, a Poincare section Ω is defined by $\Omega = \{(x_1, x_2, y_1, y_2) \in \mathbb{R}^4 | y_2 = 0\}$. The set Ω defines a hyperplane in $\mathbb{R}^4$which has the property that all the solutions of the system in (28.2) cross it transversely. This can be validated by proving that the tangent on the solutions of the system (28.2) when they cross this hyperplane, i.e.

$$\frac{d}{dt}\begin{bmatrix} x_1 \\ x_2 \\ y_1 \\ y_2 \end{bmatrix}_{y_2=0} = \begin{bmatrix} \dot{x}_1 \\ \dot{x}_2 \\ \dot{y}_1 \\ \dot{y}_2 \end{bmatrix}_{y_2=0} = \begin{bmatrix} 0 & 0 & 1 & 0 \\ 0 & 0 & 0 & 1 \\ -2-\frac{3}{2}x_1^2 & 1 & 0 & 0 \\ 1 & -2 & 0 & 0 \end{bmatrix} \begin{bmatrix} x_1 \\ x_2 \\ y_1 \\ y_2 \end{bmatrix}_{y_2=0} = \begin{bmatrix} y_1 \\ 0 \\ -2x_1 + x_2 - \frac{3}{2}x_1^3 \\ x_1 - 2x_2 \end{bmatrix}, \tag{28.4}$$

is non-zero. One can readily show that the tangent vector (28.4) is almost always non-zero, except at the origin which is the fixed point of the system (28.1). Next, a cross-section of fixed points of the mentioned Poincare map defined by the plane $y_1 = 0$, a contour of the Poincare map, is shown in Fig. 28.4. In addition, fixed points in this cross-section of the Poincare map are shown for varying f_s in Fig. 28.5 where three groups of ICMs can be recognized. First, denoted by ICM I and ICM II, are the loci of all the nonlinear modes (periodic orbits) that are continuations of linear modes of the system. Second, shown in cyan, is a group of ICMs that resemble contours of two saucer-shape surfaces sitting on top of the ICM II. The last group consists of two types of ICMs; a saddle-shape and a group of inverted saddle-shape ICMs. The last two groups are products of bifurcations from the periodic orbits (modes) on ICMs I and II. This will be further investigated in Sects. 28.4 and 28.5.

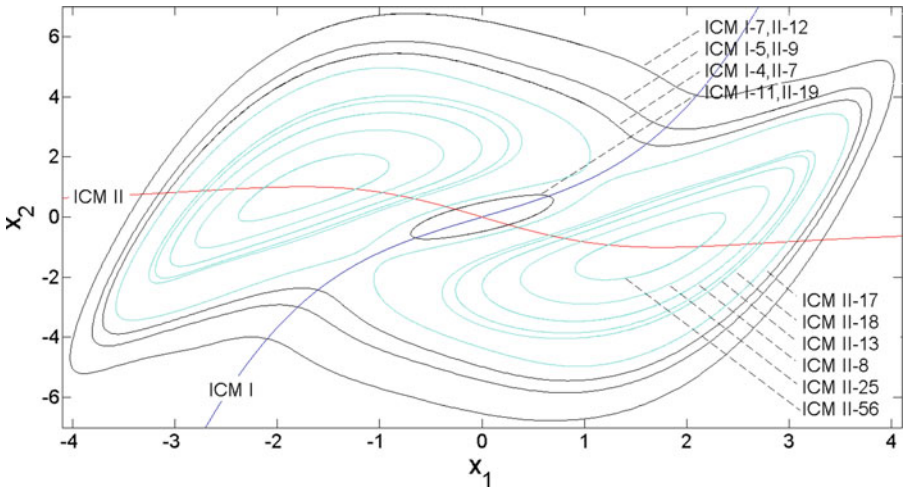

Fig. 28.4 Cross-section of a Poincare map is shown for the solutions with energies less than 35. Other than ICM I and ICM II, which are the loci of all the linear modes and their nonlinear continuations two other groups of ICMs are identified. First, shown in *cyan*, is a group of ICMs that only cross the ICM II. The second group, shown in *black*, consists of ICMs that cross both ICMs I and II

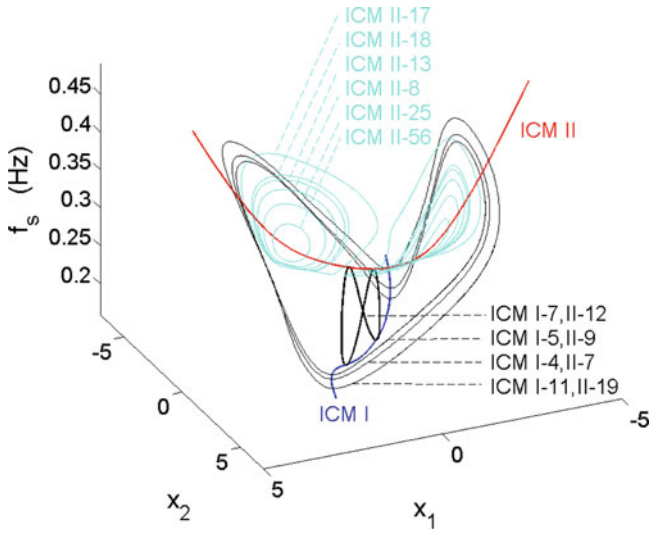

Fig. 28.5 Scaled frequencies of periodic orbits on ICMs are shown versus the fixed points of the Poincare map. Scaled frequencies are calculated using Eq. (28.3)

28.3 Orientability of Invariant Manifolds

To understand the dynamics of conservative vector fields, one typically looks for attractors (stable limit cycles or periodic orbits), their basin of attraction and, in particular, the boundaries of these attracting domains. Invariant manifolds often act as basin boundaries, and it is important to know where they are located and what they look like [36, 37]. These manifolds are sometimes called separating manifolds, as they separate the state space into two invariant regions. Orbits starting on one side of the manifold are confined to this region since they cannot pass through an invariant manifold. In particular, a separating manifold must have two sides, namely an inside and an outside. However, there are two-dimensional invariant manifolds that do not have two sides. Such manifolds are called nonorientable manifolds.

The classical example of a nonorientable manifold is the Mobius strip. A Mobius strip can be easily made by wrapping a strip of paper around a circle and gluing its ends together after giving it half of a twist (see Fig. 28.6). This surface only has one side since any trajectory that starts on the top surface will end up on the opposite surface after one cycle. In other words, orbits can advance through this type of surface without crossing it. Two examples of orientable surfaces, i.e. a twisted strip and a torus, are also shown in Fig. 28.6. Orbits that starts on one side of the twisted strip or inside of a torus can not move through these surfaces without crossing them.

The Mobius strip is the only two dimensional non-orientable manifold that can be embedded in $\mathbb{R}^3$ without self-intersection. For example, for the system in (28.1), the local invariant manifolds of the period lengthened periodic orbits form complicated manifolds that intersect themselves. However these manifolds, a few of which are shown in Fig. 28.7 are nonorientable and have very similar structures to that of the Mobius strip. The complexity of these manifolds is caused by the shape of their periodic orbits (mode shapes). In other words, to construct theses manifold, like the Mobius strip, one can

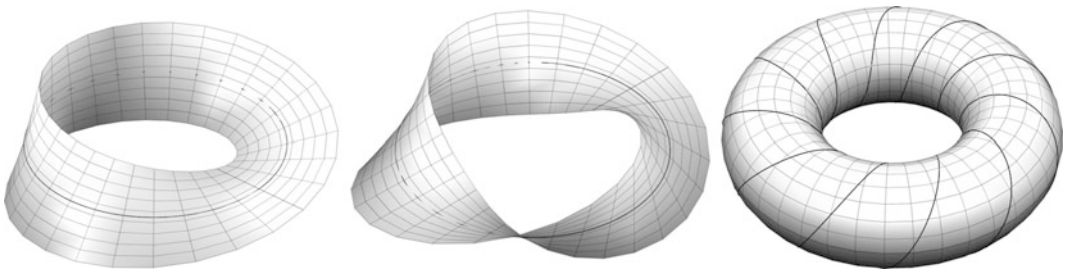

Fig. 28.6 *Left*: The Mobius strip is a nonorientable surface. *Middle*: A twisted strip represents an orientable surface. *Right*: Torus is also an orientable surface

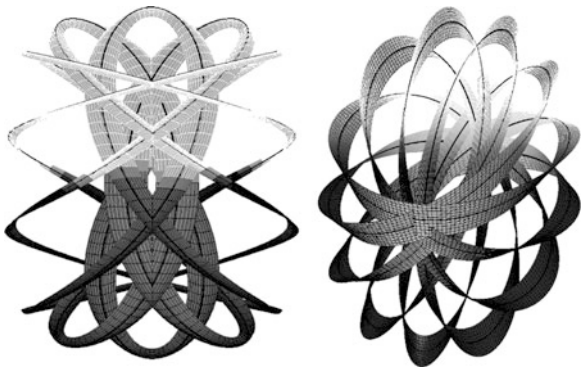

Fig. 28.7 Examples of nonorientable manifolds. *Left*: A local ICM representing a twisted strip with $(5+8)\times\frac{1}{2}$ (thirteen half) twists around a periodic orbit, shown with a *solid black line*, with 5:8 resonance. *Right*: A local ICM representing a twisted strip with $(16+1)\frac{1}{2}$ (seventeen half) twists

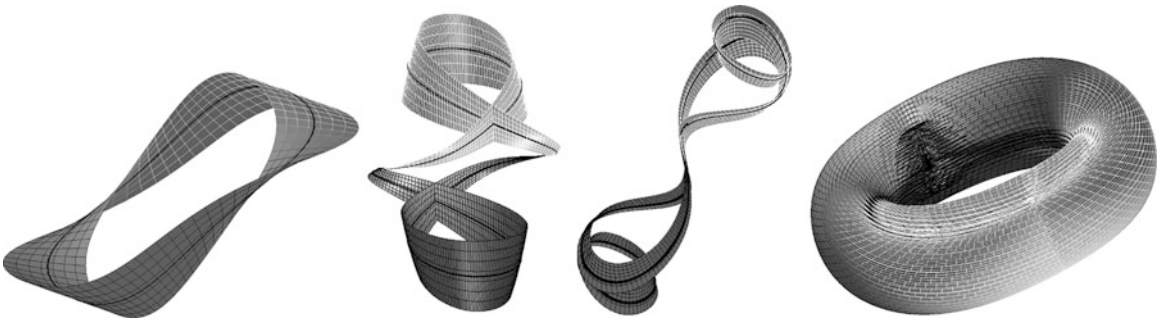

Fig. 28.8 Examples of orientable manifolds. *Left*: A local ICM representing a twisted strip. *Middle-Left*: Local ICM of a periodic obit with 3:1 resonance. This surface can be made by wrapping a strip of paper along the mode shape of the periodic orbit, shown in *black*, and gluing its ends after $(3+1)\times\frac{1}{2}$ twists. *Middle-Right*: Local ICM of a periodic obit with 5:1 resonance. *Right*: A torus local ICM

start with a strip of paper but, in this case, the strip needs to be wrapped along the mode shape of the periodic orbit instead of a circle. Also, its ends now need to be glued together after an odd number of half twists.

The system (28.1) also has several periodic orbits along orientable manifolds. For example, Fig. 28.8 represents three cases of twisted strips with, respectively, one, four and six full twists and a case of a torus local ICM.

These local invariant manifolds are key building blocks in shaping the orbits of nonlinear conservative systems, since, they can be seen as the gates and walls of the state space that the orbits of these systems can move through and cannot cross, respectively. In this regard, one needs a quantitative tool to determine the orientability (or nonorientability) of these local ICMs. This can be done through the stability analysis of their corresponding periodic orbits.

28.4 Stability of Periodic Orbits and Orientability of Their Invariant Manifolds

In this section, the relation between the orientability of local ICMs and the stability of their defining periodic orbits is explained. In order to determine the stability of periodic orbits of nonlinear systems, one needs to perform a Floquet analysis. In this regard, Floquet theory is explained briefly next.

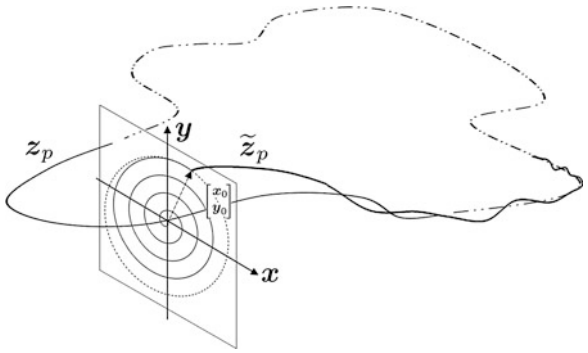

Fig. 28.9 Floquet theory essentially replaces the nonlinear system by its corresponding linear system at each point along the periodic solution. The perturbed periodic solution $\tilde{z} = \bar{z}(t*+T) + \begin{bmatrix} x_0 \\ \dot{x}_0 \end{bmatrix}$, $\begin{bmatrix} x_0 \\ \dot{x}_0 \end{bmatrix} \lll \bar{z}(t*+T)$, where $\bar{z}(t*+T)$ represent an arbitrary point along the periodic solution $\bar{z}$ and $\begin{bmatrix} x_0 \\ \dot{x}_0 \end{bmatrix}$ is the perturbation term, will asymptotically converge (will not diverge) to the periodic solution $\bar{z}$ if the solution of linear system (28.6) is stable (marginally stable), i.e. the response to the perturbation term is bounded

28.4.1 Stability of Periodic Solutions (Floquet Theory at a Glance)

Stability of periodic solutions of nonlinear system is assessed by analyzing the boundedness or otherwise of the solutions of the linearization of the system around its periodic orbit. In this sense, considering a n DOF nonlinear, conservative system defined by

$$\dot{z} = \begin{bmatrix} \dot{x} \\ \dot{y} \end{bmatrix} = \begin{bmatrix} y \\ f(x) \end{bmatrix} = F(z) \tag{28.5}$$

with a periodic solution represented by $\bar{z} = [\bar{x}^T, \bar{y}^T]^T$, Floquet theory replaces (28.5) with its linear approximation about the periodic solution $\bar{z}$

$$\dot{z} = \begin{bmatrix} \dot{x} \\ \dot{y} \end{bmatrix} = \begin{bmatrix} 0 & I \\ \mathbb{J}_f(\bar{x}) & 0 \end{bmatrix} \begin{bmatrix} x \\ y \end{bmatrix} = \mathbb{J}_F(\bar{z})z,\ i,j = 1,\ldots,n, \tag{28.6}$$

and studies the boundedness of its solutions in order to determine the stability of the periodic solution of the original nonlinear system (Fig. 28.9).

Since $\bar{z}$ has a period T, so does the Jacobian matrix $\mathbb{J}_F(\bar{z})$ and based on Floquet theory, solutions of the (28.6) accept the form

$$e^{\mu t} p(t) \tag{28.7}$$

where $p(t)$ is also periodic with period T. This way, Floquet concluded that the solutions of the linear system (28.6) are bounded, and consequently the periodic solution of the nonlinear system (28.5) is stable, if for all the Floquet exponents μ_i, $\mathtt{Re}\{\mu_i\} \leq 0, i = 1,\ldots,2n$.

In order to calculate the Floquet exponents of the system (28.6) one may first find its characteristic multipliers. Denoting the fundamental matrix of the system in (28.6) by $Z(t) = \left[z_1 \vdots \cdots \vdots z_n\right]$, where $z_1,\ldots,z_n$ are n linearly independent solutions of the system (28.6), the characteristic multipliers of the system (28.6), i.e. $\rho_1,\ldots,\rho_n$, can be defined as the eigenvalues of the monodromy matrix

$$B = Z(0)^{-1} Z(T). \tag{28.8}$$

The characteristic exponents or Floquet exponents of the system (28.6) are then defined as $\mu_1,\ldots,\mu_n$ satisfying

$$e^{\mu_i T} = \rho_i. \tag{28.9}$$

Figure 28.10 shows the Floquet exponents of the system (28.1) for the ICMs I-11,II-19 and II-2. All regions with at least one positive Floquet exponent represent unstable periodic orbits.

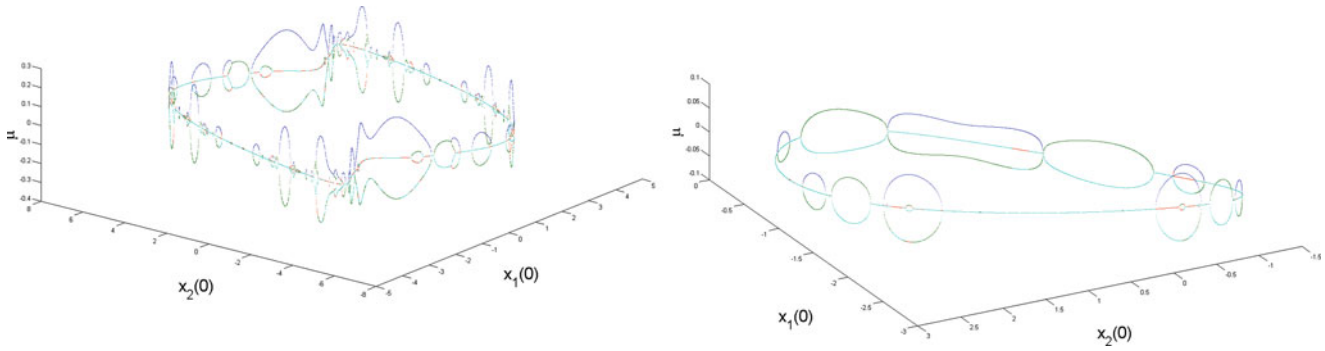

Fig. 28.10 Real parts of Floquet exponents are shown for the ICMs I-11,II-19 (*left*) and II-25 (*right*) over the cross-section of the Poincare map defined in Sect. 28.2. When one or more exponent is positive, the corresponding periodic orbit is unstable

28.4.1.1 Range of Validity of Floquet Stability Analysis

As mentioned above, the stability of the periodic solution of (28.5) is evidenced by (the signs of) the (largest) Floquet exponents of its associated linear system. Frequently, the eigenvalues computed based on a numerical solution to Eq. (28.6) are not accurate enough to allow stability to be assessed as clearly as is shown in Fig. 28.10. That is because, the periodic solution of the original nonlinear systems (28.5), its period and also the solutions of its associated linear system used in (28.8) are all prone to approximation error. Therefore, in order to assure the validity of the stability analysis, one has to show that all the aforementioned sources of approximation errors would lead to an acceptable error $|\delta Re\{\mu\}| < |Re\{\mu\}|$. This can be done by finding the maximum approximation error caused, first, when calculating the periodic solution of the nonlinear system and its period and, second, when integrating the solution of the linear system (28.6). To find periodic solution of the system (28.1), one can approximate these solution with harmonic terms [31].Then the sum of the mentioned error, i.e. $\delta Re\{\mu\}$ must satisfy $|\delta Re\{\mu\}| < |Re\{\mu\}|$. The following inequality expresses the constraint obtained using this approach.

$$\begin{aligned} &\frac{1}{2|\mu_i|}\left|e_i^T\left\{\delta\mathbb{J}_f(\bar{x}_M(0))-2\frac{\delta T_M}{T_M}\left[\mathbb{J}_f(\bar{x}_M(0))-\mu_i^2 I\right]\right\}e_i\right| \\ &+\frac{1}{T}\left|\log\left(1+\frac{x_N(t)^T\left\{\mathbb{J}_f(\bar{x}(T))-3\mu_N^2 I+(N+1)^2\omega^2 I\right\}\delta x_N(t)-2\mu_N^2\frac{\dot{x}_N(T)^T\delta\dot{x}_N(T)}{\dot{x}_N(T)^T\dot{x}_N(T)}x_N(t)^T x_N(t)}{x_N(t)^T\left\{\mathbb{J}_f(\bar{x}(T))-5\mu_N^2 I+(N+1)^2\omega^2 I\right\}x_N(t)}\right)\right| \\ &<|\mu_i|\,. \end{aligned} \tag{28.10}$$

Where e_i is the $i-$th column of the identity matrix, $\bar{x}_k$ is the periodic solution of the system (28.5) approximated by k harmonic terms, $\mathbb{J}_f$ is the Jacobian of the vector field f, T_k represents the period of the solution $\bar{x}_k$ (proof will be given in a forthcoming paper). This condition is used to determine how accurate the approximation of the periods, T_k, of the periodic orbits of the system (28.1) had to be in order to perform the stability analysis in Fig. 28.10. In contrast, Fig. 28.11 compares this approach with a more standard approach in which a fixed accuracy is used and the validity is not checked. The results in that case are highly inaccurate and hence difficult to interpret.

28.4.2 Stability of Periodic Orbits and Orientability of Their Local Invariant Manifolds

Orientability is a geometric property. In this sense, the orientability of an invariant manifold, such as those shown in Fig. 28.6, can always be determined by finding its geometry. However, for more complicated geometries like the ones shown in Figs. 28.7 and 28.8, determining the orientability, although possible, is not trivial. For invariant manifolds of dynamical systems, however, one can find the orientability of such manifolds by analyzing the behavior of the solutions of the system. For example, the geometries of the invariant manifolds of periodic orbits are shaped by the asymptotic behavior of the solutions that are initiated close to the orbits. The dynamics of such solutions, as mentioned earlier in this section, are governed by Eq. (28.6). Furthermore, since the Floquet exponents of the system in (28.6) dictate the asymptotic behavior of the mentioned solutions, they consequently determine the geometry of the invariant manifolds of their associated periodic orbit. In this regard, stability analysis (using Floquet exponents or multipliers) is essential for any quantitative approach to

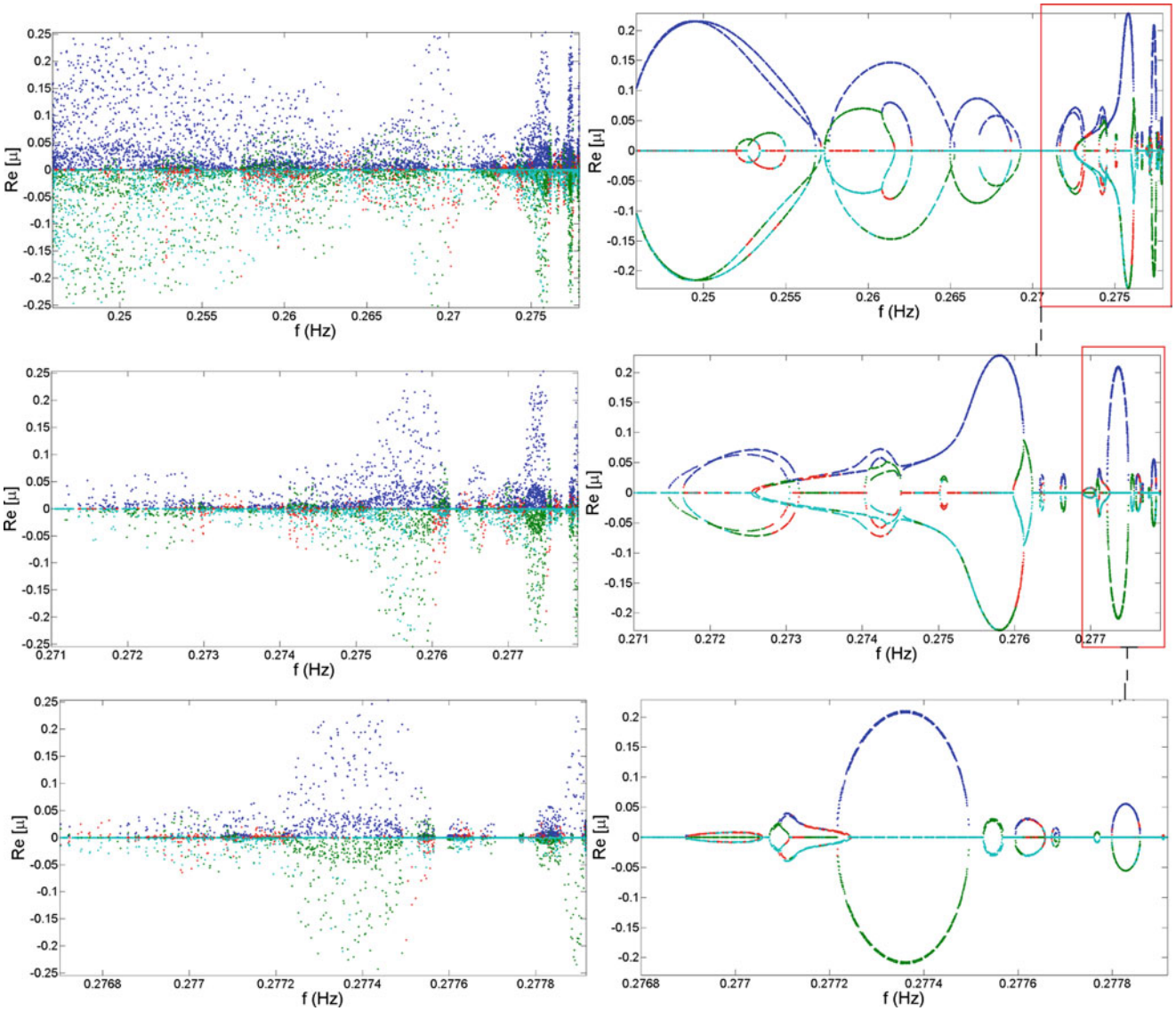

Fig. 28.11 Floquet exponents calculated without satisfying the inequality (28.10) (*left*) and after satisfying (28.10) are shown for the ICM I-11,II-19 in Fig. 28.10. Three regions, as shown in the *right*, have been magnified in both sets of valid and invalid computed Floquet exponents

determine the orientability of the local invariant manifolds of periodic orbits. Explaining the relation between the stability of periodic orbits and the geometry of their local invariant manifold is the main focus of the (global) bifurcation theory.

Roughly speaking, bifurcation theory explains how fixed points of systems turn into (branches of) simple periodic orbits and how simple periodic orbits change into more complicated ones when they lose stability. The mechanisms that govern such transformations between different types of equilibrium are important, not only because they explain why and how such changes happen, but also because they can be used to predict when the changes happen and what they are. The latter feature of such mechanisms is the main tool for determining the orientability of invariant manifolds of periodic orbits. For example, when a simple periodic orbit, such as a solution that orbits on a circle on a cylinder, loses its stability, it may transform into a periodic orbit that moves on the surface of a twisted strip or a torus. What determines the geometry, where the resultant unstable periodic orbit travels on, is the mechanism, through which, the simple periodic orbit loses its stability. If the simple periodic orbit loses its stability through Andronov-Hopf bifurcation (torus bifurcation), then the resultant periodic orbit will travel on the surface of torus.

A thorough study of all possible types of bifurcation is beyond the scope of this paper. However, for the system (28.1), nine types of periodic orbits have been identified and are provided in Appendix A. Also two cases of bifurcations and their associated mechanisms of losing stability are presented in Appendix B.

28.5 Numerical Simulation of Jump Phenomena

Analysis of the free response of oscillatory systems is the foundation of many identification methods [38–41]. In some, such as [42, 43], free responses of a slightly damped system have been used to identify the nonlinear modes of vibration of the underlying undamped system. Theses approaches use the decaying response of the system, initiated on a branch of nonlinear modes, to extract the frequency-energy dependence of the branch using time-frequency analysis tools such as a wavelet transform. This section reveals the sensitivity of such algorithms to the amount of damping and also the accuracy of the initial conditions. This is explicated by presenting examples of jump phenomena in the frequency of the response of the system for a set of different damping ratios and also accuracy of the initial conditions. This section also provides an explanation of these jumps using catastrophe theory, which describes the jump phenomena as a sudden change in the state of the system passing through local manifolds which are tangent to each other or manifolds with different orientability properties. In this sense, this study can help to extend the application of the aforementioned approaches, since, jumps are one of the primary factors preventing broader adoption of this type of identification.

28.5.1 Non-conservative System

The non-conservative system shown in Fig. 28.1 is considered herein with non-zero damping coefficients with the same underlying conservative system as the system in (28.1). The EOM of this system can be written as

$$\begin{bmatrix} \ddot{x}_1 \\ \ddot{x}_2 \end{bmatrix} = -\begin{bmatrix} 2 & -1 \\ -1 & 2 \end{bmatrix} \begin{bmatrix} x_1 \\ x_2 \end{bmatrix} - C \begin{bmatrix} \dot{x}_1 \\ \dot{x}_2 \end{bmatrix} - \begin{bmatrix} 0.5x_1^3 \\ 0 \end{bmatrix}. \tag{28.11}$$

or equivalently

$$\begin{bmatrix} \dot{x}_1 \\ \dot{x}_2 \\ \dot{y}_1 \\ \dot{y}_2 \end{bmatrix} = \begin{bmatrix} 0_{2\times 2} & \mathbf{I}_{2\times 2} \\ \begin{bmatrix} -2 & 1 \\ 1 & -2 \end{bmatrix} & -C \end{bmatrix} \begin{bmatrix} x_1 \\ x_2 \\ y_1 \\ y_2 \end{bmatrix} + \begin{bmatrix} 0 \\ 0 \\ -0.5x_1^3 \\ 0 \end{bmatrix} \tag{28.12}$$

where the damping matrix C is defined by

$$\begin{bmatrix} 0_{2\times 2} & 0_{2\times 2} \\ 0_{2\times 2} & -C \end{bmatrix} = V^T \begin{bmatrix} 0_{2\times 2} & 0_{2\times 2} \\ 0_{2\times 2} & \begin{bmatrix} 2\zeta_1\omega_1 & 0 \\ 0 & 2\zeta_2\omega_2 \end{bmatrix} \end{bmatrix} V \tag{28.13}$$

in which, $(i\omega, V)_i$ define the linearized modes of the conservative part of the system in (28.11). This way, one can readily find the damping matrix

$$\begin{aligned} C &= V^T \begin{bmatrix} 2\zeta_1\omega_{n1} & 0 \\ 0 & 2\zeta_2\omega_{n2} \end{bmatrix} V = 2 \begin{bmatrix} -\frac{\sqrt{2}}{2} & -\frac{\sqrt{2}}{2} \\ -\frac{\sqrt{2}}{2} & \frac{\sqrt{2}}{2} \end{bmatrix}^T \begin{bmatrix} \zeta_1 & 0 \\ 0 & \sqrt{3}\zeta_2 \end{bmatrix} \begin{bmatrix} -\frac{\sqrt{2}}{2} & -\frac{\sqrt{2}}{2} \\ -\frac{\sqrt{2}}{2} & \frac{\sqrt{2}}{2} \end{bmatrix} \\ &= \zeta_1 \begin{bmatrix} 1 & 1 \\ 1 & 1 \end{bmatrix} + \sqrt{3}\zeta_2 \begin{bmatrix} 1 & -1 \\ -1 & 1 \end{bmatrix}. \end{aligned} \tag{28.14}$$

that should be used to give two desired modal damping ratios in the system (28.11).

28.5.2 Cases of Jump Phenomena in the Free Response of the Non-conservative System

In this section, the system described in (28.11) is initiated at an initial condition that is on one of the periodic orbits on ICM I or ICM II, but with a small deviation δ. The time evolution of the solution is then calculated using the EOM defined in (28.11) for different values of ζ and δ. Then, the short time Fourier transform is used to obtain the spectrogram of the solution. The dominant frequency at each time instant is then extracted from the spectrogram. Figures 28.13–28.16 show

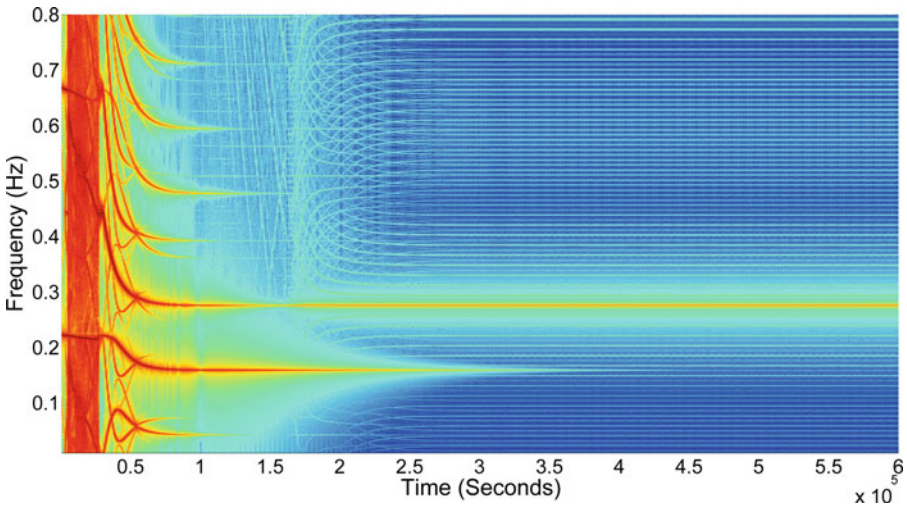

Fig. 28.12 Time-frequency history of the solution of the system, initiated on the ICM II, is calculated using short-window Fourier transform

the results of a few of these simulations in which jump phenomena are observed as the system looses energy along different invariant manifolds of the underlying conservative system. Two (out of many possible) scenarios are outlined next to explain these jumps as the interaction between invariant manifolds of the system.

In order to explain the jumps in the dominant frequency of solution of the system, for example in the time-frequency plot shown in Fig. 28.12, some background could be beneficial. This is provided next. Moving along an invariant manifold of the system, in this case the local center manifold or local ICM, the solution of the system may change its path from one manifold to another manifold that comes to contact with it. In this scenario, in order for such a change to happen, two ingredients are required. First, the two mentioned manifolds should be tangent to each other at the state where the solution changes its course from one to another. This tangency or non-transversality can be captured by the resonance condition or equivalently in the transversality condition. At the resonance condition, the Jacobian of the linearized system around the equilibrium becomes singular, indicating that its manifold may have more than one tangent plane at that equilibrium. The non-transversality condition described in Eq. (28.17) expresses the same concept in terms of (real part of) Floquet exponents and the change in the stability of the equilibrium. Second, the solution of the system needs to be perturbed (or be in a perturbed state) while passing through the neighborhood of the non-transversal intersection. In this regard, the initial perturbation δ is imposed to the solution of the system on the local ICMs. Note that when the manifold (NNM branch) is stable, the deviation δ will gradually decay due to damping until it is no longer strong enough to cause a jump in the path of the solution.

Jump phenomena may also occur when the solution of the system changes its path because of the orientability properties of the manifolds on its path. The manifold described by one of the NNM branches is typically a curvilinear plane or a twisted strip. It may be intersected by a variety of other manifolds. For example, suppose that the second manifold is a closed orientable manifold such as a torus. In this case, the solution of the system cannot lose energy by orbiting outside of the torus and needs to move to the inside. That is not possible because torus defines an orientable manifold. In such cases, a jump to the next open manifold is likely to happen. On the other hand, a twisted Mobius stripes and twisted strips are both open (nonorientable and orientable) manifolds where the solution of the system can lose energy while orbiting on one side of the manifold without having to cross it, and so, the response of the system is likely to stay on this type of manifold and not exhibit a jump.

Figure 28.13, shows an example where the solution was initiated on the ICM II with $\delta = 0.05\,\%$ deviation in its initial condition. The damping ratio was set to $\zeta_{1,2} = 1e-7$. Each neighborhood of the points marked with circles (denoted by letters A to F) houses two consecutive jumps which will be explained next. Starting (almost) on ICM II, the solution of the system begins losing energy on one side of ICM II (an orientable Twisted strip) until it hits point A. Two consecutive jumps, one because of non-transversality and another because of an orientable torus happens in the neighborhood A. First, the solution jumps from ICM II to ICM I-5,II-15 because of non-transversal intersection of the ICM II and the ICM I-5,II-15 manifolds become tangent (15:1 resonance). However, this jump is not evident in the dominant frequency shown in Fig. 28.13, because, the scaling function described in (28.3) is used to scale the dominant frequency. In the absence of this scaling function, the dominant frequency would be seen to jump to 1/15th of the ICM II frequency. Then, since the manifold ICM I-5,II-15, at the neighborhood of A is a torus, the solution jumps again to ICM I in the neighborhood B where ICM I is locally a orientable twisted Mobius strip. The solution continues to lose energy until it reaches the end of the neighborhood B where the local ICM I is tangent to ICM II (3:1 resonance-the local ICM of this point is visualized in Fig. 28.8- Middle-Left). At this point, the solution jumps back on the ICM II and continues to lose energy on one side of its orientable twisted strip until it enters

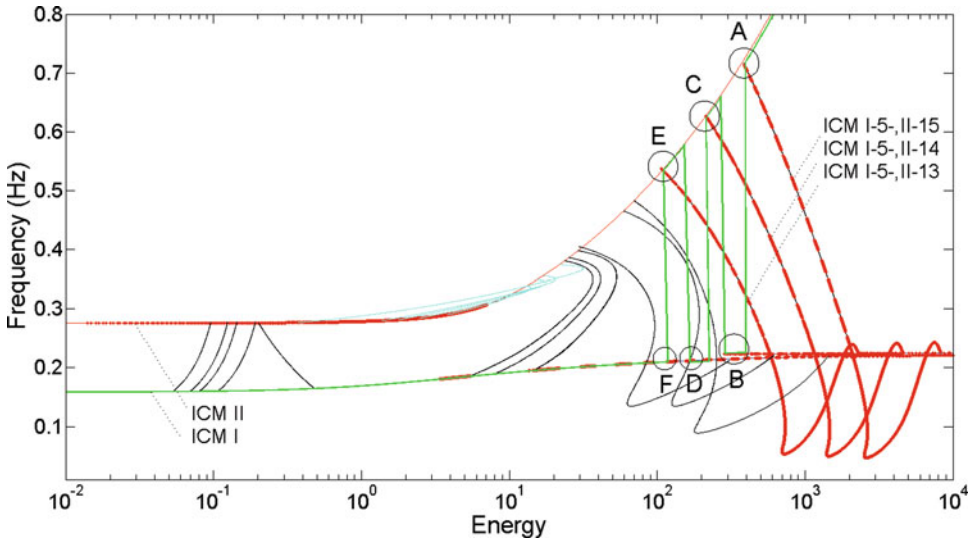

Fig. 28.13 Dominant frequency of the decaying solution of the system is overlaid on top of ones from identified ICMs of the underlying conservative system. Unstable periodic orbits are shown in *red dots* for five of the ICMs, i.e. ICM I, ICM II, ICM I-5,II13,ICM I-5,II14 and ICM I-5,II15. Jumps occur at six neighborhood labeled A to F

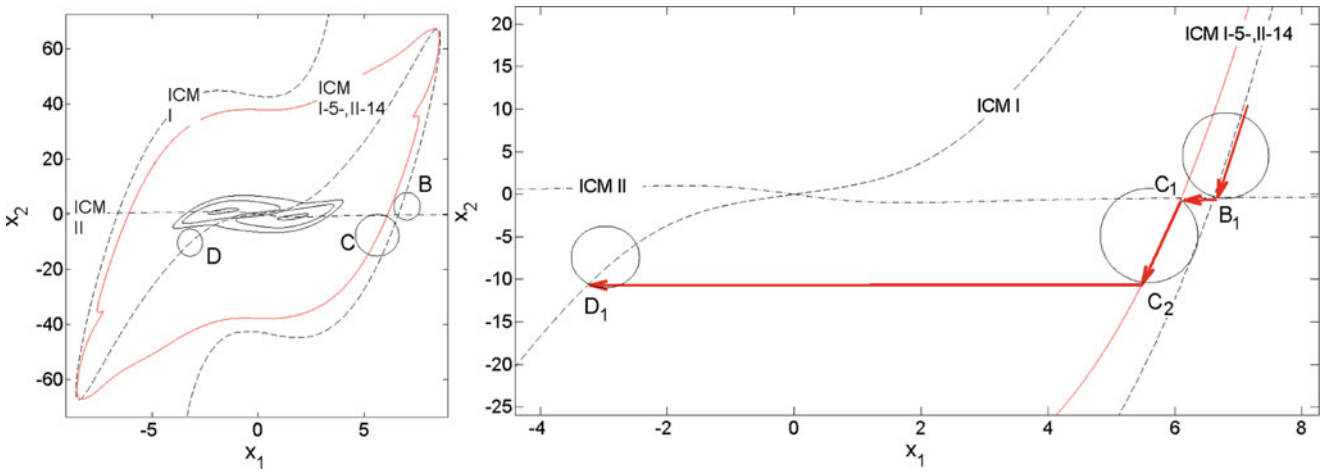

Fig. 28.14 *Left*: Poincare map sowing the ICMs I, II and I-5,II-14. *Right*: Magnified view showing the solution of the system at the neighborhood B and C highlighted by *red arrows*

in the neighborhood C. Same set of jumps as in the neighborhood A happens in neighborhood C causing the solution to jump down on the ICM I which is locally an orientable twisted strip in the neighborhood D. Another sets of two consecutive jumps similar to neighborhoods A and C, send the solution back up to the ICM II (neighborhood E) and then down to ICM I (neighborhood F). However, at this point, the deviation δ has decayed to a level that is not enough to cause any other jumps at the upcoming points prone to jump at its path on ICM I.

These jumps are examined in more detail in Fig. 28.14, which shows a cross section of a Poincare map of the system (defined in Sect. 28.2) that shows several of the ICMs of the system in the neighborhoods B and C that were marked in Fig. 28.13. Moving along the ICM I, the solution reaches the non-transversal intersection between the ICM I and ICM II at the point B_1 in the neighborhood B. At this point the deviation δ causes the solution to jump from ICM I to ICM II and continue on it until it reaches the point C_1 in the neighborhood C. At this point the ICM II and ICM I-5-II-14 intersect non-transversaly and the solution jumps onto the ICM I-5-II-14 and it continues on ICM II until point C_2. The point C_2 represents a periodic solution that orbits on the surface of a torus (its local ICM). The periodic orbit at C_2 is the product of the periodic orbit at C_1 after losing stability through torus bifurcation. At this point, since the solution cannot lose energy by orbiting outside of a torus and also cannot move through it, since the torus is orientable, it jumps again onto the ICM I in the neighborhood D.

In another case, shown in Fig. 28.15, the solution, which was initiated on ICM I, reveals a similar set of jumps at the neighborhood B, C, and D and finally rest at ICM II.

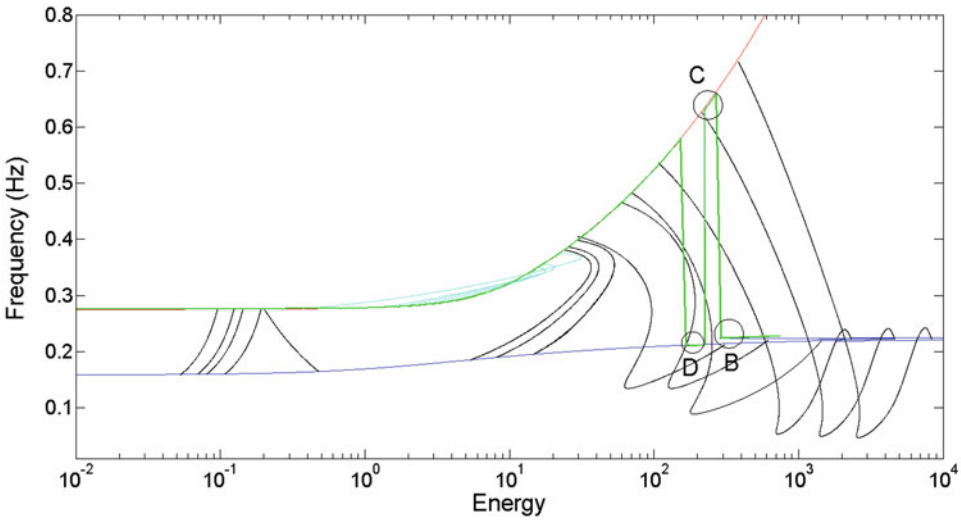

Fig. 28.15 Dominant frequency of the decaying solution of the system initial (almost) on the ICM I with $\delta = 0.05\,\%$ and $\zeta = 1e-6$. At the neighborhood B, C, and D the divination of the solution from the periodic orbits of the underlying conservative system forces the solution to move form one ICM to another one at their non-transversal intersections causing the frequency of the solution to jump. It's worth noting that although the solution was initiated on the ICM I, it reaches the origin through losing energy on the ICM II

As explained earlier, damping also causes the deviation to decay as the solution advances. This effect is evident at the neighborhood F where the deviation has decayed to such an extent that it is not enough to cause another jump despite the existing potential for another set of jumps at its next encounters with non-transversal intersections. This effect can be further examined by recomputing the response with a damping ratio $\zeta_{1,2} = 1e-6$, that is ten times larger than what was used in Fig. 28.13. To illustrate this effect, the dominant frequency of the solution of the system (for the same set of initial conditions and deviation) are obtained for damping ratios $\zeta_1 = \zeta_2 = \{5e-7, 1e-6, 12e-6\}$. As shown in Fig. 28.16, increasing the damping ratio will cause a the initial deviation to decay more quickly so that it falls below the level at which it is sufficient to cause a jump at a non-transversal intersection. At $\zeta = 12e-6$, the initial deviation is damped enough before the solution reaches the first non-transversal intersection. It is worth mentioning that decreasing the initial deviation has the exact same effect as increasing the damping ration on the behavior of the solution at non-transversal intersections on its path.

28.6 Conclusion

This paper has showed that catastrophe theory and bifurcation theory can be used to understand abrupt discontinuities in the response of a dynamical system. While this is a concept that has attracted scientists and engineers for centuries and the bifurcation and catastrophe theory that have been employed are not new, this work has sought to connect these concepts to modes of vibration and (internal) resonance. In this regard, this paper presented a brief introduction of an extended definition of modes of vibration, i.e. nonlinear modes, through the concept of ICM. Three different representation of such modes are provided for a two DOF nonlinear conservative system. One key tool that is needed in this type of analysis is a means of calculating the stability of periodic orbits. Although the concept is well established, this is incredibly challenging for a nonlinear system based on numerical ICMs or NNMs. Here a new criteria was presented that makes this possible

This study discussed the effect of nonlinear modes on the solutions of nonlinear systems through geometric concepts such as the loci of nonlinear modes (ICMs) and their orientability. These concepts are explicated by few examples of orientable and nonorientable ICMs of the nonlinear modes of the case study. An explanation is provided at two qualitative and quantitative levels that relates the bifurcation theory, catastrophe theory and the geometric properties of the ICMs of nonlinear systems. Furthermore, a slightly damped adaptation of the cases study is presented. Decaying response of the system is studied using time-frequency analysis. Results reveal multiple cases of jump phenomena which were explained through catastrophes and bifurcations caused by non-transversal (tangential) intersection of ICMs.

The findings presented here can be used in several ways. As mentioned previously, they explain why it is sometimes difficult to force a system to decay along one of its NNMs as is required in the identification method in [43]. This may lead to a better understanding of what classes of systems are most suitable for that identification method and how to increase the probability of success. One other application, is to utilize to find the ICMs (branches of nonlinear modes) that are not continuations of linear modes. Regions that exhibits jump phenomena can be searched for new nonlinear modes by initiating continuation algorithms at different directions.

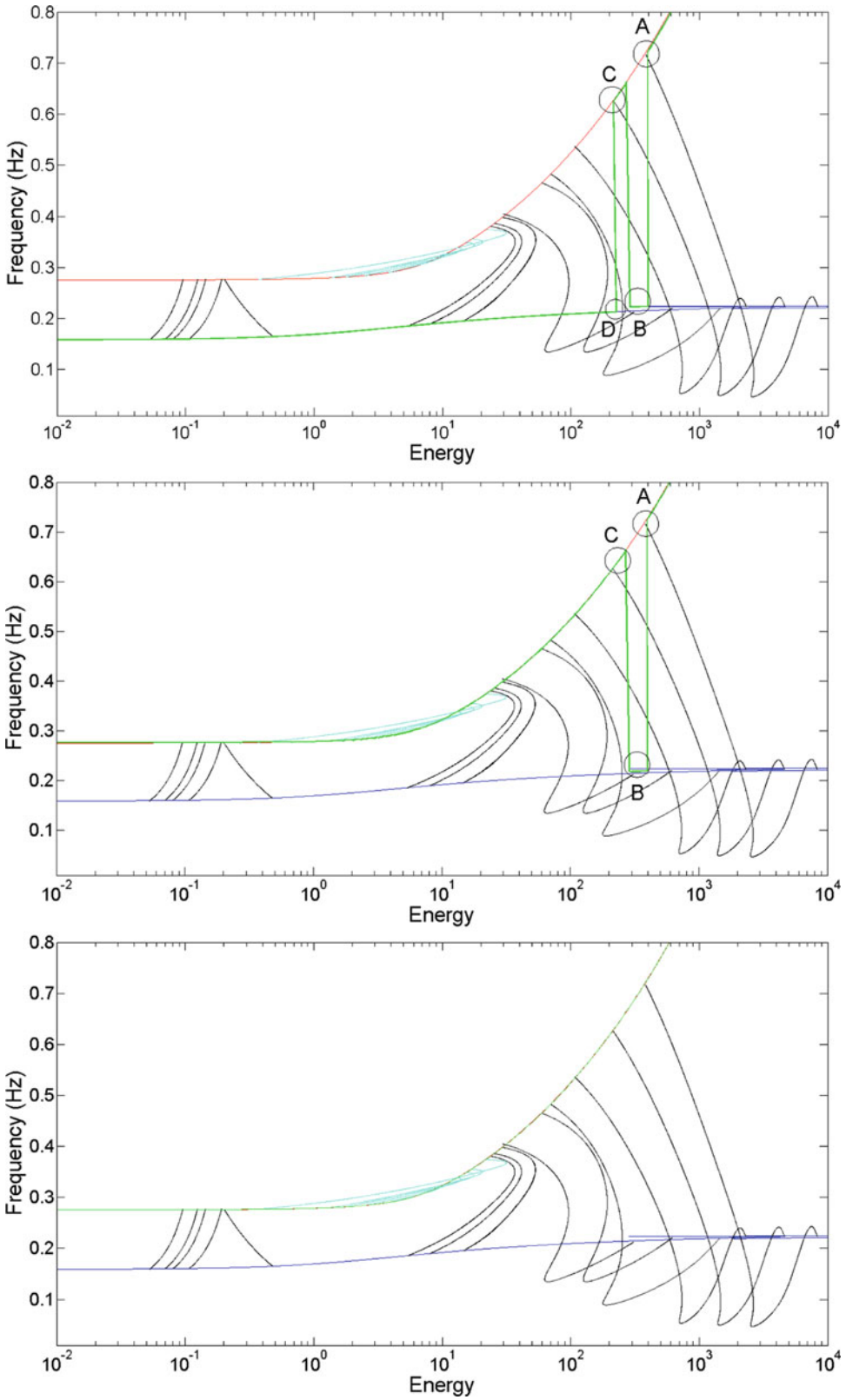

Fig. 28.16 Dominant frequency of the solution of the damped system, shown with a *solid green line*, obtained for damping ratios $\zeta = \{5e-7, 1e-6, 12e-6\}$. Increasing the damping ratio, while the initial deviation was held fixed, has caused the initial deviation to decay quickly to below the level at which it is large enough to perturb the solution at its first encounter with the non-transversal intersection at neighborhood A and at all subsequent intersections. It is also interesting to note that the response continues to decay along the ICM II even though many of the periodic orbits are unstable for energies below 10^1

Appendix A: Orientability of Periodic Solutions

This section explains a quantitative approach that can determine the orientability property of local invariant manifolds using the Floquet multipliers and exponents of the corresponding periodic orbit about which the manifold was created. In this approach, first, periodic orbits are categorized based on their Floquet exponents as shown in Table 28.1. Then, the

Table 28.1 Nine types of periodic orbits are identified for the system (28.1) based on their Floquet multiplier and exponents. Floquet multipliers and exponents are denoted by ρ and μ respectively

Periodic orbit type	Floquet exponent	Stable manifold/unstable manifold	Center manifold/ICM
1. Center 1	$\mu_1 = i\psi_1$	$\emptyset$	4D orientable surface (curvilinear planes)
(center-center)	$\mu_2 = -i\psi_1$	$\emptyset$	
	$\mu_3 = i\psi_2$		
	$\mu_4 = -i\psi_2$		
2. Sink 1	$\mu_1 = -\lambda_1 + i\psi_1$	4D $\rho_i\|_{i=3}^4 = \begin{cases} \in \mathbb{R}^+ & \text{onorientable} \\ otherwise & \text{nonorientable} \end{cases}$ stable	$\emptyset$, 2D $p+q = \begin{cases} 2k+1 & \text{nonorientable} \\ 2k & \text{orientable} \end{cases}$ surface
(sink-sink)	$\mu_2 = -\lambda_1 - i\psi_1$		
	$\mu_3 = -\lambda_2 + i\psi_2$		
	$\mu_4 = -\lambda_2 - i\psi_2$		
3. Sink 2	$\mu_1 = i\psi_1$	2D $\rho_i\|_{i=3}^4 = \begin{cases} \in \mathbb{R}^+ & \text{onorientable} \\ otherwise & \text{nonorientable} \end{cases}$ stable	2D orientable torus
(sink-center)	$\mu_2 = -i\psi_1$		
	$\mu_3 = -\lambda_2 + i\psi_2$		
	$\mu_4 = -\lambda_2 - i\psi_2$		
4. Source 1	$\mu_1 = \lambda_1 + i\psi_1$	4D $\rho_i\|_{i=1}^4 = \begin{cases} \in \mathbb{R}^+ & \text{onorientable} \\ otherwise & \text{nonorientable} \end{cases}$ unstable	$\emptyset$, 2D orientable torus
(source-source)	$\mu_2 = \lambda_1 - i\psi_1$		
	$\mu_3 = \lambda_2 + i\psi_2$		
	$\mu_4 = \lambda_2 - i\psi_2$		
5. Source 1	$\mu_1 = i\psi_1$	2D $\rho_i\|_{i=3}^4 = \begin{cases} \in \mathbb{R}^+ & \text{onorientable} \\ otherwise & \text{nonorientable} \end{cases}$ unstable	2D orientable torus
(source-center)	$\mu_2 = -i\psi_1$		
	$\mu_3 = \lambda_2 + i\psi_2$		
	$\mu_4 = \lambda_2 - i\psi_2$		
6. Saddle 1	$\mu_1 = \lambda_1$	2D orientable stable	$\emptyset$, 2D $p+q = \begin{cases} 2k+1 & \text{nonorientable} \\ 2k & \text{orientable} \end{cases}$ surface
(saddle-saddle)	$\mu_2 = -\lambda_1$	2D orientable unstable	
	$\mu_3 = \lambda_2$		
	$\mu_4 = -\lambda_2$		
7. Saddle 2	$\mu_1 = \lambda_1$	1D stable curve	2D orientable torus
(saddle-center)	$\mu_2 = -\lambda_1$	1D unstable curve	
	$\mu_3 = i\psi_1$		
	$\mu_4 = -i\psi_1$		
8. Saddle 3	$\mu_1 = -\lambda_1 + i\psi_1$	2D $\rho_i\|_{i=}^2 = \begin{cases} \in \mathbb{R}^+ & \text{onorientable} \\ otherwise & \text{nonorientable} \end{cases}$ stable	$\emptyset$, 2D orientable torus
(source-sink)	$\mu_2 = -\lambda_1 - i\psi_1$	2D $\rho_i\|_{i=3}^4 = \begin{cases} \in \mathbb{R}^+ & \text{onorientable} \\ otherwise & \text{nonorientable} \end{cases}$ unstable	
	$\mu_3 = \lambda_2 + i\psi_2$		
	$\mu_4 = \lambda_2 - i\psi_2$		
9. Saddle 4	$\mu_1 = -\lambda_1 + i\psi_1$	2D $\rho_1 = \begin{cases} \in \mathbb{R}^+ & \text{onorientable} \\ otherwise & \text{nonorientable} \end{cases}$ stable	$\emptyset$, 2D orientable torus
(source-sink)	$\mu_2 = -\lambda_1 - i\psi_1$	2D $\rho_1 = \begin{cases} \in \mathbb{R}^+ & \text{onorientable} \\ otherwise & \text{nonorientable} \end{cases}$ unstable	
	$\mu_3 = \lambda_1 + i\psi_1$		
	$\mu_4 = \lambda_1 - i\psi_1$		

orientability of both the local stable and unstable manifolds, if they exist, are determined using Floquet multipliers. This orientability property is the key to understanding whether a periodic orbit can be reached by the system from a particular region in the state space, and hence whether the system is likely to jump or remain on a particular solution branch. For example, in the damped system studied herein, since the system is losing energy, it will always approach any periodic orbit, on its path, from its local stable manifold. Therefore, if the stable manifold of a periodic orbit is orientable, the periodic orbit in question will not affect the path of the solution of the system. In this study, these periodic orbits are referred to as isolated periodic orbits. Next, the orientability of local center manifold is determined using Floquet multipliers. However, local center manifold do not always exist. In such cases, one can assign the orientability of the local ICM to the periodic orbit. That is because, the orientability of the local center manifold and the local ICM should agree at all times since ICMs are the loci of all periodic orbits of the system. In other words, in such cases , periodic orbits adopt the orientability of the center manifolds of periodic orbits in their neighborhood on the local ICM.

The basis in identifying the orientability property of local stable and unstable manifolds of periodic orbits is the fact that Floquet multipliers of a periodic orbit are the same as eigenvalues of its Poincare map [37, 44, 45]. In [46–48] it was shown that a local manifold is orientable if all of the eigenvalues of its Poincare map are real and positive. This was done using the fact that the Poincare map is an orientation preserving map.[2]

The orientability of a local center manifold is based on the type of bifurcation that has generated it. In this study, the system exhibits, mostly, three types of bifurcations, namely, Hopf-Hopf bifurcations, Period-Doubling bifurcations and Andronov-Hopf (or Torus) bifurcations. One can determine which type of bifurcation one has based on the Floquet multipliers of the periodic orbit, as will be discussed in the next section. In this regard, the local center manifold of a periodic orbit is:

- An orientable curvilinear plane if it is originated from a Hopf-Hofp bifurcation,
- A twisted strip with k half-twists (orientable for even k and nonorientable for odd k) if it is originated from a Period-Doubling bifurcation, or
- An orientable torus if it is originated from an Andronov-Hopf (torus) bifurcation.

In cases where the local center manifolds do not exist, such as cases of periodic orbits with Period-Doubling bifurcations, the local ICMs can be used to determine the orientability property of the periodic orbits. In this regard, since, all coordinates of a periodic solutions are also periodic, one can assume an analytical representation of the ICMs [31] of the system (28.1) as

$$\begin{aligned} x_1 &= \Sigma A_m^{(1)} \cos m\phi_1 = \cos\phi_1 \left(A_1^{(1)}(T) + \Sigma_{m=2} \left[A_m^{(1)} \cos m\phi_1 \right] \right) \\ H_{x_1} &= \Sigma A_m^{(1)} \sin m\phi = \sin\phi_1 \left(A_1^{(1)} + \Sigma_{m=2} \left[A_m^{(1)} \sin m\phi_1 \right] \right) \\ x_2 &= \Sigma A_m^{(2)} \cos m\phi_2 = \cos\phi_2 \left(A_1^{(2)} + \Sigma_{m=2} \left[A_m^{(2)} \cos m\phi_2 \right] \right) \end{aligned} \tag{28.15}$$

where ϕ_i's, in general, are

$$\begin{aligned} \phi_1 &= q\phi_0 \\ \phi_2 &= p\phi_0 \end{aligned} \tag{28.16}$$

and, $\phi_0 = \frac{2\pi}{T}t$ and T represents the period of the periodic orbits. Equation (28.15), in general,[3] defines a twisted strip with $p+q$ half-twists (see ruled surfaces in [49, 50]). In this sense, following the discussed in Sect. 28.3, if $p+q$ is odd, then (28.15) defines a nonorientable surface. On the other hand, the surface is orientable if $p+q$ is even.

To this end, nine types of periodic orbits are identified and the orientability of their local invariant manifolds (including the local ICM) are summarized in Table 28.1. It is importance to mention that Table 28.1 is obtained applies only to a 2 DOF conservative oscillatory system and is far from providing a complete list for a general dynamical system in $\mathbb{R}^4$.

Appendix B: Mechanisms of Losing Stability (Cases of Local and Global Bifurcations)

Section 28.4.1 discussed how the stability of a periodic orbit manifests itself through Floquet multipliers (or exponents). Section 28.4.2 presented the relationship between the Floquet multipliers (or exponents) and the orientability of the local

[2] Poincare map is a rotation matrix with unity determinant.

[3] In some special cases, such as where $\phi_2 = \frac{(2k+1)\pi}{2} - \frac{l}{2}\phi_1, k, l \in \mathbb{N}$, Eq. (28.15) generates Tori.

invariant manifolds of the periodic orbits. This section, explains some of the mentioned relations based on mechanisms through which fixed points or periodic orbits lose stability and as a result new periodic orbits come to exist. These mechanisms describe the change in the structure of the geometry of the periodic orbits and their local invariant manifolds as a function of the change in their period. In this regard two mechanisms explaining two types of bifurcations, with an eminent role in the system (28.1), are presented. Note that the system in (28.1) exhibits a very rich set of different types of bifurcations, including some special cases. However, the study of all such cases of bifurcations is beyond the scope of this paper. For more details on different types of bifurcation, specially in $\mathbb{R}^4$, readers are referred to [35, 37, 45, 51].

28.6.1 Bifurcations of Periodic Orbits from a Fixed Point

Hopf-Hopf Bifurcation An equilibrium point is referred to as a Hopf-Hopf point (or double Hofp point) if, at the mentioned point; first, the system has only two pairs of purely imaginary eigenvalues, i.e. $\pm i\omega_1, \pm i\omega_2$ and, second, if the change in the imaginary part of the Floquet exponents with respect to the period is zero, or specifically, the transversality (generosity) condition (see [35, 37, 51])

$$\frac{d}{dT}\mu_i = 0 \tag{28.17}$$

is satisfied. This is a broad definition that also includes unusual Hopf points. In a four dimensional system, at a Hopf-Hopf point many cases of bifurcation can occur which are described in [51]. In the case of the system (28.1), bifurcation of double Hopf points is the birthplace of four (half) branches of periodic orbits on two dimensional invariant linear (and later curvilinear) planes. These branches of periodic orbits include linear modes of vibration and their nonlinear continuation. In this sense, one can state that the Hopf-Hopf bifurcation of the fixed point of the system (28.1) is the birthplace of the modes of vibration in that neighborhood (Fig. 28.17).

28.6.2 Bifurcations of Periodic Orbits from a Periodic Orbit

Neimark-Sacker Bifurcation Neimark-Sacker (Torus) bifurcation[4] is characterized by a pair of complex conjugate multipliers crossing the unit circle at

$$\rho = e^{\pm i\phi}, \ \phi \neq 0, \pi. \tag{28.18}$$

The bifurcation into a torus only happens in three or higher dimensional systems. In this case, a periodic orbit, that has lost its stability, spirals around a torus. This is schematically shown for a 3 dimensional case in Fig. 28.18. Moreover, as shown in Fig. 28.18, in case of a torus bifurcation, the fixed point of Poincare map becomes unstable and generates limit cycles.

Numerous cases of torus bifurcations occur in the system (28.1). This can be observed in Fig. 28.19 which shows the Floquet multipliers of two branches of periodic orbits. For example, in ICM I-5,II-9, the type-4 periodic orbits (in Table 28.1) bifurcate from the periodic orbit with multipliers shown in solid black circles through torus bifurcation. Both pairs of multipliers move outside the unit circle. The type-8 periodic orbits shown in red solid circles are the products of torus bifurcation of the periodic orbit with multipliers shown in solid green circles. In addition, in ICM II-56, the type-9 periodic orbits are created through torus bifurcation of the periodic orbit with multipliers shown in solid black circles. A pair of multipliers move inside the unit circle while the other one move inside.

[4]It is sometimes called Hopf bifurcation of periodic orbits, secondary Hopf bifurcation or generalized Hopf bifurcation.

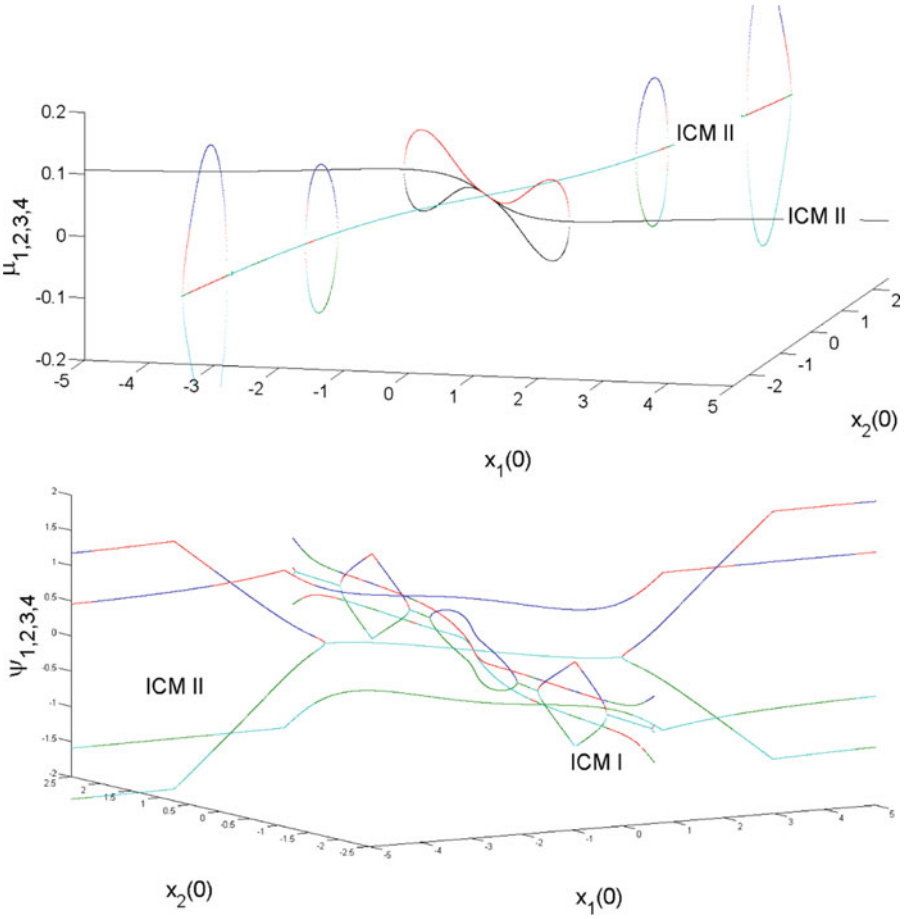

Fig. 28.17 *Top*: Real parts of Floquet exponents calculated for ICM I and ICM II and shown on the cross-section of the Poincare map described in Sect. 28.2. The period T is defined as an descending variable along theses branches as they move away from the fixed point at the origin. The transversality (generosity) condition, i.e. $\frac{d\mu_i}{dT} = 0$, is satisfied at the fixed point of the system (28.1) at the origin. Therefore, the fixed point at the origin is double Hopf point for the system (28.1). *Bottom*: Imaginary parts of Floquet exponents calculated for ICM I and ICM II

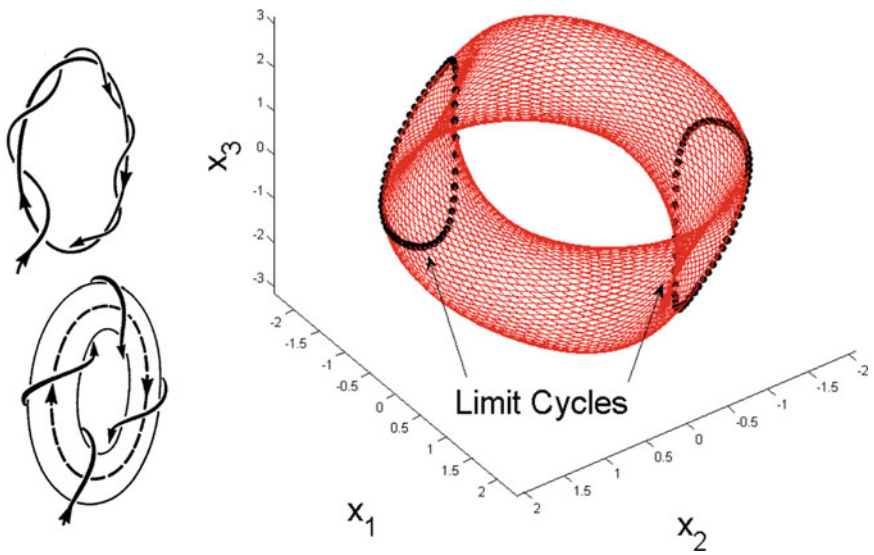

Fig. 28.18 *Left*: A schematic illustration of torus bifurcation. A stable periodic orbit becomes unstable surrounded by a stable 2D torus. *Right*: Poincare map (shown with *black dots*) of a periodic orbit (shown in *solid red*) initiated at (0.9061 -1.6894, 0, 0). Appearance of limit cycles in the Poincare map reveals a case of torus bifurcation

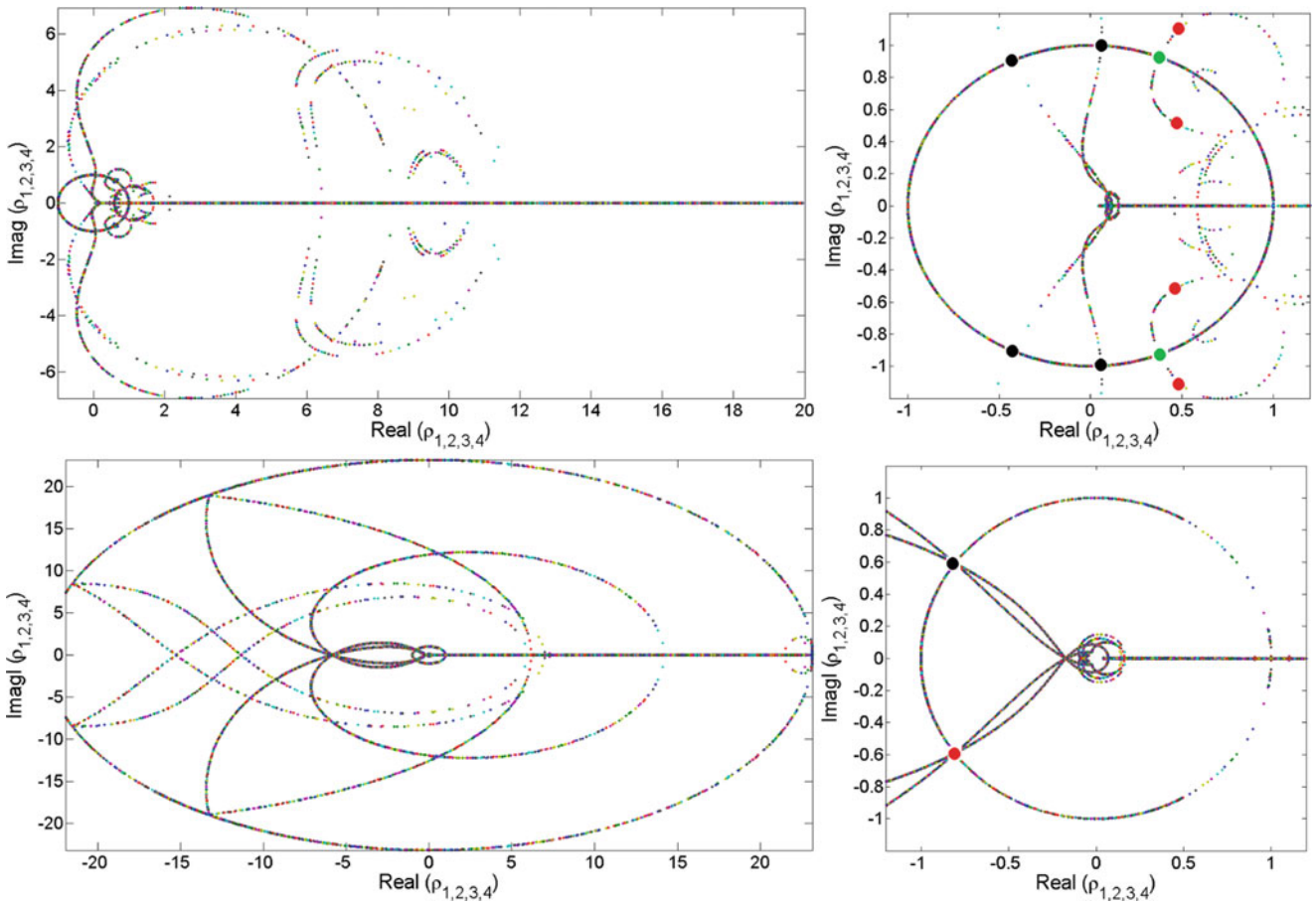

Fig. 28.19 *Left*: Real part of Floquet multipliers calculated for ICM I-5,II-9 (*Top*) and ICM II-56 (*Bottom*). *Right*: Floquet multipliers of ICM I-5,II-9 (*Top*) and ICM II-56 (*Bottom*) in the neighborhood of the unit circle

References

1. Yasui H, Marukawa H, Momomura Y, Ohkuma T (1999) Analytical study on wind-induced vibration of power transmission towers. J Wind Eng Ind Aerodyn 83(1):431–441,
2. Shaw J, Shaw SW, HaddowA G (1989) On the response of the non-linear vibration absorber. Int J Non-Linear Mech 24(4):281–293
3. Oueini SS, Chin CM, Nayfeh AH (1999) Dynamics of a cubic nonlinear vibration absorber. Nonlinear Dyn 20(3):283–295
4. Jiang X, McFarland DM, Bergman LA, Vakakis AF (2003) Steady state passive nonlinear energy pumping in coupled oscillators: theoretical and experimental results. Nonlinear Dyn 33(1):87–102
5. Murata A, Kume Y, Hashimoto F (1987) Application of catastrophe theory to forced vibration of a diaphragm air spring. J Sound Vib 112(1):31–44
6. Shimozawa K, Tohtake T (2008) An air spring model with non-linear damping for vertical motion. Q Rep RTRI 49(4):209–214
7. Huang Y, Iwamoto S (1995) Analysis of a possible reason for oscillation phenomena in a diesel-generator set through catastrophe theory. IEEE Trans Energy Convers 10(4):700–705
8. Ewins DJ (1970) A study of resonance coincidence in bladed discs. J Mech Eng Sci 12(5):305–312
9. Ewins DJ (1973) Vibration characteristics of bladed disc assemblies. J Mech Eng Sci 15(3):165–186
10. Afolabi D, Alabi B (1992) Catastrophe theory, curve veering and the vibration of bladed discs. In: Proceedings of the institution of mechanical engineers, part C. J Mech Eng Sci 206(2):143–144
11. Adams WM (1972) Analytic prediction of airplane equilibrium spin characteristics, vol 6926. Natl Aeronaut Space Administration, Washington, DC
12. Hacker T (1974) A discussion of the roll-coupling problem. Prog Aerosp Sci 15:151–180
13. Schy AA, Hannah ME (1977) Prediction of jump phenomena in roll-coupled maneuvers of airplanes. J Aircr 14(4):375–382
14. Holmes PJ, Rand DA (1976) The bifurcations of duffing's equation: an application of catastrophe theory. J Sound Vib 44(2):237–253
15. Fang T, Dowell EH (1987) Numerical simulations of jump phenomena in stable duffing systems. Int J Nonlinear Mech 22(3):267–274
16. Ueda Y (1979) Randomly transitional phenomena in the system governed by duffing's equation. J Stat Phys 20(2):181–196
17. Brennan MJ, Kovacic I, Carrella A, Waters TP (2008) On the jump-up and jump-down frequencies of the duffing oscillator. J Sound Vib 318(4):1250–1261

18. Thom R (1972) Stabilité structurelle et morphogénèse. WA Benjamin: Reading
19. Zeeman EC (1971) The geometry of catastrophe. Times Lit Suppl 10:1556–7
20. Ardeh HA, Negrut D (2011) Instantaneous center manifolds: an approach for approximating the dynamics of nonlinear systems. ASME J Comput Nonlinear Dyn
21. Rosenberg RM, Atkinson CP (1959) On the natural modes and their stability in nonlinear two-degree-of-freedom systems. J Appl Mech 26:377–385,
22. Rosenberg RM (1959) Normal modes of nonlinear dual-modes systems. Institute of Engineering Research, University of California
23. Rosenberg RM, American Society of Mechanical Engineers (1961) The normal modes of nonlinear n-degree-of-freedom systems. ASME, New York
24. Rosenberg RM (1962) On normal vibrations of a general class of nonlinear dual-mode systems. J Appl Mech 29:7–14
25. Rosenberg RM (1966) On nonlinear vibrations of systems with many degrees of freedom. Adv Appl Mech 9(155–242):6–1
26. Shaw SW, Pierre C (1991) Non-linear normal modes and invariant manifolds. J Sound Vib 150(1):170–173
27. Shaw SW, Pierre C (1993) Normal modes for non-linear vibratory systems. J Sound Vib 164(1):85–124. ISSN 0022-460X
28. Shaw SW, Pierre C (1994) Normal modes of vibration for non-linear continuous systems. J Sound Vib 169(3):319–347
29. Kerschen G, Peeters M, Golinval JC, Vakakis AF (2009) Nonlinear normal modes, part I: a useful framework for the structural dynamicist. Mech Syst Signal Process 23(1):170–194. ISSN 0888-3270
30. Peeters M, Viguié R, Sérandour G, Kerschen G, Golinval JC (2009) Nonlinear normal modes, part ii: toward a practical computation using numerical continuation techniques. Mech Syst Signal Process 23(1):195–216
31. Ardeh HA, Allen MS (2012) instantaneous center manifolds and nonlinear modes of vibrations. In: Proceedings of the ASME 2012 international design engineering technical conferences & computers and information in engineering conference. ASME, Chicago, IL
32. Poston T, Stewart I (1996) Catastrophe theory and its applications, vol 2. Dover, Mineola
33. Stewart I (1975) The seven elementary catastrophes. New Scientist 68(976):447–454
34. Stewart I (1983) Elementary catastrophe theory. IEEE Trans Circuits Syst 30(8):578–586
35. Arnol'd VI (2007) Lectures on bifurcations in versal families. Russ Math Surv 27(5):54
36. Hirsch MW, Pugh CC, Shub M (1977) Invariant manifolds. Springer, Berlin/New York. ISBN 3540081488
37. Kuznetsov IUA (1998) Elements of applied bifurcation theory, vol 112. Springer, New York
38. Masri SF, Miller RK, Saud AF, Caughey TK (1987) Identification of nonlinear vibrating structures: part i–formulation. J Appl Mech 109(4):918–922
39. Masri SF, Miller RK, Saud AF, Caughey TK (1987) Identification of nonlinear vibrating structures: part ii–applications. J Appl Mech 109(4):923–929
40. Giannakis GB, Serpedin E (2001) A bibliography on nonlinear system identification. Signal Process 81(3):533–580. ISSN 0165-1684
41. Kerschen G, Worden K, Vakakis AF, Golinval JC (2006) Past, present and future of nonlinear system identification in structural dynamics. Mech Syst Signal Process 20(3):505–592. ISSN 0888-3270
42. Bellizzi S, Guillemain P, Kronland-Martinet R (2001) Identification of coupled non-linear modes from free vibration using time-frequency representations. J Sound Vib 243(2):191–213
43. Peeters M, Kerschen G, Golinval JC (2011) Phase resonance testing of nonlinear vibrating structures. Nonlinear Model Appl 2:159–169
44. Hinke MO (2003) Nonorientable manifolds in three-dimensional vector fields. Int J Bifurc Chaos 13(03):553–570
45. Seydel RU (2009) Practical bifurcation and stability analysis, vol 5. Springer, New York
46. Kuipers JB (1999) Quaternions and rotation sequences. Princeton University Press, Princeton
47. Krauskopf B, Osinga H (1999) Two-dimensional global manifolds of vector fields. Chaos 9(3):768–774
48. Osinga HM (2000) Non-orientable manifolds of periodic orbits. In: Proceedings international conference on differential equations, Equadiff 99, Berlin, Germany, vol 2. pp 922–924
49. Dubrovin BA, Fomenko AT, Novikov SP (1984) Modern geometry: methods and applications. The geometry of surfaces, transformation groups, and fields. Springer, New York. ISBN 0387961623
50. Gray A, Abbena E, Salamon S (2006) Modern differential geometry of curves and surfaces with mathematica. Chapman & Hall/CRC, Boca Raton
51. Guckenheimer J, Holmes P (2002) Nonlinear oscillations, dynamical systems, and bifurcations of vector fields. Springer, New York. ISBN 0387908196

Chapter 29
Modelling of Gear Meshing: A Numerical Approach for Dynamic Behavior Estimation of Thin Gears

Francesca Curà and Carlo Rosso

Abstract The paper deals with the numerical analysis of thin gears. In particular, a brief overview of literature modeling techniques is reported in order to understand the best way for analyzing the dynamic behavior of gears. Then a multibody commercial software is used for implementing different complexity levels of models. The study starts with a simplified model that considers rigid the gears and concentrates the stiffness in the contact between teeth. The second, and more complex, model considers the stiffness in the contact and adds the compliance of the teeth. Stiffness of tooth is depicted as a rotational stiffness placed at the tooth root. Then, the third model increases the complexity, in fact the second model is complicated introducing the compliance of the gear body. In order to do that, a modal analysis of the gears is conducted and the synthetized modal shapes of the gears are introduced in the multibody model. The comparison highlights how the dynamic behavior of thin gears is really important in the meshing force estimation, in fact the transmission error becomes more irregular and the contact forces increase. As a second aspect, this analysis emphasizes the influence of the contact damping and the contact friction in the backlash phenomenon.

Keywords Nonlinear dynamics • Gear meshing • Dynamic behavior

29.1 Introduction

The analysis of the dynamic behavior of gears, related to engaging problems, is a very interesting topic, widely investigated in literature over the years.

In particular, many aspects may influence the dynamic of engaged gears, above all for as concerns both reliability and endurance [1]. As an example, it may be point out the effect stress variations, damage entity, transmission efficiency, loading conditions of bearings, stability regions, natural frequencies and forced vibrations, and so on.

From the 1920s to 1930s of the last century, a primary goal of engineers is to analyze the engaging dynamic problems in order to quantify the entity of teeth loadings by means of both analytical and experimental methodologies.

From the 1950s, very simplified lumped parameters systems (as mass-spring systems) have been set up to study dynamic effects on gears, becoming more and more sophisticated during the 1970s and 1980s. These models may include complex effects as the tridimensional stiffness of teeth, nonlinearities of the system, damping and friction parameters.

Nowadays, reference models available in literature show the peculiarity to take into account global dynamic phenomena as torsion, flexural and axial vibrations, allowing to obtain both transitory and operating responses, also if different typologies of engaging errors are considered.

Aim of the present work is to set up a combined multibody/FEM numerical technique, on the basis of a commercial code, in order to simulate the engaging phenomenon in aerospace gears, whose peculiarity is a high flexibility of the body gear with respect teeth ring.

F. Curà • C. Rosso (✉)
Politecnico di Torino, Corso Duca degli Abruzzi, 24 – 10129, Torino, Italy
e-mail: francesca.cura@polito.it; carlo.rosso@polito.it

G. Kerschen et al. (eds.), *Topics in Nonlinear Dynamics, Volume 1: Proceedings of the 31st IMAC, A Conference on Structural Dynamics, 2013*, Conference Proceedings of the Society for Experimental Mechanics Series 35,
DOI 10.1007/978-1-4614-6570-6_29,

29.2 State of Art

On the basis of the mathematical models review very well summarized in [1] and referring to the main aspects related to the gear dynamics, engaging phenomena analysis may be classified as follows:

1. *"Dynamic factor" calculation.* This group of studies (involving also Fatigue Standards) describes how the rotating velocity of gears may cause an overloading conditions on teeth and takes it into account by means of a global parameter.
2. *Tooth elasticity and gears dynamic*. In the basic model, involving one degree of freedom, the tooth stiffness is considered as an elastic element to store the potential energy in the system; the flexibility of shafts and bearings is neglected. More complicated models include also the flexibility of other elements.
3. *Shaft dynamic and torsion vibrations*. Simplified models involve only flexible shafts and rigid gears, but some more complex aspects may be taken into account if also flexural vibrations and whirl phenomena of shafts are considered.

29.2.1 Dynamic Factor

Effective load in engaging teeth involves two principal components, a mean (corresponding to the transmitted torque) and a vibratory one (related to the stress variations).

The "Dynamic factor" or "Velocity factor" (as later identified) has been firstly suggested by Walker in 1868 [1] and defined as:

$$DF = SL/DL \tag{29.1}$$

where DF is the Dynamic factor, SL is the static loading value and DL is the dynamic one.

This factor was empirically determined by comparing the rupture stress values of gears obtained for different rotating velocities.

Then, Barth [1] calculated the Dynamic factor by means of another expression, reported in the following:

$$DF = 600/(600+V) \tag{29.2}$$

where V is the tangential velocity of the gear (calculated at the pitch circumference in *feet per minute* (fpm)). The above quoted relationship provides overestimated dynamic effects, due the fact that other aspects may contribute to dynamic behavior of gears, as manufacturing errors and inertia terms of both gear and pinion.

In 1927 Ross [1, 2] modified the Barth expression (29.2) as:

$$DF = 78/(78+\sqrt{V}) \tag{29.3}$$

Both Barth equation (29.2) and its modified versions (as an example Eq. (29.3)) are still today utilized, being reported in Gears Standards and mechanical handbooks.

During the 1950s, lumped parameters models have been developed for the dynamic analysis of gears.

The first one, set up by Tuplin [3, 4] and involving a mass-spring system, was based on the hypothesis of a constant equivalent engaging stiffness and engaging errors were modeled by means of different wedges at the spring extremity. If only transitory exciting phenomena (without periodic contributions and far from resonance conditions) have to be taken into account, the above quoted model may provide a good information about dynamic factors.

The first work considering the presence of periodic contributions goes back to the 1953 [5]; Strauch introduced in its model the stiffness step variation due to the loading transfer from one to two engaging teeth or vice versa.

In 1970 Houser [6] developed a semi-empirical formulation for the dynamic loading in engaged teeth on the basis of both experimental results and geometrical considerations. Related equation provides a general dynamic factor for straight and helical gears (running below the resonance of the whole system), considering also loading and velocity conditions together with manufacturing errors.

AGMA (American Gear Manufacturing Association) Standard refers to the following relationship for the Dynamic factor:

$$DF = \sqrt{78/(78+\sqrt{V})} \tag{29.4}$$

providing very similar value to those obtained by Ross [2].

In 1971 Tucker [7] combined the Tuplin approach to a new model involving teeth stiffness of straight and helical gears obtained by considering the gear tooth as a cantilever beam with a concentrate mass parameter at the pitch circumference.

Wang [8] in 1985 proposed a new method to calculate the dynamic loading entity by utilizing the mechanical formulas for rigid bodies and by introducing the dynamic *Transmission Error* as input.

29.2.2 Tooth Elasticity and Gears Dynamic

General peculiarity of the models referring to this class of phenomena is that only the elasticity of teeth gears is taken into account, while other elements of the system are considered as completely rigid. This way, the models are only translational or torsional (degrees of freedom translational or torsional, as required by the object under study).

In torsional models the system may be represented as two inertial elements connected by a spring that allows relative motion; in these cases, the study of torsional vibrations is the main goal.

In translational models, the tooth is considered as a cantilever beam, allowing a simple analysis of the forced oscillations.

For both models (torsional and translational) the excitation of the system is provided by the *Transmission Error*, that is an imposed displacement $e(t)$ as a function of time.

First approaches were related to the hypothesis of constant engaging stiffness, while the following ones considered the stiffness variable during the engaging period.

One of the most popular models is that of Kahraman and Singh [9]. This model considers the *Transmission Error* as the main exciting force causing the *backlash* non linear phenomenon, represented by a discontinuous and non derivable function in the following differential equation governing the system, whose integration in the time domain t needs numerical techniques:

$$\ddot{q}(t) + 2\varsigma\dot{q}(t) + f(q(t)) = F_m + F_{ah}\Omega_{\mathrm{h}}^2 \sin(\Omega_{\mathrm{h}} t + \phi_{\mathrm{h}}) \tag{29.5}$$

where q represents the difference between static and dynamic transmission error (acting along the direction of forces and starting from the contact point) and its derivatives respectively velocity and acceleration, ς the damping parameter, F_m and F_{ah} mean and alternate components of the global force and Ω_{h} the engaging frequency. By integrating equation (29.5) three solutions may be obtained: (a) no impact; (b) impacts related only to one side of the tooth; (c) impacts related to two sides.

Equation 29.5 is the basis of the more complex models available in literature [10, 11].

A recent and widely cited in the works involving engagement dynamic studies is that proposed by Velex [12] in 2005. The peculiarity of the above quoted paper is that the teeth stiffness is modeled as a function of the position of the contact point between gears. This approach allows to gain a very good precision in both loading distribution and contact parameters, providing critical seed conditions strongly influenced by the gears deformations.

Generally, it may be observed that in dynamic simulations a good approximation may be gained by using appropriate parameters for the contact stiffness.

29.2.3 Shafts and Gears Dynamic

Theoretical models reported in Sects. 29.2.1 and 29.2.2, even neglecting both mass and stiffness of shafts, well match experimental measurements. Furthermore, in order to investigate all aspects involving the dynamic of gears, the improvement of the so quoted models has to be taken into account, above all for as concerns the flexibility characteristics of shafts and bearings. In particular, stiffness magnitude of shafts and bearings is substantially different with respect to engaging phenomena; nevertheless, dynamic aspects related to the flexibility of these components may substantially modify the global response of the system.

Models referring to this group may be classified as torsional and torsion-flexural.

Torsional models only involve the torsion stiffness of shafts, while torsion-flexural ones consider both stiffnesses.

More complex models refer to gears vibrations in two perpendicular directions; this case joins dynamic and rotor dynamic of systems.

29.2.4 Multibody/FEM Models

Numerical models available in literature are in most cases *quasi*-static or related to a few engaging steps. As a matter of fact, complex phenomena related to gear systems may limit the modeling reliability.

Multibody codes together with FEM codes may overcome these difficulties, allowing a good comprehension and analysis capability for system time varying.

The base approach in multibody studies consists of identify the system dynamic by means of one degree of freedom (torsion) model for each gear; this way, only torsion modes may be taken into account.

More refined models involve six degrees of freedom for each gear and the connections to shafts and bearings may be obtained by lumped parameter systems as spring-damper.

Finally, the more complex models consist of combined MBS-FEM models, where macro elements may be analyzed by FEM approaches.

The most captivating goal is well modeling the contact in engaged teeth. This problem has been investigated in literature by considering the engaging stiffness as distributed and as function of time [13] or by means combined approaches MBS-FEM in order to also represent the stiffness space variation [13–16].

29.3 Models

The dynamics involved in the gear meshing is a key point in the study of gear lasting and noise emission. In fact, by knowing with a good accuracy the behavior of a gearset, it is possible to define lighter and more strength gears. In order to do that, more precise and accurate models have to be set up, starting from the latest literature analytical models [17–19], using the implementation of multibody models, coming to the use of flexible elements provided by a finite element discretization. In the present paper, a commercial multibody software is used (Recurdyn, FunctionBay) in order to study the dynamic behavior of a couple of aerospatial gears. This gearset presents very thin webs and very flexible shafts, so it is expected that the body flexibility of each gear deeply affects the meshing dynamics. For highlighting this effect, three models are set up: they simulate the same working conditions using different levels of formulation complexity.

The Recurdyn software uses the recursive formulation of motion equation instead of the traditional Cartesian approach implemented in the most famous commercial multibody software. The Cartesian approach refers all the system degrees of freedom to the global coordinate system, so all the movements and the body positions are computed with respect to the same origin. In the recursive formulation, positions of bodies are related to the joints that link the bodies each other. In other word, the position of each body is known and computed with respect to the relative link between the studied body and the structure. This approach allows to eliminate a great number of relative constraints between bodies, reducing the computational efforts. For this reason, recursive formulation seems to be the more effective strategy for studying meshing dynamics. In addition, Recurdyn presents a tailored tool for the gear analysis, where it is possible to implement different model formulation, starting from complete rigid model coming to full flexible model. Flexibility of bodies could be considered in two different ways, using the modal superposition (RFLEX, *reduced flexibility model*) or considering the overall body flexibility by means of the discretized mass and stiffness matrices of the body (FFLEX, *full flexibility model*). The last one is probably the best way to analyze the gear dynamics, but the computational effort required is very high, so in the present paper, the RFLEX approach is implemented. All the flexibility features of bodies are derived using FE approach.

All the studied models are set up with the same working conditions, in particular two spin speeds are considered, low (0.2 rad/s) and high (942 rad/s). The first condition is analyzed for verify the accuracy and the capabilities of the model. The second is simulated for evaluating the gearset actual behavior; for obtaining feasible results in reasonable computational time, the maximum spin speed is reached by the system using a constant acceleration of 188.4 rad/s^2. The spin speed is applied to the drive gear, whereas a drawn torque is applied to the driven gear. All the other working parameters are set equal for all the models, in particular a meshing damping of 0.3 N s/mm is set, and no friction is considered. These two elements are object of an on going analysis.

29.3.1 Full Rigid Model (FRM)

The first model, the most simple, consists in two rigid gears linked by a contact condition between teeth. In this model, the bodies are completely rigid and the unique flexibility is located in the contact between teeth. The model implementation is very easy, in fact by means of the Recurdyn*Toolkit Gear*, the gear set parameter can be defined in terms of macro and micro geometry. Using the tool *Gear Contact*, the two rigid gears defined can be coupled, setting the stiffness value of the teeth

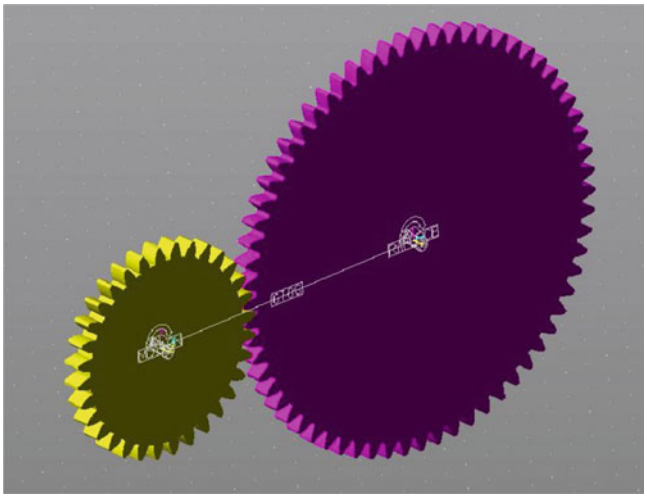

Fig. 29.1 Full rigid model: only a flexibility is considered, the contact stiffness between teeth

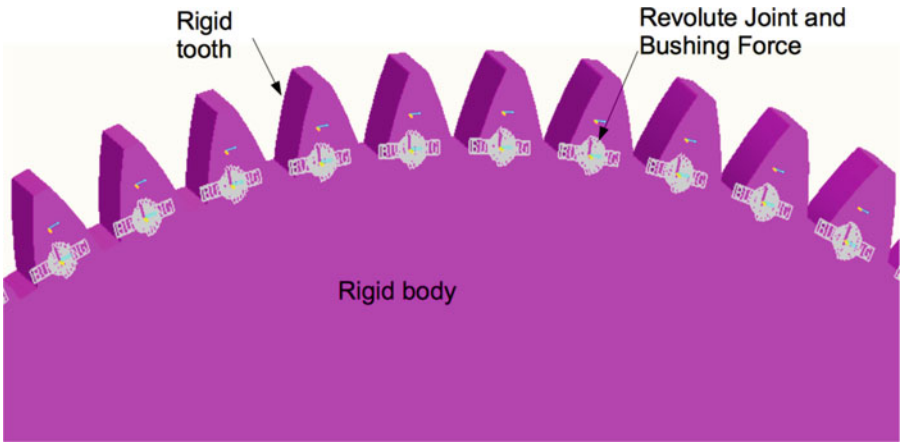

Fig. 29.2 Revolute joint and bushing force for depicting the compliance of the tooth

contact. This value is computed using an analytical approach [20] based on the Hertzian formulation (Bochman formula) and the geometrical data of the gears. As far as the boundary conditions are concerned, two *Revolute Joints* are defined. These links only allow rotation around the axes of the gears. In Fig. 29.1 it is shown the graphical aspect of the realized model.

29.3.2 Flex Teeth Model (FTM)

In order to increase the model complexity, the compliance of gear teeth is considered. For each gear and for each tooth a value of stiffness is defined. The tooth compliance is modeled considering the gear and the tooth bodies as rigid and introducing a spring between them. As depicted in Fig. 29.2, a *Revolute Joint* is defined in each tooth root, in that way tooth has only three degrees of freedom that allow it to rotate around the three axes. These degrees of freedom are controlled by means of a *Bushing Force* element that sets the stiffness values of the three torsional springs that link the tooth. Two of these springs have a very high level of stiffness in order to lock the rotations around the vertical and frontal axis of the tooth, instead the stiffness that depicts the flexibility of tooth is defined in order to allow the tooth rotation around the axis that passes through the tooth root and that is parallel to the rotation axis of the gear. The model definition is performed by means of the *QFBGear*tool of Recurdyn. The contact parameter remains the same of the FRM and the definition is already done by means of *Toolkit Gear*. In order to estimate the tooth compliance, a tailored FE model is made. In Fig. 29.3 the numerical model used for the stiffness estimation is presented. The value introduced in the *Bushing Forces* is computed imposing a torque to a gear sector and measuring the deflection of each tooth. It must be noted that the hypothesis of a unique contact pair is done. In Fig. 29.4 the FTM is depicted with particular emphasis to the representation of tooth compliance. Working conditions, contact stiffness value and damping are the same of the FRM.

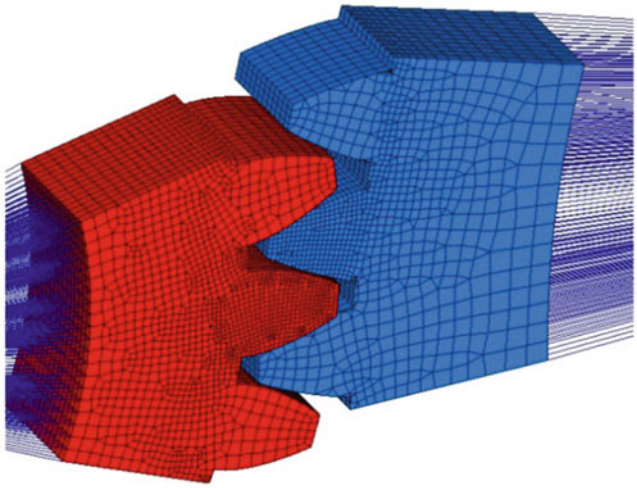

Fig. 29.3 Finite element model for the computation of tooth stiffness

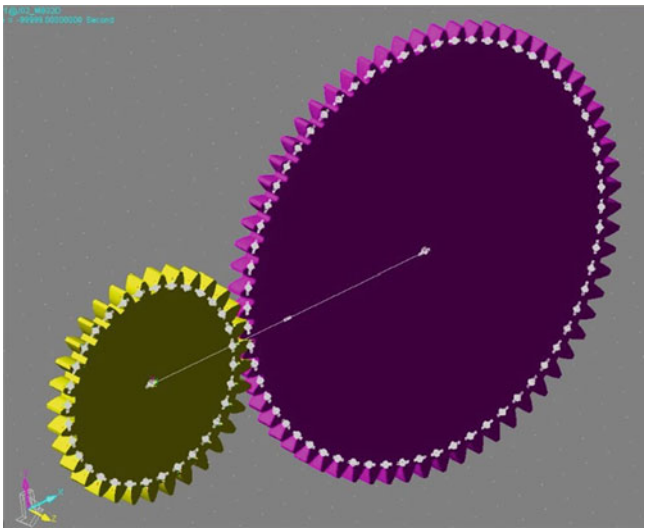

Fig. 29.4 Flexible teeth model: flexibility is defined in the contact between teeth and in the teeth compliance

29.3.3 Full Flexible Model (FFM)

The third model, the more complex, is characterized by the presence of the teeth compliance and the flexibility of the whole gear bodies. The peculiarities of this case study are:

1. very thin web with respect to the overall thickness of the mesh
2. the gears are made in a unique piece with the transmission shaft
3. the thickness of the transmission shaft is very thin with respect to the dimensions of the shaft.

In Figs. 29.5 and 29.6 the geometry of the two gears is depicted.

The compliance of the teeth is simulated as in FTM. The flexibility of the gears is computed by means of a reduced FE model. The gear FE models are realized identifying interface nodes where the components are linked. In these nodes the meshing conditions and the external constraints (bearing and spline couplings ...) are placed. In particular rigid elements (RBE2 in Nastran FE software) are used for linking the teeth to the gear body and the shaft to the nodes that depict the constraint condition.

Using the Craig-Bampton [21] approach, reduced stiffness and mass matrices are obtained. Then the modal properties of the gears are computed and the mode shapes of interest are collected in a metafile that is imported in Recurdyn. With this approach, it is possible to depict the flexibility of the gears using few nodes, reducing the computational effort.

All the other model features remain the same of the previous FRM and FTM.

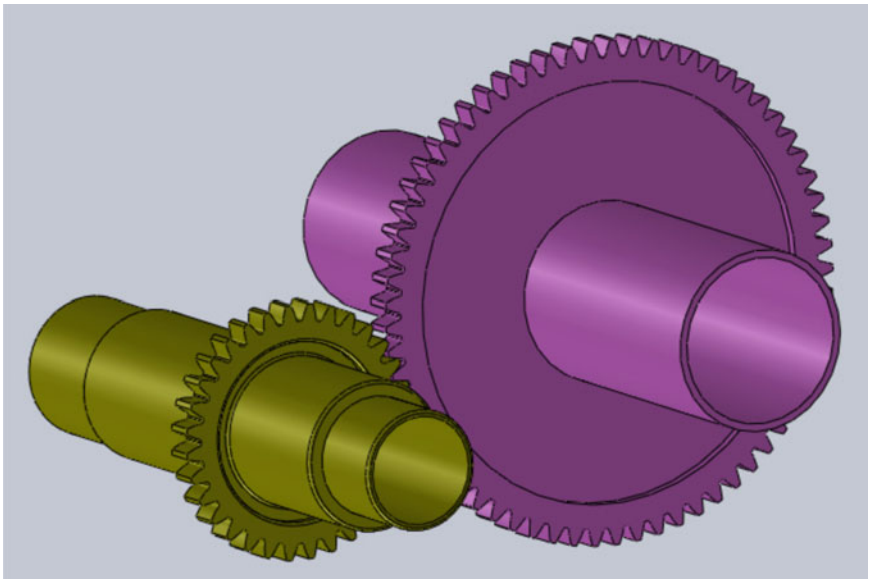

Fig. 29.5 Geometrical model of the full flexible model

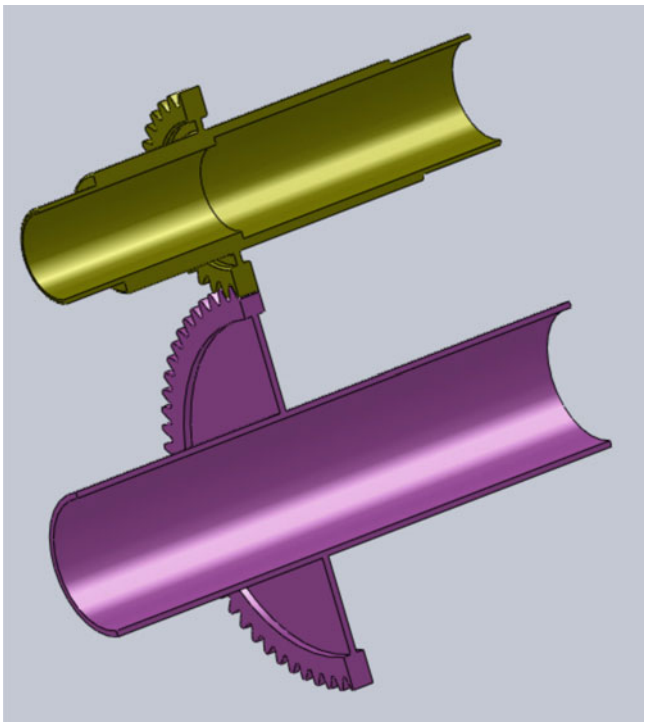

Fig. 29.6 Section of the FFM, very thin walls are used for gears and shafts

29.4 Results

In order to analyze some aspects of the meshing, tailored Matlab scripts have been developed. In particular transmission error, number of contact pairs and its variation during the meshing and forces between teeth are highlighted. Results are then summarized in the following and the differences between all the three models are presented.

29.4.1 Transmission Error

The transmission error is defined as the angular difference between the instantaneous angular position of the gear and the theoretical position. This value is zero in the nominal conditions, instead in working conditions it represents the irregularities of the motion. The plots shown in this paper represent the gap of the gear position with respect to the nominal one. In Fig. 29.7 it is possible to compare the transmission error computed by the three different models in the same conditions at low speed. It is worth noting that the aspects of the results coming from FRM and FTM are quite the same, whereas an appreciable difference is highlighted in the results of FFM. The maximum value of transmission error is slightly different between FRM and FTM, and in FFM it becomes the double of the results for rigid gear models. For FRM and FTM models the transmission error is about 6e- 5 rad, for the FFM the value increases, reaching 1.2e - 4 rad.

In Fig. 29.8 the transmission error of the three models at high velocity are depicted. Reaching the maximum spin speed of 942 rad/s, the FRM model provides a maximum transmission error of 3.1e-4 rad, whereas for the FTM the maximum is 5.7e-4 rad. Observing the results of the FFM, the transmission error becomes very high, reaching 0.04 rad and presenting a really chaotic shape.

29.4.2 Contact Forces and Contact Pairs

In the same manner, the contact forces are represented in the charts of Fig. 29.9, for the low speed conditions and Fig. 29.10 for high speed. At low speed, no great differences are appreciable between results of FRM and FTM and the behavior of the transmission is similar to the theoretical one. The FFM presents variations in the shape of response. In particular, it introduces a change in the duration of contact; with in fact the exchanged force has the same value during the five meshing, but the duration of contact is different. This is due to the not regular movement of the gears. As depicted by the transmission error and by the chart reporting the number of contact pairs (Figs. 29.11 and 29.12), it can be noted that contact duration is changing at every engaging phase. By analyzing the obtained results for the low speed models, it can be noticed that the teeth flexibility does not affect the behavior of the gears in an appreciable way; instead, the compliance of gears and shafts introduces a substantial variation in the meshing behavior.

This phenomenon is highlighted when the speed increases, in fact, observing the chart of Fig. 29.10, a great difference between FRM and FFM is shown. In particular the behavior of the FRM and FTM is really closed to the one computed by the single-mass-single-spring model proposed in [20]. Otherwise the trend of contact forces computed by the FFM is completed different and no relationship to the literature can be highlighted. The actual value of the forces is surely dependent on the damping and friction present in the meshing, but considering that models are made with the same operating conditions, the comparison emphasizes only the differences between them. It can be concluded that the compliance of gear bodies could deeply affects the transmission behavior, acting on motion regularities and improving the contact forces. The more gears have modal behavior that intersects the working conditions, the more the transmission dynamics is different with respect to the theoretical predictions.

29.5 Conclusions

In the present paper the transmission dynamics of a very thin couple of gears is studied. Three models with increasing complexity are compared. The most remarkable result is referred to the importance of the compliance of the thin bodies of the gears. In fact, both contact force and transmission error increase considering the flexibility of the bodies. In that case the contribution of each flexible element of the gear, i.e. the shaft and the web, is not under investigation, but the overall behavior of the system is analyzed. This is due in order to understand the sensibility of the design to the gear flexibility. It is possible to conclude that, if the gear has flexible modes interacting with the working condition of the gearset, the dynamic overload on the transmission can be really remarkable. So this approach, where a combine Finite Element and Multibody model is used, proves to be effective in the right design of gears. In order to build a solid design methodology, some aspects have to be cleared, in particular the contribution of lubrication, friction and damping. These topics are under investigation with more accurate models and tailored test campaigns.

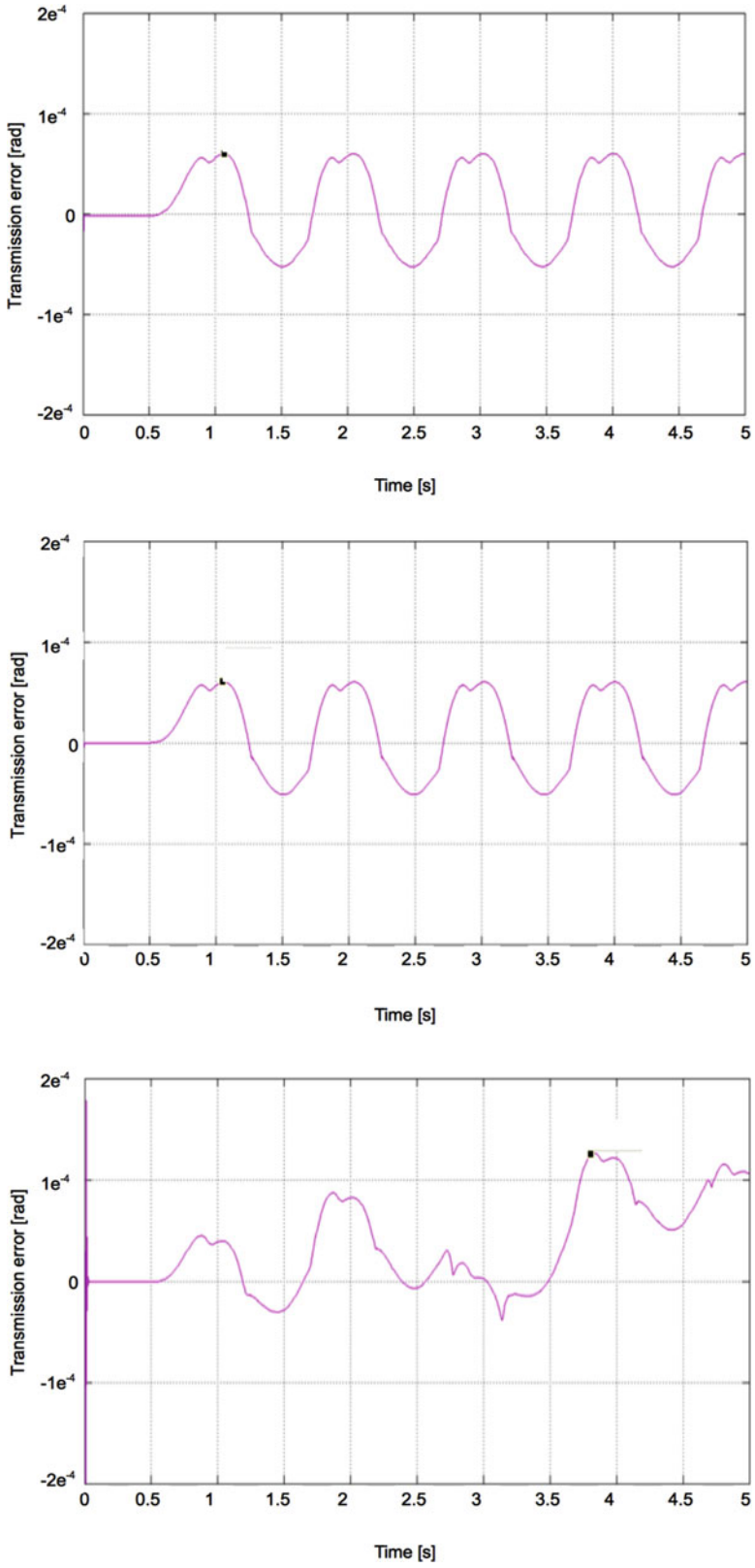

Fig. 29.7 Transmission error for the three models (*upper* FRM, *middle* FTM, *lower* FFM) for low speed condition

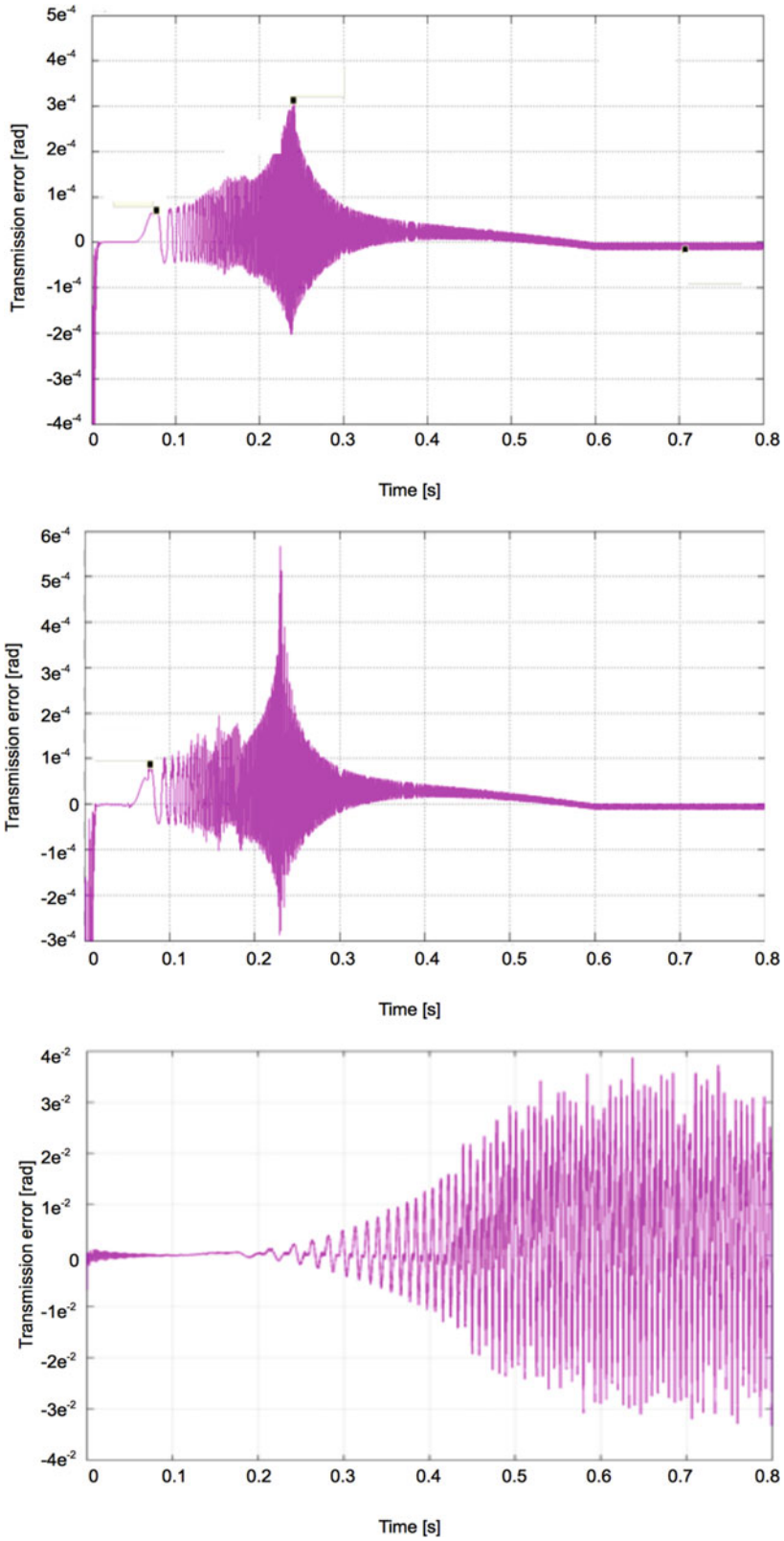

Fig. 29.8 Transmission error for the three models (*upper* FRM, *middle* FTM, *lower* FFM) for high speed condition

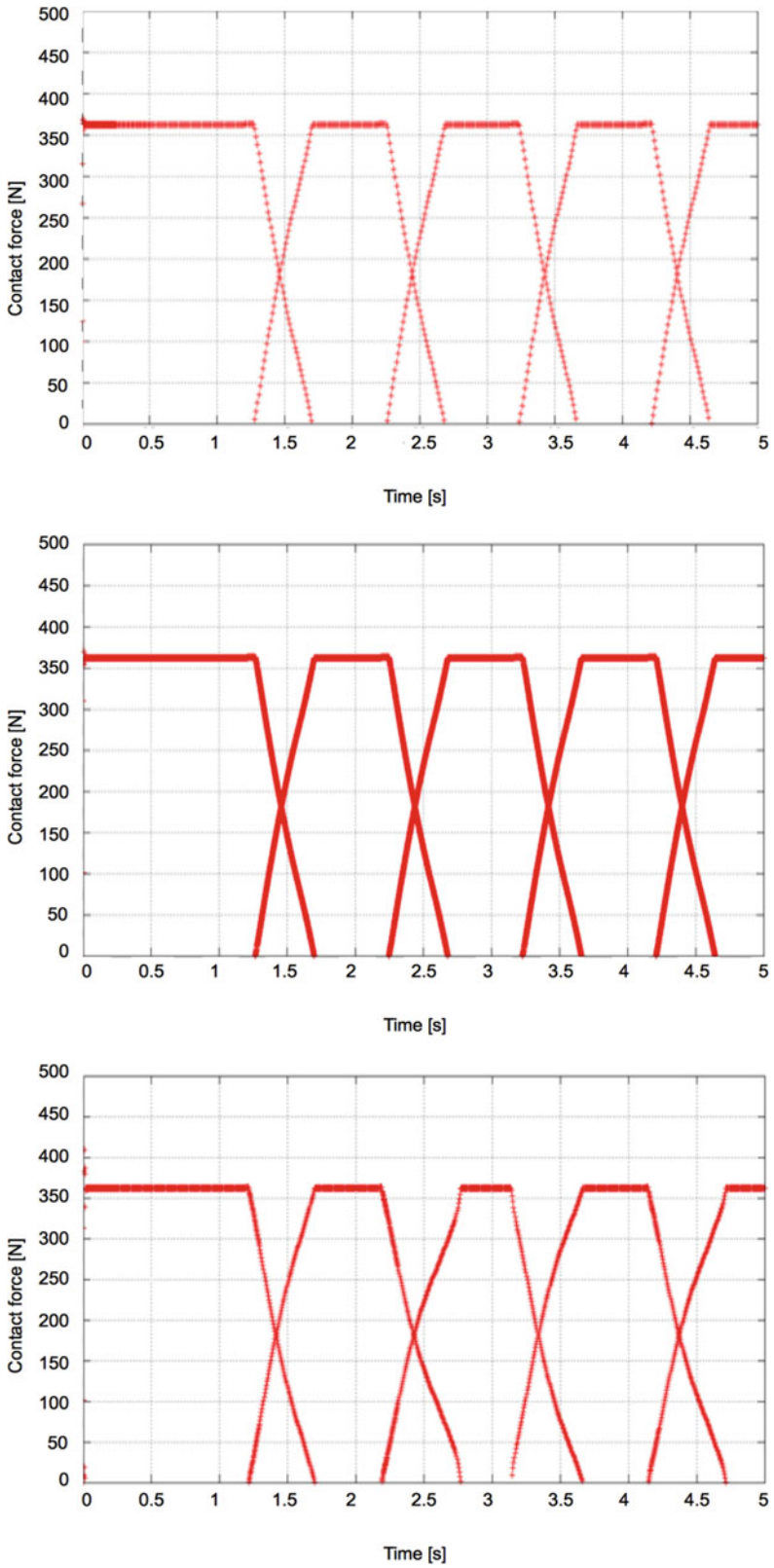

Fig. 29.9 Contact force for the three models (*upper* FRM, *middle* FTM, *lower* FFM) for low speed condition

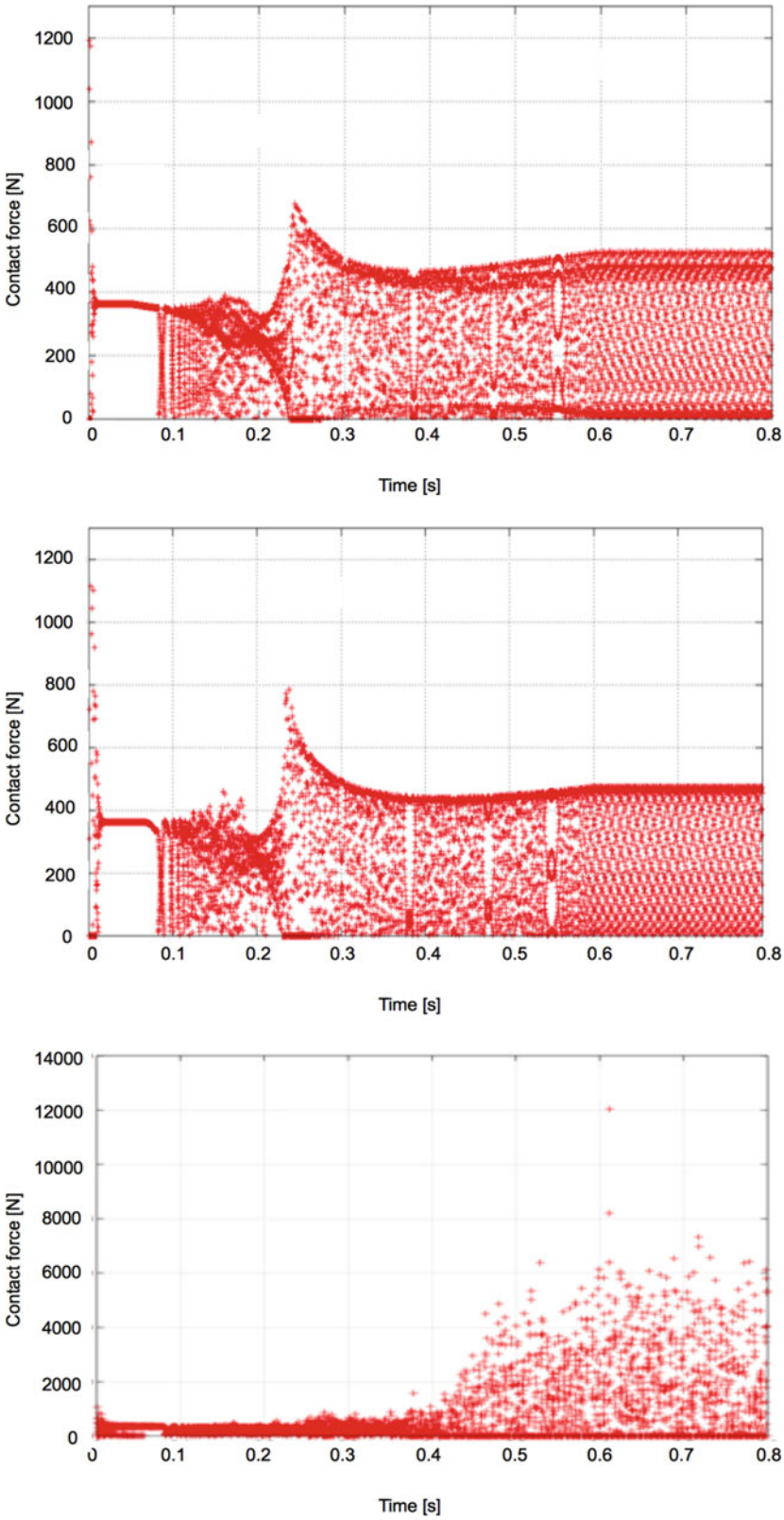

Fig. 29.10 Contact force for the three models (*upper* FRM, *middle* FTM, *lower* FFM) for high speed condition

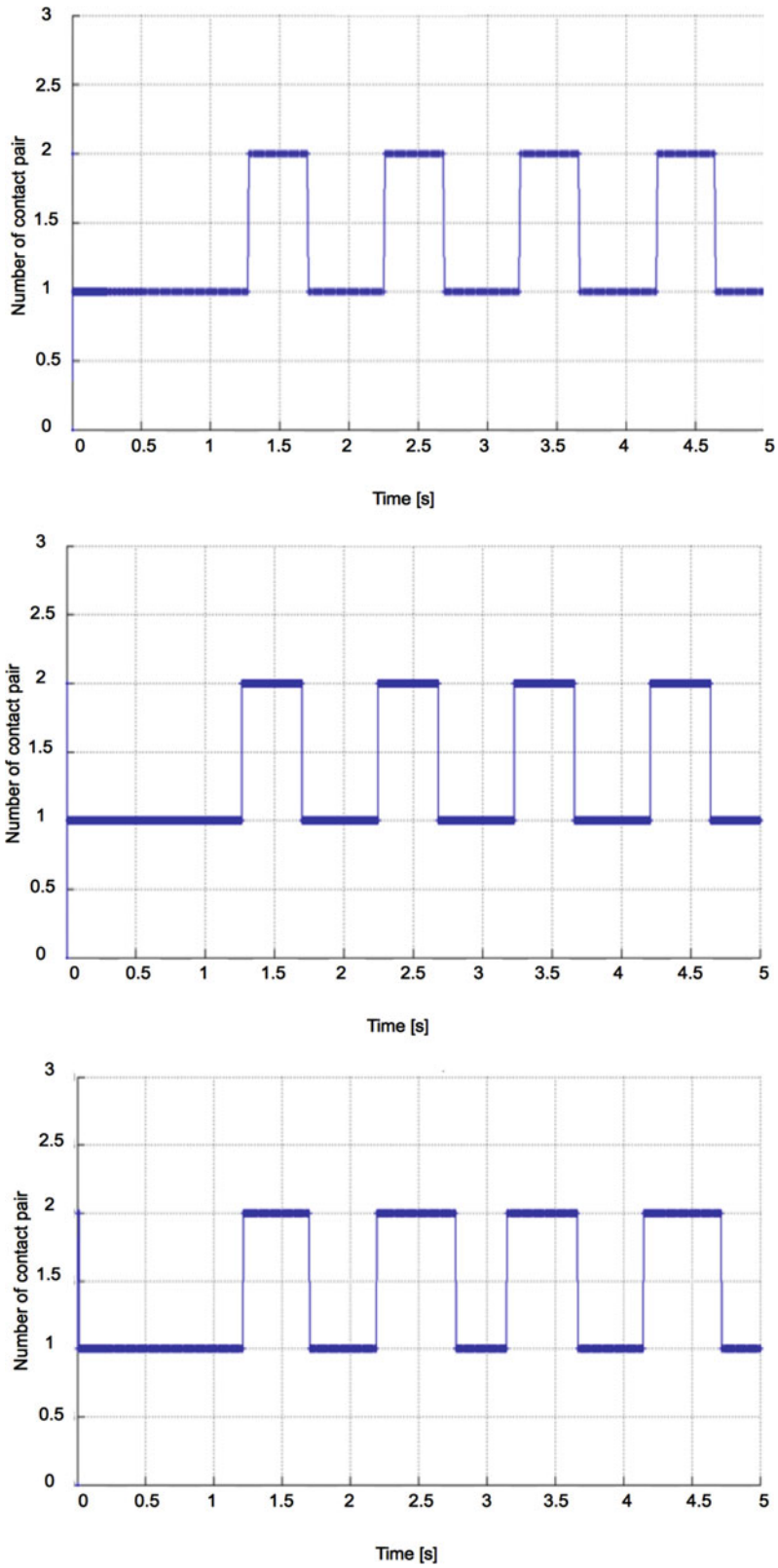

Fig. 29.11 Contact pairs for the three models (*upper* FRM, *middle* FTM, *lower* FFM) for low speed condition

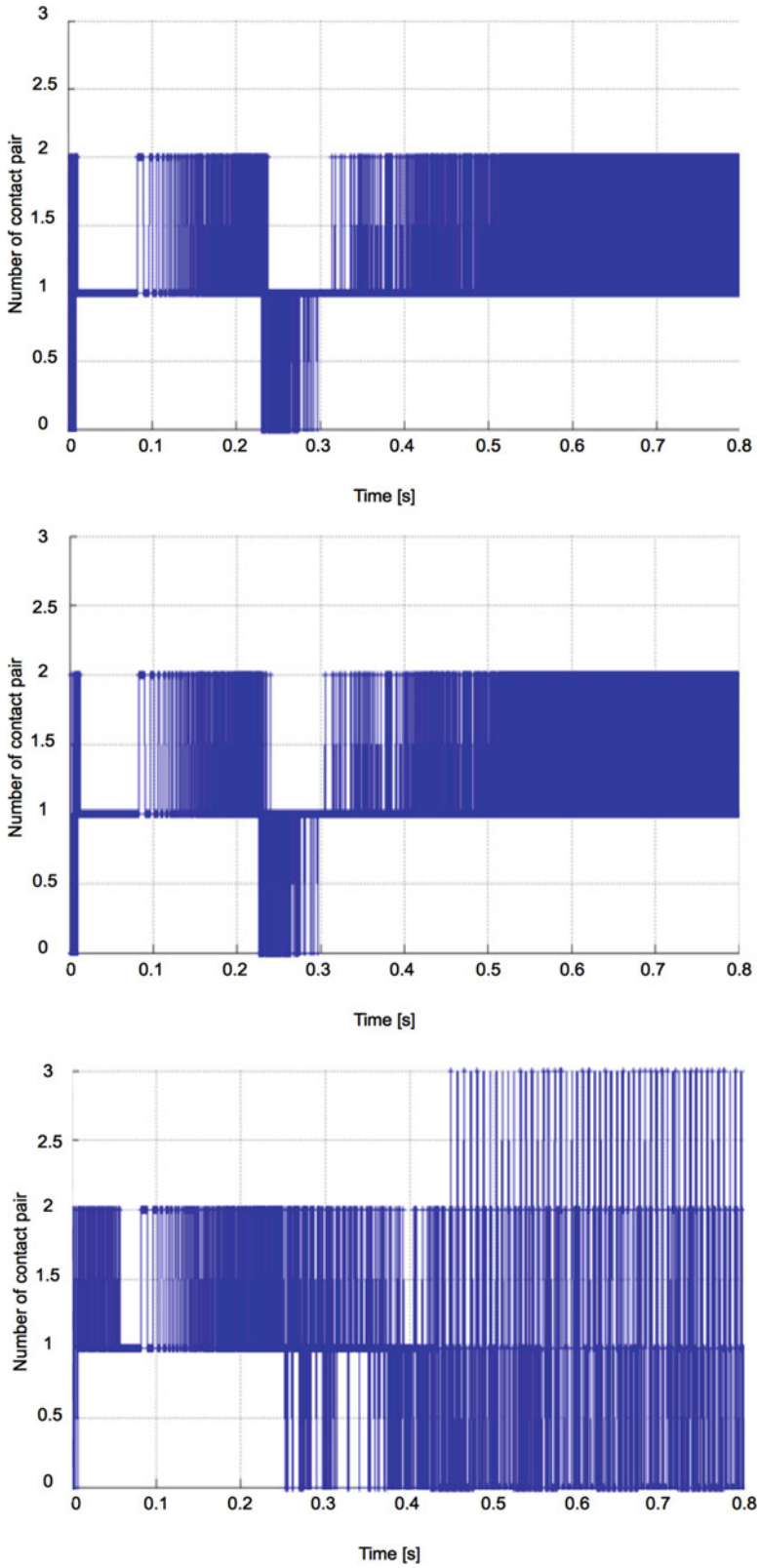

Fig. 29.12 Contact pairs for the three models (*upper* FRM, *middle* FTM, *lower* FFM) for high speed condition

References

1. NevzatOzguven H, Houser DR (1988) Mathematical models used in gear dynamics – a review. J Sound Vib 121(3):383–411
2. Ross AA (1927) Tooth pressures for high speed gears. Machinary 34(2):110–112. NY
3. Tuplin WA (1950) Gear tooth stresses at high speed. Proc Inst Mech Eng 16:162–167
4. Tuplin WA (1953) Dynamic loads on gear teeth. Mach Des 25:203–211
5. Strauch H (1953) Zahnradschwingungen (gear vibrations). Z Ver Dtsch Ingiere 95:159–163
6. Seireg A, Houser DR (1970) Evaluation of dynamic factors for spur and helical gears. J Eng Ind 192:495–503
7. Tucker AI (1971) Dynamic loads on gear teeth, design applications. American society of mechanical engineers paper, 71-DE-1. ASME, New York
8. Wang CC (1985) On analytical evaluation of gear dynamic factors based on rigid body dynamics. J Mech Transm Autom Des 107:301–311
9. Kahraman A, Singh R (1990) Non-linear dynamics of a spur gear pair. J Sound Vib 142(1):49–75
10. Kahraman A, Singh R (1991) Interactions between time-varying mesh stiffness and clearance non-linearities in a geared system. J Sound Vib 146(1):135–156
11. Li S, Kahraman A (2011) A spur gear mesh interface damping model based on elastohydrodynamic contact behavior. Int J Powertrains 1(1):4–21
12. Ajmi M, Velex P (2005) A model for simulating the quasi-static and dynamic behavior of solid wide-faced spur and helical gears. Mech Mach Theory 40:173–190
13. Vinayak H, Singh R, Padmanabhan C (1995) Linear dynamic analysis of multi-mesh transmissions containing external, rigid gears. J Sound Vib 185:1–32
14. Amirouche FML, Shareef NH, Xie M (1991) Dynamic analysis of flexible gear trains/transmissions: an automated approach. Mach Dyn Elem Vib 36:257–262
15. Amirouche FML (1992) Computational methods in multibody dynamics. Prentice Hall, Englewood Cliffs
16. Ebrahimi S, Eberhard P (2006) Rigid-elastic modeling of meshing gear wheels in multibody systems. Multibody Syst Dyn 16:55–71. doi:10.1007/s11044-006-9021-7
17. Pimsarn M, Kazerounian K (2002) Efficient evaluation of spur gear tooth mesh load using pseudo-interference stiffness estimation method. Mech Mach Theory 37:769–786
18. Kuang JH, Yang YT (1992) An estimate of mesh stiffness and load sharing ratio of a spur gear pair. In: International power transmission and gearing conference, vol 1, DE-vol, pp 43–1. ASME, New York
19. Vaishya M, Singh R (2003) Strategies for modeling friction in gear dynamics. J Mech Des 125:383–393. ASME
20. Niemann G, Winter H (1986) Elementi di macchine, vol II. Springer
21. Craig RR, Bampton MCC (1968) Coupling of Substructures for Dynamic Analyses. AIAA J 6(7):1313–1319

Chapter 30
Influence of the Support Conditions in the Modal Parameters of a Cantilever Beam

Rubén Arenillas, Manuel L. Aenlle, Pelayo Fernández, and Alfonso Fernández-Canteli

Abstract In modal analysis, previously to the modal testing, it is very common to assembly a finite element model, in order to know the frequency range of interest and the mode shapes of a structure. This information is very helpful for planning and developing the modal testing.

On the other hand, the proper modeling of the support conditions and the joints are the main difficulties in model assembly and model updating. For these reasons, the results obtained in the modal tests are, sometimes, unexpected.

In this paper it is studied the effect of the support conditions in the modal parameters of a steel cantilever beam with different kinds of foundations. Moreover, a technique based on the analysis of the singular value decomposition of the responses, using different number of sensors, is proposed and validated by experimental test carried out on a steel cantilever beam tested in the lab.

Keywords Operational modal analysis • Damage • Support conditions • Foundation • Singular value decomposition

30.1 Introduction

The proper modeling of the joints and the support conditions are the main difficulties in model assembly and model updating. For these reasons, the results obtained in the modal tests are, sometimes, unexpected and the numerical models difficult to update.

On the other hand, wind turbines are structures being subject of continuous vibration-induced forces throughout their working life. Wind turbulences and the periodic excitation due to the blade's rotation are the most important loadings to consider in the design. Thus, the turbine operational frequencies should be sufficiently separated from the structural natural frequencies in order to avoid very high dynamic forces, which could cause immediate malfunctioning and possible progressive fatigue damage of the foundation [1].

In this work it is studied the effect of the support conditions in the modal parameters of a cantilever beam tested in the lab. Moreover, the analysis of the singular value decomposition is proposed as a technique to detect damage in the foundation of wind turbines.

30.2 Motivation

After a few years of operation under normal wind conditions, two wind turbines (denoted here A and B) of a wind farm, began to show an anomalous vibration level. No visual damage was detected so that damage, if any, was generated in the inner part of the concrete foundation. As a possible way to identify the reason for such a behavior, operational modal analysis was considered before deciding on the repairing method to be used for the concrete foundation [2].

R. Arenillas • M.L. Aenlle (✉) • P. Fernández • A. Fernández-Canteli
Department of Construction and Manufacturing Engineering, University of Oviedo, Campus de Gijón s/n. Ed. Oeste, Bloque 7, 33203, Gijón, Spain
e-mail: aenlle@uniovi.es; UO173127@uniovi.es; fernandezpelayo@uniovi.es; afc@uniovi.es

G. Kerschen et al. (eds.), *Topics in Nonlinear Dynamics, Volume 1: Proceedings of the 31st IMAC, A Conference on Structural Dynamics, 2013*, Conference Proceedings of the Society for Experimental Mechanics Series 35,
DOI 10.1007/978-1-4614-6570-6_30,

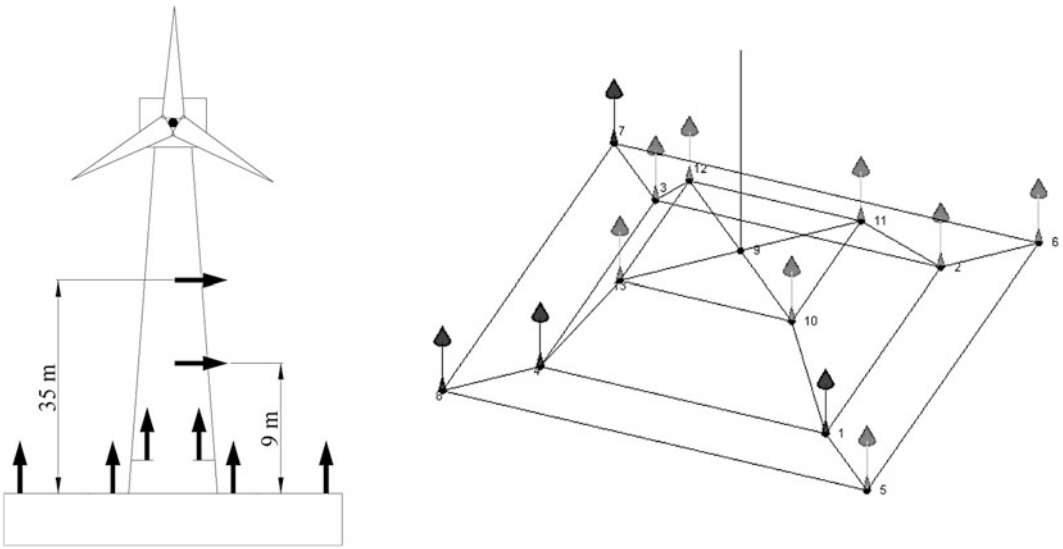

Fig. 30.1 Measurement points at wind turbines

If structures are continuously or periodically monitored, damage detection techniques can be applied to detect and localize damage. As it was not the case, another wind turbine C, located in the same area and working correctly up to present without exhibiting high vibration levels, was also tested as a reference for comparison. For all of these wind turbines, the first operational frequency (1P) is 0.513 Hz (30.8 rpm).

The test configuration used in the tests is presented in Fig. 30.1. Considering the goal to be achieved, measurement points were concentrated on the foundation region. In their usual state of operation, the concrete foundations are covered by a layer of loose soil material of about 1 m depth. To allow access to the foundation this layer was partly removed. Possible sensor locations were therefore limited to the free foundation surface.

The tower behavior was determined by disposing two bi-axial horizontal measurement points at two different heights. As a consequence, several modes with different frequency but quite similar shape in the tower region were identified. To separate such modes according to their shape, a higher number of measurement points in the tower and in the blade's region would have been necessary.

It was possible to identify damage in turbines A and B by comparing the modal parameters of these turbines with those turbine C. On one hand, the natural frequencies of turbines A and B are less than the natural frequencies of wind turbine C. On the other hand, the relative movement between the tower and the concrete foundation in wind turbines A and B is larger than wind turbine C. This relative movement can practically be identified irrespective of the modes and it can only be explained if the tower and the foundation are not rigidly but elastically connected.

On the other hand, the responses of the foundation must be different depending on the stiffness of the connection between the tower and the foundation. Moreover, if the foundation is damaged in the connection area, this effect should be reflected in the responses of the foundation. In this paper, the comparison of the singular value decomposition of the responses, using different DOF's in each analysis, is proposed as a technique to detect damage in the connection between the tower and the foundation of cantilever beam structures.

The singular value decomposition of the responses of turbine A, when all the sensors are included in the analysis, is shown in Fig. 30.2a. The first two modes of the tower, indicated by arrows, are clearly identified. These modes are in pairs (closely spaced or repeated modes) due to inherent symmetry of the geometry of the structures.

Figure 30.2b shows the same representation when only the vertical sensors are considered (sensors on the foundation and in the tower at the foundation level). The same modes of the tower can still be identified.

Finally, Fig. 30.2c shows the singular value decomposition when only the sensors on the foundation are considered. In the figure we can see that the second mode of the tower can still be identified whereas it is not possible to identify the first mode (the peak corresponding to mode 1 has disappeared).

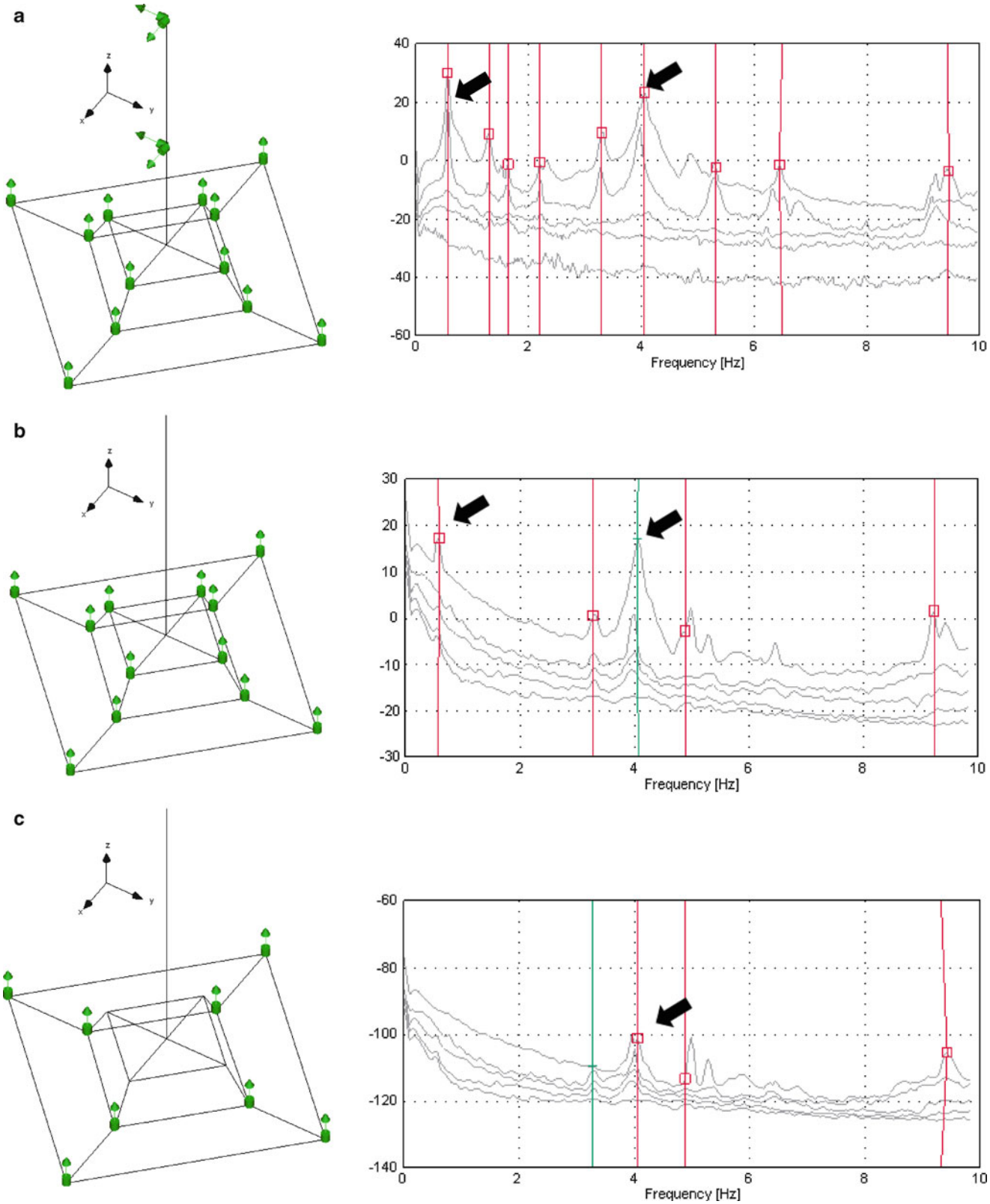

Fig. 30.2 Singular value decomposition of the responses. (**a**) With all sensors. (**b**) Only vertical sensors. (**c**) Vertical sensors on the foundation

30.3 Experimental Tests

30.3.1 Steel Foundation

In order to validate the methodology proposed in the previous section, some experimental tests were carried out on a steel cantilever beam. The beam was 1.75 m long, showing a 100 × 40 × 4 mm tube rectangular section. The beam had a plate 200 × 200 × 15 mm welded at the bottom (Fig. 30.3) and it was connected to a rigid steel structure (which simulates the foundation) with four M10 bolts.

Two different tests were performed using the test configuration shown in Fig. 30.3. In the first one, a torque wrench was used to tighten the bolts with a 30 Nm torque. In the second one, the bolts were tighten by hand. The beam was excited applying hits along the beam and the responses were measured using 8 accelerometers 100 mv/g, located as shown in Fig. 30.3. The tests were carried out at a sampling frequency of 2,000 Hz during a period of approximately 3 min.

The modal parameters were identified by Enhanced Frequency Domain Decomposition (EFDD) [3]. The first three natural frequencies are shown in Table 30.1. As it was expected, the configuration with bolts tightened to a 30 Nm torque presents the highest natural frequencies.

Figure 30.4 shows the singular values when all the sensors are considered. It can be seen that all the modes can be identified in both cases (tightened with a 30 Nm torque and by hand).

On the other hand, the singular value decomposition considering only the sensors attached to the steel rigid support, are presented in Fig. 30.5. All the modes can be identified when the bolts are highly tightened whereas the peak corresponding to the first mode is not present for the case tightened by hand.

Thus, it can be concluded that the singular value decomposition of the responses, considering only the sensors on the foundation, can be considered a good indicator of damage in the connection between a cantilever and its foundation.

30.3.2 Wooden Foundation

Due to the fact that the steel foundation shows a high stiffness compared to that made of the concrete, new experimental tests were performed using a wooden foundation (see Fig. 30.6). The beam and foundation were again connected with four M10 bolts.

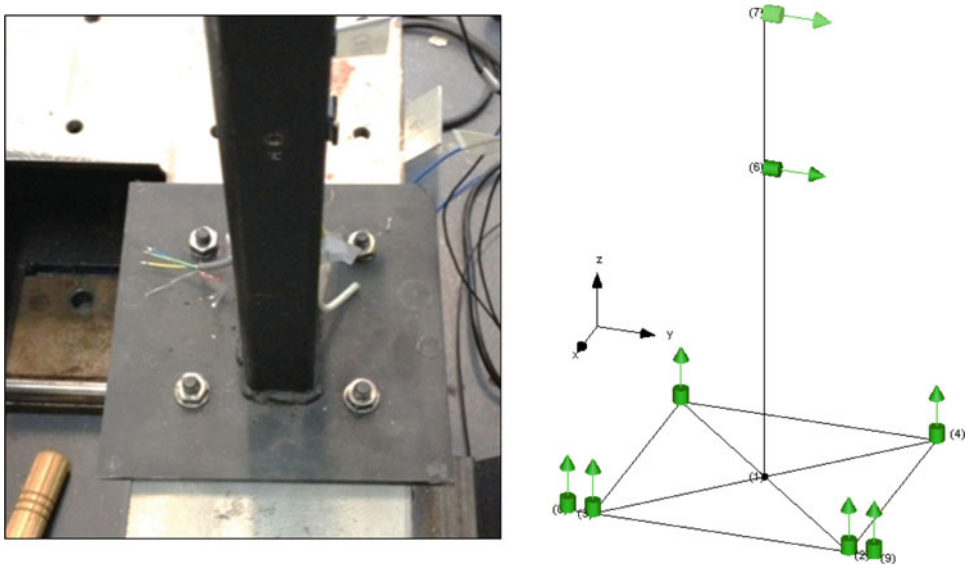

Fig. 30.3 Steel cantilever beam connected to a steel structure

Table 30.1 Natural frequencies, in Hz, of the steel cantilever beam with steel foundation

Steel foundation	Mode		
Tighten by	1 (weak axis)	2 (weak axis)	3 (weak axis)
Torque 30 Nm	12.39	79.47	222.6
Hand	3.56	63.36	197.8

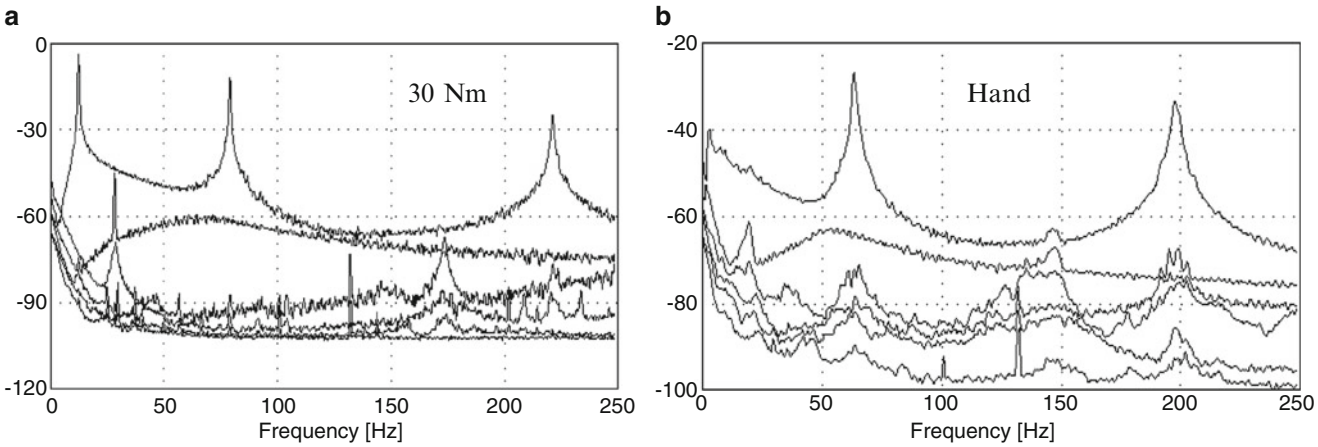

Fig. 30.4 Singular value decomposition using all sensors (steel foundation)

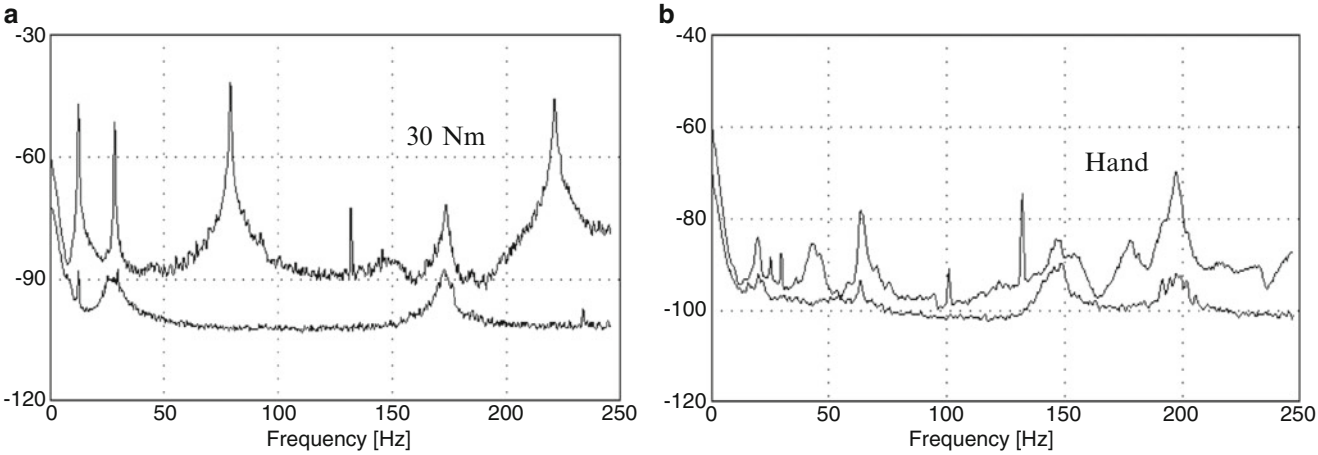

Fig. 30.5 Singular value decomposition using only the sensors attached to the steel rigid structure (steel foundation)

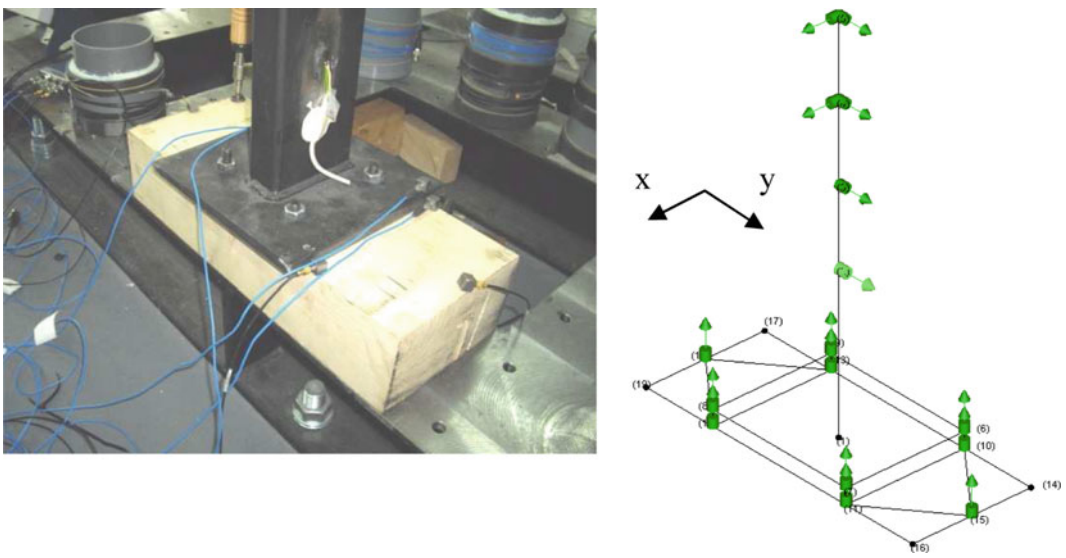

Fig. 30.6 Cantilever beam on a wooden foundation and testing configuration used

Again, two different test configurations were considered in the tests: bolts tightened with a 30 Nm torque and bolts tightened by hand. The beam was excited applying hits along the beam and the responses were measured using 16

Table 30.2 Natural frequencies, in Hz, of the steel cantilever beam with wood foundation

Wooden foundation	Mode				
Tightened by	1 (weak axis)	1 (strong axis)	2 (weak axis)	2 (strong axis)	3 (weak axis)
Torque 30 Nm	12.37	13.44	80.33	126	223.6
Hand	7.79	9.89	69.92	123.1	207.5

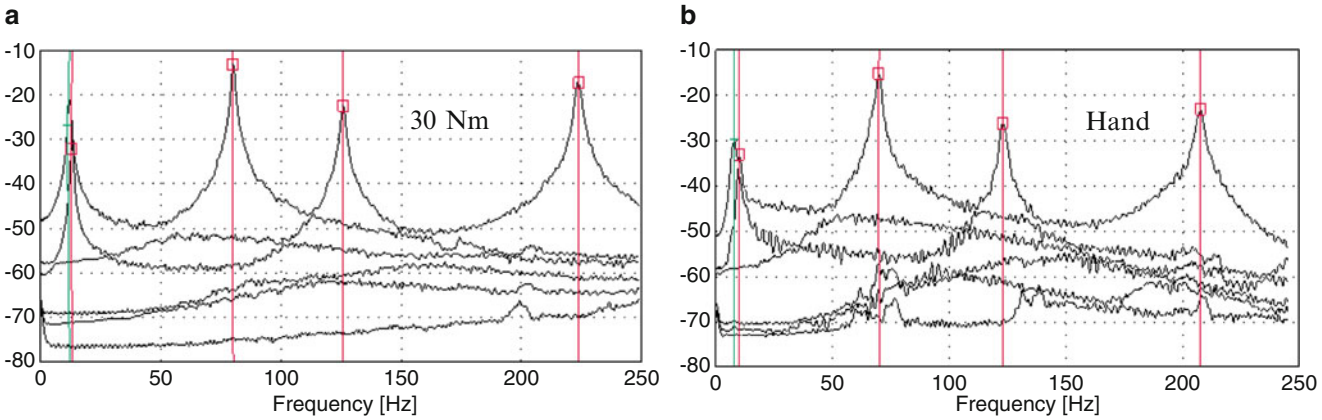

Fig. 30.7 Singular value decomposition using all sensors (wooden foundation)

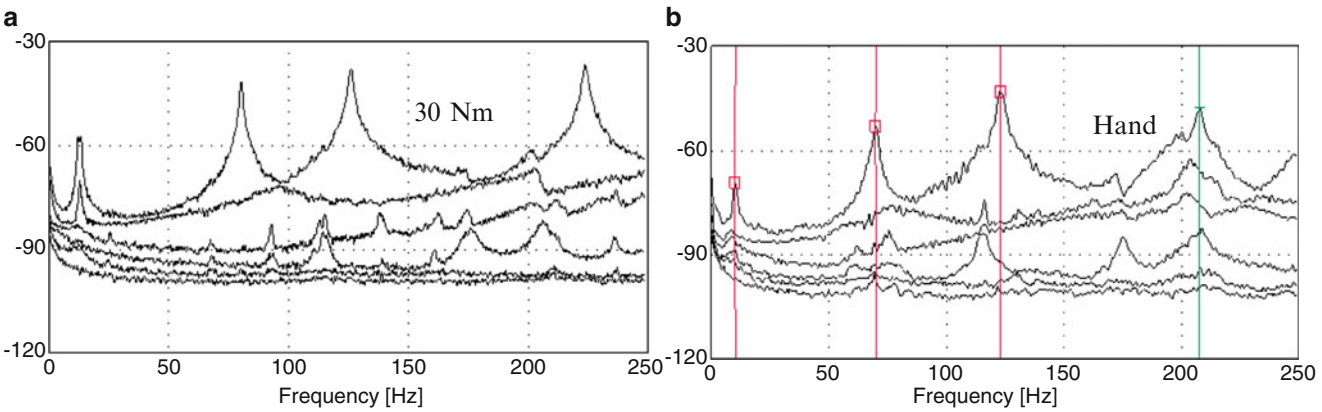

Fig. 30.8 Singular value decomposition using only the sensors attached to wooden foundation

accelerometers 100 mv/g, located as shown in Fig. 30.6. The tests were carried out at a sampling frequency of 2,000 Hz during a period of approximately 3 min. The modal parameters were identified by the frequency domain decomposition (EFDD), being the natural frequencies shown in Table 30.2.

The singular value decomposition of the responses, considering all sensors and considering only those located on the foundation, are presented in Figs. 30.7 and 30.8, respectively.

Due to the fact that the wooden block does not have the same stiffness in each direction and that the steel plate is wider than the foundation in the x direction (see Fig. 30.6), the first weak and strong axis bending modes are closely spaced (Figs. 30.7 and 30.8).

The singular value representation in Fig. 30.8 corresponding to the case tightened with a torque of 30 Nm and using only the sensors on the foundation, shows that the two peaks corresponding to the first bending modes can be clearly identified.

However, in the case tightened by hand, the peak corresponding to weak-axis bending has disappeared. The peak corresponding to strong axis bending can be explained by the small stiffness of the foundation in that direction.

The same conclusions as those derived for the steel foundation can be established for this case. Thus, it is confirmed that this methodology can be used to detect damage or a not rigid connection between the beam and the foundation.

30.4 Conclusions

A technique to detect damage between a cantilever beam and the foundation, based on the analysis of the singular values of the responses and using only the sensors located on the foundation, has been presented.

The methodology has been validated by experimental testes carried out on a steel cantilever beam, tested in the lab with different foundations and different stiffness in the connection.

Acknowledgements The economic support given by the Spanish Ministry of Science and Innovation through the project BIA 2011-28380-C02-01 is gratefully appreciated.

References

1. Tcherniak D, Basurko J, Salgado O, Urresti I, Chauhan S, Cargangiu CE, Rossetti M (2011) Application of OMA to operational wind turbine. In: 4th international operational modal analysis conference (IOMAC), Istambul
2. Pelayo F, López-Aenlle M, Fernández-Canteli A, Cantieni R (2011) Operational modal analysis of two wind turbines with foundation problems. In: 4th international operational modal analysis conference (IOMAC), Istambul
3. Brincker R, Zhang L, Andersen P (2001) Output-only modal analysis by frequency domain decomposition. Smart Mater Struct 10:441–445